Imperial College London

Structural Integrity Assessment of Clad Nuclear Steel

ALISON NOREEN O'CONNOR

DEPARTMENT OF MECHANICAL ENGINEERING

FIRST SUPERVISOR: Prof. Kamran Nikbin

SECOND SUPERVISOR: Dr Catrin Mair Davies

A thesis submitted for the degree of

Doctor of Philosophy

March 2019

Abstract

Many of the world's nuclear power plants are reaching the end of their design lives and will have to demonstrate adequate structural integrity to continue operating. Critical components, such as the reactor pressure vessel (RPV), are manufactured from a combination of materials so as to economically provide the required mechanical properties. Typical combinations include ferritic carbon steel and austenitic stainless steels. Generally, these multi-material components are manufactured by welding processes and referred to as dis-similar metal welds (DMWs) consisting of a base (ferrite, grade SA508) and a cladding (austenite, stainless steel grades 308 and 309). Current industry practise often neglects the benefits of the cladding resulting in overly-conservative assessments. The aim of this work is to improve current methods in assessing DMWs by demonstrating how the presence of cladding impacts strain distributions compared to homogeneous materials. The impact of incorporating DMWs into components was investigated by analysing the fracture performance of multi-material (inhomogeneous) samples compared to homogeneous material counterparts for multiple initial defect sizes. The influence of initial defect location with respect to the weld boundary (surface breaking and sub-surface defects) and, the impact of residual stresses were also considered. The original contribution to knowledge is the direct comparison of strain distributions, during fracture toughness testing, for homogeneous and inhomogeneous samples. Results clearly indicate that the distribution of strain in inhomogeneous samples differs significantly compared to homogeneous samples.

Due to the clad welding process the microstructure of the cladding was found to be complex with multiple HAZs resulting in the formation of undesirable microstructure (martensite) and significant variability in the direction of grain growth. Digital Image Correlation (DIC) was used to monitor the development of strain during unloading compliance fracture toughness testing and it was shown that the cladding material absorbs significantly more energy compared to base material samples. Hence the presence of cladding material undoubtedly impacts the structural integrity of a RPV but quantifying that impact is shown to be highly dependent upon initial defect size, type

(i.e. surface breaking or sub-surface) and orientation with respect to the weld boundary. Local hotspot regions in the cladding were identified using DIC and indicate that the undesirable and complex microstructure may provide preferential locations for defect initiation and/or propagation due to increased strains in hotspot areas. The mechanical properties and microstructure of the DMW studied in this work were found to be in agreement with literature data.

Standard sample geometries were used to simulate different defect orientations: Sub-surface defects were analysed using Compact Tension (CT) samples while surface breaking defects were analysed using Single Edge Notch Bend (SENB) samples. Sub-surface defects were oriented parallel to the weld boundary and were found to propagate in the lower strength material. This resulted in deviation of the defect from the expected path (i.e. perpendicular to the loading direction) into the softer material. This is in agreement with literature data. Finite element (FE) analyses showed good agreement with experimental data when 2D plane strain conditions or 3D conditions were assumed. A parametric study investigating the impact of cladding thickness indicated that sub-surface defects are less likely to propagate when the thickness of the cladding is increased. It was additionally shown that the proximity of the notch to the weld boundary impacted the strain distribution with notches in closer proximity to the weld boundary being increasingly asymmetrical this was as expected. Surface breaking defects were found to propagate along the expected path (i.e. perpendicular to the loading direction) irrespective of sample type (i.e. defect deviation remained perpendicular to the loading direction for both inhomogeneous and homogeneous samples). The influence of notch proximity to the weld boundary was addressed by varying the initial notch depth. It was found that inhomogeneous samples notched through the thickness of the cladding (i.e. notch tip in the base material) acted in a similar manner to unclad samples. Samples notched in the cladding were found to have strain distributions significantly different to similarly notched homogeneous samples. Shallow notches in the cladding exhibited more influence from the cladding microstructure compared with notches located in the cladding close to the weld boundary. FE 2D plane strain

analyses showed good agreement, in terms of strain distribution, with experimental data despite neglecting local microstructural effects. It was further shown that explicitly modelling the martensitic HAZ region significantly impacted the predicted strain distribution.

Residual stresses were measured experimentally and modelled using 3D FE analyses. Two types of residual stress modelling were investigated: block dump modelling (BDM) where the weld was assumed to be laid down in chunks and, a moving heat source model (MHS) where the weld torch was explicitly defined based on known weld procedure data. Neither BDM nor MHS could be shown to accurately describe the experimental data however, both models incorporated an initial assumption that materials used in the analyses were in a 'stress free' condition. This assumption was later shown, using experimental results, to be inaccurate. Despite the inaccuracies in initial assumptions residual stresses in individual test samples were shown to be in good agreement with experimental data.

Declaration of Originality

I, Alison Noreen O'Connor, declare that the work presented in this thesis has been undertaken by myself, except where explicit reference and acknowledgement is made to the contribution of others. This work has not been submitted in support of another degree or qualification at Imperial College London nor in any other University or institute of learning.

Copyright Declaration

The copyright of this thesis rests with the author. Unless otherwise indicated, its contents are licensed under a Creative Commons Attribution-Non Commercial 4.0 International Licence (CC BY-NC). Under this licence, you may copy and redistribute the material in any medium or format. You may also create and distribute modified versions of the work. This is on the condition that: you credit the author and do not use it, or any derivative works, for a commercial purpose. When reusing or sharing this work, ensure you make the licence terms clear to others by naming the licence and linking to the licence text. Where a work has been adapted, you should indicate that the work has been changed and describe those changes. Please seek permission from the copyright holder for uses of this work that are not included in this licence or permitted under UK Copyright Law.

For my parents, my heroes.

Without you none of this would be possible.

I'm so grateful that you're mine.

For my sisters Amy and Andrea, and their children

Katie, Jodie, Conor, Abbie, Lucy, Maggie, Ruby and Callum

*ye drive me mad in the **best** of ways. Never stop.*

For Jennifer, related by birth, friends by choice.

You're my proof that the best kind of friendships are fierce lady friendships

where you aggressively believe in each other, defend each other,

and think the other deserves the world.

Acknowledgements

I would like to thank my academic supervisors Dr Davies and Professor Nikbin for their support and encouragement at all stages of this work. Your knowledge, advice and continued guidance has been invaluable. Words are a poor substitute for the gratitude I feel, thank you.

To my industrial sponsors Dr. Peter James and John Sharples, many thanks are due to you both, for your support, technically and financially, over the past four years. I especially appreciate your insightful technical comments which have undoubtedly resulted in a better, more industrially applicable, piece of work.

Additional thanks to Professor Stephen J. Garwood, Dr Robert Wimpory, Dr Priyesh Kapadia, and Dr Keith Tarnowski for many interesting technical conversations. Special thanks to Dr Wimpory for his support at Helmholtz-Zentrum Berlin (HZB) during measurement of residual stresses. Dr Kapadia deserves special recognition for his help with regards to my early abilities, or rather lack thereof, with Python scripting language and the 3D digital image correlation system. Thanks to Nivantha Bandara for the microstructure imaging and hardness test results.

Thanks are also extended to the other students and their academic supervisors involved in the larger project: William Brayshaw and Professor Andrew Sherry of the University of Manchester. Sam Oliver, Professor Martyn Pavier, and Dr Mahmoud Mostafavi of the University of Bristol. Our yearly meetings always resulted in interesting technical conversations and the work that you undertook certainly influenced my own.

Final thanks go to Professor John Brouchard for kindly donating the materials used in this work.

Contents

1 Introduction **1**

1.1 Motivation 1

1.2 Aims and Objectives 3

1.3 Organisation 5

2 Literature Review **7**

2.1 Background 7

2.2 Reactor Pressure Vessels 7

2.3 Factors influencing structural integrity 10

2.3.1 Material properties and fabrication 10

2.3.2 Loading and stress concentration factors 14

2.3.3 Temperature 18

2.4 Fracture Mechanics 19

2.4.1 Linear Elastic Fracture Mechanics (LEFM) 20

2.4.2 Fatigue 23

2.4.3 Elastic Plastic Fracture Mechanics (EPFM) 25

2.5 Engineering Critical Assessments (ECAs) 31

2.6 Chapter 2 Summary 33

3 Specimen Manufacture and Testing **35**

3.1 As Received material 35

3.2 Specimen machining 36

3.2.1 Standard tensile specimens 36

3.2.2 Micro tensile specimens 37

3.2.3 Standard SENB specimens 39

3.2.4 CT specimens 40

3.3 Testing Parameters . . . 43
3.3.1 Neutron Diffraction . . . 43
3.3.2 Metallography and Hardness Testing . . . 46
3.3.3 Tensile testing . . . 52
3.3.4 CT Fracture Toughness Testing . . . 53
3.3.5 SENB Fracture Toughness Testing . . . 58
3.3.6 Digital Image Correlation . . . 62
3.4 Compliance Functions for SENB specimens . . . 63
3.5 Chapter 3 Summary . . . 69

4 Mechanical Properties **72**
4.1 Metallography and Hardness . . . 72
4.2 Experimental tensile test results . . . 80
4.2.1 Standard tensile testing . . . 80
4.2.2 Sub-size tensile testing . . . 83
4.2.3 Comparison of full size and micro-size data . . . 87
4.3 3D Modelling of tensile test . . . 92
4.4 Temperature Dependent Material Properties . . . 98
4.5 Chapter 4 Summary . . . 102

5 Residual Stresses **107**
5.1 Introduction . . . 107
5.2 Neutron Diffraction Results . . . 108
5.2.1 As-welded plate . . . 108
5.2.2 Stress-free (d_0) Specimens . . . 109
5.2.3 Tensile Specimens . . . 110
5.2.4 Block A . . . 113
5.2.5 CT Specimens . . . 113
5.3 3D Modelling of Welding Processes . . . 116
5.3.1 Block Dump Laser Welding Analysis . . . 120

5.3.2 Mesh sensitivity study . . . 120
5.3.3 Mapping stress to a modified mesh . . . 128
5.3.4 Moving Heat Source Laser Welding Analysis . . . 137
5.3.5 Machining CT specimens from welded component . . . 142
5.4 Chapter 5 Summary . . . 152

6 Fracture Toughness of Defects Oriented Parallel to Materials Boundary 159
6.1 Experimental Fracture Toughness of CT specimens notched in austenite 159
6.2 2D Modelling of CT specimens . . . 178
6.2.1 Defects located in austenite material . . . 178
6.2.1.1 Impact of varying the thickness of austenite region . . . 189
6.2.1.2 Impact of varying the proximity of the notch to the materials interface . . . 195
6.2.2 Inverting material properties . . . 202
6.3 3D Modelling of CT Specimens . . . 210
6.4 Chapter 6 Summary . . . 216

7 Fracture Toughness of Defects Oriented Perpendicular to Materials Boundary 224
7.1 Experimental Fracture Toughness of SENB specimens . . . 224
7.1.1 Defects in base material . . . 227
7.1.2 Defects close to the interface . . . 235
7.1.3 Defects in the cladding . . . 247
7.2 2D Modelling of SENB specimens . . . 258
7.2.1 Comparison of homogeneous and combined material models . . . 258
7.2.2 Incorporating the HAZ into the combined material model . . . 274
7.3 Chapter 7 Summary . . . 281

8 Application to Industry 287
8.1 Synthesis . . . 287
8.2 Conclusions . . . 294
8.3 Future work . . . 307

A Appendix Chapter 4 Mechanical Properties and Metallography **321**

B Appendix Chapter 5 Residual Stresses **329**

B.1 Tensile Residual Stress Measurements 329

B.2 Block A 336

B.3 CT Residual Stress Measurements 338

C Appendix Chapter 6 Defects oriented parallel to materials boundary **343**

C.1 Experimental 343

C.2 Finite element 2D: Defect in austenite 353

C.3 Finite element 2D: Defect in ferrite 362

C.4 Assessment of CT's using 3D Finite Element 368

D Appendix Chapter 7 Defects oriented perpendicular to materials interface **373**

D.1 Compliance Functions for Austenite Material 373

D.2 Force versus Displacement curves for individual samples 378

D.3 2D FEA 389

List of Figures

2.1 Typical Westinghouse PWR [IAEA, 1999] 9
2.2 Effect of welding on fatigue strength [Maddox, 2000] 15
2.3 Effect of removing weld toes on fatigue strength [Maddox, 2000] 15
2.4 Three modes of loading that can be applied to a crack [Anderson, 2005] . 22
2.5 Paris' law for fatigue crack growth [British Standards Institute, 2015*a*] . 24
2.6 CTOD estimation using three point bend specimen with effective crack tip estimated from notch opening and rotation around hinge point [Anderson, 2005] 26
2.7 Plastic zone size calculations for plane strain assumption using elastic and elastic-plastic material properties. [Anderson, 2005] 30
2.8 Plastic zone size calculations for plane strain assumption using elastic and elastic-plastic material properties. [Anderson, 2005] 30
2.9 Failure Assessment Diagram. Modified from [British Standards Institute, 2015*a*] 32

3.1 As received large clad plate 36
3.2 As received small clad plate 36
3.3 Specimens to be cut from the large clad plate 37
3.4 Full size tensile specimen orientation in the plate 38
3.5 Full size tensile specimen dimensions 38
3.6 Grouping of micro tensile specimens with respect to clad weld direction 39
3.7 Micro size tensile specimen 39
3.8 Orientation of standard size SENB specimens with respect to cladding . 41
3.9 Orientation of CT specimens with respect to cladding 42
3.10 Laser welded component from which CT specimens were manufacture . 42

3.11 Dimensions of Block B CT specimens 43
3.12 Neutron diffraction measurements on Block A 45
3.13 Neutron diffraction measurement locations on CT specimens 46
3.14 Neutron diffraction measurement locations on tensile specimens 46
3.15 Location of hardness measurements taken from Block B 48
3.16 Location of microstructural imaging on ferrite section (Figure 3.16a) and austenite section (Figure 3.16b) 49
3.17 Hardness measurement locations on original clad weld 50
3.18 Regions of which micrographs were taken 51
3.19 Tensile testing of standard and micro size specimens 53
3.20 GOM 5M system used to take images during fracture testing 62
3.21 Linear elastic model for derivation of compliance coefficients. Crack depth of 0.05 mm. Boundary conditions shown on rollers. 64
3.22 Load-line compliance as a function of crack depth, including polynomial fit 65
3.23 Crack depth as a function of crack mouth opening, including polynomial fit 66
3.24 Comparison of polynomial fit for ASTM coefficients and FE derived coefficients 67
3.25 Percentage difference in calculated crack depth compared to the known crack depth for $0 \geq a/W \leq 0.85$ 68
3.26 Polynomial fit for elastic stress intensity factor coefficients derived from FE 69

4.1 Martensitic layer at materials interface of original TIG weld plate at 10X magnification, position 1 73
4.2 Figures 4.2a, 4.2b, and 4.2c detailing grain structure in ferrite region of original TIG weld plate at 100× magnification, respectively. Figures 4.2d, 4.2e, and 4.2f showing micrographs of grain structure in austenite region of original TIG weld plate at 10× magnification, respectively . 74

4.3 Surface plot of HV10 hardness on original TIG weld plate 75
4.4 Micrographs of grain structure in ferrite region 76
4.5 Micrographs of grain structure in austenite region of EB welded section at 100× magnification. Images taken in the mid-width of sample, i.e. where the weld overlaps through thickness direction from TIG weld towards the EB weld. 78
4.6 Surface plots of HV10 hardness on Block B weld start and end positions 79
4.7 Engineering stress-strain curves for standard size tensile specimens . . . 81
4.8 True stress-true strain plot for standard sized ferritic, austenitic and HAZ specimens based on average power law data 83
4.9 Stress-strain data for Group B3-2. Specimens oriented longitudinal to clad weld direction. 85
4.10 Stress-strain data for Group B3-3. Specimens oriented transverse to clad weld direction. 85
4.11 Stress-strain data for Group B3-4A. Specimens oriented perpendicular to clad weld direction. 86
4.12 Stress-strain data for Group B3-4B. Specimens oriented perpendicular to clad weld direction. 86
4.13 Stress-strain data for sub-sized specimens comprised of ferritic material only 90
4.14 Comparison of standard size and sub-sized size power law curves for ferritic material 90
4.15 Comparison of full size and micro size power law curves for austenite material 91
4.16 Stress-strain data for sub-sized specimens comprised of mixed ferrite/austenite material 91
4.17 Force versus displacement response for each model 94
4.18 FE stress-strain response for 3D tensile testing 95

4.19 Direct stress (σ_{yy}) through thickness of specimen in Figure 4.19a. Predicted values of stress normalised against measured yield strengths shown in Figure 4.19b 95
4.20 Mises stresses at final displacement for homegeneous material models 4.20a) Austenite, 4.20b) Ferrite and 4.20c) HAZ regions 96
4.21 Mises stresses at final displacement for multi material models: 4.21a) Combined austenite and ferrite model and 4.21b) Combined austenite, ferrite and HAZ model 97
4.22 Ferritic temperature dependent true stress - true strain curves. Comparison of data from from literature [Serasli, 2014] with data provided by industrial sponsor 99
4.23 Ferrite temperature dependent true stress - true strain curve. Comparison of data from industrial sponsor with experimental data derived as part of this project (shown as solid lines see Section 4.2) 99
4.24 Temperature dependent true stress - true strain for austenite material from data in the NeT project [Ficquet et al., 2009] 101
4.25 Comparison of temperature dependent true stress - true strain for austenite material from data in the NeT project [Ficquet et al., 2009] and Serasli [Serasli, 2014] 101
4.26 Comparison of room temperature true stress - true strain for austenite material from data in the NeT project [Ficquet et al., 2009] and experimental work from this project. Shifting the original NeT data (blue curve) by 50 MPa results in a good agreeement with specimens tested as part of this project. 102

5.1 Instrument E3 setup, [Boin, 2015] 108
5.2 Residual stresses measured by Serasli using neutron diffraction (From [Serasli, 2014]). Measurements taken offset mid-width, offset from the mid-section (35 mm), through thickness of plate up to a depth of 30 mm from the clad surface. 109

5.3 Surface plot of normal residual stress in tensile specimens 111
5.4 Surface plot of residual stress in tensile specimen 2 using austenite d_0 value 112
5.5 Surface plot of residual stress in tensile specimen 2 assuming plane stress condition 112
5.6 Residual stresses in Block A post EB welding 113
5.7 Comparison of measured residual stresses in CT specimens using d_o values 115
5.8 Comparison of measured residual stresses in CT specimens assuming plane stress 115
5.9 Heat flux distribution in double ellipsoid (Figure 5.9a), conical (Figure 5.9b) and combined (Figure 5.9c) heat source model (Figure from [Kapadia, 2014]) 118
5.10 Low and high density meshes (Figures 5.10a and 5.10b, respectively) used to assess mesh sensitivity of the analysis 121
5.11 Heat transfer model weld partitions 122
5.12 Boundary conditions applied to all block dump structural models. Node used for output of temperature values shown using red circle. 123
5.13 Comparison nodal temperatures from the original structural model (34,000 elements) and heat transfer MAP_1_3 (250,000 elements) 124
5.14 Comparison of residual stresses in the transverse (Figure 5.14a), longitudinal (Figure 5.14b) and normal (Figure 5.14c) directions for the low and high density structural models. 125
5.15 Orientation of contour plots with respect to weld boundary locations . . 125
5.16 Contour plots of the transverse, longitudinal and normal residual stress on the surface and in the mid-thickness of the component for low density structural analysis 126

5.17 Contour plots of the transverse, longitudinal and normal residual stress on the surface and in the mid-thickness of the component modelled using block dump heat source for high density mesh structural analysis . . 127
5.18 Original and final structural block dump model partitioning. Model shown in Figure 5.18b was used in the MAP_2 series of analyses 129
5.19 Mesh density used in mapping analyses (see Table 5.1) 132
5.20 Comparison of nodal temperatures from a specific node for the original heat transfer and original structural model 133
5.21 Comparison of residual stresses in the transverse (Figure 5.21a), longitudinal (Figure 5.21b) and normal (Figure 5.21c) directions for the original model and the various *MAP SOLUTION techniques (see Table 5.1) . . . 134
5.22 Comparison of experimentally measured residual stresses on Block A with predicted residual stress from the original structural model 135
5.23 Contour plots of the transverse, longitudinal and normal residual stress on the surface and in the mid-thickness of the component modelled using block dump heat source for MAP_2_3 analysis 136
5.24 Mesh density and structure used in heat transfer (Figure 5.24a) and structural (Figure 5.24b) moving heat source analysis 138
5.25 Nodal temperatures for the moving heat source model, both heat transfer and structural model results depicted 139
5.26 Comparison of estimated residual stresses from moving heat source model with experimentally measured residual stresses 140
5.27 Contour plots detailing the transverse, longitudinal and normal stresses on the surface and mid-thickness of the component modelled using moving heat source 141
5.28 Mesh density used in structural analyses. Figure 5.28a showing mesh used in moving heat source weld simulation. Figure 5.28b showing the mesh used for mapping stresses. 142

5.29 Contour plots detailing the transverse, longitudinal and normal stresses on the surface and mid-thickness of the component. Nodal displacements mapped using data from moving heat source and *MAP SOLUTION keyword 145
5.30 Contour plots detailing the transverse, longitudinal and normal stresses on the surface and mid-thickness of the component after relaxation of stresses 146
5.31 Contour plots detailing the transverse, longitudinal and normal stresses on the surface of specimen blanks before and after relaxation of stresses 147
5.32 Annotated image of specimen orientation with respect to the component. Figure 5.32a showing first outer surface of the specimen, corresponding to approximate mid-thickness region of the component. Figure 5.32b showing the second outer surface of the specimen, corresponding to the weld 1 surface of the laser welded component 148
5.33 Contour plots detailing the transverse, longitudinal and normal stresses on the surface and mid-thickness of Specimen 1 before and after relaxation of stresses 149
5.34 Contour plots detailing the transverse, longitudinal and normal stresses on the surface and mid-thickness of Specimen 2 before and after relaxation of stresses 150
5.35 Contour plots detailing the transverse, longitudinal and normal stresses on the surface and mid-thickness of Specimen 3 before and after relaxation of stresses 151
5.36 Comparison of nodal temperatures estimated using block dump and moving heat source model. Figure 5.36a showing the position of the node used to output temperature values. Figure 5.36b plotting temperatures for entire welding process. Figure 5.36c showing magnified view of heating cycles. 156

5.37 Comparison of residual stresses in mid-thickness of CT specimen 1. Showing a) longitudinal, b) transverse, and c) normal directions. Contour map limited to ± 200 MPa, applicable to all directions as shown 158

6.1 CT specimen with annotations showing material boundaries 161

6.2 Force versus displacement for CT specimens with initial defect in austenite material 161

6.3 J-Integral versus crack extension (Δa) for CT specimens notched in austenite 163

6.4 DIC data for CT specimen S3 with initial defect length $a/W = 0.45$. Figures 6.4a and 6.4d showing the true major strain and Figures 6.4e and 6.4h showing strains in thickness direction. Results of first, fifth, mid-test and final peak (force) unloading positions, respectively. 166

6.5 DIC data for CT specimen S5 with initial defect length $a/W = 0.55$. Figures 6.5a and 6.5d showing the true major strain and Figures 6.5e and 6.5h showing strains in thickness direction. Results of first, fifth, mid-test and final peak (force) unloading positions, respectively. 167

6.6 DIC data for CT specimen S6 with initial defect length $a/W = 0.55$. Figures 6.6a and 6.6d showing the true major strain and Figures 6.6e and 6.6h showing strains in thickness direction. Results of first, fifth, mid-test and final peak (force) unloading positions, respectively. 168

6.7 Annotated images showing approximate locations of TIG and EB weld boundaries and paths investigated. Figure 6.7a showing sections parallel to crack depth. Local co-ordinate system in use. Remaining ligament from crack tip to back face of sample shown in green with positive displacement representing movement away from the crack tip. Individual DIC paths for strain analysis showing Path '0' at the crack tip to Path '9' 4.5 mm vertically offset from crack tip. Each section subsequent to Path '0' located 0.5 mm from preceding path. Figure 6.7b showing sections oriented perpendicular to the crack depth. Local co-ordinate system at the bottom of image. Section moving from 'bottom' of image towards the top passing through the austenite region. Four sections labelled 'A' through 'D' as shown, section 'A' located at the crack tip, subsequent sections offset by 1 mm from preceding section. 170

6.8 Major strain along the remaining ligament at various positions. Positions are positive relative to the crack tip towards the TIG weld boundary. Results shown for Samples S3, S5 and S6 at first and final sequences, respectively. 171

6.9 Normalised relative strain along the remaining ligament at various positions. Positions are positive relative to the crack tip towards the TIG weld boundary. Results shown for Samples S3, S5 and S6 at first and final sequences, respectively. 173

6.10 Post-test inspection of CT sample S1. Figure 6.10a detailing the bifurcation at the crack tip on the surface of the sample with defects oriented towards both material boundaries. Figure 6.10b showing defect in the mid-thickness region with defect oriented towards the EB weld boundary. 176

6.11 Major strain parallel to loading direction. Path 'A' at the crack tip, Paths 'B' to 'D' offset from preceding section by 1 mm. Results shown for Samples S3, S5 and S6 at first and final sequences, respectively. 177

6.12 Boundary condition and meshing applied to 2D models. Notch tip postulated to be 1 mm below TIG weld boundary. Figure 6.12a showing 6 mm thick austenite layer. Figures 6.12b and 6.12c showing 4 mm and 8 mm thick austenite layers, respectively. 180
6.13 Maximum force and displacement for multiple crack depths at plastic collapse 181
6.14 J-integral values at plastic collapse 181
6.15 Plane stress analysis contour plots of direct strain (ϵ_{yy}) for multiple values of pin displacement (Δ) 183
6.16 Plane strain analysis contour plots of direct strain (ϵ_{yy}) for multiple values of pin displacement (Δ) 183
6.17 Reaction force versus load-line displacement (LLD) for multiple crack depths (a_0) for plane stress and plane strain analyses 184
6.18 Average J-integral values for multiple crack depths (a_0) for plane stress and plane strain analyses 184
6.19 Direct strain (ϵ_{yy}) along the remaining ligament for multiple initial crack depths (a_0) for plane stress and plane strain analyses at a displacement (Δ = 0.4 mm) 185
6.20 Direct strain (ϵ_{yy}) along the materials boundary for multiple initial crack depths (a_0) for 2D plane strain (Figure 6.20a) and plane stress (Figure 6.20b) analyses at a displacement (Δ = 0.4 mm). Cracktip positions marked with circle. 187
6.21 Direct strain (ϵ_{yy}) along the materials boundary when $\frac{a}{W}$ = 0.45 for multiple load-line displacement values for plane strain (Figure 6.21a) and plane stress (Figure 6.21b) conditions. 188
6.22 Reaction force versus load-line displacement (LLD) for crack depth (a/W = 0.45) for plane stress and plane strain analyses at each austenite thicknesses shown. 190

6.23 Comparison of direct strain ϵ_{yy} along the remaining ligament for plane strain and plane stress conditions varying the austenite thickness. 191
6.24 Comparison of σ_{yy} along the remaining ligament for plane strain and plane stress conditions varying the austenite thickness. 191
6.25 Comparison of direct strain ϵ_{yy} along the materials interface for plane strain and plane stress conditions varying austenite thickness. Displacement Δ = 0.4 mm. 193
6.26 Contour plots for the plane stress and plane strain conditions varying the austenite thickness. Applied force = 20 kN. 194
6.27 Varying the proximity of the notch to the materials interface with Figure 6.27a: 1 mm from materials interface, Figure 6.27b: 2 mm from the materials interface, Figure 6.27c 3 mm from the materials interface (i.e. in the centre of the austenite material). Austenite material properties shown in green, ferrite material properties in cream. 196
6.28 Reaction force versus load-line displacement (LLD) for crack depth ($\frac{a}{W}$ = 0.45) for plane stress and plane strain analyses varying the proximity of the notch to the materials interface. 197
6.29 Average J-integral estimation for crack depth (a/W = 0.45) for plane stress and plane strain analyses, varying both the thickness of the austenite region and the proximity of the notch to the materials interface. . . . 197
6.30 Average J-integral estimation for crack depth (a/W = 0.45) for plane stress and plane strain analyses, varying both the thickness of the austenite region and the proximity of the notch to the materials interface. Results limited to small-scale yielding zone. 198
6.31 Comparison of direct strain ϵ_{yy} along the remaining ligament for plane strain and plane stress conditions varying the proximity of the notch to the materials interface (Δ = 0.4 mm). 199

6.32 Comparison of direct strain ϵ_{yy} along the materials interface for plane strain and plane stress conditions varying the proximity of the notch to the materials interface Δ = 0.4 mm. 200
6.33 Comparison of direct stress σ_{yy} along the materials interface for plane strain and plane stress conditions varying the proximity of the notch to the materials interface Δ = 0.4 mm. 200
6.34 Contour plots for the plane stress and plane strain conditions varying the proximity of the notch to the materials interface. Applied force = 20 kN 201
6.35 Boundary condition and meshing applied to 2D models. Austenite material properties assigned to the gray region, ferrite material properties assigned to the green regions. 203
6.36 Plane stress analysis contour plots of direct strain (ϵ_{yy}) for multiple values of pin displacement (Δ). Notch region consisting of ferrite material properties. 203
6.37 Plane strain analysis contour plots of direct strain (ϵ_{yy}) for multiple values of pin displacement (Δ) Notch region consisting of ferrite material properties. 204
6.38 Reaction force versus load-line displacement (LLD) for multiple crack depths (a_0) for plane stress and plane strain analyses 204
6.39 Direct strain (ϵ_{yy}) along the remaining ligament for multiple initial crack depths (a_0) for plane stress and plane strain analyses at a displacement (Δ = 0.4 mm) 206
6.40 Direct strain (ϵ_{yy}) along the remaining ligament for initial crack length (a_i) 13.5 mm for plane stress and plane strain analyses at a displacement (Δ = 0.4 mm) 207

6.41 Direct strain (ϵ_{yy}) along the materials boundary for multiple initial crack depths (a_0) for 2D plane strain (Figure 6.20a) and plane stress (Figure 6.20b) conditions at a displacement (Δ = 0.4 mm). Cracktip positions marked with dashed line. 208

6.42 Comparison of direct strain (ϵ_{yy}) along the materials boundary for initial crack depth (a_i=13.5 mm) for 2D plane strain (Figure 6.42a) and plane stress (Figure 6.42b) conditions at a displacement (Δ = 0.4 mm) for specimens notched in austenite material and specimens notched in ferrite material 209

6.43 Image of boundary conditions and mesh strategy applied to the 3D model.211

6.44 Force versus displacement at the load-line and crack mouth opening (CMOD) for 3D fracture models 212

6.45 Contour plots of direct strain ϵ_{yy} in 3D model of fracture toughness test during peak loading conditions. Notched region consisting of austenite material properties. Figures 6.45a to 6.45c showing estimated strain on surface. Figures 6.45d to 6.45f showing strains in the mid-thickness region.214

6.46 Contour plots of direct strain ϵ_{yy} in 3D model of fracture toughness test during peak loading conditions. Notched region consisting of ferrite material properties. Figures 6.46a to 6.46c showing estimated strain on surface. Figures 6.46d to 6.46f showing strains in the mid-thickness region.215

6.47 Comparison of measured major strain using DIC to predicted equivalent plastic strain (PEEQ) using 2D modelling with plane strain assumption. Specimens compared at various applied displacements. 218

6.48 Comparison of fracture surface of the surface of specimen S1 with 2D FEA plane stress analysis. Showing direct strain ϵ_{yy}. 219

6.49 Comparison of mid-thickness fracture surface of specimen S1 with 2D plane strain analysis. Showing direct strain ϵ_{yy}. 220

6.50 Comparison of measured major strain using DIC to predicted equivalent plastic strain (PEEQ) using 3D model notched in austenite. Specimens compared for identical test sequences. 222
6.51 Comparison of equivalent plastic strain (PEEQ) using 3D models notched in austenite and ferrite. Specimens compared for identical test sequences. 223

7.1 Force versus displacement for specimens with initial defect length $a/W = 0.45$229
7.2 J-Integral versus crack extension (Δa) for C1 group. Original notch size $a/W = 0.45$ 230
7.3 Post-test imaging of mid-thickness defect in specimen C11 (combined austenite and ferrite) 231
7.4 DIC data for specimen C11 with initial defect length $a/W = 0.45$. Figures 7.4a and 7.4b showing the true major strain for the initial loading cycle and the final unloading, respectively. Figures 7.4c and 7.4d showing the thickness reduction for the initial loading cycle and the final unloading, respectively. 231
7.5 Post-test imaging of mid-thickness defect in specimen C13 (ferrite only) 231
7.6 DIC major strain for specimen C13 with initial defect length $a/W = 0.45$. Figures 7.6a and 7.6b showing the initial loading cycle and the final unloading, respectively, for test one. Figures 7.6c and 7.6c showing the initial loading cycle and the final unloading, respectively, for test two. . 233
7.7 DIC strain in thickness direction for specimen C13 with initial defect length $a/W = 0.45$. Figures 7.7a and 7.7b showing the initial loading cycle and the final unloading, respectively, for test one. Figures 7.7c and 7.7d showing the initial loading cycle and the final unloading, respectively, for test two. 233
7.8 Post-test imaging of mid-thickness defect in specimen C31 (combined austenite and ferrite) 236

7.9 Post-test imaging of clad embedded defects in specimen C31 (combined austenite and ferrite) at 7.9a) the edge of the original plate and 7.9b) in the mid-thickness of the original plate 237
7.10 Post-test imaging of mid-thickness defect in specimen C34 (combined austenite and ferrite) 7.10a) showing possible fatigue pre-crack and 7.10b) showing secondary crack. 237
7.11 Force versus displacement for specimens with initial defect length $a/W = 0.30$ 238
7.12 J-Integral versus crack extension (Δa) for C3 group. Original notch size $a/W = 0.30$ 239
7.13 DIC data for combined specimen C31 with initial defect length $a/W = 0.15$. Figures 7.13a and 7.13d showing the true major strain and Figures 7.13e and 7.13h showing strains in thickness direction. Results of first, fifth, mid-test and final peak (force) unloading positions, respectively. 243
7.14 DIC data for combined specimen C34 with initial defect length $a/W = 0.30$. Figures 7.14a and 7.14d showing the true major strain and Figures 7.14e and 7.14h showing strains in thickness direction. Results of first, fifth, mid-test and final peak (force) unloading positions, respectively. 244
7.15 Annotated view of Figure 7.13h (Figure 7.15a) and Figure 7.13h (Figure 7.15b), respectively. Showing idealised profile shape for strain in thickness direction beneath the weld boundary 245
7.16 DIC data for homogeneous specimen C35 with initial defect length $a/W = 0.30$. Figures 7.16a and 7.16d showing the true major strain and Figures 7.16e and 7.16h showing strains in thickness direction. Results of first, fifth, mid-test and final peak (force) unloading positions, respectively. 246
7.17 Force versus displacement for specimens with initial defect length $a/W = 0.15$ 250
7.18 J-Integral versus crack extension (Δa) for C2 group. Original notch size $a/W = 0.15$ 251
7.19 Post-test imaging of mid-thickness defect in specimen C21 (combined austenite and ferrite) 252

7.20 Post-test imaging of clad embedded defects in specimen C21 (combined austenite and ferrite) 252
7.21 Post-test imaging of mid-thickness defect in specimen C24 (combined austenite and ferrite) 252
7.22 DIC data for combined specimen C21 with initial defect length $a/W = 0.15$. Figures 7.22a and 7.22d showing the true major strain and Figures 7.22e and 7.22h showing strains in thickness direction. Results of first, fifth, mid-test and final peak (force) unloading positions, respectively. 253
7.23 DIC data for combined specimen C24 with initial defect length $a/W = 0.15$. Figures 7.22a and 7.22d showing the true major strain and Figures 7.22e and 7.22h showing strains in thickness direction. Results of first, fifth, mid-test and final peak (force) unloading positions, respectively. 254
7.24 DIC data showing crack propagation on surface of combined sample C24 255
7.25 DIC data for homogeneous ferrite specimen C26 with initial defect length $a/W = 0.15$. Figures 7.25a and 7.25d showing the true major strain and Figures 7.25e and 7.25h showing strains in thickness direction. Results of first, fifth, ninth and eighteenth peak (force) unloading positions, respectively. 256
7.26 FE models showing boundary conditions and meshing for notch depths: 7.26a) $a/W = 0.15$, 7.26b) $a/W = 0.30$, 7.26c) $a/W = 0.45$ 260
7.27 Comparison of force versus displacement curves for defects of size a/W=0.15 under plane stress and plane strain conditions 261
7.28 Principal stresses (σ_{xx}) along the remaining ligament for combined material model assuming plane strain conditions 262
7.29 Normalised stress along the ligament for combined material model assuming plane strain conditions. Figures 7.29a and 7.29b showing the entire section along the specimen height. Figures 7.29c and 7.29d showing the region surrounding the materials interface. 264

7.30 Contour plots of plane strain analyses for equivalent plastic strain (PEEQ) and Mises stress for $a/W = 0.15$ and $a/W = 0.30$. Force$\approx$ 5 kN 265
7.31 Direct stresses along the materials interface for $a/W = 0.15$ 267
7.32 Direct stresses along the materials interface for $a/W = 0.30$ 268
7.33 Direct stresses along the materials interface for $a/W = 0.45$ 269
7.34 Normalised stresses along the materials interface for $a/W = 0.15$ 272
7.35 Normalised stresses along the materials interface for $a/W = 0.30$ 273
7.36 Normalised stress in remaining ligament for $a/W = 0.15$ when HAZ is neglected (Figure 7.29a) and included (Figure 7.36b) 275
7.37 Normalised stress in remaining ligament for $a/W = 0.30$ when HAZ is neglected (Figure 7.29b) and included (Figure 7.37b) 275
7.38 Comparison of contour plots for plane strain analyses. Combined austenite and ferrite model results for PEEQ strains and Mises stress shown in Figures 7.38a to 7.38c. Combined austenite to HAZ to ferrite model in Figure 7.38d to 7.38f. Force$\approx$ 5 kN, except for Figures 7.38c and 7.38f where the maximum force was estimated to be $\approx$ 4.6 kN. 276
7.39 Normalised stresses along the materials interface for $a/W = 0.15$ 279
7.40 Normalised stresses along the materials interface for $a/W = 0.30$ 280

List of Tables

2.1 Chemical composition of the ferritic and austenitic materials (From: [Washko and Aggen, 1990; IAEA, 1999]) 12

3.1 Coefficients for calculation of load-line compliance. 64

3.2 Coefficients for calculation of crack depth from crack mouth opening displacements. Note: ASTM coefficients only valid for surface measurements. 68

3.3 Coefficients for calculation of elastic stress intensity factor 68

4.1 Average mechanical properties for ferritic, austenitic and HAZ materials, derived from standard size tensile specimens 80

4.2 Average power law constants for standard size true stress-strain properties 82

4.3 Average power law constants for upper, lower and average bounding curves for sub-sized specimens. 88

4.4 Average power law constants for upper, lower and average bounding curves for sub-sized austenite specimens only 88

4.5 Average power law constants for upper, lower and average bounding curves for mixed material sub-sized specimens 89

5.1 Mapped structural analyses for block dump modelling 130

6.1 Fracture toughness of CT specimens notched in austenite 164

7.1 Fracture toughness of SENB Group C1. Initial machined notch a_0 = 8.1 mm. 226

7.2 Fracture toughness of SENB Group C3. Initial machined notch a_0 = 5.4 mm. 240

7.3 Fracture toughness of SENB Group C2. Initial machined notch a_0 = 2.7 mm. 257

Nomenclature

α	Materials constant
γ_s	Surface energy
γ_p	Plastic work per unit area of surface created
δ_{el}	elastic CTOD
δ_{pl}	elastic CTOD
$\Delta\sigma$	Stress range
ΔK	Range of stress intensity factor
ϵ	Strain
ϵ_0	Normalising strain parameter in Ramberg-Osgood material model
ϵ_e	Engineering strain
ϵ_{ij}	Strain tensor
ϵ_t	True strain
η	Strain hardening parameter or weld efficiency
η_j	Unit vector normal to path-integral
θ	Angle measurement in degrees
λ	Neutron wavelength
ν	Poisson's ratio
σ_e	Engineering stress
σ_{eff}	Effective stress
σ_f	Fracture stress
σ_{ij}	Stress tensor
σ_o	Reference stress, typically taken to be σ_y
σ_t	True stress
σ_y	Yield stress
ω	Strain energy density
$A_{pl_{(i)}}$	Plastic area under J versus Δa curve at unloading increment
a	Crack length or half crack length

a_0	Initial crack length
a_i	Current crack length at current unloading increment
a_f	Final crack length
b_i	Remaining ligament at current unloading increment
B	Fracture toughness specimen thickness
B_e	Fracture toughness effective specimen thickness
B_N	Fracture toughness net specimen thickness
C	Material constant
$C_{C_{(i)}}$	Rotationally corrected compliance
C_{LL}	Load-line compliance
C_v	Charpy impact energy
da	Increment of crack growth
d_{hkl}	Lattice spacing in crystalline material
dN	Incremental number of cycles (fatigue)
d_s	length of increment along contour
E	Young's modulus
G	Energy release rate
I	Measure of electrical current
J	Non-linear energy release rate
J_{el}	Elastic fracture toughness
J_{pl}	Plastic fracture toughness
J_{total}	Summation of elastic and plastic fracture toughness
J_{limit}	Maximum allowable value of energy
K	Stress intensity factor (also SIF)
K_I	Stress intensity for Mode 1 loading
K_{mat}	Fracture toughness
m	Material constant or dimensionless constant
N	Number of cycles (fatigue)

P_f	Maximum applied load during elastic fracture toughness testing
P_{fail}	Factor representing probability of failure
P_i	Load at current unloading increment
Q	Heat input parameter
q	Heat flux
q_e	Heat flux of double ellipsoid
q_c	Heat flux of conical shape
r_p	Plastic rotational factor
S	Span between centre of loading positions
T	Temperature
T_i	Traction vector components
T_K	Temperature describing scatter
T_0	Temperature for fracture toughness of 100 MPa$\sqrt{\text{mm}}$
u_i	Displacement vector components
V	Measure of electrical voltage
V_p	Plastic displacement at crack mouth
$V_{pl(i)}$	Plastic displacement at measuring position at current unloading increment
V_{LL}	Displacement at load-line
W	Specimen height
Y	Geometrical constant
AUS	Austenite
AUT	Automated ultrasonics
BCC	Body center cubic
BWR	Boiling water reactor
BPVC	Boiler pressure vessel code
CT	Compact tension
CDF	Crack driving force

CMOD	Crack mouth opening displacement
COD	Crack opening displacement
CTE	Coefficient of thermal expansion
CTOD	Crack tip opening displacement
DIC	Digital image correlation
EB	Electron beam
ECA	Engineering critical assessment
EDM	Electro-discharge machining
EPFM	Elastic plastic fracture mechanics
FCC	Face center cubic
FCGR	Fatigue crack growth rate
FEA	Finite element assessment
FER	Ferrite
FFP	Fitness for purpose
FPA	Focussed phased array
GWe	Gigawatt electricity
HAZ	Heat affected zone
IAEA	International atomic energy agency
LLD	Load line displacement
LWR	Light water reactor
LEFM	Linear elastic fracture mechanics
MMA	Manual metal arc
MHS	Moving heat source
MVC	Microvoid coalescence
NPP	Nuclear power plant
PE	Plane strain
PM	Parent material
PMZ	Partially mixed zone
PS	Plane stress

PWHT	Post-weld heat treatment
PWR	Pressurised water reactor
RBM	Rigid body motion
RF	Reaction force
RPV	Reactor pressure vessel
SAW	Submerged arc weld
SCF	Stress concentration factor
SENB	Single edge notch bend
SHC	Specific heat capacity
SIF	Stress intensity factor
SSY	Small-scale yielding
TT	Transition temperature
TIG	Tungsten Inert Gas
TOFD	Time-of-flight diffraction
USA	United states of America
WM	Weld metal

Chapter 1: Introduction

1.1 Motivation

The commercial nuclear industry began expanding rapidly from the 1950's with the first commerical nuclear power plant (NPP) being connected to a Soviet power grid in 1954 [Chater, 2005]. In 2008 up to 350 GWe (gigawatt electricity) accounting for 16% of the world's power was generated by 439 NPPs. It has been estimated that by 2030 the amount of electricity generated will increase to between 400-640 GWe [IAEA, 2009*b*]. One of the alternative uses for nuclear energy is propulsion particularly in the shipping industry. Indeed the first nuclear powered vessel, a submarine, became operational in the United States of America (USA) in 1955 two years prior to the first USA commercial NPP [Chater, 2005; Hirdaris et al., 2014; World Nuclear Association, 2015]. One of the major issues facing the nuclear industry today is the safe operation of aging reactor pressure vessels (RPVs). Many RPVs were designed to have an operational life of 40 years based on the fatigue usage calculations [IAEA, 2009*b*]. The International Atomic Energy Agency (IAEA) has stated that approximately 25% of the world's NPPs have been in operation for 30 years and about 70% for more than 20 years [IAEA, 2015].

Structural integrity procedures for NPPs were redeveloped after two significant nuclear accidents – the Three Mile Island incident (1979) and the Chernobyl accident (1986) both of which have been well documented [Chater, 2005; Cooper, 2015; IAEA, 2014; Rathod et al., 2015; Rowinski et al., 2015]. The 'new' structural integrity procedures were rigorous methodologies assessing the level of risk in a quantifiable manner and were generally resubmitted to government overseers every 10 years [Tomkins, 2003]. The process of reassessment, where operators submit a quantifiable measurement of reliability (a safety case) to the relevant overseeing body, is still active today. One of the benefits of the safety case methodology is that should the NPP be deemed fit-for-purpose (FFP) the operational life may be extended beyond that of the original

design. In the UK the R6 code [British Energy, 2008] specifically addresses the assessment of defects in critical components and has a major influence on whether a NPP is deemed to have sufficient structural integrity.

Prior to the discovery of irradiation embrittlement the main method of fabricating an RPV was by welding plate material [IAEA, 1999]. Welding is a process whereby two materials are joined together typically using heat and a filler material. One of the major disadvantages of welding is that it leads to a weaker material when compared to the base material. Older RPVs typically contained both circumferential and longitudinal welds that were fabricated using copper coated electrode wires. It was later established that higher percentages of copper and phosphorous resulted in welds that were more susceptible to irradiation damage. To avoid irradiation damage later designs used forged materials thus eliminating the need for longitudinal welds. Copper coated electrode wire was also eliminated from use [IAEA, 2009*a*, 1999].

This particular work investigates Light Water Reactor (LWR) RPVs which are generally constructed from a combination of low alloy carbon steel, stainless steel and/or nickel based alloys [IAEA, 1999; Choi et al., 2000; Dolby et al., 2005; Hanninen et al., 2006]. The main body of the RPV is comprised of forged rings of ferritic steel. The inside is generally lined with 3-10 mm of corrosion resistant material. The welding process used to apply the lining is referred to as cladding. Hence a clad material consists of ferritic base metal and several layers of stainless steel (or another corrosion resistant material). The most common grades of cladding used for nuclear purposes are: CF8 and CF8M which are cast, and Type 304 (equivalent to CF8), 308, 309 and 316 (equivalent to CF8M) which are wrought [Hanninen et al., 2006; IAEA, 2009*a*]. Stainless steels are incorporated due to their high resistance to corrosion and creep, even at elevated temperatures, when compared to ferritic materials [ASM International Handbook Committee, 2010]. Both cast and wrought stainless steels are used. In addition to stainless steels nickel based alloys, in particular Inconel alloys (alloy 600, 625 and filler metal 82), are widely adopted [IAEA, 1999; Daw et al., 2010; Kiser et al., 2005]. These

alloys are similar in performance to stainless steels and can be wrought or cast [ASM International Handbook Committee, 2011].

Structural integrity procedures, such as that outlined in R6 [British Energy, 2008], use fracture mechanics theory (see Section 2.4) with specific component information such as material properties, loading conditions and postulated defect size. The postulated defect size is generally dependent on the type of non-destructive test (NDT) technique used to assess the component. BS 7910 [British Standards Institute, 2015*a*] standard provides some guidance on appropriate minimum defect size for a variety of NDT techniques but these are specified as being relevant to homogeneous material welds only (i.e. they may not be appropriate for DMWs). In addition NDT techniques often struggle to find and size defects in DMWs due to the changes in how acoustic or phased-array waves propagate through materials of differing densities. Hence defects may exist in multiple orientations with respect to the weld boundary. To account for inaccuracies in NDT measurements and ensure the integrity procedure is conservative initial defect sizes are, typically, much larger (both in terms of depth and length) than those used for homogeneous or similar welded materials. A separate integrity procedure must be conducted for each postulated defect size for each defect orientation. As the number of uncertainties increases so to does the number of required integrity assessments.

1.2 Aims and Objectives

The overall project aim of the project is to advance industry related standards for engineering critical assessments (ECAs) with respect to the performance of dissimilar clad welded materials. One of the issues with the clad welding process is that the residual stresses post in the structure post welding are not comprehensively understood. This leads to difficulties in assessing defect initiation and, particularly, defect propagation, both of which are considered critical input parameters to ECAs [British Standards Institute, 2015*a*; British Energy, 2008].

ECA parameters are generally derived from standard, small-scale, specimens taken from larger components that are similar (in terms of material properties, fabrication methods etc.) to the in-service component. By addressing the likelihood of defect initiation and propagation in standard specimens the performance of the larger in-service component can be assessed more comprehensively. As discussed earlier current codes and standards provide little guidance on how DMWs should be analysed. In terms of DMWs ECAs generally do not consider the cladding material as contributing to structural integrity. Defects are postulated at numerous locations: through clad, sub-surface clad, sub-surface base, etc. and are, generally, assumed to be of a conservatively large length and depth. Understanding the likelihood of defect initiation and propagation in combined components would ensure that ECAs could be conducted in a more streamlined manner by 1: reducing the overall number of assessments to be conducted 2: providing insight to NDT operators on locations likely to initiate defects 3: provide insight into the likely direction of defect propagation.

The following research questions were derived based on the current state of the art:

- Does the cladding contribute to structural integrity? Can we quantify the contribution, if any, of the cladding?
- Are there locations where defects are likely to initiate? Are sub-surface defects more prevalent than surface breaking defects?
- If defects exist in multiple locations is one more likely to propagate in comparison with another? Are sub-surface or surface breaking defects more likely to propagate?
- Does the weld boundary influence defect propagation direction? Do defects oriented perpendicular to the weld boundary deviate along the weld interface (i.e. delamination of cladding)? Or, do they propagate through the weld boundary into the base material? Do defects oriented parallel to the weld boundary continue propagating along the boundary? Or, do they deviate into one of the materials specifically?
- How accurate is finite element modelling at predicting defect propagation in DMWs?

The following objectives, based on the research questions, were derived:

- Manufacture suitable inhomogeneous (combined clad and base material) and homogeneous (base material only) samples
- Assessment of material microstructure and measurement of mechanical properties
- Assessment and measurement of welding residual stresses
- Comparison of performance of combined samples to homogeneous samples during fracture testing
- Assessment of defect initiation and propagation with respect to the weld boundary

1.3 Organisation

Chapter 2 discusses the importance of the nuclear industry to society in terms of power consumption. The critical components of a nuclear power plant, and the implications of failure are discussed. A brief overview of historical materials, fabrication methods and safety assessments is provided so that the reader can understand how the current work relates to the wider nuclear industry. To provide some understanding of how factors (such as material properties, loading, and defect location) specific to this work relate to engineering critical assessments (ECAs) Chapter 2 provides an overview of fracture mechanics theory.

The purpose of Chapter 3 is to provide the reader with specific details on specimen manufacture. Given that multi-material and homogeneous material specimens were utilised in this work, the location of specimens with respect to material boundaries is considered essential information. The types of testing conducted and basic test parameters are also provided. Material properties and details on the microstructure are provided in Chapter 4. Three dimensional (3D) finite element assessment (FEA) of the mechanical properties are also presented. The impact of material boundaries on tensile test results are assessed. Additional tables and plots for Chapter 4 are provided in Appendix A.

Chapter 5 discusses the experimental residual stress measurements in the plate material and in the manufactured specimens. FEA of the welding processes for 3D models are presented for two types of heat source model: 1) block dump and 2) moving heat source. Additional data is provided in Appendix B.

Chapter 6 presents experimental results of fracture tests on samples with defects oriented parallel to the materials boundary. 2D FEA results assessing the impact of varying the multi-material thickness ratios and the impact of notch proximity to the material boundary are also presented. A 3D model assessment of the fracture test is presented for two cases: 1) considering zero initial residual stresses and 2) incorporating residual stresses, from Chapter 5. Additional plots and results are provided in Appendix C. Chapter 7 is presented in a similar format to that of Chapter 6 with experimental results presented first followed by both FE modelling. Additional plots and results are provided in Appendix D.

While short discussion sections are included in the relevant Chapters, Chapter 8 is a discussion of the broader implications of this research. Results detailed in Chapters 2 to 7 are drawn together and presented to the reader. Conclusions that can be drawn from the tests conducted and future work recommendations are additionally provided.

Chapter 2: Literature Review

2.1 Background

One of the major issues facing the nuclear industry today is the safe operation of aging RPVs. Many RPVs were designed to have an operational life of 40 years, the IAEA has stated that approximately 25% of the world's NPPs have been in operation for 30 years and about 70% for more than 20 years [IAEA, 2015] indicating the end of design life is close for a significant percentage of the worlds active NPPs. The main benefit of structural integrity procedures is that should the NPP be deemed fit-for-purpose (FFP) the operational life may be extended beyond that of the original design. In the UK the R6 code [British Energy, 2008] specifically addresses the assessment of defects in RPVs and has a major influence on whether a NPP is deemed to have sufficient structural integrity.

This particular work investigates Light Water Reactor (LWR) RPVs, spcifically the dissimilar metal weld in the RPV. The main body of the RPV is comprised of forged rings of ferritic steel. The inside of RPVs are generally lined with 3-10 mm of corrosion resistant material. Hence a clad material consists of ferritic base metal and several layers of stainless steel (or another corrosion resistant material). Stainless steels are incorporated due to their high resistance to corrosion and creep, even at elevated temperatures, when compared to ferritic materials [ASM International Handbook Committee, 2010].

2.2 Reactor Pressure Vessels

The electricity from a nuclear reactor is typicalled generated via the fission process which relies on the attraction and the associated energy between electrons and protons in atoms. A 1938 experiment bombarded a uranium atom with neutrons. The uranium

atom subsequently became 'excited' or unstable and split into parts releasing additional neutrons and a small amount of heat into the system. As additional neutrons are released into the system it is almost inevitable that a second atom will become excited thereby starting a chain reaction increasing the total amount of heat generated [Cooper, 2015; Chater, 2005; Rowinski et al., 2015]. The main concept of a nuclear reactor is to use the heat generated by the fission chain reaction to produce electricity.

The key component in a nuclear reactor is the reactor pressure vessel (RPV). This component is considered to be an irreplaceable critical component. A single event resulting in damage to the RPV could potentially lead to the fission products being released into the environment [IAEA, 2009*b*]. Within the RPV nuclear fuel pellets are stored in rods of zirconium alloy. These are generally referred to as 'fuel rods' [Cooper, 2015]. Control rods, which can be lowered and retracted from the system, absorb neutrons in the system without becoming unstable, thereby slowing, or stopping, the fission chain reaction. A fluid (water in the case of LWRs) is circulated around the fuel rods. As the fission process occurs, heat is generated converting water into steam. The steam is used to drive a turbine which in turn generates electricity.

There are several RPV designs. These have been broadly categorised into 'generations' based on the year of design and manufacture [Rowinski et al., 2015; IAEA, 2009*b*; Chater, 2005]. Several of the early prototype vessels were subject to substantial modification in later years most notably the *reaktor bolshoy moshchnosty kanalny* or RBMK RPV which was deemed to have an insufficient emergency protection system and was never adopted outside the Soviet Union. The focus of this work is specifically on light water reactors (LWRs) as these vessels are used extensively in the Western hemisphere, in both the marine and power generation industries [IAEA, 1999; Hirdaris et al., 2014].

Light water reactors (LWRs) are RPVs that use normal water as the coolant. There are two types of LWR: pressurised water reactors (PWRs) and boiling water reactors (BWRs). The PWR is the most common type of RPV currently in operation followed by

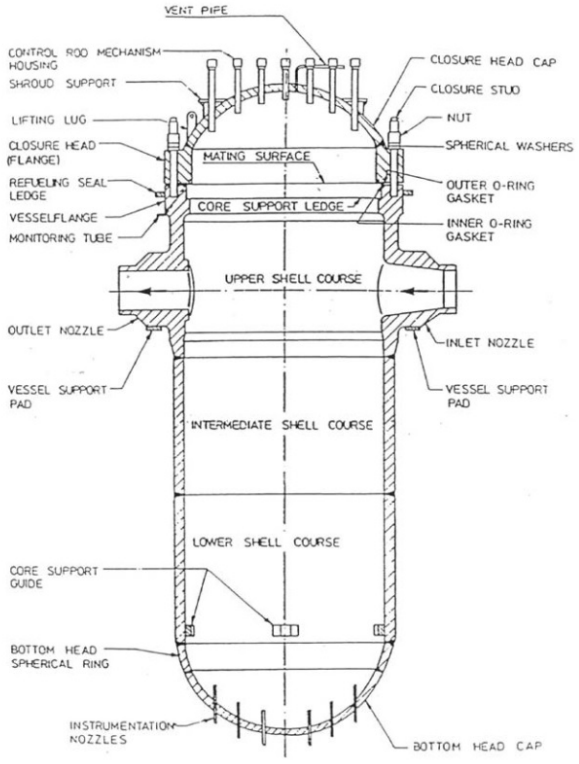

Figure 2.1: Typical Westinghouse PWR [IAEA, 1999]

the BWR [Rowinski et al., 2015; IAEA, 1999, 2009*b*,*a*]. There are many types of design of this form and they vary in terms of size, fabrication and operating parameters [IAEA, 1999]. The main difference between a PWR and a BWR is the number of cooling circuits and the associated operating pressures. The water in a PWR has two circuits where the BWR has only one. In a PWR the first circuit the water is circulated around the fuel rods where it becomes heated by the fission process. The water is pressurised so that it maintains its liquid form even under high temperatures. In the secondary coolant system the hot water is heated further until it begins to boil and produces steam. The steam drives a turbine which generates electricity. The condensed steam is then returned to the primary circuit.

Pressurised water reactors (PWRs) are generally keep at a relatively high pressure to ensure the coolant remains in a liquid form. The Westinghouse design (Figure 2.1) is a typical example of the types of LWR found in the Western hemisphere [IAEA, 1999, 2009*a*]. It should be noted that Figure 2.1 does not show the second cooling circuit. The Westinghouse RPV is designed to by operated at a pressure of 15.51 MPa

at temperatures between 280-325 °C [IAEA, 1999]. In comparison BWRs have only a single coolant circuit and the steam is generated inside the RPV. As a result BWR vessels operate at a significantly lower pressure (approximately 7 MPa) in comparison to PWRs [Buongiorno, 2010].

Both PWRs and BWRs are fabricated using low alloy carbon steels (for the vessel shell) and internal austenitic stainless steel cladding between 3-10mm in depth. The specific materials in use are very much dependent on the year of design and manufacture. Earlier vessels typically used ASTM SA302 Grade B while later vessels used ASTM SA533 Grade B Class 1 [IAEA, 1999, 2009*a*]. To accommodate additional equipment BWRs are larger in diameter than PWRs.

2.3 Factors influencing structural integrity

There are three main contributors to the structural integrity of a component: material properties, load history and the presence, or absence, of a defect [Vitale, 1989; IAEA, 2010]. These factors, in relation to relevant materials and fabrication processes, are discussed in more detail in the following sections.

2.3.1 Material properties and fabrication

Materials, specifically metals, can fail in either a brittle or a ductile manner. Brittle fracture occurs almost instantaneously upon initiation of a defect and absorbs little energy. The mechanism controlling brittle fracture is known as cleavage and can be described as a 'separation along specific crystallographic planes' [Anderson, 2005]. Ductile failures, in comparison, occur slowly and absorb significantly more energy than brittle failures. Fracture occurs via micro-void coalescence (MVC) where yielding of the materials leads to the formation of 'voids'. Over time these voids grow in frequency and diameter and the ligament between subsequent voids plastically collapses. The voids then join together (coalesce) this is typically seen as extension of a defect. One characteristic of the ductile failure mechanism is the formation of deformation bands. These

deformation bands typically form at 45° to the applied stress resulting in the formation of 'shear lips' in the case of rectangular shaped specimens, or, 'cup and cone' in the case of spherical shaped specimens. The fracture surface of ductile failures are dimpled and appear dull, the fracture surfaces of specimens having failed by cleavage fracture are comparatively flat and 'shiny'.

With regards to metals the crystallographic structure can impact the failure mechanism. In ferritic, body center cubic (BCC) materials the primary deformation mechanism occurs via screw dislocations, which are controlled by the interaction between the dislocation and the crystal lattice. For BCC materials deformation is dominated by strain rate and lattice friction, the latter of which is temperature dependent. Hence BCC materials can transition between brittle and ductile failure mechanisms. Austenitic steels have a face-center cubic (FCC) structure which primarily deform via edge dislocations. For austenitic materials the resistance to deformation is primarily controlled by the number of dislocations, where an increasing number of dislocations will increase the materials ability to resist deformation, at the cost of decreasing the ductility of the material. Similar to BCC structures, the dislocation density of FCC materials are also affected by strain rate and temperature [Dunnett, 2014].

The thickness of a material can also impact the failure mode due to the change in constraint when moving from the surface of a component to the mid-thickness. On the surface stress in the thickness direction is negligible in comparison to other directions this is often referred to as 'plane stress condition'. In the mid-thickness region, due to the constraining effect of the surrounding bulk material, the stresses in the thickness direction are no longer negligible. Therefore a state of triaxiality exists (i.e. there are stresses in all three orthogonal directions). Materials behave in a more brittle manner when subject to triaxial stress states [Anderson, 2005]. Fracture testing of materials promotes brittle fracture mechanisms, typically through specimen design, to ensure conservative results. For a ductile material triaxiality promotes fracture in the mid-thickness region but deformation bands may still form on the surfaces. As a result a defect is more likely to propagate in the mid-thickness region. This phenomena is gen-

erally referred to as 'crack tunnelling'. Fracture specimens can be machined so as to reduce the cross sectional area in the region of a defect. Specimens manufactured in this way are called 'side-grooved' specimens and are less likely to be subject to crack tunnelling.

In this work a dissimilar metal weld comprised of base material (SA508) and cladding (stainless steel) was utilised. The base material is generally clad using a welding process. The cladding consisted of three layers of stainless steel, the first layer was comprised of grade 309, the following two layers of grade 308. The chemical compositions for the materials are given in Table 2.1. The composition at the materials boundary is complex and lies somewhere between that of the base material and that of the first layer of cladding due to dilution effects. Dilution describes the change in composition of the cladding material during the welding process. A high dilution indicates that more than one layer of cladding needs to be deposited to ensure the required material properties and/or microstructure is achieved [Gooch, 1976]. From a structural integrity perspective the carbon content of the material is of significance in that it will essentially control the hardness and potentially the ductility of the region [Ashby and Jones, 2006].

RPVs are welded in numerous locations generally at, or close to, global stress concentrating features. A welded component can be broken down into three zones: parent material (PM), heat affected zone (HAZ) and weld metal (WM). The PM refers to areas which remain unchanged by the heat input of the welding process. The HAZ describes the region close to the weld where the application of heat has changed the microstruc-

Table 2.1: Chemical composition of the ferritic and austenitic materials (From: [Washko and Aggen, 1990; IAEA, 1999])

Type	C	Mn	Si	Cr	Ni	P	S	Mo	V
308	0.080	2.000	1.000	21.000	12.000	0.045	0.030	-	-
309	0.200	2.000	1.000	24.000	15.000	0.045	0.030	-	-
SA508 G3	0.250	1.500	0.400	0.250	1.000	0.015	0.015	0.600	0.050

ture of the PM. The WM zone typically describes the area in which a filler material has been used to join the two pieces together.

There are many different types of welding including manual, semi-automatic and automatic processes. The specific processes typically used in RPVs are submerged arc welding (SAW) and manual metal arc welding (MMA) [IAEA, 1999]. The MMA and SAW techniques use electricity to form an arc between the workpiece and an electrode. The arc generates heat causing the surface of the workpiece to melt, this region is often referred to as the weld pool. With MMA the electrode is consumable and often coated with flux. The weld parameters are stated to be 'greatly influenced by the chemical composition of the flux coating' [*Submerged-arc welding*, n.d.]. When the electrode and flux melt they form a gas shield around the weld pool essentially protecting the area from the atmosphere. The MMA process is manual and therefore weld quality is highly dependent on the skill of the welder. Unlike MMA the SAW process can be either semi or fully automatic. A consumable continuously fed bare wire is used to form the arc. Flux powder is placed directly on the workpiece prior to welding and this forming a protective shield around the weld pool. As the arc is covered by the flux powder the thermal efficiency of this method is 'as high as 60%' compared with the 25% efficiency of the MMA process [*Submerged-arc welding*, n.d.; *The manual metal arc process (MMA Welding)*, n.d.]. However, as the weld pool is not visible to the operator the input parameters (such as current, voltage and travel speed) must be carefully selected.

Davis [Davis, 1994] defined a weld overlay as 'the deposition of a filler metal on a base metal (substrate) to impart some desired property to the surface that is not intrinsic to the underlying base metal'. In the case of RPVs the inside of the vessel is generally clad, or overlay, with an austenitic stainless steel or a nickel based alloy as these materials have an improved resistance to corrosion compared to carbon steels resulting in longer service lifetimes [Davis, 1994; Hanninen et al., 2006; IAEA, 1999]. While there are a number of methods to clad a material RPVs are generally clad using multiple wire, single wire or strip cladding techniques [IAEA, 1999; Wei et al., 2010; Server

and Nanstad, 2015]. Gooch [Gooch, 1976] additionally noted the use of metal inert gas (MIG), tungsten inert gas (TIG) and plasma welding processes.

2.3.2 Loading and stress concentration factors

In addition to the variation in material properties welded details generally exist at, or close to, regions of stress concentration. Typical stress concentrating details can be defined as either local or global geometrical effects: Global effects are defined as regions such as large openings, curved beams, and eccentricity, while local effects are regions subjected to nonlinear stresses in addition to the structural stress [International Institute of Welding, 2008]. The welding process results in a change of shape to a component and hence, a local stress concentration exists in welded geometries. The weld toe, described by Maddox as 'the junction of the plate surface and weld metal' [Maddox, 1991], is typically the location at which the highest stress occurs. The weld toes are generally considered the locations most at risk of cracking.

Figure 2.2 [Maddox, 2000] clearly shows the influence of stress concentrating details under fluctuating loads. Figure 2.2 shows that welded geometries have a severe reduction in fatigue life in comparison to both parent materials and global stress concentrators. The effect of material strength on fatigue life for parent material and welded components is shown in Figure 2.3 [Maddox, 2000]. As can be seen the parent materials have an increased fatigue strength with increasing yield strength, even in the presence of a global stress concentrating feature. Welded geometries however do not exhibit this behaviour - the fatigue strength remains the same, regardless of the materials strength, due to the stress concentrating features at this location. Maddox showed that removing the weld toe offers some return of benefit from the material strength for fatigued welds.

Pollard and Cover [Pollard and Cover, 1972] investigated the fatigue strength of various geometries and welding processes. They reported that the SAW process 'appears to be capable of superior welds' when compared to MMA processes in terms of the weld shape and soundness. Indeed many sources surmise that the weld shape (i.e. geomet-

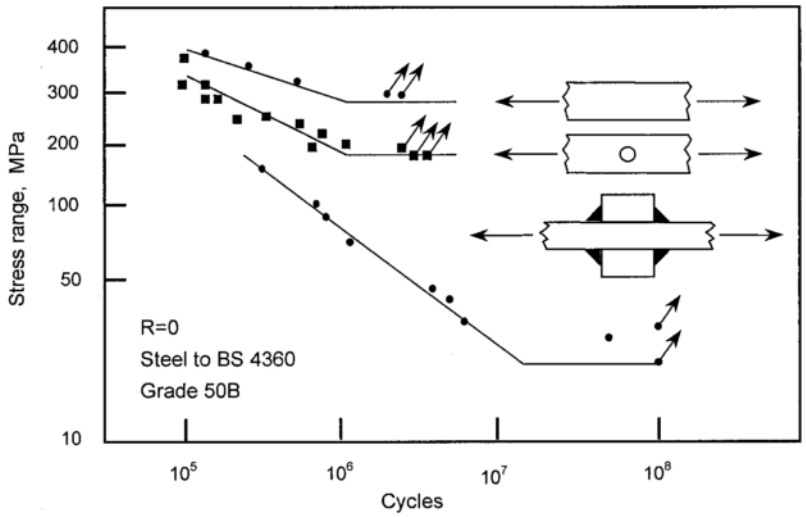

Figure 2.2: Effect of welding on fatigue strength [Maddox, 2000]

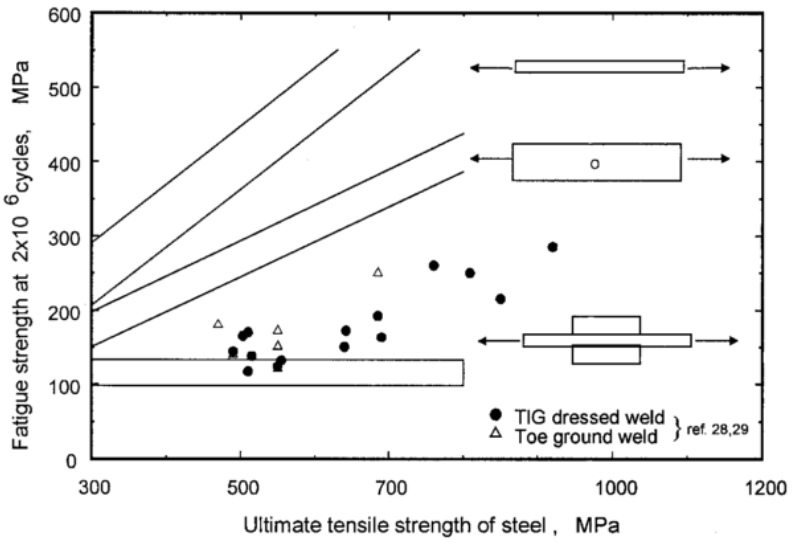

Figure 2.3: Effect of removing weld toes on fatigue strength [Maddox, 2000]

rical parameters such as weld toe/root radius and angle) is crucial to the fatigue life, and that the welding process itself is only relevant in terms of the geometrical parameters that can be expected from each type of process [Branco et al., 1999; Caccese et al., 2006; Crupi et al., 2009]. It should be noted however that automatic welding processes tend to provide better weld profiles than MMA processes which are, by their nature, highly dependent on the skill of the welder [Crupi et al., 2009]. Given the dependancy of geometrical parameters to fatigue life many codes and standards advocate the use of suitably qualified welders for MMA applications [British Standards Institute, 2015*b*; British Energy, 2008; British Standards Institute, 2018*a*; IAEA, 1966].

It is clear from the preceding comments that the structural integrity of an RPV is paramount in terms of safety. As previously stated there are a number of design codes and standards for the design and fabrication of RPVs namely: ASME Boiler and Pressure Vessel Code (BPVC) [American Society of Mechanical Engineers ASME, 2015*c*,*a*,*b*], PD5500 [British Standards Institute, 2015*b*] and BS EN 13445 [British Standards Institute, 2018*a*]. The background and development of these standards is complex and the result of many years of research and experience in industrial applications [Spence and Nash, 2004; IAEA, 1966].

The original structural integrity assessments of RPVs were based on the maximum stresses on the vessel during operation or accidental loading. The majority of pressure vessels are tested between 1.5 to 2 times the design pressure prior to service to ensure the integrity of the vessel. Engineering knowledge has progressed significantly since the 1950's and the design codes and standards have been subjected to many changes to reflect progress in various fields. However, the vast majority of RPVs in service today have been operating for over 20 years and are now reaching the end of their original design lives. As these RPVs were designed to earlier versions of the codes and standards there may be a significant amount of conservatism in the estimated design lives. In order to reduce the conservatism a full understanding of the factors influencing material and component performance must be understood. Furthermore regardless of the

amount of conservatism present in the original design of a RPV the structural integrity must be maintained.

The majority of life extension techniques adopted by industry are based on fracture mechanics theory which assesses the structural integrity of a component in the presence of a postulated defect. There are many specific codes and standards outlining such techniques such as BS7910 and R6 [British Standards Institute, 2015*a*; British Energy, 2008]. There are differences in the assessment methods depending on the standard or code adopted. BS7910 is applicable to any industry whereas the R6 code is specific to the nuclear industry (though it may be adopted for other industries). Irrespective of the chosen assessment method an initial defect size and location is critical required information. It is clear from the previous sections that welding introduces defects to components. For clad welds the weld root is not accessible, furthermore defects will be located sub-surface. To locate and size sub-surface defects non-destructive testing (NDT) inspection techniques such as ultrasonics are typically applied. There are a range of ultrasonic inspection methods available; automated ultrasonics (AUT), focussed phased array (FPA), and time-of-flight diffraction (TOFD). Each method has benefits and limitations and, similar to welding, results are operator dependent. BS7910 Annex T provides some information on the minimum flaw size that can be reliably detected and sized. It states that, for the aforementioned techniques, defects of greater than 2×7 mm can be reliably sized, in homogeneous ferritic materials. The sizing accuracy of defect length can vary by ±7 mm while the depth accuracy may vary by ±1.5 mm. Hence any identified defect may range in ultimate size from anywhere between 0.5×1 mm to 3.5×14 mm. As previously stated these defect sizes are relevant only to sub-surface defects in homogeneous ferritic materials. Special consideration is required for austenitic stainless steels where coarse microstructure effects can negatively impact the accuracy (i.e. resulting in an increase to postulated defect sizes). Clad welds in particular are subject to significant accuracy issues due to a combination of variable microstructure, variable material densities and the relative thickness of each material [British Standards Institute, 2015*a*].

2.3.3 Temperature

The majority of RPVs operate at temperatures that differ from room temperature. Temperature has a significant impact on materials performance, both austenitic and ferritic steels have crystal structures that are susceptible to changes in failure mode dependent on temperature. At colder temperatures failure is more likely to occur by brittle fracture, at higher temperatures metals are more likely to fail in a ductile manner. The change in failure mode does not occur at a specific temperature but rather over a range of temperatures. The 'transition temperature' (TT) is the temperature at which the impact energy lies between the upper shelf (ductile failure) and the lower shelf (brittle failure). A Charpy impact test is the simplest and most often adopted method of estimating the toughness of a material, furthermore Charpy impact energy can be used to estimate fracture toughness using various correlations such as that shown in Equation 2.3.1 [British Standards Institute, 2015*a*]. These correlations are known however to be overly conservative. Therefore life extension assessments often require full thickness fracture toughness testing.

While it is ideal to have fracture toughness testing conducted at the operating temperature of the vessel this is not always possible. Wallin [Törrönen et al., 1984] showed that the fracture toughness at specific temperatures could be calculated from Charpy correlated data in with a known performance of 25 mm thick specimens at other temperatures. This method is often referred to as the 'master curve' method and is calculated as shown in Equation 2.3.2. The benefit of the master curve method is that by defining the fracture toughness performance for a known specimen thickness (e.g. 25 mm) over a range of temperatures the impact of other factors such as environmental degradation and geometrical changes, can be represented as a shift of the entire curve along the temperature axis. Smith and Rolfe [Smith and Rolfe, 1994] showed that for an RPV steel (A533-B) modifying constraint had a significant affect on measured fracture toughness. They showed that shallow cracked samples (i.e. sample with low in-plane constraint) had higher values of fracture toughness in comparison to deep cracked

samples, hence the position of T_0 shifts to the left (i.e. lower value of T_0) in comparison to the curve representing that of deeply cracked specimens.

$$K_{mat} = \left[\left(12\sqrt{C_v} - 20 \right) \left(\frac{25}{B} \right)^{0.25} \right] + 20 \tag{2.3.1}$$

Where K_{mat} is the fracture toughness, C_v the Charpy impact energy and B represents the thickness of the sample.

$$K_{mat} = 20 + \{11 + 77e\left[0.019\left(T - T_0 - T_K\right)\right]\} \left(\frac{25}{B} \right)^{\frac{1}{4}} \left[ln\left(\frac{1}{1 - P_{fail}} \right) \right]^{\frac{1}{4}} \tag{2.3.2}$$

Where K_{mat} is the fracture toughness, T is the temperature at which K_{mat} is to be determined, T_0 is the temperature for a median toughness of 100 MPa$\sqrt{\text{m}}$ in a 25 mm thick sample, T_K is the temperature describing scatter (generally assumed to be 25°C), B represents the thickness of the sample and P_{fail} represents the probability that the fracture toughness is less than estimated (BS 7910 recommends a value of $P_{fail} = 0.05$ [British Standards Institute, 2015*a*]).

2.4 Fracture Mechanics

Research in the field of fracture mechanics can be broadly split into two sections: Linear-elastic fracture mechanics (LEFM) and elastic-plastic fracture mechanics (EPFM) [Anderson, 2005; Kapadia, 2014]. LEFM and EPFM were originally derived to investigate static loads only and are described in more detail in the following sections. However it is clear that the majority of components in service are exposed to fluctuating loads. RPVs for example are exposed to fluctuating temperatures and pressures. The initiation and propagation of cracking due to a fluctuating elastic load is known as the fatigue mechanism. This type of loading mechanism is particularly important in welded geometries and in many cases it is the structural integrity of the weld that dic-

tates the safe life of a component. The application of LEFM to fatigue cracking is well established. The effect of large scale plasticity on fatigue crack growth (FCG) has yet to be adequately defined. In this report the fracture mechanics for loading in fatigue is described as a subset of LEFM.

2.4.1 Linear Elastic Fracture Mechanics (LEFM)

Griffith investigated the global energy balance and found that the fracture stress (σ_f) could be expressed in terms of the material properties as shown in Equation 2.4.1. Equation 2.4.1 is suitable only for brittle materials such as glass and underestimated the fracture strength for ductile materials substantially. Later modifications included a function to account for additional plasticity effects (Equation 2.4.2), however Equation 2.4.2 was found to be suitable for materials with a moderate amount of yielding at the crack tip only. Materials that exhibit substantial amounts of plasticity (i.e. such as metals) cannot be comprehensively analysed using these methods [Anderson, 2005].

$$\sigma_f = \sqrt{\frac{2E\gamma_s}{\pi a}} \tag{2.4.1}$$

$$\sigma_f = \sqrt{\frac{2E(\gamma_s + \gamma_p)}{\pi a}} \tag{2.4.2}$$

Where: E represents Young's modulus, γ_s the surface energy, γ_p the plastic work per unit area of surface created, a the half crack length.

Irwin proposed that crack extension was a measure of the energy release rate (G). Where the energy release rate was defined as the rate of change in potential energy with respect to the crack area. The benefit of Irwin's approach compared to Griffith's is that it is much more suitable for engineering purposes. The energy release rate is also referred to as the crack driving force (CDF) as crack extension will only occur when

the CDF reaches a critical value. Irwin showed that the energy release rate for a wide plate, in plane stress conditions, with a flaw could be calculated using Equation 2.4.3 .

$$G = \frac{\pi\sigma^2 a}{E} \tag{2.4.3}$$

Where: σ represents the stress, a the half crack length, and E the Young's modulus.

Further work in the field led to a closed form solution around the crack tip suitable for linear elastic isotropic materials known as the stress intensity factor (SIF, denoted using 'K'). The SIF is a single parameter that completely describes the conditions at the crack tip for a particular mode of loading and geometrical constraint. The three modes of loading are depicted in Figure 2.4. Where as shown: Mode I represents crack opening, Mode II in-plane shear loading, and Mode III out-of-plane shear loading.

The SIF equation for mode I loading is shown in Equation 2.4.4. For linear elastic materials under plane stress or plane strain conditions these parameters have the relationships described by Equation 2.4.5. For plane stress conditions the Young's Modulus remains as given (Equation 2.4.6), for plane strain conditions the Young's Modulus is recalculated as per Equation 2.4.7. It should however be noted that the energy release rate (G) is a global parameter while the SIF (K) is a local parameter.

$$K_I = Y\sigma\sqrt{\pi a} \tag{2.4.4}$$

$$G = \frac{K_I^2}{E'} \tag{2.4.5}$$

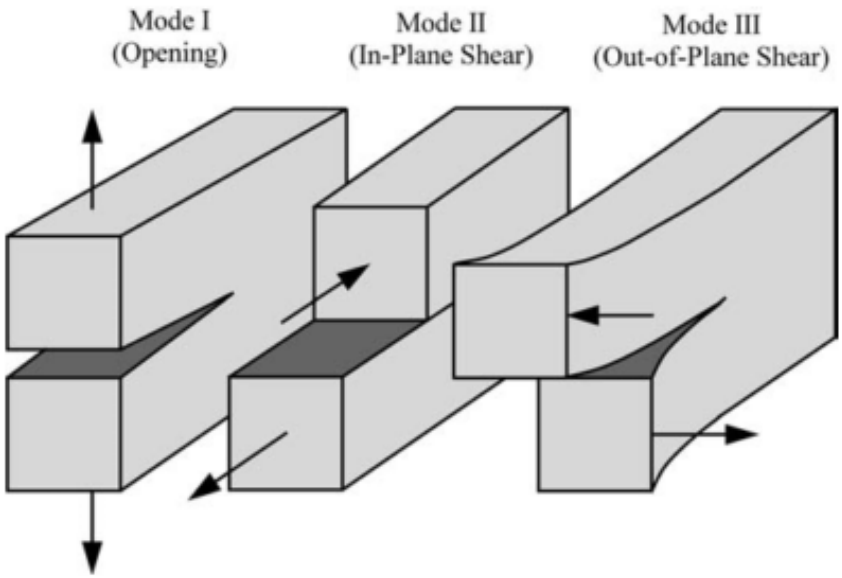

Figure 2.4: Three modes of loading that can be applied to a crack [Anderson, 2005]

Where E′ is calculated for either the plane stress condition:

$$E' = E \tag{2.4.6}$$

or, for the plane strain condition as:

$$E' = \frac{E}{1 - \nu^2} \tag{2.4.7}$$

Where: K_I is the SIF, Y a geometrical constant, σ the stress, a crack length, G energy release rate, E Young's modulus, and ν Poisson's ratio.

From Equations 2.4.4 to 2.4.7 it is clear that crack growth cannot occur until the CDF reaches a critical value (i.e. either K_{IC} or G_c depending on the method used) this critical value is known as the fracture toughness.

The main drawback of LEFM is that it is only applicable when the plastic region sounding a cracked body is small in relation to the overall structural dimensions. This is commonly referred to as small-scale yielding (SSY). When materials fail in an inelastic manner LEFM analyses are no longer valid and elastic-plastic analyses should be applied [Anderson, 2005; IAEA, 2010; Kamel, 2010].

2.4.2 Fatigue

As previously stated fatigue cracking can be defined as the initiation and propagation of a flaw under repeated or cyclic elastic loading. It is therefore a time dependent parameter. Paris and Erdogan found a power-law relationship in fatigue crack growth [Anderson, 2005] for metallic materials which can be described using Equation 2.4.8.

$$\frac{da}{dN} = C(\Delta K)^m \tag{2.4.8}$$

Where: da/dN is the rate of crack growth in mm/cycle, C and m are material constants. The range of SIF is calculated from $\Delta K = K_{max} - K_{min}$, where K_{max} and K_{min} represent the SIF at maximum and minimum loads, respectively.

Figure 2.5 shows a typical fatigue crack growth rate (FCGR) curve for metallic materials. It should be noted that the FCGR of a material is highly dependent on the stress ratio (the ratio between minimum and maximum stresses) and environmental factors. Higher stress ratios generally result in lower FCGR thresholds while materials in corrosive environments generally crack at a faster rate than those in air. It is important to note that the power-law equation Equation 2.4.8 is only applicable when steady-state crack growth occurs (Stage II). It is not relevant during the initiation phase (Stage I) of crack growth nor during the final stages of crack growth (Stage III).

Fatigue generally occurs under elastic conditions in regions of stress concentrating details [Maddox, 1991]. For a stationary crack the crack tip parameters have been defined using the SIF, K, (Equation 2.4.4). Modifying Equation 2.4.4 to account for cyclic stresses, as opposed to a static stress, gives Equation 2.4.9. The SIF for a crack under cyclic conditions is defined as the difference between the SIF at a maximum load and the SIF at a minimum load [Anderson, 2005].

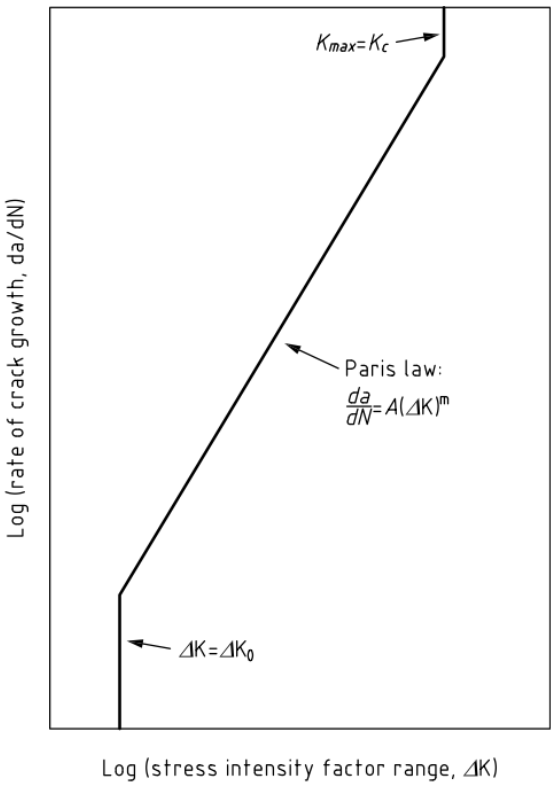

Figure 2.5: Paris' law for fatigue crack growth [British Standards Institute, 2015*a*]

$$\Delta K = Y\Delta\sigma\sqrt{\pi a} \tag{2.4.9}$$

Where: $\Delta\sigma$ is the stress range calculated from $\Delta\sigma = \sigma_{max} - \sigma_{min}$. σ_{max} and σ_{min} represent the stress at maximum and minimum loads, respectively.

From Equation 2.4.8 and Equation 2.4.9 the crack growth rate can now be defined as a function of crack size, stress, materials properties and geometrical constraint (Equation 2.4.10). By integrating Equation 2.4.10 the number of cycles required for a crack to grow from an initial size (a_i) to a final size (a_f) can be calculated (Equation 2.4.11).

$$\frac{da}{dN} = C(Y(\Delta\sigma)\sqrt{\pi a})^m \tag{2.4.10}$$

$$N = \int_{a_i}^{a_f} \frac{da}{C(Y(\Delta\sigma)\sqrt{\pi a})^m} \tag{2.4.11}$$

As specified earlier LEFM is not applicable to materials that undergo significant plasticity. However, it should be noted that fatigue cracking generally occurs when the applied loads are within the materials elastic region. It is therefore considered acceptable to apply LEFM fatigue theory to materials such as metals for the purposes of life assessment [British Standards Institute, 2015*a*; British Energy, 2008].

2.4.3 Elastic Plastic Fracture Mechanics (EPFM)

Assessment of elastic-plastic fracture mechanics (EPFM) is generally conducted using either crack-tip-opening displacement (CTOD) or the J-integral methods. The CTOD method assumes that large scale yielding in elastic-plastic materials results in crack tip blunting and that the degree of crack tip blunting is proportional to the toughness of the material [Anderson, 2005]. Plasticity ahead of the crack tip results in an effective crack length which is longer than the blunted notch. For a relatively small plastic zone (i.e. LEFM conditions) under plane stress conditions the CTOD can be estimated from the displacement at the physical crack tip and related to K_I and G as shown in Equation 2.4.12. The amount of plasticity in the specimen can be calculated using experimental methods to measure the crack mouth displacement (V) assuming that the two halves of the specimen rotate around a hinge point. The CTOD of a non-linear material is simply assumed to be equal to the summation of the elastic and plastic parts as shown in 2.4.13. Specimen dimensions are shown in Figure 2.6.

$$\delta_{el} = \frac{4}{\pi}\frac{K_I^2}{\sigma_y E} = \frac{4}{\pi}\frac{G}{\sigma_y} \tag{2.4.12}$$

Where: δ_{el} is the elastic CTOD, K_I the mode I stress intensity factor, σ_y the yield stress, E the Young's modulus, and G the energy release rate.

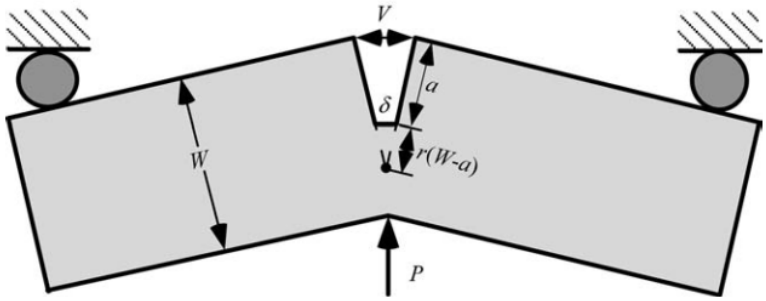

Figure 2.6: CTOD estimation using three point bend specimen with effective crack tip estimated from notch opening and rotation around hinge point [Anderson, 2005]

$$\delta = \delta_{el} + \delta_{pl} = \frac{K_I^2}{m\sigma_y E'} + \frac{r_p(W+a)V_p}{r_p(W-a)+a} \tag{2.4.13}$$

Where: m is a dimensionless constant, E' the effective Young's modulus (see Equations 2.4.6 and 2.4.7), r_p a plastic rotational factor (typically 0.44 for test specimens), W is a specimen dimension, a the crack length, V_p is the measured plastic displacement at the crack mouth (see Figure 2.6).

The alternative EPFM method is the J-integral method proposed by Rice [Anderson, 2005]. Rice showed that the elastic component of the energy release rate for a linear-elastic material could be calculated using Equation 2.4.14. For plane stress conditions the Young's Modulus remains as given, for plane strain conditions Equation 2.4.7 should be applied. Hence it can be seen that for linear elastic case: $J = G$.

$$J = \frac{K_I^2}{E'} \tag{2.4.14}$$

Where: J is the non-linear energy release rate, K_I the mode I SIF, E' is the Young's modulus for the appropriate boundary condition (see Equations 2.4.6 and 2.4.7), ν the Poisson's ratio, G is the global energy release rate for an elastic material.

The J-integral can also be used as a stress intensity parameter when certain conditions are met. Rice derived the J-integral for an arbitrary path around the crack tip in the anti-clockwise direction to be as shown in Equation 2.4.15 to Equation 2.4.17 [Anderson, 2005; Kapadia, 2014; Bettinson, 2001].

$$J = \int_{\Gamma} \left(w dy - T_i \frac{\delta u_i}{\delta x} ds \right) \tag{2.4.15}$$

Where: w is the strain energy density, T_i the components of the traction vector, u_i the displacement vector components, ds the length of an increment along the contour Γ.

$$w = \int_{\epsilon_{ij}}^{0} \sigma_{ij} d\epsilon_{ij} \tag{2.4.16}$$

$$T_i = \sigma_{ij} \eta_{ij} \tag{2.4.17}$$

Where: σ_{ij} is the stress tensor, ϵ_{ij} the strain tensor, η_j the unit vector normal to the path integral.

Elastic-plastic materials can be successfully modelled as a non-linear materials, provided no elastic-plastic unloading occurs, by assuming appropriate non-linear relationships between stress and strain. The Ramberg-Osgood power law relationship (Equation 2.4.18), is one such example. For J to remain path independent the stress-strain close to the crack tip must vary. Additionally, regions close to the crack tip are domi-

nated by plastic strains and the stress-strain behaviour reduces back to the non-linear relationship. By applying boundary conditions the stress (σ_{ij}) and strain (ϵ_{ij}) tensors were derived as shown in Equation 2.4.20 and Equation 2.4.21 respectively. These are commonly referred to as the near-tip singularity fields, the HRR solution or the HRR stress field [Anderson, 2005; Bettinson, 2001; Kamel, 2010; Kapadia, 2014; Hutchinson, 1983].

$$\frac{\epsilon}{\epsilon_o} = \frac{\sigma}{\sigma_o} + \alpha \left(\frac{\sigma}{\sigma_o}\right)^n \tag{2.4.18}$$

and;

$$\epsilon_o = \frac{\sigma_o}{E} \tag{2.4.19}$$

Where: σ_o represents the reference stress (typically the yield stress), α is a dimensionless constant, η the strain-hardening exponent.

$$\sigma_{ij} = \sigma_o \left(\frac{EJ}{\alpha \sigma_o^2 I_n r}\right)^{\frac{1}{n+1}} \tilde{\sigma_{ij}}(n, \theta) \tag{2.4.20}$$

$$\epsilon_{ij} = \frac{\alpha \sigma_o}{E} \left(\frac{EJ}{\alpha \sigma_o^2 I_n r}\right)^{\frac{n}{n+1}} \tilde{\epsilon_{ij}}(n, \theta) \tag{2.4.21}$$

Where: I_n is a function of n, $\tilde{\sigma_{ij}}$ and $\tilde{\epsilon_{ij}}$ are functions of n and θ.

The J-integral in Equation 2.4.20 and Equation 2.4.21 defines the amplitude of the HRR field and the conditions within the plastic zone.

Plastic zone size and shape

Dodds [**?**] investigated the shape of the plastic zone for plane stress and plane strain conditions under Mode I loading conditions. For elastic materials Equations 2.4.22 and 2.4.23 can be used to calculate the shape of the plastic zone. However, for elastic-plastic materials, particularly those with a power-law hardening relationship (Equation 2.4.18), there is no definite yield point and relatively small changes to the chosen value of yield stress can have a significant impact on the size and shape of the plastic zone. Figure 2.7 shows the plastic zone size and shape calculated for both an elastic material (dashed black line) and an elastic-plastic power-law hardening material with a low strain hardening effect. In the case of the elastic-plastic material two cases are investigated: firstly the effective stress is assumed to be equal to the yield stress of the material (dark grey area, $\sigma_e/\sigma_y = 1.00$), as was the assumption used in the elastic calculation. Secondly the ratio of effective stress to yield stress is reduced slightly (light grey area, $\sigma_e/\sigma_y = 0.92$. As shown by comparing the elastic case to that of the elastic-plastic case where $\sigma_e/\sigma_y = 1.00$) it can be seen that elastic-plastic analysis results in a significantly smaller plastic zone size. Comparing the two elastic-plastic cases show that a small change in the ratio of σ_e/σ_y increases the size of the plastic zone considerably.

$$r_y(\theta) = \frac{1}{4\pi}\left(\frac{K_I}{\sigma_y}\right)^2\left[1 + cos\theta + \frac{3}{2}sin^2\theta\right] \tag{2.4.22}$$

$$r_y(\theta) = \frac{1}{4\pi}\left(\frac{K_I}{\sigma_y}\right)^2\left[(1+2\nu)^2(1 + cos\theta) + \frac{3}{2}sin^2\theta\right] \tag{2.4.23}$$

Figure 2.8 plots the shape of the plastic zone size for three values of η when the ratio of σ_e/σ_y is assumed to be 1.00. The three values of strain hardening (η): 5, 10, and 50, are broadly representative of materials with high, medium and low strain hardening

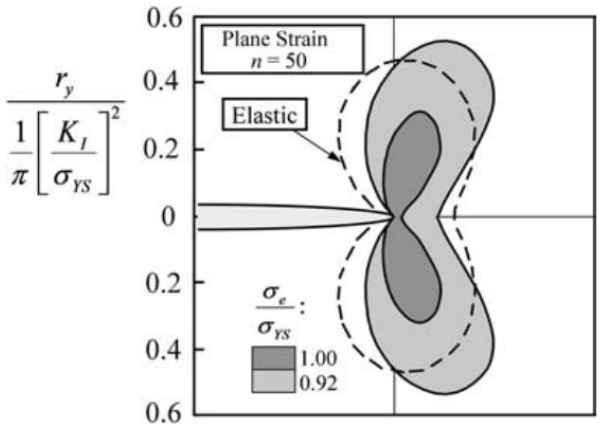

Figure 2.7: Plastic zone size calculations for plane strain assumption using elastic and elastic-plastic material properties. [Anderson, 2005]

ability respectively. It is interesting to note that η appears to influence not only the size of the plastic zone but also the shape. Materials with low and medium strain hardening capabilities appear to have plastic zones smaller than that of the high strain hardening material and, as discussed previously, the high strain hardening material exhibits a plastic zone size significantly smaller than that predicted using the elastic analysis.

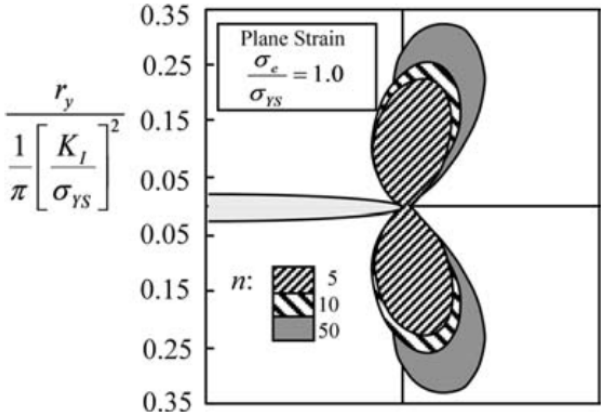

Figure 2.8: Plastic zone size calculations for plane strain assumption using elastic and elastic-plastic material properties. [Anderson, 2005]

2.5 Engineering Critical Assessments (ECAs)

Engineering Critical Assessment (ECA) procedures such as those outlined in R6 and BS 7910 [British Energy, 2008; British Standards Institute, 2015*a*] assess the impact of a postulated defect on a known material under presumed operating parameters. The size and location of any postulated defect is of significance in this type of assessment. The defect may be idealised to some 'worst case' scenario, or where applicable, may be based on estimated defect sizes from some NDT method. The likelihood of failure due to the presence of a defect is visualised using a failure assessment diagram (FAD). Figure 2.9 shows a typical FAD. The L_r and K_r point/(s) for a specific defect with known loading condition/(s) is bounded by the curve (generally based on material properties). The position of the L_r and K_r points relative to the bounding curve stipulate the level of risk to the overall structural integrity. Points of (L_r, K_r) that lie within the bounding curve are 'safe', points that lie on, or outside, the bounding curve are considered to be 'unsafe' [O'Connor et al., 2019].

The L_r point represents the ratio of applied load to plastic collapse load, L_r (Equation 2.5.1), while the K_r point represents the ratio of stress intensity to fracture toughness taking due account of residual stresses (Equation 2.5.2. K_I is calculated as per Equation 2.5.3). As can be seen the location of the (L_r, K_r) (for any given input parameters) can be relatively easily assessed as to be being 'safe' or 'unsafe' using the FAD.

$$L_r = \frac{\sigma_{ref}}{\sigma_y} \tag{2.5.1}$$

$$K_r = \frac{K_I}{K_{mat}} \tag{2.5.2}$$

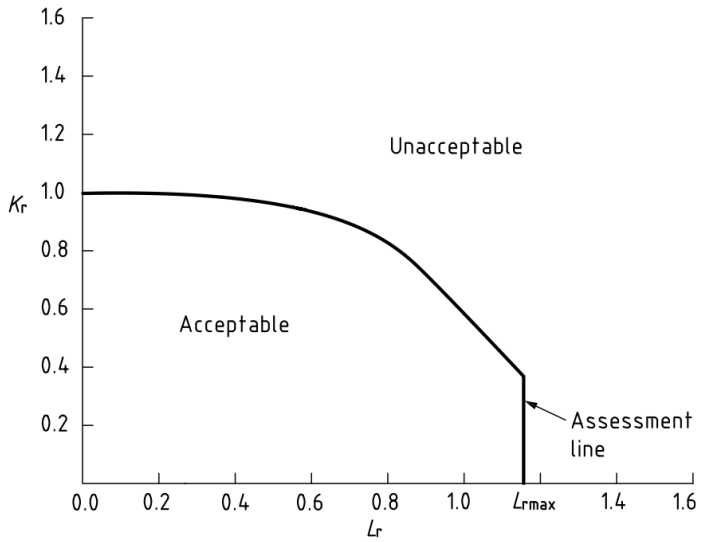

Figure 2.9: Failure Assessment Diagram. Modified from [British Standards Institute, 2015*a*]

$$K_I = K_I^P + VK_I^S \tag{2.5.3}$$

The reference stress σ_{ref} (Equation 2.5.1) is a function of the geometry, loading and defect size. The stress intensity parameter, K_I (Equation 2.5.2), is dependent on contributions from both primary and secondary loads (Equation 2.5.3). The parameter V *combines the mechanical relief of residual stress and plasticity correction,* ρ*, into a single factor* [Smith, 1997]. This plasticity correction factor, V, should be calculated as per Equation 2.5.4 for $L_r < 1.05$ and assumed to be 1 for $L_r > 1.05$.

$$V = \min \begin{cases} 1 + 0.5L_r + 0.02K_I^s \left(\frac{L_r}{K_I^P}\right)(1 + 2L_r) \\ 3.1 - 2L_r \end{cases} \tag{2.5.4}$$

The fracture toughness, K_{mat}, can be calculated in a variety of ways. The preferred method is from fracture toughness testing, conducted to a relevant test method, on full thickness specimens.

2.6 Chapter 2 Summary

In this chapter we have discussed how a significant number of the world's NPPs are reaching the end of their design lifetimes. It has been shown that while many factors contribute to structural integrity the material properties and crystallographic structure of the material have a major impact on the failure mechanism. Materials that have BCC crystallographic structures, such as ferritic materials, undergo a temperature transition whereby failure can occur in a brittle manner at, generally, lower temperatures. Austenitic materials, such as stainless steel, have an FCC crystal structure which is less temperature dependent in comparison to ferrite materials. For the nuclear industry where vessels generally operate at relatively high temperatures (approximately 300 °C) the impact of transition temperature might appear less relevant. However as briefly mentioned in Chapter 1.1 irradiation of RPV materials can reduce the mechanical performance substantially [IAEA, 1999]. The reduction in material performance is assessed using the master curve approach which as shown (see Equation 2.3.2) is dependent on T_0 which is in turn dependent on the transition temperature of the material. Hence for engineering critical assessments (ECAs) understanding the relationship between temperature, failure mechanism and environmental damage is of significance.

Dis-similar metal welds (DMWs) are a combination of materials where the base material, generally, provides the strength and the cladding provides corrosion resistance. Cladding material is typically joined to the base material using a welding procedure. While there are a variety of welding procedures it has been shown that each one inherently introduces defects to a component. Under loading conditions the performance, in terms of lifetime, of welded components is significantly reduced in comparison to base materials alone. Some benefits can be retained by post-weld treatments of the weld toes but for cladding weld toes are often not accessible. It has further been shown that the heat input during welding can cause mixing of the dissimilar metals resulting in undesirable microstructures.

The basic theory of fracture mechanics was also reviewed and the importance of various modes of loading (see Figure 2.4), with respect to fracture mechanics, was presented. It was shown that the ratio of stress intensity fracture to a materials fracture toughness dictates, at least in part, whether a component is 'safe' or 'unsafe' from a structural integrity perspective. The fracture toughness used in an ECA (K_{mat}) is generally assumed to be the fracture toughness under Mode I loading conditions and hence K_{mat} is often replaced with K_{IC}. It should be noted that, in operation, components are rarely subject to one specific mode of loading and are more often subjected to multi-mode or mixed mode conditions. There are several factors that contribute to mixed mode loading conditions such as residual stresses and/or constraint due to the thickness effect which we touched on briefly above. Residual stresses will be discussed in more detail later in this work. Regardless it should be noted that both, or indeed either, residual stress and constraint can impact the mode of loading.

Current guidance on methods to conduct ECAs (R6, BS 7910) contain little information on how DMWs should be addressed [British Energy, 2008; British Standards Institute, 2015*a*]. Current practise is to conduct a multitude of ECAs each investigating the impact of various input parameters on the overall integrity of a component. The cladding is typically addressed in two ways: 1. Cladding does not contribute to the structural integrity of the vessel and hence the ECA may assume a homogeneous ferritic welded component or, 2. The lower strength property (from either the base or cladding materials) are used as input parameters. While neither of these approaches are accurate they will provide some indication of the overall structural integrity. If however, as in the case of DMWs, there are multiple possible defect orientations and multiple directions of defect propagation, the number of ECAs required for analysis purposes quickly becomes inhibitive. This is exacerbated by the requirement for exceptionally large initial defect sizes due to difficulties various non-destructive testing (NDT) techniques incur when analysing DMWs.

Chapter 3: Specimen Manufacture and Testing

3.1 As Received material

A ferritic steel clad welded with stainless steel was sourced from previous work conducted by the University of Bristol (UOB) and the Open University (OU) [Serasli, 2014; Naveed, 2015]. The base material is A508 – a nuclear reactor pressure vessel steel, measuring approximately 300 × 180 × 50 mm in dimension. Three layers of cladding were welded to the top surface of the base metal. The first layer of cladding was made using stainless steel grade 309, the second and third layers were made using stainless steel grade 308. The chemical compositions are provided in Table 2.1. The total thickness of cladding, post-welding, was measured to be approximately 8.5 mm. The three cladding layers were applied using the TIG welding process, a manual arc welding process widely used in the nuclear industry. These types of welds are typically conducted with qualified welding procedures carried out by highly trained, competent weld operators. Documentation on the welding procedure was not provided but it is known that the base was pre-heated to a temperature of 170 °C. A primary and background current of 315 and 180 Amps respectively, were used in conjunction with a voltage of 12 V. The travel speed of the TIG weld was specified to be 150 mm/min and the weld interpass temperature was specified to be 250 °C [Serasli, 2014; Naveed, 2015].

Post welding residual stress measurements were conducted on the welded component. Hence the material received by Imperial was received in machined sections due to the destructive techniques (deep hole drilling, contour measurements etc.) previously employed. Two sections of plate were provided. One section measured approximately 150 × 180 × 58.5 mm and a second, smaller section, measuring 70 × 180 × 58.5 mm.

The larger section (Figure 3.1) had several cuts in the central region of the plate to facilitate residual stress measurements. The smaller section of material is shown in Figure 3.2.

(a) Top view (b) Front view

Figure 3.1: As received large clad plate

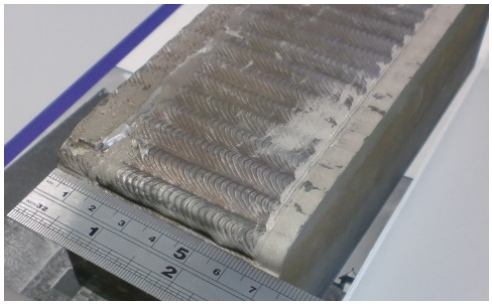

Figure 3.2: As received small clad plate

3.2 Specimen machining

The large section of clad plate was machined to remove as many specimens as reasonably possible for materials testing. Figure 3.3 shows a top view of the large clad plate and the outline of specimens that were to be machined. To facilitate machining the plate was first cut into several smaller regions corresponding to the type of specimen to be removed these cuts are depicted in Figure 3.3.

3.2.1 Standard tensile specimens

A total of 17 standard tensile specimens were machined from the large clad plate. Due to the specimen size, in comparison to the as received plate dimensions, specimens were machined transverse to the clad weld direction only. Specimens were machined

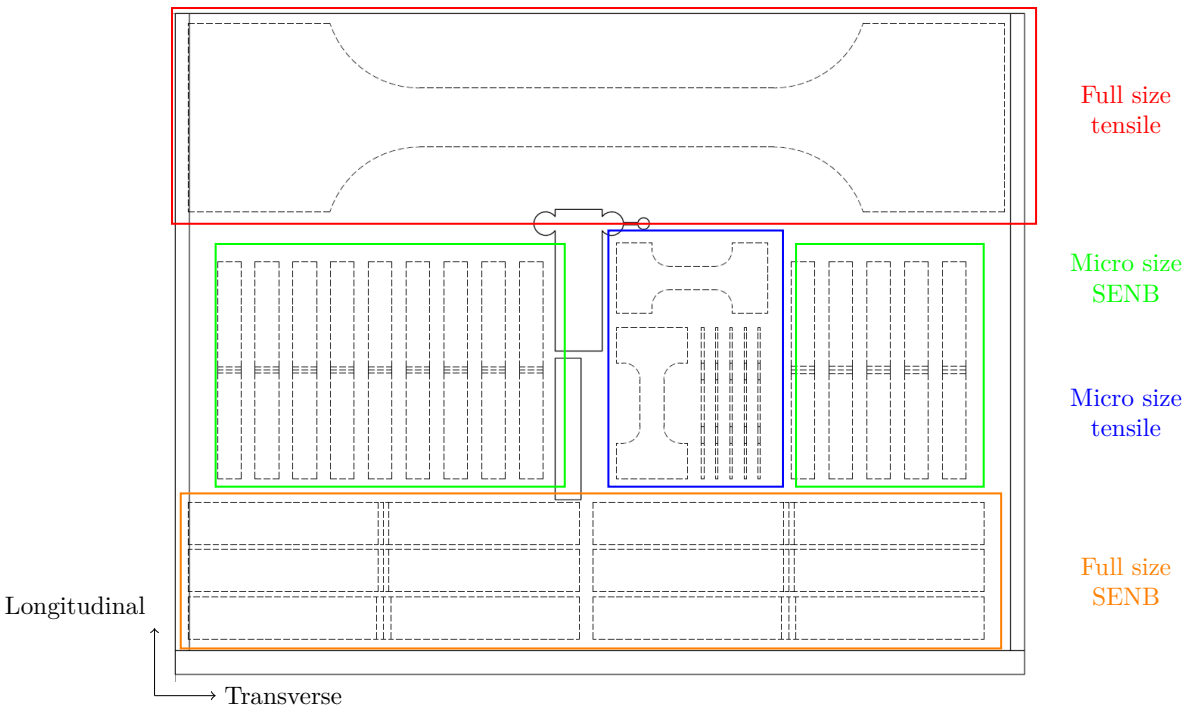

Figure 3.3: Specimens to be cut from the large clad plate

through the thickness of the plate from the clad surface. The orientation of the specimens with respect to the as received material is shown in Figure 3.4. Specimens were numbered with respect to their location to the cladding so that Specimen 1 refers to a specimen located near the 'top' of the plate (in the austenitic cladding) and Specimen 17 refers to a specimen located close to the 'bottom' of the plate (ferritic base material). Full size tensile specimens 3, 4 and 5 were located close to the interface between the austenitic and ferritic materials. During manufacture it was noted that removed material deformed significantly. This deformation is considered likely to be due to residual stresses in the section. As a result of the deformations specimens 1 and 2 deviated from the requested dimensions (see Figure 3.5). Specimen 1 was considered unusable.

3.2.2 Micro tensile specimens

A total of 54 micro sized tensile specimens were machined from the plate as detailed in Figure 3.6. Two sets, each consisting of 19 specimens, were machined in the transverse and longitudinal directions (Figure 3.6 Group B3-2 and B3-3). The specimen number-

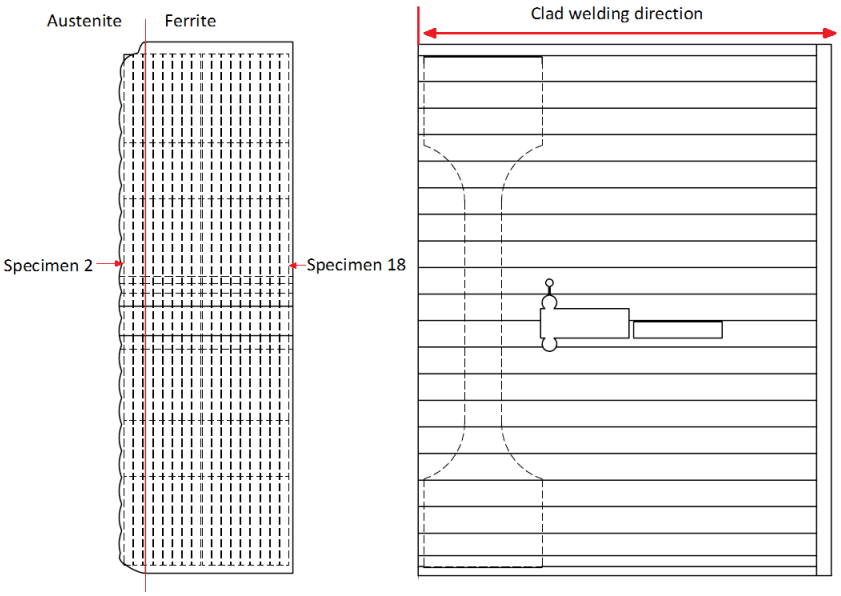

Figure 3.4: Full size tensile specimen orientation in the plate

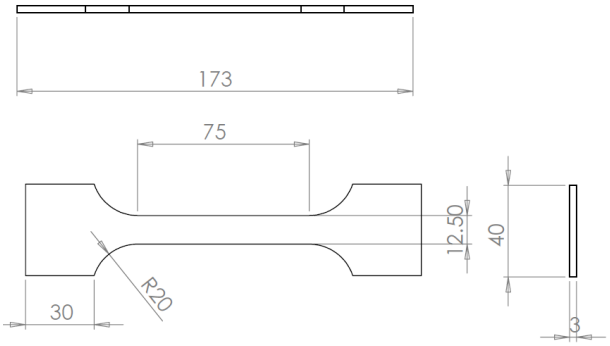

Figure 3.5: Full size tensile specimen dimensions

ing system was identical to that described above for the standard tensile specimens (i.e. first specimens removed from austenitic material, nineteenth specimen from the ferritic only specimen). A set of 16 specimens were machined perpendicular to the weld boundary. Eight of these specimens contained both austenitic and ferritic material with the weld boundary appearing roughly in the centre of the specimen (Figure 3.6 Group B3-4A). A further eight specimens were machined in the same orientation, deeper into the plate, and hence contained ferritic base material only. The dimensions of the specimens and are shown in Figure 3.7.

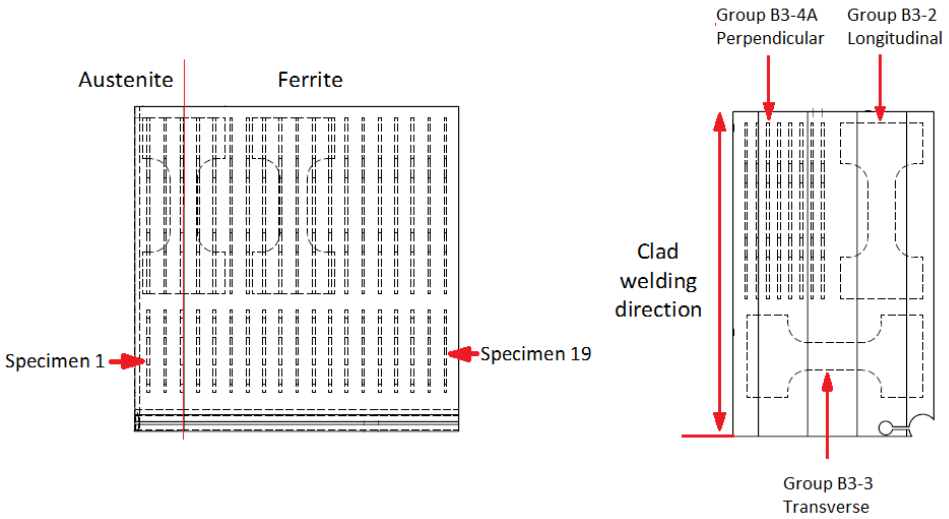

Figure 3.6: Grouping of micro tensile specimens with respect to clad weld direction

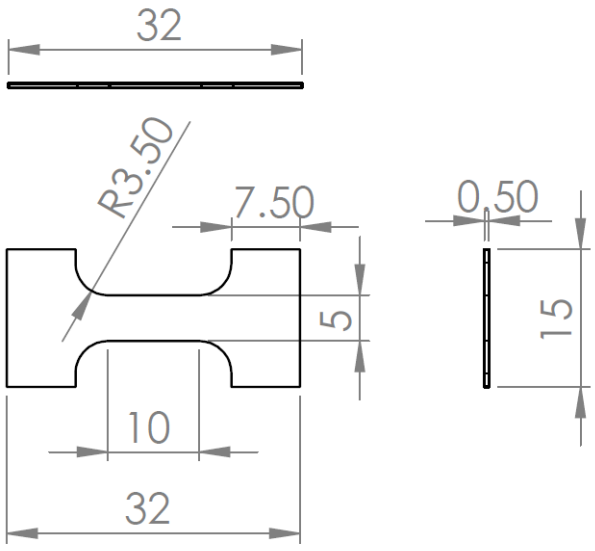

Figure 3.7: Micro size tensile specimen

3.2.3 Standard SENB specimens

A total of 18 standard single end notch bend (SENB) specimens were machined. Again, for spacing purposes specimens were oriented transverse to the clad welding direction only. Specimens were notched through the thickness of the specimen, in the plate thickness direction. Three notch sizes were to be investigated: $a/W = 0.15$, $a/W = 0.30$, $a/W = 0.45$. A total of six specimens per notch size were machined. To prevent residual stresses resulting in machining errors (such as was noted during the removal of standard size tensile specimens) the section of material was first machined into slices

representing each notch size. The six specimens for each notch size where then removed from the relevant slice. Figure 3.8 shows the orientation of specimens with respect to the cladding material. As shown each batch of specimens comprises of two mixed material specimens (combined specimens) and four homogeneous (ferritic base) material specimens.

3.2.4 CT specimens

Compact tension (CT) specimens were manufactured from the smaller section of as-received plate (Figure 3.10a). It was not possible to machine CT specimens directly from the as-received plate due to the plates geometry and the required notch location. To facilitate the manufacture of CT specimens the plate was modified as follows: The as-received section was machined into four sub-sections. Two sub-sections comprised of both cladding and base materials (the original TIG weld boundary remained intact) and two sub-sections of homogeneous ferrite base material. All sub-sections were machined square. Where relevant the cladding surfaces were machined flat. Each homogeneous section was tack welded to the austenitic side of a combined material section, effectively sandwiching the austenitic material in the centre of two ferritic sections. Small end plates were tacked on the sides of the 'sandwich' component. Two such sandwich components (Block A and Block B) were manufactured. The orientation of the CT specimens with respect to the cladding is shown in Figure 3.9.

Subsequent to tack welding the sandwich components were electron beam (EB) laser welded. The travel speed of the beam was 400 mm/min. The voltage was specified to be 150 kV with a beam current of 30 mA. The beam size was calculated to be approximately 2 mm in diameter. The depth of penetration was estimated to be 20 mm. To ensure full root fusion the components were welded from both sides. Both components (Blocks A and B) were placed in the weld chamber, the chamber was then pressurised to provide a stable laser beam. Block A was EB welded, followed by Block B. The chamber was de-pressurised and a temperature measurement of one component

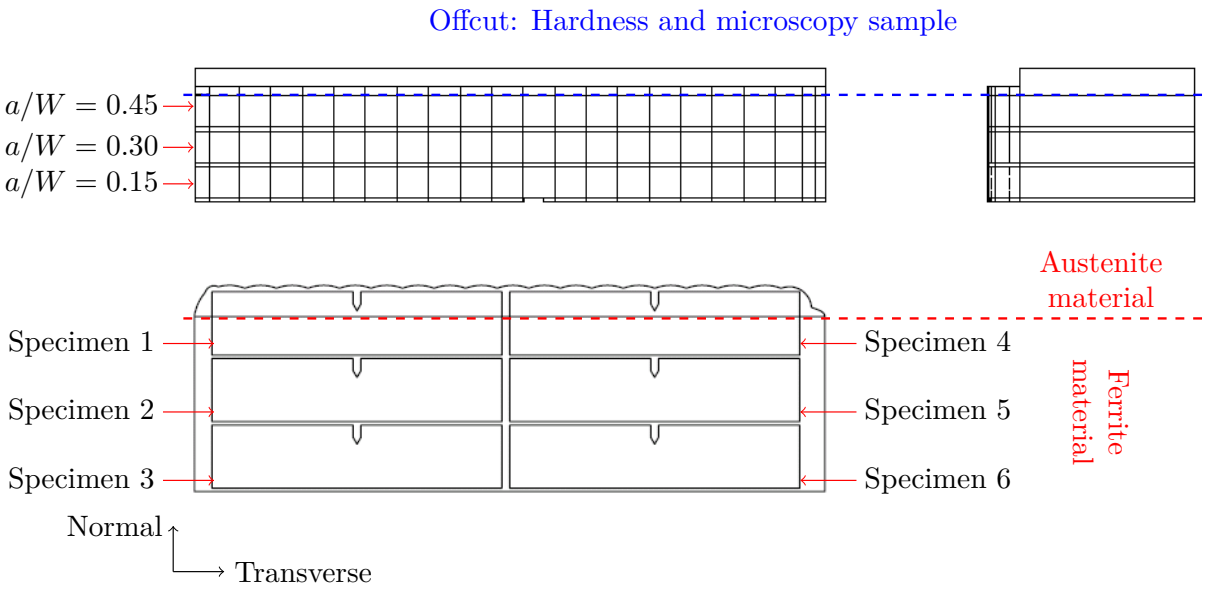

Figure 3.8: Orientation of standard size SENB specimens with respect to cladding

was made using a temperature probe. Ventilation of the chamber took approximately five minutes. Each component was flipped over 180° and placed back in the chamber. The chamber was re-pressurised and each component was again EB welded. As before Block A was welded first followed by Block B. The chamber was vented for a final time and a second temperature measurement was made. Approximately 4 mm of weld overlap in the mid-thickness of each Block A and Block B was achieved. The finished EB weld on the surface of one sandwich component is shown in Figure 3.10a. The temperature after the first ventilation was measured to be 110 °C, the second was measured to be 120 °C.

Post welding the sandwich components were machined to remove the end blocks and any weld caps. The interface between the cladding and the ferritic steel was marked and CT specimens were machined from positions as shown in Figure 3.9. Machining was conducted using electro-discharge machining (EDM) process with a 0.25 mm diameter wire. A total of six CT specimens measuring $37.5 \times 36 \times 15$ mm were machined from Block B. Specimens were machined in pairs beginning 10 mm from the weld start position, with 12.5 mm distance between each subsequent pair of specimens. The specimens were oriented so that the notches were approximately 1 mm offset from the

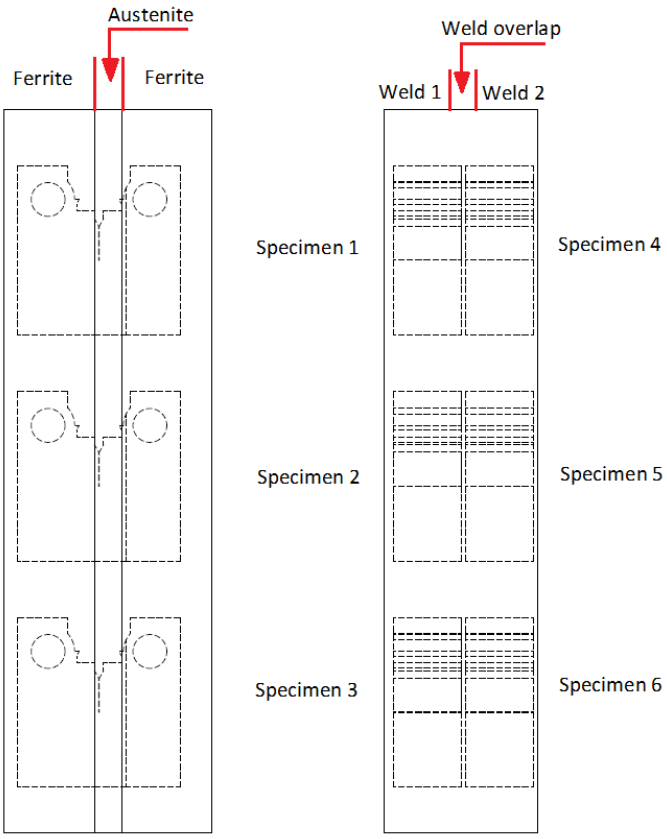

Figure 3.9: Orientation of CT specimens with respect to cladding

(a) Laser welded component (b) Notch orientation CT specimens

Figure 3.10: Laser welded component from which CT specimens were manufacture

original TIG weld interface. Figure 3.10b shows the notch location for specimens taken from Block B. As shown in Figure 3.10b the original TIG weld is undulating, this is a function of the method of laying down the TIG weld. The laser weld is comparatively straight. Post-machining the notch tip was measured to be approximately 2 mm from the TIG weld boundary. Prior to fracture toughness testing the notch length was extended using EDM machining with a 0.10 mm diameter wire to the initial crack length required for fracture toughness testing. It was additionally decided to incorporate integrated knife edges aligned with the central point of the pin holes. Due to the specimen

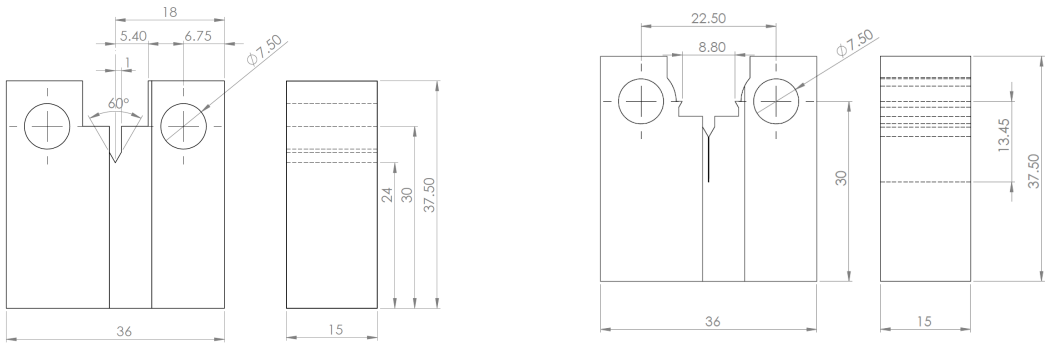

(a) Block B: Original CT dimensions

(b) Block B: Final CT dimensions

Figure 3.11: Dimensions of Block B CT specimens

dimensions there was insufficient clearance for the clip gauge around the pin holes. To combat the clearance issue additional material was also removed from regions above the load-line. The original and final dimensions of the Block B specimens are shown in Figure 3.11.

3.3 Testing Parameters

3.3.1 Neutron Diffraction

The crystalline structure of metals allows residual stresses to be estimated using non-destructive testing (NDT). In this work components were bombarded by a beam of neutrons which are diffracted from crystallographic planes at an angle. The angle of scatter is dependent on the lattice spacing. The crystallographic planes (in terms of Miller indices, hkl) are related to the interplanar spacing, d_{hkl}, by Equation 3.3.1 where a represents the length of the unit cell edge. By applying Bragg's law (Equation 3.3.2) the scattering angle can be calculated. Changes to the scattering angle therefore reflect changes in the lattice spacing. By comparing results from a component to that of a known stress free (d_0) measurement the strain in the component can be calculated.

$$d_{hkl} = \frac{a}{\sqrt{h^2 + k^2 + l^2}} \tag{3.3.1}$$

$$n\lambda = 2d_{hkl} \sin \theta_B \tag{3.3.2}$$

Neutron diffraction measurements were made on the EB welded sandwich component Block A, on three CT specimens located at the weld start, mid-weld and weld end positions of Block B, side 1 and on four tensile specimens. The measurements were taken using instrument E3 at Helmholtz Zentrum Berlin (HZB). To ensure accurate residual strain measurements the reference lattice parameter, d_0, was determined using two individual cubic samples, each measuring $2 \times 2 \times 2$ mm^3, comprised of: homogeneous ferritic base material and homogeneous austenitic cladding material. The beam was oscillated around five angles in two directions (i.e. a total of 10 angles measured, $\pm 5°$).

Due to the relative thickness of Block A measurements were made transverse to the EB weld along the mid-weld mid-plane only. Measurements were biased towards the weld region. Locations close to the material boundary were measured twice, once for ferritic material and once for austenitic material as the composition of material in these regions was not clear. Figure 3.12 shows the measurement locations. To keep the count times reasonable a $2 \times 2 \times 10$ mm^3 gauge volume was utilised in the transverse and normal directions. A smaller gauge volume measuring $2 \times 2 \times 6$ mm^3 was utilised for the longitudinal measurements to increase the accuracy of the result.

The CT specimens were relatively thin in comparison with the welded component therefore a gauge volume of $1 \times 1 \times 2$ mm^3 was utilised. A total of 12 measurements were taken in the mid-thickness of each specimen, starting from the crack tip continuing in increments of 2 mm to the end of the sample. The location of the measurements is shown in Figure 3.13.

The four tensile specimens tested for residual stresses were numbered as follows: Specimen 2, homogeneous austenitic cladding material (surface cladding). Specimen 3,

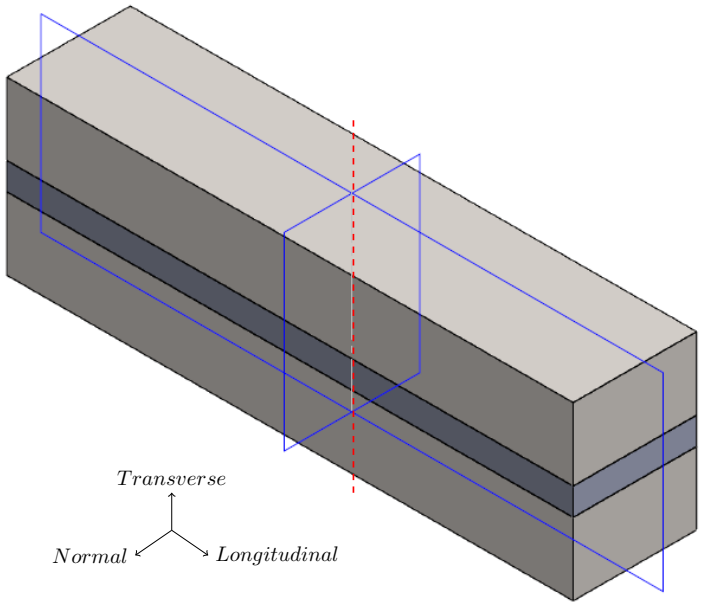

(a) Isometeric view of measurement location

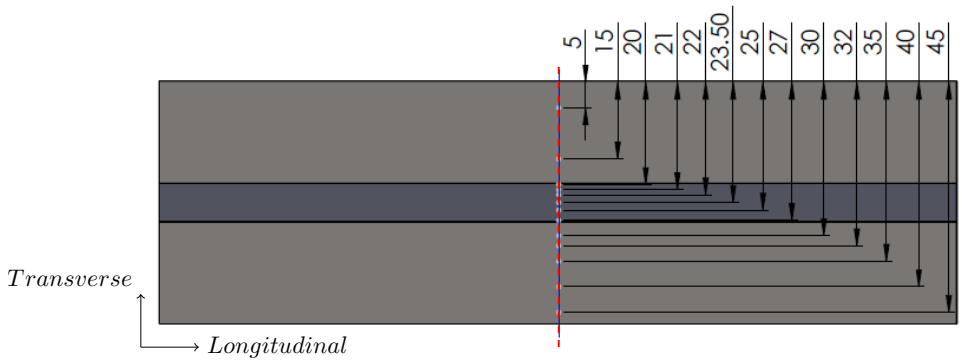

(b) Specific measurement locations

Figure 3.12: Neutron diffraction measurements on Block A

homogeneous austenitic cladding material (mid-clad). Specimen 4, unknown composition mixed material machined from region along the weld boundary. Specimen 18, homogeneous ferritic base material. A gauge volume of $2 \times 2 \times 2$ mm^3 was utilised for all measurements. A total of nine measurements in the gauge section of each specimen was taken as shown in Figure 3.14. The distance between measurements was 35 mm in the transverse (with respect to the cladding orientation) direction. Measurements in the transverse direction were taken from the central gauge width position and 5 mm offset either side of the central position.

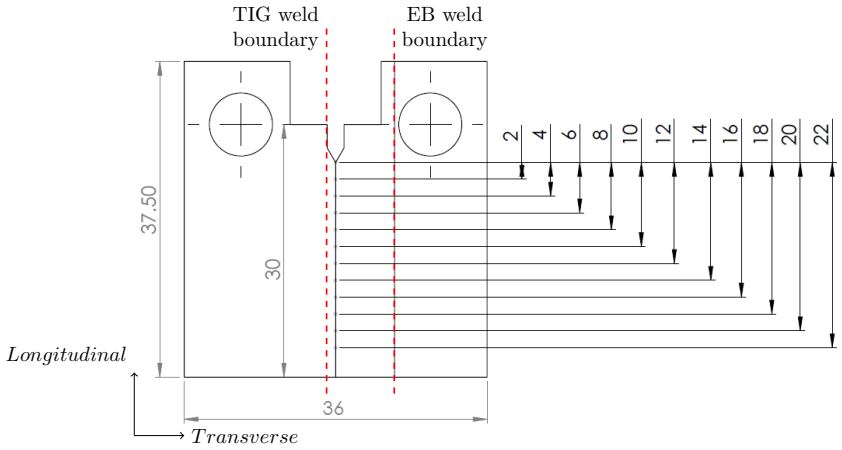

Figure 3.13: Neutron diffraction measurement locations on CT specimens

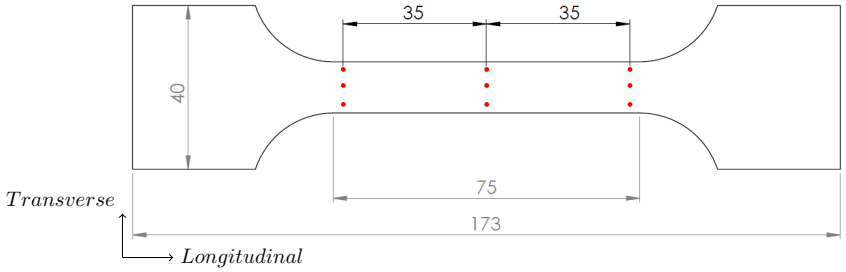

Figure 3.14: Neutron diffraction measurement locations on tensile specimens

3.3.2 Metallography and Hardness Testing

Offcuts from both the original plate and the EB welded component were used for metallography and hardness testing. The location of the TIG weld offcut, with respect to the original plate, is shown in Figure 3.8. The EB weld offcut is shown in Figure 3.15a. Offcuts were manually ground using a SAPHIR 330 grinding and polishing machine at 400 rpm. European 'P' grade sandpapers were used successively as follows: P60, P180, P320, P600, P800, P1200, P2500. Water was run throughout the polishing process to provide lubrication. After each change of sandpaper specimens were rotated by 90 °to ensure a smooth surface was achieved. Final polishing of the surfaces used micro-polishing cloths of 6 μm, 3 μm, 1 μm. Specimens were washed and dried between each cloth to ensure no cross-contamination of particles. Hardness testing was conducted using a Vicker's hardness testing machine.

The original TIG weld was assumed to be of symmetrical properties across the width of the plate, hence only one half of the offcut was tested. Specific measurement points

for microscopy and hardness testing are shown in Figures 3.16 and 3.17, respectively. A total of 17 hardness measurements were made along each of the hardness measurement lines 2-5, fifteen measurements were taken along measurement line 1 due to the geometry of the cladding. The distance between each subsequent measurement point was 5 mm starting from the left hand side of the section to the center of the plate.

Two sections were tested from the EB welded sandwich component Block B. The sections were located at the extremities of Block B and are analogous to the weld start and end positions of the laser weld (see Figure 3.15a). Specific measurement positions are shown in Figure 3.15b. As can be seen measurements were biased towards the weld region.

Post hardness testing specimens were re-polished and micrographs of the ferrite, austenite and HAZ regions were made. The original plate section was etched using 5% Nital solution at intervals of 10 seconds until the microstructure was revealed. The austenite region was resolved using an electro-chemical process involving 10% oxalic acid for 90 seconds. One section from Block B was polished and etched for micrographs. The specimen was etched using 1% Nital solution for 40 seconds to resolve the ferrite region. The austenite region was etched using the electro-chemical etching process with 10% oxalic acid for 25 seconds. Prior to the application of oxalic acid all specimens were re-ground and polished.

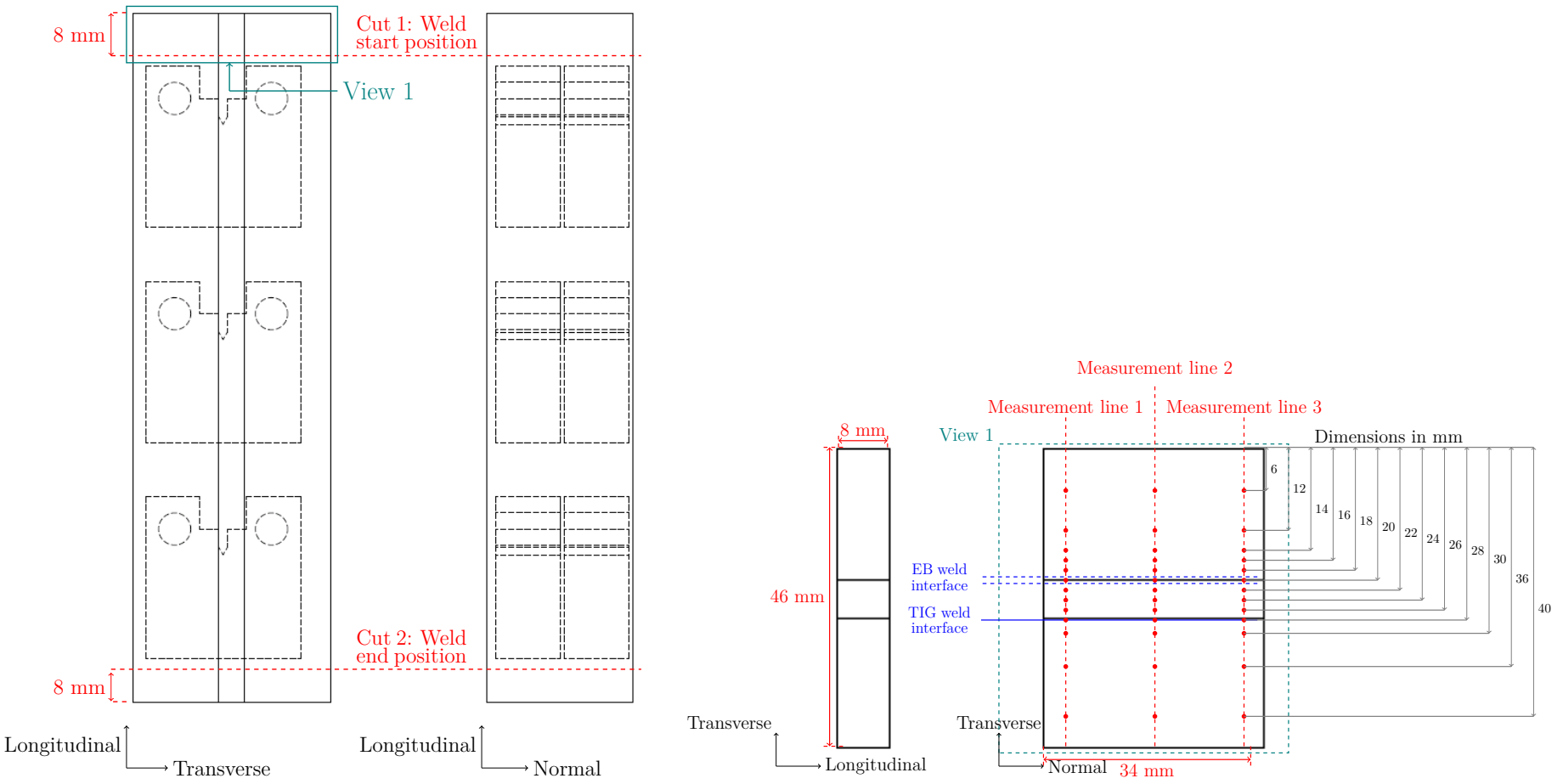

(a) Block B sections used for measurements

(b) Location of measurements on section

Figure 3.15: Location of hardness measurements taken from Block B

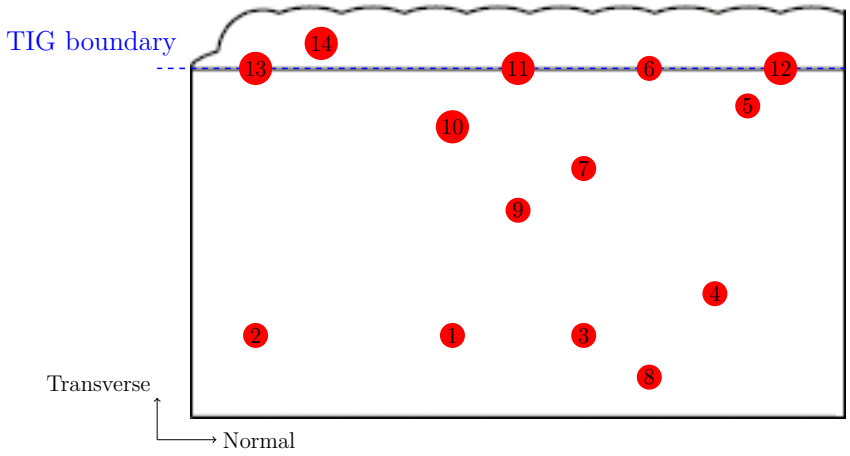

(a) Ferritic region of original clad weld

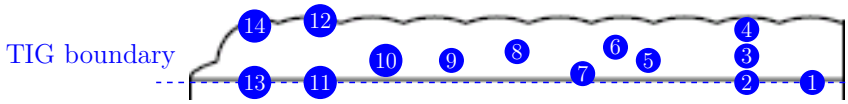

(b) Austenite regions of original clad weld

Figure 3.16: Location of microstructural imaging on ferrite section (Figure 3.16a) and austenite section (Figure 3.16b)

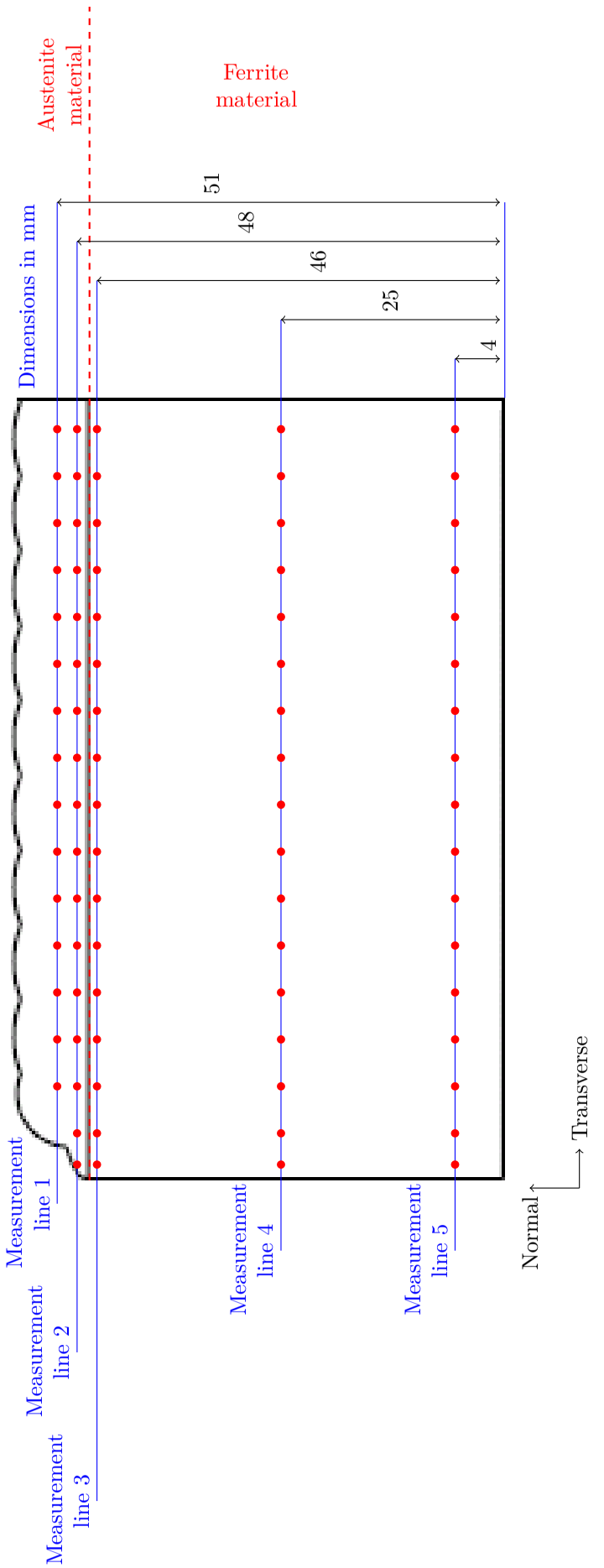

Figure 3.17: Hardness measurement locations on original clad weld

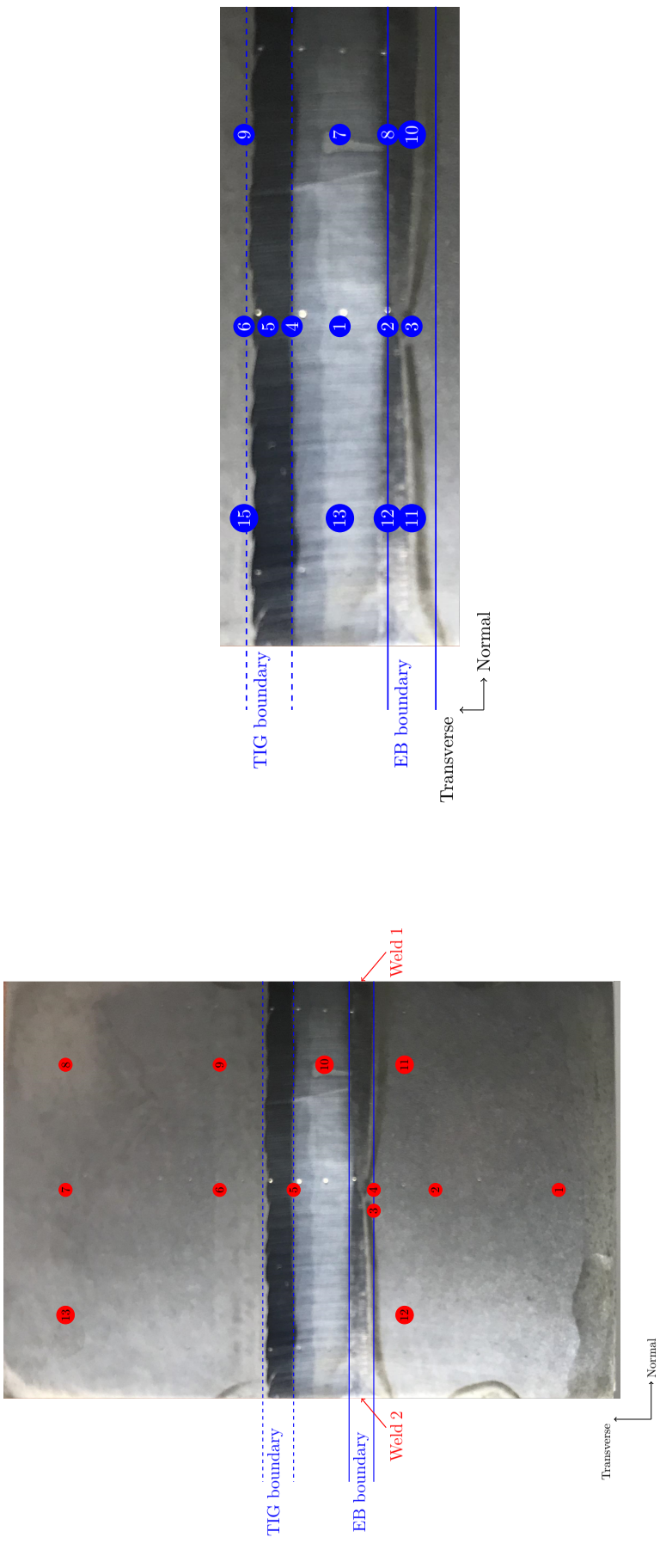

(a) Regions sampled using Nital solution

(b) Regions sampled using Oxalic acid solution

Figure 3.18: Regions of which micrographs were taken

3.3.3 Tensile testing

Testing of standard tensile specimens was conducted in a 150 kN Instron servo-electric tensile testing machine. Hydraulic jaws were used to grip each specimen in position prior to loading. Specimens were tested in accordance with test method BS EN 10002-1 [British Standards Institute, 2001]. Specimens were loaded at a rate of 1 mm/min to failure. Failure was defined as full separation of the specimen. Testing was conducted in a temperature controlled environment with an ambient temperature of approximately 20 °C.

The load and crosshead displacements were monitored throughout each test. Strain in the gauge section of each specimen was measured using an extensometer with a gauge section 50 mm and an travel of 5 mm. To avoid damage to the extensometer it was removed mid-way through testing. Figure 3.19a shows a specimen during testing.

Digital Image Correlation (DIC) was utilised on several specimens for additional strain measurements. The results were inconclusive. In the elastic region DIC data is subject to noise errors. During the latter stages of testing the speckle pattern could not be resolved as, due to the ductility of the samples, the paint had separated from the surface of the samples. The data are not presented in this work as they are considered insufficient.

Testing of micro size tensile specimens was conducted in a 50 kN Instron servo-electric tensile testing machine. Mechanical jaws were used to grip specimens. Testing was conducted in a temperature controlled environment at ambient temperature (approximately 20 °C). Originally two methods of measuring strain: a) extensometer and b) DIC were planned. During testing group B3-2 however it was noted that the extensometer did not have sufficient clearance between the jaws of the machine leading to unreliable data. Consequently half of group B3-2 were discarded from the analysis and DIC measurements alone were relied upon for the remaining specimens.

All specimens were tested at a crosshead displacement of 1 mm/min. The applied load and the crosshead displacement were measured during testing. DIC images were

taken at a rate of 1 Hz. Data from the machine (displacement in terms of crosshead movement and applied load) and DIC results were cross-referenced by time. Figure 3.19b shows the DIC imaging of specimen 2 from Group B3-4A during testing.

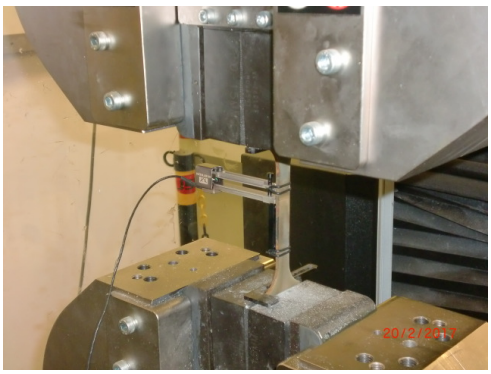

(a) Standard size tensile test setup

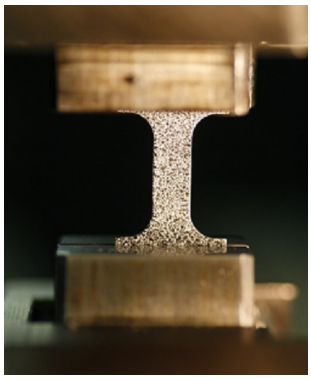

(b) Micro tensile during testing

Figure 3.19: Tensile testing of standard and micro size specimens

3.3.4 CT Fracture Toughness Testing

Compact tension specimens were tested in a 150 kN Instron servo-hydraulic test machine. Testing was conducted at room temperature in a temperature controlled environment. The unloading compliance test method [ASTM International, 2001] was utilised. Previous tests on dissimilar metal weld specimens showed that the materials boundary and/or any residual stresses in the specimens may influence the direction of crack growth [Rathod et al., 2017]. Hence one requirement of the test method, pre-fatigue cracking, was not implemented so as to avoid crack deviation. Test results were processed in real time, in-situ, using Labview J_{IC} unloading compliance software V8.5 Build 21 [Instron, 2010*b*].

The force, cross-head displacement and crack-opening displacement (COD) were measured at a frequency of approximately 0.33 Hz. COD was measured using an Instron gauge with a gauge length of 10 mm and a travel of 4 mm located along integrated knife edges at the load-line of the CT specimens. Prior to beginning the unloading compliance test the sample was subjected to 20 bedding in cycles.

The fracture toughness (J_{1C}) was calculated in real time using data from the clip gauge and the load cell. Prior to testing three elastic unloading sequences are conducted to

estimate the initial crack length (a_0). The elastic sequences are labelled as curves 1-3 inclusive and the maximum applied load is no greater than that derived by Equation 3.3.3. The software [Instron, 2010*b*] segregates test data into sequences. Each fracture toughness sequence is numbered sequentially $(1, 2, 3....n)$ with sub-values assigned to differentiate whether the data belongs to a load (0), unload (1), or reload (2) segment. Hence the initial fracture toughness loading will have a sequence number of 10, the corresponding unload 11, and the corresponding reload 12. The subsequent test segments will have sequence numbers of: $n0$, $n1$, and $n2$, respectively. The unload sequences ($n1$) were set to occur at specific increments of crack mouth opening displacement (CMOD) measured from the clip gauge. At the relevant value of CMOD a 20 % reduction in load (compared to the maximum load attained in the corresponding load sequence ($n0$)) was applied. Any crack growth is assumed to occur during the loading sequence ($n0$) only. Both the unload ($n1$) and reload ($n2$) sequences are assumed to be elastic.

The compliance of the specimen was measured at each unloading sequence ($n1$) as a function of load-line displacement (LLD), specimen dimensions and material properties as shown in Equations 3.3.4 to 3.3.9. The fracture toughness (J_{1C}) was estimated for each unloading increment (i) as per ASTM E813 [Instron, 2010*b*] since superseded by ASTM E1820 [ASTM International, 2001].

$$P_f = \frac{0.4B\left(W - a_0\right)^2 \sigma_y}{\left(2W + a\right)} \tag{3.3.3}$$

$$\begin{aligned} C_{LL} = \left(\frac{1}{B_e E}\right)\left(\frac{W + a_i}{W - a_i}\right)^2 \Bigg[2.1630 + 12.219\left(\frac{a}{W}\right) - 20.065\left(\frac{a}{W}\right)^2 \\ - 0.9925\left(\frac{a}{W}\right)^3 + 20.609\left(\frac{a}{W}\right)^4 - 9.9314\left(\frac{a}{W}\right)^5\Bigg] \end{aligned} \tag{3.3.4}$$

$$B_e = B - \frac{\left(B - B_N\right)^2}{B} \tag{3.3.5}$$

$$u = \frac{1}{\left(B_e E C_{C(i)}\right)^{\frac{1}{2}} + 1} \tag{3.3.6}$$

$$C_{C(i)} = \frac{C_i}{\left[\frac{H*}{R}\sin\theta_i - \cos\theta_i\right]\left[\frac{D}{R}\sin\theta_i - \cos\theta_i\right]} \tag{3.3.7}$$

$$\theta = \arcsin\left[\frac{\frac{d_m}{2} + D}{\sqrt{D^2 + R^2}}\right] - \arctan\left(\frac{D}{R}\right) \tag{3.3.8}$$

$$\begin{aligned}\frac{a}{W} = \Big[&1.000196 - 4.06319\,(u) + 11.242\,(u)^2 - 106.043\,(u)^3 \\ &+ 464.335\,(u)^4 - 650.677\,(u)^5\Big]\end{aligned} \tag{3.3.9}$$

Where: a_i is the current crack length, B is the specimen thickness, B_e is the effective thickness, B_N is the net thickness, $C_{C(i)}$ is the rotationally corrected compliance, C_i is the elastic compliance at the load-line, D is the distance from edge of one measuring point to the centreline of the specimen, d_m is the total measured load-line displacement, E is Young's Modulus, H^* is the distance from centre of one pin to centreline of the specimen, R is the radius of rotation (assumed to be $(W + a)/2$), W is the width of the specimen, and θ_i the angle of rotation of a rigid body.

The total fracture toughness was estimated to be a summation of a specimens elastic and plastic parts (Equation 3.3.10). The elastic fracture toughness is calculated as shown in Equation 3.3.11 where the stress intensity factor K is calculated from Equations 3.3.12 and 3.3.13. Unloading compliance testing results in multiple fracture toughness values, each value is associated with an incremental growth in defect depth. The plastic part of the fracture toughness is a function of incremental crack growth, energy absorption, and applied load (see Equation 3.3.14). At each unloading point the incremental crack growth and the energy required to grow the crack to the current

length is estimated from the area under the force versus CMOD curve. Superposition of energy absorption is assumed for subsequent increments of crack growth.

$$J_{total} = J_{el} + J_{pl} \tag{3.3.10}$$

$$J_{el} = \frac{K^2(1-\nu^2)}{E} \tag{3.3.11}$$

$$K_i = \left[\frac{P_i}{\sqrt{BB_N W}}\right] f\left(\frac{a_i}{W}\right) \tag{3.3.12}$$

$$f\left(\frac{a_i}{W}\right) = \frac{\left[\left(2+\frac{a_i}{W}\right)\left(0.886+4.64\left(\frac{a_i}{W}\right)-13.32\left(\frac{a_i}{W}\right)^2+14.72\left(\frac{a_i}{W}\right)^3-5.6\left(\frac{a_i}{W}\right)^4\right)\right]}{\left(1-\frac{a_i}{W}\right)^{\frac{3}{2}}} \tag{3.3.13}$$

$$J_{pl} = \left[J_{pl(i-1)} + \left(\frac{\eta_{(i-1)}}{b_{(i-1)}}\right)\left(\frac{A_{pl(i)} - A_{pl(i-1)}}{B_N}\right)\right]\left[1-\gamma_{(i-1)}\frac{a_{(i)}-a_{(i-1)}}{b_{(i-1)}}\right] \tag{3.3.14}$$

$$\eta_{(i-1)} = 2.0 + 0.522\left(\frac{b_{i-1}}{W}\right) \tag{3.3.15}$$

$$\gamma_{(i-1)} = 1.0 + 0.76\left(\frac{b_{i-1}}{W}\right) \tag{3.3.16}$$

$$A_{pl(i)} = A_{pl(i-1)} + \frac{\left[P_{(i)} + P_{(i-1)}\right]\left[v_{pl(i)} - v_{pl(i-1)}\right]}{2} \tag{3.3.17}$$

The test method [ASTM International, 2001] provides limits, outside of which, test data are not considered valid. The limit of energy, J_{limit}, is calculated as a function of specimen geometry as shown in Equation 3.3.18. Valid test data are also constrained in terms of crack extension. The maximum crack extension is limited as per Equation 3.3.19. The minimum valid crack extension is estimated by way of a 'construction line'. The construction line is used to estimate the fracture initiation point, J_Q, and is estimated as per Equation 3.3.20. The value of M in Equation 3.3.20 is representative of a particular material for a specific, minimum level of constraint (i.e. thickness effect). ASTM guidance states M should initially be assumed to have a value of 2.0 which is associated with plane strain conditions for the strip yield model [Croften, 2007]. The test method qualifies that the value of M may be re-estimated to higher values at later stages of data assessment.

$$J_{limit} = min\left(\frac{b\sigma_y}{20}; \frac{B\sigma_y}{20}\right) \tag{3.3.18}$$

$$\Delta a_{max} = 0.25(W - a) \tag{3.3.19}$$

$$J = M\sigma_y \Delta a \tag{3.3.20}$$

Where b in Equation 3.3.18 represents the remaining ligament $(W - a)$.

3.3.5 SENB Fracture Toughness Testing

SENB specimens were tested in a 150 kN Instron servo-hydraulic test machine. Testing was conducted at room temperature in a temperature controlled environment. Specimens were fatigue pre-cracked, using loads outlined in the test method [ASTM International, 2001], to specific depths depending upon specimen type. Labview software was used to track crack depth during the pre-cracking phase of work [Instron, 2010*a*]. Fatigue pre-cracking was conducted at a rate of 10 Hz. The force, cross-head displacement and crack-opening displacement were measured at all stages of the test. The clip gauge was located on knife-edges attached to the specimen surface. Initially the COD was measured using an Instron clip gauge with a gauge length of 5 mm and a travel of 2 mm. The software, reliant upon clip gauge data, was unable to continue testing once the maximum travel of the clip gauge was exceeded. As the maximum travel was exceeded prior to any significant crack growth these samples, and the remaining untested samples, were re-tested using a clip gauge of 10 mm gauge length with a travel of 4 mm.

Unloading compliance fracture toughness testing was conducted and processed using Labview J_{IC} software Version 8.5 Build 22. The force, crosshead displacement and COD were measured for all stages of the test. Specimens were additionally monitored using ARAMIS 4M adjustable base cameras with 50 mm lens allowing resolution of strains in three dimensions. Prior to beginning the unloading compliance test the sample was subjected to a minimum of 20 bedding in cycles. Additionally three elastic unloading cycles were utilised to estimate the initial defect size.

Testing was conducted using Instron da/dN software [Instron, 2010*a*] under constant load conditions. The maximum stress applied was, in all cases, less than or equal to the maximum elastic load limit calculated as per Equation 3.3.21. A frequency of 10 Hz and a stress ratio of 0.1 was applied.

$$P_f = \frac{0.5B\left(W - a_0\right)^2 \sigma_y}{S} \tag{3.3.21}$$

As noted in Section 3.3.4 the fracture toughness (J_{1C}) was calculated in real time using data from the clip gauge and the load cell. The software [Instron, 2010*b*] segregates test data into sequences. Prior to testing three elastic unloading sequences are conducted to estimate the initial crack length (a_0). The elastic sequences are labelled as curves 1-3 inclusive and the maximum applied load is no greater than that derived by Equation 3.3.21. Each fracture toughness sequence is numbered sequentially $(1, 2, 3....n)$ with sub-values assigned to differentiate whether the data belongs to a load (0), unload (1), or reload (2) segment. Hence the initial fracture toughness loading will have a sequence number of 10, the corresponding unload 11, and the corresponding reload 12. The subsequent segments will have sequence numbers of $n0$, $n1$, and $n2$, respectively. The unload sequences ($n1$) were set to occur at specific increments of crack mouth opening displacement (CMOD) measured from the clip gauge. At the relevant value of CMOD a 20 % reduction in load (compared to the maximum load attained in the corresponding load sequence ($n0$)) was applied. Any crack growth is assumed to occur during the initial loading sequence ($n0$) only. Both the unload ($n1$) and reload ($n2$) sequences are assumed to be elastic.

The compliance of the specimen was measured at each unloading sequence ($n1$) as a function of load-line displacement (LLD), specimen dimensions and material properties as shown in Equations 3.3.22, 3.3.23 and 3.3.24. The crack length is estimated as a function of the measured crack mouth opening and test parameters as per Equations 3.3.25 to 3.4.2. The co-efficients of the compliance and CMOD functions used in the calculations were derived from finite element analyses and are discussed in detail in Section 3.4. The fracture toughness (J_{1C}) was estimated for each unloading increment (i) as per ASTM E813 [Instron, 2010*b*] since superseded by ASTM E1820 [ASTM International, 2001].

$$C = \frac{v_{LL}}{P} \tag{3.3.22}$$

$$C = \left(\frac{Y^2}{BE}\right)\left[A_0 + A_1\left(\frac{a}{W}\right) + A_2\left(\frac{a}{W}\right)^2 + A_3\left(\frac{a}{W}\right)^3 + A_4\left(\frac{a}{W}\right)^4 + A_5\left(\frac{a}{W}\right)^5\right] \tag{3.3.23}$$

$$Y = \frac{S}{W - a} \tag{3.3.24}$$

Where: v_{LL} is the load-line displacement, P is the load, E is Young's Modulus, B is the specimen thickness, S is the span of the rollers, W is the height of the specimen, a_0 is the known crack length.

$$u = \frac{1}{(BEC_i)^{\frac{1}{2}} + 1} \tag{3.3.25}$$

$$C_i = \frac{\Delta v_{LL}}{\Delta P} \tag{3.3.26}$$

$$\frac{a}{W} = \left[U_0 + U_1(u) + U_2(u)^2 + U_3(u)^3 + U_4(u)^4 + U_5(u)^5\right] \tag{3.3.27}$$

The total fracture toughness was estimated to be a summation of a specimens elastic and plastic parts (Equation 3.3.28). The elastic fracture toughness is calculated as shown in Equation 3.3.29 where the stress intensity factor K is calculated from Equations 3.3.30 and 3.3.31. Unloading compliance testing results in multiple fracture

toughness values, each value is associated with an incremental growth in the initial defect. The plastic part of the fracture toughness is a function of incremental crack growth, energy absorption, and applied load (see Equation 3.3.32). At each unloading point the incremental crack growth and the energy required to grow the crack to the current length is estimated from the area under the force versus CMOD curve. Superposition of energy absorption is assumed for subsequent increments of crack growth.

$$J_{total} = J_{el} + J_{pl} \tag{3.3.28}$$

$$J_{el} = \frac{K^2(1-\nu^2)}{E} \tag{3.3.29}$$

$$K_i = \left[\frac{P_i S}{\sqrt{BB_N}\sqrt[3]{W}}\right] f\left(\frac{a_i}{W}\right) \tag{3.3.30}$$

$$f\left(\frac{a_i}{W}\right) = \frac{3\sqrt{\frac{a_i}{W}}\left[1.99 - \left(\frac{a_i}{W}\right)\left(1-\frac{a_i}{W}\right)\left(2.15 - 3.93\left(\frac{a_i}{W}\right) + 2.97\left(\frac{a_i}{W}\right)^2\right)\right]}{2\left(1+2\left(\frac{a_i}{W}\right)\right)\left(1-\left(\frac{a_i}{W}\right)\right)^{3/2}} \tag{3.3.31}$$

$$J_{pl} = \left[J_{pl(i-1)} + \left(\frac{2}{b_{(i-1)}}\right)\left(\frac{A_{pl(i)} - A_{pl(i-1)}}{B_N}\right)\right]\left[1 - \frac{a_{(i)} - a_{(i-1)}}{b_{(i-1)}}\right] \tag{3.3.32}$$

$$A_{pl(i)} = A_{pl(i-1)} + \frac{\left[P_{(i)} + P_{(i-1)}\right]\left[v_{pl(i)} - v_{pl(i-1)}\right]}{2} \tag{3.3.33}$$

3.3.6 Digital Image Correlation

Digital image correlation (DIC) utilises image tracking to compute strain on the surface of a component by comparing a 'reference' image to subsequent images. A stochastic pattern is applied to the relevant component(s) surface. For this work generic acrylic spray paint was applied. The pattern consisted of two layers of white base paint followed by a 'speckle' pattern in black paint. The density of speckle required is dependent on the area of the component under investigation. Black speckle on a white background ensures a good colour contrast to aid image processing.

For 2D analyses (plane stress) a single camera is sufficient for resolving strains in two orthogonal directions. For 3D analyses a minimum of two cameras is required. Tensile tests were assumed to be predominately in plane stress hence a single Cannon camera with 50 mm lens was used. For fracture toughness testing the GOM Aramis 5M system, shown in Figure 3.20, consisting of two camera's, both with 50 mm lens, located a fixed distance apart was utilised [*ARAMIS: User Information - Hardware*, 2013]. Prior to testing the 5M system was calibrated using a calibration block capturing a volume of approximately $30 \times 20 \times 10\text{mm}^3$. Image post-processing was conducted using GOM Correlate Professional 2017 software [GOM, 2017]. The reference image is assumed to be strain free. The software identifies the stochastic pattern on the component. Strains are estimated by comparing the relative displacement of the stochastic pattern at each stage of the test to that of the reference image.

Figure 3.20: GOM 5M system used to take images during fracture testing

3.4 Compliance Functions for SENB specimens

Compliance coefficients provided in the test method [ASTM International, 2001] are only valid for crack ratios in the range of $0.45 \geq a/W \leq 0.8$. As SENB specimens used in this work are outside of this range, new coefficients, for the compliance calculation were estimated using 2D linear elastic FE modelling.

The crack tip was modelled using collapsed wedge elements with duplicated nodes. A midside position of 0.25 were applied to the first contour. Structured elements were used in all other areas. A boundary condition was applied to one node in the center of the specimen to prevent rigid body motion (U1 = 0) of the specimen. The rollers were modelled as analytical rigid bodies with a frictionless, hard contact specified between the surface of the specimen and the surface of the pins. Boundary conditions were applied to reference nodes in the center of the pins which were then kinematically coupled to the surface of the pins so that (U1 = U2 = UR1 = UR2). The two supporting rollers were constrained using the encastre boundary condition (U1 = U2 = UR1 = UR2 = 0), the third roller was displaced in the Y-direction to a maximum displacement of 1 mm. Specimens were meshed using element type CPE8R for plane strain. The mesh and boundary conditions are shown in Figure 3.21. Figure 3.21 also shows three elements extending upwards above the surface of the model. These elements measured 1×1 mm^2 and were used to estimate the change in CMOD as a function of distance from the surface of the specimen. The bulk of the specimen geometry was meshed with 1×1 mm^2 sized elements, a denser mesh was used in the region surrounding the crack tip. The values of Young's Modulus and Poisson's Ratio were 217,439 MPa and 0.3, respectively.

A number of crack depths were investigated, from a minimum of 0.05 mm (see Figure 3.21) to a maximum to 16.0 mm. The load line displacement and the reaction force at the fixed rollers were used to calculate compliance as per Equation 3.3.22. The compliance was then non-dimensionalised and plotted as shown in Figure 3.22. For comparison purposes Figure 3.22 also plots the results calculated using ASTM coefficients.

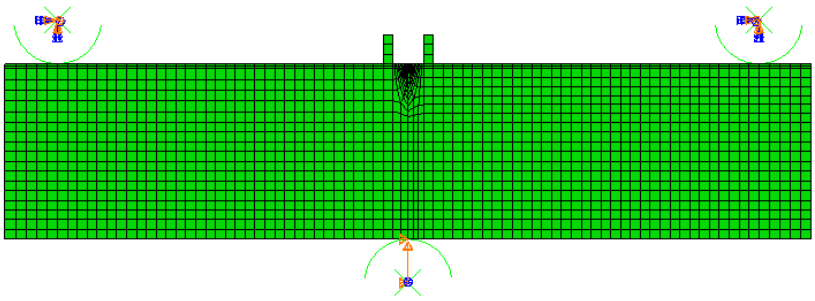

Figure 3.21: Linear elastic model for derivation of compliance coefficients. Crack depth of 0.05 mm. Boundary conditions shown on rollers.

The ASTM data is valid only for initial crack sizes in the range $0.45 \geq a/W \leq 0.8$. A polynomial of degree five was fitted to the FE results and coefficients of the polynomial were derived as per Equations 3.3.22 to 3.3.24. Table 3.1 tabulates the results from the FE analysis and shows the ASTM derived values. As shown in Table 3.1 the ASTM coefficients are limited to a three significant figures with the final coefficient forced to zero. The differences between the ASTM and FE data plotted in Figure 3.21 are due to variations in the polynomial.

From the FE analysis the crack opening displacement at several positions relative to the cracked surface were investigated: CMOD0, CMOD1, CMOD2 and CMOD3. CMOD0 represents the crack opening displacement assuming measurements were taken directly from the cracked surface. CMOD1, CMOD2 and CMOD3 represent the crack opening displacements should the crack opening displacements be located 1 mm, 2 mm and 3 mm above the cracked surface of the specimen respectively. The crack opening displacements and reaction forces were used to calculate u as per Equation 3.3.25. The known crack depths were plotted against 'u' as shown in Figure 3.23. A fifth order polynomial was fitted to the data and the coefficients of the curve were derived. The

Table 3.1: Coefficients for calculation of load-line compliance.

Analysis	A_0	A_1	A_2	A_3	A_4	A_5
ASTM	1.193	-1.980	4.478	-4.443	1.739	0
FE	1.2362765	-2.5022540	6.9989134	-9.4586760	5.4604376	-0.7496926

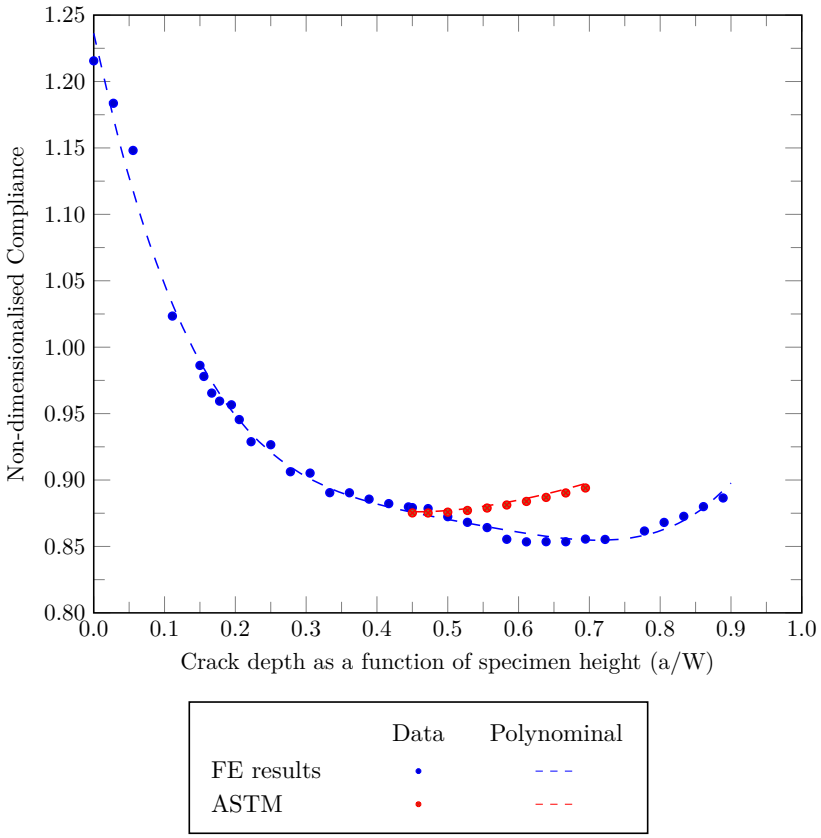

Figure 3.22: Load-line compliance as a function of crack depth, including polynomial fit

derived coefficients from the FE model are tabulated in Table 3.2, ASTM coefficients are included for comparison.

As previously stated the ASTM coefficients are valid for a relatively small range of crack depths and assumes that measurements are made on the cracked surface of the specimen. Figure 3.24 compares polynomial fit derived from FE with the ASTM data. The valid ASTM region is encapsulated by the red markers. The dashed red line plots the resulting fit if the ASTM coefficients were assumed valid outside of the validity range. As can be seen there is a good correlation between the FE data and ASTM data in the valid region. For shorter defects, $a/W \leq 0.2$, there is a large discrepancy between the FE data and the ASTM data. Given that the minimum crack depth of specimens used in the experimental aspects of this work exceeded this ratio the coefficients derived from FE are considered reasonable in terms of the correlation to ASTM coefficients.

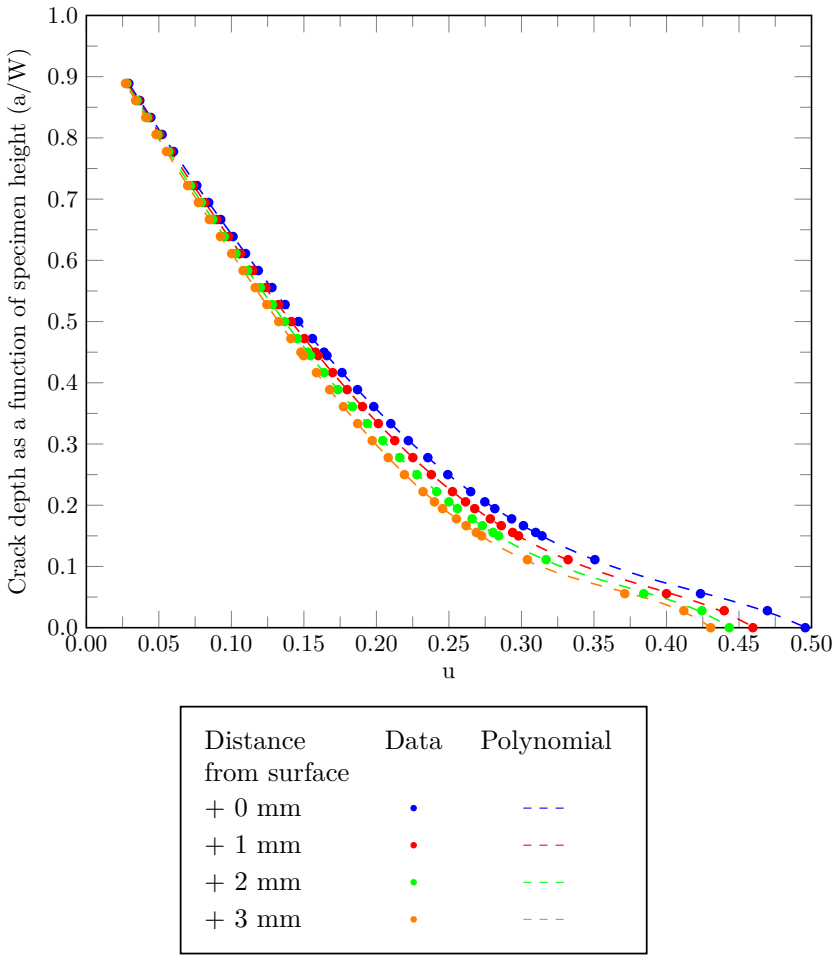

Figure 3.23: Crack depth as a function of crack mouth opening, including polynomial fit

The crack depth can be estimated as a function of the crack opening displacement using Equation 3.3.27. Figure 3.25 shows the percentage difference between the calculated crack depth (using Equation 3.3.27) and the known crack depth. As shown a exponential relationship exists indicating the coefficients are unreliable for short crack depths. Specimens used for this work had a minimum crack depths of at least 2.7 mm the percentage difference in estimating crack depth using CMOD falls to less than 10 % once a crack depth of approximately 3 mm is achieved and is negligible thereafter.

The above analysis was repeated using the austenite material properties (Young's Modulus: 202,220 MPa. Poisson's ratio: 0.3). Results are similar to those discussed above (see Appendix D.1). Hence the ferrite derived results are deemed appropriate for use regardless of whether test specimens comprised of homogeneous ferritic material or combined materials.

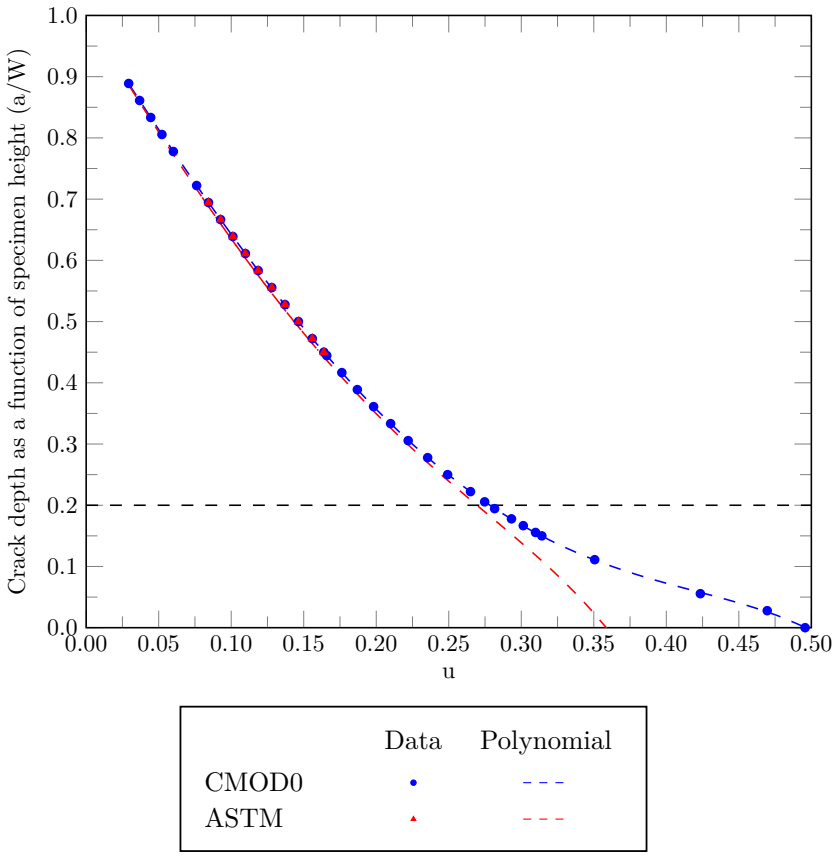

Figure 3.24: Comparison of polynomial fit for ASTM coefficients and FE derived coefficients

The coefficients used for the calculation of the elastic stress intensity factor (SIF) were also assessed. The SIF and reaction forces were estimated for each crack depth over 15 contours. The average SIF was calculated for contours 3-15 (inclusive) to negate any computational errors. Using Equations 3.4.1 and 3.4.2 the estimated SIF was normalised and plotted against the various crack depths as shown in Figure 3.26. A quartic polynomial was fitted to the data. The derived coefficients are shown in Table 3.3, ASTM coefficients are included for comparison.

$$K = \left[\frac{P}{\sqrt{BB_N W}}\right] f\left(\frac{a}{W}\right) \tag{3.4.1}$$

Table 3.2: Coefficients for calculation of crack depth from crack mouth opening displacements. Note: ASTM coefficients only valid for surface measurements.

Analysis	U_0	U_1	U_2	U_3	U_4	U_5
ASTM	0.9997480	-3.9504	2.9821	-3.21408	51.51564	-113.031
CMOD0	0.9981489	-3.8066119	2.2539319	1.1460084	19.4204780	-32.6231450
CMOD1	1.0008508	-4.0494949	4.5163173	-14.9002510	69.7981020	-85.8348500
CMOD2	1.0016542	-4.2067747	5.6726330	-24.9923070	106.9139600	-128.6245800
CMOD3	1.0018754	-4.3352971	6.4937910	-33.6093560	142.6154000	-172.7990300

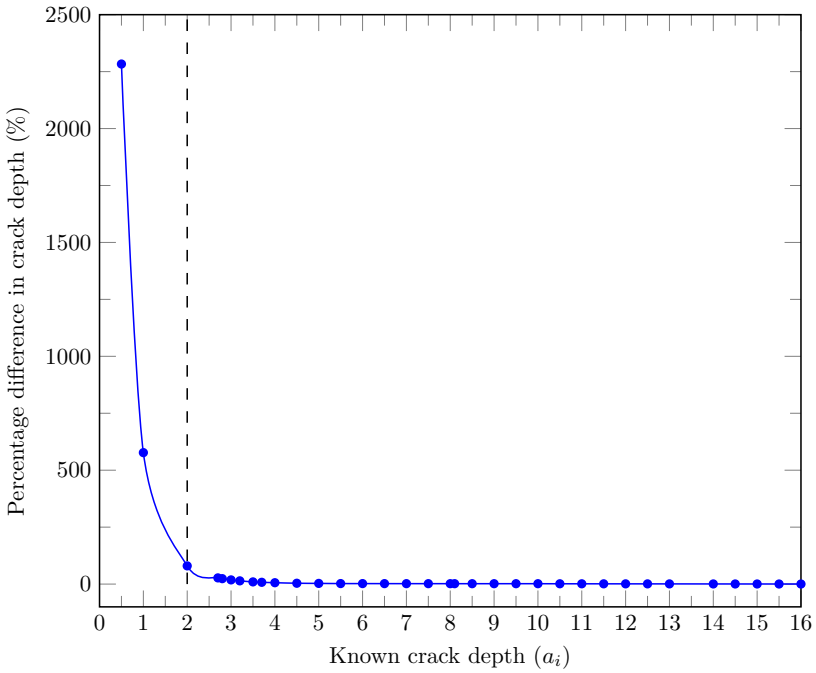

Figure 3.25: Percentage difference in calculated crack depth compared to the known crack depth for $0 \geq a/W \leq 0.85$

$$f\left(\frac{a}{W}\right) = \left(\frac{3\left(\frac{S}{W}\right)\left(\sqrt{\frac{a}{W}}\right)}{2\left(1+2\left(\frac{a}{W}\right)\right)\left(\sqrt[3]{1-\frac{a}{W}}\right)}\right)\left[C_O + C_1\left(\frac{a}{W}\right) + C_2\left(\frac{a}{W}\right)^2 + C_3\left(\frac{a}{W}\right)^3 + C_4\left(\frac{a}{W}\right)^4\right] \tag{3.4.2}$$

Table 3.3: Coefficients for calculation of elastic stress intensity factor

Analysis	C_0	C_1	C_2	C_3	C_4
ASTM	1.99	-2.15	6.08	-6.63	2.7
FE	0.000259	-0.000172	0.016415	-0.036364	0.029513

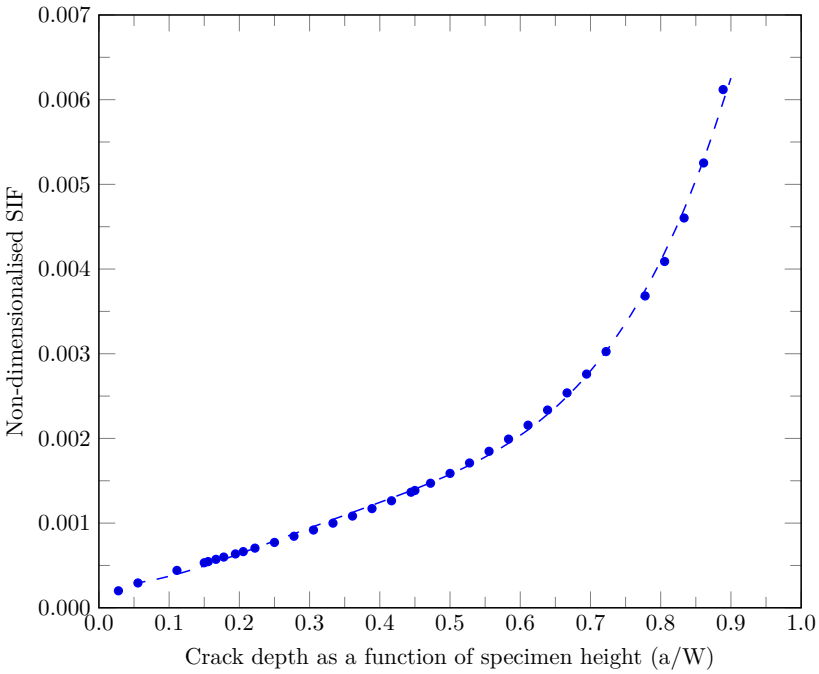

Figure 3.26: Polynomial fit for elastic stress intensity factor coefficients derived from FE

3.5 Chapter 3 Summary

In this chapter the materials used in this work have been introduced. The dis-similar metal weld (DMW) used comprised of A508 base material, approximately 50 mm thick, to which three layers of austenitic stainless steel were welded. Welding was conducted using the TIG welding process the first layer of cladding was stainless steel grade 309 while the remaining two layers were grade 308. As mentioned in Chapter 2 welding can cause microstructural changes in materials. Grade 309 was selected to reduced the amount of dilution that could occur between the base material and the subsequent layers of 308 material.

The test specimens manufactured and the testing parameters were outlined. With regards to fracture toughness specimens, as discussed in Chapter 2, high triaxiality at the crack tip promotes brittle fracture. Given that brittle fracture is to be avoided for in-service failures it is typical for ECAs to incorporate low values of fracture toughness to ensure conservatism and thus safety. To force triaxial conditions the in-plane constraint of a specimen is modified to incorporate a 'deep' defect. A defect is considered to be deep should the ratio of defect depth to specimen height be in the range $a/W \geq 0.45$.

This is why the ASTM test standard [ASTM International, 2001] incorporates validity limits on minimum and maximum defect depths. The out-of-plane constraint (i.e. the thickness effect) is, for small scale specimens, a function of the specimen height (W). Hence ASTM rules effectively limit the geometry and crack depth conditions under which a 'valid' fracture toughness measurement can be made.

Compact tension (CT) specimens were not fatigue pre-cracked which deviates from the recommended ASTM test standard guidance [ASTM International, 2001]. Others have shown that the crack propagation direction may not remain perpendicular to the loading direction. Hence a crack tip originally existing in the base material may propagate to other regions of a DMW [Brayshaw et al., 2018]. It is unclear however what mechanism/(s) may be promoting propagation in unexpected regions. To avoid this from occurring the notch tip was extended using EDM machining as opposed to fatigue pre-cracking.

As presented here several of the SENB specimens have notch parameters that do not follow ASTM guidance. While this is limiting in terms of 'validity' it should be noted that the main focus of this work is on investigating how defects initiate and/or propagate with respect to the weld boundary. Hence, given the geometrical constraints of the original plate, it was not possible to remain 'valid' to ASTM guidance while still fulfilling the research objectives.

It should be noted that the ASTM validity limits were derived somewhat arbitrarily. Finite element analysis of various ligament ratios (i.e. a/W) for a number of material hardening parameters were investigated. The limits were derived to ensure crack tip strains remained similar to those predicted by the HRR field solution within a particular range of the crack tip [Dodds et al., 1991]. In other words the validity limits ensure small scale yield conditions exist at the crack tip. Furthermore the original analysis [Dodds et al., 1991] was conducted with homogeneous material properties only, DMWs were not addressed.

Compliance functions representing the SENB specimens were derived using 2D finite element analysis for the geometry of specimen given. It was shown that there is a disparity between the predicted crack depth using ASTM polynominal values and those derived here. However the disparity is limited to crack depths smaller than that used in this work and hence will not unduly influence test results.

Chapter 4: Mechanical Properties

4.1 Metallography and Hardness

Details relating to the position of samples in the plate sections or, information pertaining the specific location of measurements are provided in Section 3.3.2.

Original TIG weld

The microstructure of the original clad weld plate shows a distinct layer of martensite at the materials interface. This is shown in Figure 4.1 (Figures in this section refer to positional locations which are shown in Figure 3.16b). The martensite layer exists along the entire width of the plate at the weld boundary between the austenite cladding and ferritic base materials. Martensite is a supersaturated solid solution of carbon in ferritic iron and the hardness of this phase is significantly dependent on the amount of carbon present in the ferrite material [Bhadeshia and Honeycombe, 2017]. The formation of martensite requires steel to be cooled from an austenite phase at a rate that is fast enough to avoid solid-state transformations such as ferrite and pearlite. Figure 4.2 shows high magnification (100×) images of positions 1, 9 and 10 (Figures 4.2a, 4.2b and 4.2c, respectively). A banitic microstructure is shown. By comparing these figures it can be seen that position 10, which is closer to the materials interface than either positions 1 or 9, has less carbon compared to the other locations. The reduction in carbon occurs due to the temperature in the plate during the welding process. At high temperatures the diffusion of carbon is rapid and there is little opportunity for carbides to precipitate in the ferrite material. At lower temperatures (i.e. locations further from the weld) carbon precipitates as fine carbides into the ferrite while the remainder partitions into the austenite. Other researchers have shown similar results for these types of materials [Rathod et al., 2017; Kim et al., 2009; Slaughter and Housely, 1962].

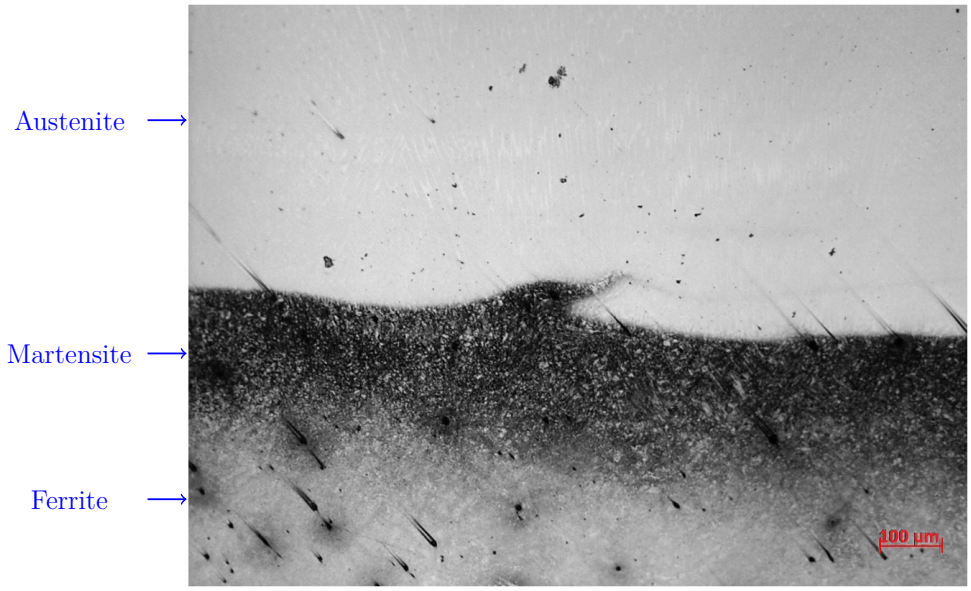

Figure 4.1: Martensitic layer at materials interface of original TIG weld plate at 10X magnification, position 1

The austenite region is shown in Figures 4.2d, 4.2e and 4.2f for each clad layer. Clad layer one (Figure 4.2d) is the layer adjacent to the ferrite, clad layer three (Figure 4.2f) represents the 'top' or surface layer of the plate. From Figures 4.2d, 4.2e and 4.2f it is clear that the grain growth in each layer of cladding is significantly different from the previous/subsequent layer(s). This is is not unexpected when given the variable number of heat cycles that each subsequent layer of cladding is subjected too. Each successive layer will heat treat the underlying microstructure to some extent which introduces a reheated or secondary microstructure [Bhadeshia and Honeycombe, 2017].

Specific measurement points for hardness testing are shown in Figure 3.17. The hardness measurement results are tabulated in Appendix A Table A.3 and plotted in Figure 4.3. Figure 4.3 is a surface plot based on interpolated values between each measurement line and specific measured hardness values of the original TIG welded plate. From Figure 4.3 it can be seen that there is an increase in hardness as one moves from the bottom of the plate towards the weld boundary. Additionally Figure 4.3 shows that the hardness is higher in the mid-width of the plate compared to the outer edge (see measurement line 2 on Figure 3.17 and Appendix A Table A.3). An average increase

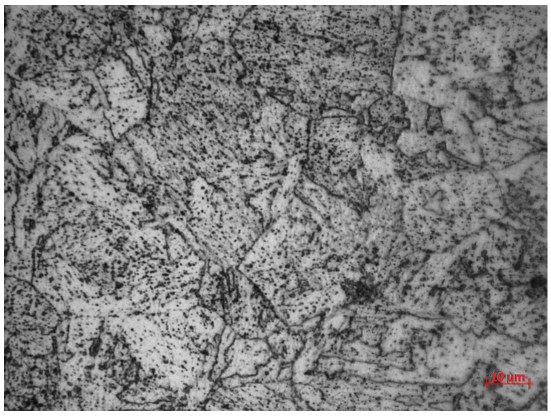

(a) Position 1

(d) Position 2: Clad layer 1

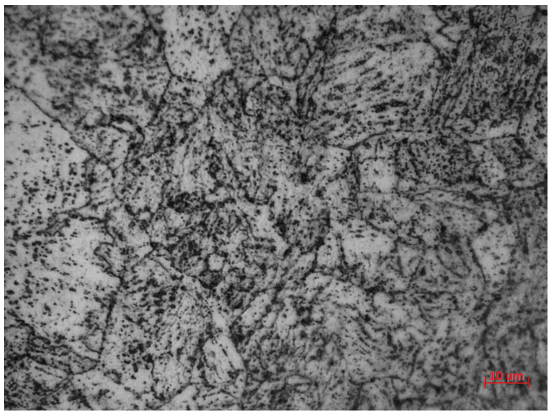

(b) Position 9

(e) Position 3: Clad layer 2

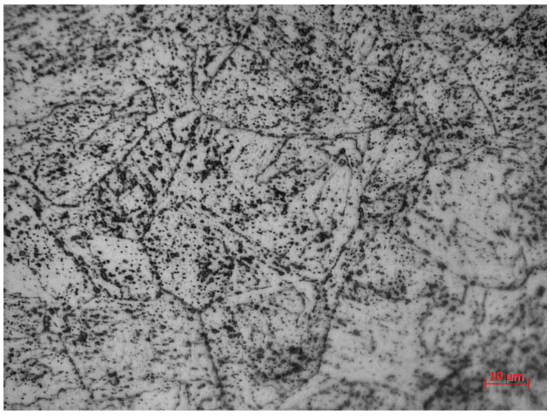

(c) Position 10

(f) Position 4: Clad layer 3

Figure 4.2: Figures 4.2a, 4.2b, and 4.2c detailing grain structure in ferrite region of original TIG weld plate at 100× magnification, respectively. Figures 4.2d, 4.2e, and 4.2f showing micrographs of grain structure in austenite region of original TIG weld plate at 10× magnification, respectively

in hardness of approximately 25 % was found when comparing points from the ferrite side of the materials boundary (Figure 3.17 measurement line 3) to corresponding points on austenite materials boundary (Figure 3.17 measurement line 2). A reduction in hardness of approximately 19 % was found to exist when comparing measurement

lines in the cladding (Figure 3.17 measurement lines 2 and 1). As previously stated (Section 2.3.1) Gooch [Gooch, 1976] stated that due to the dilution effects of the welding process the exact composition at the weld boundary is likely to lie somewhere between that of both the base and cladding materials. Considering that increasing the carbon content of steel typically results in an increase in hardness due to the formation of martensite it not unexpected that an increase in hardness is noted in this location.

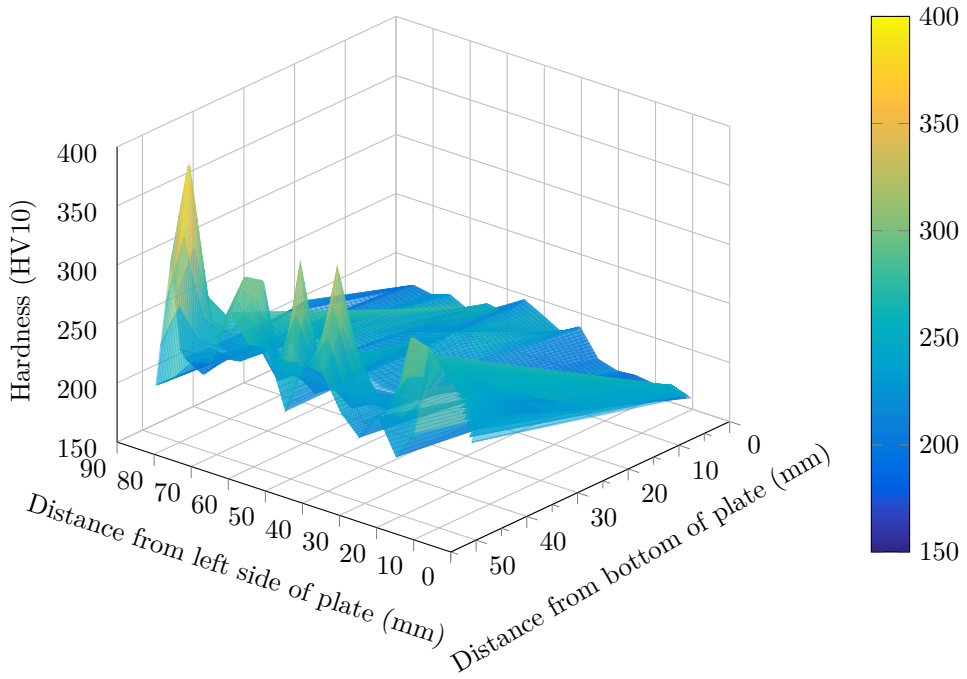

Figure 4.3: Surface plot of HV10 hardness on original TIG weld plate

EB welded section

The microstructure of the EB welded section is shown in Figures 4.4 and 4.5 for the base (ferrite) and cladding (austenite) regions respectively. Micro-structural analysis was conducted on the weld start position only as hardness measurements (discussed below) showed little variation between the weld start and weld stop positions. Figure 4.4 shows position 6 (Figure 3.18a, close to the TIG weld) and region 2 (Figure 3.18a, close to the laser weld). As can be seen the base material appears to have a bainitic microstructure. As shown the microstructure at both positions are broadly similar.

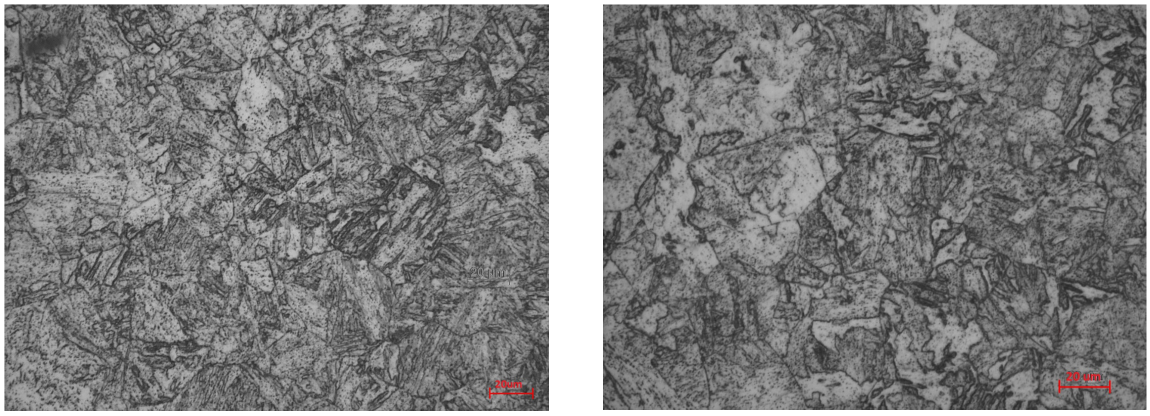

(a) Position 6 (b) Position 2

Figure 4.4: Micrographs of grain structure in ferrite region

The microstructure in the cladding material is shown through the thickness of the weld, from the TIG weld boundary towards the laser weld boundary (see Figure 3.18b for position details). Figure 4.5 clearly demonstrates a significant change in microstructure through the thickness of the austenite region. David [David, 1981] identified four types of ferrite morphologies: vermicular, lacy, acicular and globular. He postulated that the morphologies were related to the transformation temperatures (i.e. the cooling rate) and the diffusion rate. Figure 4.5a shows that, close to the TIG weld boundary, significant mixing of austenite and ferrite phases occur and furthermore this extends some distance into the austenite region. The type of microstructure in the region is not clear. The microstructure shown at the bottom of Figure 4.5a and in Figure 4.5b is the globular form with very low volume fractions of ferrite. Figure 4.5c shows a distinct boundary and change in microstructure between the first and second clad layers. The top of Figure 4.5c is similar, in terms microstructure, to that shown in Figure 4.5b while the bottom shows the globular morphology which is characterised as a random distribution of ferrite in austenite matrix. David suggests that this morphology is the result of thermal instability during the formation of acicular type microstructure. Figure 4.5c shows the vermicular morphology which, according to David, is aligned along the heat flow direction. The ferrite phase is the result of an incomplete $\delta \rightarrow \gamma$ transformation. Figure 4.5e shows the boundary between clad layer 3 (top of the image) and the laser weld. The top Figure 4.5e appears to be somewhere between the lacy and glob-

ular morphologies which indicates the material has undergone several thermal cycles. During each subsequent cycle, depending on temperature and cooling rates it's likely different morphologies formed, broke down and re-formed. The microstructure in this region could not be ascertained in detail.

Tabulated values of hardness for the EB welded sections (both weld start and weld stop positions) are provided in Appendix A Tables A.1 and A.2, surface plots based on the interpolated tabular values are shown in Figure 4.6 for the weld start (Figure 4.6a) and end (Figure 4.6b) positions. Figure 4.6 shows the highest hardness exists at a location analogous to the EB weld materials interface. A peak in hardness occurs at each outer edge, at least in comparison to the mid-width measurement. The reduction in hardness in the centre of the specimen is likely due to annealing in the central region where the two welds overlap. Similarly this may account for the variation in hardness when comparing the edge measurements. Additionally an increase of hardness was noted close to the original TIG weld boundary.

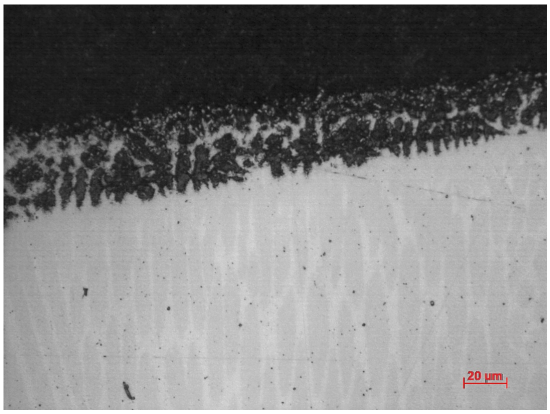

(a) Position 6: TIG boundary

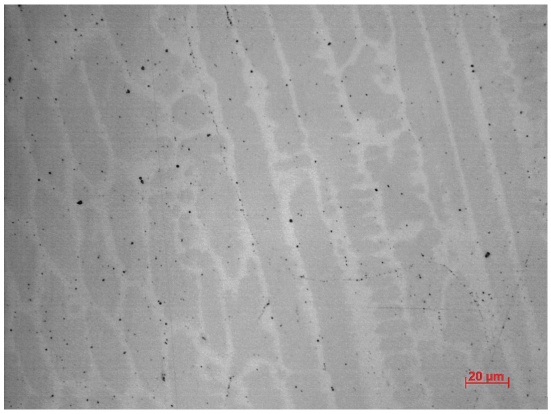

(b) Position 5: Clad Layer 1

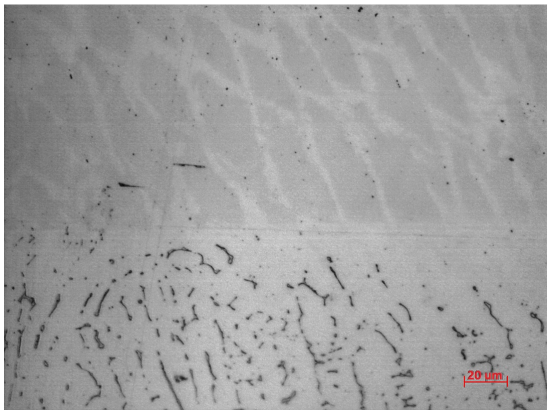

(c) Position 4: Boundary between clad layers 1 and 2

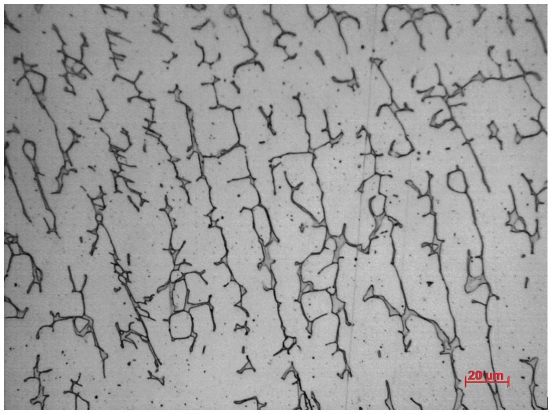

(d) Position 1: Clad layer 2 mid thickness of austenite

(e) Position 2: Boundary between clad layers 3 and laser weld

Figure 4.5: Micrographs of grain structure in austenite region of EB welded section at 100× magnification. Images taken in the mid-width of sample, i.e. where the weld overlaps through thickness direction from TIG weld towards the EB weld.

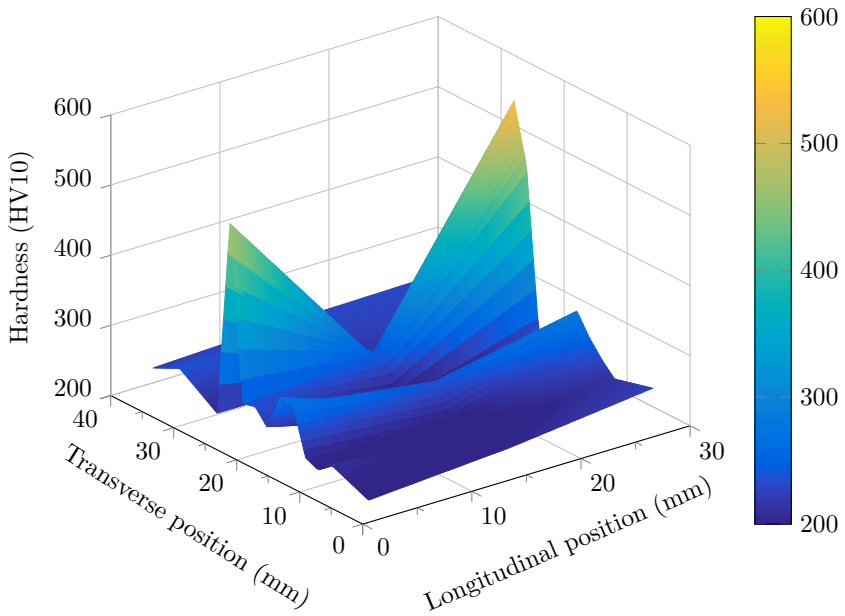

(a) Weld start position

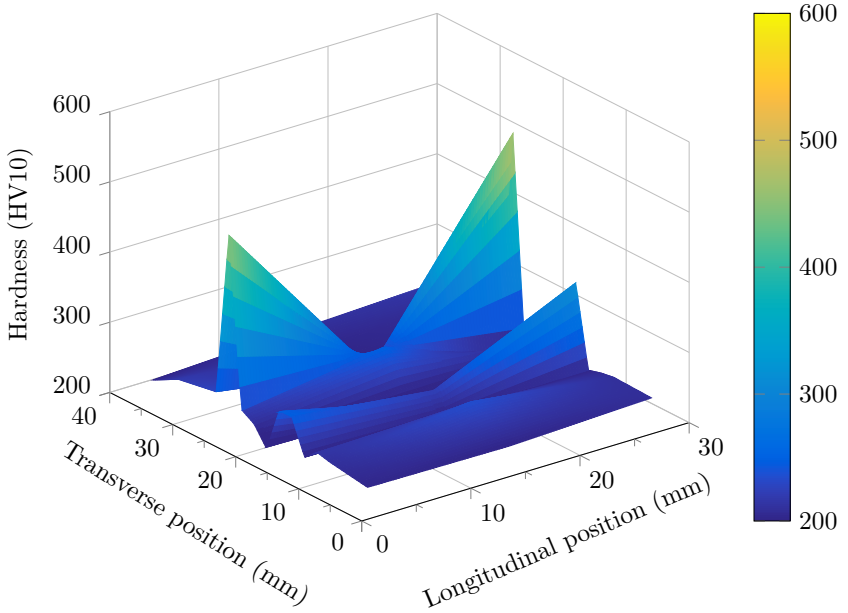

(b) Weld end position

Figure 4.6: Surface plots of HV10 hardness on Block B weld start and end positions

4.2 Experimental tensile test results

4.2.1 Standard tensile testing

The engineering stress-strain curves for the ferritic and austenitic materials are shown in Figure 4.7. Figure 4.7a plots the homogeneous ferrite specimens and, as shown, samples exhibited similar magnitudes of yield and UTS (ultimate tensile stress). Figure 4.7b plots homogeneous austenite specimens (S2 and S3) and specimens of unknown chemical composition (mixed specimens S4 and S5). Considering the complex microstructure in and around this region (see Section 4.1 for microstructural analysis) it is not unusual to have such disparity in terms of mechanical performance. Yield stress, UTS and Young's Modulus were estimated from the relevant curves in Figures 4.7a and 4.7b and are tabulated in Appendix A Table A.4. The proof stresses were calculated assuming an offset of 0.2 % strain in conjunction with the estimated Young's Modulus. The average mechanical properties for the ferrite, austenite and HAZ zones were calculated from Appendix A Table A.4 and are shown in Table 4.1.

Table 4.1: Average mechanical properties for ferritic, austenitic and HAZ materials, derived from standard size tensile specimens

Specimen Number	**Units**	**Ferritic**	**Austenitic**	**HAZ**
Yield Strength	MPa	436	300	486
0.2% proof stress	MPa	440	350	510
Young's Modulus	GPa	217.44	203.22	173.28
UTS	MPa	590	440	620
Failure strain	%	20	43	13

The true-stress true-strain curves were calculated for each specimen using Equations 4.2.1 and 4.2.2. Hardening was assumed to follow a power law relationship (Equation 4.2.3) and the parameters α and n were calculated based on the best fit for each individual true-stress true-strain curve. The power law fit for each of the regions (ferrite, austenite and HAZ) were calculated from the average values of α and η provided in Appendix A Tables A.5 and A.6. The overall averages are tabulated in Table 4.2. Figure 4.8 shows the average true-stress true-strain plots.

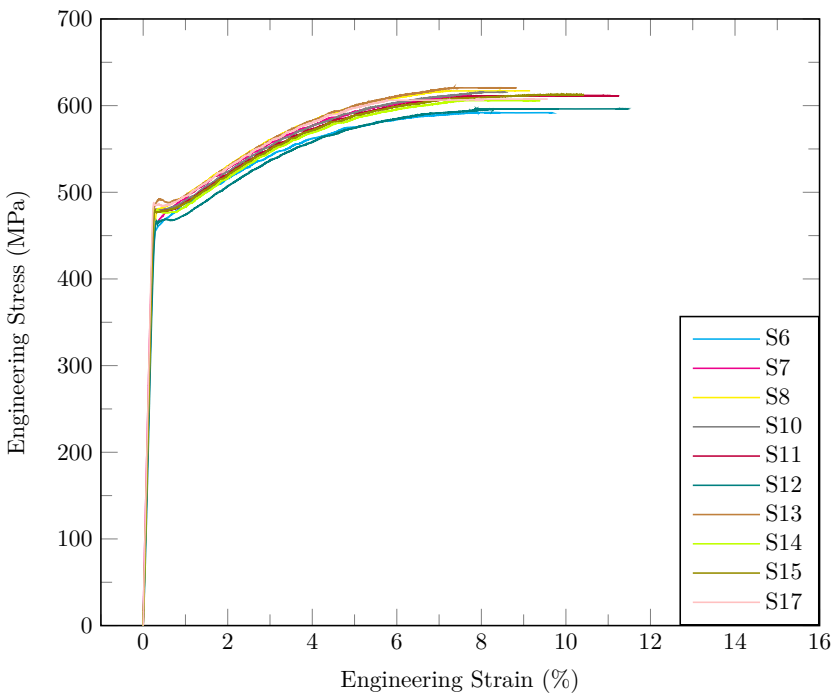

(a) Ferrite only specimens.

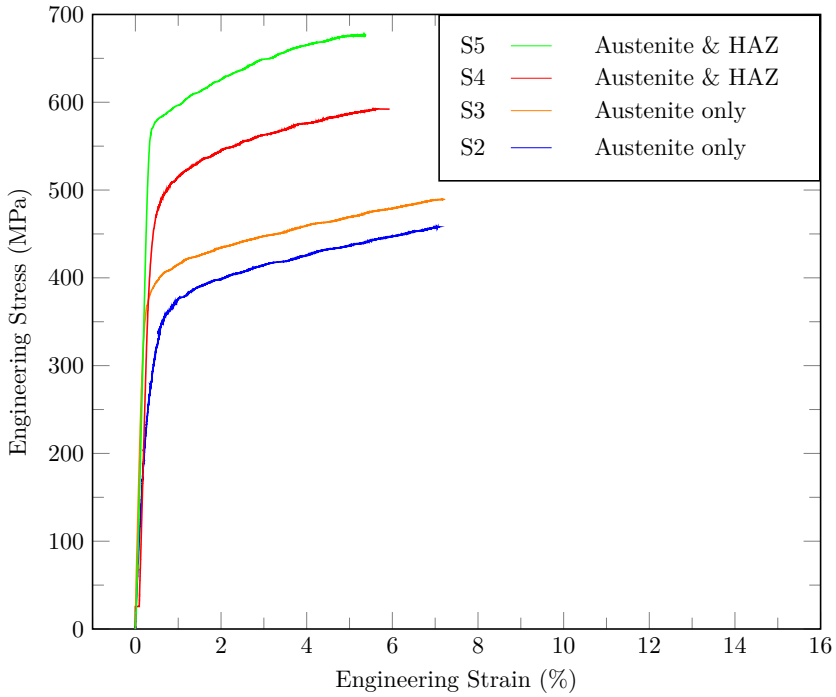

(b) Austenite and mixed specimens

Figure 4.7: Engineering stress-strain curves for standard size tensile specimens

$$\epsilon_t = ln(1 + \epsilon_e) \tag{4.2.1}$$

$$\sigma_t = \sigma_e(1 + \epsilon_e) \tag{4.2.2}$$

Where: ϵ_t represents true strain, ϵ_e the engineering strain, σ_t the true stress, and σ_e the engineering stress.

$$\epsilon_p = \alpha\sigma^n \tag{4.2.3}$$

Where: α is a constant fitting parameter and n is the strain-hardening exponent.

Table 4.2: Average power law constants for standard size true stress-strain properties

Parameter	**Ferrite**	**Austenite**	**HAZ**
α	4.54×10^{-13}	2.20×10^{-16}	6.04×10^{-14}
n	4.02	5.24	4.65

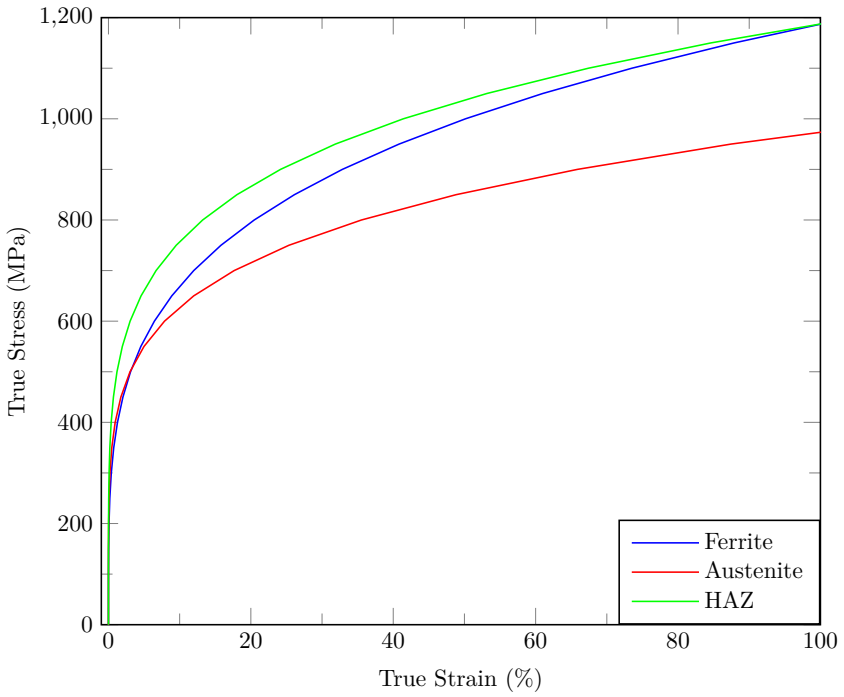

Figure 4.8: True stress-true strain plot for standard sized ferritic, austenitic and HAZ specimens based on average power law data

4.2.2 Sub-size tensile testing

For clarity the following section is divided by specimen orientation (see Section 3.2 for details on orientation). Experimental data was modified assuming a power law fit as detailed Equation 4.2.3. As previous discussed (Section 3.2.3) strains were estimated using the DIC technique.

B3-2

The DIC stress-strain data for group B3-2 are shown in Figure 4.9. From Figure 4.9 it can be seen that some specimens have excessive scatter (specimen 10, 12, and 14) this was attributed to the resolution of the attained images. The austenitic specimen (Specimen 2) has a hardening trend which is significantly different from that of the other specimens.

Group B3-3

Results for group B3-3 are shown in Figure 4.10. As shown specimens 1 and 2, both homogeneous cladding specimens, again show significantly different hardening when compared to other specimens in the group.

As shown specimen 3 reaches a yield and UTS significantly higher than any other specimen. This is attributed to the thickness of the specimen (0.5 mm) and the region of the plate sampled. It is considered likely that specimen 3 measured pure HAZ material rather than mixed HAZ to austenite or HAZ to ferrite that is likely to have been sampled by standard sized specimens taken from a similar location. This is due to the relative thickness of standard specimens compared to sub-size specimens.

Group B3-4A

Figure 4.11 shows the results for specimens machined perpendicular to the materials interface centred at the materials boundary. These specimens consisted of 50 % ferrite and 50 % austenite with the weld boundary located in the central width of the specimen. Due to the small size of the samples and the undulation of the materials interface it was difficult to ensure the 50:50 ratio on all samples which may account for some of the variation seen in the results. Additionally it should be noted that due to sample size the 'ferrite' material is likely to consist largely of HAZ material as opposed to homogeneous ferrite.

Group B3-4B

Figure 4.11 shows the results for homogeneous ferrite specimens machined perpendicular to the weld boundary. As can be seen the majority of specimens have similar yield stress of 450-500 MPa excepting specimens 7 and 8 which show yield stresses of 550 to 600 MPa respectively. Specimen 7 has a UTS of approximately 580 MPa, slightly lower than that noted for other specimens. It is not clear why specimens 7 and 8 differ from other data in this group. It may be that they existed in an area that was microscopi-

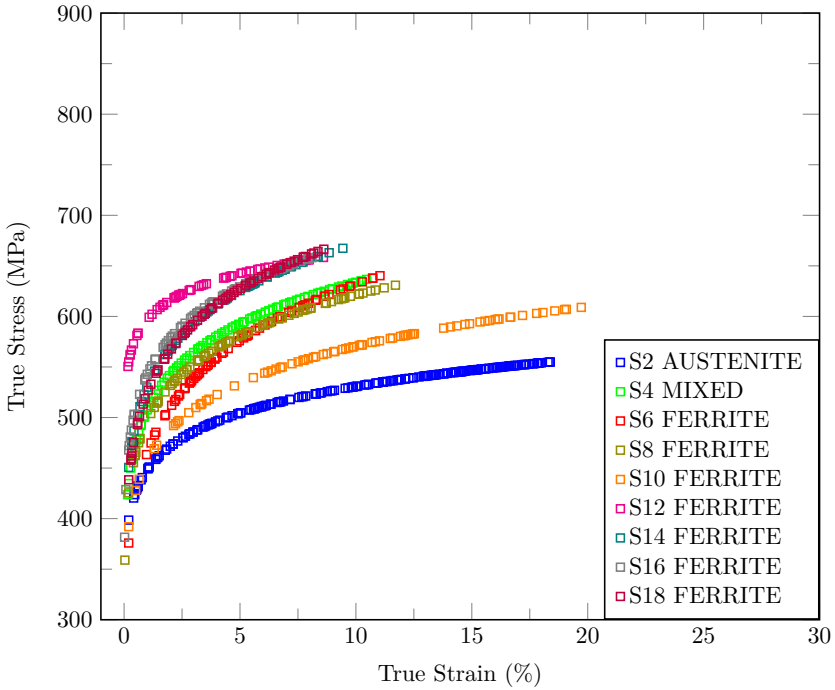

Figure 4.9: Stress-strain data for Group B3-2. Specimens oriented longitudinal to clad weld direction.

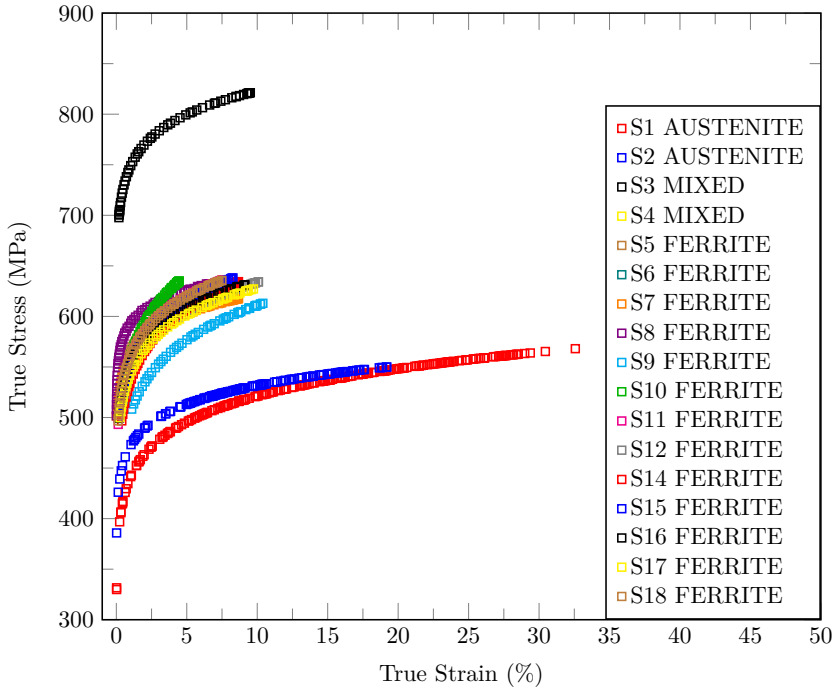

Figure 4.10: Stress-strain data for Group B3-3. Specimens oriented transverse to clad weld direction.

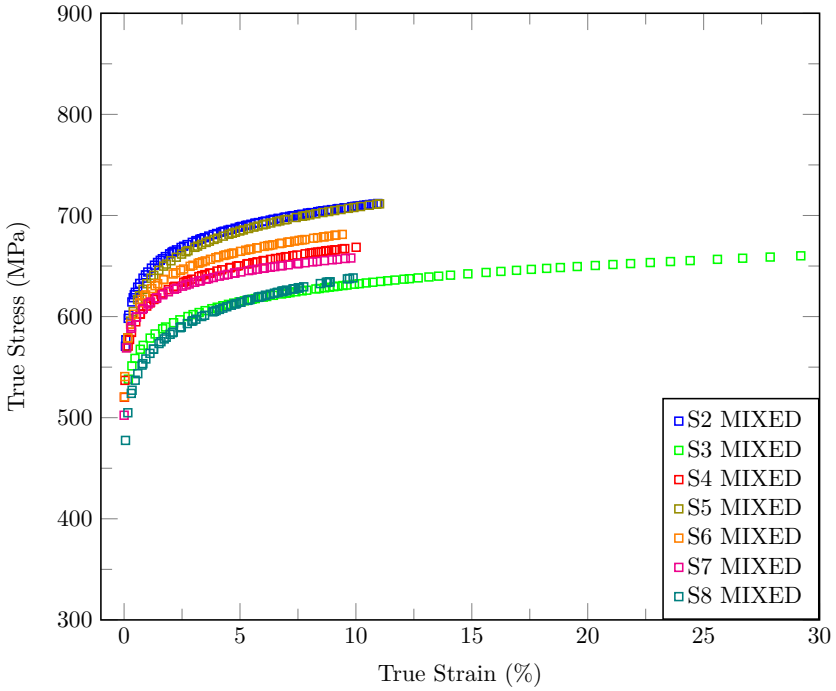

Figure 4.11: Stress-strain data for Group B3-4A. Specimens oriented perpendicular to clad weld direction.

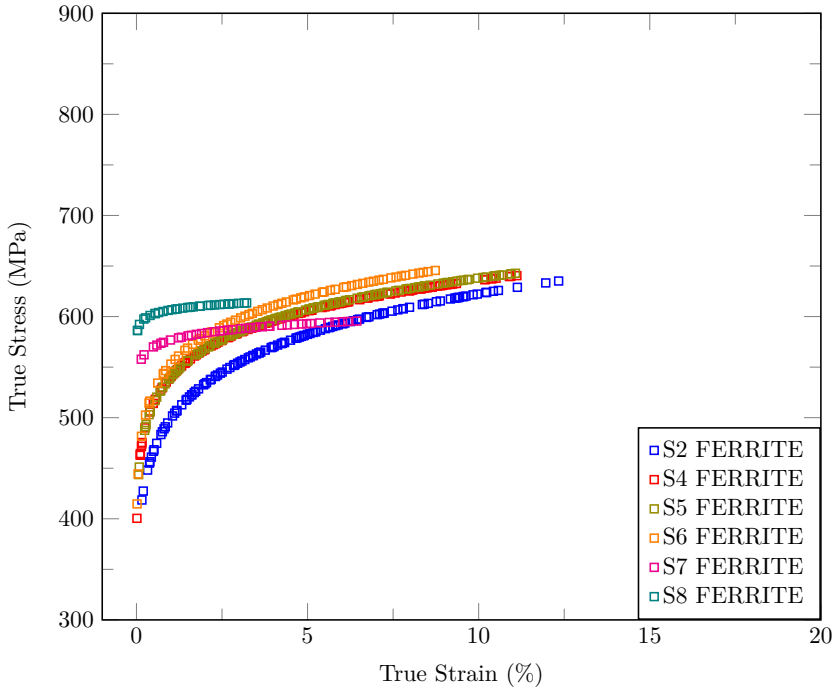

Figure 4.12: Stress-strain data for Group B3-4B. Specimens oriented perpendicular to clad weld direction.

cally different to other samples (i.e. HAZ region), further microscopic analysis of the specimens would be required to confirm.

4.2.3 Comparison of full size and micro-size data

Figure 4.13 plots homogeneous ferrite sub-sized specimens irrespective of orientation. From these data the upper, lower and average bounding curves were calculated. As can be seen the majority of sub-sized specimens fall between the upper and average bounding curves. Additionally the largest deviations in true stress - true strain response occur between specimens of the same group. This implies that the orientation of the specimens, with respect to the cladding, has less influence on the measured data than other factors such as local microstructure, variations in test method and/or variation in measurement technique.

A comparison of the derived power law curves for both full size and micro size ferrite data sets is shown in Figure 4.14. As can be seen there is no agreement between the data sets. The yield stress and hardening coefficients of the data sets are tabulated in Table 4.2 and Table 4.3 for the full size and sub-sized data sets respectively. Significant variations exist in both the material constant α and the hardening co-efficient n. As previously discussed (Section 3.3.2) the sub-sized test specimens were tested at a cross-head displacement of 1 mm/min, identical to that of the standard size specimens. However, comparing the relative size of each specimen in terms of dimensions, it can be seen that the strain rate applied to the sub-sized specimens would be significantly higher than that applied to the standard size specimens which likely a contributing factor to the variation in mechanical response. Dunnett [Dunnett, 2014] stated that 'an increase in variability is a characteristic of microstructure influencing the behaviour' when comparing geometrically small samples to larger samples manufactured from the same material.

Figure 4.15 plots homogeneous austenite sub-sized specimens. From this data the upper, lower and average bounding curves of all data sets were calculated and are tabu-

Table 4.3: Average power law constants for upper, lower and average bounding curves for sub-sized specimens.

Parameter	Lower	Upper	Average
α	1.814×10^{-28}	1.215×10^{-123}	2.465×10^{-51}
n	10.42	43.86	18.23

lated in Table 4.4. The equivalent standard size power law curve is included in the plot for comparison. Figure 4.15 shows good agreement was found between all sub-sized curves with little variation in bounding curves. The sub-sized data does not however agree with the equivalent standard size data. Given that there is relatively good agreement between sub-sized specimens it is considered likely that the variation, when comparing the standard size data to the sub-sized data, is due in part to the difference in the strain rates applied to each data set, and in part to the local microstructural effects.

Figure 4.16 plots sub-sized specimen data for mixed material specimens. As shown the sub-sized data fall below the average bound curve. The power law curve for full size HAZ specimens is included in the curve for comparison. Specimen B3-3 S3 is significantly different from all other specimens but this specimen is likely to contain a significant amount of martensite microstructure due to its location in the plate (see Figure 3.6). Data for the mixed sub-sized specimens is tabulated in Table 4.5. As noted for other comparison the standard HAZ data do not agree with sub-sized specimen data.

Given the difference in mechanical properties for the sub-sized specimens in comparison to the results generated for standard size specimens it was decided that, for the

Table 4.4: Average power law constants for upper, lower and average bounding curves for sub-sized austenite specimens only

Parameter	Lower	Upper	Average
α	4.758×10^{-37}	7.960×10^{-51}	5.340×10^{-37}
n	13.74	18.70	13.70

Table 4.5: Average power law constants for upper, lower and average bounding curves for mixed material sub-sized specimens

Parameter	**Lower**	**Upper**	**Average**
α	4.359×10^{-33}	1.73×10^{-70}	1.220×10^{-48}
n	11.98	24.30	17.3

purposes of FE modelling, only data generated by the full size specimens (i.e. data as shown in Figure 4.8 and Table 4.2) would be utilised.

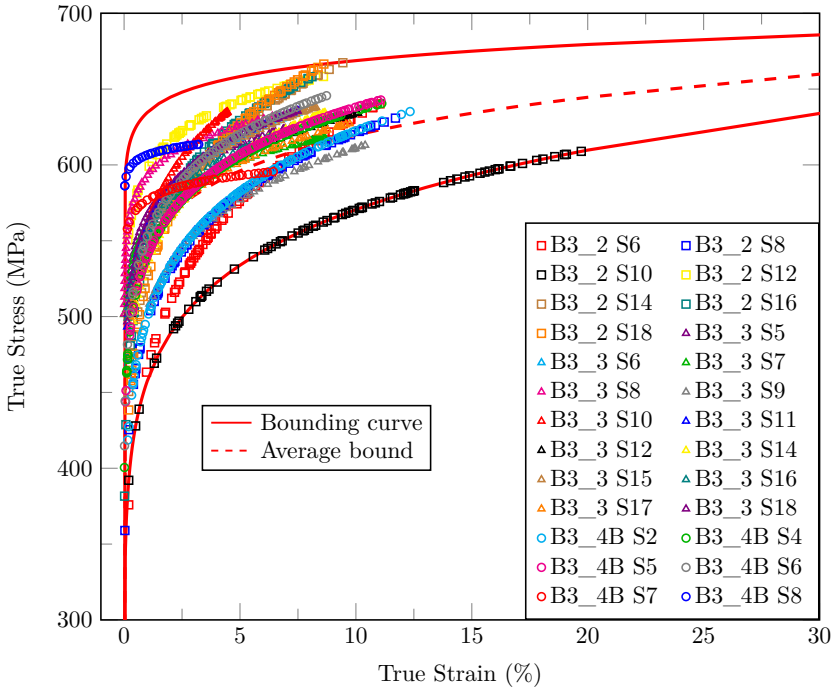

Figure 4.13: Stress-strain data for sub-sized specimens comprised of ferritic material only

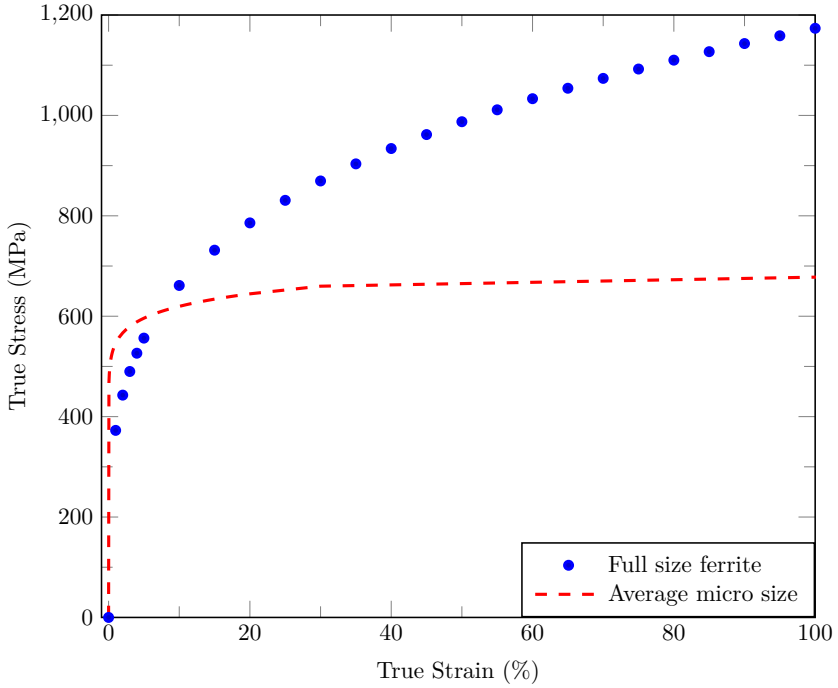

Figure 4.14: Comparison of standard size and sub-sized size power law curves for ferritic material

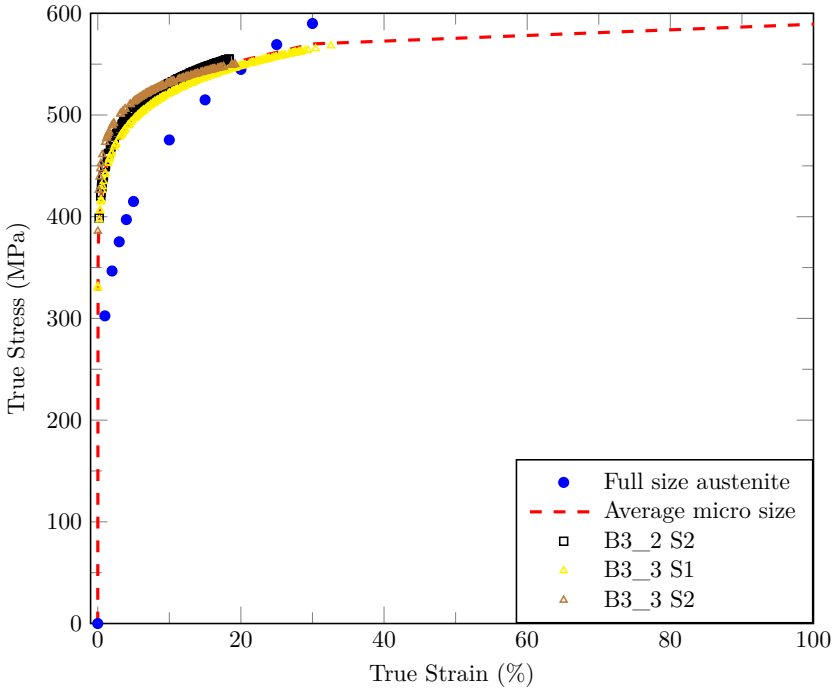

Figure 4.15: Comparison of full size and micro size power law curves for austenite material

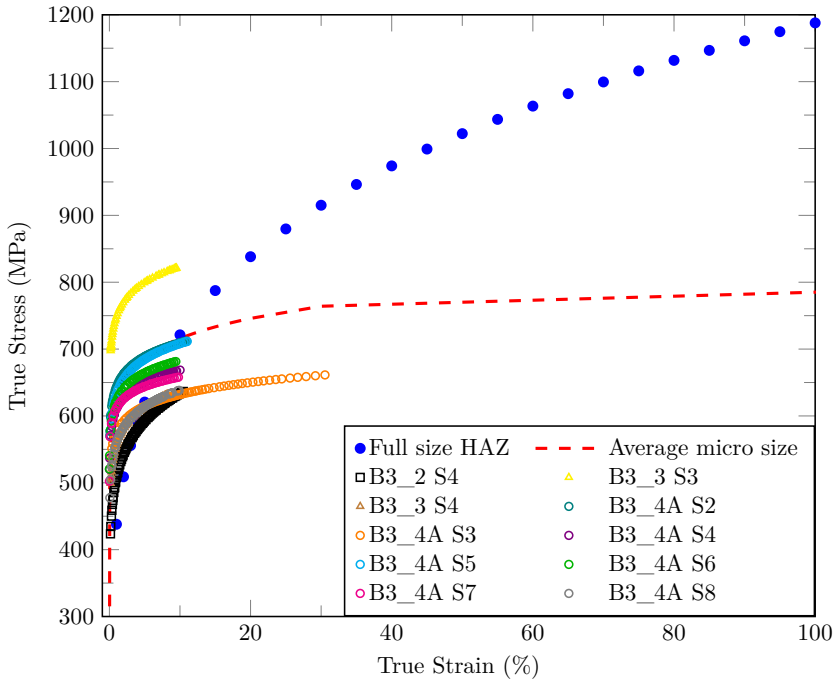

Figure 4.16: Stress-strain data for sub-sized specimens comprised of mixed ferrite/austenite material

4.3 3D Modelling of tensile test

Numerical simulation of tensile testing was conducted using ABAQUS v6.14 [Dassault Systemes Simulia Corp, 2014]. Material properties for ferrite, austenite and HAZ material were based on power law data derived as discussed in Section 4.2.1. An isotropic hardening relationship was assumed. The specimen geometry was identical to that shown in Figure 3.5.

Identical boundary conditions were applied to all models. An encastre boundary condition was applied to the bottom surface of the model (U1 = U2 = U3 = UR1 = UR2 = UR3 = 0). A displacement of 30 mm (U2 = 30) was applied to a reference point. The reference point was kinematically coupled to the top surface of the model (U1 = U3 = UR1 = UR2 = UR3 = 0, U2 = 30).

During experimental testing the presence of stress concentrating defects due to the clad welding process were noted. The experimental tensile samples were machined transverse to the direction of welding. As displacement increased during testing areas of high stress appeared at the inter-pass locations, indeed failure of the austenite frequently occurred along these inter-pass weld runs. This is not wholly unexpected given that (as discussed in Section 2.3) each weld inter-pass will have a unique weld toe, each introducing stress concentrating defects. The likelihood of failure in these regions is further increased due to the comparative change in microstructural properties for each weld bead. Figure 4.5 clearly shows the change in microstructure for each clad layer, the change in grain growth seen in these images is representative of the change in cooling for each subsequent weld bead, and each subsequent clad layer. It is considered likely that multiple HAZ regions exist not only at the materials interface but also between each weld bead and each clad layer in the austenite material. The impact of multiple HAZ regions and stress concentrating defects in the austenite material zone were not incorporated into the models.

Five types of model were investigated for comparison purposes. Three models, each assuming one of the three individual material properties: homogeneous austenite ma-

terial, homogeneous ferrite material and HAZ material. Additional models assuming a combination of material properties were analysed. The first assumed a combined austenite to ferrite condition (combined AF), a second model assumed a austenite to HAZ to ferrite combination (combined AHF). The purpose of these analyses is to investigate the influence of the HAZ region on the estimated stress-strain response.

Combination models assumed a materials boundary existed along the length of the specimen through the mid-thickness of the specimen - mimicking the materials interface in the standard size experimental specimens. For the austenite and ferrite combination the materials were assumed to be split evenly across the thickness (i.e. 1.5 mm of austenite material and 1.5 mm of ferrite material). The model investigating the influence of all three types of material properties assumed a HAZ zone of thickness 0.1 mm existing in the ferrite region at the boundary with austenite (i.e. austenite region 1.5 mm, HAZ region 0.1 mm and a ferrite region of 1.4 mm).

Figure 4.17 plots the force versus displacement curve for the five models. The response of specimens comprised of homogeneous material properties are as expected. The combined austenite to ferrite specimen response falls approximately in-between the homogeneous ferrite and austenite results. The model comprised of all three materials responded identically to that of the combined ferrite to austenite model.

Figure 4.18 plots the stress-strain response of a single node located in the center of the specimen (i.e. mid-gauge section, mid-thickness). Results for the homogeneous materials (Figure 4.18a) are as expected. The combined material models (Figure 4.18b) show two values of strain for each value of stress. This is due to the position of the materials boundary with respect to the position of the node. The direct stress (σ_{yy}) through the thickness of each model was investigated. Results for the homogeneous samples were as expected, results for the combined models are shown in Figure 4.19. From Figure 4.19a it can be seen that the combined material models have stagnant stresses across homogeneous sections and distinct deviations at the weld boundaries. In the case of the combined austenite and ferrite material model that change occurs,

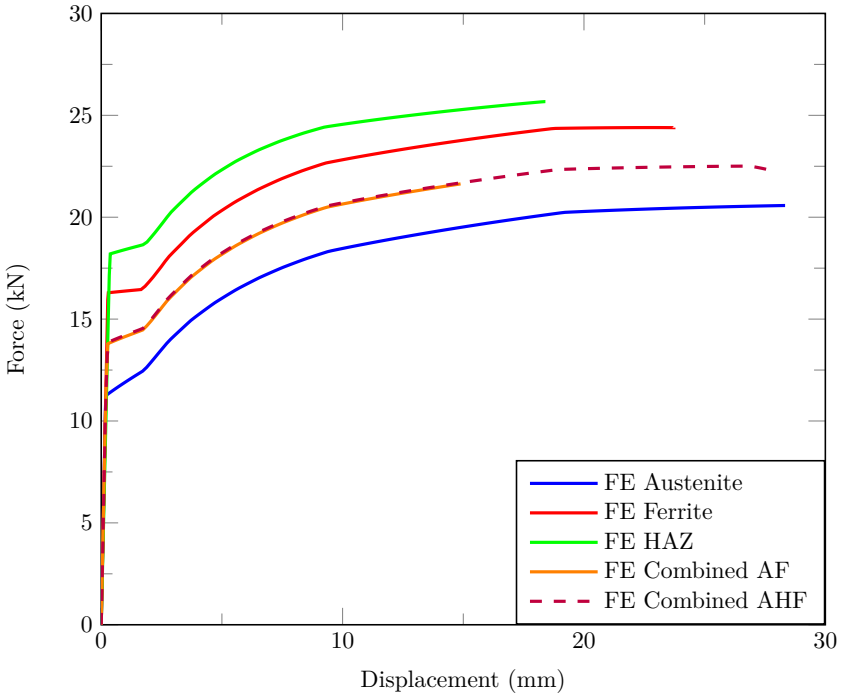

Figure 4.17: Force versus displacement response for each model

as expected, in the mid-thickness (position 1.5 mm) with nodes associated with ferrite material having higher stresses than those estimated for the austenite material. For the combined ferrite, HAZ, austenite model (Figure 4.19a) there are two distinct changes, one at the materials boundary between the ferrite and HAZ, and a second between the HAZ and the austenite. Again the highest magnitude of stress exists in the ferrite material region. Figure 4.19b plots the results in Figure 4.19b normalised by the yield strength of the respective material (see Table 4.1). It is clearly shown (Figure 4.19b) that the peak magnitude of stress exists in the austenite material and at the interface between the austenite and HAZ boundary. The stress in the HAZ region is lower, in relative terms, than those predicted in either the ferrite or austenite regions, this correlates well with experimental results.

Figures 4.20 and 4.21 are contour plots of the von Mises stress distributions for the singular and multi-material models respectively.

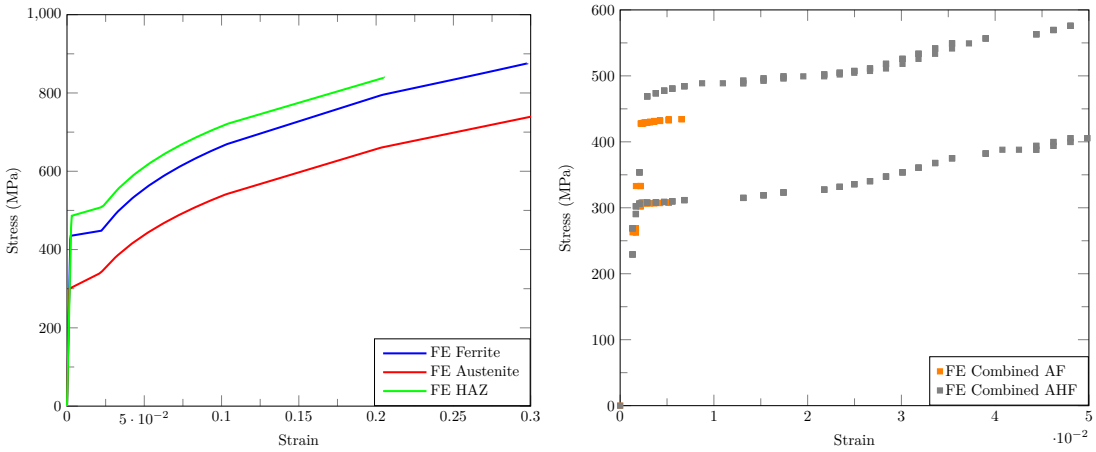

(a) Homogeneous material models (b) Multi-material models

Figure 4.18: FE stress-strain response for 3D tensile testing

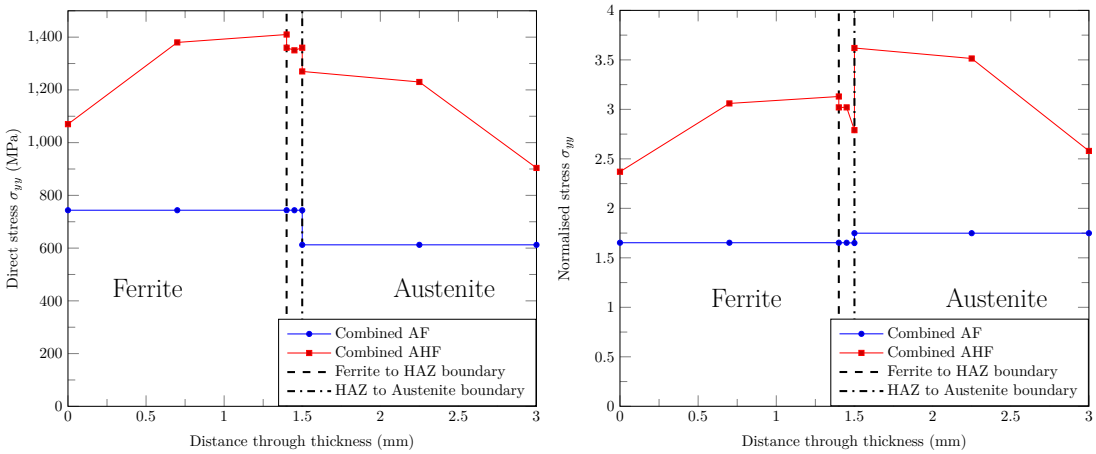

(a) Multi-material models (b) Normalised multi-material models

Figure 4.19: Direct stress (σ_{yy}) through thickness of specimen in Figure 4.19a. Predicted values of stress normalised against measured yield strengths shown in Figure 4.19b

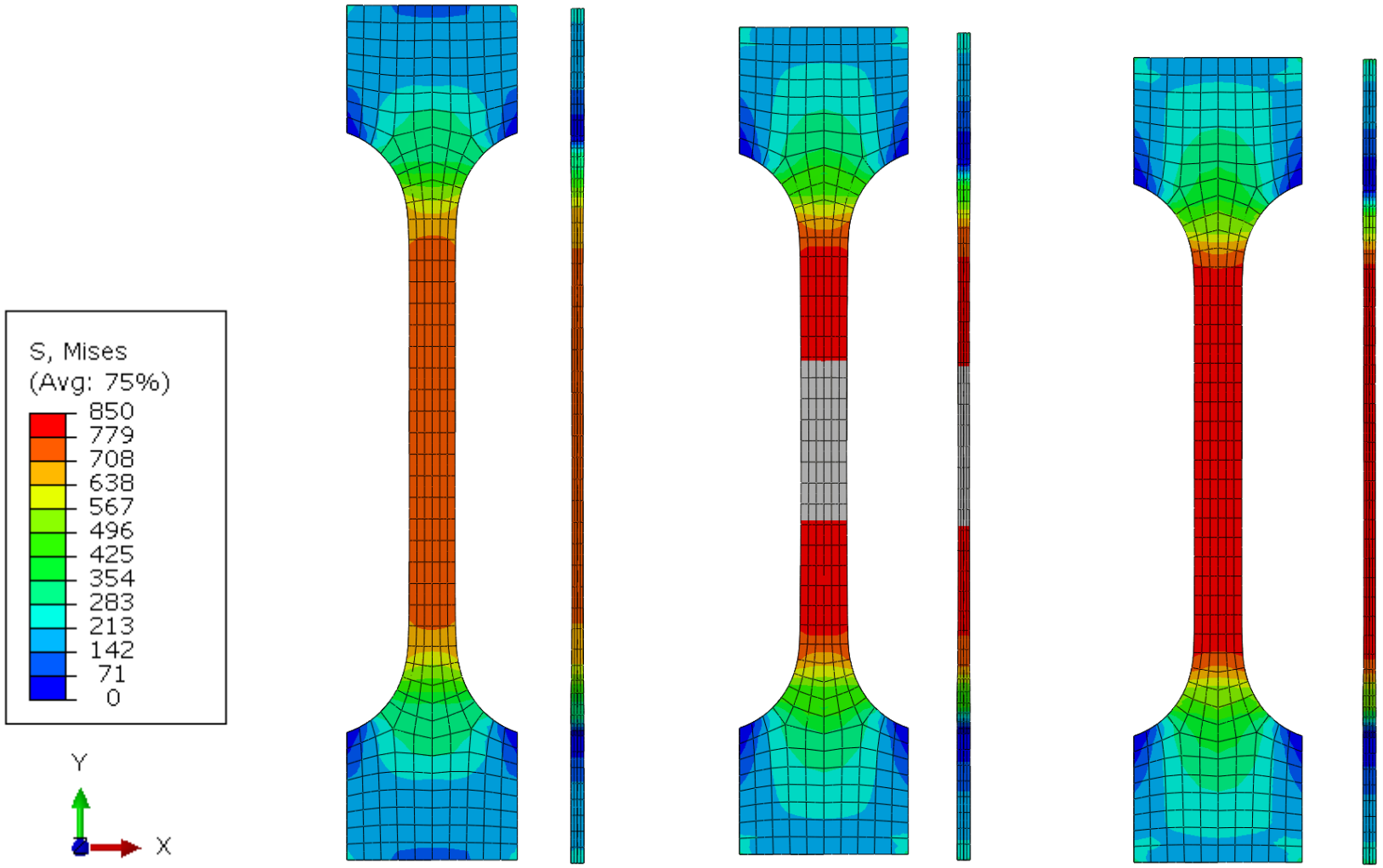

(a) Austenite (b) Ferrite (c) HAZ

Figure 4.20: Mises stresses at final displacement for homegeneous material models 4.20a) Austenite, 4.20b) Ferrite and 4.20c) HAZ regions

(a) Combined austenite and ferrite

(b) Combined austenite, HAZ and ferrite

Figure 4.21: Mises stresses at final displacement for multi material models: 4.21a) Combined austenite and ferrite model and 4.21b) Combined austenite, ferrite and HAZ model

4.4 Temperature Dependent Material Properties

Finite element (FE) work was initially conducted using material properties provided by a literature [Serasli, 2014]. Plots for these data are shown in Appendix A Figures A.1 to A.4. The temperature dependent true stress-true strain data for the ferrite material are plotted in Appendix A Figure A.5. Due to difficulty in digitalising data at strains < 0.5 % some data are not included. The temperature dependent austenite material properties reported by Serasli [Serasli, 2014] are shown in Figure A.6. Few data were provided for this material and results showed that an identical mechanical response was found for tests conducted at 260 °C and 370 °C.

Temperature dependent true stress-true stain data, for a similar grade of ferrite material, was provided by the industrial sponsor. Figure 4.22 is a comparison of the industrial sponsor's data and that of the literature [Serasli, 2014]. As can be seen there is little agreement between the data for tests conducted at similar temperatures. The data reported by Serasli appears to underestimate the yield strength and hardening ability of the ferrite material. Figure 4.23 compares the true stress-true strain data derived as part of this project (see Section 4.2.1 for more details) with true stress-true strain data from the industrial sponsor. A slight offset exists between data provided by the industrial sponsor and the experimental data but the variation is within the acceptable statistical parameters for forging materials (i.e. approximately 50 MPa).

Temperature dependent material properties for the specific grade of austenite used in this work could not be sourced from additional literature. However, a European collaborative project - the NeT project conducted a significant amount of experimental and numerical work on a stainless steel grade 316L [Ficquet et al., 2009] which has a similar chemical structural and similar mechanical properties to stainless steel grades 308 and 309. The NeT project data is shown in Figure 4.24. Figure 4.25 compares the NeT material with literature data [Serasli, 2014]. As shown a good agreement was not found. The data reported by Serasli appears to have a much higher rate of hardening in comparison to the NeT data for all temperatures.

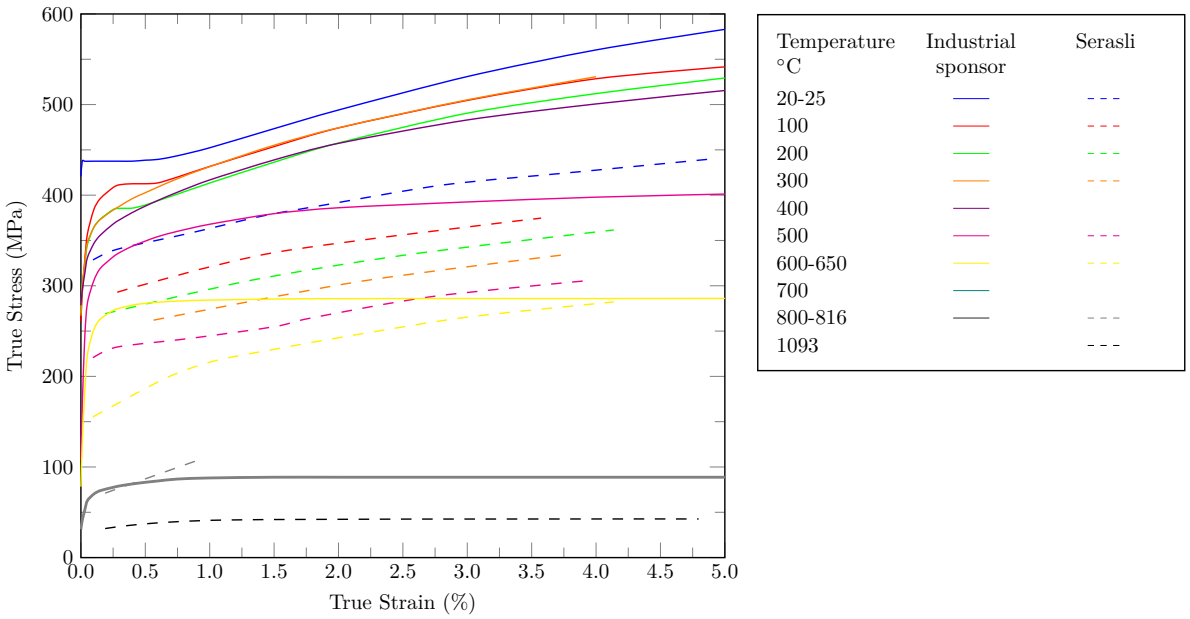

Figure 4.22: Ferritic temperature dependent true stress - true strain curves. Comparison of data from from literature [Serasli, 2014] with data provided by industrial sponsor

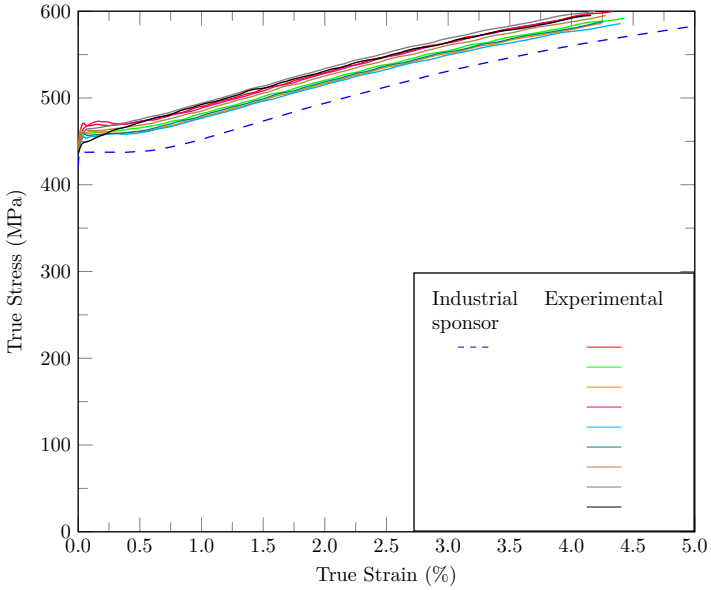

Figure 4.23: Ferrite temperature dependent true stress - true strain curve. Comparison of data from industrial sponsor with experimental data derived as part of this project (shown as solid lines see Section 4.2)

Figure 4.26 is a comparison of the room temperature NeT data with experimental tensile test results conducted as part of this project. The NeT data specified a yield strength of 250 MPa for the 316L grade stainless steel, slightly lower than that of the material tested in this work (300 MPa for austenite specimens see Section 4.2.1). However comparing the NeT data with the curve derived experimentally it is shown that the shape of the curves are almost identical and that by simply shifting the NeT data +50 MPa (black dashed curve) a curve very similar to that measured experimentally can be obtained.

It is clear from these comparisons that the experimental work conducted is in good agreement with data from other sources [Ficquet et al., 2009] for tests conducted at room temperature. The temperature dependent data provided by Serasli [Serasli, 2014] was significantly different from both literature and experimental work conducted as part of this project and was therefore not used in computations for this work. Data derived experimentally was used for simulations at room temperature. For simulations requiring the use of temperature dependent material properties literature values provided by the industrial sponsor and the NeT project [Ficquet et al., 2009] where used for the ferrite and austenite materials, respectively.

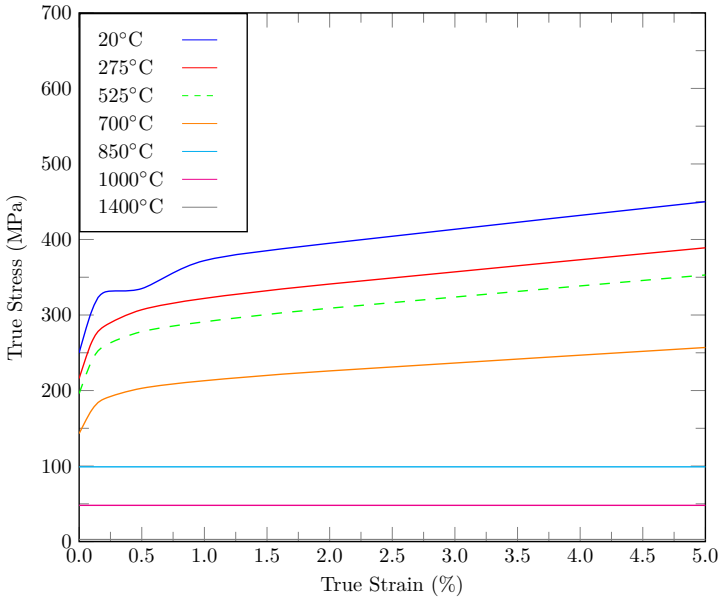

Figure 4.24: Temperature dependent true stress - true strain for austenite material from data in the NeT project [Ficquet et al., 2009]

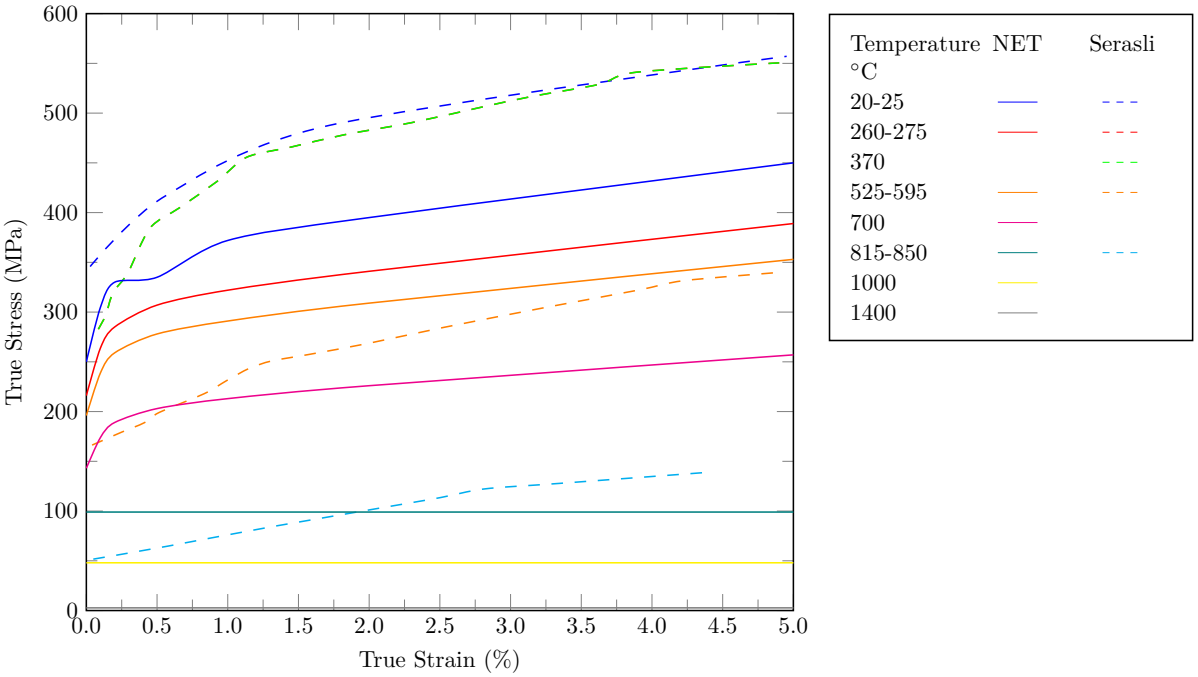

Figure 4.25: Comparison of temperature dependent true stress - true strain for austenite material from data in the NeT project [Ficquet et al., 2009] and Serasli [Serasli, 2014]

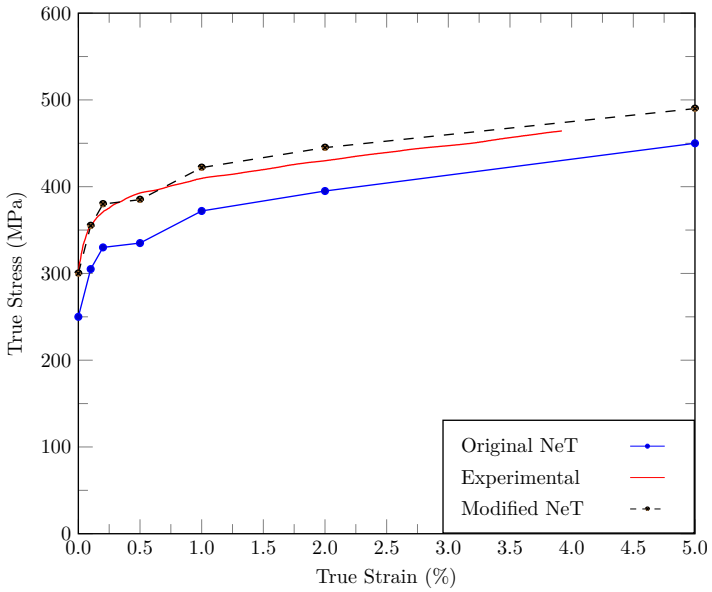

Figure 4.26: Comparison of room temperature true stress - true strain for austenite material from data in the NeT project [Ficquet et al., 2009] and experimental work from this project. Shifting the original NeT data (blue curve) by 50 MPa results in a good agreeement with specimens tested as part of this project.

4.5 Chapter 4 Summary

Tensile testing was conducted on standard and non-standard sized specimens. During machining it was noted that the tensile specimens deformed significantly, indicating a high level of residual stress was present in the TIG welded plate. Homogeneous ferrite tensile testing results were found to be in good agreement for samples machined through the thickness of the plate indicating that the microstructure in the base material was consistent. Samples taken from the cladding, that were known to consist of cladding material only, agreed broadly with one another. A maximum of two specimens were tested and difficulties incurred during the testing process likely accounts for the deviations in tensile test results. Two specimens taken from the materials boundary performed significantly differently to one another and other specimens (Figure 4.7).

A power law fit was applied to true-stress, true-strain data based on the mechanical testing results. The austenite material was found to be of lower yield strength in comparison to the base and HAZ regions with a higher hardening parameter. The mechanical properties are provided in Table 4.1, power law constants are given in Table

4.2. The standard size tensile specimens performed as expected and were shown to be in good agreement with additional data provided by the industrial sponsor.

While the results for the sub-sized tensile specimens are limited in the elastic region predominately good agreement were found when comparing base material specimens for all orientations. This indicates that the orientation of homogeneous base material specimens does not influence the mechanical properties. Greater variability was found when comparing sub-size samples manufactured from the HAZ and austenite regions. Given the variability in microstructure in these locations it is considered reasonable to assume, taking the relative size of the sub-size specimens into consideration, that the local microstructural effects are impacting the test results. Given the variability noted in sub-sized specimen results material properties used in finite element (FE) models were limited to standard size specimen test data results only.

FEM of full size homogeneous material tensile specimens showed good agreement with data derived experimentally. The presence of the weld boundary was also assessed and it was shown (Figure 4.19) that, for specimens comprised solely of base and clad materials, the stress in the cladding was higher than that in the base. Incorporating the HAZ region resulted in an increase in stress in both the base and cladding sections (compared to base to clad only). Further it was noted that the stress in the HAZ region was lower than that of either the base or the clad section. By normalising the result by the respective material yield strength it was shown that the clad region was likely to yield prior to the base. The HAZ region was the least likely to yield. These results were as expected for the given mechanical properties. The likelihood of failure of each material is more difficult to ascertain as results show the cladding has significantly greater ductility in comparison to either the base or HAZ materials.

Given the geometry of the original plate it was not possible to orientate the notch, with respect to the TIG weld boundary, without further processing. To this end, the section was machined and laser welded, into a 'sandwich' component. Six CT specimens were

manufactured from various positions in the sandwich component as shown in Figure 3.9.

Once the CT samples were removed from the sandwich component, sections close to the weld start and stop positions were removed and used for microstructural and hardness measurements. The microstructure of the ferrite region was sampled at positions close to the TIG weld and laser weld (see Figures 3.18 and 3.15 for positional details pertaining to the microstructural imaging and hardness testing, respectively). The microstructure in these regions were shown to be broadly similar with respect to one another, irrespective of their position relative to the applied welding procedure. While this may be construed as implying that the welding procedure had no effect on the ferritic microstructure it should be noted that, positionally, these images were taken a significant distance (in terms of micro-scale), from the weld boundaries. Hence is it considered more likely that both image locations are positioned far enough away from their respective weld that mixing of the ferrite and austenite materials is not captured. It is clear however that the austenite region undergoes severe and significant changes in microstructure morphology when moving through thickness from the TIG weld to the laser weld, Figure 3.18b demonstrates this quite clearly. While it was outside of the remit of this work to conduct an in-depth microstructural assessment, it is not unexpected that significant changes in microstructure, such as those seen in Figure 3.18b, could impact defect initiation and propagation. Jang et al. [Jang et al., 2010] investigated a narrow gap laser weld in a 316L stainless steel. They conducted fatigue testing on samples notched in the direction of the dendritic microstructure. It was shown that the fatigue crack path occurred, generally, along the austenite/ferrite boundary. In areas were dendrite alignment was not favourable the crack path deviated and secondary cracking occurred. It is not possible to quantitatively define the impact of microstructure on crack initiation and propagation on the experimental fracture testing conducted in this work. Microstructural imagining was limited to one plane only (transverse and normal, with respect to the weld) while the defects were oriented in a direction plane (readers are referred to Figure 3.15). Additionally, given the complexity of the austen-

ite region in this work (Figure 3.18b) compared to that of others [Jang et al., 2010] the direction of crack growth, with respect to the microstructure, cannot be stated with any certainty without extensive further work.

As stated previously (see Section 4.1) hardness measurements were taken along three sections across the width of the sample encapsulating the first weld, weld overlap region, and the second weld region. Measurements were made through the thickness of the sample, encapsulating the ferrite material, the TIG weld boundary, the austenite material and the laser weld boundary in order. Readers are referred to Figure 3.15 for a comprehensive diagram of measurement locations. The hardness was shown to be approximately identical in the longitudinal direction. That is to say, there was no significant difference between the weld start and weld stop positions (see Figure 4.6). The hardness was found to be demonstrably greater, in the region of the laser weld, compared to elsewhere in the sample. Furthermore a significant reduction in hardness was noted in the mid-width of the sample, analogous to the region of weld overlap. Taking the manufacturing positions of the samples into consideration this implies that the hardness will be of greater magnitude on one surface of each CT sample, reducing through the thickness. The TIG weld was also noted to have higher magnitude of hardness in comparison to the surrounding ferrite and austenite materials but the magnitude of hardness was considerably less than that in the region of the EB weld.

The connection between hardness, yield strength and ductility are well established. For homogeneous materials with comparative grain sizes, increasing hardness will increase the yield strength and reduce ductility. Grain size however impacts the relationships considerably. By reducing the grain size both hardness and yield strength can be increased without a substantial loss of ductility. Given the complex microstructure discussed previously it is not clear whether the increase in hardness in the region of the laser weld resulted in a loss of ductility. Tensile testing of the laser welded component was not conducted as part of this work. Comparing Figures 4.5a and 4.5e show that the microstructure at the TIG boundary is not comparable with that at the laser weld boundary. Hence it is considered inappropriate to attribute tensile testing conducted

on the HAZ region of TIG welded plate to the laser welded region. Further tensile testing on the laser welded component would be required to measure the mechanical properties in this region. This was not conducted as part of this work due to lack of available material.

Temperature dependent material properties from literature were presented and compared to test data. It was shown that there was a good agreement between data provided by the industrial sponsor and test data for the base material. Poor agreement was found when comparing other literature values [Serasli, 2014]. Therefore temperature dependent material properties provided by the industrial sponsor were used in the appropriate FE models.

Some literature data [Serasli, 2014] was found to be in poor agreement with true stress - true strain properties for the cladding (austenite) material test data. Additional literature data [Ficquet et al., 2009] for a different grade of stainless steel (316L) was found to be in better agreement. The temperature dependent true stress - true strain data in Ficquet [Ficquet et al., 2009] was modified by increasing the yield strength by 50 MPa which gave excellent agreement with test data. Hence for FE models the true stress - true strain data was taken from Ficquet [Ficquet et al., 2009]. Other relevant material properties were taken from Serasli [Serasli, 2014] which were confirmed to be in general agreement with other literature.

Chapter 5: Residual Stresses

5.1 Introduction

As briefly discussed in Chapter 2, residual stresses can significantly impact the structural integrity of components. To fully assess the performance of specimens used in this work the magnitude of residual stress present in any sample prior to testing must be understood. The neutron diffraction method is a non-destructive technique used to measure residual stress. The lattice spacing of a nominally 'stress-free' specimen (the d_0 specimen) of identical material is compared to the lattice spacing of the 'stressed' specimen. Assuming no other stresses are applied to the specimen any changes in lattice spacing can be attributed to residual stress.

Neutron diffraction measurements were carried out at Helmholtz-Zentrum Berlin für Materialien und Energie, on instrument E3. The setup for the instrument is shown in Figure 5.1. The sample is placed on a transition table at an angle to the incoming neutron beam. The crystallographic planes within the material cause the beam to diffract at various angles while the scattered neutrons are counted by the detector. The measurement of the lattice spacing is based on Bragg's law (Section 3.3.1, Equation 3.3.2) where d_{hkl} represents the lattice spacing of planes with Miller indices hkl, θ is the scattering angle, λ is the neutron wavelength, and n is the small integer number, assumed to be 1.0 for this work. Elastic strain is calculated by comparing the change in position of the scattering angle (θ) between the reference (unstressed) and stressed samples calculated as shown in Equation 5.1.1, where ϵ_{hlk} is the lattice strain, $d_{0,hkl}$ is the reference lattice spacing, d_{hkl} is the specimen lattice spacing [British Standards Institute, 2018*b*].

$$\epsilon_{hkl} = \frac{d_{hkl} - d_{0,hkl}}{d_{0,hkl}} \tag{5.1.1}$$

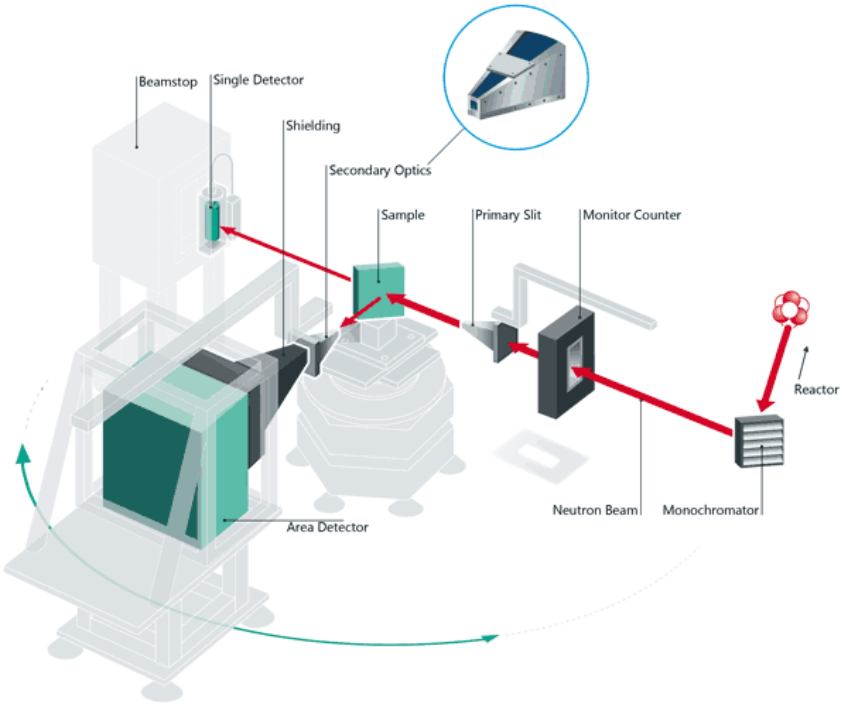

Figure 5.1: Instrument E3 setup, [Boin, 2015]

5.2 Neutron Diffraction Results

5.2.1 As-welded plate

As previously mentioned in Section 3.1 this project obtained material from the remaining sections of an as-welded plate that were previously used for research. The previous works [Serasli, 2014; Naveed, 2015] both focussed specifically on residual stress and thus multiple measurements of residual stress were made using a variety of techniques. It was not possible to reproduce this data independently, due to destruction of the sample. This section provides key residual stress measurements made on the original plate in the as-welded condition by [Serasli, 2014] and [Naveed, 2015]. Prior to neutron diffraction measurement, a 'window' was made in the plate by removing ferritic material from the bottom of the plate. The measurements were conducted in the center of the window from the clad surface to a depth of 30 mm. A gauge volume of $3.0 \times 3.4 \times 5.8$ mm was used, measurements were conducted using ENGIN-X at ISIS in the United Kingdom. Results are shown in Figure 5.2 where the directions are with respect to the clad weld layer (i.e. the longitudinal direction is along the 300 mm dimension, the transverse direction is along the 180 mm direction and, the normal di-

rection is through the thickness of the plate). The error was specified to remain within $\pm$ 10 MPa except at a depth of 24 mm where the error was measured to be in the range of $\pm$ 67 to 112 MPa. The authors also conducted residual stress measurements using incremental deep hole drilling, deep hole drilling and contour methods. A good agreement was found when comparing neutron diffraction measurements to the other techniques.

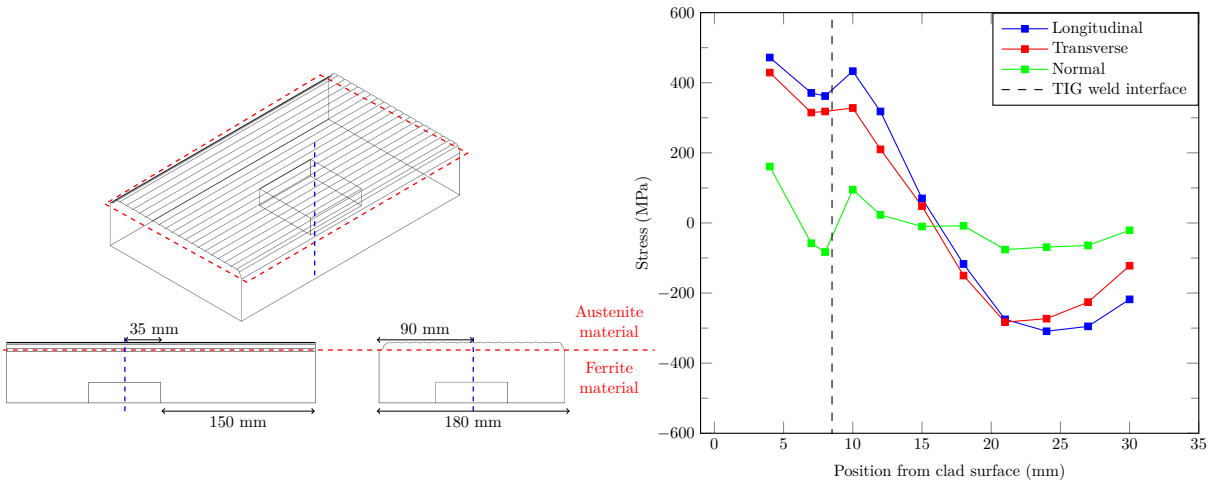

Figure 5.2: Residual stresses measured by Serasli using neutron diffraction (From [Serasli, 2014]). Measurements taken offset mid-width, offset from the mid-section (35 mm), through thickness of plate up to a depth of 30 mm from the clad surface.

5.2.2 Stress-free (d_0) Specimens

Two stress free d_o specimens each measuring $2 \times 2 \times 2$ mm^3 were provided. One sample was homogeneous base ferritic material, the second homogeneous clad austenite material. These specimens were machined from offcuts taken from EB welded Block B (Section 3.3.4) and, given their small size, were assumed to be stress free. The peak 2θ value for ferrite was found to be 77.80° with an error of 1.03×10^{-3}, for austenite it was found to be 85.52° with an error of 2.00×10^{-3}.

Cladding processes are known to develop 'a coarse strongly textured, columnar grain structure' [Gooch, 1976]. These regions of textured material can result in localised areas of discontinuous partially mixed zones (PMZs) that can lead to difficulties in acquiring diffraction peaks of sufficient intensity. One method of overcoming the texture effect is

to oscillate the sample at various angles. The d_o specimens were oscillated around ten different angles. [Dodge, 2014; IAEA, 2005]

5.2.3 Tensile Specimens

The measured residual stresses and associated error for specimens 2, 3, 4 and 18 are shown in Appendix A Tables B.1 to B.3 for the longitudinal, transverse and normal directions, respectively. As specimen 4 consisted of an unknown mixture of materials residual stresses were calculated for results based on both the austenite d_0 and the ferritic d_0 values. A d_0 value for the HAZ region could not be obtained. While the ferritic scan showed residual stresses of higher magnitudes compared to the austenitic scan the error measurements associated with the ferritic scan were significantly larger than those noted for the austenite scan. Surface plots depicting the interpolated values between measured data can be seen in Figure 5.4 for specimen 2 and Appendix A Figures B.1 to B.5 for the specimens 3, 4, and 18. Plotted data for specimen 4 is limited to data measured during the ferrite scan only as several data points could not be measured during the austenitic scan.

Figure 5.3 shows the normal stresses measured on all four specimens. Considering the thickness of the samples (3 mm) relatively small magnitudes of residual stress were anticipated in the normal direction. However, as shown in Figure 5.3 the range of residual stress measured in the normal direction were measured to be significant (over 100 MPa) for specimens 2, 3 and 4 (in the range of $\pm$250 MPa). While other works [Köhler et al., 2014; James et al., 2014] have found similar magnitudes of compressive stress at bimetallic interfaces the results were based on as-welded specimens rather than specimens machined from an as-welded section. The normal stress for specimen 18 was measured to be in the range of 60 MPa, which is within the error margin. As specimen 18 was taken from the bottom of the large clad plate, furtherest from the original TIG weld, and was not subject to external stresses (not considering machining stresses) the magnitude of measured stress (60 MPa) was unexpected. Given that the

measurement lies within the expected error margin, results were re-analysed assuming a plane stress condition (stress in the normal direction equals zero) rather than the application of the d_0 measurement. Results are tabulated in Appendix A Tables B.4 to B.6. Figure 5.5 plots the results for specimen 2 when the plane stress condition is assumed.

By comparing Figure 5.4 to Figure 5.5 it can be seen that reducing the magnitude of normal stress from 160 MPa (Figure 5.4c) to zero (Figure 5.5c) increases the magnitude of residual stress from 160 MPa to 250 MPa in the longitudinal direction, and decreases the range of magnitude of residual stress from 140 MPa to 120 MPa in the transverse direction. Similar plots for specimens 3, 4 and 18 can be viewed in Appendix A Figures B.2 to B.6.

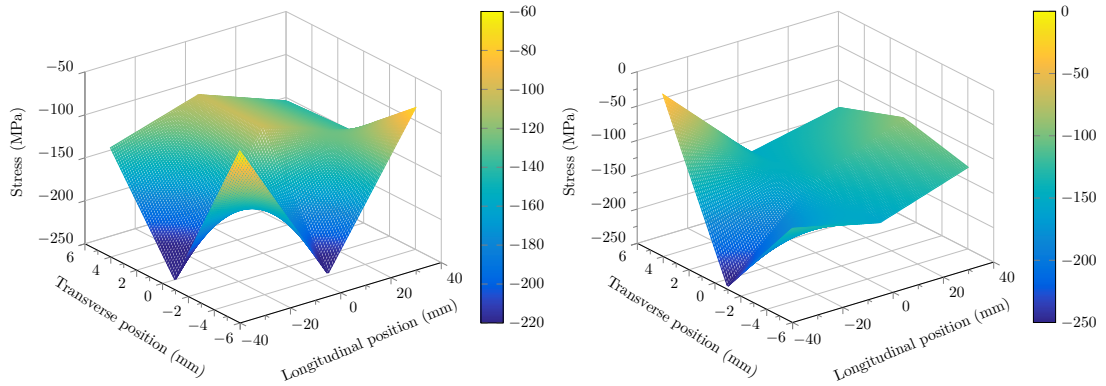

(a) Specimen 2

(b) Specimen 3

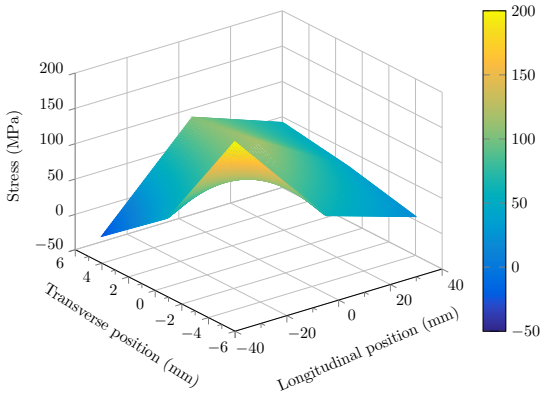

(c) Specimen 4: Ferrite results only

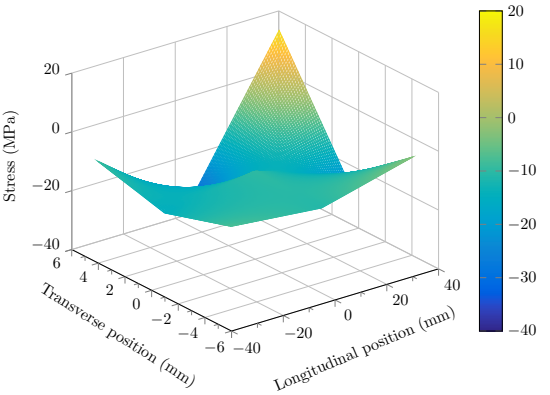

(d) Specimen 18

Figure 5.3: Surface plot of normal residual stress in tensile specimens

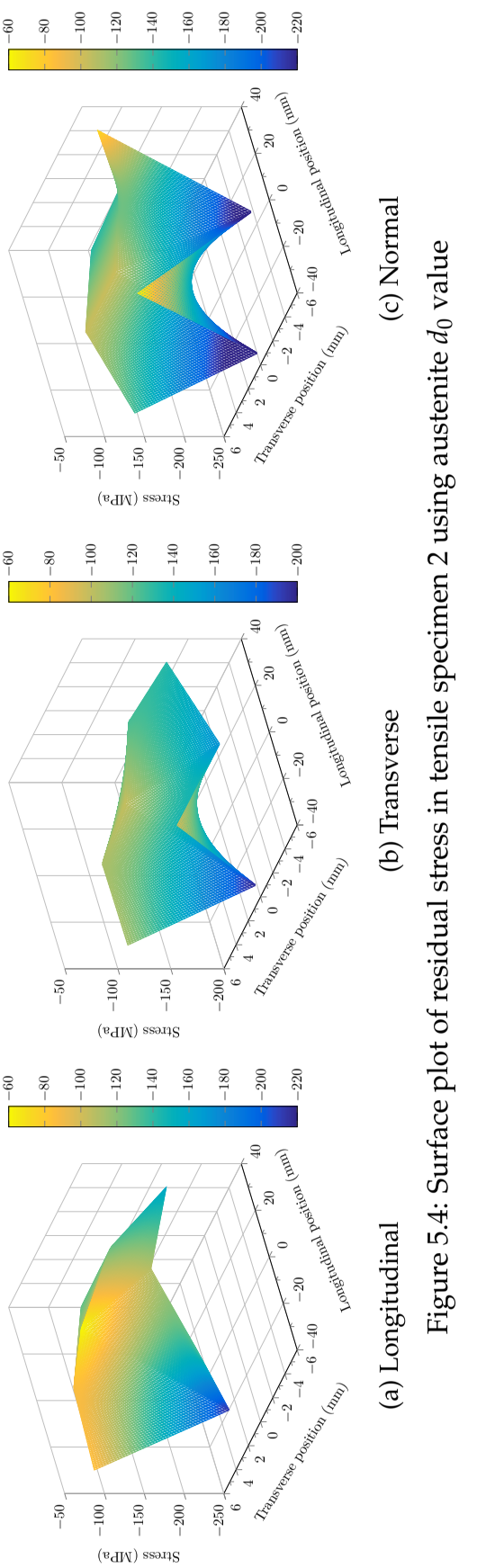

(a) Longitudinal (b) Transverse (c) Normal

Figure 5.4: Surface plot of residual stress in tensile specimen 2 using austenite d_0 value

(a) Longitudinal (b) Transverse (c) Normal

Figure 5.5: Surface plot of residual stress in tensile specimen 2 assuming plane stress condition

5.2.4 Block A

The measured values of residual stress in the transverse, normal and longitudinal directions for Block A, including the estimated errors, can be seen in Appendix B Table B.7. Data are plotted in Figure 5.6. From Figure 5.6 stresses appear to be predominately compressive through the thickness of the cladding material becoming increasingly tensile heading towards either weld interface. The peak tensile stresses for the longitudinal, transverse and normal directions were measured to be 130 MPa, -12 MPa and 327 MPa, respectively.

Both the longitudinal and normal direction peak values occur at the TIG weld interface. The peak value in the transverse direction occurs close to the free surface. The value of transverse stress at the TIG weld interface however was measured to be -31 MPa which, when the error measurement is considered, could exceed the previous value of -12 MPa. The largest range of residual stress was found to be compressive in nature and with a magnitude of approximately 540 MPa in the transverse direction.

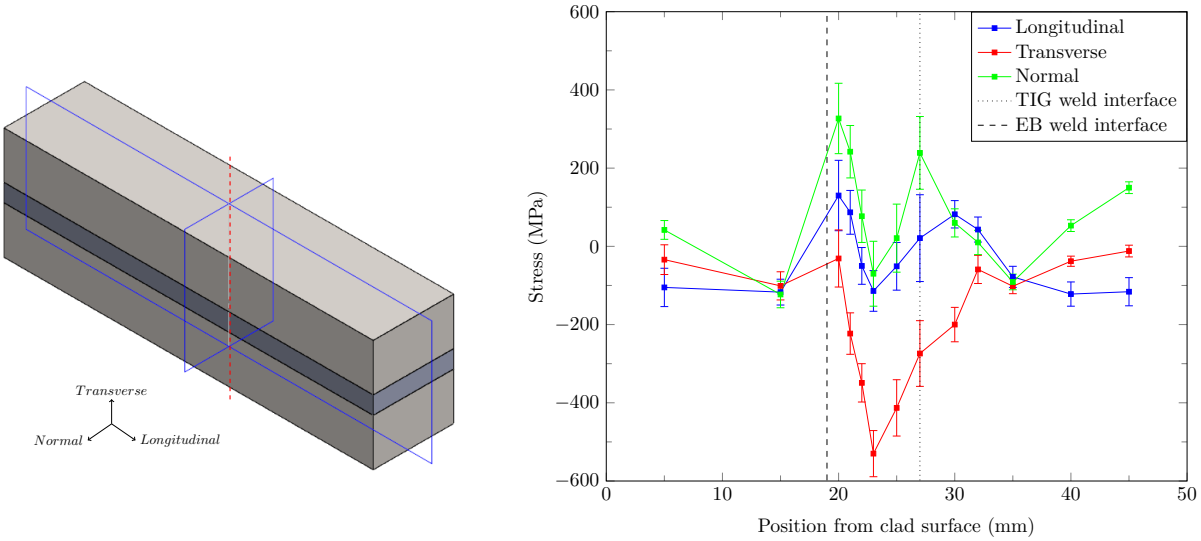

Figure 5.6: Residual stresses in Block A post EB welding

5.2.5 CT Specimens

The measurements of residual stress calculated using the d_0 values are plotted in Figure 5.7. As can be seen in Figure 5.7b residual stresses of approximately 300 MPa were

noted in the normal direction for specimens 2 and 3. This is similar to the maximum tensile stress noted in the normal direction of the EB welded block (see Figure 5.6). Considering that the thickness of each CT specimen is less than half of that Block A it is considered unlikely that stresses of this magnitude would remain present in the CT specimens post-machining. Therefore the analysis was re-considered assuming plane stress conditions the results are plotted in Figure 5.8. Tabulated data are available in Appendix B Table B.8 to B.10.

It should be noted that the neutron diffraction measurements were taken prior to extending the notch tip (see Section 3.2.4) to the initial testing crack depth. Therefore the stresses in Figure 5.8 not wholly representative of any residual stress in the tested specimens. Indeed Figure 5.8 shows that the largest magnitudes of longitudinal and transverse stresses were located close to the notch tip which was later machined away. Taking the further relaxation of specimens due to additional machining at the crack tip, it is considered unlikely that residual stresses of high magnitude remained in the test specimens prior to fracture toughness testing.

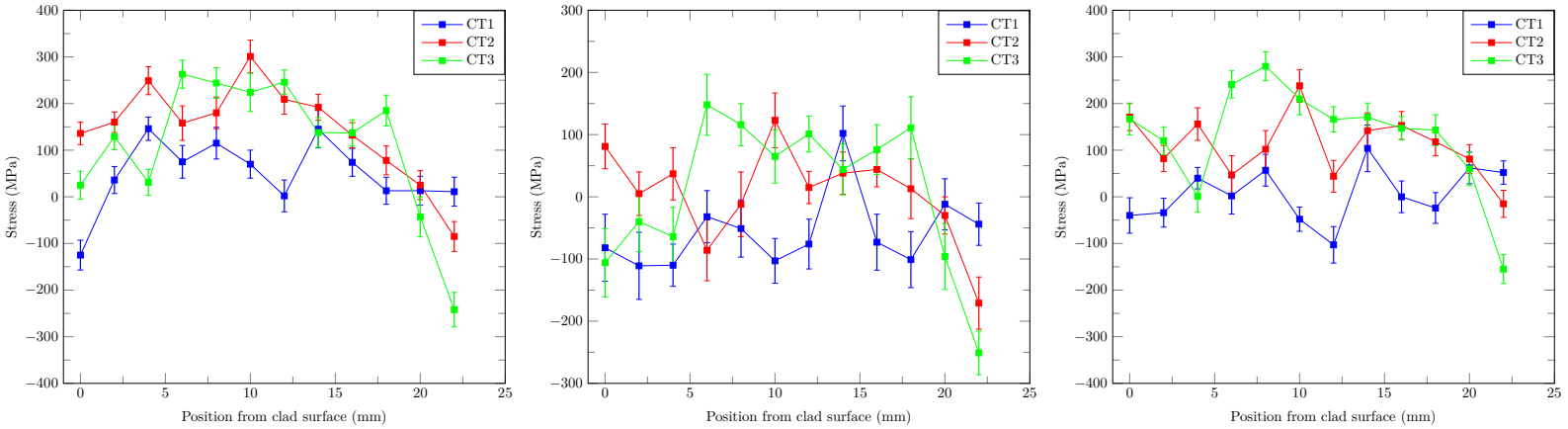

(a) Longitudinal (b) Transverse (c) Normal

Figure 5.7: Comparison of measured residual stresses in CT specimens using d_o values

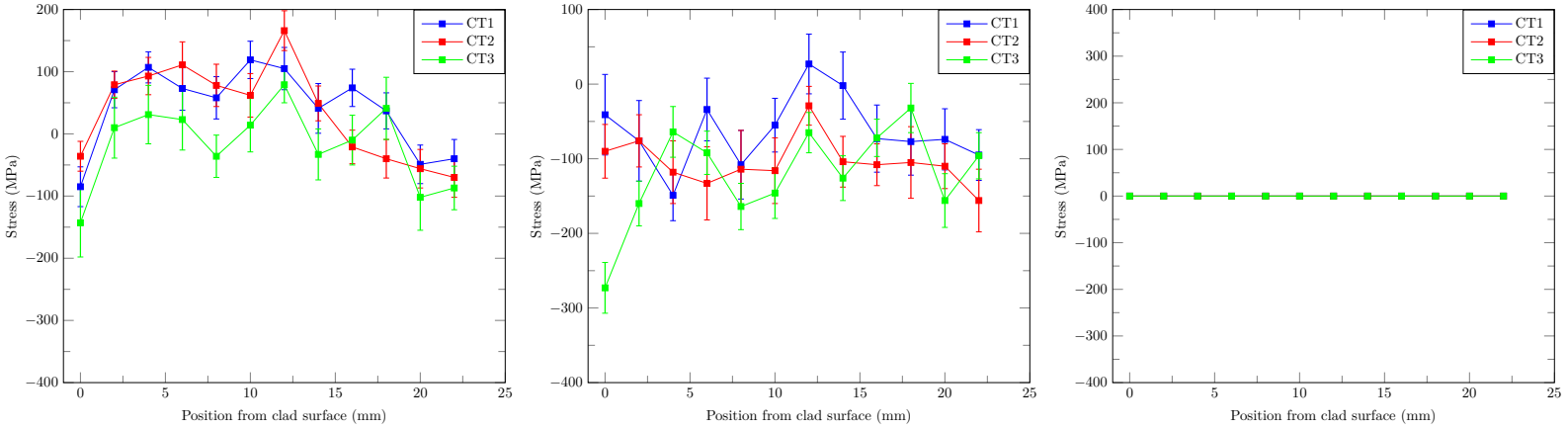

(a) Longitudinal (b) Transverse (c) Normal

Figure 5.8: Comparison of measured residual stresses in CT specimens assuming plane stress

5.3 3D Modelling of Welding Processes

Temperature dependent material properties will significantly influence numerical simulation of residual stresses due to welding. It was considered inappropriate to use the Serasli [Serasli, 2014] elastic-plastic temperature dependent properties for either the ferrite or austenite materials as the data did not represent material tested during this work (see Section 4.4). As previously discussed a good agreement was found when comparing room temperature data provided by the industrial sponsor to experimental work conducted as part of this project. Hence for the weld models, unless otherwise stated, the industrial sponsor's temperature dependent elastic-plastic ferrite material properties were used. Similarly the austenite material properties provided by Serasli [Serasli, 2014] did not represent experimental work. A better representation was found by modifying data found in literature [Ficquet et al., 2009]. Other temperature dependent material properties such as thermal conductivity, thermal expansion, Young's modulus (elastic material properties) and specific heat were taken from Serasli's work [Serasli, 2014] as similar results were reported elsewhere.

The laser welding process, described in Section 3.2.4, was analysed. Modelling of welding processes is complex particularly for ferritic materials like A508 as phase changes occur at higher temperatures, and reoccur upon cooling. These phase changes can increase strains (due to changes in grain size etc.) and are likely to significantly impact any estimated residual stress profile [Ficquet et al., 2009; Francis et al., 2007; Honeycombe and Gooch, 1985]. In this work the impact of phase changes in the ferrite material were neglected.

Two types of heat source were analysed. A static volumetric heat source and a moving heat source. A static volumetric heat source, often referred to as a block dump model (BDM), applies the heat flux to a specific volume of material. There is no fixed classification of what constitutes an appropriate volume, though clearly the smaller the volume the more accurate the analysis is likely to be. In some cases authors have assumed entire layers of cladding as appropriate [Serasli, 2014], in others individual

weld beads are analysed [Smith and Smith, 2009; Aird et al., 2013; Abburi Venkata, Truman, Smith and Bhaduri, 2016].

In block dump analyses the heat input is calculated using welding parameters for current (I) and voltage (V). The welding process is also assigned an efficiency parameter, η where a value of unity represents a fully efficient process.

$$Q = \eta IV \tag{5.3.1}$$

The heat flux is calculated as follows:

$$q = \frac{Q}{volume} \tag{5.3.2}$$

Where Q is calculated from Equation 5.3.1 and $volume$ represents the volume of material to be heated.

Comparatively a moving heat source models the movement of the torch with respect to the specimen. Several types of heat source models can be used to describe the heat flux distribution from basic Gaussian distributions to more complex double ellipsoid distributions [Kapadia, 2014]. As the EB laser welding process has a significant variation along the depth of the weld (in comparison with MMA welding techniques). The moving heat source (MHS) applied to this weld model was a combined double ellipsoidal and conical heat source as shown in Figure 5.9. According to Kapadia [Kapadia, 2014] this type of heat source provides better accuracy for welds that penetrate deep into the base material.

The heat flux of the double ellipsoid, q_e, depends on its position relative to the EB. For positions ahead of the EB the heat flux is defined as:

$$q_{e(x,y,z,t)} = \frac{6\sqrt{3} f_{ef} Q}{a_e b_{ef} c_e \pi^{\frac{3}{2}}} e^{\left(-3\frac{x^2}{a_e^2}\right)} e^{\left(-3\frac{(y-vt^2)}{b_e f^2}\right)} e^{\left(-3\frac{z^2}{c_e^2}\right)} \tag{5.3.3}$$

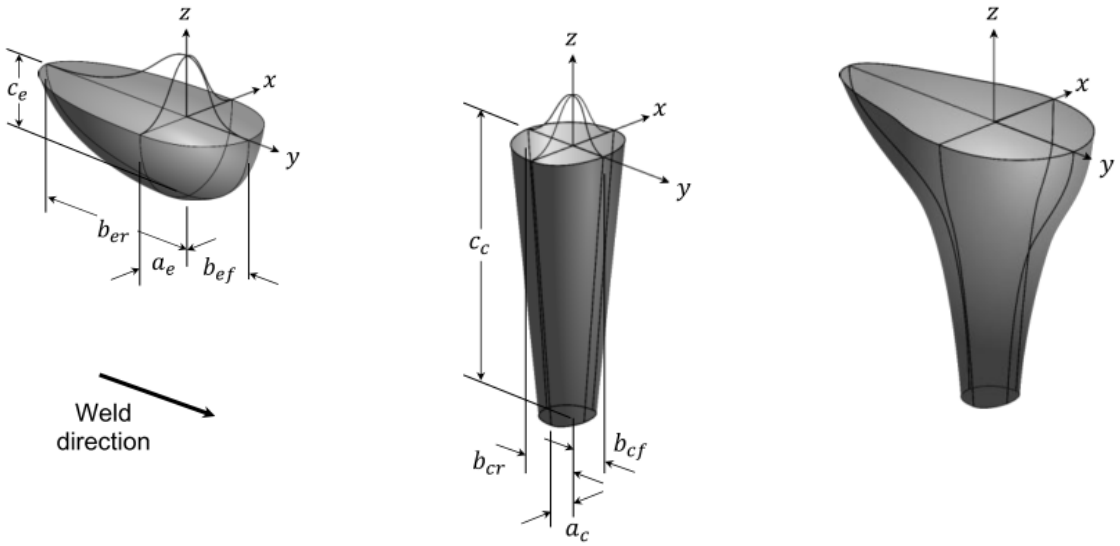

(a) Double ellipsoidal (b) Conical (c) Combined

Figure 5.9: Heat flux distribution in double ellipsoid (Figure 5.9a), conical (Figure 5.9b) and combined (Figure 5.9c) heat source model (Figure from [Kapadia, 2014])

For postions behind the EB it is:

$$q_{e(x,y,z,t)} = \frac{6\sqrt{3}f_{er}Q}{a_e b_{er} c_e \pi^{\frac{3}{2}}} e^{\left(-3\frac{x^2}{a_e^2}\right)} e^{\left(-3\frac{\left(y-vt^2\right)}{b_e r^2}\right)} e^{\left(-3\frac{z^2}{c_e^2}\right)} \tag{5.3.4}$$

Where a_e, b_e, and c_e are the distances associated with Gaussian distribution of the torch and are defined in Figure 5.9a. The subscripts f and r describe the dimensions in the front and rear of the weld, respectively. The constants f_{ef} and f_{er} are described as follows:

$$f_{ef} = \frac{2b_{ef}}{b_{ef} + b_{er}} \tag{5.3.5}$$

$$f_{ef} + f_{er} = 2 \tag{5.3.6}$$

The energy input rate, Q, is determined from welding parameters as per Equation 5.3.1. Where I represents the current of the beam, V the voltage and η is the efficiency of the heat transfer from the beam to the work piece. EB laser welding processes are

extremely efficient due to the vacuum conditions and the are generally estimated to be in the region of 90-95% [Kapadia, 2014]. For simplicity the current model assumed a weld efficiency of unity.

For the conical model the heat flux ahead of the torch is defined as:

$$q_{e(x,y,z,t)} = \frac{6 f_{cf} Q}{a_c b_{cf} c_c \pi \left(1 - d_c\right)} e^{\left(-3\frac{x^2}{a_e^2}\right)} e^{\left(-3\frac{\left(y-vt^2\right)}{b_c f^2}\right)} \left[1 - \frac{\left(1 - d_c\right) z}{c_c}\right] \tag{5.3.7}$$

and behind the torch as:

$$q_{e(x,y,z,t)} = \frac{6 f_{cr} Q}{a_c b_{cr} c_c \pi \left(1 - d_c\right)} e^{\left(-3\frac{x^2}{a_e^2}\right)} e^{\left(-3\frac{\left(y-vt^2\right)}{b_c r^2}\right)} \left[1 - \frac{\left(1 - d_c\right) z}{c_c}\right] \tag{5.3.8}$$

Where a_c, b_c, and c_c are the distances associated with Gaussian distribution of the torch and are defined in Figure 5.9b. The heat input rate, Q, is calculated as per Equation 5.3.1. The dimensionless parameter d_c defines the linear change of heat flux in the y direction, this work assumes $d_c = 1$. The constants f_{cf} and f_{cr} are defined as:

$$f_{cf} = \frac{2 b_{cf}}{b_{cf} + b_{cr}} \tag{5.3.9}$$

$$f_{cf} + f_{cr} = 2 \tag{5.3.10}$$

The total heat flux distribution for the combined model (Figure 5.9c), q is defined by:

$$q_{comb(x,y,z,t)} = \beta q_{e(x,y,z,t)} + \left(1 - \beta\right) q_{c(x,y,z,t)} \tag{5.3.11}$$

Where β represents the contribution from the ellipsoid q_e relative to the conical q_c.

5.3.1 Block Dump Laser Welding Analysis

5.3.2 Mesh sensitivity study

It is of paramount importance in FEA modelling to ensure that the mesh used is sufficiently dense to accurately predict displacements, strains and stresses from applied loading conditions. Should the mesh density used in the heat transfer analysis lack the ability to successfully model the nodal temperatures then the structural analysis will be inaccurate.

To ensure that the mesh density used in the original heat transfer and structural analyses were robust enough to resolve nodal displacements accurately a heat transfer and structural analyses on two meshes, of varying densities, were conducted. The densities of the mesh are shown in Figure 5.10. As the component was machined prior to EB welding the plates were assumed to be in a state of zero residual stress, that is to say any stresses due to the original TIG weld were assumed to be negligible. The influence, on residual stress, of the tack welds was neglected from the analysis under the assumption that the stresses introduced during EB welding would far exceed any that may have been present during the tack welding phase of the experiment. Additionally the run-on, run-off plates were not included. Run-on, run-off plates are used experimentally to allow the beam time to stabilise, as theoretical analyses assumes an immediately stable beam the plates were considered unnecessary.

The analysis consisted of six steps: An initial step for application of boundary conditions, a heating step simulating the first weld, a cooling step to simulate the time required to vent the EB chamber and move the sample experimentally. A second heating step simulating the second weld, a second cooling step simulating the time required to vent the EB chamber and a final step to simulate cooling to room temperature completed the assessment. A sequentially coupled heat transfer and structural analysis was conducted. The heat input was calculated using the experimental welding parameters (see Section 3.2.4) and Equation 5.3.1. Laser welding is considered to be highly efficient with efficiencies generally in the 90 % range [Kapadia, 2014]. For simplicity

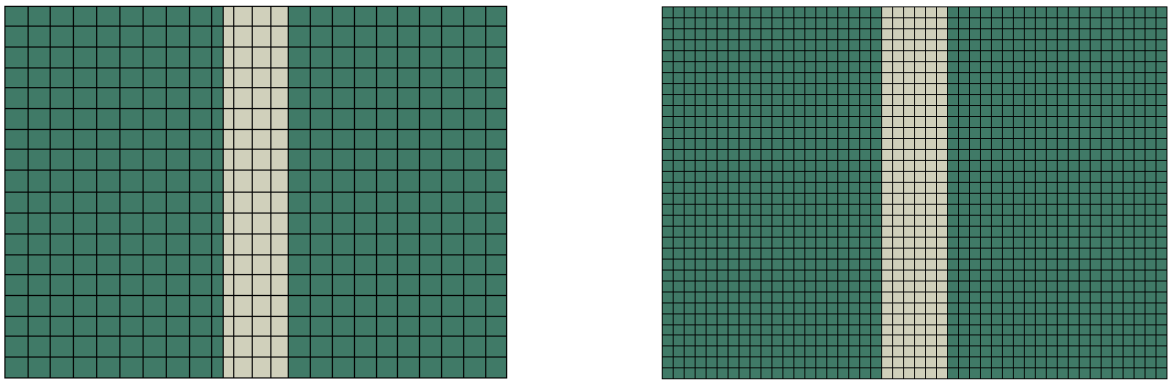

(a) Low density mesh: 34,000 elements

(b) High density mesh: 295,000 elements

Figure 5.10: Low and high density meshes (Figures 5.10a and 5.10b, respectively) used to assess mesh sensitivity of the analysis

the weld efficiency was assumed to be unity. For a simple 3D analysis a body heat flux (see 5.3.2) was applied to each area in which welding occurred. The weld volume was calculated from the diameter of the weld bed, the depth of penetration of the weld and the length of the weld. The body heat flux was calculated to be 703 MW/m^3 assuming each bead takes 24 seconds to lay down. Radiation conditions were applied to the relevant surfaces during the first and second cooling steps.

The depth of penetration of the weld was specified to be approximately 20 mm. The overall thickness of the component was approximately 34 mm, resulting in an area of overlap between the two welds. This was incorporated into the analysis. The areas to which the body heat flux were applied are shown in Figure 5.11. Subsequent to each weld step the component was allowed to cool for approximately 5 minutes to simulate the length of time required for the EB chamber to vent (first and second cooling steps). After the second cooling step, a third cooling step allowed the component to equilibrate to room temperature. Cooling was implemented assuming radiation for all three cooling steps. Radiation was assumed to occur on all surfaces except for the surface in contact with the EB chamber which was assumed to be completely insulated. The radiation emissivity was assumed to be 0.60 while the film conditions (to simulate convection) were assumed to be 25 W/m.

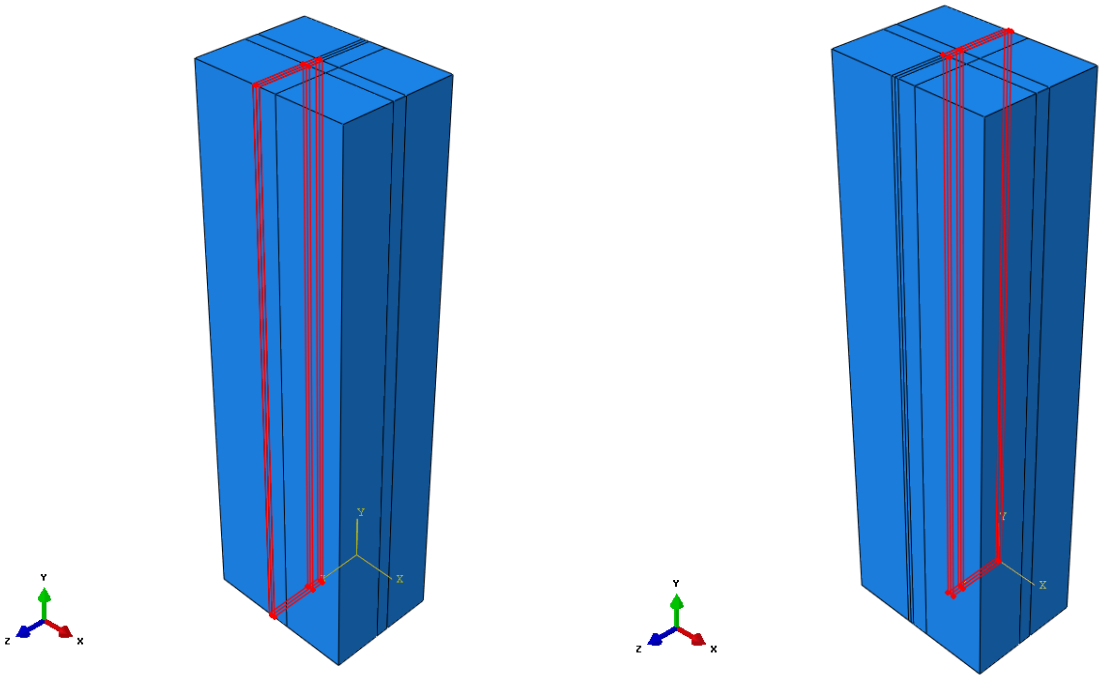

(a) Weld 1

(b) Weld 2

Figure 5.11: Heat transfer model weld partitions

The heat transfer model consisted of approximately 34,000 elements of type DC3D20R. The structural model calculated stresses from the nodal temperatures resulting from the heat transfer analysis. The model was identical to the heat transfer model in terms of geometry and applied material properties. The mesh was modified to use C3D20R structural elements but contained the same number of nodes and elements as the heat transfer model. Boundary conditions to constrain rigid body motion were applied to corner nodes on one surface of the sample. All four corner nodes were constrained from moving in the z-direction (U3=0). One node was additionally constrained in both the x and y directions (U1=U2=U3=0), one node was additionally constrained in the x-direction (U1=U3=0). The applied boundary conditions are shown in Figure 5.12.

The nodal temperatures derived from the original structural analysis are compared to those derived from the heat transfer increased mesh density model in Figure 5.13. As shown the results are identical indicating that the original mesh density of 34,000 elements is robust enough for the heat transfer calculation. The heat transfer to structural analysis for the high density model were also confirmed to be identical to one another.

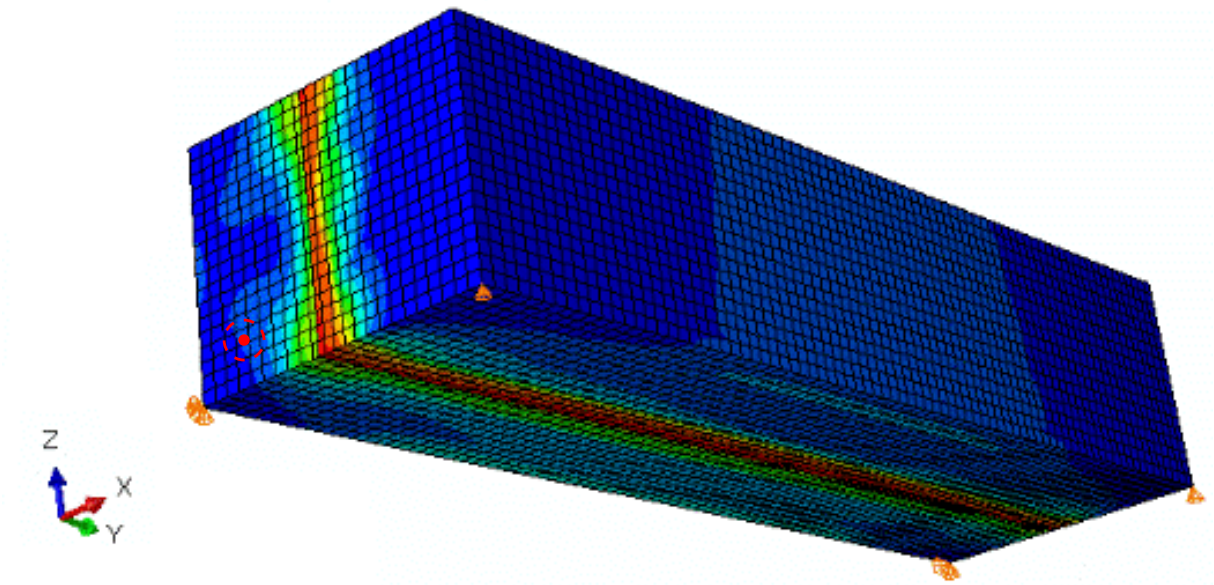

Figure 5.12: Boundary conditions applied to all block dump structural models. Node used for output of temperature values shown using red circle.

Residual stresses in the transverse, longitudinal and normal directions were taken from a path of nodes in the center of the specimen in the mid-thickness from the 'top' surface to the 'bottom' surface, similar to the location of the experimental measurements (Section 5.2.4). Figure 5.14 compares the estimated residual stresses in the transverse, longitudinal and normal directions for the low and high density models. There are some differences in resolved stresses when comparing the original model and the high density model, most noticeably in Figure 5.14b. However, the differences between the two analyses is less than 20MPa which is considered to be an acceptable error given the computational resources required for the high density analysis.

Figure 5.16 and Figure 5.17 show contour plots for the low density and high density analyses, respectively. Results are provided for both the surface and mid-thickness orientations in three orthogonal directions. The orientation of the contour plots, with respect to the weld boundaries is shown in Figure 5.15. By comparing Figure 5.16 with Figure 5.17 it can be seen that the contours for both analyses are similar, though not identical. The low density model (34,000 elements) appears to have over-estimated the transverse stresses on the surface and underestimated the longitudinal stress. A good match was found for both analyses in the normal stress direction. Contour plot results are in good agreement with the results plotted in Figure 5.14.

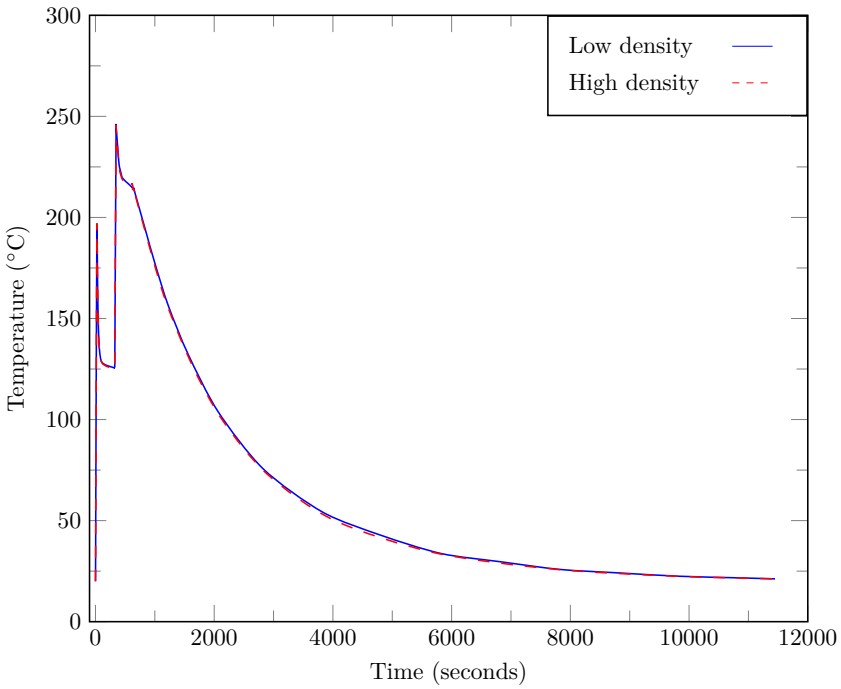

Figure 5.13: Comparison nodal temperatures from the original structural model (34,000 elements) and heat transfer MAP_1_3 (250,000 elements)

In conclusion: Although an error in the estimation of residual stresses is noted when comparing results from the low density model and those of the high density model, the error is small enough that it is considered acceptable, given the benefits in terms of computational cost of running the lower density mesh. The error does not impact the results in terms of the overall shape of the residual stress profiles, nor do the contour plots indicate much difference either on the surface, nor, the mid-thickness regions.

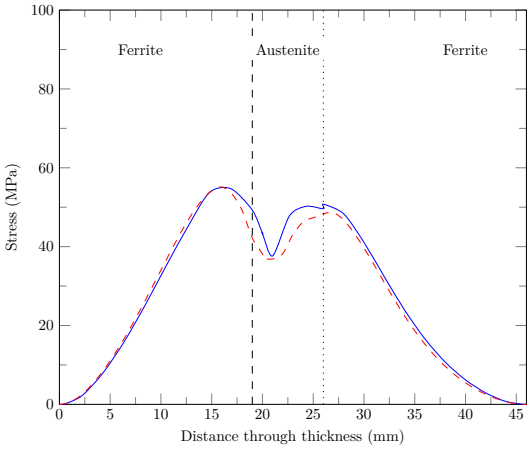

(a) Transverse

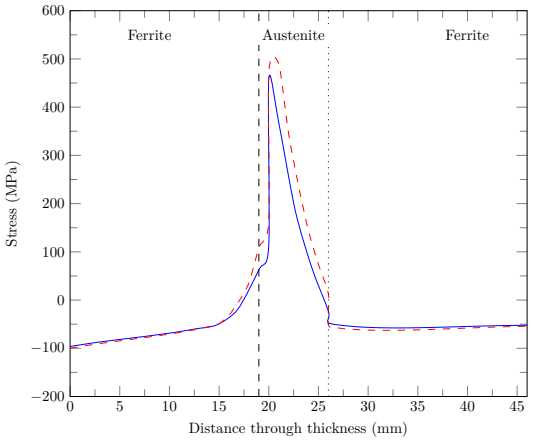

(b) Longitudinal

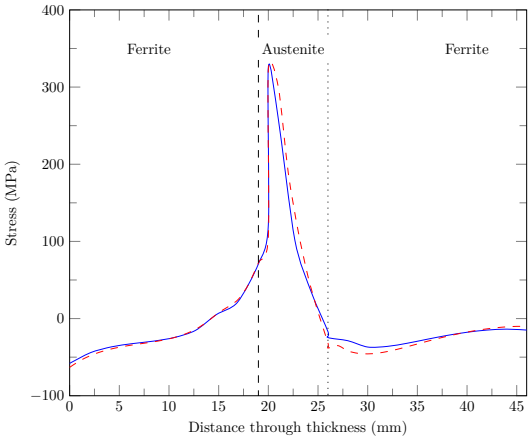

(c) Normal

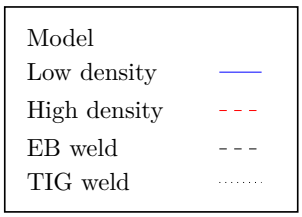

Figure 5.14: Comparison of residual stresses in the transverse (Figure 5.14a), longitudinal (Figure 5.14b) and normal (Figure 5.14c) directions for the low and high density structural models.

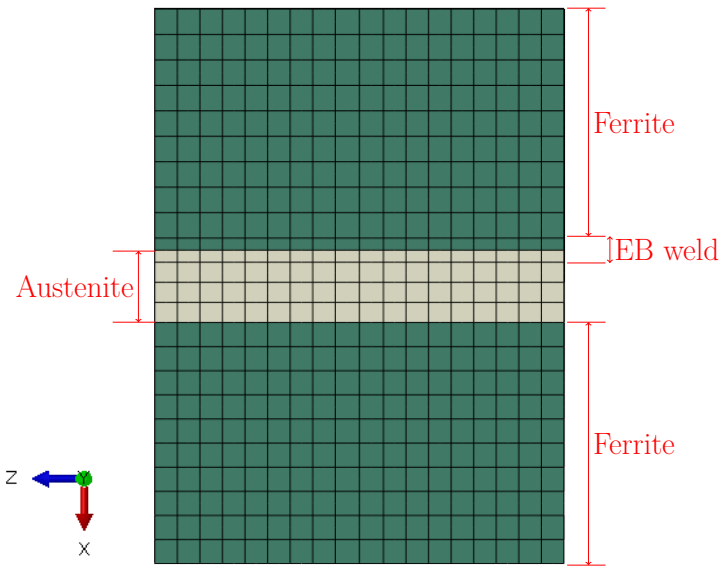

Figure 5.15: Orientation of contour plots with respect to weld boundary locations

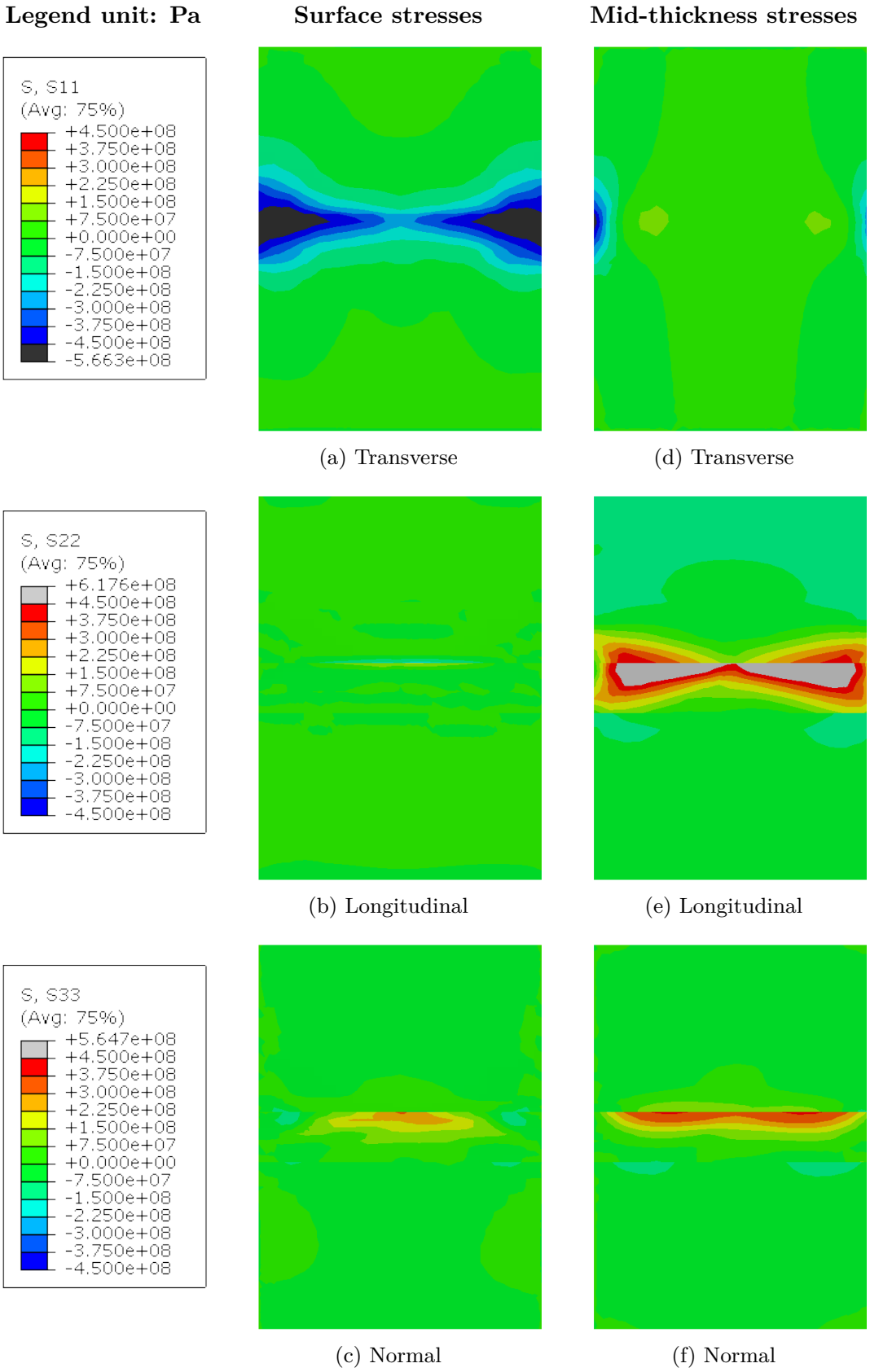

(a) Transverse (d) Transverse

(b) Longitudinal (e) Longitudinal

(c) Normal (f) Normal

Figure 5.16: Contour plots of the transverse, longitudinal and normal residual stress on the surface and in the mid-thickness of the component for low density structural analysis

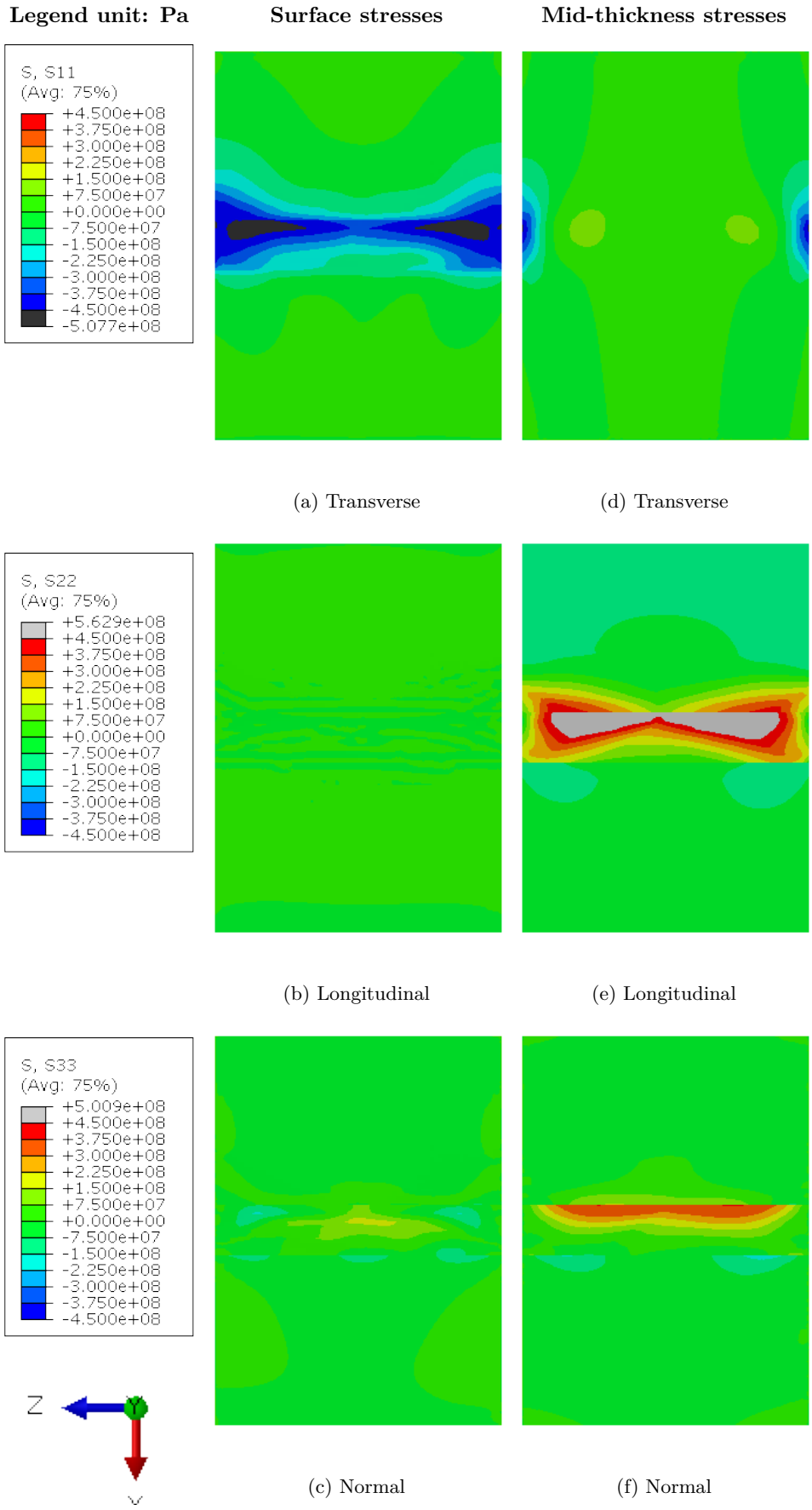

(a) Transverse (d) Transverse

(b) Longitudinal (e) Longitudinal

(c) Normal (f) Normal

Figure 5.17: Contour plots of the transverse, longitudinal and normal residual stress on the surface and in the mid-thickness of the component modelled using block dump heat source for high density mesh structural analysis

5.3.3 Mapping stress to a modified mesh

The analyses described in the following section are, in terms of analysis technique (e.g. element type, boundary conditions, loading parameters etc.), identical to that outlined in the previous section. The purpose of this work is to investigate the estimated residual stresses in both the EB welded block and on individual CT specimens. Partitioning the block geometry to allow for deletion of elements, i.e. material removed during the machining process, is not required for the heat transfer analysis. It is not possible to transfer nodal temperatures directly to a mesh which differs significantly from that of the heat transfer analysis. Therefore rather than transferring nodal temperatures to a potentially unstable mesh it was decided to conduct the heat transfer and structural model on a simple geometry (Figure 5.18a) identical to that used in the earlier low density analysis. This is referred to as the original model. The structural solution could then be mapped from the original structural model onto separate analyses that were partitioned and meshed in a more desirable fashion, such as that shown in Figure 5.18b.

Abaqus provides a number of methods to map solutions from one structural model to another. Two were investigated: the mapping of stresses using the predefined field method within Abaqus CAE software and, the mapping of stresses by modifying the input file to include the *MAP SOLUTION keyword. The predefined field method is unsuitable when the mesh strategy is modified significantly in comparison to that of the original model. This is due to the change in node numbers which in turn impacts the positioning of the heat transfer model data. If the structural model is partitioned identically to that shown in Figure 5.11 then the mesh density can be increased/decreased using the predefined field method. In cases where the structural model requires further partitioning the *MAP SOLUTION method must be used.

The *MAP SOLUTION method is generally used for re-meshing analyses that are subject to severe distortion. The mapping solution results in some discontinuity in the solution of the model due to the nature of the solution mapping algorithm. How-

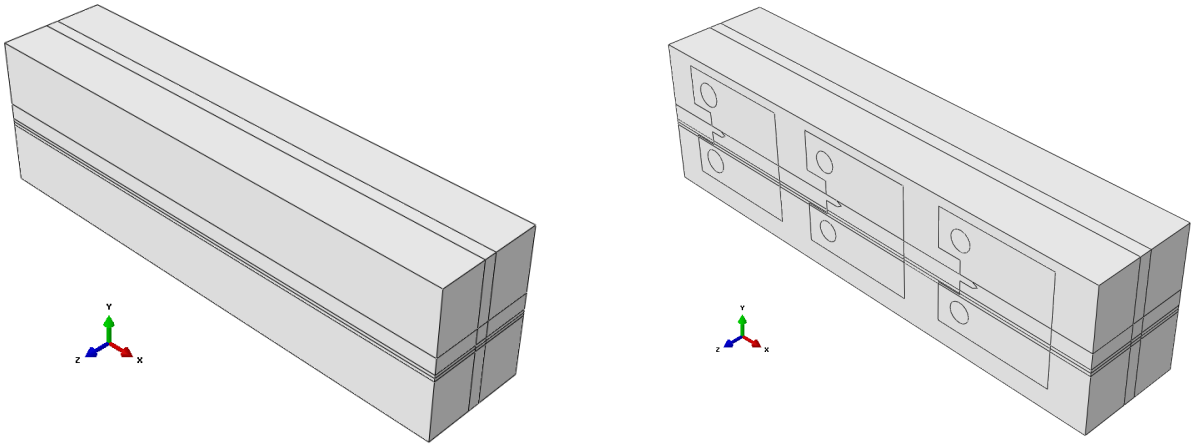

(a) Original (b) Final

Figure 5.18: Original and final structural block dump model partitioning. Model shown in Figure 5.18b was used in the MAP_2 series of analyses

ever, if the mesh is sufficiently fine and remeshing occurs prior to too much distortion then these discontinuities will be kept to a minimum [Dassault Systemes Simulia Corp, 2014]. To assess the amount of residual stress remaining in the individual CT specimens post-machining it is necessary to partition the structural model to account for material removal. Figure 5.18 shows two partitioned structures, the first (Figure 5.18a) is identical to the method used for the heat transfer model. The second partitioning method (Figure 5.18b) allows for material removal and relaxation of residual stresses due to the machining process. To assess the meshing strategy and the *MAP SOLUTION algorithm several analyses were conducted to ensure adequate transfer of nodal displacements.

Table 5.1 lists the analyses conducted to assess the mesh density. The original weld model is not a 'mapped' solution it is the structural model, identical to the heat transfer model, with the nodal temperatures taken from the heat transfer solution. The remaining analyses are all mapped solutions with strains and displacements being mapped from the original structural analysis. Figure 5.19 shows the mesh density of each analysis in Table 5.1. All analyses had structured meshes; the MAP_2 analyses were meshed using an extruded swept mesh with seeding applied to the XY surface.

Table 5.1: Mapped structural analyses for block dump modelling

Name:	Partioning type	Element type	No. of elements
Original	Figure 5.19b	C3D20R	34,000
MAP_1_1	Figure 5.19c	C3D20R	34,000
MAP_1_2	Figure 5.19d	C3D20R	104,000
MAP_1_3	Figure 5.19e	C3D20R	250,000
MAP_2_1	Figure 5.19f	C3D20R	42,000
MAP_2_2	Figure 5.19g	C3D20R	121,000
MAP_2_3	Figure 5.19h	C3D20R	295,000

To ensure the nodal temperatures where transferred correctly from the heat transfer analysis to the original structural model the nodal temperatures at a specific node (marked in Figure 5.12) were compared. The results are shown in Figure 5.20. As shown both analyses have identical results indicating a successful mapping procedure. Notably however the analysis indicates that the maximum temperature peaks at just under 250°C, realistically during a welding process the temperature must exceed the melt temperature of the material for fusion to occur. As specified in Section 3.2.4 a temperature measurement was taken after each chamber venting. The temperature probe specified a temperature of 110 °C post chamber ventilation for weld one and 120 °C after venting for weld two. However it should be noted that due to the size of the EB weld in comparison with the size of the component the location from which the measurement is taken is likely to significantly impact the measured temperature. The exact location of the measurement point taken experimentally was not noted. Hence some deviation between the experimental and model data is to be expected.

Residual stresses in the transverse, longitudinal and normal directions were taken from a path of nodes in the center of the specimen in the mid-thickness from the 'top' surface to the 'bottom' surface, similar to the location of the experimental measurements (Section 5.2.4). Figure 5.21 plots the results for the first increment (S_INC) and last increment (F_INC) for each of the analyses. As shown in the majority of cases there is a good agreement between the results from the original model and those from the mapped solutions for both the first and last increments. This indicates that the mapping algorithm successfully transfers the nodal displacements associated with the original structural

model to the new increased mesh densities in the mapped solutions. The most notable deviation exists when comparing the transverse stress direction (Figure 5.21a), however the deviations in estimated stress do not exceed ± 50 MPa which is the expected error in terms of measuring residual stresses experimentally. Also it can be seen from Figure 5.21a that the deviations in measured stresses occur for both the start increment and the final increment indicating that deviation occurs at all stages of the analyses and hence is more likely due to the change in mesh structure rather any relaxation of stresses over the mapping step.

The experimentally measured stresses are compared to the results of the original model in Figure 5.22. As shown there is a significant difference between results measured experimentally and those estimated using the block dump method. What is interesting is the experimental measurements clearly show two peaks existing in Block A while only one single peak is shown in the FE analysis. The FE analysis assumes that prior to EB welding there are no pre-existing residual stresses. It may be that the second peak seen in the experimental data is a pre-existing residual stress (presumably from the original TIG weld) although further analysis is required to show that this is the case.

Figure 5.16 shows contour plots of the residual stress distributions for the transverse, longitudinal and normal stresses on the surface and in the mid-thickness for the original structural model. The orientation of the component with respect to the location of the EB weld as shown in Figure 5.15. The mid-thickness stress distribution is significantly different from those present on the surface, this is not unexpected. Figure 5.23 plots the corresponding contours for the MAP_2_3 analysis which differs from the original structural model in mesh type and mesh density. By comparing Figure 5.16 and Figure 5.23 it can be seen that the mapped solution remains accurate, even after significantly changing the mesh structure.

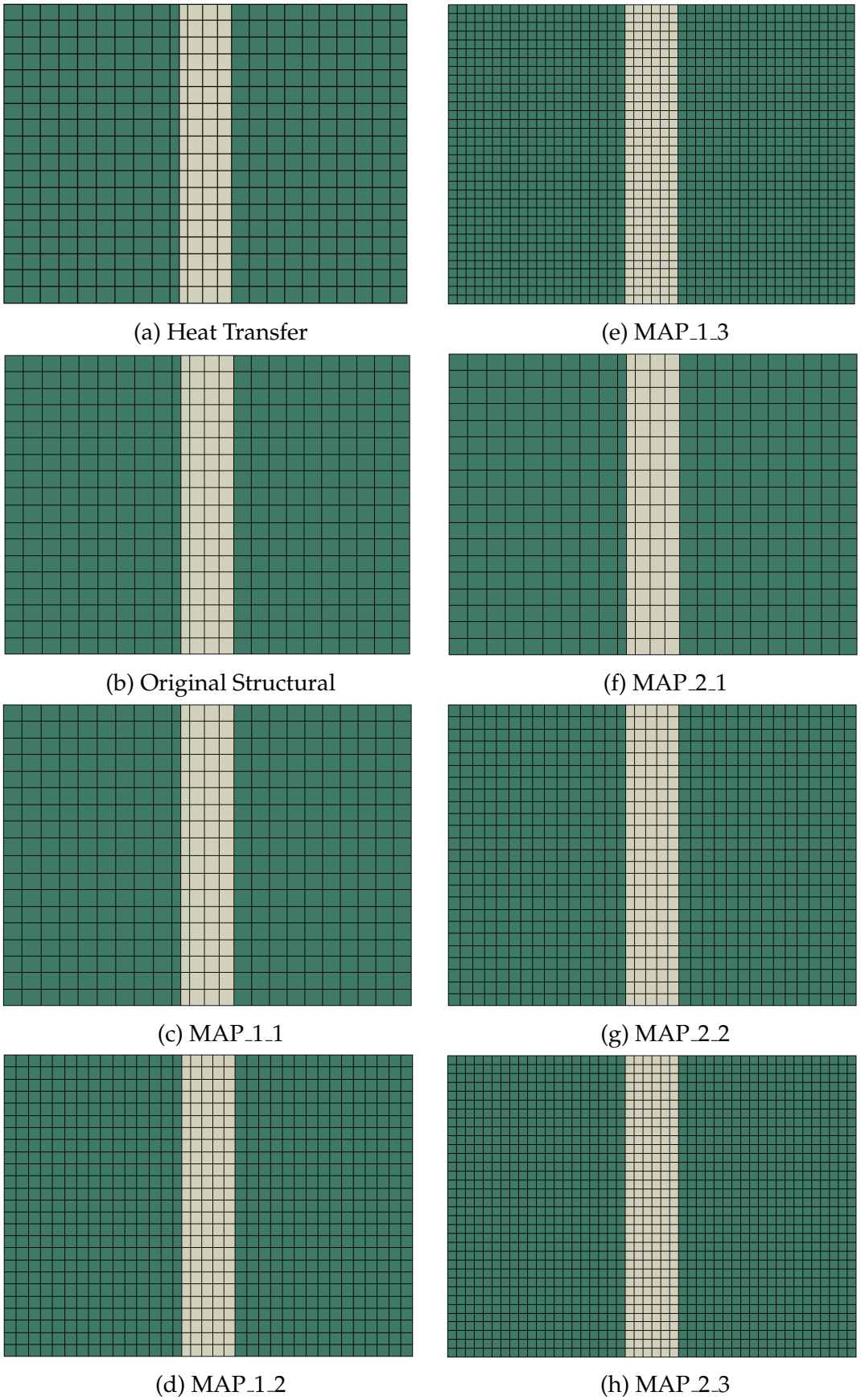

(a) Heat Transfer

(e) MAP_1_3

(b) Original Structural

(f) MAP_2_1

(c) MAP_1_1

(g) MAP_2_2

(d) MAP_1_2

(h) MAP_2_3

Figure 5.19: Mesh density used in mapping analyses (see Table 5.1)

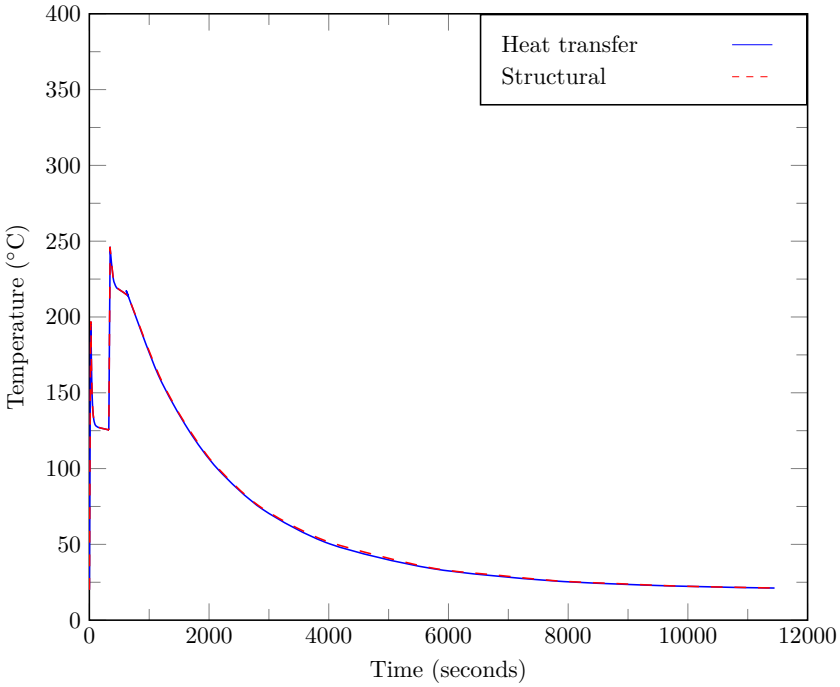

Figure 5.20: Comparison of nodal temperatures from a specific node for the original heat transfer and original structural model

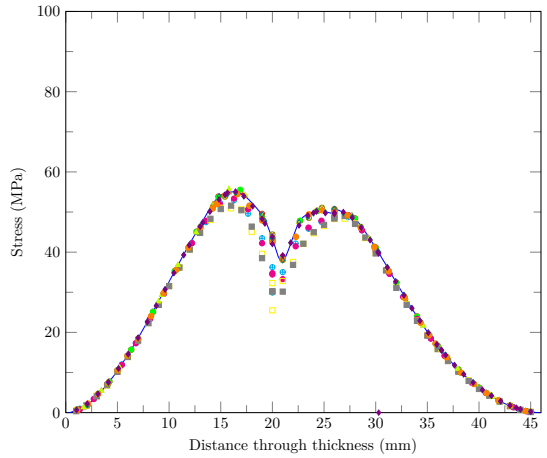

(a) Transverse

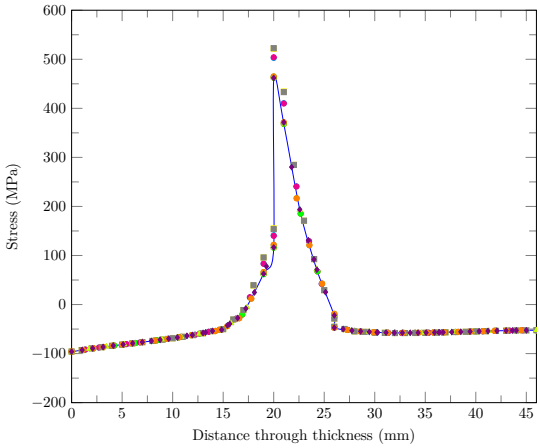

(b) Longitudinal

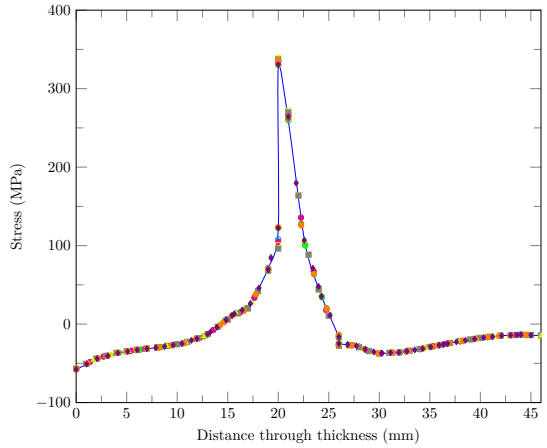

(c) Normal

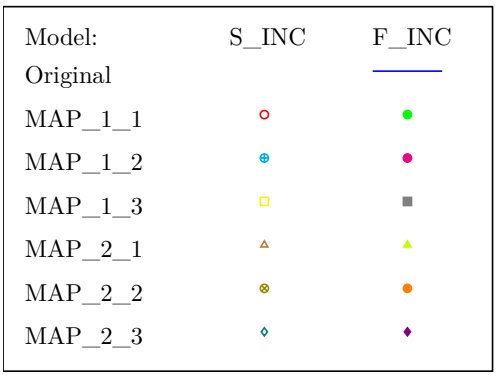

Legend

Figure 5.21: Comparison of residual stresses in the transverse (Figure 5.21a), longitudinal (Figure 5.21b) and normal (Figure 5.21c) directions for the original model and the various *MAP SOLUTION techniques (see Table 5.1)

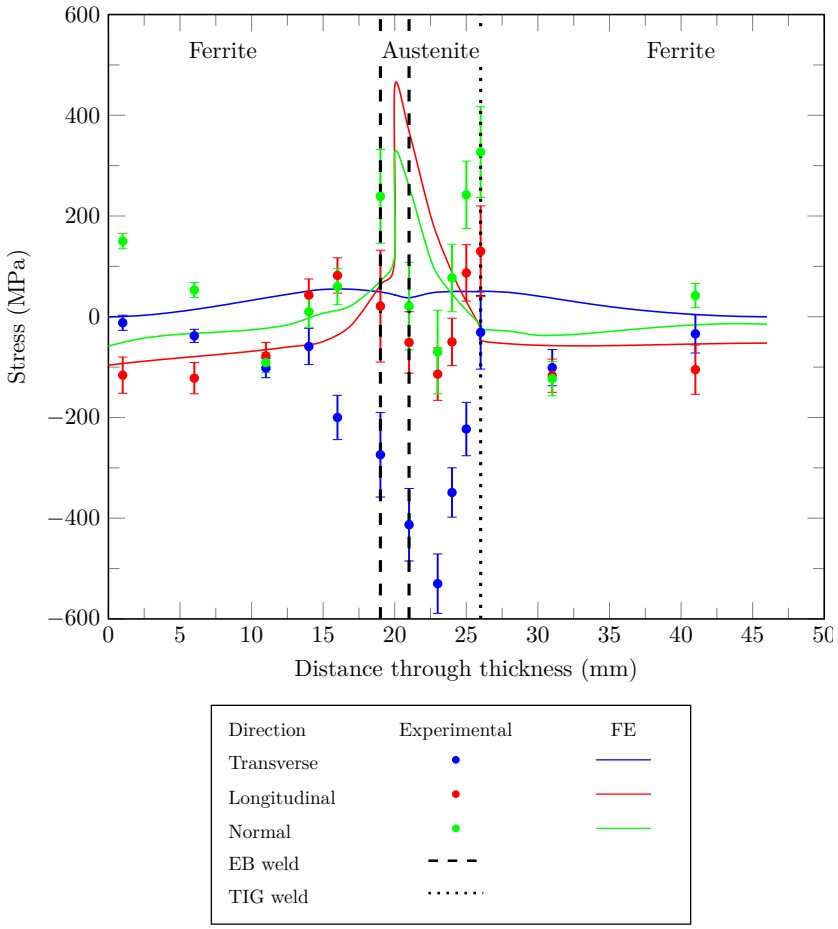

Figure 5.22: Comparison of experimentally measured residual stresses on Block A with predicted residual stress from the original structural model

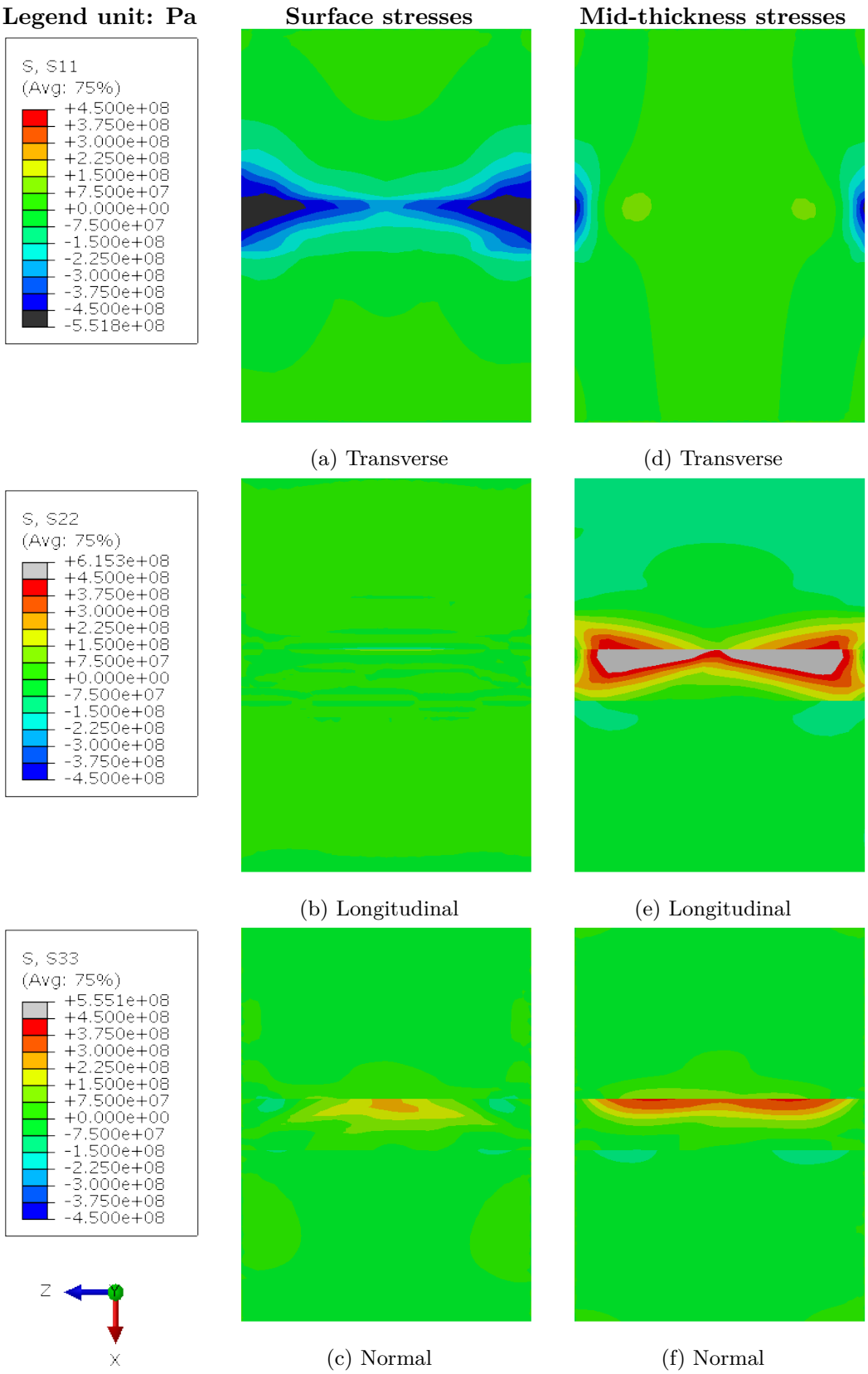

Figure 5.23: Contour plots of the transverse, longitudinal and normal residual stress on the surface and in the mid-thickness of the component modelled using block dump heat source for MAP_2_3 analysis

5.3.4 Moving Heat Source Laser Welding Analysis

The geometry of the model is identical to that described in Figure 5.18a. The mesh density was increased from 34,000 elements to over 74,000 elements to adjust for the expected increases in temperature (heat flux is applied over a much smaller volume of material). Figure 5.24 shows the mesh density used in this analysis. The heat source used in this section was the double ellipsoid and conical heat source as outlined in Section 5.3. The heat flux was applied to the model using the Abaqus subroutine *DFLUX, β was assumed to be 0.25. That is to say the ellipsoid accounts for one quarter of the total heat flux distribution. The weld efficiency η was assumed to be unity.

The application of the *DFLUX subroutine requires specific co-ordinate data to mimic the movement of the torch. Both the heat transfer and structural analyses were split into two parts, one for each weld. The first analysis investigated the first weld and the first chamber ventilation. The second analysis modelled the second weld, the second chamber ventilation and the final cool down. During chamber ventilation radiation was assumed to occur from all surfaces except the surface in contact with the chamber. Radiation and film conditions were applied during the final cool down cycle which occurred outside the EB chamber. The first heat transfer model (HT1) modelled all geometry data, the second heat transfer model (HT2) was a restart file where the initial conditions were identical to the last increment of HT1. A similar method was applied to the structural analyses where the first structural model (SA1) was based on nodal displacements derived from HT1. The second structural analyses was a restart analysis where the initial conditions were assumed to be identical to the last increment in SA1.

Due to the mesh density and the requirement for restart files the size of the output was limited to reduce computation time. Restart output and field outputs were requested every twenty increments. History outputs were exported for every ten increments of the analysis. The nodal temperatures calculated from the moving heat source (MHS) model are shown in Figure 5.25.

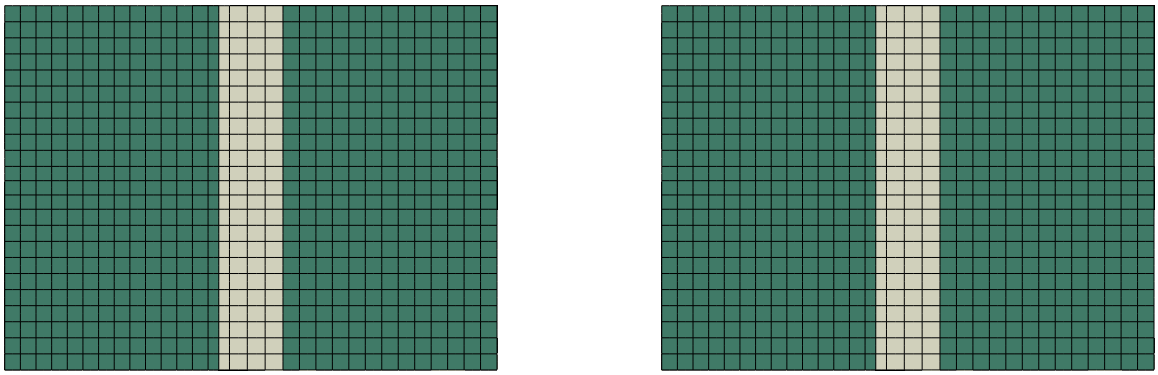

(a) Heat Transfer (b) Structural

Figure 5.24: Mesh density and structure used in heat transfer (Figure 5.24a) and structural (Figure 5.24b) moving heat source analysis

Residual stresses along the mid-section of the specimen, analogous to the position measured experimentally (see Figure 3.12) were estimated. Measurements were taken directly from nodes located along the section of interest and are compared to the experimental data in Figure 5.26. As shown the estimated residual stress profiles do not agree with the experimental data. The transverse stresses are underestimated whilst both the longitudinal and normal stresses appear to be over estimated in comparison with experimental measurements. Similar to the block dump analysis (Section 5.3.1) the MHS has failed to present a double peak for the longitudinal or normal stresses. It is possible that the double peak found experimentally was due to the pre-existing residual stress field in the component due to the original TIG weld. As specified earlier in this chapter existing residual stresses were neglected from the models under the assumption that they would have been relieved due to machining.

Figure 5.27 shows contour plots of the transverse, longitudinal and normal stresses for the surface and mid-thickness of the component. The orientation of the contour plots, with respect to the laser weld, is identical to the block dump model (BDM), Figure 5.15). Similar to the BDM (Section 5.3.1) the model predicts significant differences comparing surface and mid-thickness stresses. The BDM was modelling for multiple mesh densities ranging from fairly coarse to high density. Comparing the contour stresses for the BDM little difference was noted to have occurred in the estimated residual stresses. By comparing Figure 5.27 with either Figure 5.16 or Figure 5.23 it can be

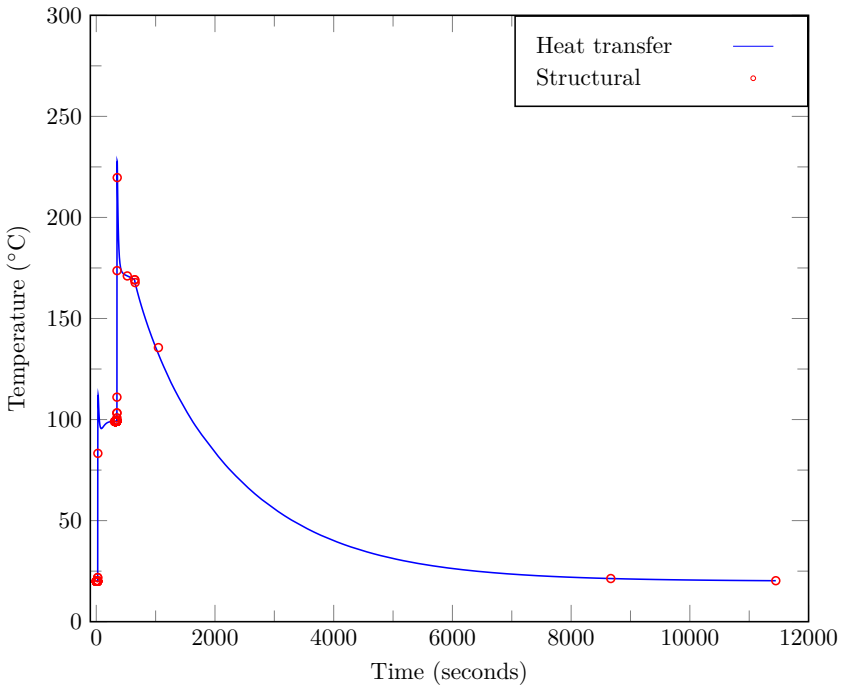

Figure 5.25: Nodal temperatures for the moving heat source model, both heat transfer and structural model results depicted

seen that the moving heat source model while similar to the BDM is not identical. The MHS predicts stresses that are larger in magnitude and extend further over area's in comparison to the BDM results. This is not unexpected given the significant variation in heat source when comparing the two analyses. The BDM and MSH models both predict similar results in the terms of the location in the component of the peak stress regions, both compressive and tensile.

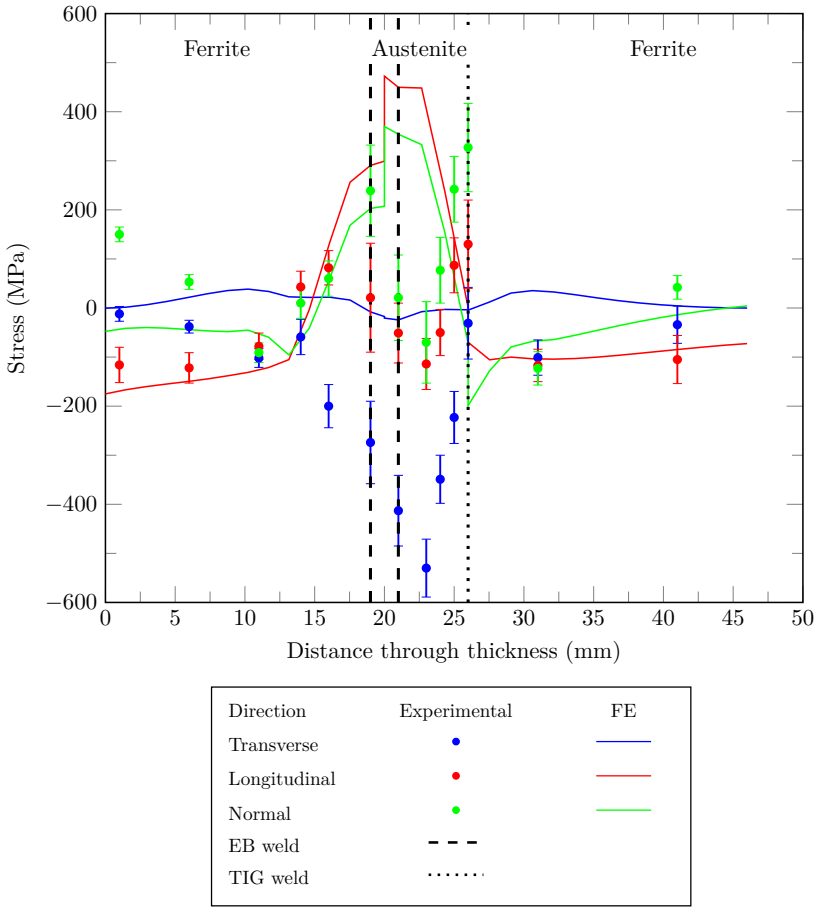

Figure 5.26: Comparison of estimated residual stresses from moving heat source model with experimentally measured residual stresses

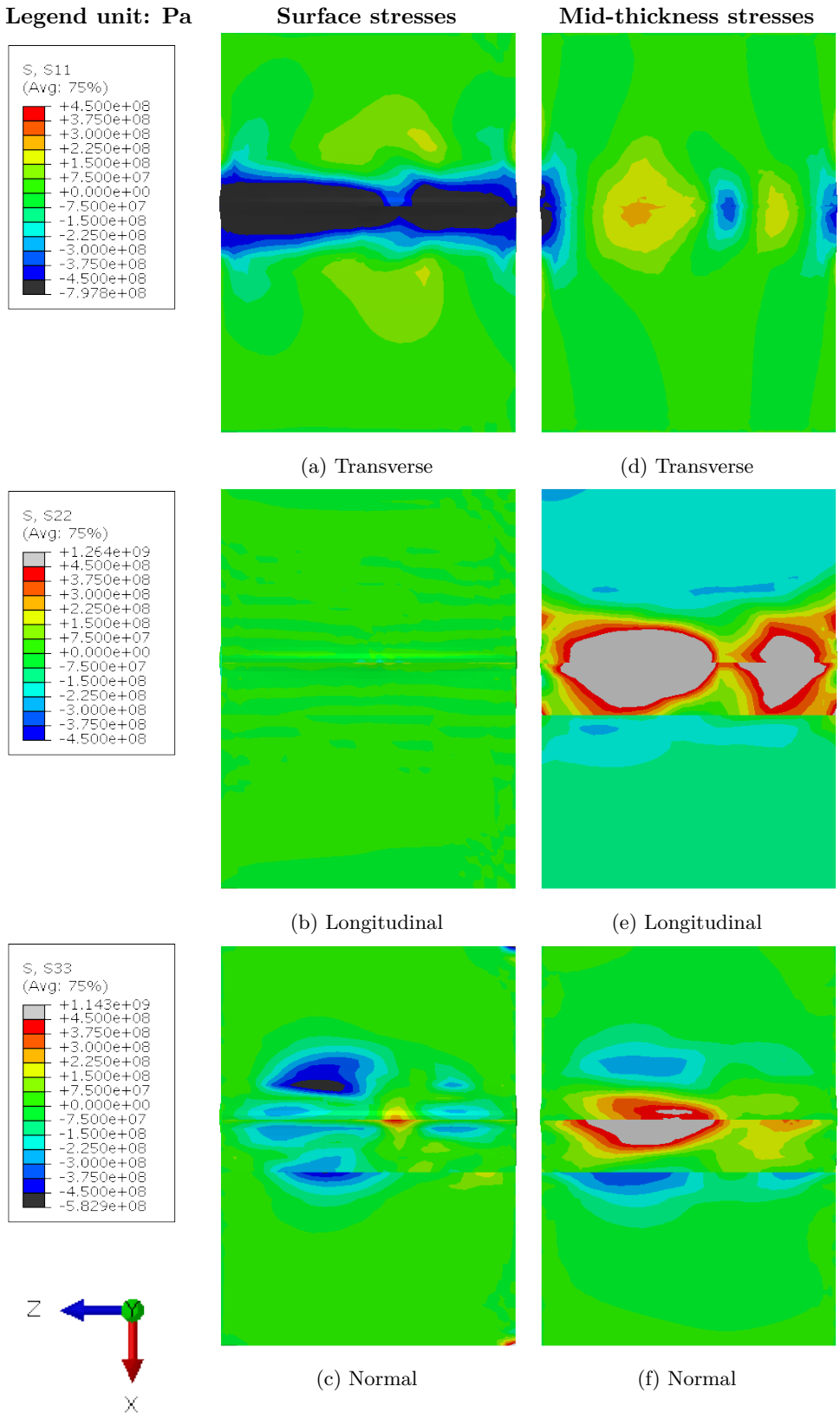

Figure 5.27: Contour plots detailing the transverse, longitudinal and normal stresses on the surface and mid-thickness of the component modelled using moving heat source

5.3.5 Machining CT specimens from welded component

To estimate the residual stresses in the CT specimens post-machining element deletion is required. As discussed in Section 5.3.3 it is not possible to retain the CT specimen geometry without the use of a complex mesh. Stresses, from the laser welded simulation, were mapped to a partitioned structure using the *MAP SOLUTION method, which was discussed in detail in Section 5.3.3. A good agreement (in comparing stresses) was found using the *MAP SOLUTION keyword, even when the structure of the mesh has been significantly modified. Figure 5.28 shows the two meshes that were utilised for this work. The first mesh (Figure 5.28a) was used in the structural weld simulation, the second (Figure 5.28b) was used for mapping purposes. In this case the mesh shown in Figure 5.28b is identical to that referred to as MAP_2_3 in Section 5.3.3 and readers are referred to that section for explicit details pertaining to the mesh.

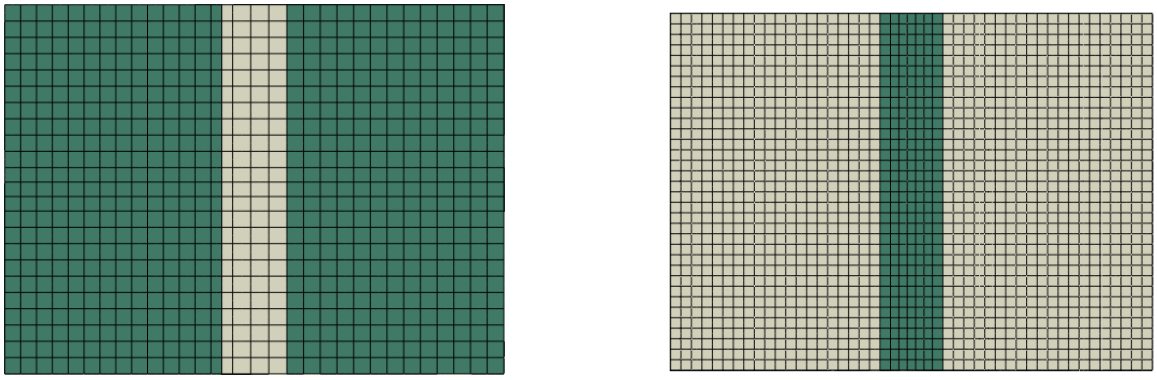

(a) MHS structural mesh (b) Mapping structural mesh

Figure 5.28: Mesh density used in structural analyses. Figure 5.28a showing mesh used in moving heat source weld simulation. Figure 5.28b showing the mesh used for mapping stresses.

Although it was noted that coarse meshes predicte stresses with reasonable accuracy, a denser mesh was utilised to account for the larger magnitudes of nodal displacements expected in the MHS when compared to the BDM. Identical boundary conditions, to the BDM and MHS models, were applied to the initial stages of mapping (see Figure 5.12). Figure 5.29 shows the initial results on the surface and in the mid-thickness region after the mapping procedure was conducted. Comparing Figure 5.29 to Figure 5.27 shows that a good agreement between the analyses indicating that nodal displace-

ments were mapped successfully. Figure 5.30 shows the contours after the component was allowed to reach equilibrium conditions. Comparing Figure 5.29 to Figure 5.30 it can be seen that the stresses in the component have not reduced significantly. Hence any relaxation that occurs from this point are due exclusively to element deletion and equilibrium effects due to element deletion, as opposed to equilibrium effects from the mapping solution.

The CT specimens were machined via the electro-discharge machining (EDM) process. First three 'blanks' of material, each in the shape of the outline of the CT specimen, were machined. Subsequently, the pin holes were machined using an electric drill. Finally individual CT specimens were machined by slicing each block to remove material in the mid-thickness region. The model mimicked the procedure as closely as reasonably possible. In each step, if elements were deleted, stresses were allowed to relax linearly over the duration of the time step. Figure 5.31 shows the estimated stresses in the blank specimen shapes before and after stress relaxation was allowed to occur. As shown and, as expected, a significant reduction in residual stress is noted to have occurred in each of the three blanks. Furthermore the stress distribution in each of the blanks differs when compared to one another. This is not unexpected when one considers the movement of the heat source with respect to specimen location. Experimental residual stress measurements showed distinct differences between CT specimens depending on their location in the component and it is well understood that variations in residual stresses are linked to the relative placement of a sample with respect to the motion of the heat source.

Figure 5.33 shows contour plots of estimated stress in three orthogonal directions before and after element deletion. The location of the specimen corresponds to that of Specimen 1 shown in Section 3.2.4, Figure 3.9. As per Figure 5.32, both surfaces of the specimen are shown. The 'surface' represents the sample surface closest to the first pass of the laser weld, and 'mid-thickness' represents the opposing surface that is to say the approximate mid-thickness of the sandwich component. Figure 5.33 shows contour plots for each orthogonal direction. As shown the residual stress is significantly differ-

ent on the surface of the sample in comparison with the mid-thickness region. This is not unexpected as a double-sided weld, such as that used here, involves some material in the mid-thickness region being exposed to high temperature gradients twice. The second weld pass would have acted similar to a post-weld heat treatment (PWHT) on material in the mid-thickness region, resulting in a reduction of residual stress. What is clear is that, upon relaxation, the transverse stresses are predicted to be compressive close to the laser weld and more tensile close to the TIG weld, in the austenite material. For the transverse, longitudinal and normal directions the stresses in the mid-thickness region are more tensile when compared to those on the surface.

The longitudinal stress is somewhat similar to the transverse stress in that it is predicted to be more tensile close to the TIG weld compared to the EB weld. Though the longitudinal stress is of a notably higher magnitude than the transverse stress. During relaxation the longitudinal stress in the mid-thickness region increases. Compressive stresses, that were predicted to occur at the weld boundaries in the ferrite material, relax to negligible magnitudes which forces the austenite region close to the EB weld to be more tensile. Longitudinal stresses on the surface do not change significantly during relaxation. It is interesting to note that upon relaxation the normal stresses on both the surface and in the mid-thickness are predicted to negligible, at least in comparison to the transverse and longitudinal directions. Given that prior to element deletion, high magnitudes of normal stress were estimated on the surface of the sample, this gives some validation to the assumption of plane stress condition applied to the experimental neutron diffraction data (see Section 5.2.5, Figure 5.8).

Contour plots for specimen 2 and specimen 3 are shown in Figures 5.34 and 5.35, respectively. Prior to relaxation the stresses, in both the mid-thickness and surface regions, were predicted to be of similar magnitudes and locations to those noted in specimen 1. After relaxation there are some differences in the redistribution of stress but, overall, the specimens (specimens 1, 2 and 3) are predicted to be broadly similar to one another.

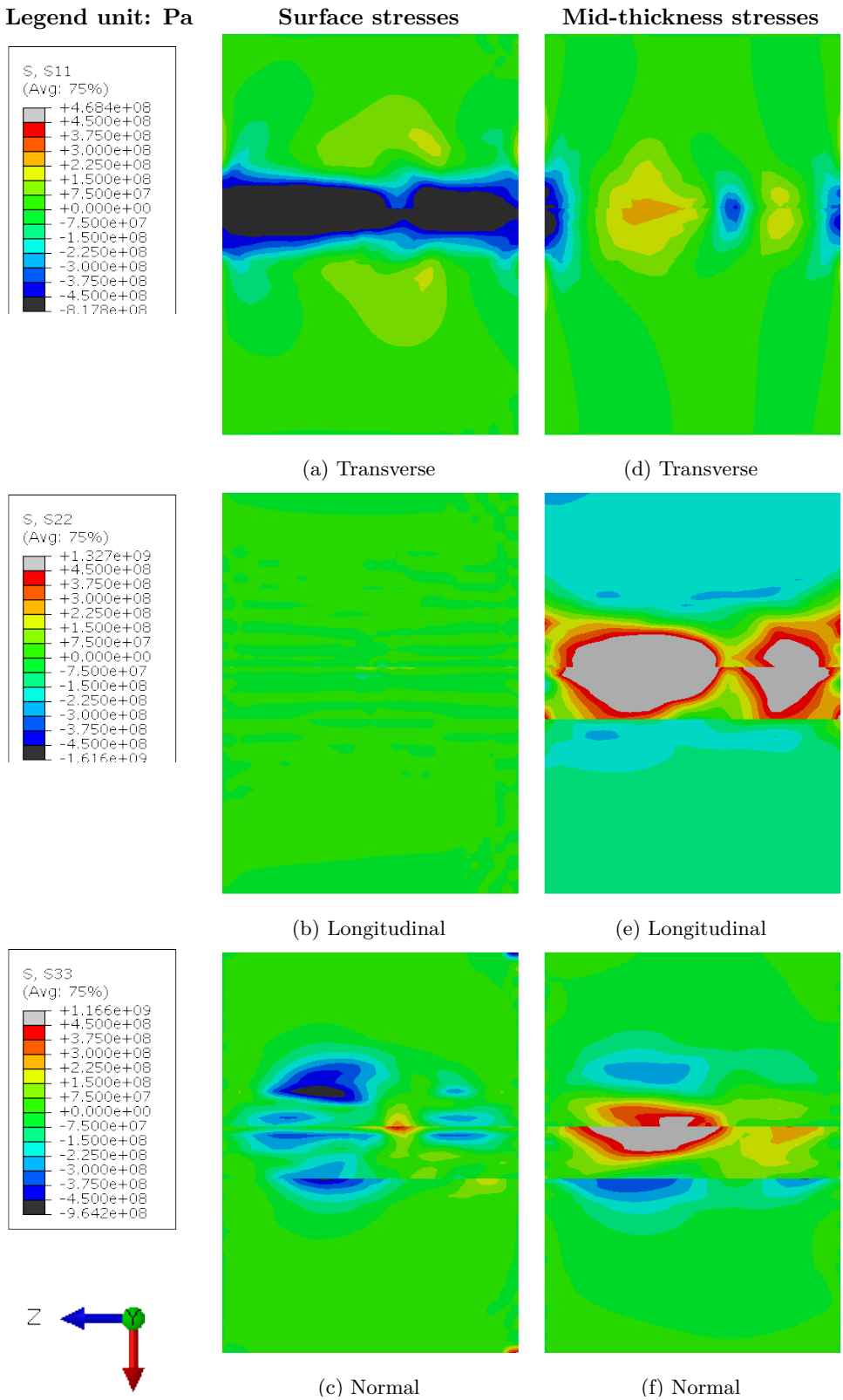

(a) Transverse (d) Transverse

(b) Longitudinal (e) Longitudinal

(c) Normal (f) Normal

Figure 5.29: Contour plots detailing the transverse, longitudinal and normal stresses on the surface and mid-thickness of the component. Nodal displacements mapped using data from moving heat source and *MAP SOLUTION keyword

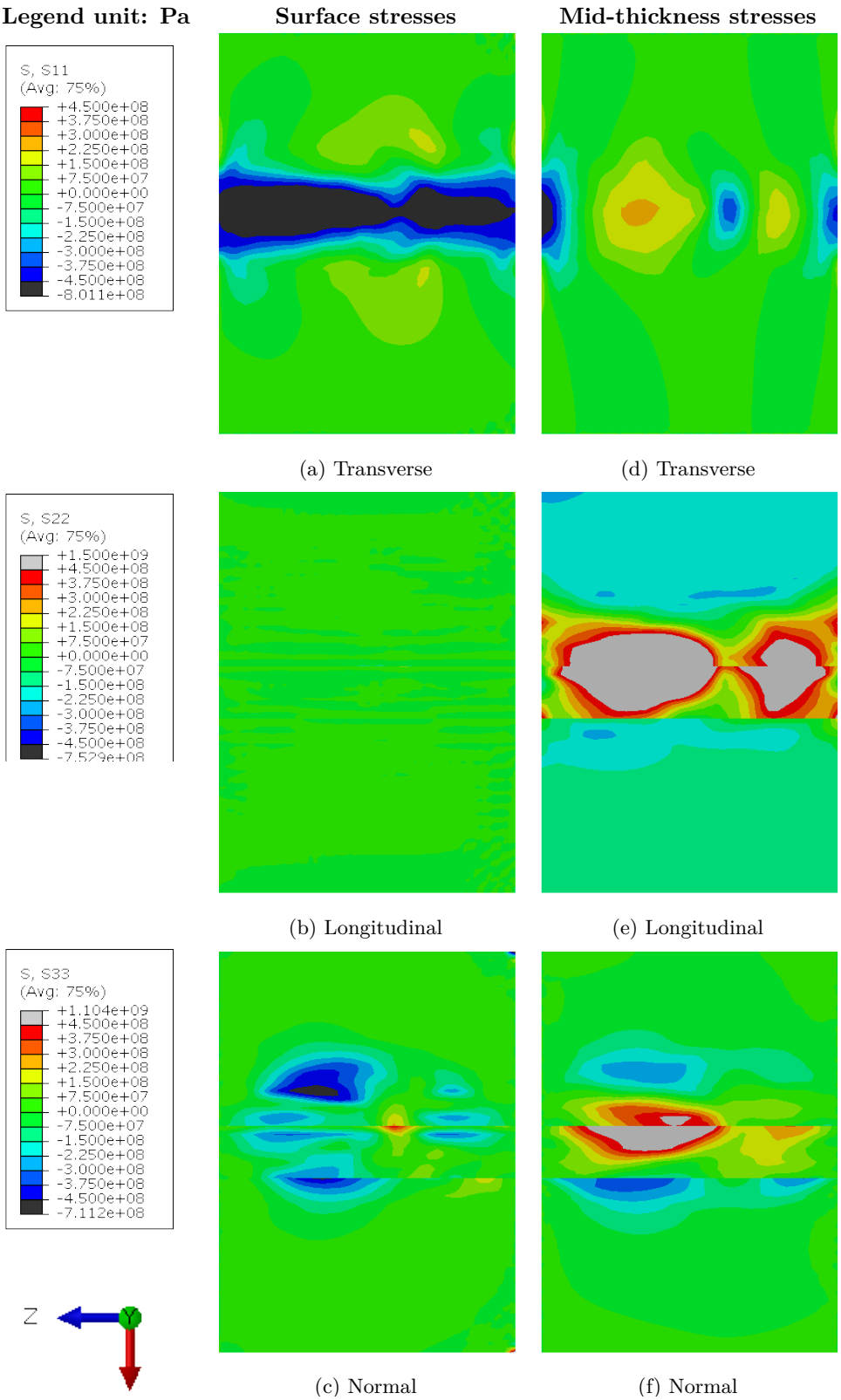

Figure 5.30: Contour plots detailing the transverse, longitudinal and normal stresses on the surface and mid-thickness of the component after relaxation of stresses

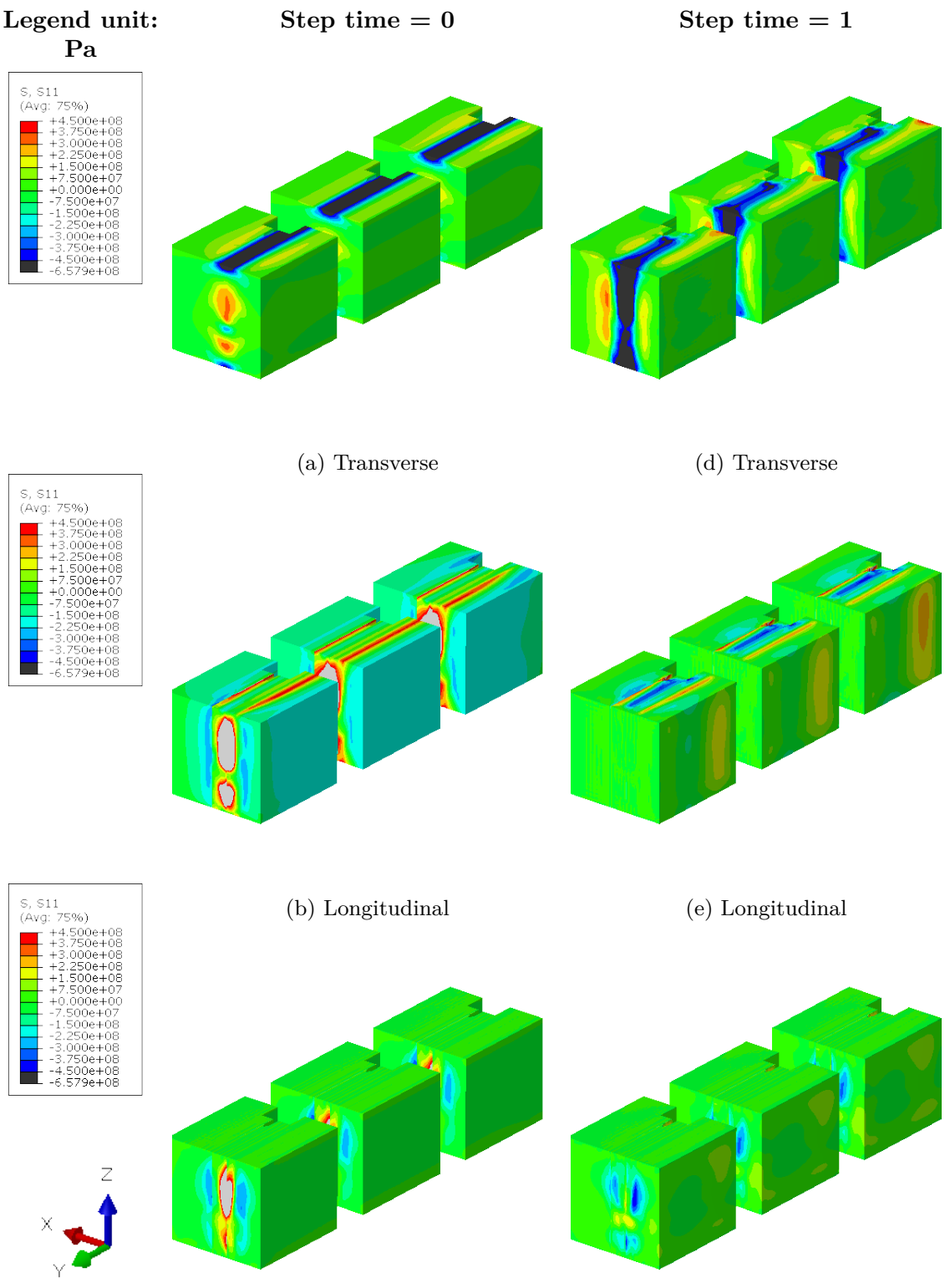

(a) Transverse

(d) Transverse

(b) Longitudinal

(e) Longitudinal

(c) Normal

(f) Normal

Figure 5.31: Contour plots detailing the transverse, longitudinal and normal stresses on the surface of specimen blanks before and after relaxation of stresses

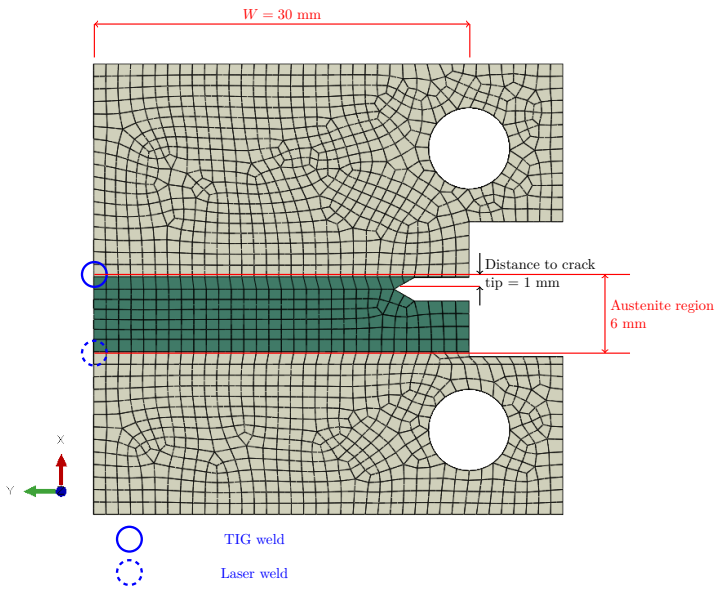

(a) Mid-thickness

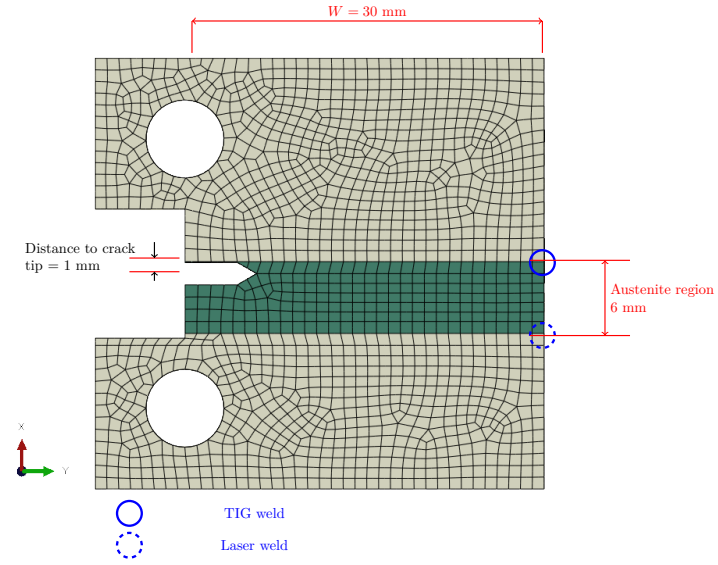

(b) Surface

Figure 5.32: Annotated image of specimen orientation with respect to the component. Figure 5.32a showing first outer surface of the specimen, corresponding to approximate mid-thickness region of the component. Figure 5.32b showing the second outer surface of the specimen, corresponding to the weld 1 surface of the laser welded component

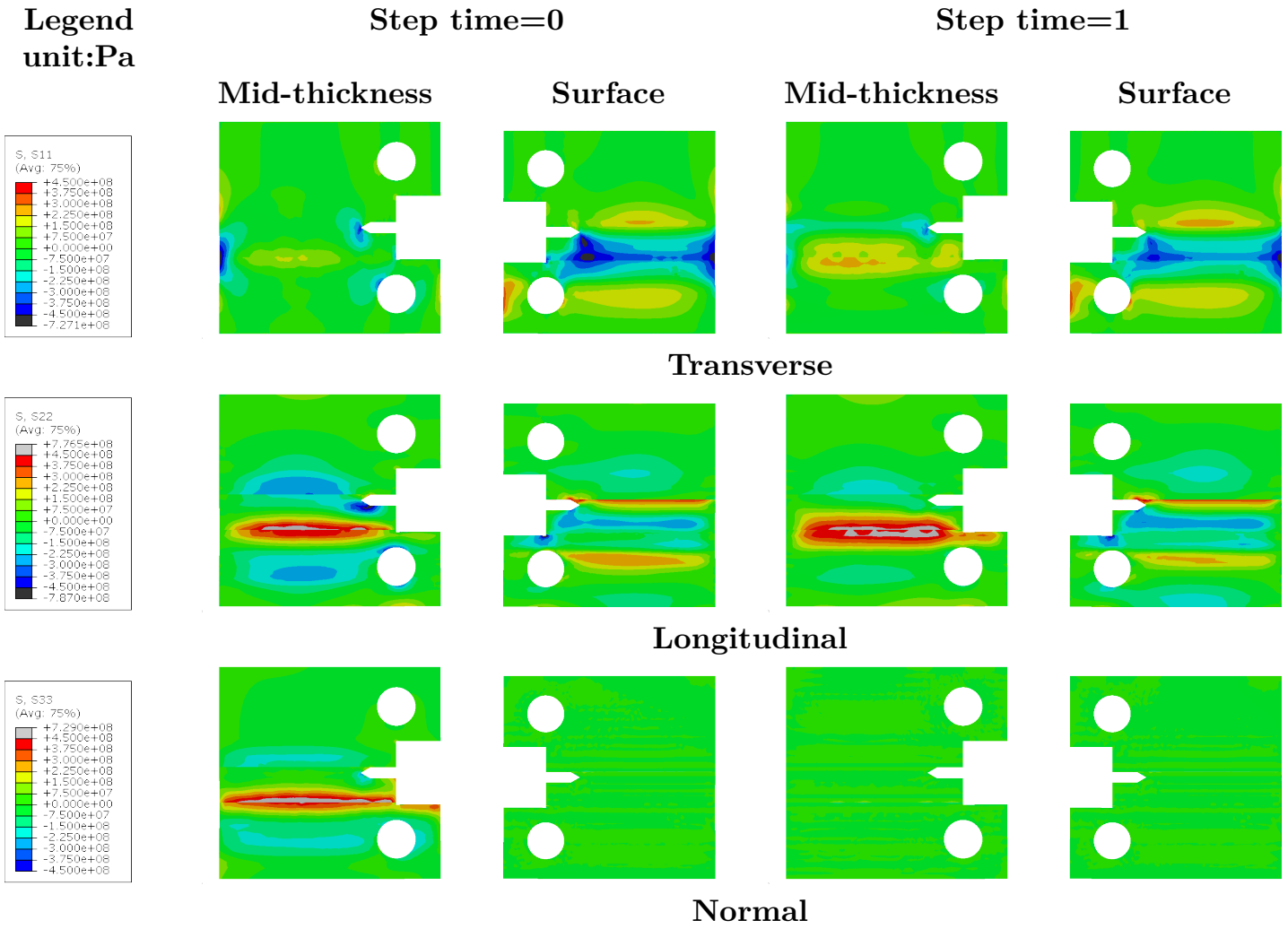

Figure 5.33: Contour plots detailing the transverse, longitudinal and normal stresses on the surface and mid-thickness of Specimen 1 before and after relaxation of stresses

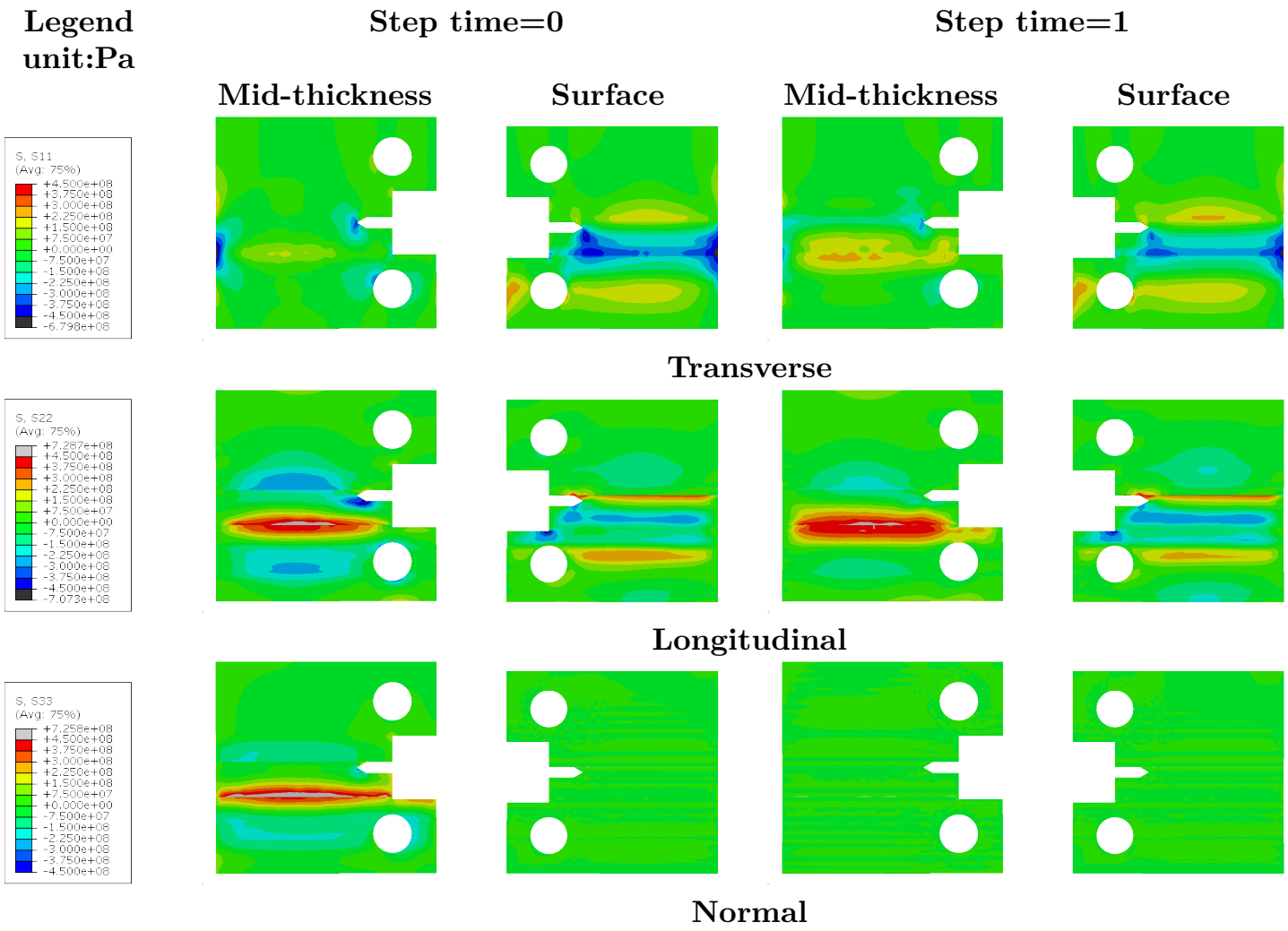

Figure 5.34: Contour plots detailing the transverse, longitudinal and normal stresses on the surface and mid-thickness of Specimen 2 before and after relaxation of stresses

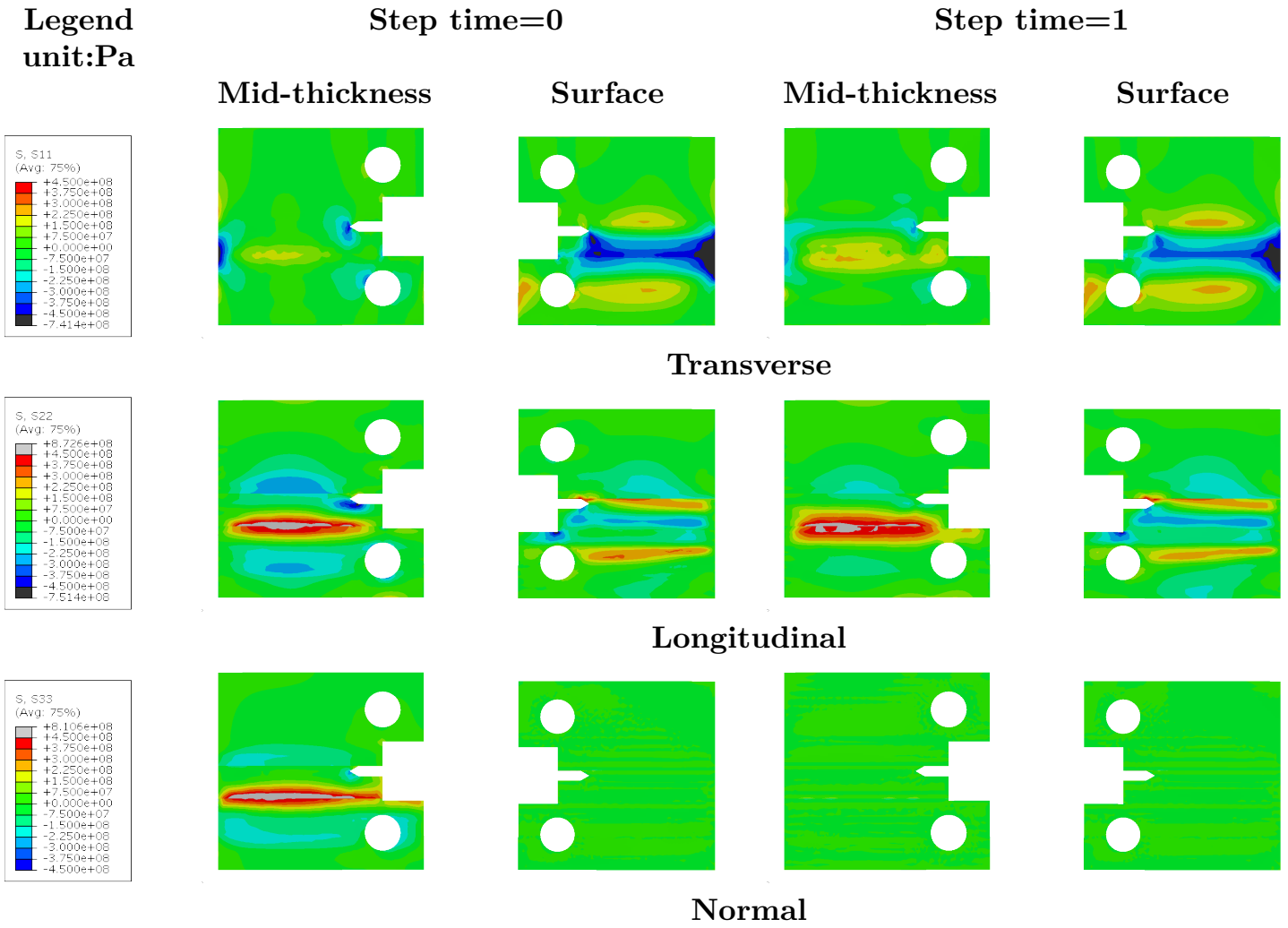

Figure 5.35: Contour plots detailing the transverse, longitudinal and normal stresses on the surface and mid-thickness of Specimen 3 before and after relaxation of stresses

5.4 Chapter 5 Summary

In this chapter the residual stress measurements, using neutron diffraction, conducted on both the laser welded block (also referred to as the 'sandwich component') and on individual CT specimens were presented. Baseline, d_0, lattice measurements were taken from stress-free samples manufactured from both the ferrite (base) and austenite (clad) regions. While the base material d_0 measurements are reasonable the austenite material measurements are subject to large errors. This is not unexpected given the complex textured type microstructure present (see Chapter 3). Given the large error associated with the austenite stress-free measurement relatively thin samples like the tensile and CT specimens were re-assessed using a plane stress assumption. For tensile specimens this resulted in an increase in estimated residual stresses in the longitudinal and transverse directions of welded specimens. This is as expected. The base material tensile specimen was found to have maximum estimated residual stresses in the longitudinal and transverse directions similar to the range of the error measurement. This is as expected.

In the sandwich component the stress was shown to be tensile at the TIG weld boundary, compressive in the mid-weld region, and tensile at the laser weld boundary. This double tensile peak result indicates that significant amounts of residual stress were likely present in the component prior to additional laser welding. The peak tensile stress was measured to be approximately 300 $\pm$ 50 MPa in the normal direction (i.e. with respect to the weld) at the TIG weld boundary. The peak compressive stress was noted to have occurred roughly in the center of the austenite material and was measured to be 500 $\pm$ 50 MPa.

Finite element modelling of the laser welding process was conducted to determine residual stresses in the sandwich component. Two heat sources were investigated, a block dump model (BDM) and a moving heat source (MHS) model. The differences, in terms of heat source, are discussed in-depth in Section 5.3 but to briefly re-iterate: the block dump model (BDM) assumes the application of a heat flux to the entire volume

of each weld. The moving heat source (MHS) applies a relatively complex combined ellipsoid-conical heat flux that passes along the weld in the longitudinal direction. It is generally accepted that MHS models are more accurate in comparison to their BDM counterparts but this benefit is offset by the additional computing resources required in comparison to the BDM approach.

A mesh sensitivity study was conducted on a BDM analysis to ensure the density of mesh applied was sufficient for the applied temperature gradients. Two models were compared in terms of temperature and estimated residual stresses. The first had a mesh of approximately 34,000 elements while the second had just under 300,000 elements. Similar results were found when comparing the coarse and fine mesh densities. The high density mesh model deviated slightly compared to the less dense mesh (Figures 5.14a and 5.14b, respectively) but in all cases the deviation was less than 50 MPa, which is equivalent to the error on the experimental results. Hence the lower density mesh was considered robust enough and was used in the majority of BDM analyses.

To estimate stresses from nodal temperatures, the nodal displacements are mapped from the heat transfer solution to a structural solution. There are a number of methods that can be implemented but some cases, notably when the structural model mesh differs immensely from that of the heat transfer model, require mesh-to-mesh solution mapping [Dassault Systemes Simulia Corp, 2014]. While the mesh-to-mesh solution method allows the user additional freedoms in terms of geometry the main drawback is the requirement for equilibrium. Essentially, for mapping temperature to structural models, this results in a reduction of residual stress in the mapped analysis. The magnitude of reduction in residual stress is dependent on the level of deformation in the heat transfer model.

One of the objectives of this work was to estimate the residual stresses in CT specimens manufactured from the sandwich component. This requires element deletion in the structural model. The shape of the CT specimens are complex, at least in comparison to the component itself which was modelled as a rectangular volume with perfectly

square or rectangular element shapes. It is not possible to delete square elements and retain the required geometry of the CT specimens. Hence a second, extensively partitioned model (see Figure 5.18b) was created. The partitioned model required somewhat distorted element shapes which implies that the validity of the mesh sensitivity analysis conducted for the BDM was no longer applicable. To assess the robustness of the mapping method a parametric study investigating the impact on residual stresses was conducted. It was shown, see Figure 5.21, that there was little impact on the estimated residual stresses when the mesh-to-mesh mapping solution was applied. Contour plots of stresses on the surface and mid-thickness regions were comparable, in each of the three orthogonal directions, with those obtained in BDM mesh sensitivity study.

The nodal temperatures for the BDM and MHS models are compared in Figure 5.36. As can be seen the MHS model has a lower temperature when compared to the BDM. The nodal temperatures plotted are taken from a specific node located on the outer surface of the block for comparison to experimental measurements made during the welding process. The experimental measurements were 110°C after the first weld deposition and 118°C after the second weld deposition. From Figure 5.36c it can be seen that, for the first weld deposition cycle, the nodal temperature for the MHS is approximated well with the experimental value while the BDM appears to overestimate the temperature. During the second weld deposition cycle both models appear to significantly overestimate the temperature on the outer surface. While the model takes into account the time required to vent the electron beam chamber it does not allow additional time for re-pressurisation prior to the second weld deposition. This likely accounts for some of the disparity in comparing experimental temperatures to FE temperatures for the second weld deposition. The impact of cooling parameters (surface film and radiation coefficients) on estimated temperatures should also be investigated more thoroughly. The variation, of temperature, in comparing the two models is unsurprising when one considers the profile of the heat source applied. The BDM heat source profile is significantly larger than that of the MHS. The distance of the node, from which the tem-

peratures plotted in Figure 5.36 were estimated, to the heat source is different for each case and hence the temperature measured at said node is a function of the applied heat source due to the influences of the surface coefficient (i.e. conduction) and the relative distance of the node to the heat source.

A comparison was made between experimental data and residual stresses estimated using the BDM in Section 5.3.1 Figure 5.22. A good agreement between experimental and modelling was not achieved. Both the BDM and MHS models underestimate the transverse stresses and over estimate longitudinal and normal stresses. It should be noted however that both models neglected the influence of phase transformation. It was made clear earlier (see Section 2.3.3) that temperature has a profound impact on particular crystalline structures which impacts the microstructure, the mechanical properties and the fracture mode of materials, particularly those of a body center cubic (BCC) structure. Modelling phase transformations has been investigated by others [Arun, 2015; Duffy, 2014; Abburi Venkata et al., 2015; Abburi Venkata, Truman, Khayatzadeh and Coules, 2016; Francis et al., 2007]. Arun [Arun, 2015] stated that the phase transformation from austenite to martensite results in an increase in volume due to additional carbon insertion to the crystal lattice structure. The increase in volume essentially results in compressive residual stresses which must be balanced by tensile residual stresses elsewhere in the system. Abburi [Abburi Venkata et al., 2015; Abburi Venkata, Truman, Khayatzadeh and Coules, 2016] showed a similar result for a phase-transformation finite element model of a P91 to 316L dissimilar metal weld. Duffy [Duffy, 2014] attempted to use a cooling curve to model the formation and transformation of phases in an EB welded dissimilar metal weld, similar in material type to that used in this work. Duffy found that the cooling curve for A508 grade 3 had a critical influence on microstructure formation. Furthermore it was shown that without detailed data of cooling modelling the phase transformations was only partially successful when compared to experimental microscopy and hardness testing results.

Clearly phase transformation in BCC structures has a large impact on any estimated residual stresses and will account for at least some of the disparity seen in the results

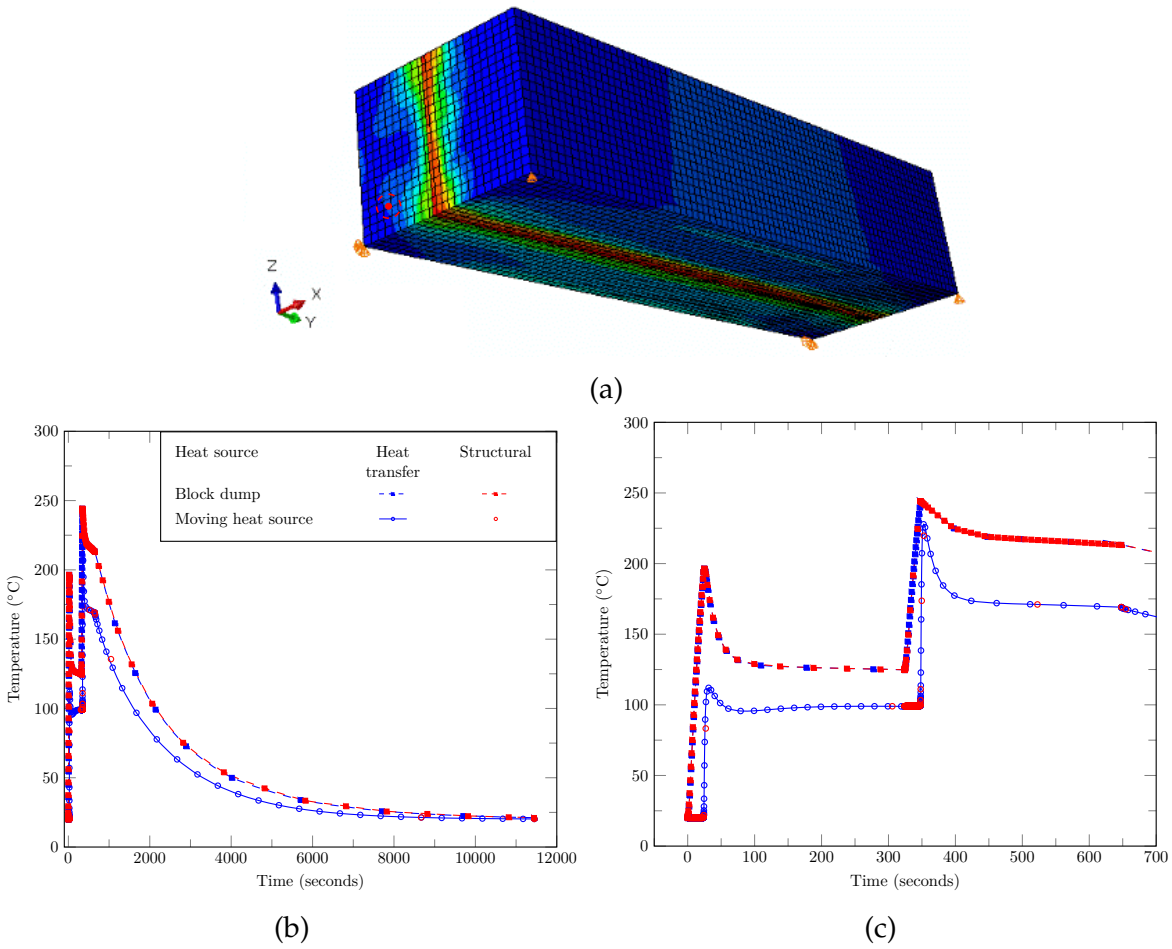

Figure 5.36: Comparison of nodal temperatures estimated using block dump and moving heat source model. Figure 5.36a showing the position of the node used to output temperature values. Figure 5.36b plotting temperatures for entire welding process. Figure 5.36c showing magnified view of heating cycles.

presented in this work. Other variables that might improve the comparison are: modelling the estimated residual stresses prior to EB welding (i.e. those due to the original TIG welding procedure), estimating the impact, if any, of the tack welds, and averaging FE data to more closely resemble that of the neutron diffraction measurements. In Chapter 3.3.1 neutron diffraction measurements were taken over a gauge volume measuring $2 \times 2 \times 10$ mm^3 whereas FE data was presented from specific nodal values. Averaging the data in the current work would likely result in a better agreement to experimental data. Additionally incorporating phase transformations would improve the accuracy of the model. These tasks are recommended for future work in weld modelling assessment.

Experimental neutron diffraction was also conducted on specimens machined from the laser welded component. When the d_0 result for austenite material was used to assess the data residual stresses in the normal direction were measured to be up to 300 MPa. Given the thickness of the samples (15 mm) this magnitude of stress was not considered a reasonable approximation. It is worth noting that the results (Figure 5.7) were based on the austenite material d_0 values. Measurements were taken from the crack tip region along the remaining ligament of the sample at 2 mm intervals with a gauge volume of $1 \times 1 \times 2\text{mm}^3$. Considering the proximity of the notch to the TIG weld boundary, and given the aforementioned complex microstructure, it's not surprising that the results were inconsistent with expectation. By adopting a plane stress approach (as opposed to the d_0 measurement) the stresses were re-estimated. Experimental data for the plane stress assumption was plotted in Figure 5.8. The longitudinal stress was measured to be compressive at the notch tip, becoming more tensile along the remaining ligament, and slightly compressive on the back surface. The trend was similar for the three tested specimens. Figure 5.37 shows contour plots of the predicted residual stresses, after removal of material (by element deletion, see Section 5.3.5). As shown the longitudinal stresses are predicted to be compressive at the crack tip, tensile along the remaining ligament, and less tensile on the back surface. While the magnitude in the predicted model differs from that measured experimentally the approximately is predicts the location of the peak stresses very well. Good agreements were also noted for the transverse and normal directions when comparing to experimental data.

One might question how the residual stress measurements in the CT specimens were predicted more accurately, when comparing with experimental data, than the component. As discussed earlier the comparison at a component level was conducted using explicit nodal values, along a direction similar to the experimental measurement. At a component level the element size is significantly smaller than the experimental gauge volume. Additionally explicit nodes were used and no averaging of the data was conducted. At a specimen level however the element size is a fairly good approximation of the respective experimental gauge volume. Hence, the contour plots shown in Figure

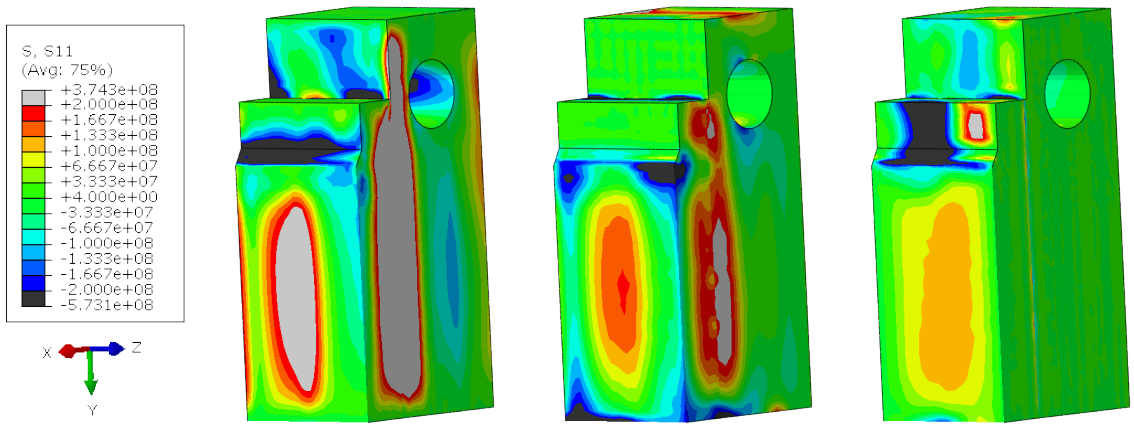

(a) (b) (c)

Figure 5.37: Comparison of residual stresses in mid-thickness of CT specimen 1. Showing a) longitudinal, b) transverse, and c) normal directions. Contour map limited to $\pm$ 200 MPa, applicable to all directions as shown

5.37 consist of stresses that are averaged over a volume similar to that used experimentally. The implication is that the good agreement between estimated residual stresses (using FE) and the experimental (neutron diffraction) results for individual CT specimens validate the MHS FE model. It has also been clearly demonstrated that the BDM and MHS models are similar, in terms of both the magnitude of estimated residual stress and the predicted residual stress profiles, within expected precision limitations for each respective heat source. Hence the disparity seen between experimental neutron diffraction data taken from the sandwich component (Block B) and the FE model of the component is likely limited to the assumption that a stress-free state existed in the combined section of material prior to laser welding.

Chapter 6: Fracture Toughness of Defects Oriented Parallel to Materials Boundary

6.1 Experimental Fracture Toughness of CT specimens notched in austenite

The purpose of this work is to assess the performance of defects oriented parallel to the materials interface. Current literature states that due to the clad welding process, sub-surface (under clad) cracking in the HAZ of the base material is a possible SCF and defect initiation point. This issue is expounded by the fact that NDT methods struggle to identify and size defects located in multi-material components. Additionally the mechanism of crack propagation in clad welded materials is not well understood and current literature has not identified whether cracking would deviate from the normal direction (perpendicular to the load) due to the presence of a materials boundary. This section of work aims to clarify the following:

- Does the presence of a materials boundary impact strain distribution in the sample? If so, does this impact the crack driving force?
- How do sub-surface defects a clad component propagate? Will they propagate perpendicular to the load direction (as with homogeneous samples) or does the crack deviate?
- In the event defects propagate to the weld boundary region does the crack direction re-align to the load direction and propagate along the boundary or, does the crack path continue deviating into the base material?
- Does the proximity of the notch to the materials boundary impact the direction of crack growth?
- What is the impact, if any, of the thickness of the cladding?

In this section the six CT specimens machined from the laser welded component (see Section 3.2.4, Block B) will be analysed. Fracture toughness testing was completed using unloading compliance method with digital image correlation (DIC) as outlined in Sections 3.3.4 and 3.3.6, respectively. Figure 6.1 shows one of the specimens, in the test machine, prior to fracture testing. The weld boundaries are clearly marked for reference. All images and plots in this section have weld boundaries in the orientation described by Figure 6.1. Table 6.1 lists the defect lengths at various points during testing. As shown in Table 6.1 samples S1 to S3 were machined to an initial crack depth of 13.5 mm while samples S4 to S6 where machined to an initial crack depth of 16.5 mm. These notch depths are representative of $a/W = 0.45$ and $a/W = 0.55$, respectively. The test method [ASTM International, 2001] specifies that samples should be pre-fatigue cracked prior to fracture testing. This was not conducted as, due to the undulating nature of the TIG weld boundary and the proximity of the notch to this boundary, the direction of crack growth could not be guaranteed. The test standard specifies that the crack must remain perpendicular to the loading direction. To ensure crack 'straightness' specimens were machine notched using a 0.1 mm wire EDM process. Figure 6.2 plots the force against LLD for the six specimens, individual plots can be seen in Appendix C Figures C.1 to C.6. As seen in Figure 6.2 specimens S1 to S3 reached forces signficantly higher than specimens S4 to S6 for comparable values of LLD, this is due to the differences in initial defect lengths between the specimens.

Table 6.1 shows that the crack length was not estimated well in the elastic region, indeed for all specimens the initial crack length was over-estimated. As a result the first estimated crack length during the unloading compliance test was, in all cases except for S2, smaller than that estimated during the elastic region. Figure 6.3 plots the fracture toughness as a function of crack extension (Δa) for data calculated by the software [Instron, 2010*b*]. As shown negative crack extension was noted to have occurred during the early stages of each test. This phenomena has been noted by other authors [Voss, 1983; Rosenthal et al., 1990; Seok, 2000] and is particularly prevalent in high

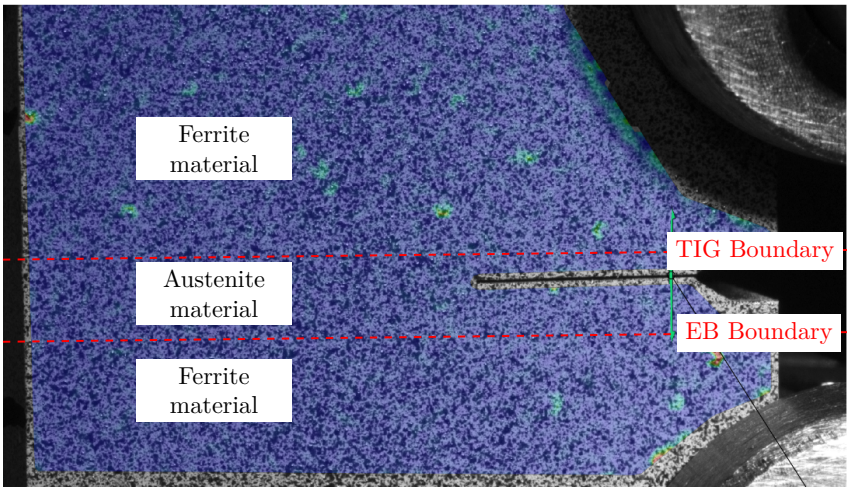

Figure 6.1: CT specimen with annotations showing material boundaries

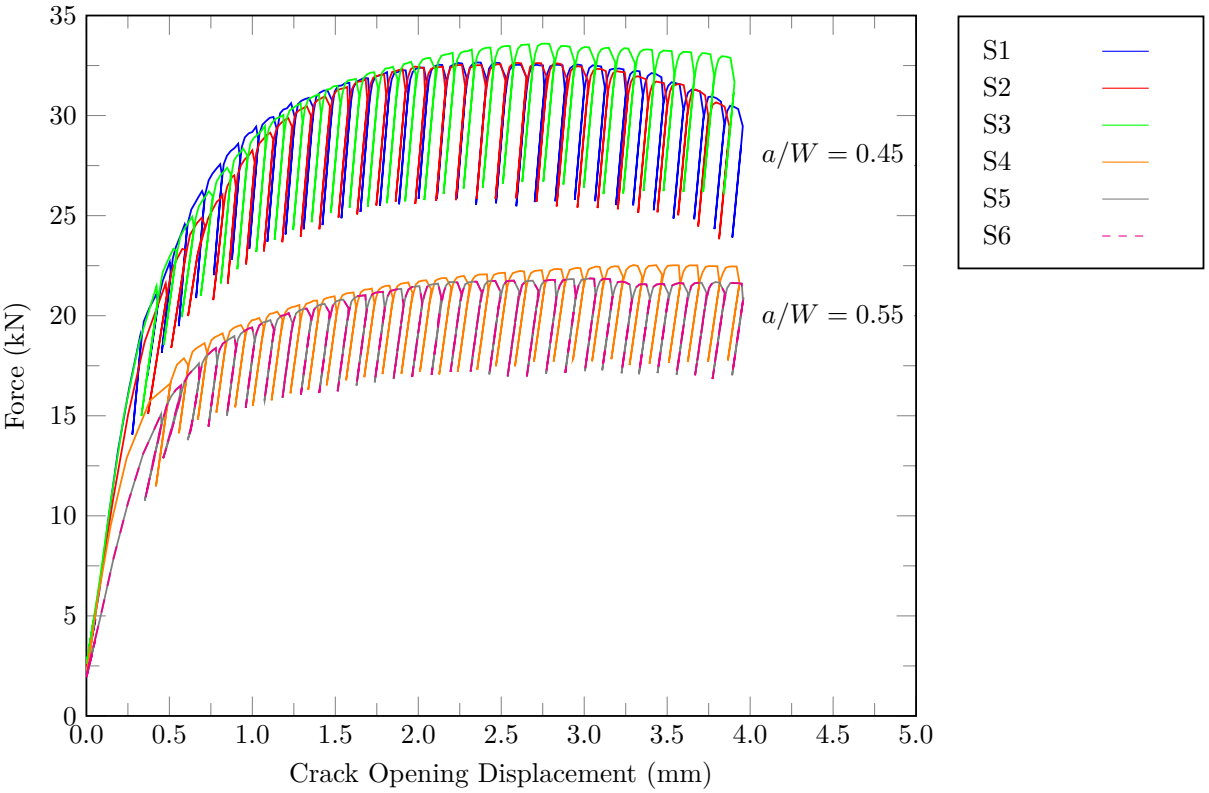

Figure 6.2: Force versus displacement for CT specimens with initial defect in austenite material

strength, ductile materials. Verstraete [Verstraete et al., 2014] stated that the negative crack extension values were calculated due to a decrease in compliance at an early loading stage while Weiss [Weiss and Nyilas, 2006] postulated it was possibly due to crack tip blunting and strain hardening of the plastic zone ahead of the crack tip. The fracture toughness testing method [ASTM International, 2001] does not provide guidance on how negative crack growth should be adjusted but common practise is to shift the crack extension (Δa) so that the most negative value of crack extension becomes the 'zero' crack extension position. This assumption has been validated experimentally by others [Rosenthal et al., 1990; Seok, 2000; Weiss and Nyilas, 2006]. Figure 6.3 includes scatter points showing the modified data (where data is shifted so that the most negative value represents zero crack growth).

The test method [ASTM International, 2001] provides limits, outside of which, test data is not considered valid. These were previously discussed in Section 3.3.4. The limit of energy, J_{limit}, is plotted for each sample in Figure 6.3. The value of M is initially assumed to be 2.0 as per recommended guidance. As shown in Figure 6.3 J_Q could not be estimated within these limits. Increasing the slope of the construction line ($M = 5$) encapsulated more test data but the J_{limit} was exceeded prior to a J_Q value for all tests. Hence a valid measure of fracture toughness could not be made. Additionally Table 6.1 shows that the crack depth in the mid-thickness exceeded the surface depth significantly which again, surpasses the validity limits of the test method. As previously discussed (see Section 2.3.1) side-grooving the samples would have reduced the likelihood of crack tunnelling, however, this method would have controlled the path of the crack and as the aim of this work was to assess the crack path with respect to the materials boundary side-grooving was considered inappropriate.

Digital Image Correlation (DIC) of the surface of CT specimen S3 is shown in Figure 6.4. Figures 6.4a to 6.4d show the true major strain in each element of the DIC generated mesh. True strain in the thickness direction are shown in Figures 6.4e to 6.4h. From Figures 6.4a to 6.4d it can be seen that initially higher strains are present in the region of the crack tip with a slight attraction towards the original TIG weld boundary, located

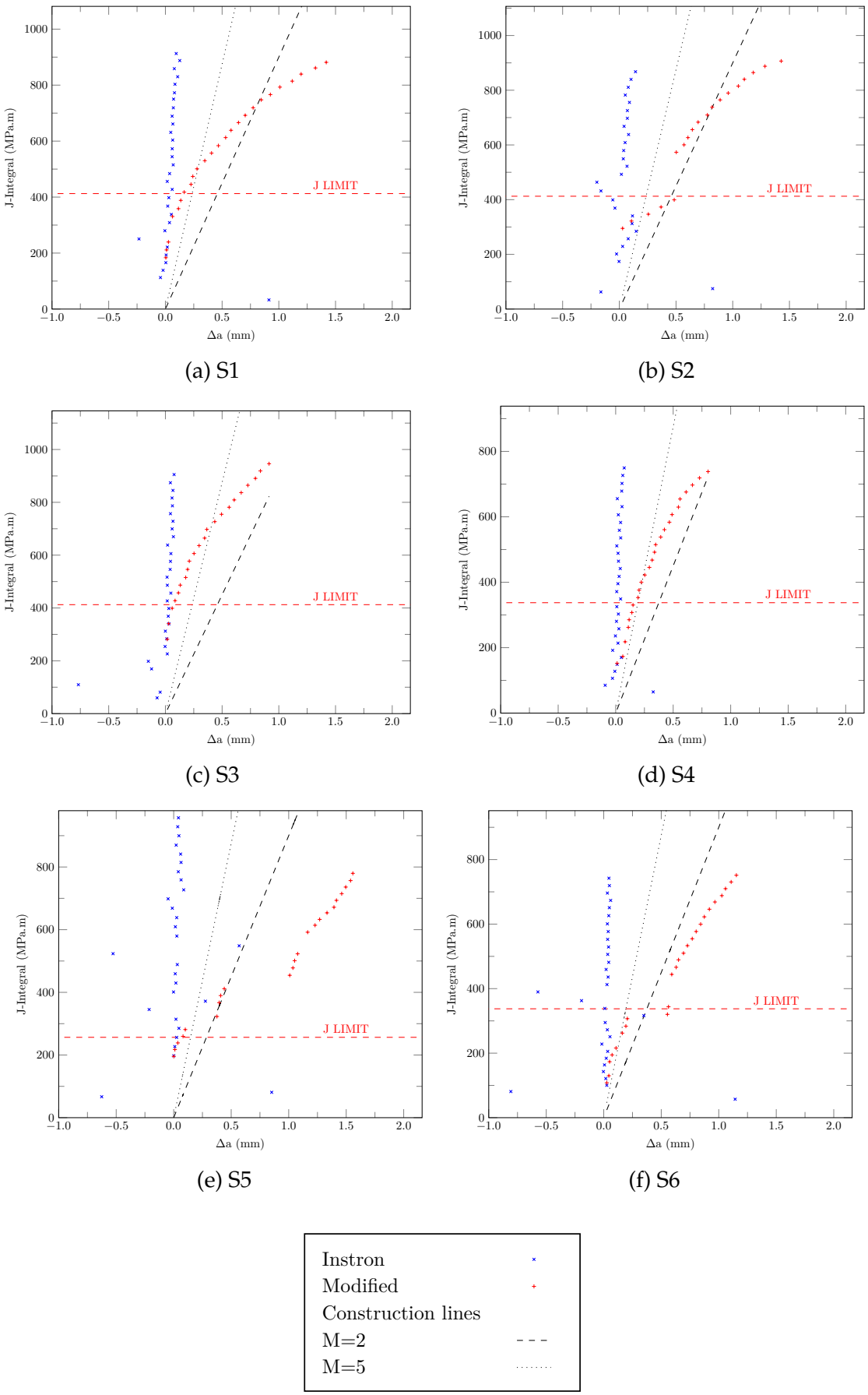

Figure 6.3: J-Integral versus crack extension (Δa) for CT specimens notched in austenite

Table 6.1: Fracture toughness of CT specimens notched in austenite

Sample No.	**Machined notch**	$a_{0\ elastic}$	$a_{0\ test}$	$a_{f\ test}$	$a_{f\ measured}$	**Comments**
	mm	mm	mm	mm	mm	
S1	13.5	18.73	14.41	14.92	17.25	Bifurcation of defect on outer surfaces with slight deviation towards the TIG weld boundary. In the mid-thickness defect curved away from the TIG boundary towards the bulk of the austenite region.
S2	13.5	17.32	17.48	14.87	16.57	Little/no crack growth on outer surfaces. Defect in the mid-thickness growing perpendicular to load direction.
S3	13.5	17.38	16.84	15.00	15.54	Little/no crack growth on outer surfaces. Defect in the mid-thickness growing perpendicular to load direction.
S4	16.5	16.92	16.82	17.47		
S5	16.5	19.74	19.11	17.30		
S6	16.5	17.75	17.64	17.20		

Where $a_{0\ elastic}$ represents the initial crack length estimated during the elastic unloading prior to fracture testing, $a_{0\ test}$ the initial crack length estimated after first unloading sequence (SEQ10), $a_{f\ test}$ represents the final crack length estimated from final unloading sequence, and $a_{f\ measured}$ represents the measured crack length at the mid-thickness of the sample post-test.

approximately 1 to 2 mm from the crack tip. Over time higher values of strain appear along both the TIG weld boundary and the EB weld boundary (approximately 4 mm from the crack tip). Midway through the test (Figure 6.4c) strains along the EB weld boundary extend further along the remaining ligament in comparison to those on the TIG weld boundary. In the early stages of testing the propagation of strain towards the materials boundary is not unexpected given that higher values of residual stresses are expected in these areas. By the mid-point (Figure 6.4c) of the test (SEQ150), given the considerable deformation at the crack tip, one would expect the residual stress to have been significantly reduced due to the excessive plasticity. This implies that the continued preference of strains to propagate along the weld boundaries as shown in Figure 6.4c are not due to residual stress effects but are most likely due to other factors such as local microstructure. At the end of the test sequence, Figure 6.4d, the austenite region appears to have plastically collapsed. Some strain has propagated into the ferrite, but these regions appear to be limited to regions close to the crack tip. Similar results were noted to have occurred for S5 (Figures 6.5a to 6.5d) and S6 (Figures 6.6a to 6.6d).

Strains in the thickness direction (Figures 6.4e to 6.4h) develop in a similar manner to those noted previously. Strain appears to be initially attracted towards the TIG weld boundary however they relatively quickly develop on the opposing side (i.e. along the EB weld boundary). By the middle of the test (Figure 6.5g) the distribution of strain in the thickness direction is symmetric around the crack tip. The weld boundaries do not appear to impact strains in the thickness direction to the same extent as that noted for major strain. Similar results were noted to have occurred for S5 (Figures 6.5a to 6.5d) and S6 (Figures 6.6a to 6.6d).

DIC images were further analysed investigating strains along specific paths. Figure 6.7a describes the paths perpendicular to the loading direction. Nine paths, at distances of 0.5 mm relative to one another from the crack tip (Path 0) were investigated. The final position, Path 9, is vertically offset 4.5 mm from Path 0. Each path (Path 0 to Path 9) has an identical horizontal length. A local co-ordinate system, located at

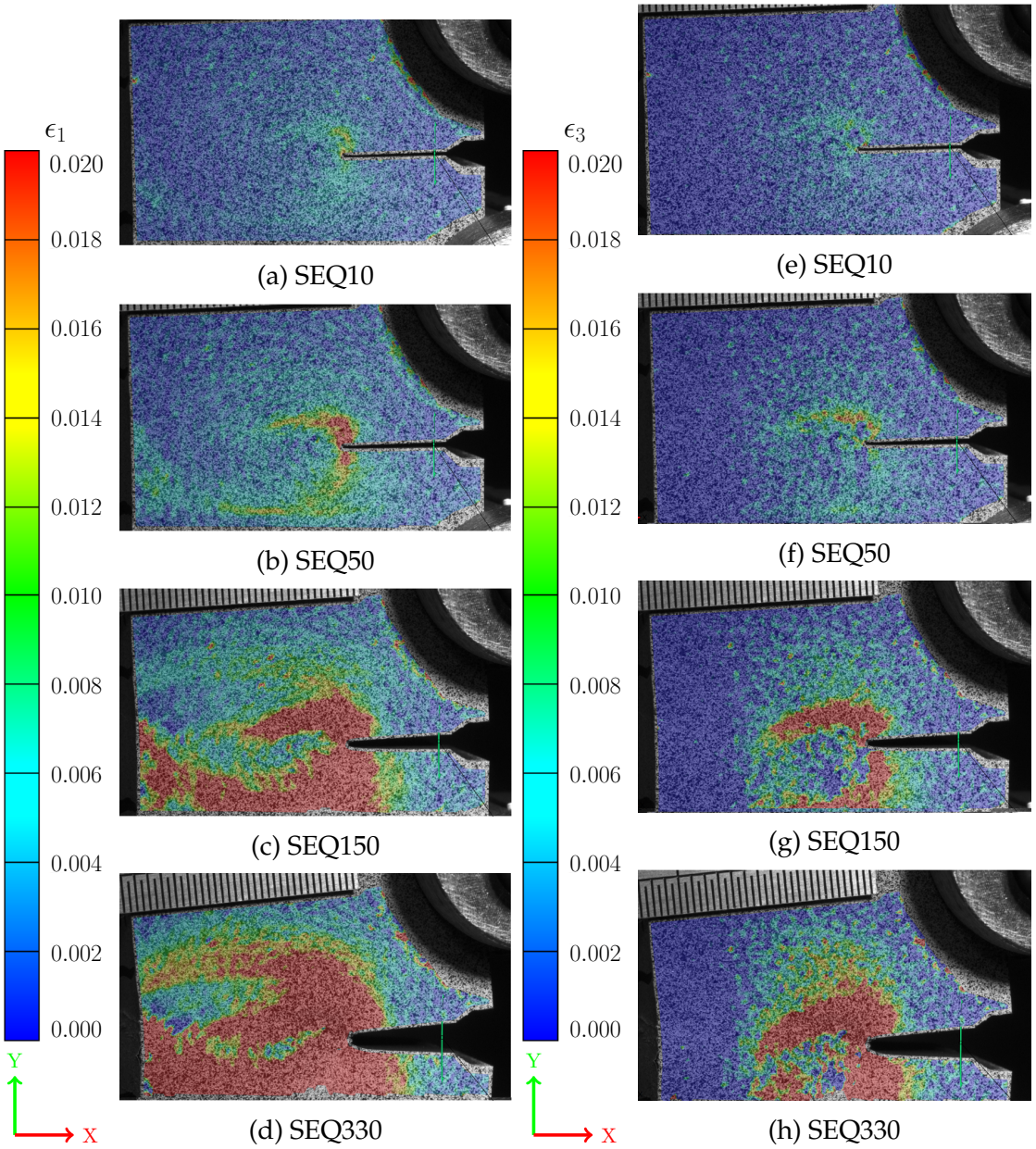

Figure 6.4: DIC data for CT specimen S3 with initial defect length $a/W = 0.45$. Figures 6.4a and 6.4d showing the true major strain and Figures 6.4e and 6.4h showing strains in thickness direction. Results of first, fifth, mid-test and final peak (force) unloading positions, respectively.

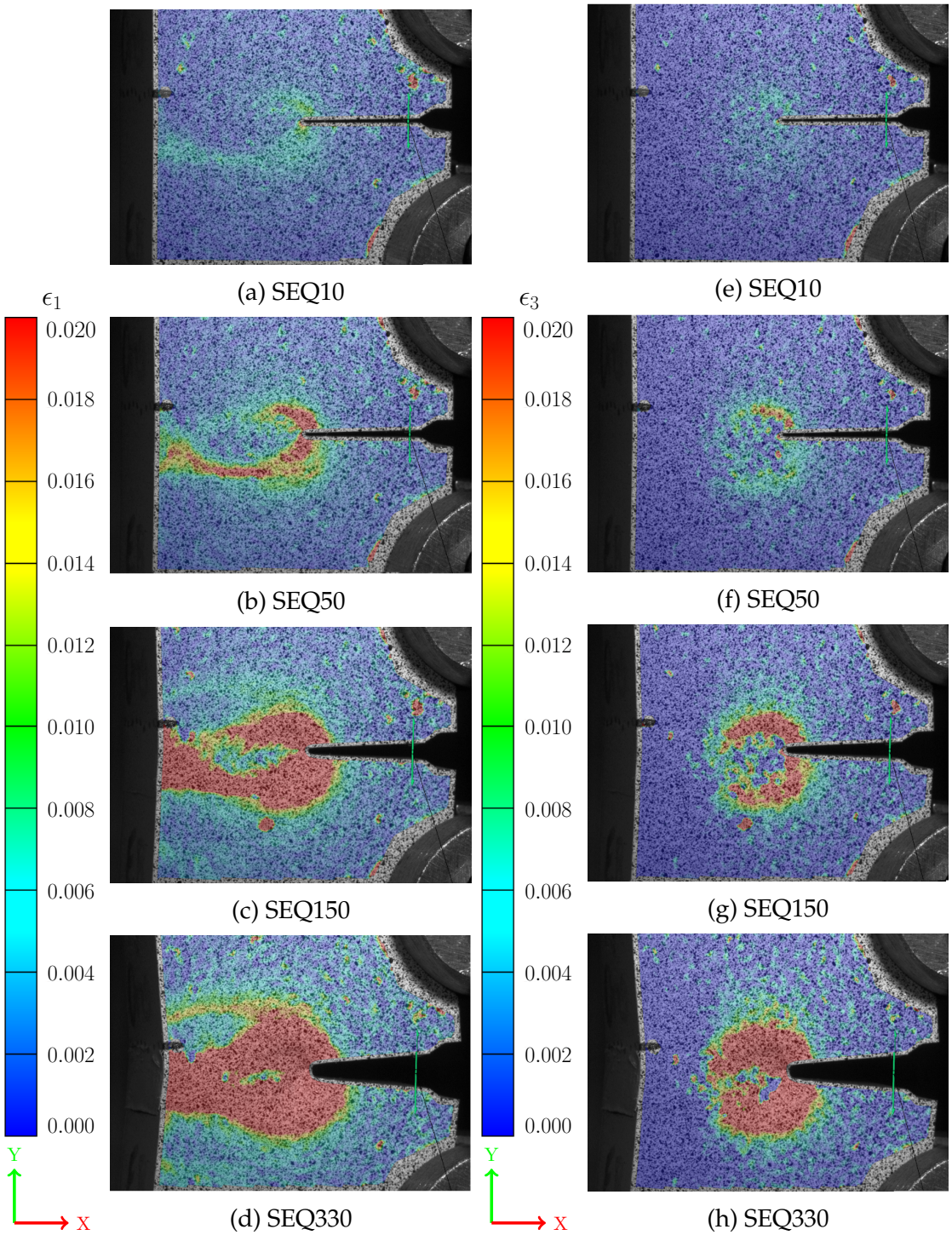

(a) SEQ10 (e) SEQ10

(b) SEQ50 (f) SEQ50

(c) SEQ150 (g) SEQ150

(d) SEQ330 (h) SEQ330

Figure 6.5: DIC data for CT specimen S5 with initial defect length $a/W = 0.55$. Figures 6.5a and 6.5d showing the true major strain and Figures 6.5e and 6.5h showing strains in thickness direction. Results of first, fifth, mid-test and final peak (force) unloading positions, respectively.

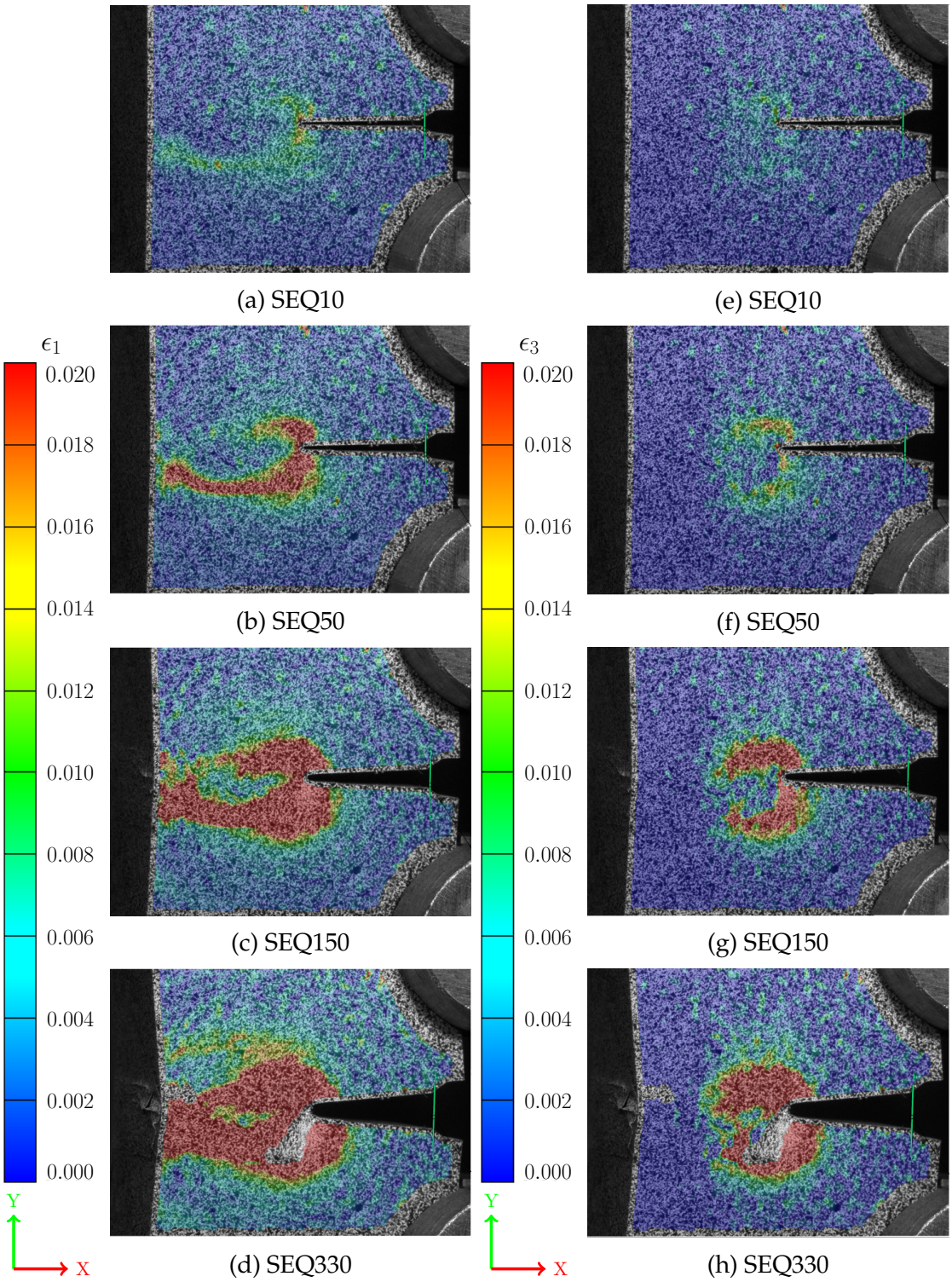

(a) SEQ10 (e) SEQ10

(b) SEQ50 (f) SEQ50

(c) SEQ150 (g) SEQ150

(d) SEQ330 (h) SEQ330

Figure 6.6: DIC data for CT specimen S6 with initial defect length $a/W = 0.55$. Figures 6.6a and 6.6d showing the true major strain and Figures 6.6e and 6.6h showing strains in thickness direction. Results of first, fifth, mid-test and final peak (force) unloading positions, respectively.

the crack tip end of each path was applied. Hence positive horizontal displacement represents movement along the path away from the crack tip. Data for each path were filtered, to reduce noise errors, using a mean filter around a window encapsulating seven points.

Figure 6.8 plots major strain for samples S3 (Figures 6.8a and 6.8b), S5 (Figures 6.8c and 6.8d) and S6 (Figures 6.8e and 6.8f) for the first and last unloading cycles, respectively. Additional stages of the analyses are plotted in Appendix C Figure C.7. For all samples the overall trend is a reduction in strain as one moves along the path away from the crack tip. This is not unexpected as an exponential reduction in strain, due to the increasing distance from an SCF (in this case the crack tip), is widely acknowledged. The strains at Path 0 and Path 2 are, in general, similar, for each sample at their respective unloading sequence. One exception was noted for sample S5 during the first unloading sequence (Figure 6.8c) where the strain at Path 2 exceeds that of Path 0 approximately 2.0 mm along the section. This localised increase in strain was not noted in Figure 6.5a, however it can be seen that strains in the region are somewhat higher than the surrounding environment. Hence the peak seen in Figure 6.8c is likely a result of the averaging technique. Figure 6.5f more clearly depicts local hotspots in the region of Path 2. The highest magnitude of strain was noted to be at Path 4 (2.0 mm vertical offset from the crack tip) for both samples S3 and S6. For sample S5 the highest magnitude was noted to exist at Path 0 but reduces significantly within 1 mm distance of the crack tip. Comparatively, at Path 4, the values of strain remain at higher magnitudes over distances much further from the crack tip. In all three samples a significant reduction in strain is noted to occur at Path 5 (2.5 mm vertical offset from Path 0). These data indicate that the TIG weld boundary exists between 2.0 - 2.5 mm from Path 0. Indeed Figure 6.7a was marked at the approximate location of the TIG boundary prior to testing and the mark lies in the region encapsulated by Path 4 and Path 5.

Comparing strains directly as shown in Figure 6.9 does not account for the changing proximity of each Path relative to the notch location. Figure 6.9 plots normalised data for the sequences and positions shown in Figure 6.7a. Data were normalised as fol-

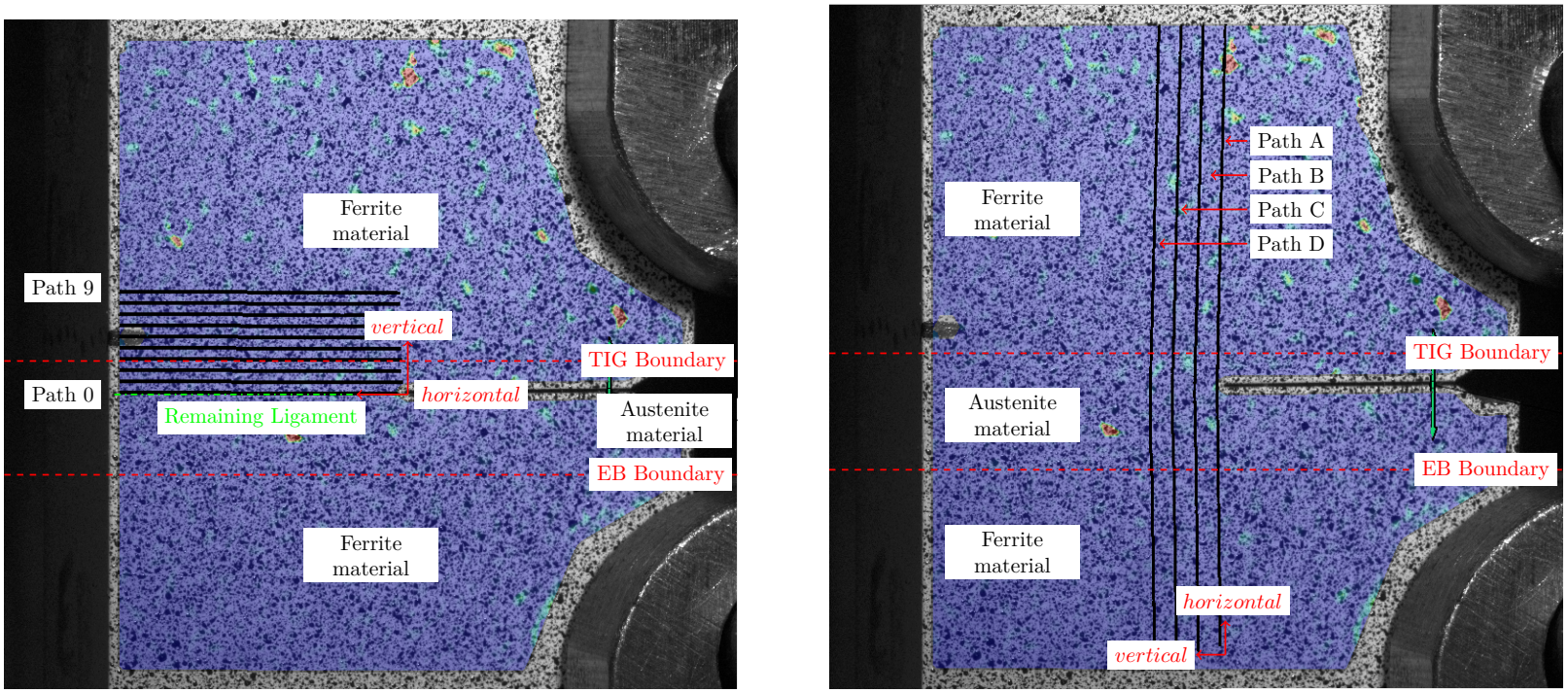

(a) (b)

Figure 6.7: Annotated images showing approximate locations of TIG and EB weld boundaries and paths investigated. Figure 6.7a showing sections parallel to crack depth. Local co-ordinate system in use. Remaining ligament from crack tip to back face of sample shown in green with positive displacement representing movement away from the crack tip. Individual DIC paths for strain analysis showing Path '0' at the crack tip to Path '9' 4.5 mm vertically offset from crack tip. Each section subsequent to Path '0' located 0.5 mm from preceding path. Figure 6.7b showing sections oriented perpendicular to the crack depth. Local co-ordinate system at the bottom of image. Section moving from 'bottom' of image towards the top passing through the austenite region. Four sections labelled 'A' through 'D' as shown, section 'A' located at the crack tip, subsequent sections offset by 1 mm from preceding section.

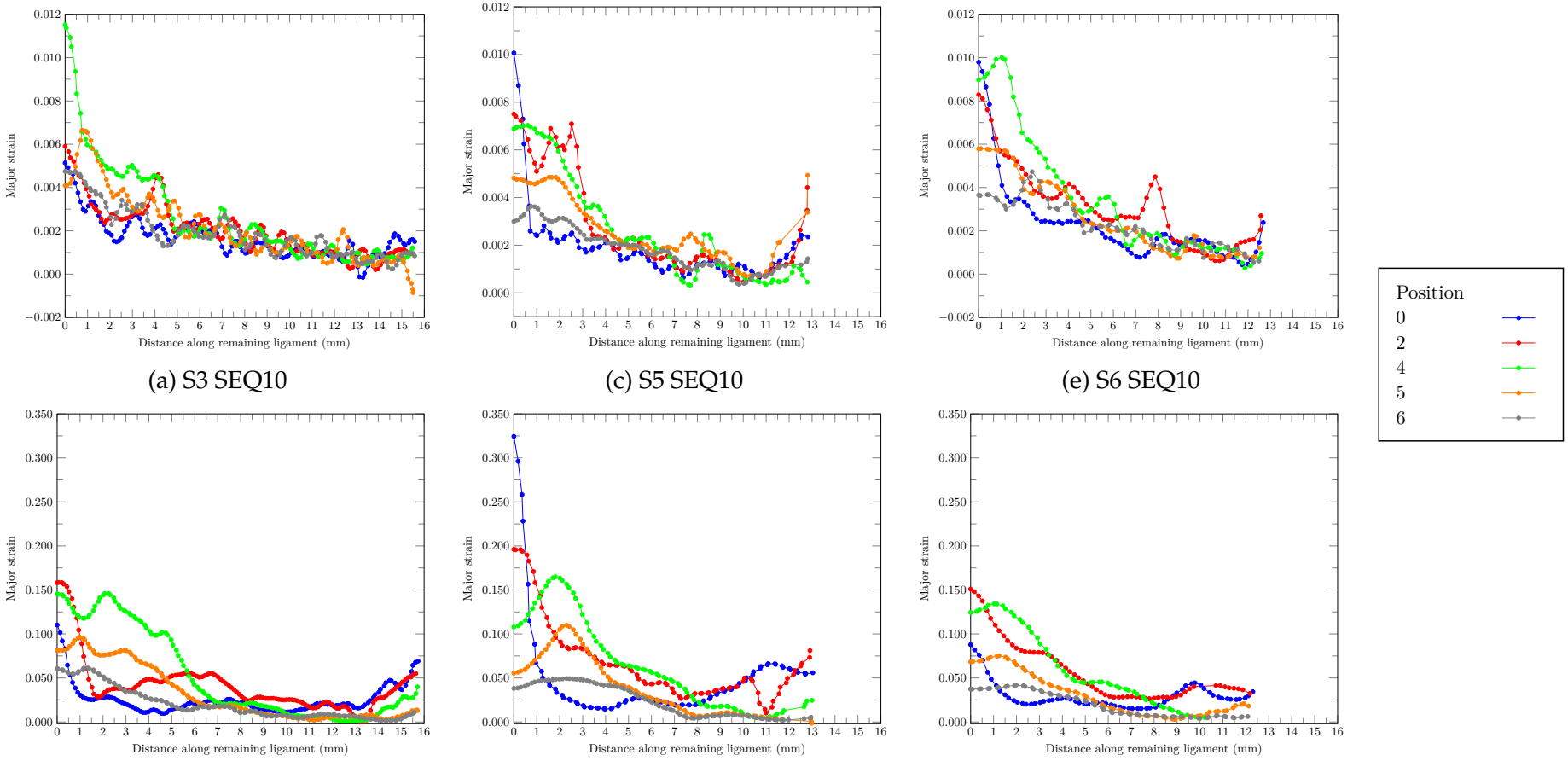

(a) S3 SEQ10 (c) S5 SEQ10 (e) S6 SEQ10

(b) S3 SEQ330 (d) S5 SEQ330 (f) S6 SEQ330

Figure 6.8: Major strain along the remaining ligament at various positions. Positions are positive relative to the crack tip towards the TIG weld boundary. Results shown for Samples S3, S5 and S6 at first and final sequences, respectively.

lows; To account for proximity to the notch tip, at each time stamp, the strains at the crack tip from Path 0 to Path 9 (i.e. parallel to the loading direction) were adjusted using Equation 6.1.1. This provided a normalised notch parameter (normalised$_{notch}$). To account for variations along the path length (i.e. perpendicular to the loading direction), for every time stamp, the strain along the remaining ligament of each Path was normalised using Equation 6.1.1. The maximum and minimum values of strain were taken from any path (i.e. Paths 0-9), irrespective of distance from the crack tip. This resulted in a normalised section parameter (normalised$_{section}$). The two normalised parameters were then multiplied as per Equation 6.1.2 to get the overall relative strain effects along the section of each Path.

$$\epsilon_{normalised} = \frac{\epsilon_{current} - \epsilon_{min}}{\epsilon_{max} - \epsilon_{min}} \tag{6.1.1}$$

$$\text{Relative normalised strain} = \text{normalised}_{notch} \times \text{normalised}_{section} \tag{6.1.2}$$

As shown in Figure 6.9, along the remaining ligament, Path 4 is strained to a significantly higher relative magnitude for longer distances, compared to other Paths. There are instances when Path 0 and Path 2 exceed the relative magnitude of Path 4 but, in general, these instances are located within 2 mm horizontal distance (i.e. inside the plastic zone along the remaining ligament) of the crack tip. Additional test sequences are plotted in Appendix C Figure C.8 and show similar trends to those noted here. Figure 6.9d is the exception to the trend. As shown, during the final sequence of testing, the relative strain at Path 4 was lower than that noted for Paths 0 or 2. Other than the final sequence however, sample S5 followed the general trend (see Appendix C Figures C.8c and C.8d).

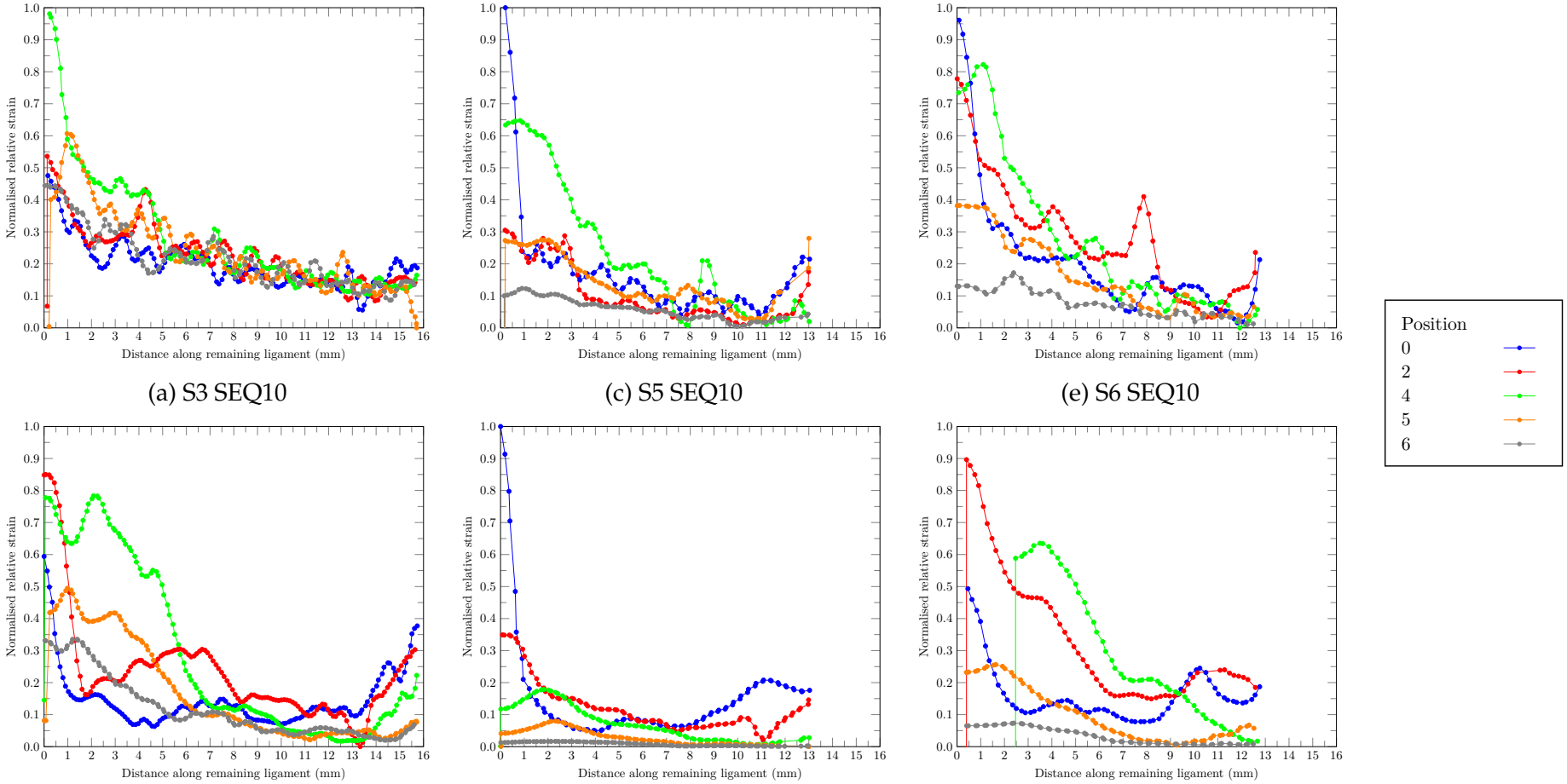

(a) S3 SEQ10 (c) S5 SEQ10 (e) S6 SEQ10

(b) S3 SEQ330 (d) S5 SEQ330 (f) S6 SEQ330

Figure 6.9: Normalised relative strain along the remaining ligament at various positions. Positions are positive relative to the crack tip towards the TIG weld boundary. Results shown for Samples S3, S5 and S6 at first and final sequences, respectively.

Figure 6.9 clearly shows that the relative strains at Path 5 are consistently lower than those at Path 4. By comparing Figures 6.9a, Appendix C Figures C.8a and C.8b and Figure 6.9b in order, it can be seen that the difference in relative normalised strain between Path 4 and Path 5 increases over time. This indicates that strains at the interface, in both the austenite and ferrite materials, are similar at the beginning of testing but diverge over the duration of the test. Similar results can be seen to have occurred in samples S5 and S6 over the duration of testing. Comparing Paths 0 and 2 over test duration shows similar divergence but to a lesser extent than that noted between Paths 4 and 5. In any case it is clear that Path 4, i.e. the weld boundary, is subjected to higher relative magnitudes of strain than any other location. Hence, should failure occur, it is more likely to occur at Path 4 (i.e. at the weld boundary) and furthermore within 2 mm horizontal distance (i.e. along the remaining ligament) from the crack tip.

Comparing the three samples to one another in terms of the relative normalised strains it can be seen that each sample S5 differs somewhat in terms of relative normalised strain. Taking Path 4 as a comparison point, sample S3 is shown to have higher relative magnitudes of strain over a larger area than either samples S5 and S6. As previously discussed in Section 3.2.4, the component was welded with a double sided EB laser weld. Samples S5 and S6 were taken from the 'back' surface of the welded component (see Figure 3.9) in the region welded by the second weld pass. The impact of temperature on fracture and microstructure is significant and has been previously addressed in Sections 2.3.3 and 4.1. The component, from which the samples were machined, was at room temperature prior to the first weld pass. Consequently, the temperature differential (ΔT), was significant. During the second weld pass ΔT would be lower compared to that of first weld pass (due to heating of the component as a result of the first weld pass). It is therefore not unexpected that some variation, in terms of the relative magnitudes of strain, would exist when comparing samples machined from different regions of the component. The variation in performance between samples S3, S5 and S6 are likely a combination of microstructural differences and the impact of residual stresses.

Figure 6.10 shows the defect initiation and propagation on the surface and in the mid-thickness of specimen S1. As shown two defects initiated on the surface of the specimen while only one initiated in the mid-thickness region. The mid-thickness defect was measured to be longer than that of the surface defect. It was known, prior to testing, that the samples were at risk of crack tunnelling. However as specified earlier, given that the purpose of this work was to assess the crack path, side-grooving was considered inappropriate.

Figure 6.7b shows sections that were taken parallel to the loading direction. Path 'A' is at the crack tip, Postions B - C are offset 1 mm from each preceding section. Data along the sections are plotted in Figure 6.11 for the first and final test sequences. Additional test sequences can be seen in Appendix C Figure C.9. As can be seen the strain in sample S3 were measured to be significantly higher in the region of the weld in comparison to samples S5 or S6. It should however be noted that as per Table 6.1 the notch depth in S3 was 3 mm shorter than that of specimens S5 and S6. Therefore it is not surprising that higher strains were seen given that the applied force is correspondingly larger. The high strains noted in the ferrite region of specimen S6 are unexpected. It was noted, at later stages of testing, that the painted speckle pattern had failed in several regions. Given that the unexpected result occurs at the early stages of testing it is not clear what the cause of the result is but it may be well due to a lack of adhesion between the paint and the surface of the sample. Hence data in this region should be interpreted cautiously.

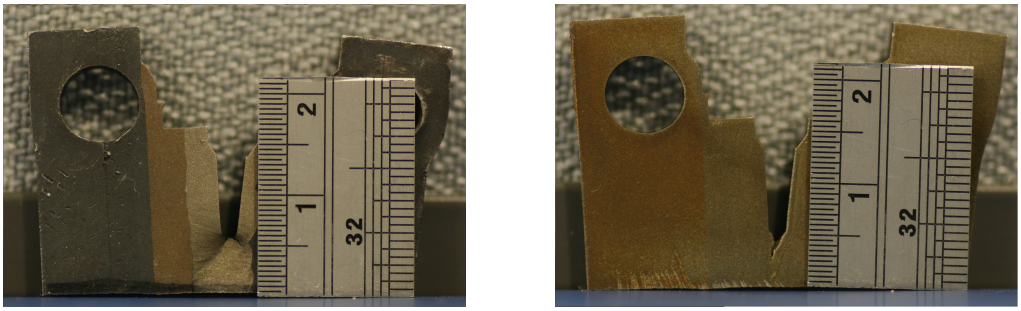

(a) Surface (b) Mid-thickness

Figure 6.10: Post-test inspection of CT sample S1. Figure 6.10a detailing the bifurcation at the crack tip on the surface of the sample with defects oriented towards both material boundaries. Figure 6.10b showing defect in the mid-thickness region with defect oriented towards the EB weld boundary.

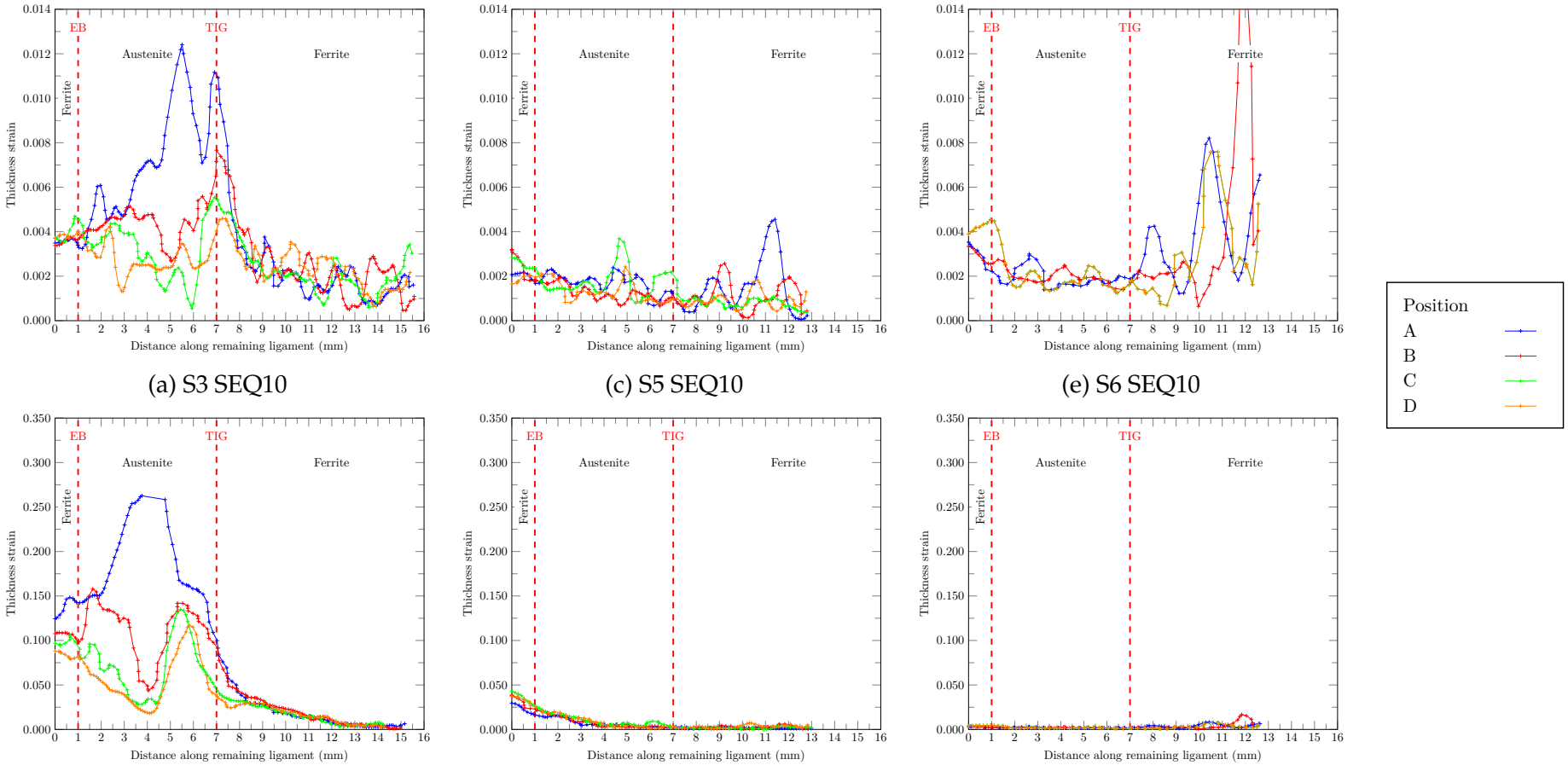

(a) S3 SEQ10 (c) S5 SEQ10 (e) S6 SEQ10

(b) S3 SEQ330 (d) S5 SEQ330 (f) S6 SEQ330

Figure 6.11: Major strain parallel to loading direction. Path 'A' at the crack tip, Paths 'B' to 'D' offset from preceding section by 1 mm. Results shown for Samples S3, S5 and S6 at first and final sequences, respectively.

6.2 2D Modelling of CT specimens

6.2.1 Defects located in austenite material

Plane stress and plane strain models of the CT specimens notched in austenite (see Figures 3.10b and 3.11b) were conducted for multiple crack depths (a/W) to assess the change in strain along both the remaining ligament and materials boundary. The model geometry was based on the experimental specimen geometry as shown in Figure 3.11b. Elastic-plastic material properties (as outlined in Table 4.2) were assigned to the relevant areas. The austenite region was assumed to be 6 mm in width, as was measured in the experimental specimens. The notch tip was located 1 mm from the materials interface in the austenite material. Finite strain analyses were conducted using the non-linear geometry option in Abaqus.

The models were meshed using CPS8 and CPE8 elements for the plane stress and plane strain analyses respectively. The crack tip singularity, for small-strain analysis, is dependent upon the material model. In the case of power-law hardening it is defined, in Abaqus, as Equation 6.2.1, where ϵ is the strain, r the distance from the crack tip, and η the hardening parameter used in the material model. Collapsed wedge elements with duplicated nodes and a midside parameter of 0.25 were applied to the first contour. This results in a combined square root and 1/r singularity which is specified to be 'the best' combination for power-law materials. As previously specified the current work used finite strain analyses rather than small-strain analyses. Generally finite strain models do not include sharp cracks and singular elements as it may lead to convergence issues. While the strains in the region directly surrounding the crack tip may be subject to inaccuracies, the contour integral is specified to remain reasonably accurate [Dassault Systemes Simulia Corp, 2014].

$$\epsilon \propto r^{-\frac{\eta}{\eta+1}} \tag{6.2.1}$$

A free mesh structure was allowed on a limited area surrounding the pin holes, structured elements were used at all other locations. The pins were not modelled, instead a reference point, at the centre of each pin hole, was kinematically coupled (U1 = U2 = UR1 = UR2) to the surface associated with each pin. Boundary conditions were applied to these reference points. The first reference point was constrained in all directions (U1 = U2 = UR1 = UR2 = 0), the second reference point was displaced in the y-direction (U2 = X mm, U1 = UR1 = UR2 = 0). Displacement control ensures that, in the event of stress redistribution, it can be readily ascertained. For longer crack lengths the analyses were considered to be small-strain (due to displacement control) rather than finite strain analysis, hence the use of crack tip singularity elements in the models. An additional boundary condition (U1 = 0) was placed on the back face of the specimen to stop rigid body motion (RBM) of the specimen. Approximately 6800 elements were used. Figure 6.12a shows the boundary conditions and meshing used for the analyses. A plastic collapse study was conducted on plane strain analyses to assess the maximum load capacity and the associated load-line displacement (LLD) for crack ratios in the range of $a/W = 0.45$ to $a/W = 0.75$. Results are plotted in Figure 6.13. As expected shorter crack depths reach higher magnitudes of load and displace less than longer crack depths. For a crack depth of 13.5 mm the maximum LLD was estimated to be approximately 1.5 mm. Therefore the analyses in the remaining section of this Chapter were limited to a maximum LLD of 1 mm (U2 = 1 mm, U1 = UR1 = UR2 = 0) unless otherwise explicitly stated. The maximum J-integral values at plastic collapse are shown in Figure 6.14.

Figure 6.15 shows the contour plots of direct strain (ϵ_{yy}) for various values of pin displacement (Δ) for a crack depth of 13.5 mm ($a/W = 0.45$). As shown the plane stress analysis predicts a high level of bias towards the materials interface region. Comparatively, the plane strain analysis (Figure 6.16), predicts strains are more likely to occur in the austenite region. Figure 6.17 plots the reaction force against load-line displacement (LLD) for multiple initial crack depths (a_0) for both plane stress and analyses. As shown in Figure 6.17 the plane strain analyses predict higher values of reaction force

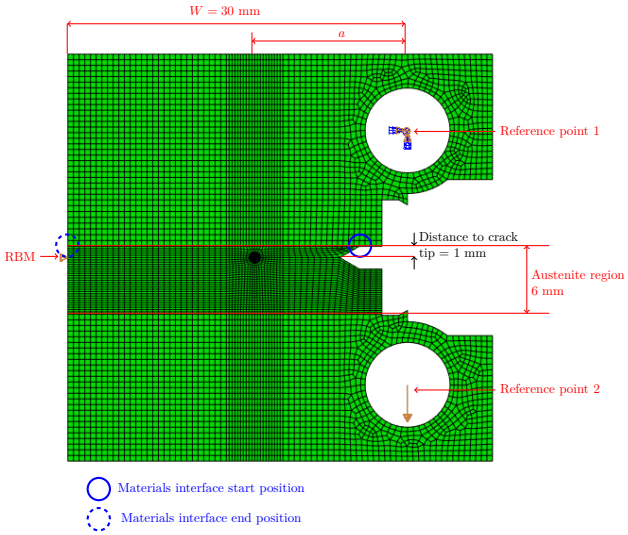

(a) 6 mm thick austenite region

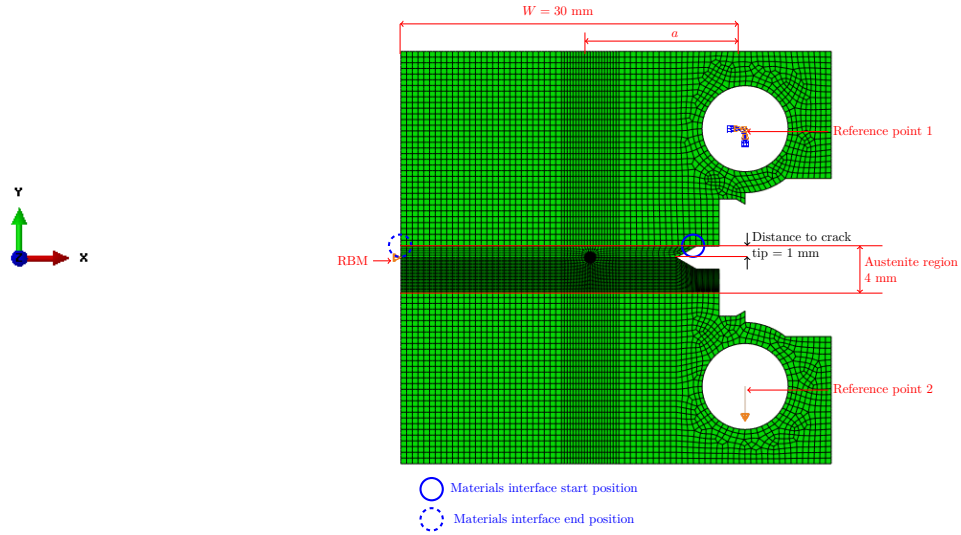

(b) 4 mm thick austenite region

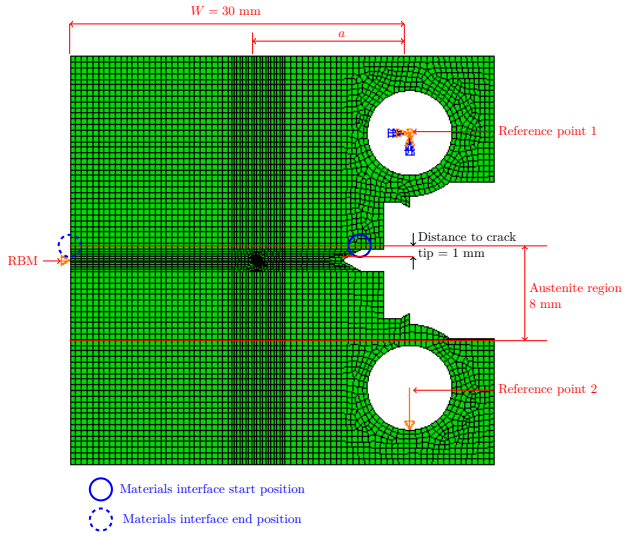

(c) 8 mm thick austenite region

Figure 6.12: Boundary condition and meshing applied to 2D models. Notch tip postulated to be 1 mm below TIG weld boundary. Figure 6.12a showing 6 mm thick austenite layer. Figures 6.12b and 6.12c showing 4 mm and 8 mm thick austenite layers, respectively.

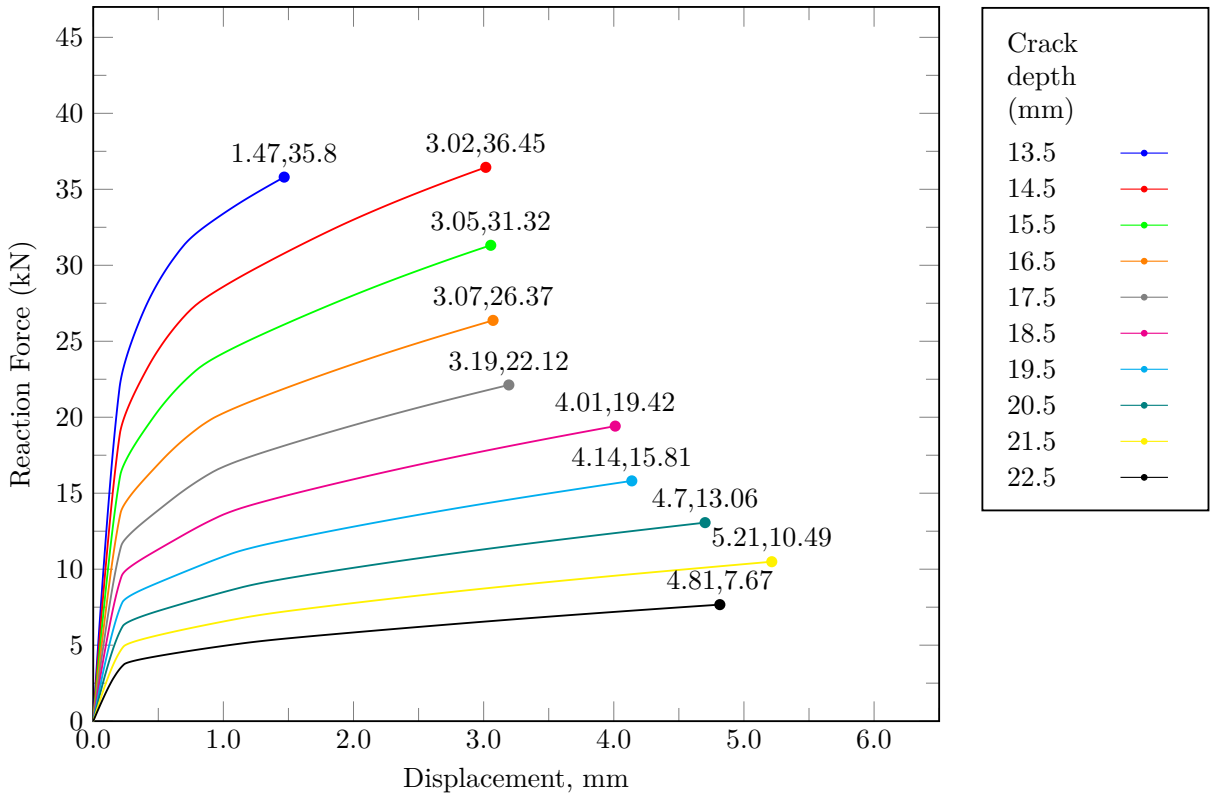

Figure 6.13: Maximum force and displacement for multiple crack depths at plastic collapse

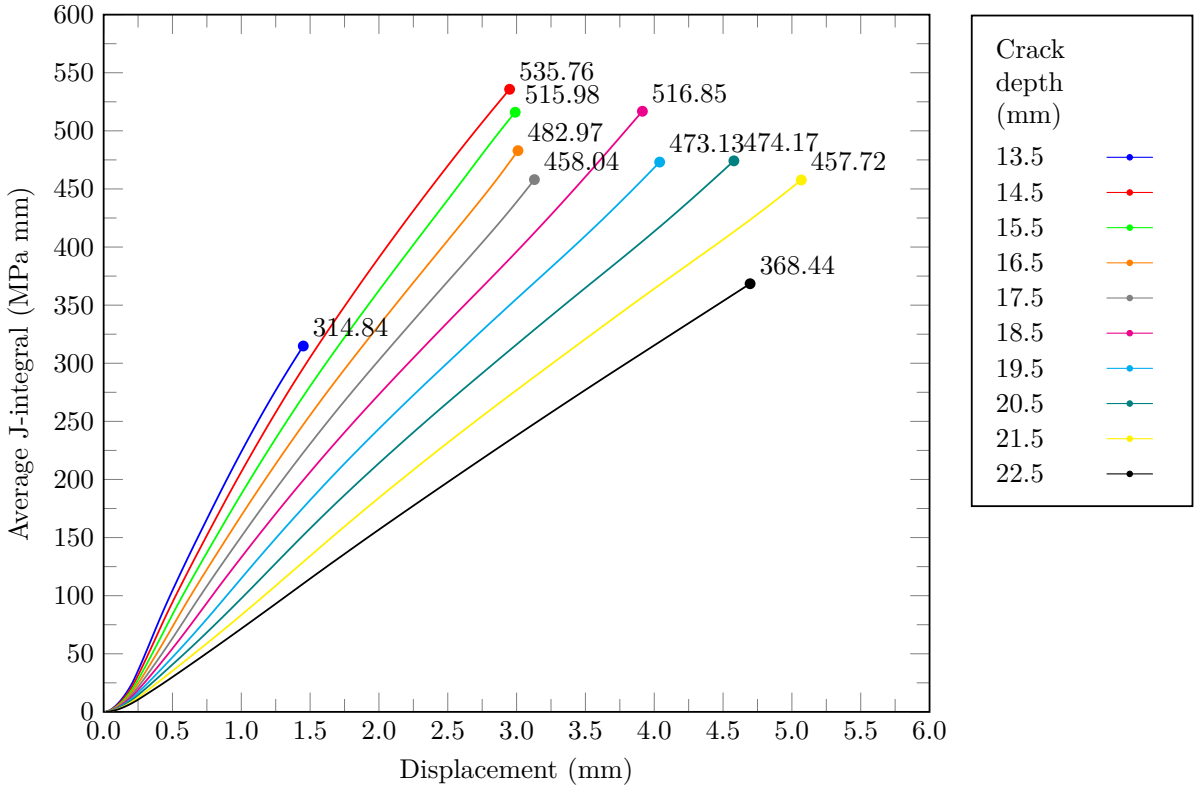

Figure 6.14: J-integral values at plastic collapse

for any given displacement value compared to the plane stress case. This accounts for the significant variation in strain when comparing Figures 6.15 and 6.16. Contour plots showing the direct stresses (σ_{yy}) are shown in Appendix C Figures C.10 and C.11.

The J-integral was estimated for each crack depth for both the plane strain and plane stress cases and can be seen in Figure 6.18. Contour integral calculations were carried out over 11 contours from the crack tip. The data presented are the average J-integral value over the total number of contours. Given the significant level of distortion in the crack tip region, the first contour was neglected from the averaging computation. As can be seen the plane strain analyses predict higher magnitudes of J-integral in comparison with the correlated plane stress analysis. This is as expected.

The strain along the remaining ligaments are shown in Figure 6.19. As shown, at a LLD displacement of 0.4 mm excessive strains are present in the region of the crack tip. The plane stress analysis predict larger magnitudes of strain at the crack tip, for comparable crack depths, compared to the plane strain cases, as expected. Appendix C Figure C.12 plots the stresses, rather than strains, in an equivalent format to that shown in Figure 6.19.

The direct strain (ϵ_{yy}) was along the materials boundary adjacent to the crack tip (i.e. the TIG weld boundary) was also investigated. Results are shown in Figures 6.20a and 6.20b for the plane strain and plane stress cases, respectively. At the weld boundary both ferrite and austenite material properties were assigned to nodes. By removing individual element sets, specific values for each individual material can be post-processed. In Figure 6.20 the results for austenite cladding material are shown with a solid line, those for the base (ferrite) are shown with a dashed line. For clarity the crack tip position is marked with a circle on each plot. Comparing Figures 6.20a and 6.20b shows that the plane stress analyses predicts much lower strains in comparison to the plane strain analyses, this is not unexpected given the variation in reaction forces noted earlier.

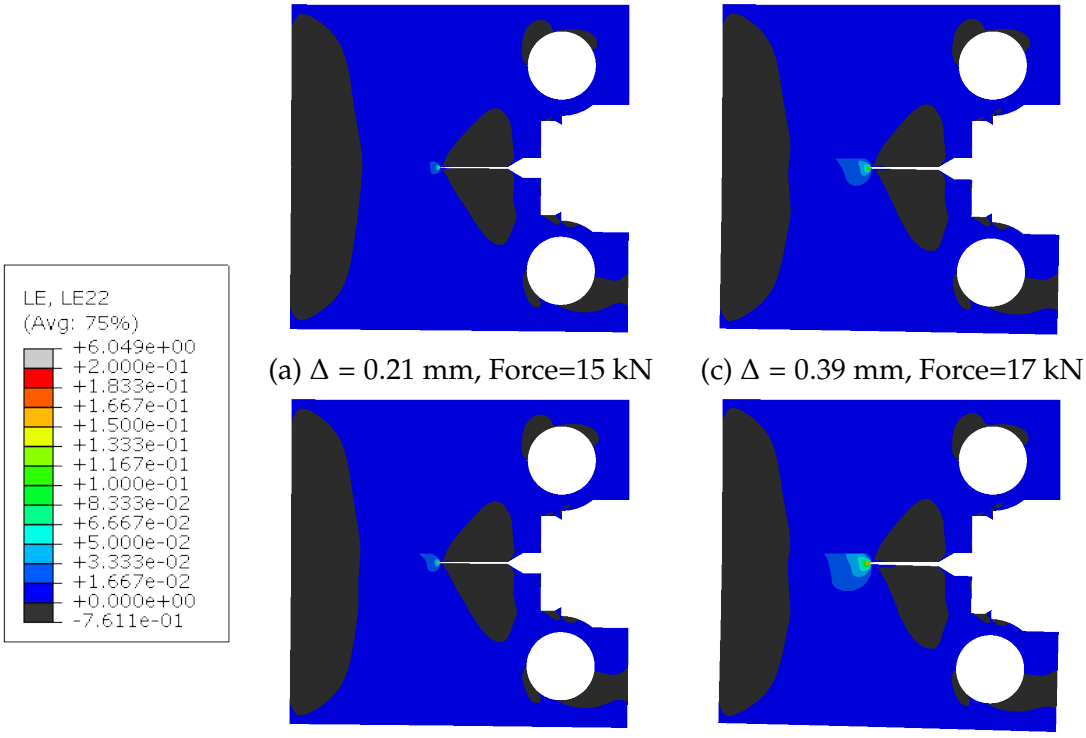

(a) Δ = 0.21 mm, Force=15 kN (c) Δ = 0.39 mm, Force=17 kN

(b) Δ = 0.25 mm, Force=16 kN (d) Δ = 0.59 mm, Force=19 kN

Figure 6.15: Plane stress analysis contour plots of direct strain (ϵ_{yy}) for multiple values of pin displacement (Δ)

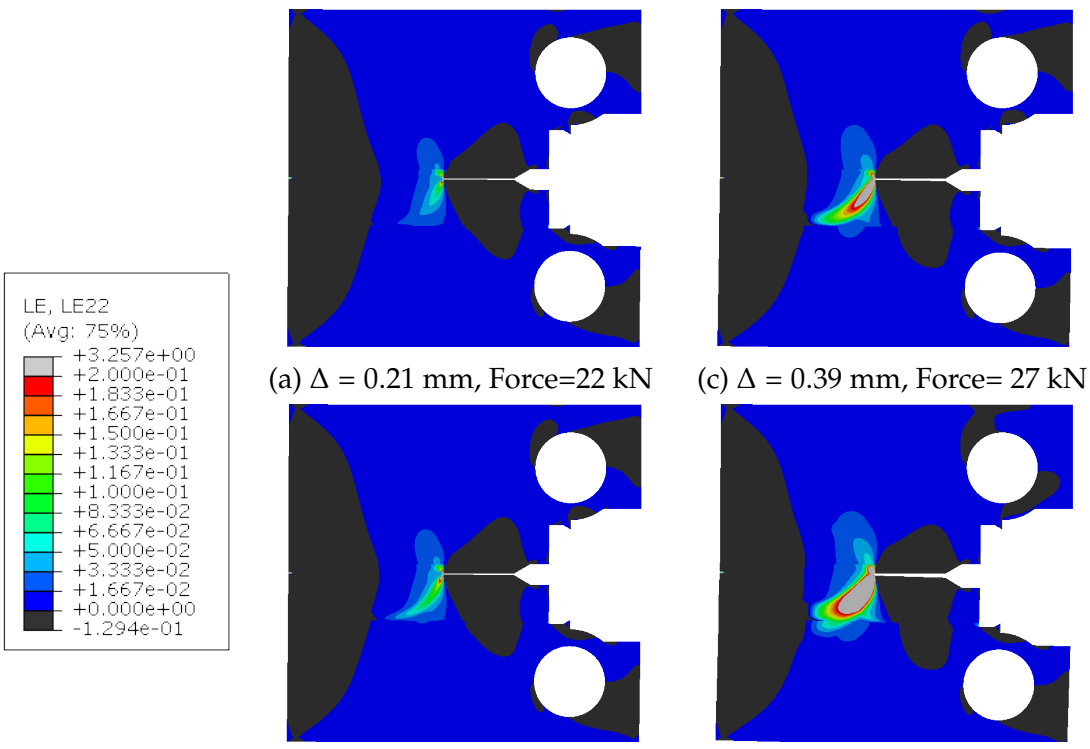

(a) Δ = 0.21 mm, Force=22 kN (c) Δ = 0.39 mm, Force= 27 kN

(b) Δ = 0.25 mm, Force=23 kN (d) Δ = 0.59 mm, Force= 30 kN

Figure 6.16: Plane strain analysis contour plots of direct strain (ϵ_{yy}) for multiple values of pin displacement (Δ)

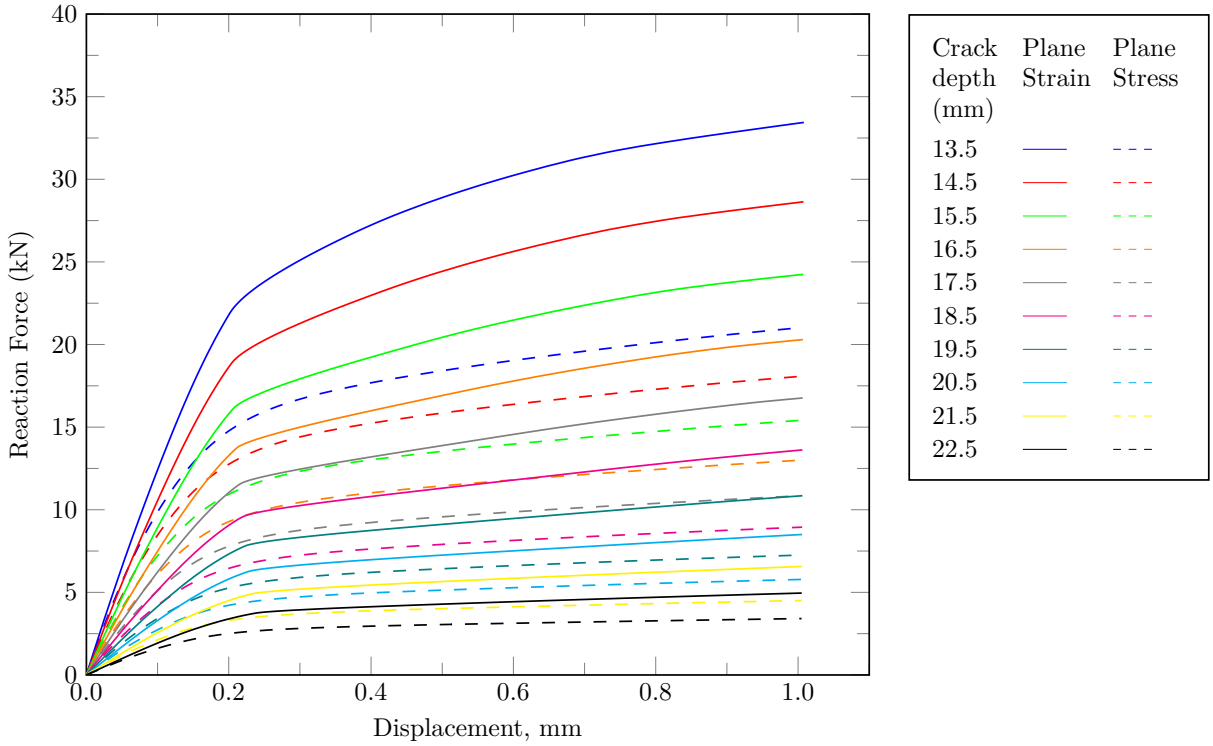

Figure 6.17: Reaction force versus load-line displacement (LLD) for multiple crack depths (a_0) for plane stress and plane strain analyses

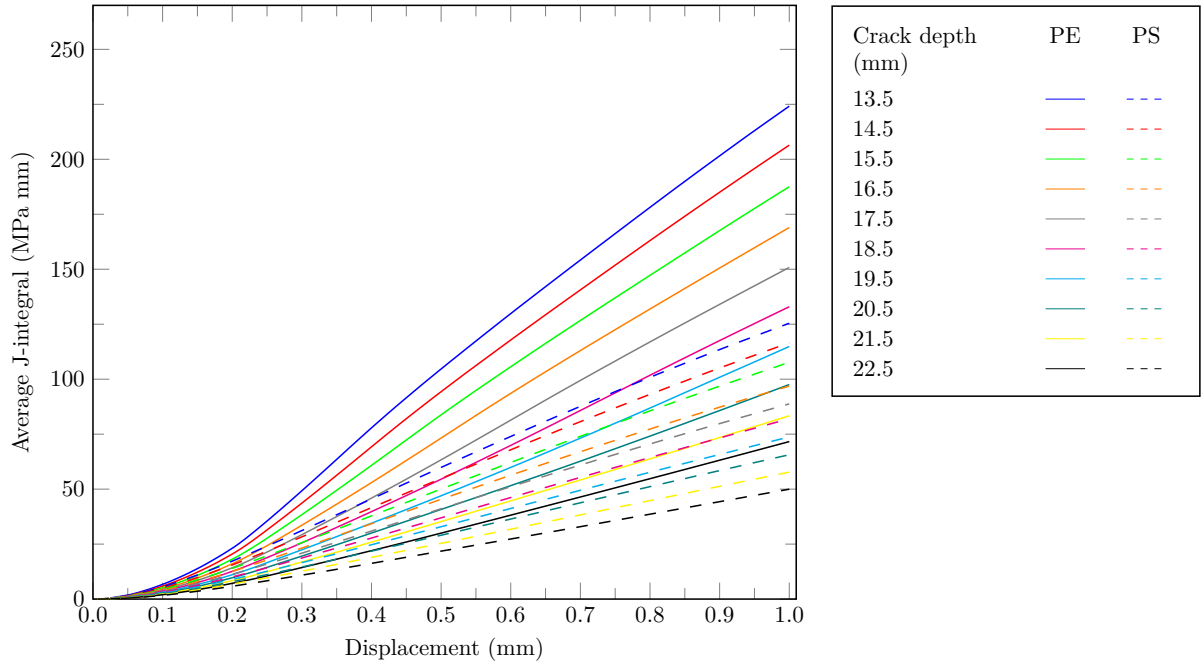

Figure 6.18: Average J-integral values for multiple crack depths (a_0) for plane stress and plane strain analyses

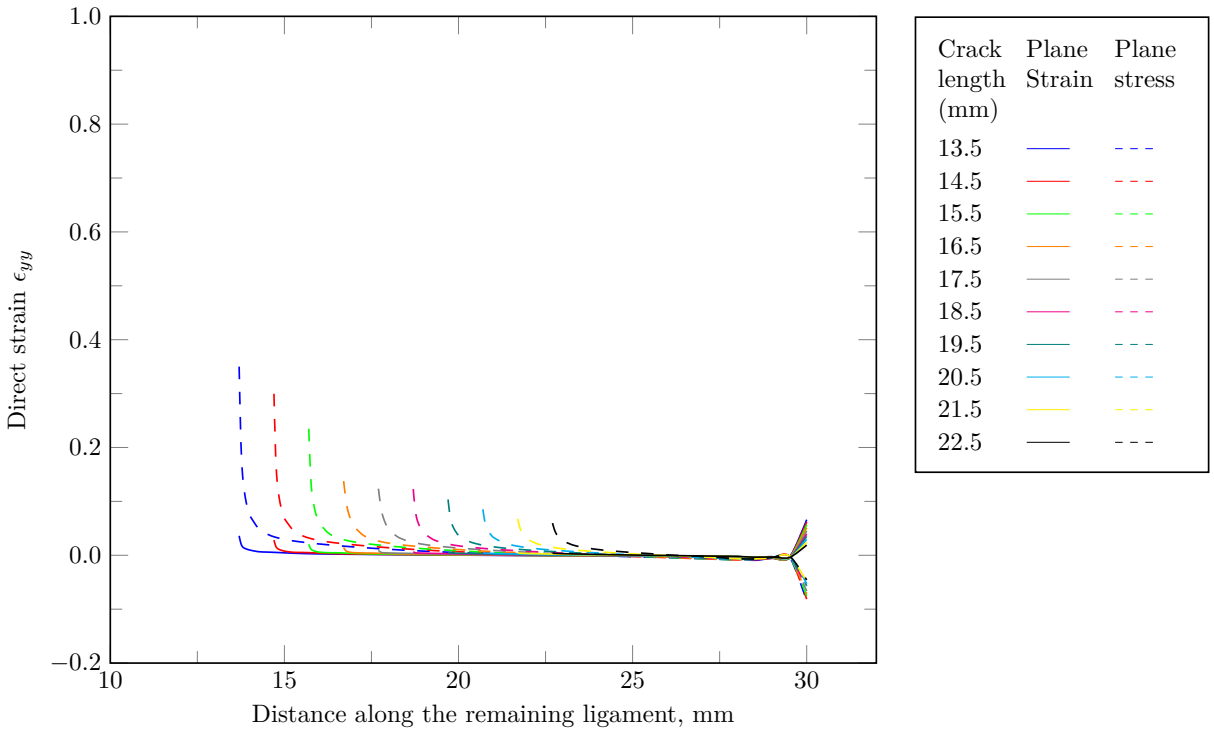

Figure 6.19: Direct strain (ϵ_{yy}) along the remaining ligament for multiple initial crack depths (a_0) for plane stress and plane strain analyses at a displacement (Δ = 0.4 mm)

Figure 6.20a plots the direct strain (ϵ_{yy}) along the materials interface for the plane strain case. For clarity the position of the crack tip along the materials interface region is circled on each plot. The peak magnitude of strain does not occur at the position of the crack tip but rather at a position approximately 1.0 to 1.5 mm beyond the crack tip. For each successive crack length (13.5 mm to 22.5 mm) the magnitude of peak strain reduces. This is a function of the applied loading parameter which was displacement based rather than force based. Longer cracks will have a smaller applied force and hence a smaller strain magnitude. A significant majority of the weld boundary is in excess of the yield strengths of both the austenite and ferrite materials at this displacement. The key point being that areas a significant distance ahead of the crack tip position are at magnitudes of strain that may initiate or propagate defects. In terms of plane stress Figure 6.20b shows dis-similar values of direct strain for both ferrite and austenite materials for all crack lengths. As noted previously the peak direct strain does not occur at the crack tip but at a position approximately 1 mm beyond. For an initial crack length of 13.5 mm material begins to yield at a position 0.5 mm ahead of the

crack tip (i.e. at position 14.0 mm) and the yield strain is reached and/or exceeded up to approximately 8.0 mm away from the crack tip. The ligament, over which yielding occurs, reduces for each subsequent crack length due to the displacement controlled nature of the model. Interestingly, in comparison to the plane strain analyses, under plane stress conditions failure is predicted for the austenite material only.

Given that Figure 6.20 is for only one value of displacement the question of how the strains evolve as displacement is increased remains unanswered. Figure 6.21 shows the evolution of strain from the initial point of yield up to a maximum displacement of $\Delta = 0.4$ mm for the plane strain analysis. Austenite material at the weld boundary reaches yield at a LLD of $\Delta = 0.06$ mm. The peak direct strain measurement occurs approximately 0.5 mm beyond the crack tip but the initial position at which yield is exceeded is somewhat lower than this value. The length of weld boundary, over which yielding occurs, increases with displacement. At small values of displacement a significant portion of the austenite interface region has yielded while yield has not yet been surpassed in the ferritic material. As the displacement increases strains begin to propagate into the ferritic material however, due to the shape of the curve, yielding is predicted to always occur first in the austenite and over a broader range of positions when compared to yielding in the ferrite. This trend is shown more clearly in Figure C.16b which shows the results of the plane stress analysis. As can be seen the ferrite and austenite have similar estimated strains for plotted values of LLD until relatively large values of displacement. At relatively small values of displacement (i.e. $\Delta < 0.1$ mm) little yielding has occurred in either the austenite or ferrite materials at positions along the materials interface. As the displacement increases the yield strains, which initially occur approximately 0.5 to 1.0 mm beyond the crack tip position and extend along the materials interface. This expansion occurs in terms of both magnitude and affected ligament. This is trend is depicted clearly in Figures 6.15b to 6.15d where is is shown that yielding occurs only in the austenite material region, extending along the remaining ligament.

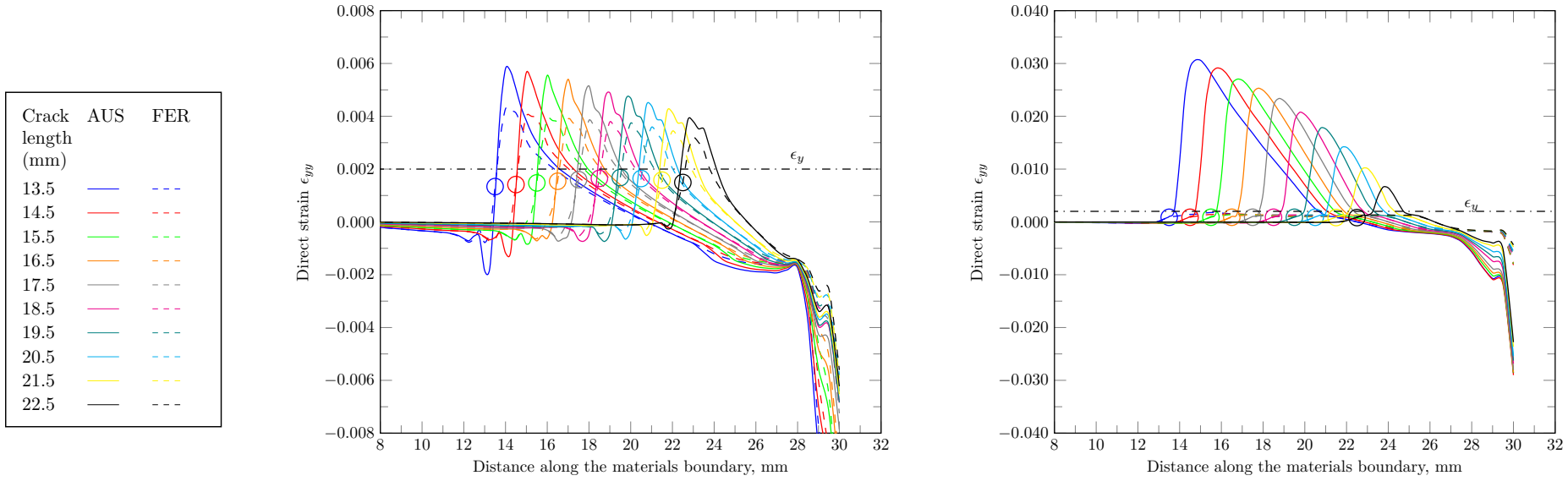

(a) Plane strain analysis

(b) Plane stress analysis

Figure 6.20: Direct strain (ϵ_{yy}) along the materials boundary for multiple initial crack depths (a_0) for 2D plane strain (Figure 6.20a) and plane stress (Figure 6.20b) analyses at a displacement (Δ = 0.4 mm). Cracktip positions marked with circle.

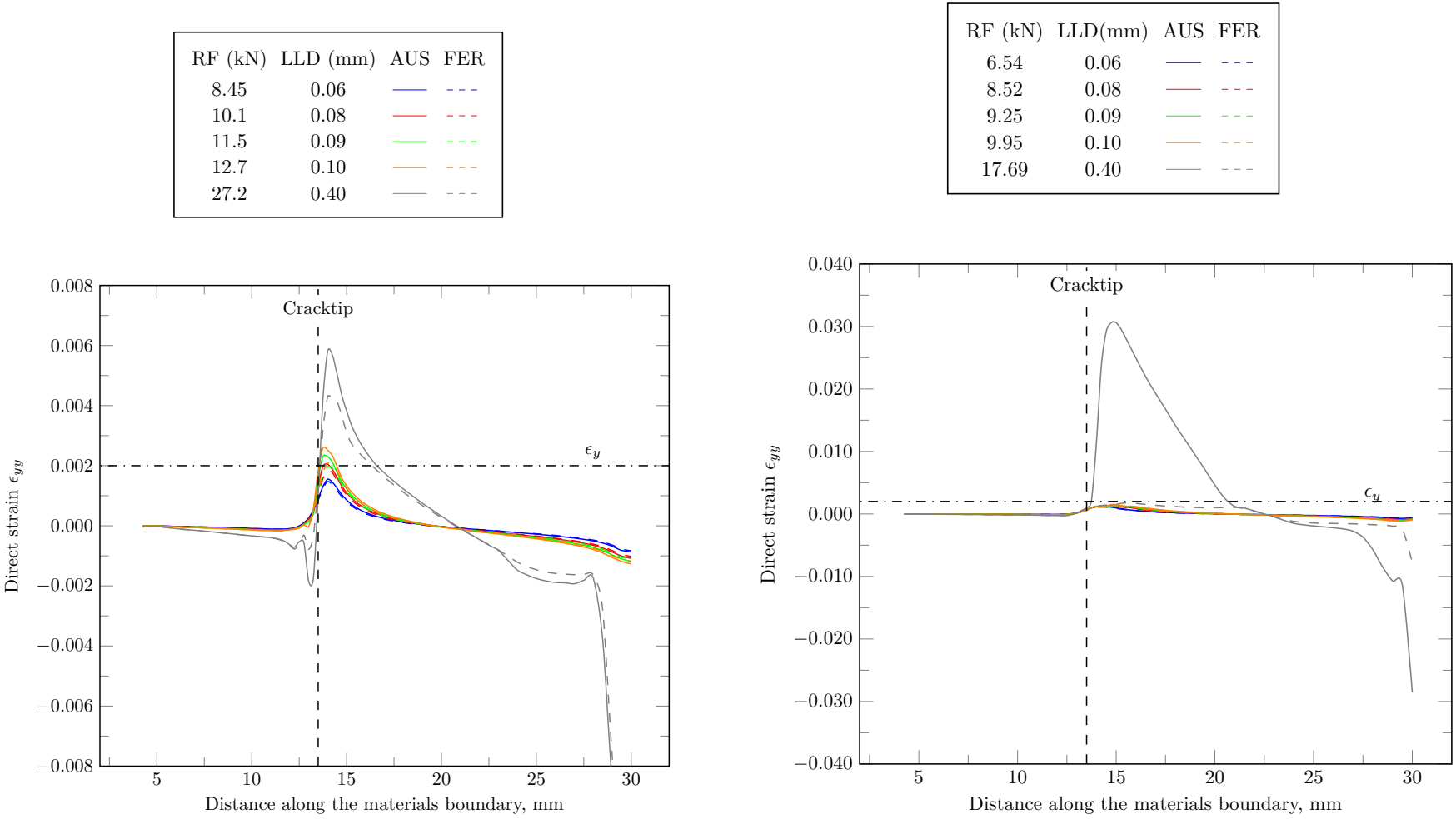

(a) Plane Strain

(b) Plane Stress

Figure 6.21: Direct strain (ϵ_{yy}) along the materials boundary when $\frac{a}{W} = 0.45$ for multiple load-line displacement values for plane strain (Figure 6.21a) and plane stress (Figure 6.21b) conditions.

6.2.1.1 Impact of varying the thickness of austenite region

While the previous section provides insight into the comparison of plane stress and plane strain conditions it is only relevant to one specific geometry, that is to say the austenite region is 6 mm thick and the notch is located 1 mm from the TIG weld boundary. As previous stated (Section 2.1) clad welds typically contain 3-10 mm of corrosion resistant material. The impact, on stress, of increasing and decreasing the width of the austenite section is not clear based on the previous section alone. The following section investigates two analyses: the first assumed the austenite section to have a width of 4 mm thickness, the second a width of 8 mm thickness. Other parameters remained identical to the analysis described in the previous section. The estimated force versus displacements for these cases are compared to the previous analyses in Figure 6.22. It is interesting to note that the reaction force for any given displacement greater than ≈ 0.2 mm differ depending on the amount of austenite present. This indicates that the overall sample material properties are influenced not only by the types of materials present but also the relative amount of each material. However, the analyses do show that changes are relative to the plastic section of the curve only, i.e. the elastic region is identical for varying austenite thickness for each condition. Furthermore there is a larger variation in result in the plane strain condition compared to the variation noted for the plane stress condition, though this is expected.

In Figure 6.23 the strains along the remaining ligament are compared for each the analyses. By comparing the plane strain analyses for the three models it can be seen that higher strains are predicted for thicker sections of austenite - at least in regions close to the crack tip. The stress distribution is shown in Figure 6.24 which shows that for the plane strain condition the model with austenite thickness of 4 mm has yielded up to 5.75 mm away from the crack tip while models with austenite thickness of 6 mm and 8 mm have yielded up to positions 5.25 mm and 5.0 mm respectively. The increased magnitude of stress, and the increased distance of affected ligament in the

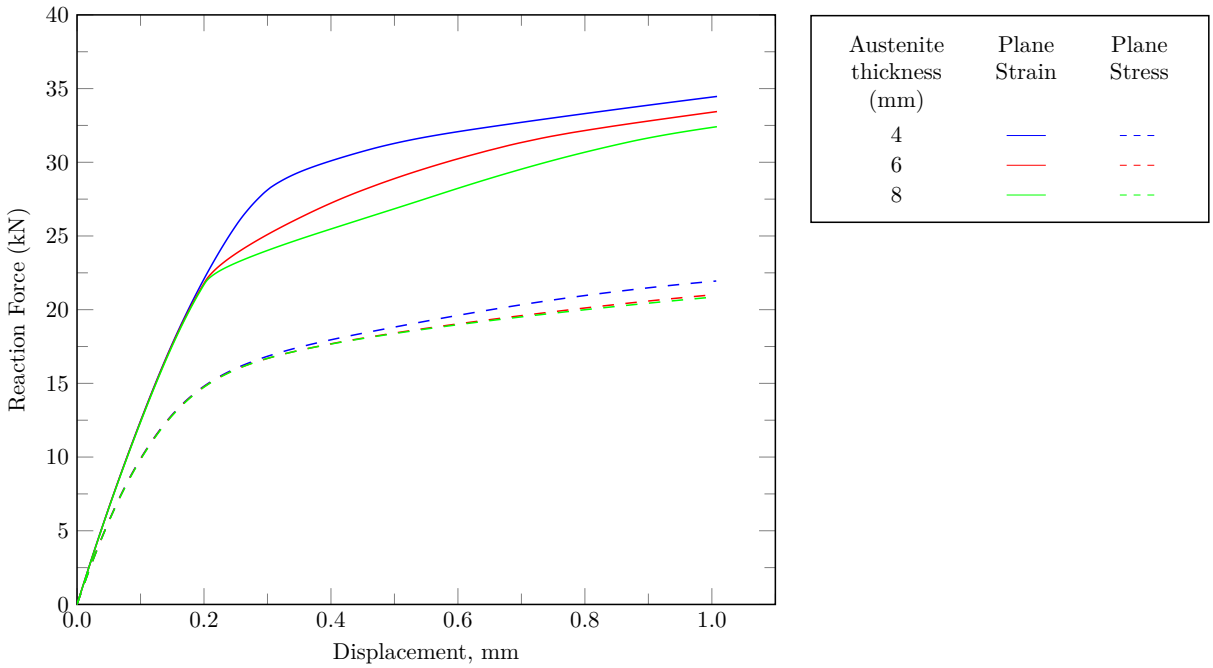

Figure 6.22: Reaction force versus load-line displacement (LLD) for crack depth ($a/W = 0.45$) for plane stress and plane strain analyses at each austenite thicknesses shown.

4 mm thick model indicates that thinner sections of austenite are less favourable under plane strain conditions. In the plane stress analyses all models predict similar distributions indicating that the thickness of the austenite region has no effect on the predicted stresses.

The direct strain along the materials interface for a displacement of 0.4 mm is compared for each condition for all three models in Figure 6.25. As shown in comparable cases (e.g. 4 mm thick austenite material, plane strain condition) the ferrite and austenite materials have similar strains. In regions where the strains are not identical there is a negligible difference between values in the ferrite and austenite materials at each position along the materials interface. In all cases, irrespective of the thickness of the austenite region, the plane stress condition is more onerous than the plane strain condition. The highest magnitude of peak strain appears to be dependent on the thickness of the austenite region with thinner sections (4 mm) resulting in higher peak stress compared to thicker (6 mm, 8 mm) sections. The length over which yielding is predicted to occur appears to be somewhat dependent on austenite thickness again,

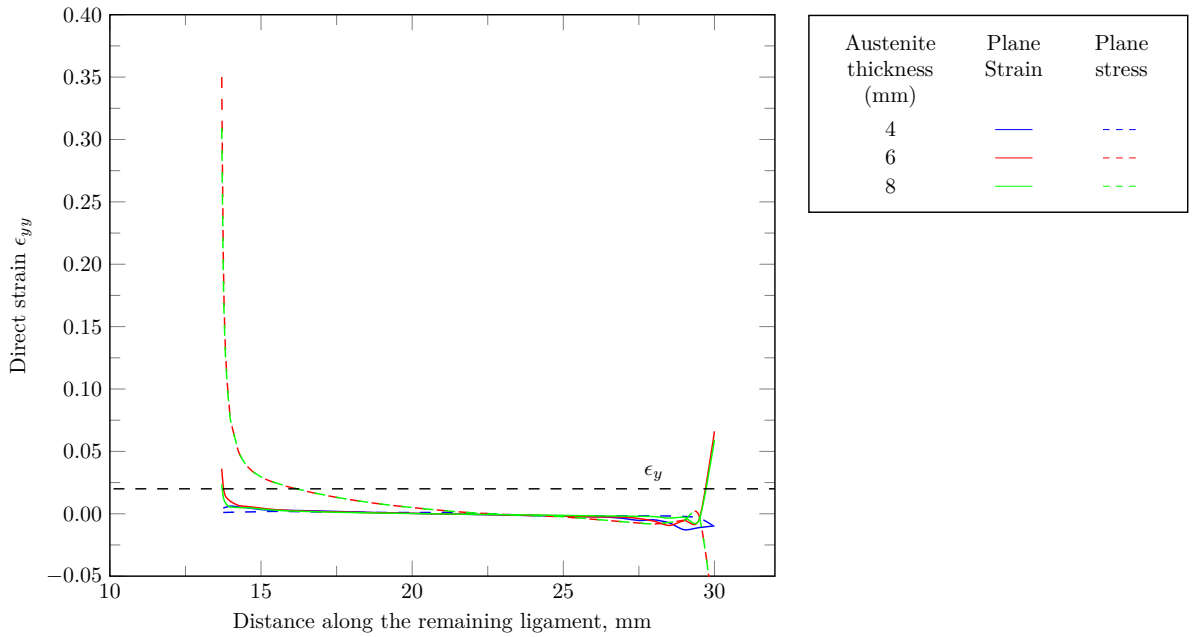

Figure 6.23: Comparison of direct strain ϵ_{yy} along the remaining ligament for plane strain and plane stress conditions varying the austenite thickness.

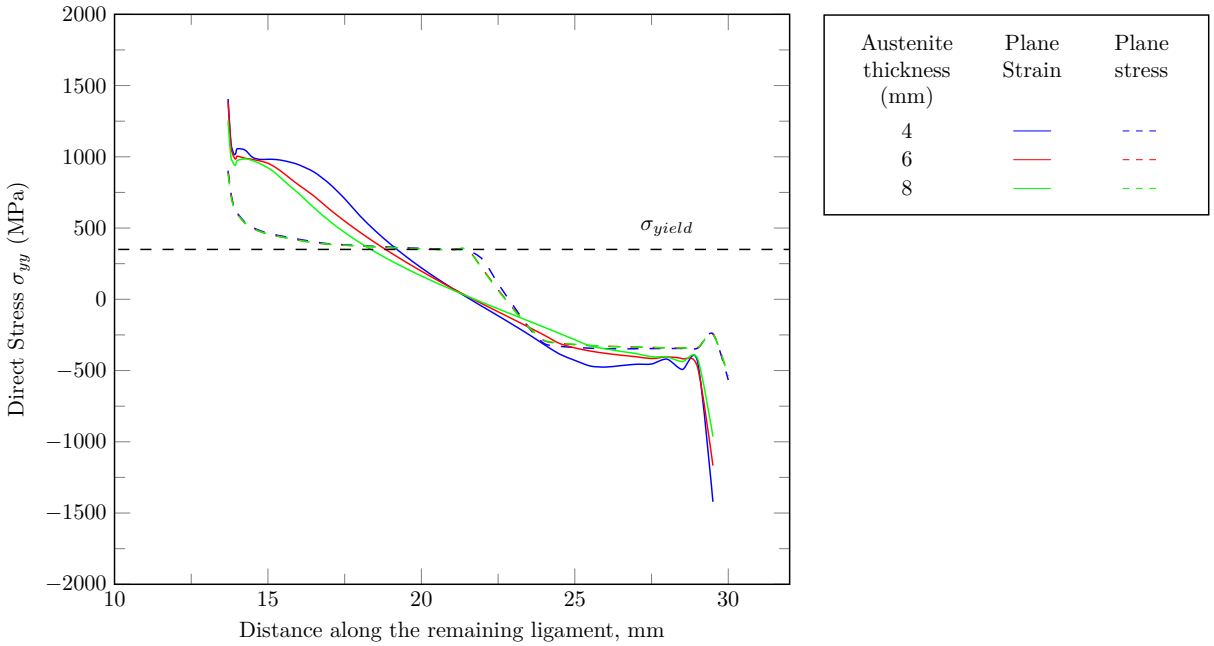

Figure 6.24: Comparison of σ_{yy} along the remaining ligament for plane strain and plane stress conditions varying the austenite thickness.

thinner sections are likely to yield over greater distances when compared to thicker sections. Results for the plane stress condition are comparable for all three thickness of austenite both in terms of peak stress magnitudes and in terms of the distance over which yielding occurs. This indicates that the plane stress condition is less sensitive to changes in the thickness of the austenite region in comparison to the plane strain condition. For details on direct stress effects see Appendix C Figure C.13.

Figure 6.26 compares the contour plots for each austenite thickness at an applied for of ≈ 20 kN, for the plane stress and plane strain conditions, respectively. Appendix C Figure C.17 plots the direct stresses. As shown in Figure 6.26 in the plane stress condition the 4 mm thick austenite region has yielded almost in totality, at an equivalent applied force significantly smaller regions of high strain exist in the 6 mm and 8 mm thick models. In the 6 mm and 8 mm models the peak strains are restricted to the cladding. In all models there are high strains predicted along the weld boundary. In the plane strain condition the 4 mm and 6 mm thick models predict bifurcation of strains at the crack tip towards both weld boundaries. In the 4 mm thick model strains have propagated through the weld boundary into the ferrite material on both sides. The distribution of strain is non-symmetrical indicating the presence of the weld boundary impacts the distribution of strain. The 6 mm model also shows some indication of bifurcation and bias in the region of the crack tip, while the 8 mm thick model shows little to no strain. The magnitude of strains in the 6 mm and 8 mm models are, similar to as noted for the plane stress condition, significantly lower than those in the 4 mm model.

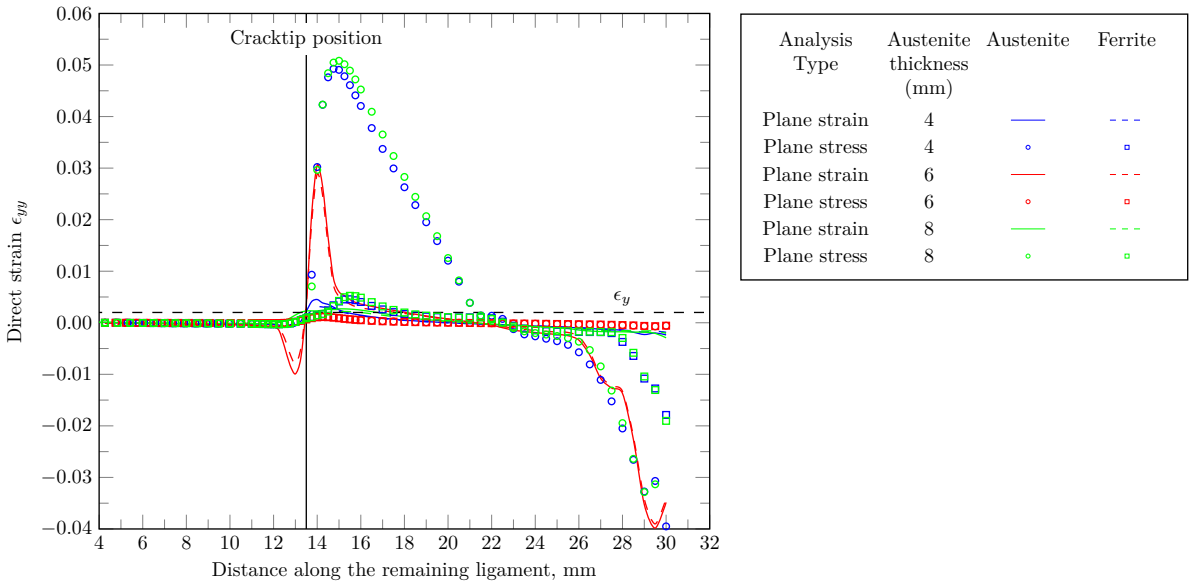

Figure 6.25: Comparison of direct strain ϵ_{yy} along the materials interface for plane strain and plane stress conditions varying austenite thickness. Displacement Δ = 0.4 mm.

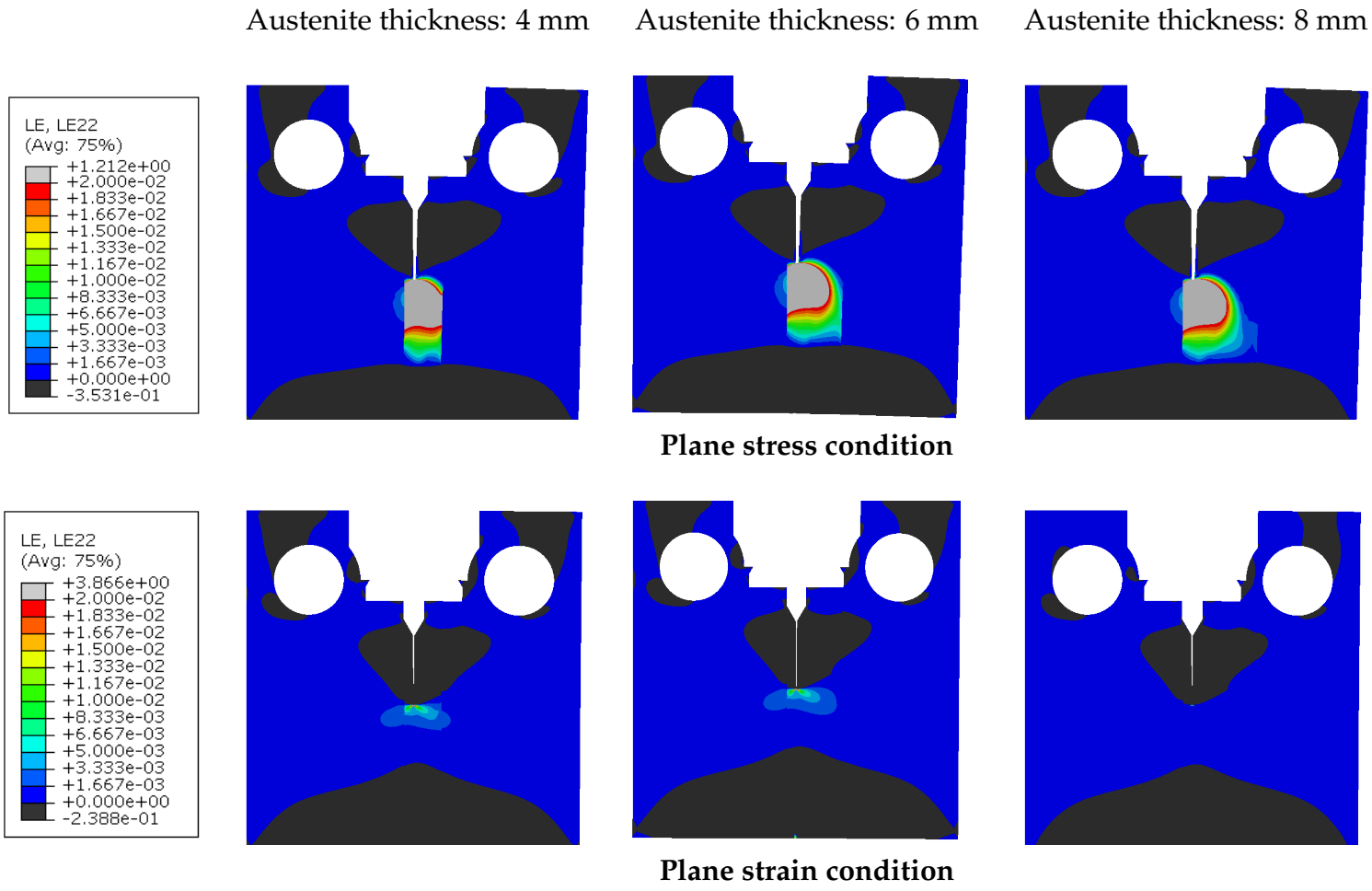

Figure 6.26: Contour plots for the plane stress and plane strain conditions varying the austenite thickness. Applied force = 20 kN.

6.2.1.2 Impact of varying the proximity of the notch to the materials interface

The FE models have idealised the materials interface as a perfectly flat boundary. In reality, due to the nature of the TIG welding process, the weld boundary undulates. Therefore, in test samples, as the crack grows the proximity of the notch tip to the materials interface can change. In this section the influence of proximity between the crack tip and the weld boundary is investigated. Figure 6.27 shows the three models. The first case is identical to that investigated in Section 6.2 with an austenite thickness of 6 mm and the crack tip located 1 mm away from the materials interface. The second and third models are similar to the first case however the crack tip is located 2 mm and 3 mm away from the materials boundary respectively. Therefore in the case of the third model the crack tip is in the central position surrounded by equal amounts of austenite on both sides (i.e the geometry is symmetric). For all three models the initial crack length (a_i) was assumed to be 13.5 mm. Boundary conditions, meshing strategy and materials properties remain identical to those discussed earlier (Section 6.2).

Figure 6.28 plots the estimated reaction force versus displacement for the plane stress and plane strain conditions, for each of the three models. As can be seen there is relatively little difference when comparing the results of the models for each condition. The largest disparity occurs when comparing the plane strain condition where Model 1 shows a slightly different shape in comparison to Models 2 and 3. This disparity results in changes of reaction force of less than 3 kN and is considered to have a negligible effect on the resulting stresses. The J-integral was estimated for each of the three models and results are shown in Figure 6.29. The plot (Figure 6.29) also includes the results for multiple values of clad thickness as discussed in the previous section. The results predict that when the cladding thickness is increased the J-integral decreases slightly. For a thickness of 4 mm, 6 mm and 8 mm (of the cladding) the J-integral was estimated to be approximately 240 MPa mm (7.6 MPa m), 225 MPa mm (7.1 MPa m), and 210 MPa mm (6.6 MPa m), respectively. While there is a clear trend of reducing fracture toughness

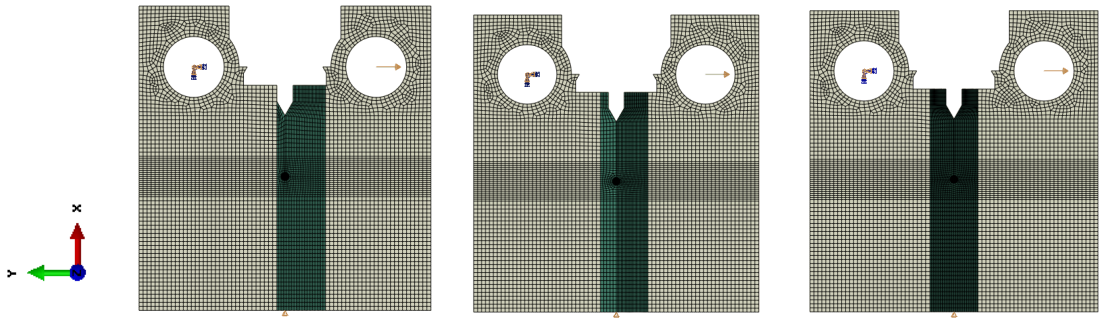

(a) Model 1 (b) Model 2 (c) Model 3

Figure 6.27: Varying the proximity of the notch to the materials interface with Figure 6.27a: 1 mm from materials interface, Figure 6.27b: 2 mm from the materials interface, Figure 6.27c 3 mm from the materials interface (i.e. in the centre of the austenite material). Austenite material properties shown in green, ferrite material properties in cream.

at a displacement of 1 mm it should be noted that at this stage of the analysis the crack tip has significantly deformed. The Abaqus manual [Dassault Systemes Simulia Corp, 2014] states that J-integral values should remain 'reasonably accurate' for this type of analysis but as shown in Figure 6.30 limiting data to the small-scale yielding zone does not predict a similar trend to that noted in Figure 6.29. In the small-scale yielding zone the J-integral estimated is similar for the three values of thickness investigated.

In terms of the notch and it's proximity to the weld boundary, at 1 mm of displacement the analysis predicts that a notch located 2 mm from the materials boundary will have a higher value of J-integral compared to notches located 1 mm or 3 mm distance. In the small-scale yielding region however the magnitude of J-integral is higher for lower values of proximity (i.e. when the notch is closer to the materials boundary the J-integral is of higher magnitude). It is clear from the above results that the J-integral values must be assessed with caution when large deformations are present in the model. It may be possible to achieve a more accurate approximation of J-integral by disregarding contours immediately adjacent to the crack tip however, given the presence of the materials boundary and the proximity of the notch to the interface between materials it is difficult to achieve a reasonable number of contours without impacting the path dependency.

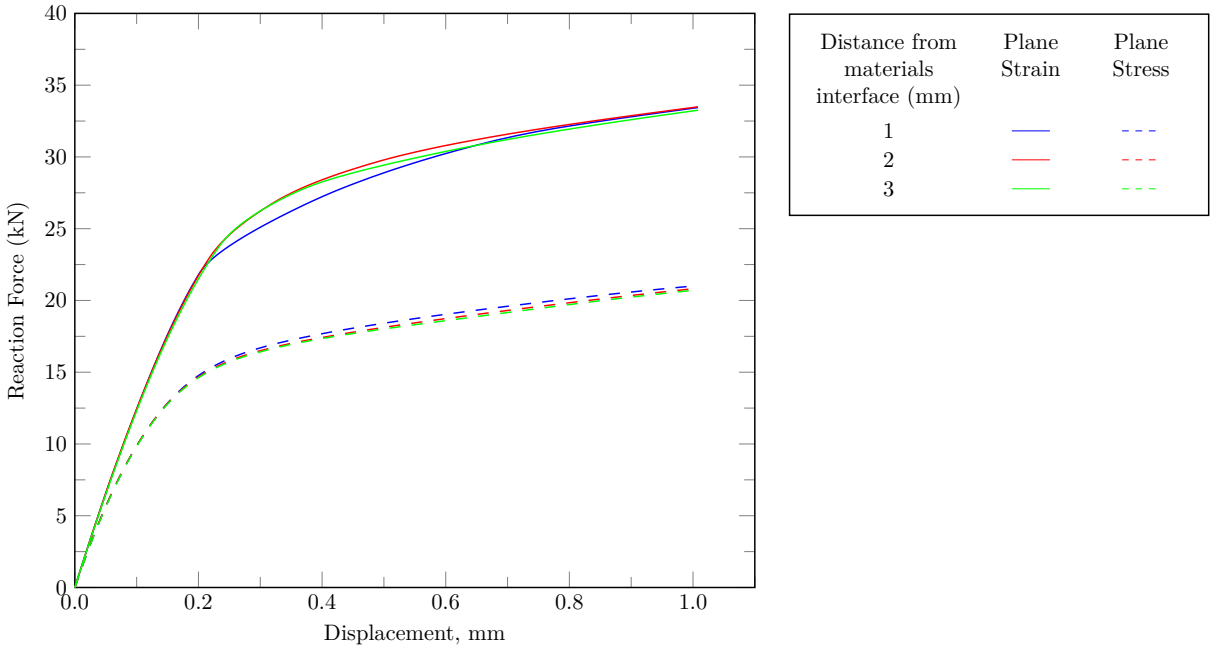

Figure 6.28: Reaction force versus load-line displacement (LLD) for crack depth ($\frac{a}{W}$ = 0.45) for plane stress and plane strain analyses varying the proximity of the notch to the materials interface.

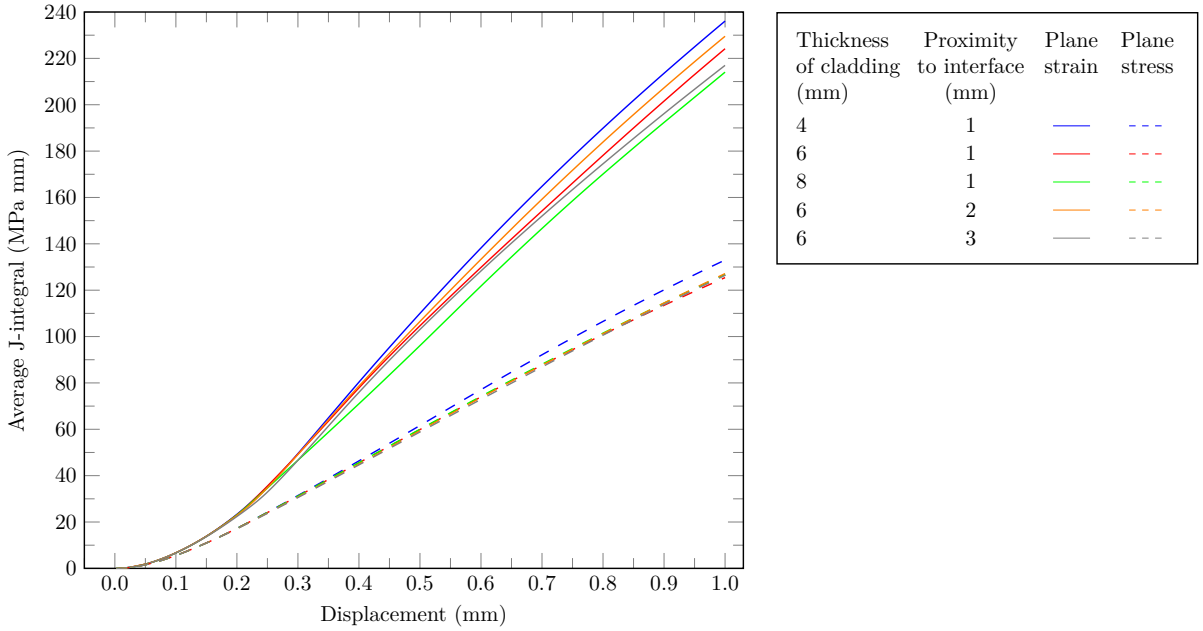

Figure 6.29: Average J-integral estimation for crack depth (a/W = 0.45) for plane stress and plane strain analyses, varying both the thickness of the austenite region and the proximity of the notch to the materials interface.

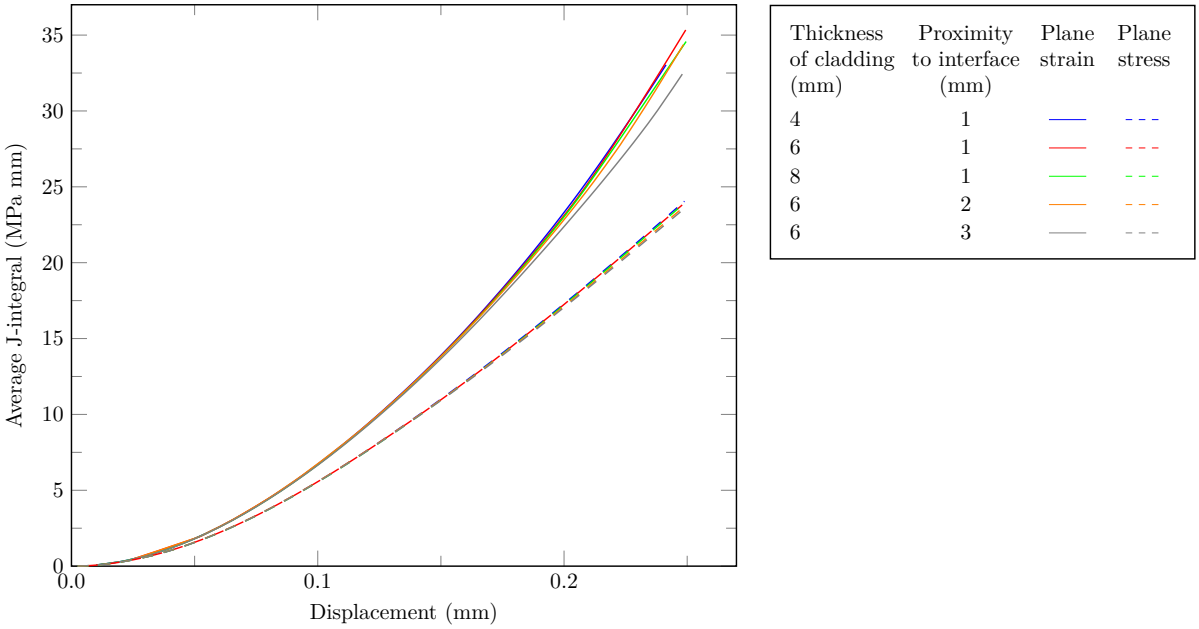

Figure 6.30: Average J-integral estimation for crack depth ($a/W = 0.45$) for plane stress and plane strain analyses, varying both the thickness of the austenite region and the proximity of the notch to the materials interface. Results limited to small-scale yielding zone.

The direct strain (ϵ_{yy}) along the remaining ligament for a displacement of 0.40 mm is shown in Figure 6.31 (direct stresses can be seen in Appendix C Figure C.18). As can be seen the results for the plane stress condition are identical for the three cases investigated. Some differences can be seen for the plane strain condition but overall there is a good agreement for the models. This indicates that stresses along the remaining ligament are not influenced by position of the crack tip with respect to the weld boundary. This is not unexpected.

The direct strain at the weld boundary at a displacement of 0.40 mm for each of the models is shown in Figure 6.32. As shown for both the plane stress and plane strain condition the direct strain is of the greatest magnitude in the austenite material under plane stress conditions. Figure 6.33 plots the same data for direct stress. As show in Figure 6.33 the proximity of the notch to the interface has a significant effect on the results. The closer the proximity the higher the stresses are the interface, this is likely due to the stress concentrating feature of the notch. In the case where the notch is located centrally with respect to the austenite material (i.e, symmetrical) the stresses

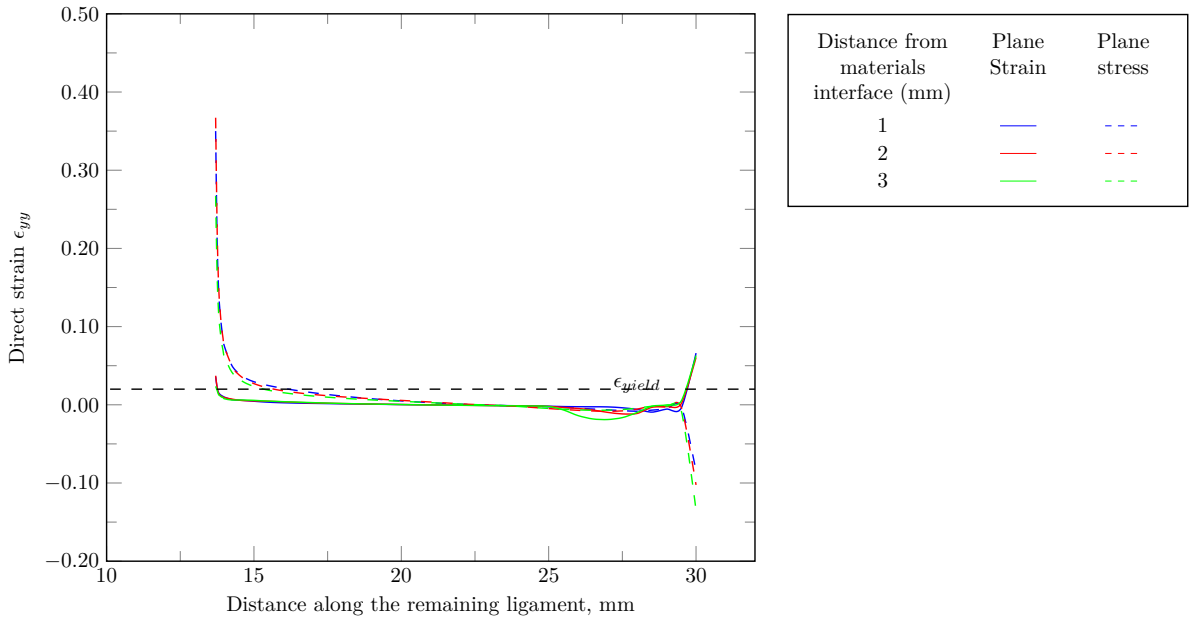

Figure 6.31: Comparison of direct strain ϵ_{yy} along the remaining ligament for plane strain and plane stress conditions varying the proximity of the notch to the materials interface (Δ = 0.4 mm).

in the austenite and ferrite materials at the boundary are identical. In cases were the notch is offset from centre, minor deviations in stress are predicted.

Appendix C Figure C.19 shows the contour plots for a displacement of Δ = 0.4 mm for the plane stress an plane strain conditions. Figure 6.34 plots the contours for a fixed load of $\approx$ 20 kN. Figure 6.34 clearly shows that Model 3 is perfectly symmetrical around the crack tip. This is not unsurprising given the crack tip is located in the centre of the austenite material. By comparing the results of Model 3 with those from Model 2 and Model 1 the influence of proximity to the materials interface can be seen. Model 1 is clearly asymmetrical with high stresses appearing to be biased towards the materials interface. Model 2 is also asymmetrical but to a lesser extend that Model 1. This indicates that stress concentrating features in close proximity to the materials boundary increase the likelihood of failure at the boundary.

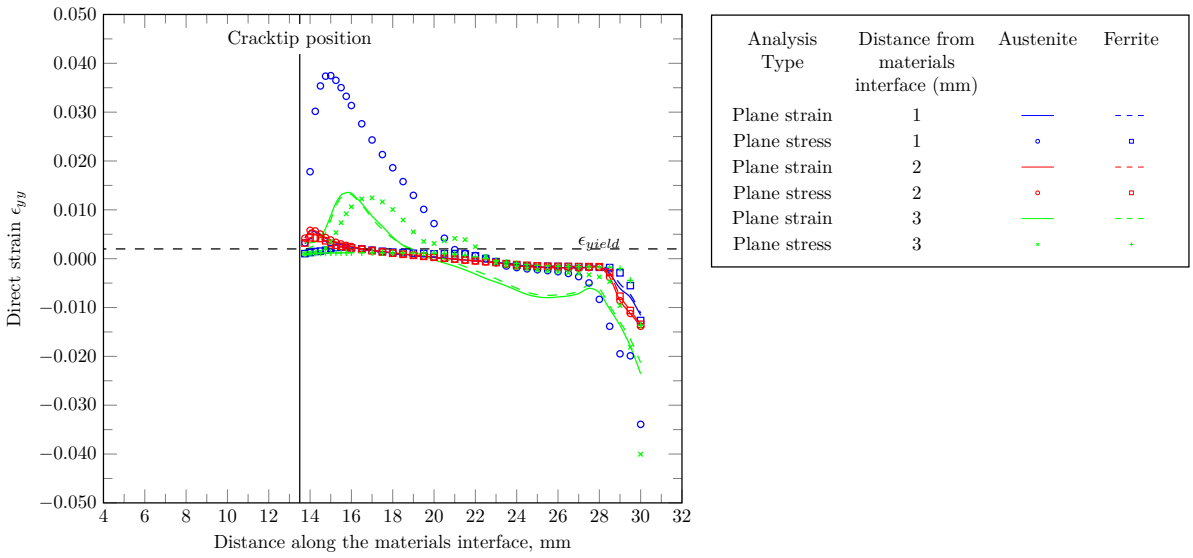

Figure 6.32: Comparison of direct strain ϵ_{yy} along the materials interface for plane strain and plane stress conditions varying the proximity of the notch to the materials interface Δ = 0.4 mm.

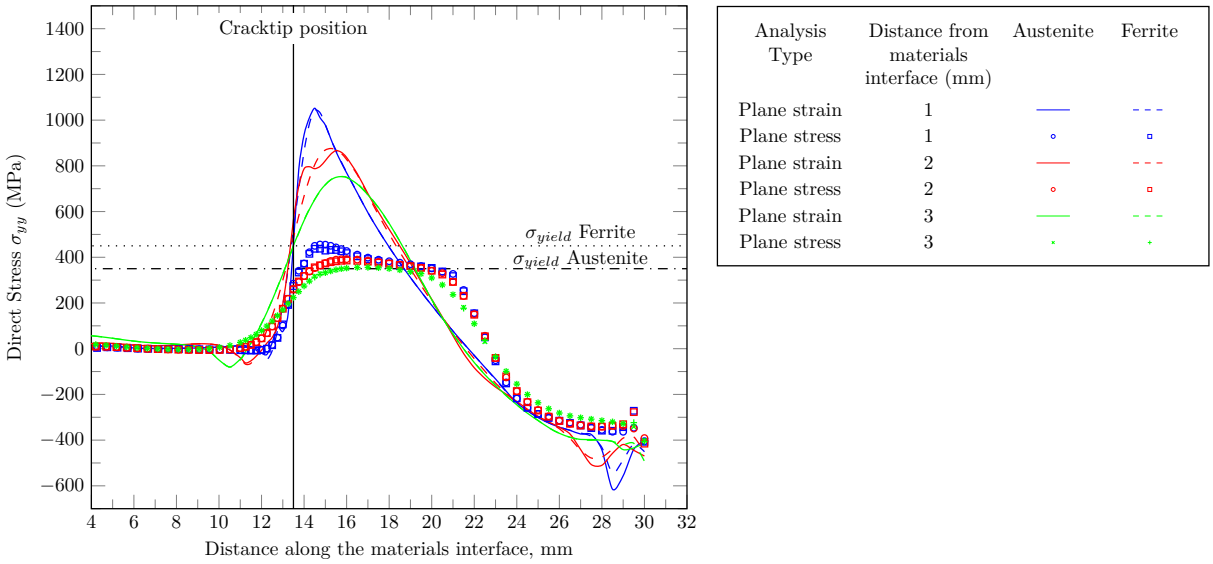

Figure 6.33: Comparison of direct stress σ_{yy} along the materials interface for plane strain and plane stress conditions varying the proximity of the notch to the materials interface Δ = 0.4 mm.

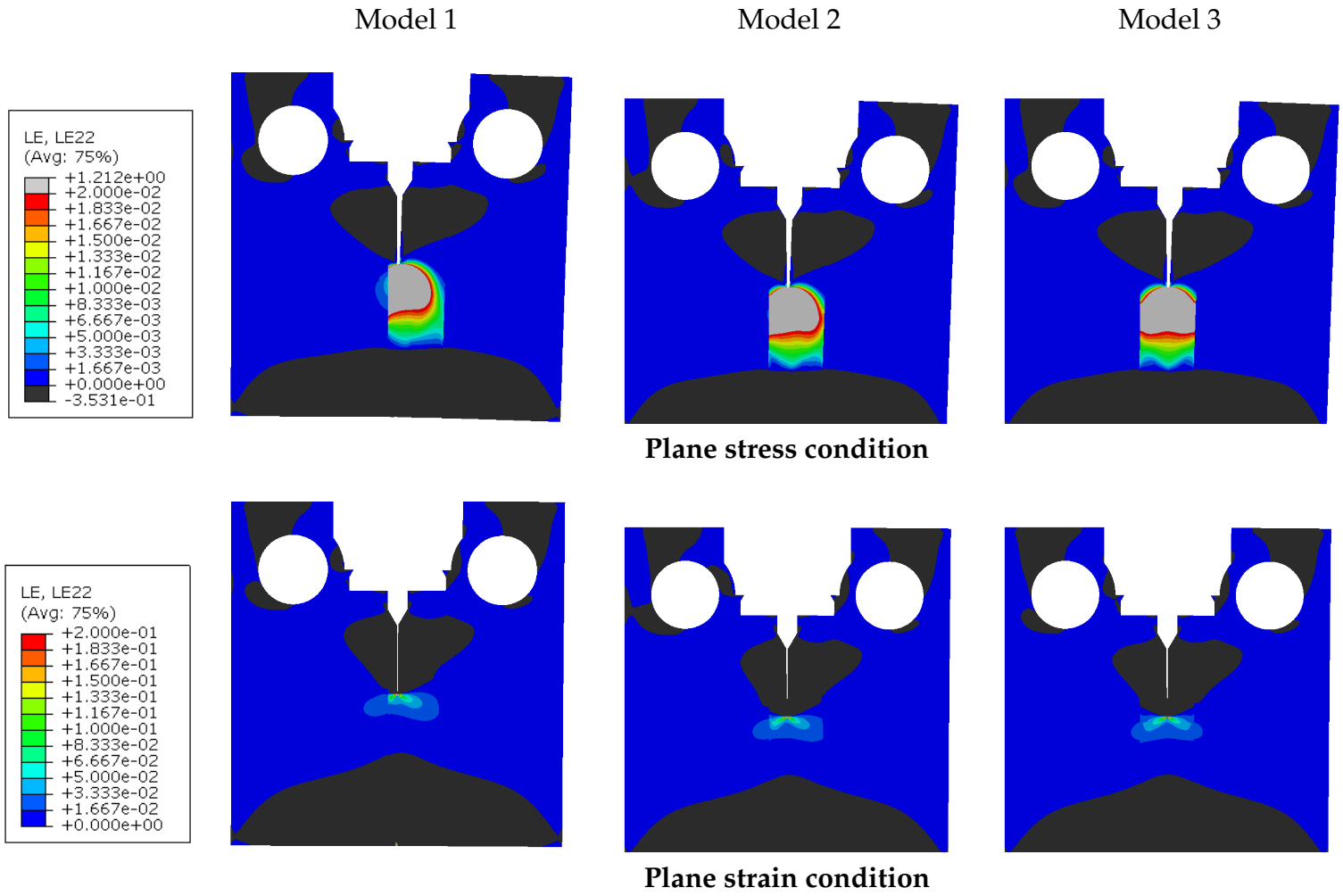

Figure 6.34: Contour plots for the plane stress and plane strain conditions varying the proximity of the notch to the materials interface. Applied force = 20 kN

6.2.2 Inverting material properties

Similar to the previous section (Section 6.2.1) plane stress and plane strain models were conducted for CT specimens assuming the material sections were inverted. The geometry, boundary conditions and meshing strategy was identical to that outlined previously. In this case the majority of the specimen was assumed to be comprised of austenite material with a 6 mm thick section of ferrite material containing a defect 1 mm from the TIG weld boundary. Again multiple crack depths (a/W) were assessed and the change in stresses along both the remaining ligament and materials boundary investigated.

Figure 6.36 shows the contour plots of direct strain (ϵ_{yy}) for various values of pin displacement (Δ) for a crack depth of 13.5 mm ($a/W = 0.45$). As shown the plane stress analysis predicts a high strains outside the region of the crack tip in the austenite material. This trend is significantly different to what was noted when the notch was located in the austenite material (see Figure 6.15b). The plane strain analysis (Figure 6.37), also shows strains in the region of the materials interface, though these are significantly lower, in terms of affected area, for comparable levels of displacement, compared to the plane stress analyses. Contour plots of direct stresses (σ_{yy}) are shown in Appendix C Figures C.20 and C.21. Figure 6.38 plots the reaction force against load-line displacement (LLD) for multiple initial crack depths (a_0) for both plane stress and plane strain analyses. Comparing Figure 6.38 with Figure 6.17 shows that the predicted force versus displacement curves for the models are identical for the plane strain assumption. A moderate increase in reaction force was found for the plane stress assumption. As shown in Figure 6.38 the plane strain analyses predict higher values of reaction force for any given displacement value compared to the plane stress case.

Figure 6.39 shows the restricted direct strain (ϵ_{yy}), a plot of direct stress is shown in Appendix C Figure C.22. As shown in Figure 6.39 at a notch depth of 16.5 mm the plane stress case is significantly higher than other analyses. Figure 6.40 plots the strain in the remaining ligament for two cases: 1 - notched in austenite as per Section 6.2.1,

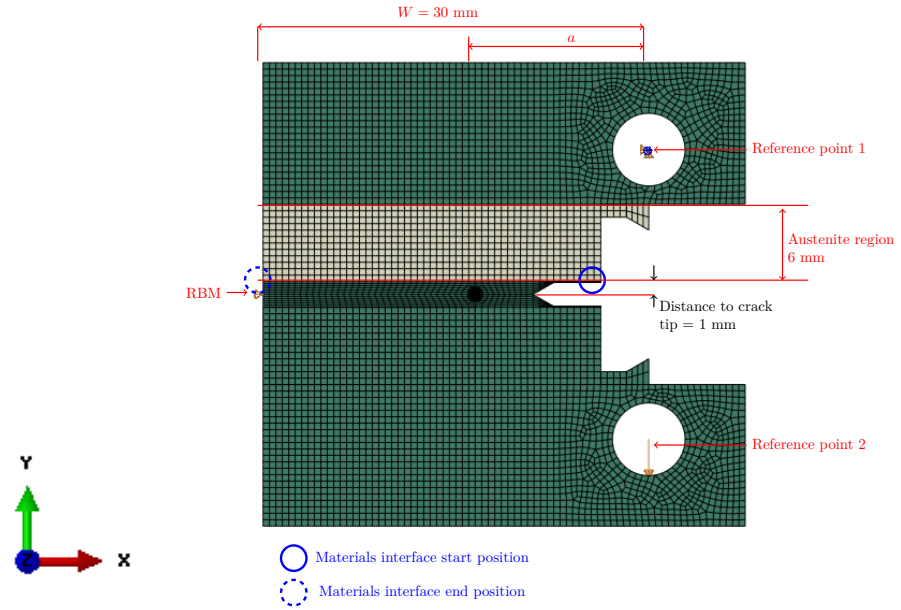

Figure 6.35: Boundary condition and meshing applied to 2D models. Austenite material properties assigned to the gray region, ferrite material properties assigned to the green regions.

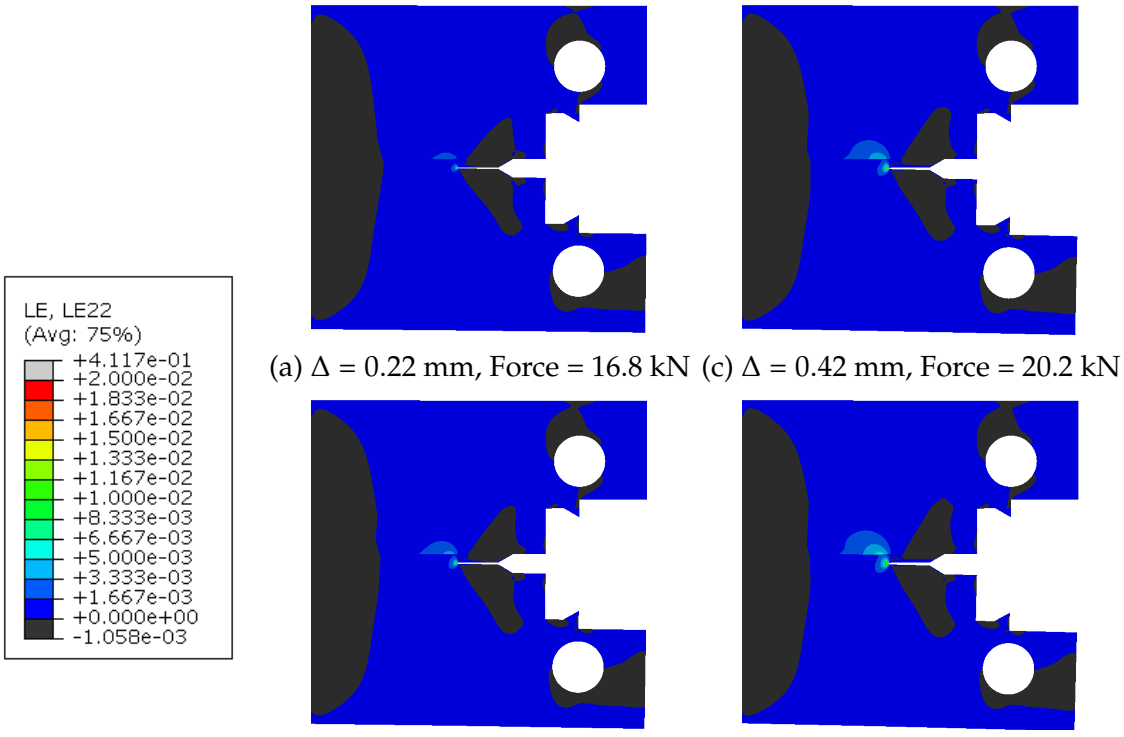

(a) Δ = 0.22 mm, Force = 16.8 kN (c) Δ = 0.42 mm, Force = 20.2 kN

(b) Δ = 0.32 mm, Force = 18.5 kN (d) Δ = 0.52 mm, Force = 17 kN

Figure 6.36: Plane stress analysis contour plots of direct strain (ϵ_{yy}) for multiple values of pin displacement (Δ). Notch region consisting of ferrite material properties.

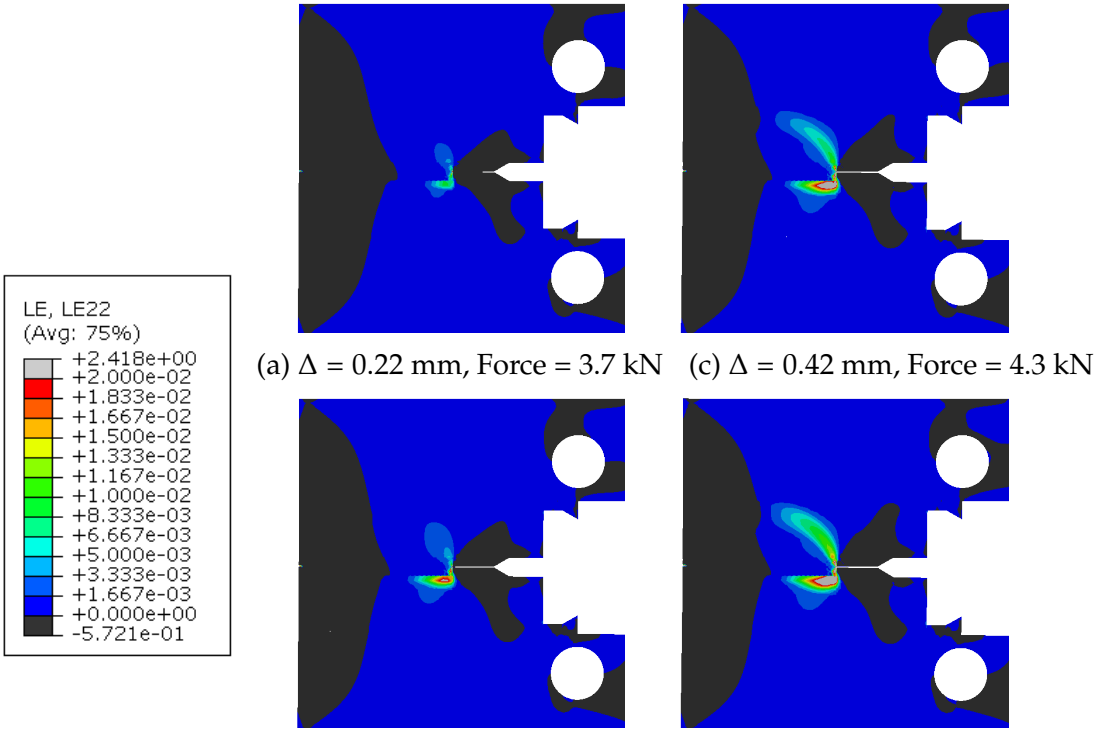

(a) Δ = 0.22 mm, Force = 3.7 kN (c) Δ = 0.42 mm, Force = 4.3 kN

(b) Δ = 0.32 mm, Force = 4.2 kN (d) Δ = 0.52 mm, Force = 4.5 kN

Figure 6.37: Plane strain analysis contour plots of direct strain (ϵ_{yy}) for multiple values of pin displacement (Δ) Notch region consisting of ferrite material properties.

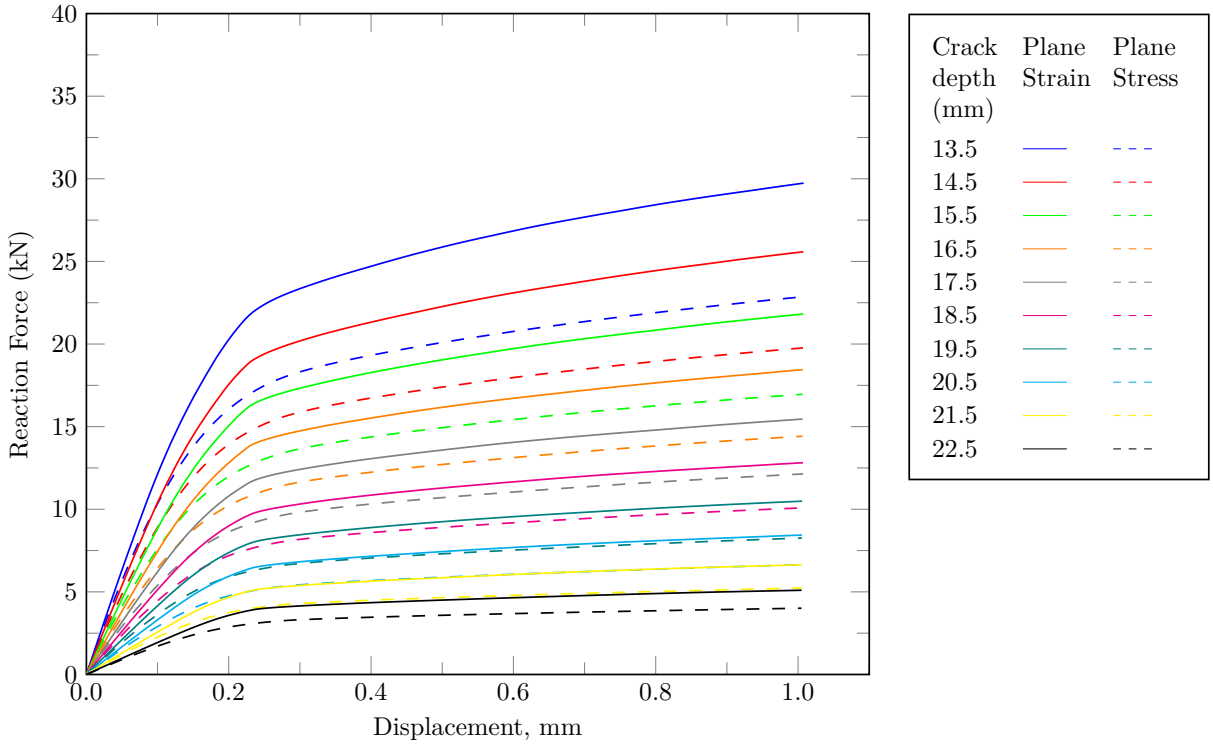

Figure 6.38: Reaction force versus load-line displacement (LLD) for multiple crack depths (a_0) for plane stress and plane strain analyses

and 2 - notched in ferrite. The crack length for both cases is 13.5 mm. As can be seen (Figure 6.40) the plane strain analyses predict similar trends and magnitudes of stress irrespective of the notch location. The plane stress analyses are not similar with the notch in austenite showing significantly higher values of strain in the crack tip region compared to a notch located in the ferrite region. This is not unexpected given that Young's modulus will the geometry is likely to be significantly different compared to the previously investigated geometry.

The direct strain (ϵ_{yy}) along the materials boundary adjacent to the crack tip was also investigated. Results are shown in Figures 6.41a and 6.41b for the plane strain and plane stress cases, respectively. At the materials interface both ferrite and austenite material properties were assigned to nodes. By removing individual element sets, specific values, pertaining to one material, can be post-processed. Figure 6.41 the results for austenite material are shown with a solid line, those for ferrite are shown with a dashed line. For clarity the crack tip position is marked on each plot. Comparing Figures 6.41a and 6.41b it can be seen that yielding is likely to occur in both materials in the mid-thickness region and is more likely to occur in the austenite material on the surface of the sample. Plots for direct stress are provided in Appendix C Figures C.25a and C.25b.

In the plane strain condition (Figure 6.41a). The peak magnitude of strain does not occur at the position of the crack tip but rather at a position approximately 1.0 to 1.5 mm beyond the crack tip. For each successive crack length (13.5 mm to 22.5 mm) the magnitude of peak strain reduces, this is due to the displacement controlled nature of the model. A small section of the weld boundary is in excess of the yield strain for shorter crack lengths ($a \leq 17.5$ mm). These trends were also noted for specimens notched in austenite region (Section 6.2.1, Figure 6.20). In terms of the plane stress condition Figure 6.41b shows dis-similar values of direct strain for the ferrite and austenite materials. For all crack lengths yielding is predicted to occur in the austenite material at positions about 0.5 mm beyond the crack tip extending a significant distance along

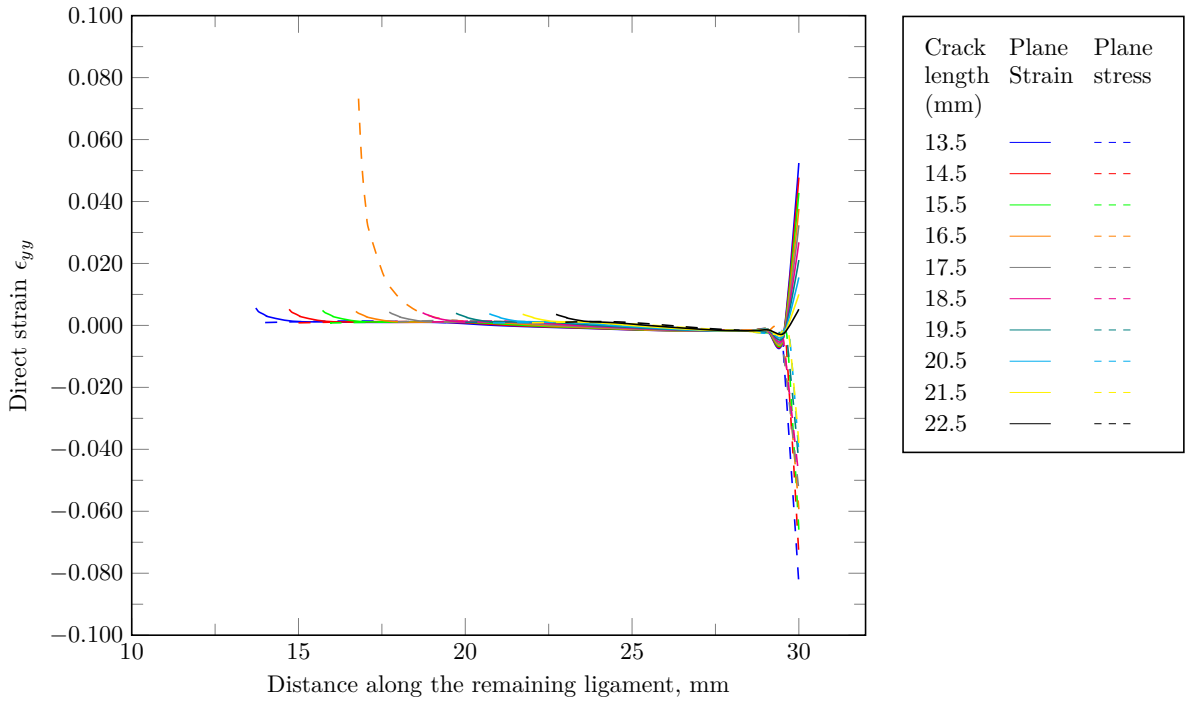

Figure 6.39: Direct strain (ϵ_{yy}) along the remaining ligament for multiple initial crack depths (a_0) for plane stress and plane strain analyses at a displacement (Δ = 0.4 mm)

the boundary. Similar trends were noted for specimens notched in austenite material (Figure 6.20b).

Figure 6.42 is a comparison of the direct strain of the two specimens types (specimens notched in austenite region as per Section 6.2.1, and specimens notched in ferrite as per Section 6.2.2) along the materials interface region at a displacement of 0.4 mm. Appendix C Figure C.26 plots the data in terms of direct stress. For direct stress plotting each curve is normalised by the associated material yield stress so ferrite regions are normalised by 450 MPa and austenite regions by 350 MPa. The direct strain plots are comparable without further data processing. In the plane strain condition (Figure 6.42a) yield is predicted to occur in both the ferrite and austenite regions the specimen notched in ferrite. In the plane stress condition (Figure 6.42b) yield is predicted to occur in the austenite region irrespective of the notch location. In the plane strain condition, Figure 6.42a, yielding is predicted to occur in both the ferrite and austenite materials when the notch is located in the ferrite region. Specimens notched in austenite material are not predicted to fail in either materials for the same level of displacement.

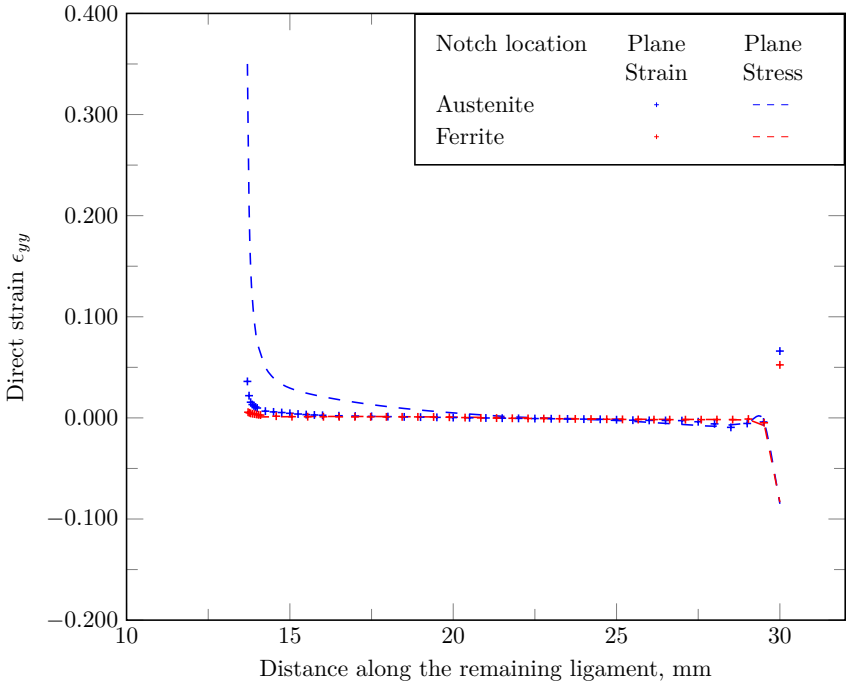

Figure 6.40: Direct strain (ϵ_{yy}) along the remaining ligament for initial crack length (a_i) 13.5 mm for plane stress and plane strain analyses at a displacement (Δ = 0.4 mm)

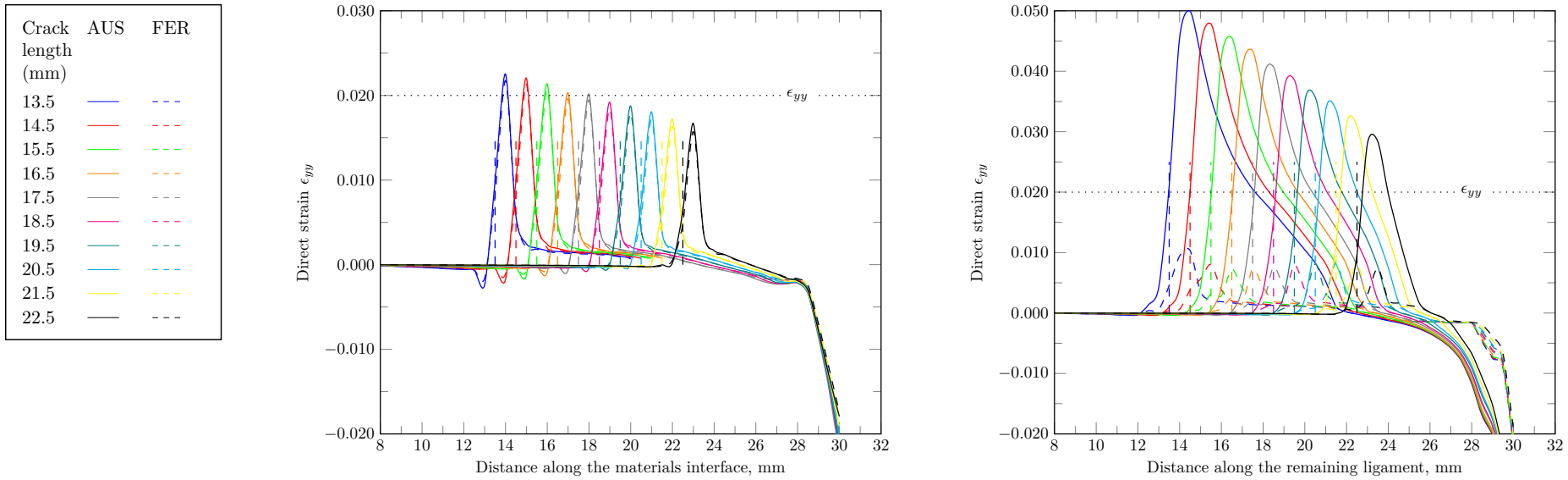

(a) Plane Strain

(b) Plane Stress

Figure 6.41: Direct strain (ϵ_{yy}) along the materials boundary for multiple initial crack depths (a_0) for 2D plane strain (Figure 6.20a) and plane stress (Figure 6.20b) conditions at a displacement (Δ = 0.4 mm). Cracktip positions marked with dashed line.

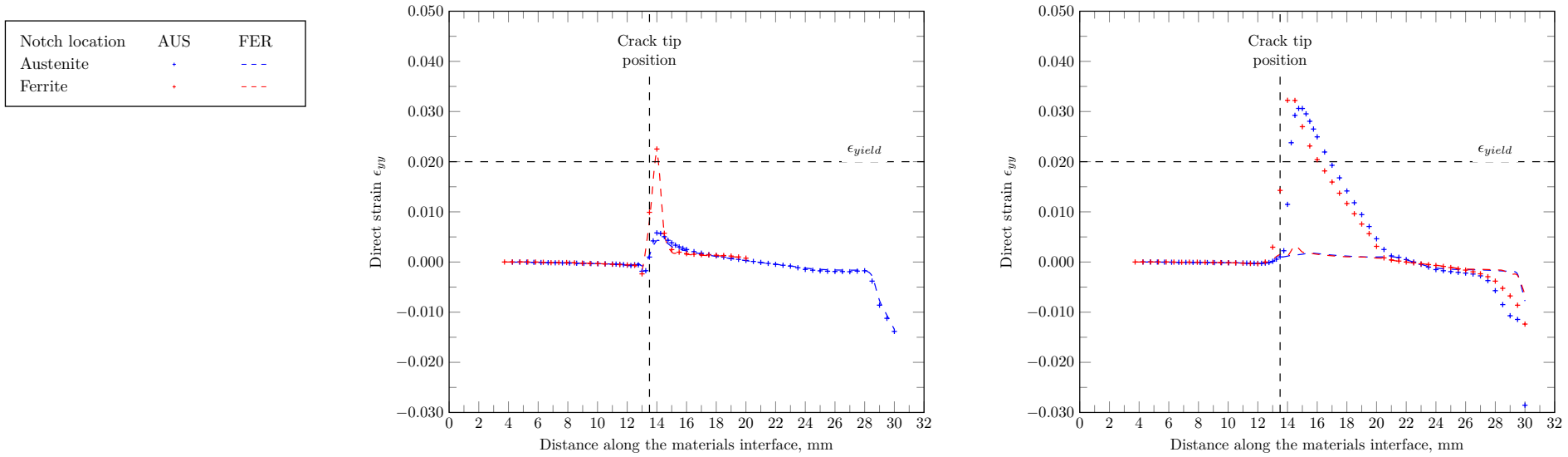

(a) Plane Strain

(b) Plane Stress

Figure 6.42: Comparison of direct strain (ϵ_{yy}) along the materials boundary for initial crack depth (a_i=13.5 mm) for 2D plane strain (Figure 6.42a) and plane stress (Figure 6.42b) conditions at a displacement (Δ = 0.4 mm) for specimens notched in austenite material and specimens notched in ferrite material

6.3 3D Modelling of CT Specimens

The purpose of this work was to investigate whether the 2D models were truly representative of the experimental work. Three dimensional (3D) finite element models of the experimental fracture toughness test were conducted for two cases. Geometrically the samples were identical to that of the experimental specimens. The first case assumed, that the specimen comprised of ferrite material with a 6 mm thick notched austenite region. The notch was positioned 1 mm from the TIG weld boundary. The second case considered an identical model with reversed material properties, so that the sample comprised of austenite material with a notched 6 mm thick ferrite region. An initial crack depth of 13.5 mm was assumed for both cases.

Elastic-plastic material properties (see Chapter 4.2) for both the austenite and ferrite materials were applied to the relevant areas. Finite strain analysis, using the non-linear geometry option, was implemented. Similar to the 2D models, the 3D models were displacement controlled. To mimic test conditions displacement data taken from clip-gauge measurements were applied to a reference node located in the center of the pin hole. One reference node was fixed (U1=U2=UR1=UR2=0), the other was displaced, in the y-direction, in accordance with test data. Both reference nodes were kinematically coupled to the relevant pin hole surface. The models were meshed using C3D8R elements with a similar meshing strategy as that used in the 2D analyses. A total 56,700 elements were used, this ensured that measurements, at less than 1 mm distances through the thickness, could be obtained. The defect was modelled as a sharp crack with collapsed wedge elements around the crack tip. Duplicated nodes with a midside parameter of 0.25 was applied to elements in the first contour. The model geometry and meshing strategy are shown in Figure 6.43.

The force versus displacement curves for the models are shown in Figure 6.44. Displacements taken at the load-line and at the crack mouth position are shown (details on the crack mouth position can be seen in Figure 6.43b). Unsurprisingly the curves vary from one another with the specimen notched in austenite material expected to

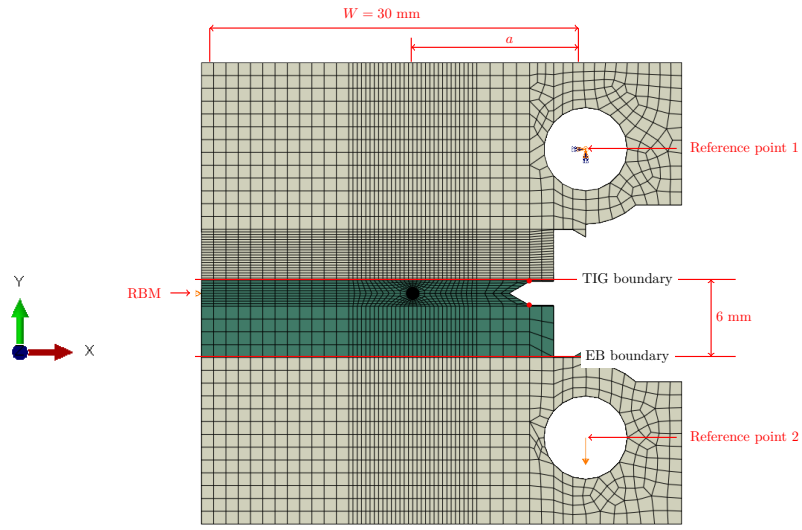

(a) LLD from reference point 2

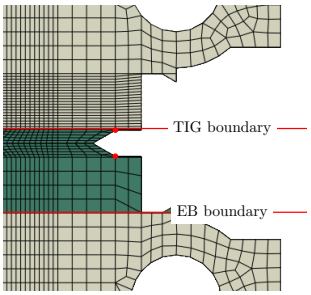

(b) Magnified view of notch, with CMOD positions marked

Figure 6.43: Image of boundary conditions and mesh strategy applied to the 3D model.

reach higher magnitudes of load for comparative values of displacement. While somewhat counter intuitive the result is realistic in terms of the relative volume of material. The austenite notched model consists of significantly more ferrite material, over the entire geometry of the specimen and, taking the relative yield strength of the materials into consideration, it is therefore expected that the austenite notch specimen would reach higher magnitudes of load. As expected, in both cases the load-line displacement (LLD) is greater than that of the CMOD. This is attributed to crack tip blunting.

Figure 6.45 plots the estimated strains at various stages of test sequencing for the surface of the sample (Figures 6.45a to 6.45c) and the mid-thickness (Figures 6.45d to 6.45f), respectively (see Section 6.1 for details on test sequencing). As shown significant plasticity occurs at the crack tip, this is not unexpected given that crack initiation and/or propagation was not assessed. In terms of the sample surface the 3D model differs significantly, in terms of strain profile, compared to similar results for the 2D plane stress model. At SEQ10 the model has been displaced approximately 0.5 mm at the load-line, by comparing Figure 6.45a with Figure 6.15d) it can be seen that the 3D model predicts a much larger area affected by high magnitudes of strain in comparison to the 2D analyses. In the mid-thickness region the area impacted (Figure 6.45d) in the 3D model is again significantly larger than that noted to have occurred for a sim-

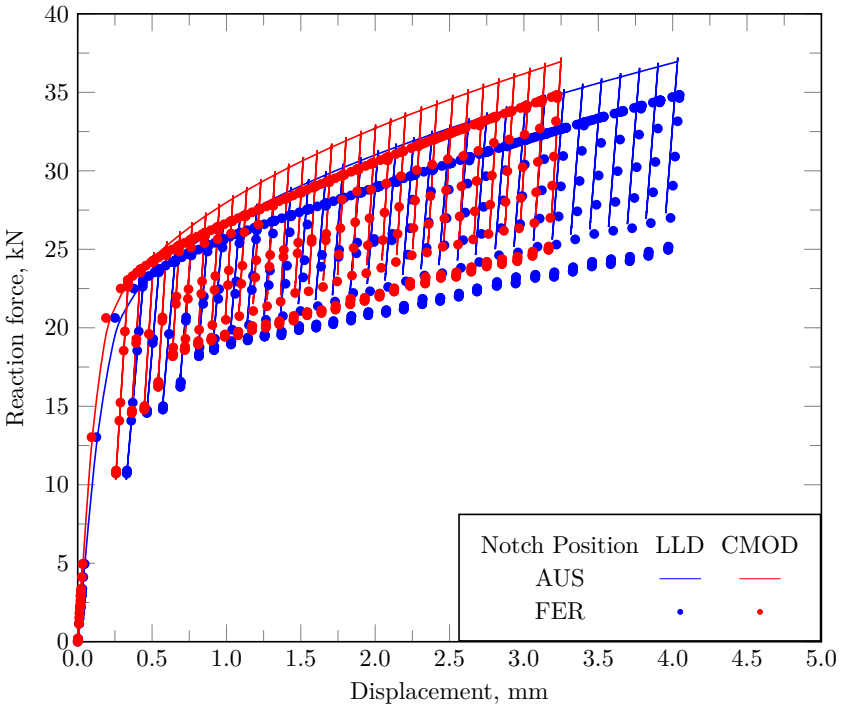

Figure 6.44: Force versus displacement at the load-line and crack mouth opening (CMOD) for 3D fracture models

ilar LLD in the 2D plane strain model (Figure 6.16d) though yielding is restricted to a smaller zone. This indicates that constraint, due to the thickness effect, is not accurately assessed when plane stress or plane strain assumptions are used.

Similar contour plots are shown in Figure 6.46 for the model notched in ferrite material. When comparing Figure 6.46 to 2D plane stress (Figure 6.36) and plane strain (Figure 6.37) analyses, trends, similar to that noted in the previous paragraph, were found (i.e. the 3D model predicts higher magnitudes of strain over larger areas in comparison to 2D analyses). Comparing specimens notched in austenite material (Figure 6.45) to those notched in ferrite (Figure 6.46) it is shown that, for similar stages of the analyses, the results differ significantly. It is clear from Figures 6.45d to 6.45f that strains in the mid-thickness are life limiting (these extend much further along the remaining ligament of the sample compared to strains on the surface). For specimens notched in ferrite however, the strains appear to the be broadly similar, in terms of magnitude and profile, on both the surface and in the mid-thickness. Additionally when the notch is located in the austenite material the strains are predicted to propagate away from

the TIG weld boundary, into the austenite material. Even at the mid-point of the test (Figure 6.45f), relatively little strain has propagated from the austenite material into the ferrite material. Conversely specimens notched in the ferrite region show that at very early stages of testing (Figure 6.46d) the strains at the crack tip and at the TIG weld boundary are of equal magnitude. Furthermore the area on the austenite side of the weld boundary is much greater than that of the crack tip. This trend is similar to that noted for the 2D plane stress and plane strain models. This indicates that defects initiating in the austenite region tend to propagate throughout the austenite region and only a limited amount of strain propagates into the ferrite material. When defects are initiated in the ferrite region strain immediately propagates through the weld boundary into the austenite material.

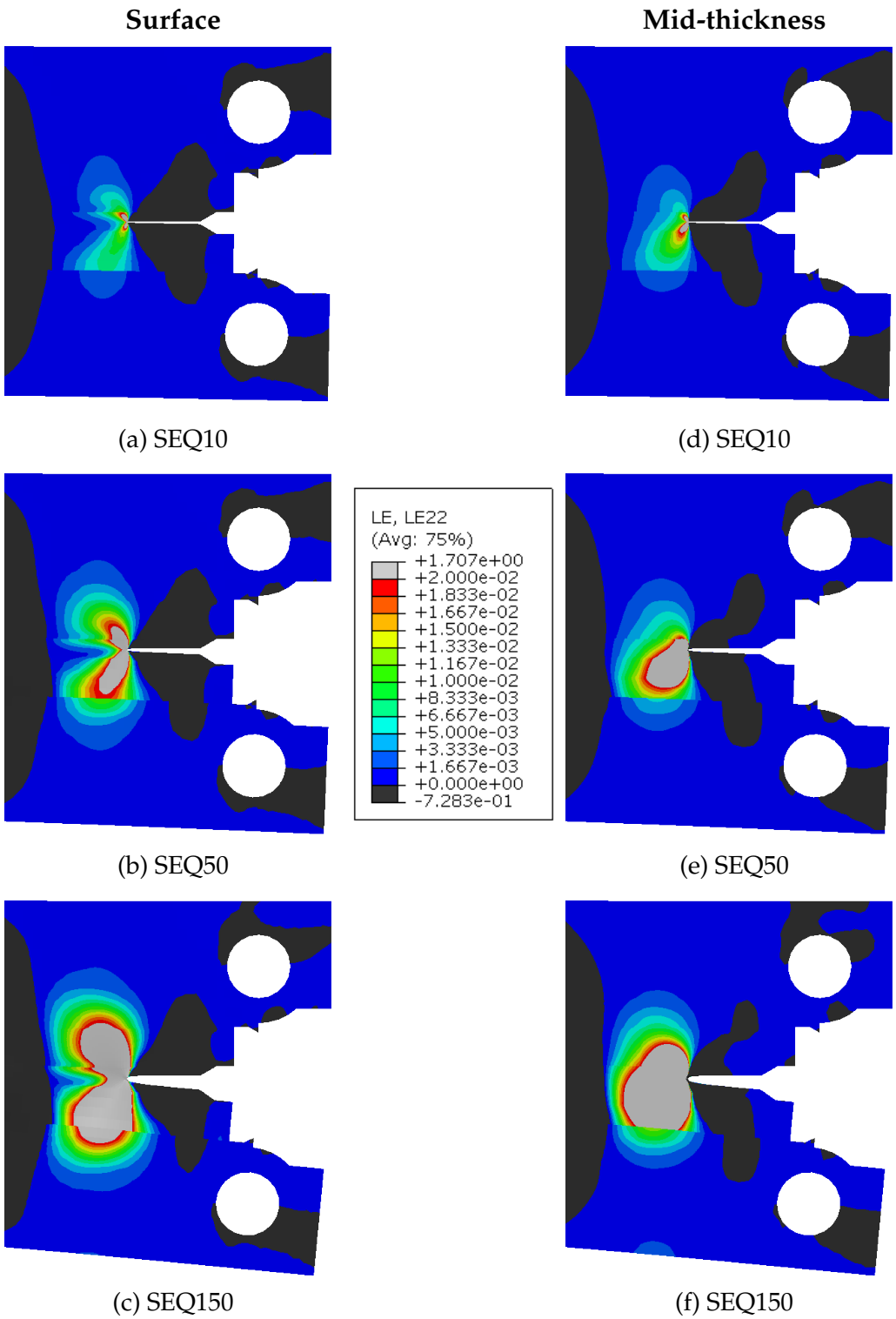

(a) SEQ10 (d) SEQ10

(b) SEQ50 (e) SEQ50

(c) SEQ150 (f) SEQ150

Figure 6.45: Contour plots of direct strain ϵ_{yy} in 3D model of fracture toughness test during peak loading conditions. Notched region consisting of austenite material properties. Figures 6.45a to 6.45c showing estimated strain on surface. Figures 6.45d to 6.45f showing strains in the mid-thickness region.

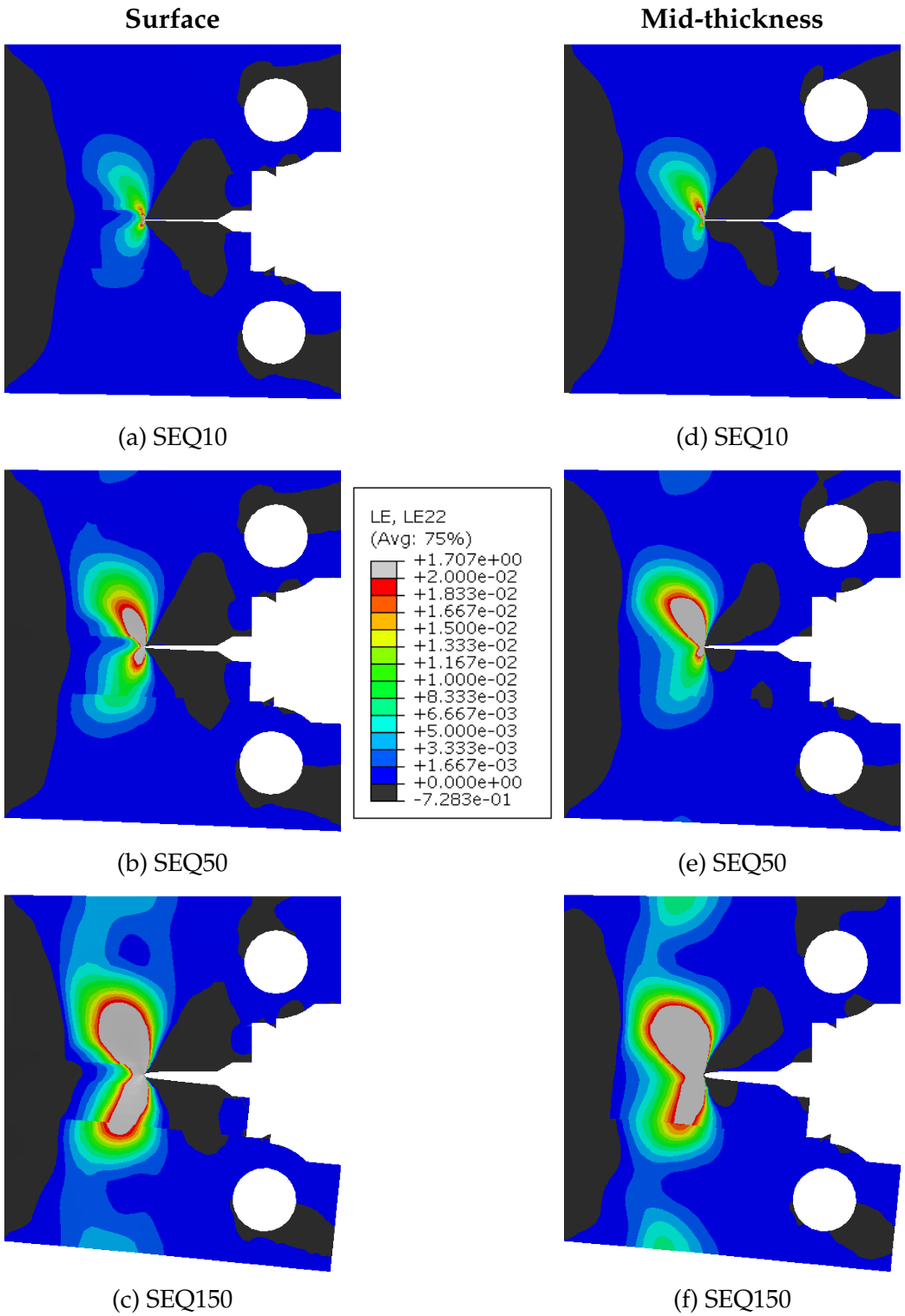

(a) SEQ10 (d) SEQ10

(b) SEQ50 (e) SEQ50

(c) SEQ150 (f) SEQ150

Figure 6.46: Contour plots of direct strain ϵ_{yy} in 3D model of fracture toughness test during peak loading conditions. Notched region consisting of ferrite material properties. Figures 6.46a to 6.46c showing estimated strain on surface. Figures 6.46d to 6.46f showing strains in the mid-thickness region.

6.4 Chapter 6 Summary

The maximum number of samples that could be machined from the laser welded component, to the standard recommended geometry [ASTM International, 2001], was six. Both the BS7910 and R6 [British Standards Institute, 2015*a*; British Energy, 2008] methods recommend that fracture toughness data used in an engineering critical assessment (ECA) is limited to the minimum measured value of three data or the second minimum measured value of six data. This method provides some statistical confidence that the fracture toughness will not be lower than experimentally measured data. The validity of a fracture toughness test cannot be ascertained until the test has completed, upon which the sample has been effectively destroyed. To ensure that a statistically meaningful value of fracture toughness was measured, testing for this work was limited to room temperature only.

Given that both the ferrite and austenite materials used in this dissimilar metal weld (DMW) have high strength and toughness at room temperature, test conditions were not ideal. However, testing at room temperature allowed for the measurement techniques, digital image correlation (DIC), that would not have been available for testing at low temperature. Additionally, given the hardness and relative brittleness of the HAZ region, defect initiation an propagation was considered likely, even for sub-optimal conditions. As presented in Chapter 6 the CT specimens did initiate and propagate defects. All specimens failed in a ductile manner and the majority exhibited a significant amount of crack tunnelling. Crack tunnelling occurs due to high shear stresses on the free surfaces (i.e. surfaces in plane stress) while the bulk material (i.e. mid-thickness region) remains under higher constraint and is subject to a triaxial stress state, resulting in larger crack driving forces in the mid-thickness region.

Fracture was modelled using 2D plane stress and strain assumptions. The EDM machined notch was modelled as a seam, where duplicate nodes along the seam allow the crack to open as loading is applied. The crack tip was modelled using collapsed elements. To model the singularity at the crack tip a combined $1/\sqrt{r}$ and $1/r$ singularity

was assumed, this is the recommended method for power-law materials [Dassault Systemes Simulia Corp, 2014]. Figure 6.48 compares cracking on the surface of specimen S1 to the predicted equivalent plastic strain (PEEQ) from a 2D FE analysis conducted with plane stress elements. As can be seen the plane stress assumption accurately predicts the damaged regions. Figure 6.49 plots a similar comparison between the mid-thickness damage to that predicted using a plane strain elements. Again the model accurately predicts higher strains in regions damaged during testing. This provides some confidence in the use of 2D modelling for DMWs.

In addition to modelling the test specimen geometry, a parametric study was conducted to assess the impact of the austenite thickness on the results. Unsurprisingly the plane strain assumption was more damaging compared to the plane stress assumption. Figure 6.15c shows contour plots of the strain for a given value of displacement for the plane stress condition. The plane strain condition is shown in Figure 6.15c. In both cases the thinner austenite region was shown to have significantly higher values of strain compared to thicker austenite regions. In terms of real structures, these results imply that additional layers of austenite cladding material provides some measure of protection to the sample against failure. However, it should be noted that in these models the influence of microstructure and HAZ regions were neglected. Further work, including additional experimental testing, would be required to adequately detail the impact of the microstructure.

As mentioned the 2D plane stress and plane strain model did not incorporate the HAZ region at either material boundary. For the cases where the notch is in close proximity to one boundary in particular (in the case of Figures 6.15c and 6.16c the notch is 1 mm from the TIG weld boundary) stresses in the austenite and the ferrite materials are likely to be higher than those in the HAZ. This is based on the results shown in Figure 4.19, which show that for identical loads the stress in the HAZ is always lower in comparison to that of either the austenite or ferrite, and similarly the stress in the austenite is always of greater magnitude than that in the ferrite. This trend was reflected in the experimental fracture toughness testing where DIC showed that strains in the austen-

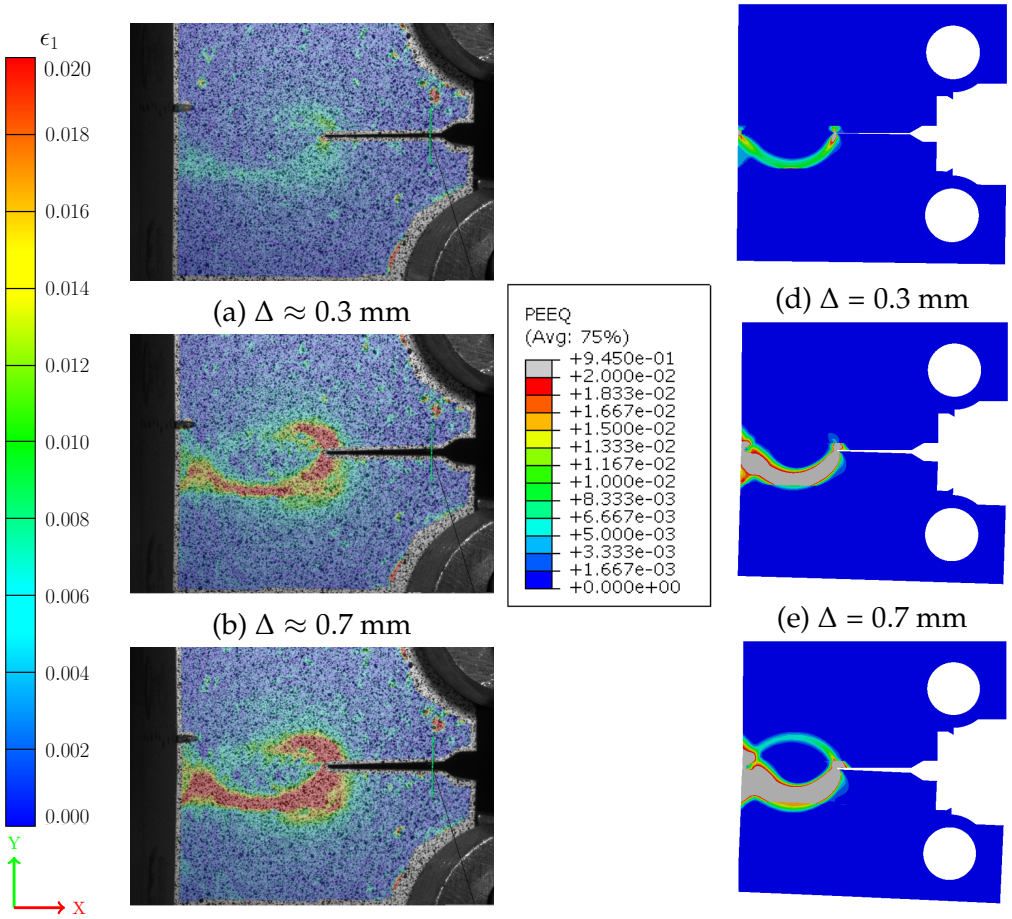

(a) $\Delta \approx 0.3$ mm

(b) $\Delta \approx 0.7$ mm

(c) $\Delta \approx 1.1$ mm

(d) $\Delta = 0.3$ mm

(e) $\Delta = 0.7$ mm

(f) $\Delta = 1$ mm

Figure 6.47: Comparison of measured major strain using DIC to predicted equivalent plastic strain (PEEQ) using 2D modelling with plane strain assumption. Specimens compared at various applied displacements.

ite and HAZ region were significantly higher in comparison to those in the austenite region (see Figure 6.9).

The proximity of the notch to the interface was also investigated. Contour plots of direct strain are shown in Figure 6.32 for the plane stress and plane strain assumptions, respectively. The symmetry, or lack thereof, is reflected in the profile of the strain distributions. The closer the notch is to the materials interface the more asymmetrical the strain distribution is estimated to be. For asymmetric plane stress conditions this translates to strains growing predominately at an angle towards the materials interface, extending into the remaining ligament. Asymmetric plane strain analyses predict high levels of strain growing away from the nearest weld boundary. This is purely a

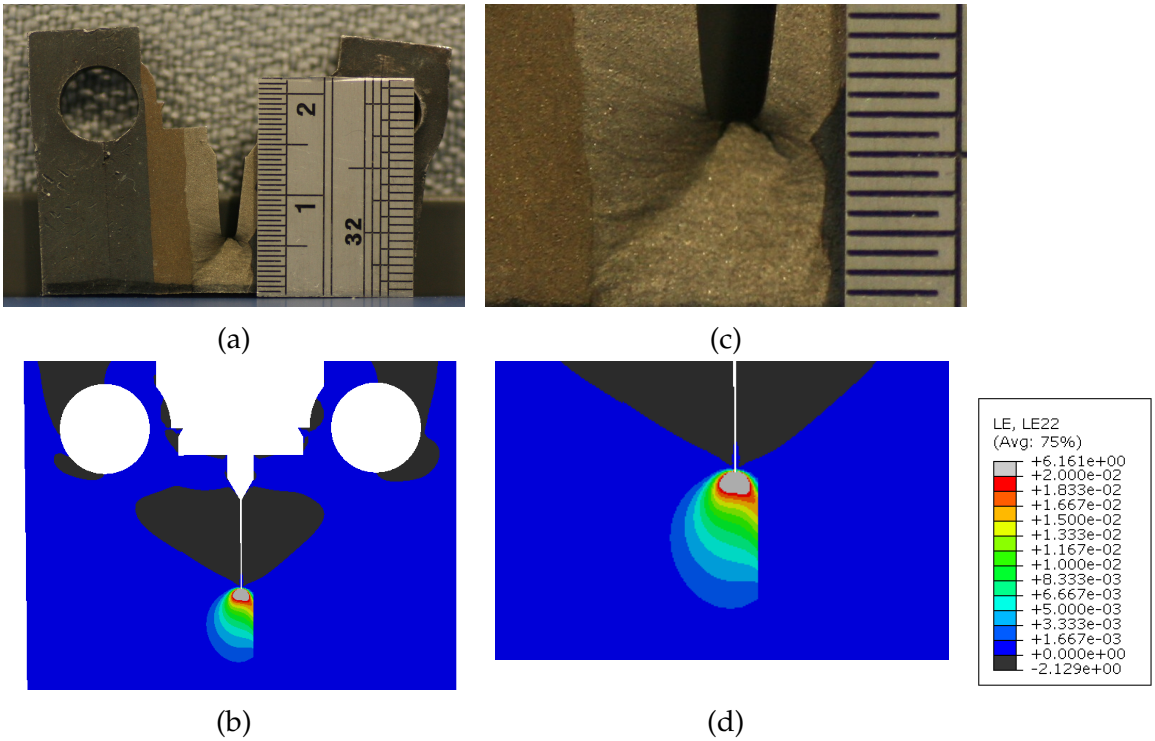

Figure 6.48: Comparison of fracture surface of the surface of specimen S1 with 2D FEA plane stress analysis. Showing direct strain ϵ_{yy}.

function of the respective yield strengths of the materials and was validated experimentally as shown in Figure 6.49.

In Section 2.3 it was shown that welding results in the stress concentration factors at the weld toe, and that these inherent defects act, in many cases, as crack initiation points [Gooch, 1976; Maddox, 1991]. For the clad weld used in this work there are a number of weld toes, the vast majority of which are sub-surface. As it is unclear whether sub-surface defects are more likely to occur on the austenite or ferrite regions of the weld boundary 2D modelling, assessing the impact of a notch located in the ferrite region was conducted (see Section 6.2.2). In this section it was shown that under plane stress assumptions, high magnitudes of strain exist not only at the crack tip region but also in the austenite material along the materials boundary (Figure 6.36). The implication is that crack initiation is equally as likely to occur at either the notch tip or at the weld boundary in the austenite material. The plane strain assumption however shows the crack tip (i.e. the ferrite material) to be the predominant location of failure.

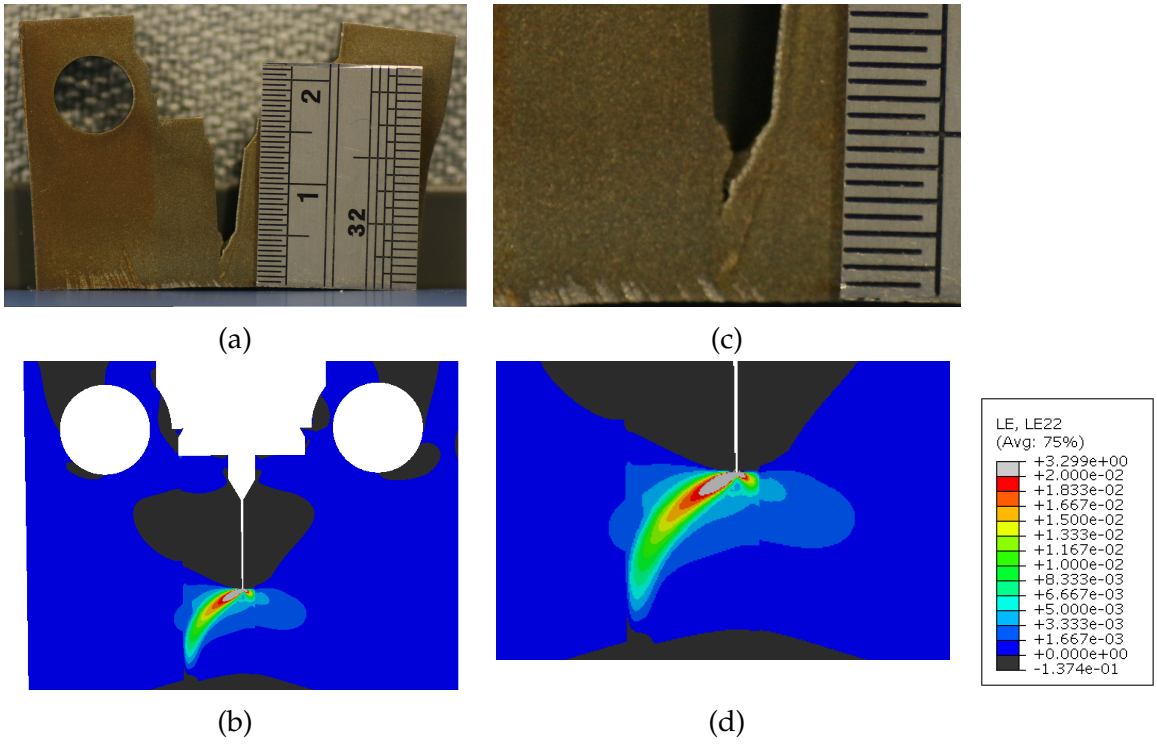

Figure 6.49: Comparison of mid-thickness fracture surface of specimen S1 with 2D plane strain analysis. Showing direct strain ϵ_{yy}.

Three dimensional finite element analysis was conducted to assess the accuracy of the 2D plane stress and plane strain assumptions. Two models were assessed, the first was similar to the specimens tested experimentally where the majority of the specimen was comprised of ferrite material with a 6 mm thick austenite region. A 13.5 mm deep notch was placed in the austenite material, offset from the TIG weld boundary by 1 mm. The second model was identical to the first in terms of geometry but the application of materials was reversed so that the majority of the specimen comprised of austenite material, with a 6 mm thick ferrite region. Experimental clip gauge data was used to apply displacements. Figure 6.50 shows the experimental major strain and the estimated equivalent plastic strain in the 3D model for identical test sequences (SEQ10, SEQ50 and SEQ70). Displacements at these sequences are analogous to the displacement values used in Figure 6.47. As shown the strain on the back surface of the specimen is over-estimated by the 3D model. It should however be noted that a boundary condition to restrict rigid body motion (RBM) was applied to a single node in this area. This likely accounts for a signficant part of the over-estimation in this re-

gion. Other regions, away from the boundary condition, are in good agreement with the experimental data. Figure 6.51 compares results for the same stages of testing for specimens notched in austenite and specimens notched in ferrite. As shown significant changes in strain profile exist between the two models. This was expected given the changes made to the geometry. It is interesting to note, that in cases notched in ferrite, strains of yield magnitude are predicted in the austenite region. This implies that defects initiating in the ferrite material may propagate through the weld boundary into the austenite material.

Specimens consisting primarily of ferrite material are predicted to reach larger magnitudes of force when compared to those comprised mainly of austenite material. Contour plots showing direct strain, ϵ_{yy} can be seen in Figures 6.45 and 6.46. Interestingly specimens comprising mainly of ferrite material (i.e. those notched in austenite, see Figure 6.45) show variations in strain magnitude and strain profile when comparing the surface and mid-thickness regions. Additionally the strain in the mid-thickness regions was noted to predominately remain within the austenite region even after significant deformation of the sample. Sample comprised mainly of austenite material (i.e. notched in the ferrite zone, see Figure 6.46) predicted notably different results. The magnitude and profiles of strain on the surface and in the mid-thickness regions were predicted to be broadly similar, particularly at the latter stages of testing. The most interesting difference between the models is that, for specimens notched in a ferrite zone, the strains at the crack tip are similar in magnitude to those in the austenite region at the weld interface. Figures 6.46d to 6.46f show that strain initiates in both materials and predominately propagates into the austenite material. This implies that, for ferritic and austenitic materials of similar fracture toughness, defects initiating in the austenite region are likely to propagate in the austenite region only. Whereas defects initiating in the ferrite region are equally likely to fail at the crack tip or at the weld boundary.

If one considers the original TIG welded plate (Figure 3.1) and postulates a defect initiating on the weld interface, then the above results imply that irrespective of whether

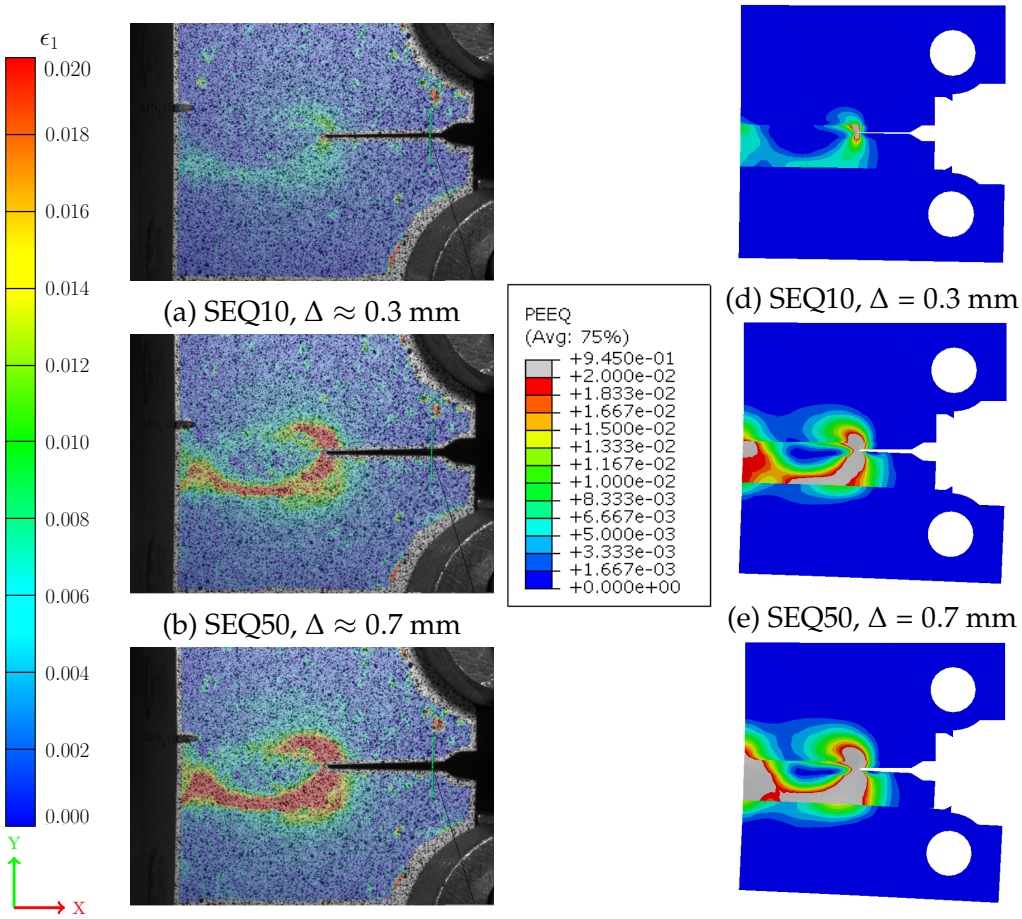

(a) SEQ10, $\Delta \approx 0.3$ mm

(b) SEQ50, $\Delta \approx 0.7$ mm

(c) SEQ70, $\Delta \approx 1.1$ mm

(d) SEQ10, $\Delta = 0.3$ mm

(e) SEQ50, $\Delta = 0.7$ mm

(f) SEQ70, $\Delta = 1$ mm

Figure 6.50: Comparison of measured major strain using DIC to predicted equivalent plastic strain (PEEQ) using 3D model notched in austenite. Specimens compared for identical test sequences.

the defect initiates in the austenite or the ferrite materials strains are more likely to propagate in the austenite. Furthermore the results shown in Figure 6.46 indicate that tearing is more likely to occur through the austenite material rather than along the weld boundary. That implies that sub-surface defects at the weld interface are more likely to propagate through austenite material, and so, become surface breaking. From a non-destructive testing (NDT) perspective surface breaking defects are more desirable than their sub-surface counterparts. This is particularly true for dissimilar metal welds (DMWs) as a surface breaking defect is much more likely to be 'found' and sized accurately. From a corrosion perspective however, a surface breaking defect through the cladding exposes ferritic base material to an environment for which it is not designed.

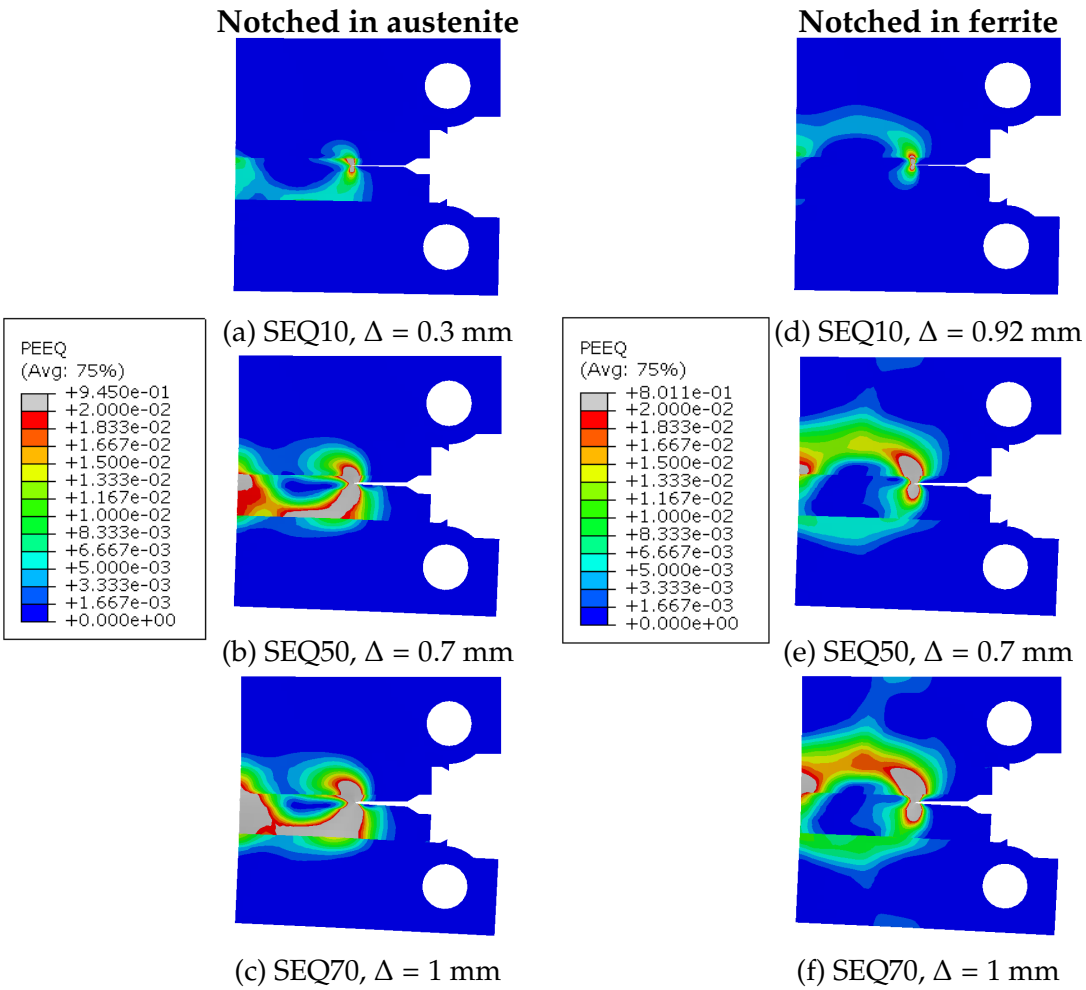

(a) SEQ10, Δ = 0.3 mm (d) SEQ10, Δ = 0.92 mm

(b) SEQ50, Δ = 0.7 mm (e) SEQ50, Δ = 0.7 mm

(c) SEQ70, Δ = 1 mm (f) SEQ70, Δ = 1 mm

Figure 6.51: Comparison of equivalent plastic strain (PEEQ) using 3D models notched in austenite and ferrite. Specimens compared for identical test sequences.

It should be considered that the results pertaining to the 3D modelling do not take account of residual stresses which, as previously discussed were measured and predicted to be of significant tensile magnitudes in both the ferrite and austenite material. The prediction of residual stress in this work was conducted for a 6 mm thick austenite cladding case only. It is not clear what the residual stresses would be were a 6 mm thick ferrite cladding assumed instead. Furthermore additional work is required to combine the predicted residual stress in the CT sample with the 3D modelling prediction. This would give further information on how the presence of residual stress impact the estimated strain propagation, and hence defect propagation, path.

Chapter 7: Fracture Toughness of Defects Oriented Perpendicular to Materials Boundary

7.1 Experimental Fracture Toughness of SENB specimens

The main purpose of this chapter is to investigate whether the presence of the cladding impacts fracture toughness test results when defects are oriented perpendicular to the weld boundary. Current industry practise is too assess dis-similar specimens as homogeneous samples using each type of material. The lowest (most conservative) value is then used to prove the safety case. Clearly this approach is overly-conservative. Currently the following questions have not been addressed in literature:

- Does the presence of an interface impact the strains in the sample? If so, does this impact the crack driving force?
- If a defect has extended beyond the cladding interface does the cladding have any further impact?
- If a defect is located close to the interface will the defect propagate along the interface or will it continue to propagate perpendicular to the loading direction?
- If a defect is located in the cladding, a significant distance from the interface, does this impact the fracture toughness result? Can we quantify the impact?

The purpose of this work was to address these questions. Section 3.2.3 details the orientation of defects associated with the SENB specimens, with respect to the weld boundary. Each of the three sets of specimens tested here contained two samples of combined material (cladding and base material) and four samples of base material only. By comparing the performance of homogeneous samples to that of the combined

samples the impact of the cladding can be addressed. Furthermore each set of specimens contained a defect located in an area of interest (i.e. in the cladding relatively distant to the weld boundary, in the cladding relatively close to the weld boundary and, through the weld boundary in the base material).

Basic test information was provided in Section 3.3.4, a brief overview follows but readers should refer to Section 3.3.4 for specific details. Prior to fracture testing each sample was subject to fatigue pre-cracking. The purpose of fatigue pre-cracking was not, in this case, to grow the crack to a greater depth, but rather to provide a short, but sharp, realistic defect in place of the machined notch. DIC was used for a small number of tests in an attempt to track crack growth. However, as the applied load was in the elastic range of the material the strains on the surface could not be differentiated from the noise. Table 7.1 shows the number of fatigue cycles for each specimen in group C1 (initial machined defect size a_0 = 8.1 mm) and the initial estimated crack length prior to fracture testing (see Table 7.1 column: $a_{0\ test}$).

As previously discussed in Section 3.3.5 several specimens were tested using a 5 mm clip gauge (T1). The travel of the gauge (2 mm) was exceeded prior to any crack growth and a valid measure of fracture toughness could not be estimated. The software used to control testing [Instron, 2010*b*] stops the test once the maximum travel of the clip gauge is met. Many of these tested samples had little/no deformation post-testing, therefore a larger clip gauge (gauge length of 10 mm and a travel of 4 mm) was used in place of the 5 mm clip gauge. The previously tested samples were re-tested with the larger clip gauge. Prior to retest (T2) samples were modified to remove existing studs (to which the 5 mm knife edges were attached). The DIC speckle pattern was cleaned off and new studs (at 10 mm positions) were applied. Following the application of new studs the DIC speckle pattern was re-applied. Specimens were pre-fatigued a second time to ensure the crack tip extended beyond any plastic zone which may have been incurred during the initial test. The remaining (non-tested) samples were tested using the 10 mm clip gauge only. The test software unloads specimens at set increments of CMOD as defined by the user. In early tests a relatively small increment was cho-

Table 7.1: Fracture toughness of SENB Group C1. Initial machined notch a_0 = 8.1 mm.

Sample & Test No.	**Material**	**Gauge length**	**Fatigue Cycles**	$a_{0\ elastic}$	$a_{0\ test}$	$a_{f\ test}$	$a_{f\ measured}$	**Comments**
		mm	N	mm	mm	mm	mm	
C11	Combined	10	55,433	9.33	9.34	9.57	10.03	Deviation of surface crack. Evidence of crack tunnelling.
C12	Ferrite	5	30,240	9.24	9.21	9.00	-	
C12_2	Ferrite	10	2,359	9.83	9.85	9.91	10.64	Deviation of surface crack. Evidence of crack tunnelling.
C13	Ferrite	5	18,532	8.17	8.10	8.15	-	
C13_2	Ferrite	10	11,456	10.40	9.70	9.62	10.36	Evidence of crack tunnelling.
C15	Ferrite	5	53,826	9.96	-	-	-	
C15_2	Ferrite	10	137,690	10.10	10.25	9.72	9.72	Deviation of surface crack. Evidence of crack tunnelling.
C16	Ferrite	5	22,251	7.32	7.37	7.39	-	
C16_2	Ferrite	10	48,352	9.06	9.13	9.52	10.80	Bifurcation of crack on surface. Evidence of crack tunnelling.

Where $a_{0\ elastic}$ represents the initial crack length estimated during the elastic unloading prior to fracture testing, $a_{0\ test}$ the initial crack length estimated after first unloading sequence (SEQ10), $a_{f\ test}$ represents the final crack length estimated from final unloading sequence, and $a_{f\ measured}$ represents the maximum measured crack length at the mid-thickness of the sample post-test.

sen to maximise data output. When the ductility of the samples became clear, larger increments of CMOD were specified.

7.1.1 Defects in base material

The force versus displacement for crack ratios of $a/W = 0.45$ are shown in Figure 7.1. Individual specimen data is shown in Appendix D.2. From Figure 7.1 it can be seen that samples C12 to C16 were tested using both a 5 mm and 10 mm clip gauge. For samples that were tested with both clip gauges the data were assumed to be correlated cumulatively. That is to say: the initial loading cycle (SEQ 10) of the second test was assumed to begin at a CMOD value analogous to the elastic unloading of the final unloading position of the previous test. In cases were samples were tested twice (with 5 mm clip gauge and 10 mm clip gauge) data for both tests are included. Similar to the CT specimens (see Chapter 6) negative crack extension was noted to have occurred during the early stages of each test. The data were modified so that the most 'negative' value of crack extension represented the 'zero' crack extension position. As shown in Figure 7.1 the combined material specimen reached much larger magnitudes of force in comparison with the other, homogeneous ferrite specimens. This was unexpected given that the crack tip exists in the ferrite material for all samples but is likely due to the initial unloading position which was specified, for C11, to be 0.5 mm CMOD. Other samples from group C1 were unloaded at CMODs of 0.2 mm. Furthermore the initial defect size during the first unloading was measured to be broadly similar for all samples (See Table 7.1, column $a_{0\ test}$) despite large variations in the number of applied number of fatigue pre-cracking cycles.

Figure 7.2 plots the J-integral as a function of crack extension for samples with initial defects of $a/W = 0.45$. The test method [ASTM International, 2001] applies additional validity constraints for test data such as a maximum capacity for J-integral (J_{limit}) and crack extension (Δa). Specific details are provided in Section 3.3.4 and 3.3.5. Equations 3.3.18 and Equation 3.3.19 indicate how the validity values are estimated from test data. A 'construction line' (Equation 3.3.20), with an assumed value of $M = 2$, was applied to

each data set as specified by the test standard. Offsets of the construction line are set at crack extension (Δa) positions of 0.15, 0.2, 0.5 and 1.5 mm. The point at which test data intersects with the 0.15 mm offset curve defines the onset of fracture instability J_Q. The crack extension associated with J_Q is denoted as Δa_{min}. Test data within the bounds of Δa_{min} to Δa_{limit} capped by J_{limit} are considered valid data points. The test method [ASTM International, 2001] does note that materials such as austenitic stainless steels often have steep initial slopes, in which case the assumption of $M = 2$ may be overly conservative. The value of M may be re-assessed at a later stage but the value of J_Q must be estimated from the $M = 2$ assumption. Figure 7.2a plots the fracture toughness data for the combined material sample C11. This sample was tested only once with the 10 mm clip gauge. As shown in Table 7.1 the initial defect was estimated to be 9.33 mm prior to testing and 9.57 mm on conclusion of testing. Comparing Figure 7.2a shows that crack extension did not occur until the fourth (SEQ40) or fifth (SEQ50) unloading at which stage the J_{limit} was almost exceeded. Post-test the defect was measured, in the mid-thickness, to be 10.03 mm (see Figure 7.3). Figure 7.4 plots DIC contours of the true major strain and through thickness strain for the combined material sample.

Sample C13 consisted of homogeneous ferrite material (see Table 7.1) and was notched in an identical manner to sample C11. Figure 7.1 shows a distinct disparity between the unloading of the first test and the initial loading of the second test attempt. Indicating that the assumed correlation (i.e. that the final unloading of the first test was elastic) may not be accurate. From Table 7.1 it can be seen that the first fracture test (T1), an estimated fatigue pre-crack length of 8.17 mm was calculated. During the initial loading sequence (SEQ10 T1) the crack was estimated to measure 8.10 mm while the final crack length was estimated to be 8.15 mm. The initial crack length of the first unloading of the second test (SEQ10 T2) was estimated to be 10.40 mm. It is not clear why this disparity occurs. Post-testing the sample was cut using EDM along the mid-thickness plane and the physical crack size in the mid-thickness was measured to be 10.36 mm (Figure 7.5).

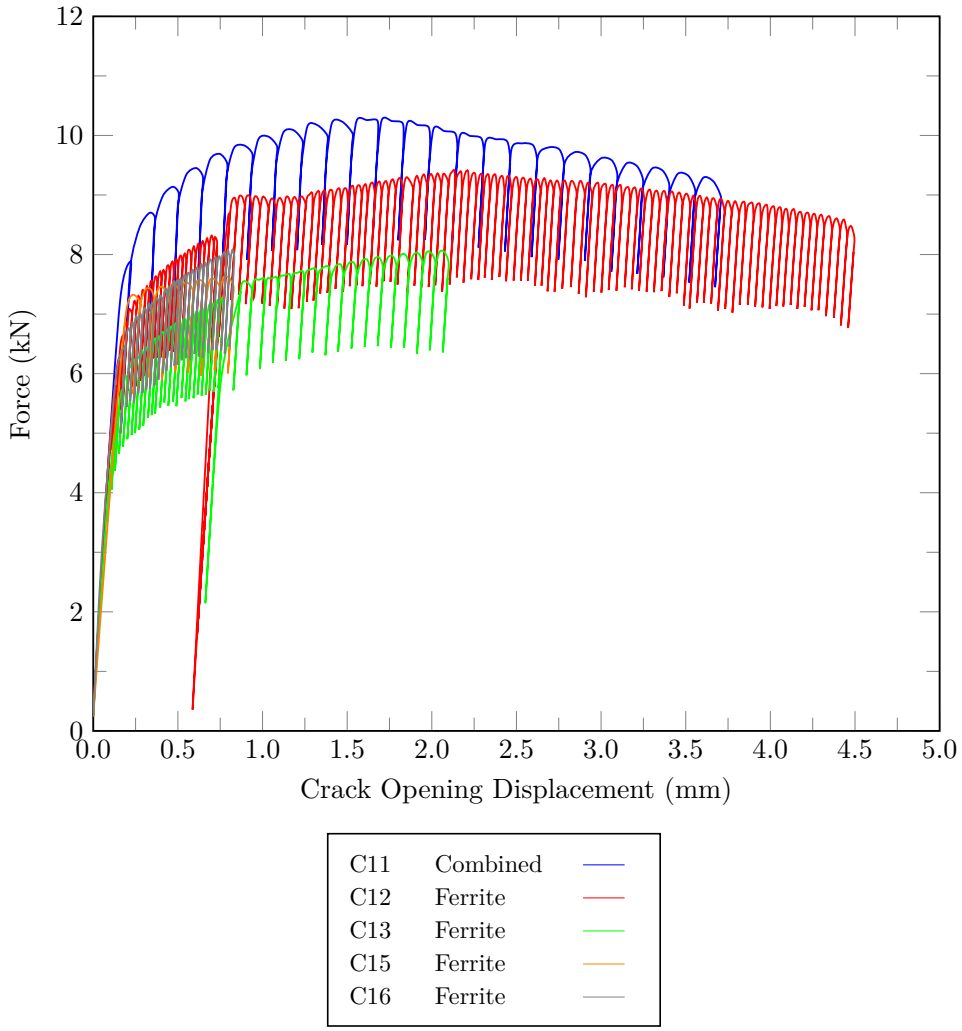

Figure 7.1: Force versus displacement for specimens with initial defect length $a/W = 0.45$

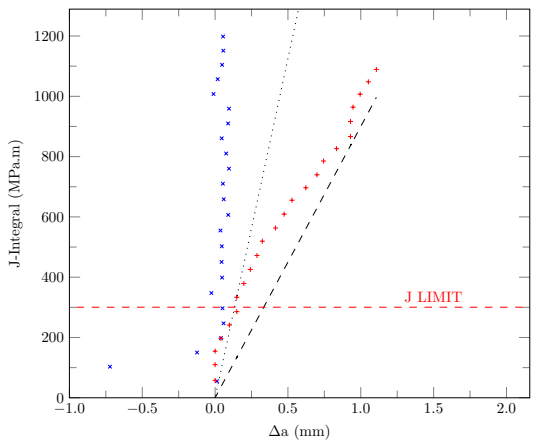

(a) C11 combined

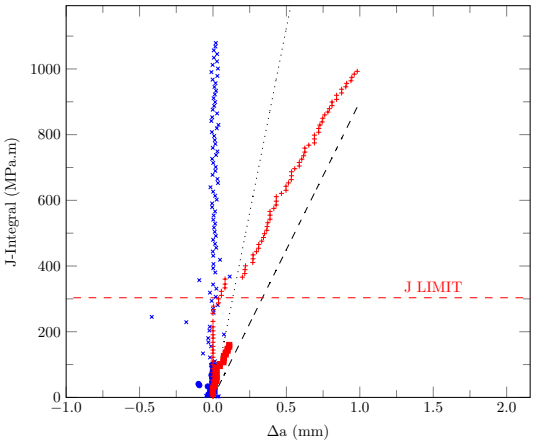

(b) C12 ferrite

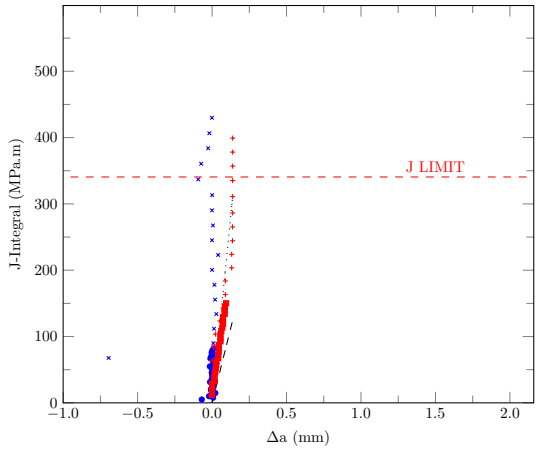

(c) C13 ferrite

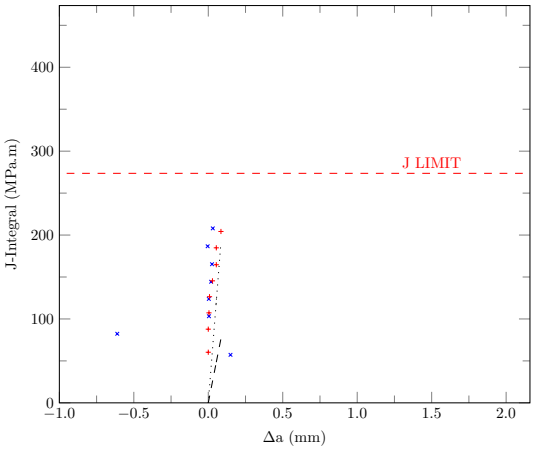

(d) C15 ferrite

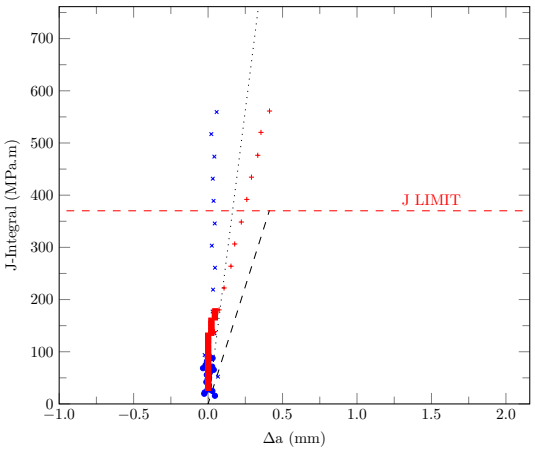

(e) C16 ferrite

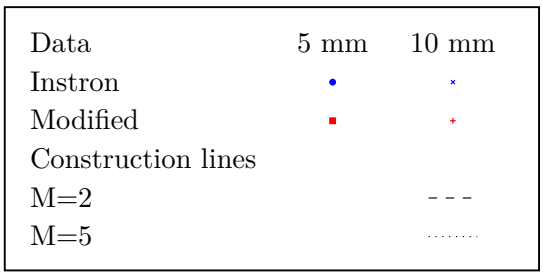

Figure 7.2: J-Integral versus crack extension (Δa) for C1 group. Original notch size $a/W = 0.45$

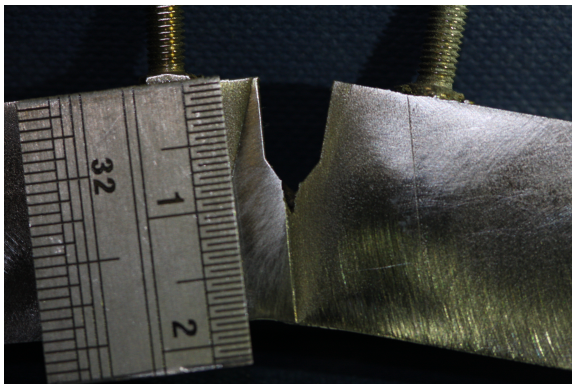

Figure 7.3: Post-test imaging of mid-thickness defect in specimen C11 (combined austenite and ferrite)

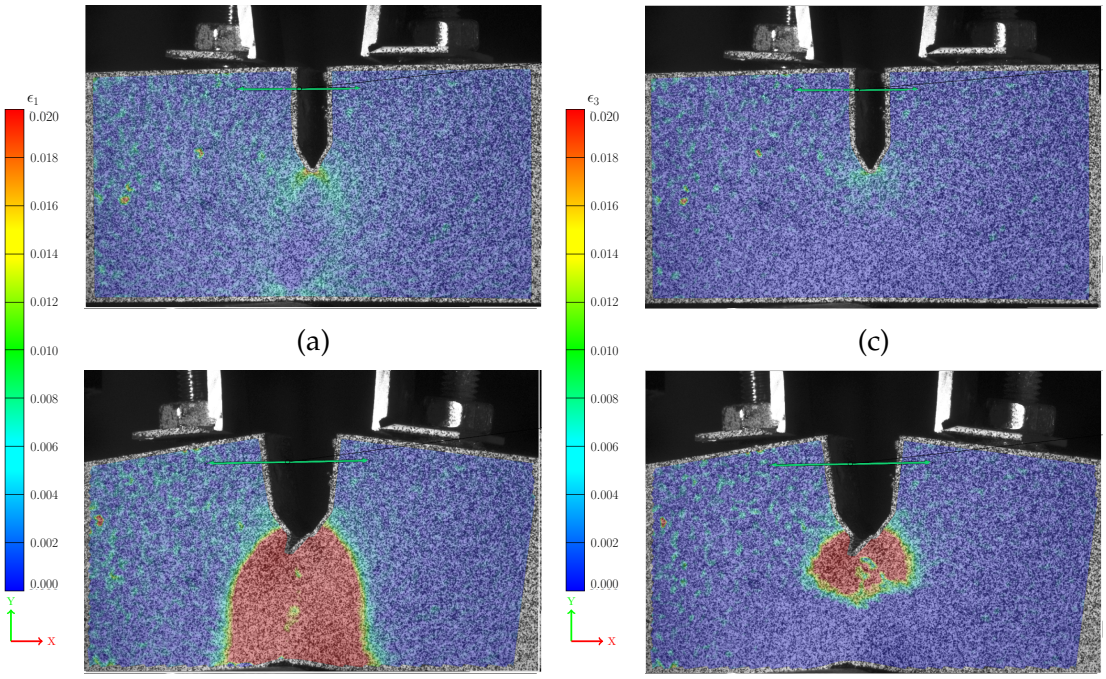

Figure 7.4: DIC data for specimen C11 with initial defect length $a/W = 0.45$. Figures 7.4a and 7.4b showing the true major strain for the initial loading cycle and the final unloading, respectively. Figures 7.4c and 7.4d showing the thickness reduction for the initial loading cycle and the final unloading, respectively.

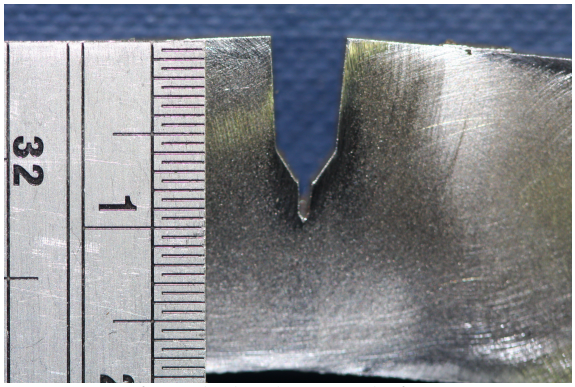

Figure 7.5: Post-test imaging of mid-thickness defect in specimen C13 (ferrite only)

Fracture toughness results for sample C13 are shown in Figure 7.2c as shown the crack extension was measured by the clip gauge to be less than 0.25 mm. When the assumption $M = 2$ is applied to the construction curve no valid J_Q value can be defined. Assuming a steeper slope ($M = 5$) results in test data that do not exceed the exclusion zone - hence the validity limits are exceeded. The true major strain in sample C13 are shown in Figure 7.6. During the initial loading cycle (SEQ10 T1, Figure 7.6a) high strains in the region surrounding the crack tip are visible. At the final unloading (Figure 7.6b) high magnitudes of strain have extended well into the specimen. Figure 7.7 shows strains in the thickness direction for sample C13, it clearly shows that significant plasticity occurred in the region surrounding the crack tip. Prior to the second test the sample was pre-fatigue cracked for an additional 11,456 cycles, the fatigue crack length was estimated to be 9.71 mm. There was some evidence of crack tunnelling in both samples with the mid-thickness defect being slightly deeper than that on the surface. The values are however within the expected range of error. Figures 7.6c and 7.6d show true major strain on the surface of sample C13 during the initial plastic loading (SEQ10 T2) and at the final loading cycle, respectively, for test two. While it is clear that the notch has opened further during the test there is no visible crack extension. The J versus Δa curve (Figure 7.2c) for the second test supports that little measurable crack extension occurred. Figure 7.7 shows strains in the thickness direction in the sample during test one (Figures 7.7a and 7.7b) and test two (Figures 7.7c and 7.7d), respectively. As shown the zone around the crack tip grows significantly in comparison to that of the first test, this is not unexpected. It should be noted that the strains (Figure7.7c) were initialised at zero. This is due to the re-application of DIC speckle pattern. The implication is that DIC cannot be initialised to the level of strain seen at the end of the first test. Hence the strains shown in Figures 7.6c and 7.6d, and Figures 7.7c and 7.7d are subject to error.

Other homogeneous ferrite samples (C12-16, excluding C14) performed similarly to C13, both in terms of J-Δa and DIC results. There was one difference of note: sample C13 did not show evidence of crack deviation on the surface of the specimen. All other

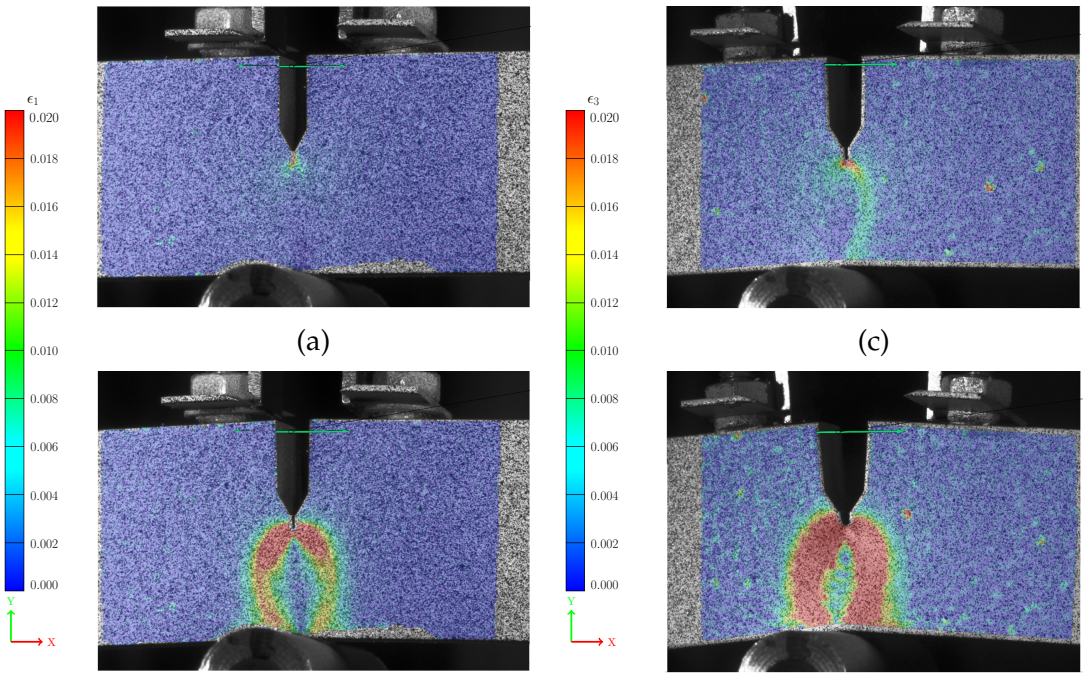

(a) (c)

(b) (d)

Figure 7.6: DIC major strain for specimen C13 with initial defect length $a/W = 0.45$. Figures 7.6a and 7.6b showing the initial loading cycle and the final unloading, respectively, for test one. Figures 7.6c and 7.6c showing the initial loading cycle and the final unloading, respectively, for test two.

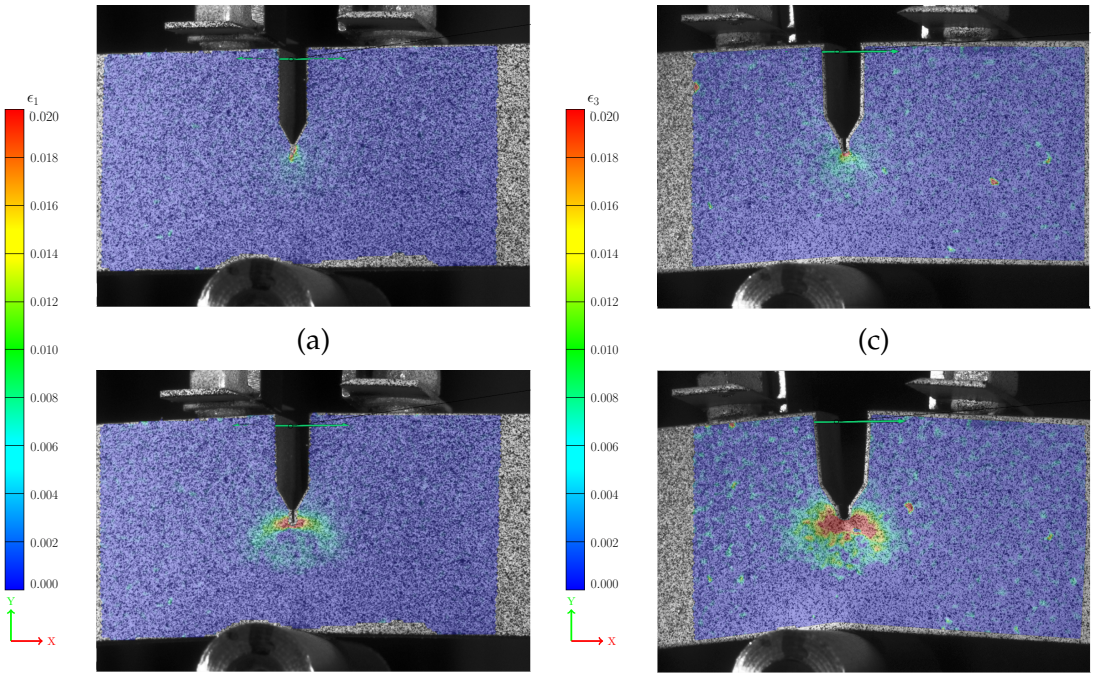

(a) (c)

(b) (d)

Figure 7.7: DIC strain in thickness direction for specimen C13 with initial defect length $a/W = 0.45$. Figures 7.7a and 7.7b showing the initial loading cycle and the final unloading, respectively, for test one. Figures 7.7c and 7.7d showing the initial loading cycle and the final unloading, respectively, for test two.

samples, both combined and homogeneous samples, showed distinct curvature of defects on the surface in comparison to the the mid-thickness. Ductile fracture occurs via a mechanism known as micro-void coalescence (MVC). This high energy absorption mechanism occurs on free surfaces, along the planes of maximum plastic strain (i.e. at 45°C to the direction of maximum principal stress), and leads to the formation of shear lips in the case of rectangular shaped specimens or, cup and cone failures for spherical shaped specimens. In this case deviations of the defects on the surface are an indication of the formation of shear lips; thus the samples are known to have failed in a ductile manner. It is not clear why sample C13 does not follow this trend. The mid-thickness region is subject to higher principal stresses than the surface due to additional constraint in the region from the surrounding material. This variation of stress along the crack front results in the the mid-thickness region being subjected to plane strain conditions (high triaxiality) and the surfaces being subjected to plane stress conditions (low triaxiality). The shift from low triaxiality to high triaxiality reduces ductility in the mid-thickness. This phenomena is called crack tunnelling.

Comparing Figure 7.4b with Figure 7.6d shows that both specimens experienced plastic collapse and similar strain profiles can be seen. The defect in sample C11 was noted to have deviated on the surface while this differs to the defect shown in sample C13 other homogeneous ferrite samples, C12, C15 and C16, had similar surface defects to that noted in sample C11. Comparing Figure 7.4d with Figure 7.7d it can be seen that both samples show a reduction in cross-sectional area surrounding the crack tip. The affected area is slightly larger in the combined sample but this trend is attributed to the greater CMOD applied to the combined sample in the initial loading stage compared with the homogeneous sample. Comparisons between the homogeneous ferrite and combined samples, do not highlight any differences in the respective strain fields that can be attributed to the presence of the cladding. The strain fields for all samples in group C1 appear identical. Hence the presence of the cladding does not appear to impact results once the defect extends beyond the weld boundary.

7.1.2 Defects close to the interface

Due to the position of samples in the original plate the depth of the cladding was somewhat variable along the length of the samples. Post-test inspection of the mid-thickness region of the combined samples (C31, C34) showed that the machined notch was within 2 mm of the weld boundary. Prior to testing, as the position of the notch relative to the weld boundary was unknown, care had to be taken during fatigue pre-cracking to ensure the crack tip did not extend beyond the weld boundary. Table 7.2 provides details on the estimated crack depths at various points during testing. In the case of C31 no fatigue pre-crack was initiated, subsequently no fracture initiation occurred. Post-test inspection of C31 showed the machined notch to be 2 mm distance from the weld boundary (see Figure 7.8). Sample C34 was consequently fatigue pre-cracked for longer and a pre-crack was successfully intitiated and propagated. Post-test inspection, Figure 7.10, shows the machined notch to have been approximately 1 mm from to the weld boundary.

Figure 7.11 plots the force against CMOD for samples from group C3, containing initial defects of 5.4 mm ($a/W = 0.30$). In comparison with homogeneous ferrite samples the combined samples were loaded to significantly higher loads to achieve comparable values of CMOD. This is not unexpected given that high magnitudes of ductility noted in the tensile testing of clad samples. The fracture toughness as a function of crack extension (J-Δa) for each specimen are shown in Figure 7.12. Similar to the previous section valid fracture toughness (J_{1C}) values could not be derived as test data exceeded validity limits as specified by the test standard. Several specimens did initiate and propagate a defect during testing but in all cases the measured crack extension was estimated to be less than 1.5 mm. As detailed in Table 7.2 and, similar to group C1, several samples exhibited signs of crack tunnelling in the mid-thickness region and evidence of ductile deformations were noted to exist on the sample surfaces.

The combined material samples (C31, C34) appear less inclined to initiate or propagate a defect in comparison with homogeneous ferrite samples from group C3. In the case

of C31 a defect of less than 0.25 mm was estimated to exist in the sample subsequent to testing. Post-test visual inspection found no indication of defect initiation despite the presence of significantly large embedded defects in the cladding, see Figure 7.9, one of which occurred on the weld boundary (albeit outside the region of maximum bending moment). The lack of fatigue pre-crack in sample C31 makes comparing the result to homogeneous samples somewhat unfair given the difference in SCF at the notch tip when comparing sharp fatigue pre-cracks to machined notches. Sample C34 may have initiated a fatigue pre-crack (Figure 7.10a) in the mid-thickness region. This is not necessarily the region from which propagation occurred as, as shown in Figure 7.10b, two defects appear to have initiated. Regardless sample C34 achieved significantly higher magnitudes of energy for comparable values of crack extension in comparison to the homogeneous samples.

Figures 7.13a to 7.13d and 7.14a to 7.14d show the true major strain for the combined samples C31 and C34, respectively, at various stages of testing. Each of the images shown represents the peak force position prior to unloading. As shown both samples show similar profiles developing over time. Some variation can be seen during the fifth unloading sequence (Figures 7.14b and 7.14b) but these differences are likely due to variations in crack length and hence, respective differences in CMOD and force. Both samples were fully plastically deformed throughout the ligament mid-way through the test (Figures 7.13c and 7.14c). Figures 7.13a to 7.13d and 7.14a to 7.14d show strains in the thickness directions at the same test positions discussed previously. Interestingly,

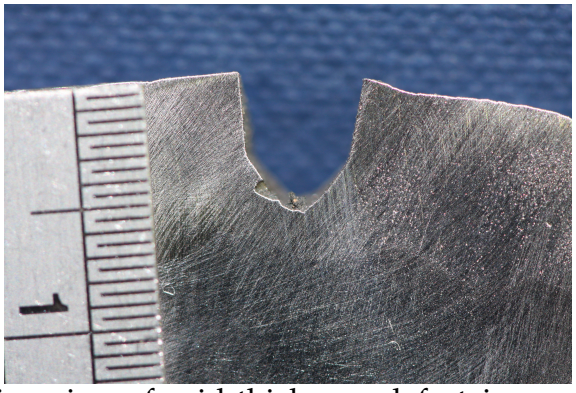

Figure 7.8: Post-test imaging of mid-thickness defect in specimen C31 (combined austenite and ferrite)

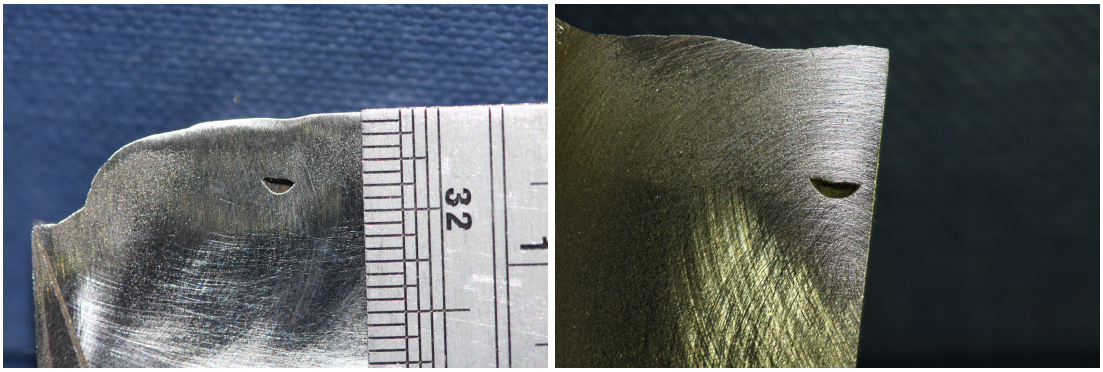

(a) (b)

Figure 7.9: Post-test imaging of clad embedded defects in specimen C31 (combined austenite and ferrite) at 7.9a) the edge of the original plate and 7.9b) in the mid-thickness of the original plate

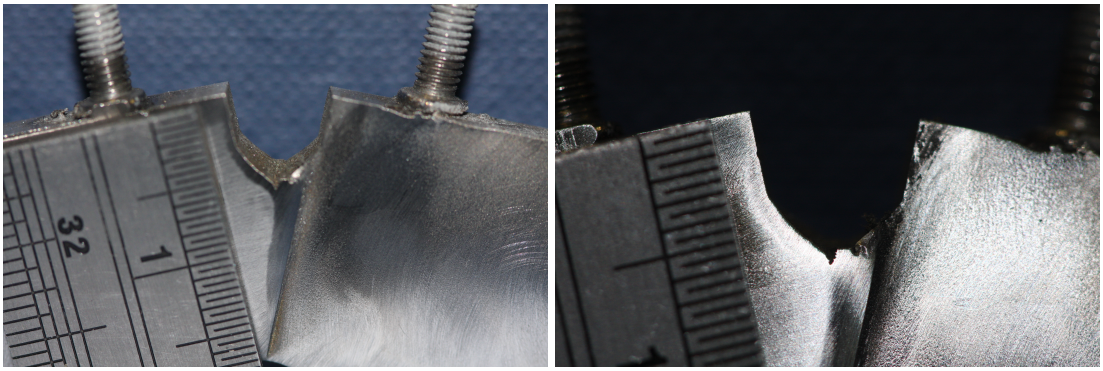

(a) (b)

Figure 7.10: Post-test imaging of mid-thickness defect in specimen C34 (combined austenite and ferrite) 7.10a) showing possible fatigue pre-crack and 7.10b) showing secondary crack.

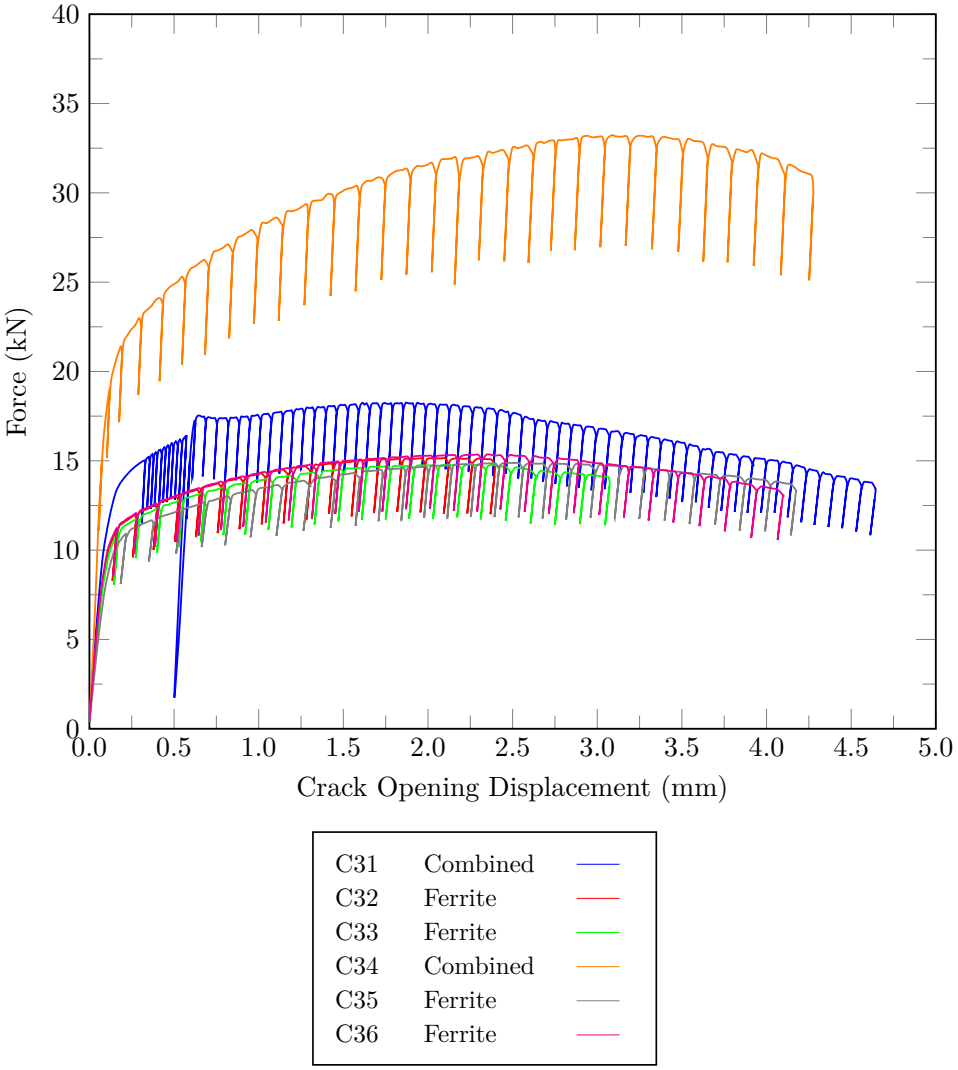

Figure 7.11: Force versus displacement for specimens with initial defect length $a/W = 0.30$

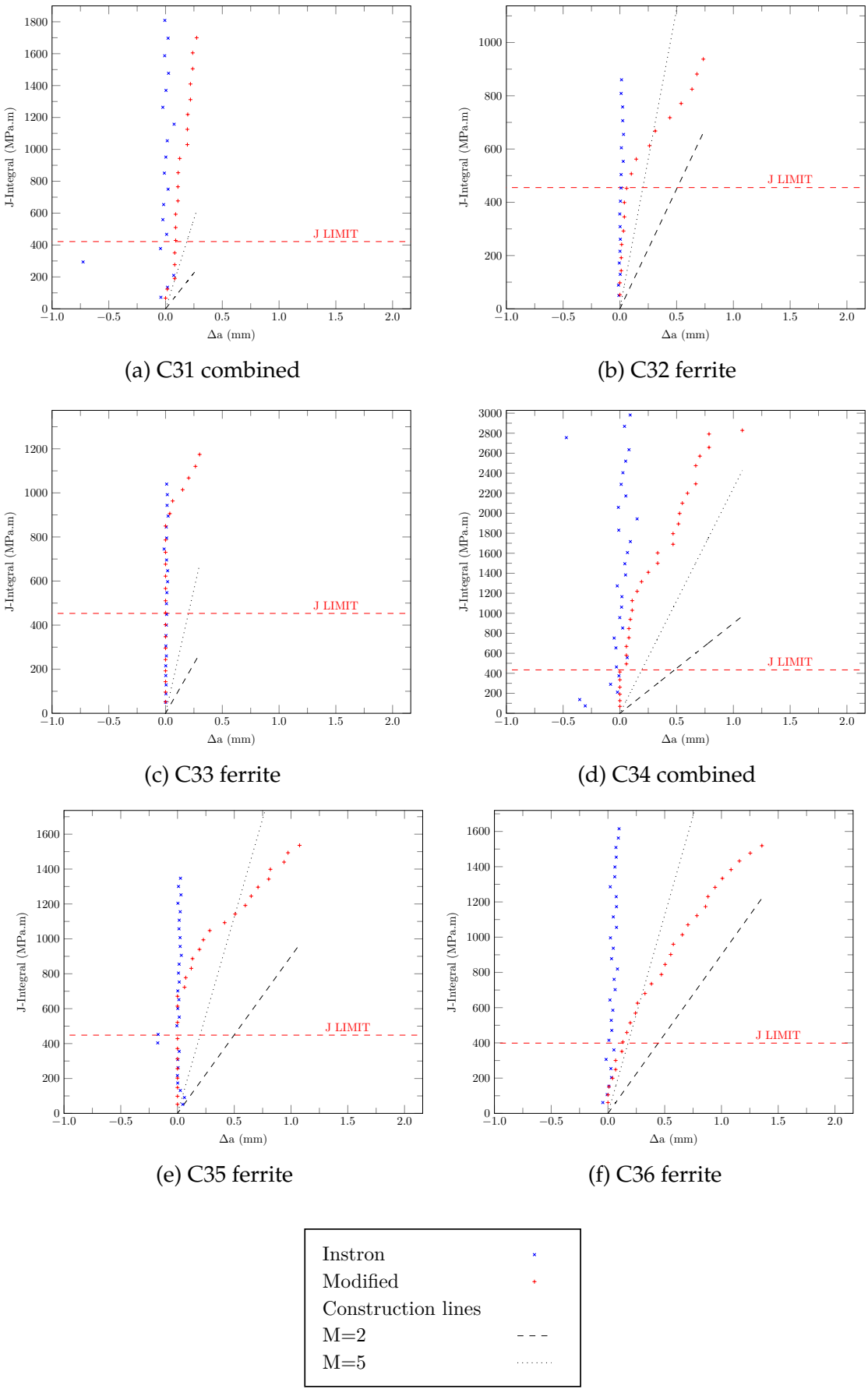

(a) C31 combined

(b) C32 ferrite

(c) C33 ferrite

(d) C34 combined

(e) C35 ferrite

(f) C36 ferrite

Figure 7.12: J-Integral versus crack extension (Δa) for C3 group. Original notch size $a/W = 0.30$

Table 7.2: Fracture toughness of SENB Group C3. Initial machined notch a_0 = 5.4 mm.

Sample & Test No.	**Material**	**Gauge length**	**Fatigue Cycles**	$a_{0\ elastic}$	$a_{0\ test}$	$a_{f\ test}$	$a_{f\ measured}$	**Comments**
		mm	N	mm	mm	mm	mm	
C31	Combined	10	15,000	5.83	5.74	5.23	-	Machined notch approximately 2 mm from interface. No visible fatigue pre-crack. Blunting of machined notch only. Several embedded defects found in the mid-thickness of cladding.
C32	Ferrite	10	38,262	4.87	4.86	5.02	7.87	Deviation of surface crack.
C33	Ferrite	10	51,900	4.92	4.92	5.09	8.34	Deviation of surface crack.
C34	Combined	10	32,000	5.48	5.18	5.09	6.74	Machined notch approximately 1 mm from interface. Significant deformation. Evidence of crack tunnelling.
C35	Ferrite	10	42,330	5.06	5.11	5.14	8.32	Bifurcation of crack on surface and in the mid-thickness.
C36	Ferrite	10	41,534	6.49	6.45	7.73	8.85	Bifurcation of surface crack. Deviation of crack in the mid-thickness.

Where $a_{0\ elastic}$ represents the initial crack length estimated during the elastic unloading prior to fracture testing, $a_{0\ test}$ the initial crack length estimated after first unloading sequence (SEQ10), $a_{f\ test}$ represents the final crack length estimated from final unloading sequence, and $a_{f\ measured}$ represents the maximum measured crack length at the mid-thickness of the sample post-test.

expected, furthermore this type of behaviour was not noted in combined samples from group C1 where the defect extended beyond the weld boundary, Figure 7.4d.

The metallography of the TIG weld has been previously discussed in detail in Section 4.1. It was shown that the hardness of the cladding was variable both along the width of the plate and through the thickness of the plate (see Section 4.1, Figure 4.3). Given the orientation of the samples (Figure 3.8) it can be presumed that the SENB samples from each group are broadly subject to similar metallurgical conditions. Considering the metallurgy of the cladding (changing grain orientations and multiple HAZ regions) the presence of hotspots in the clad region is not surprising. This metallurgy is likely contributing significantly to the growth of strain in the cladding outside areas influenced by the SCF of the notch. A defined HAZ zone, of martensitic material, was found to exist at the weld boundary (Figure 4.1). This region was shown to be significantly harder and stronger in comparison to either the cladding or base materials (see Figures 4.3 and 4.10). Given the results in Figures 7.13e to 7.13h and 7.14e to 7.14h it is possible that the HAZ acts as somewhat of a barrier to strains attempting to propagate from the cladding into the base material.

The shape of the profile in Figure 7.4d can be described as broadly elliptical with the minor axis extending from the notch tip through the remaining ligament. This profile occurs at the crack tip, a known SCF. The profiles in Figures 7.13h and 7.14h appear almost rectangular in comparison. If the HAZ were to act as barrier to strain growth then it must, by the same reasoning, be acting as a stress concentrating feature and hence the strain profile below the HAZ region would be expected to be similar to that noted in Figure 7.4d. Figure 7.15 shows annotated views of Figures 7.13h and 7.14h identifying the weld boundary and fitting an ellipsoid to the region below the boundary. As shown a reasonable approximation of an ellipsoid is found in both cases. This indicates that the weld boundary may act as a stress concentrating feature.

Unlike C31, sample C34 initiated and propagated a defect. While on the surface the defect was of negligible length (see Figure 7.15b) there was evidence of crack tunnelling.

Post-test visual inspection of the mid-thickness showed a defect extending from the notch tip through the cladding towards the materials boundary. The defect did not deviate from a central position in the mid-thickness region, in other words the weld boundary did not appear to inhibit defect propagation in any way (i.e. a straight defect tearing through the cladding into the ferrite material).

The initial defect depth of 5.4 mm ($a/W = 0.30$) used in these samples is shorter than the minimum allowable valid crack depth required by the test method [ASTM International, 2001]. The minimum crack depth recommended by the test standard ($a/W = 0.45$) ensures a high constraint condition at the crack tip which in turn promotes brittle fracture. Reducing the depth of the defect results in a loss of constraint and hence ductile failure modes are increasingly likely. The prevalence of crack tunnelling may be attributed, at least in part, to the loss of in-plane constraint (i.e. constraint due to the ratio of crack depth to specimen height). Given that the samples discussed in this section will have been subject to less triaxiality compared to the deeply notched specimens (see Section 7.1.1) comparisons between combined samples and homogeneous samples should be limited to those with similar notch depths (i.e. comparisons should be limited to samples of the same group).

Figure 7.16 plots the major strain (Figures 7.16a to 7.16d) and strains in the thickness direction (Figures 7.16e to 7.16h) for peak force positions associated with the first, fifth, mid-test and final unloading positions, respectively. In terms of major strain comparing Figure 7.16a to Figures 7.13a and 7.14a it can be seen that high magnitudes of strain exist in a greater area in the homogeneous sample when compared to the combined samples. As the test continues the strain distributions become more dis-similar (compare Figure 7.16c to Figures 7.13c and 7.14c) with strains in the clad samples (Figures 7.13c and 7.14c) tending to grow laterally to the clad tip whereas the homogeneous samples show elongated strains pointing in the direction of the remaining ligament. Mid-way through testing clad samples show high magnitudes of strain through the entire ligament of the sample (Figures 7.13c and 7.14c). Comparatively the homogeneous samples (see Figure 7.16c) show high magnitudes of strain are limited to the

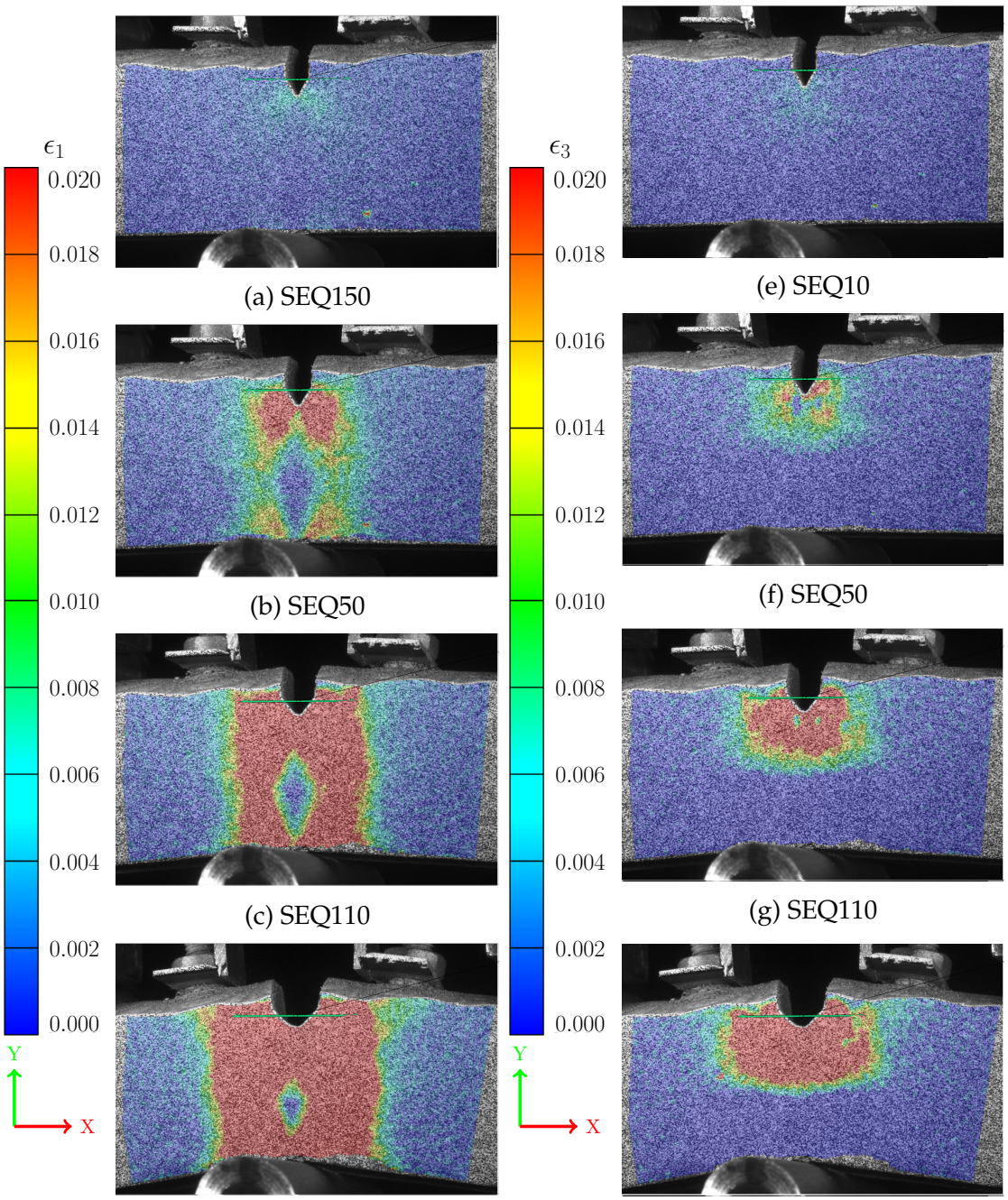

(a) SEQ150 (e) SEQ10

(b) SEQ50 (f) SEQ50

(c) SEQ110 (g) SEQ110

(d) SEQ210 (h) SEQ210

Figure 7.13: DIC data for combined specimen C31 with initial defect length $a/W = 0.15$. Figures 7.13a and 7.13d showing the true major strain and Figures 7.13e and 7.13h showing strains in thickness direction. Results of first, fifth, mid-test and final peak (force) unloading positions, respectively.

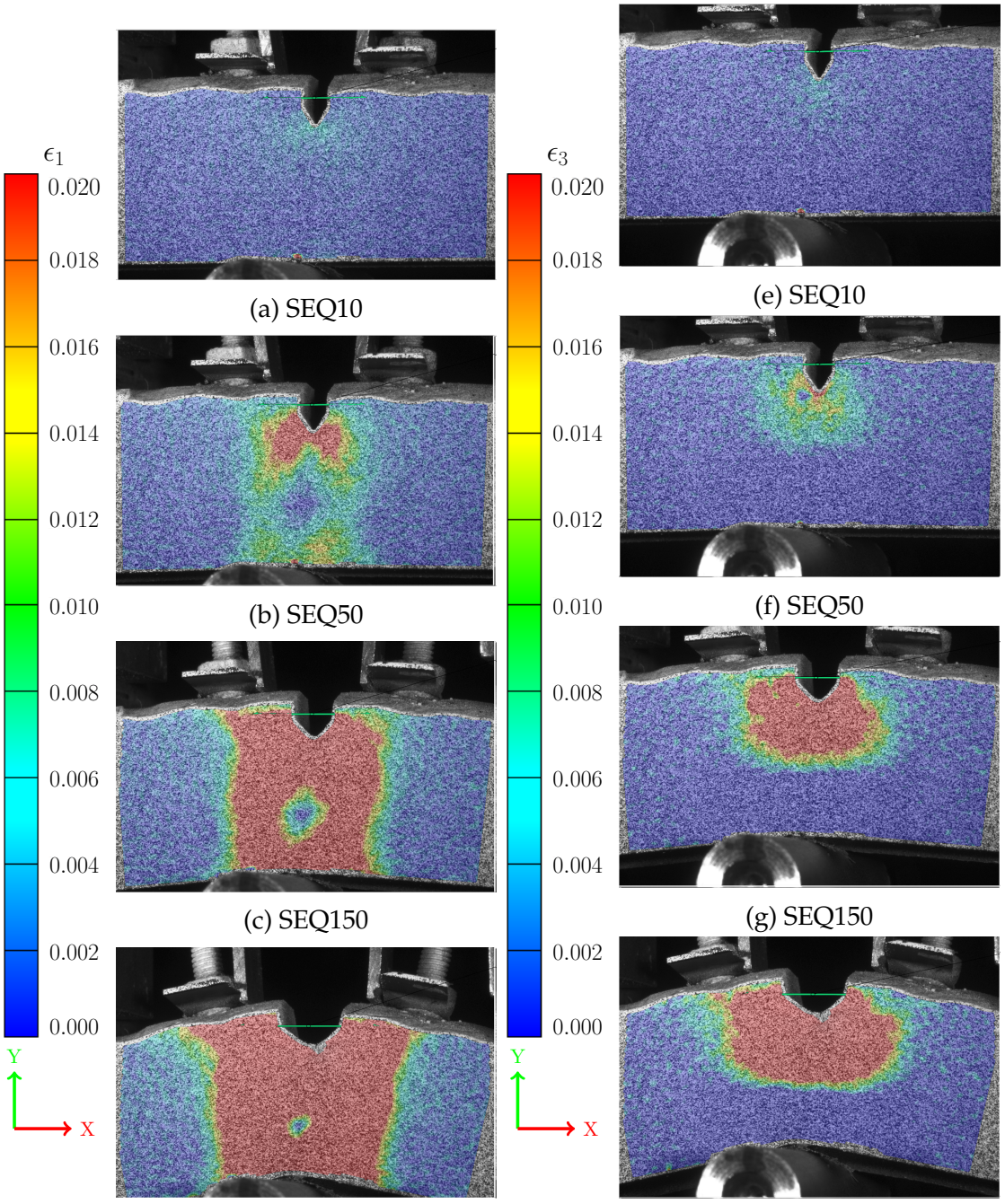

(a) SEQ10 (e) SEQ10

(b) SEQ50 (f) SEQ50

(c) SEQ150 (g) SEQ150

(d) SEQ290 (h) SEQ290

Figure 7.14: DIC data for combined specimen C34 with initial defect length $a/W = 0.30$. Figures 7.14a and 7.14d showing the true major strain and Figures 7.14e and 7.14h showing strains in thickness direction. Results of first, fifth, mid-test and final peak (force) unloading positions, respectively.

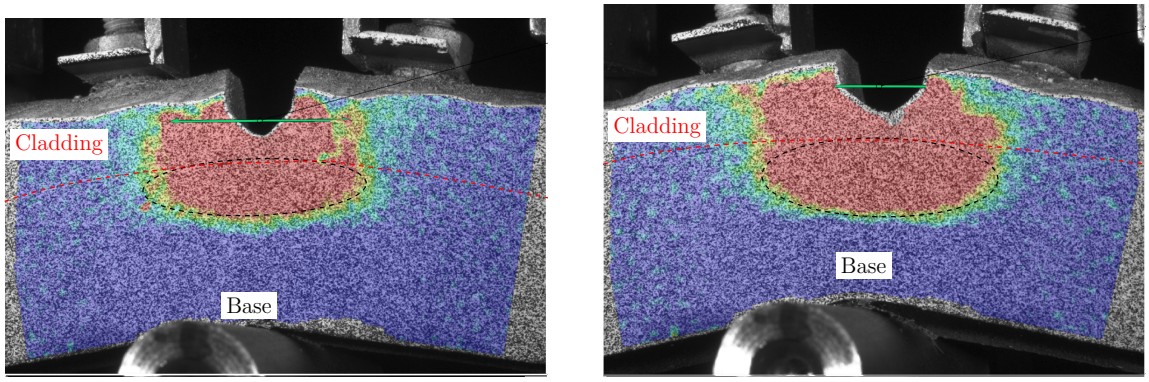

(a) (b)

Figure 7.15: Annotated view of Figure 7.13h (Figure 7.15a) and Figure 7.13h (Figure 7.15b), respectively. Showing idealised profile shape for strain in thickness direction beneath the weld boundary

area of the remaining ligament (i.e. they only occur below the crack tip region). Strains in the thickness direction for a homogeneous material of defect size $a/W = 0.30$ are shown in Figures 7.16e to 7.16h. As shown high magnitudes of strain begin in the region surrounding the crack tip. The shape of the profile up to the mid-point of testing (Figures 7.16f and 7.16g) appear broadly elliptical in shape and are similar to those seen previously for deeper notches (Figures 7.7b, 7.7a, 7.7d). The shape of the profile differs significantly from that noted for combined samples. Interestingly, the shape of the profile found in combined sample C11 (Figure 7.4d) is more similar to homogeneous samples than to that of the combined samples tested here. The main difference between samples C11, C31 and C34 was the depth of the machined notch. Where the notch in C11 extended beyond the weld boundary into the base material, the notches in C31 and C34 did not. This trend implies that once a defect has propagated through the weld boundary the impact, of the boundary, on the distribution of strain is negligible.

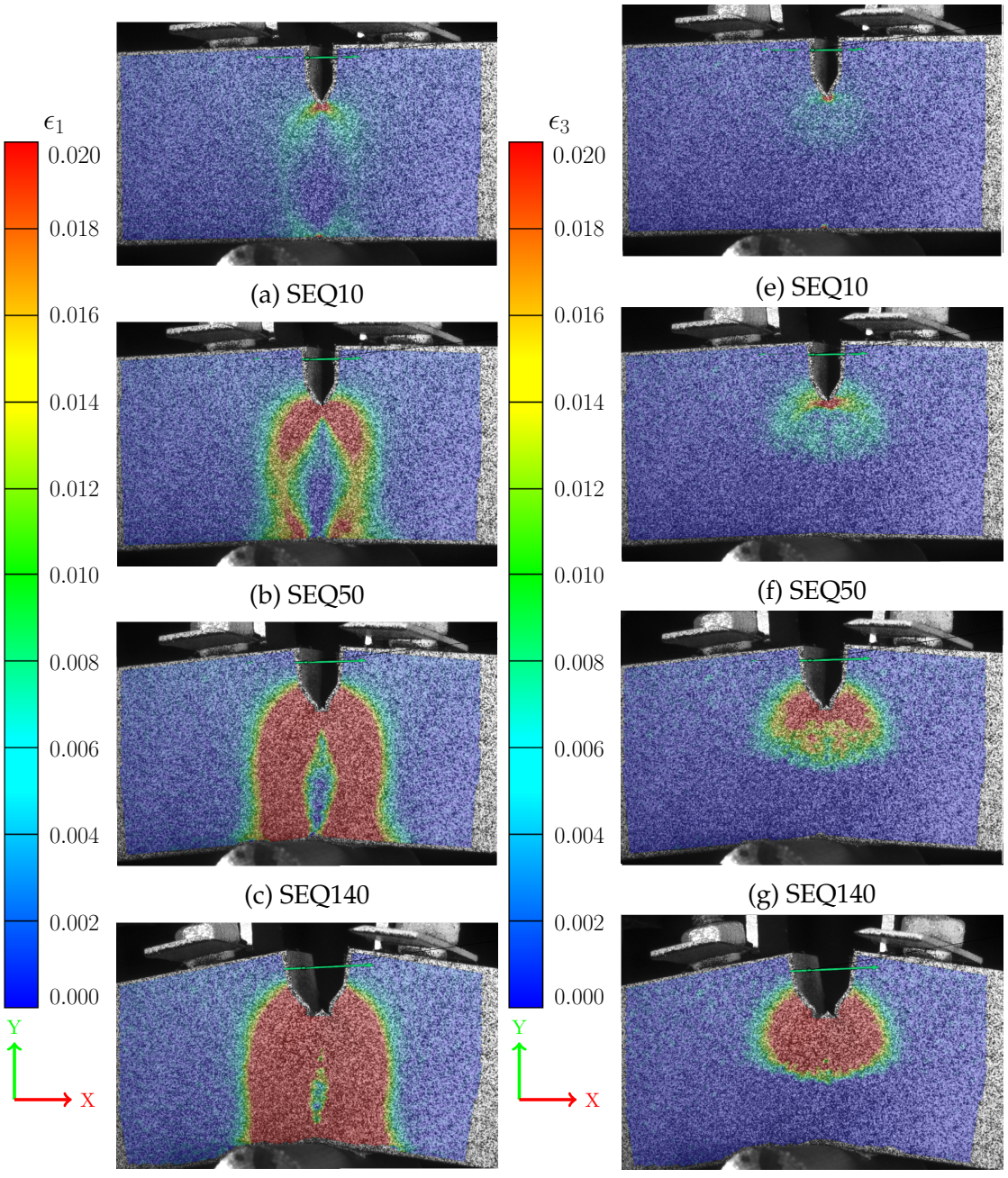

(a) SEQ10 (e) SEQ10

(b) SEQ50 (f) SEQ50

(c) SEQ140 (g) SEQ140

(d) SEQ280 (h) SEQ280

Figure 7.16: DIC data for homogeneous specimen C35 with initial defect length $a/W = 0.30$. Figures 7.16a and 7.16d showing the true major strain and Figures 7.16e and 7.16h showing strains in thickness direction. Results of first, fifth, mid-test and final peak (force) unloading positions, respectively.

7.1.3 Defects in the cladding

As discussed earlier (see Section 7.1.1) several samples were tested twice using different clip gauges. Specimens tested using the smaller clip gauge (2 mm travel) did plastically deform but did not initiate or propagate defects. Figure 7.17 plots force against CMOD for each of the specimens from group C2 which had initial defects measuring $a/W = 0.15$. Table 7.3 lists details about the defect depth at various stages of testing. The J-Δa curves are shown in Figure 7.18. Similar to the previous results (Sections 7.1.1 and 7.1.2) no valid J_{1C} or J_Q values were derived from test results when the test standard validity limits were applied. Sample C21 did not initiate a fatigue pre-crack. Post-test inspection of the mid-thickness (Figure 7.19) showed a small defect near the notch root. The defect measures less than 0.5 mm in depth and does not extend from the mid-thickness to the surface. From Figure 7.18a it can be seen that a small amount of crack growth was noted towards the end of the test. Like sample C31 a number of embedded defects were noted in the clad region, these are shown in Figure 7.20. While these defects are smaller in volume than those noted in sample C31 they were more frequent and they appeared to be distributed throughout the entire length of the specimen. Specimen C24 certainly contained a fatigue pre-crack prior to fracture testing (see Table 7.3 and Figure 7.21). The pre-crack depth was estimated to be approximately 1 mm, in the mid-thickness, prior to the fracture test. As shown in Figure 7.21 signficant crack growth occurred in comparison to other clad samples. The final crack depth in the mid-thickness region was measured to be 9.2 mm. The crack appears to have deviated from its original path at the materials boundary. Figure 7.18d shows that a significant increase in crack length was noted to have occurred twice during testing (between the ranges 0.25-0.5 mm and 1.4 - 1.8 mm of crack growth, respectively).

The true major and through thickness strains for combined samples C21 and C24 are shown in Figures 7.22 and 7.23, respectively. Figure 7.25 shows a similarly notched homogeneous specimen for reference. In terms of major strain and comparing Figures 7.13b and 7.14b (group C3) with Figures 7.22b and 7.23b (group C2) it can be seen that the shape of the profile is broadly similar. Figures 7.22c, 7.23c and 7.23d clearly indi-

cate that the strains have a tendency to grow at a faster rate in the cladding compared to the rate of growth in the base material (i.e. along the remaining ligament). Furthermore a distinct reduction in strain is noted at the approximate location of the weld boundary. Strains in the thickness direction predominately show the behaviour that was noted previously with localised hotspots. As previously stated these hotspots are likely occurring at local micro-structural changes. Unlike deeper defects (group C3) the strain distribution in the thickness direction of these samples does not exhibit an elliptical shape below the weld boundary. However, it should be noted that strains are limited, in both samples, to the clad area. Strains do not appear to propagate into the base material despite the growth of a large defect in sample C24 (see Figure 7.23j). Comparatively Figure 7.25 is comparable with homogeneous data from groups C1 and C3.

The growth of the defect in C24 occurred via a series of micro-cracks on the surface of the sample. Figures 7.24a and 7.24b show the defect initiating at 45°C to the notch tip, this is not unexpected and similar defect initiation angles have been noted in other samples. Figures 7.24c to 7.24j show multiple parallel initiation points at various steps of the test. It is interesting to note that after the defect initiates (in the expected manner) further micro-cracks initiate at lateral positions offset from the existing tear (i.e. the defect does not propagate in a straight line but rather additional micro-cracks are initiated offset laterally to the first defect). The formation of defects in this manner is likely due to a combination of factors such as: 1) Variations in local microstructure, 2) variability in constraint conditions through thickness influencing surface cracking, 3) global constraint conditions. For example the localised hotspots of strain (see Figures 7.23g and 7.23h) are postulated as resulting from local microstructural changes and possible HAZ regions in the cladding. HAZ regions are likely to be stronger but less ductile than the surrounding material, hence they can achieve higher magnitudes of strain but fail in a predominately brittle manner. If the surrounding bulk material is assumed to be failing in a ductile manner (MVC) then, as subsequent voids start to coalesce, the strain in the hotspot regions (whether due to preferentially oriented

grains or HAZ material) increases significantly. Once the strain has exceeded a critical value the region fails. If failure of the hotspot region (i.e. in the HAZ) occurs prior to plastic collapse of the surrounding bulk material then it is possible strain is re-distributed to surrounding HAZ zones. This could result in a failure such as that seen here, where a small tear is surrounded by, seemingly, undamaged bulk material (see Figure 7.24e).

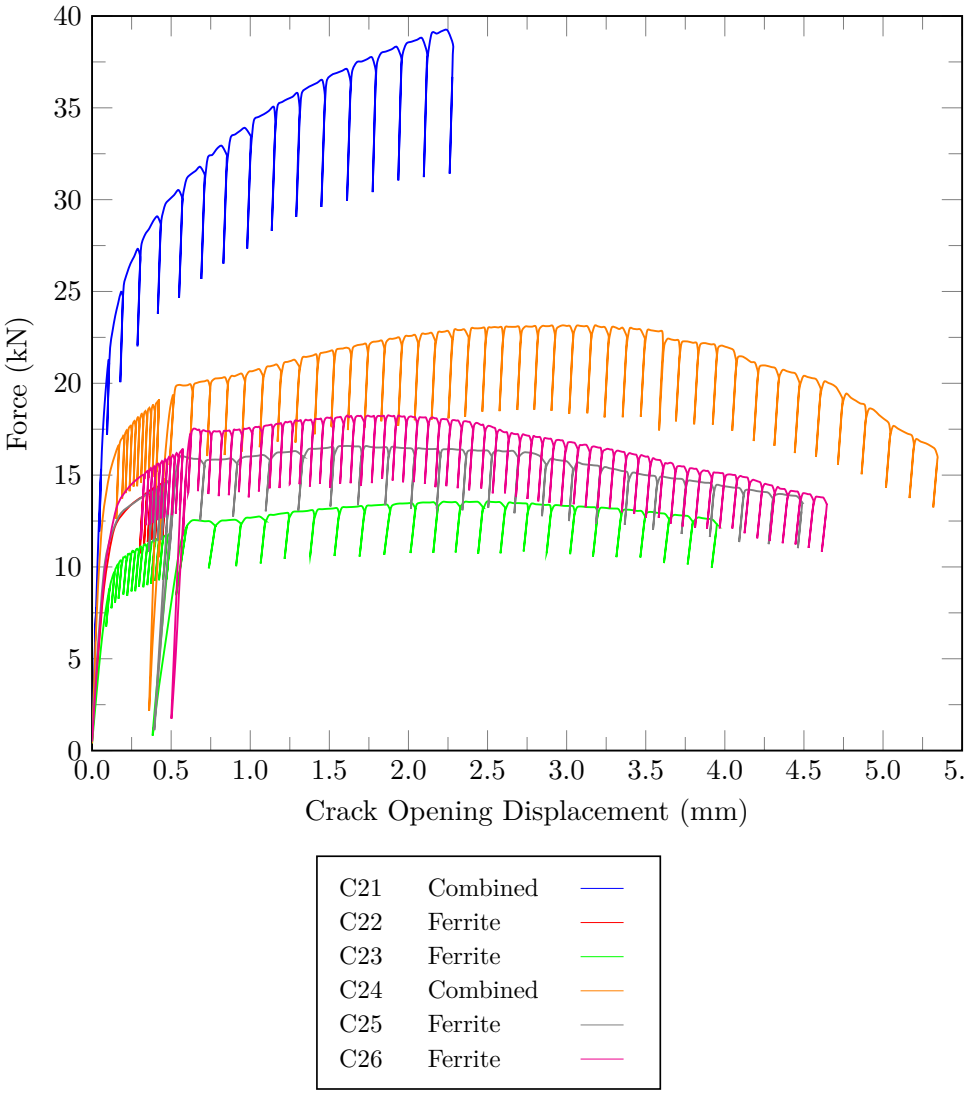

Figure 7.17: Force versus displacement for specimens with initial defect length $a/W = 0.15$

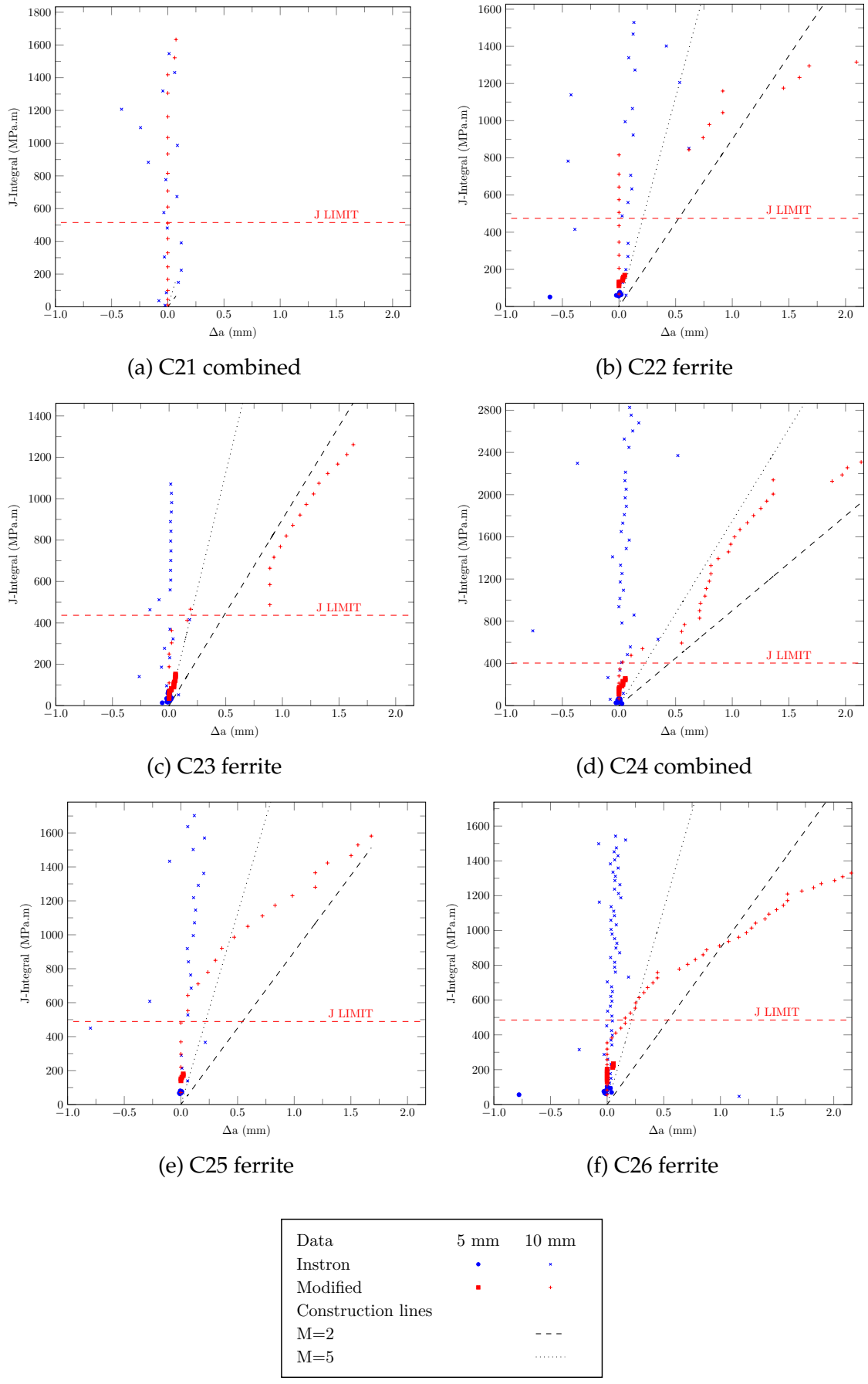

(a) C21 combined

(b) C22 ferrite

(c) C23 ferrite

(d) C24 combined

(e) C25 ferrite

(f) C26 ferrite

Figure 7.18: J-Integral versus crack extension (Δa) for C2 group. Original notch size $a/W = 0.15$

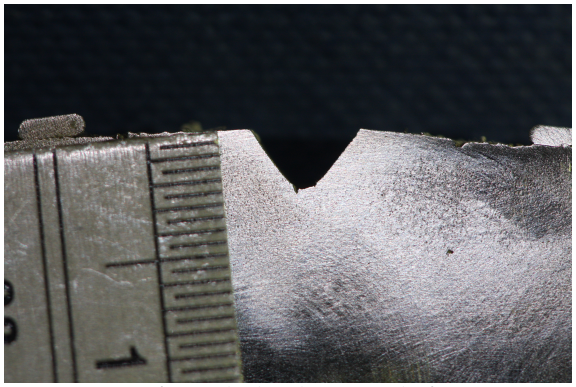

Figure 7.19: Post-test imaging of mid-thickness defect in specimen C21 (combined austenite and ferrite)

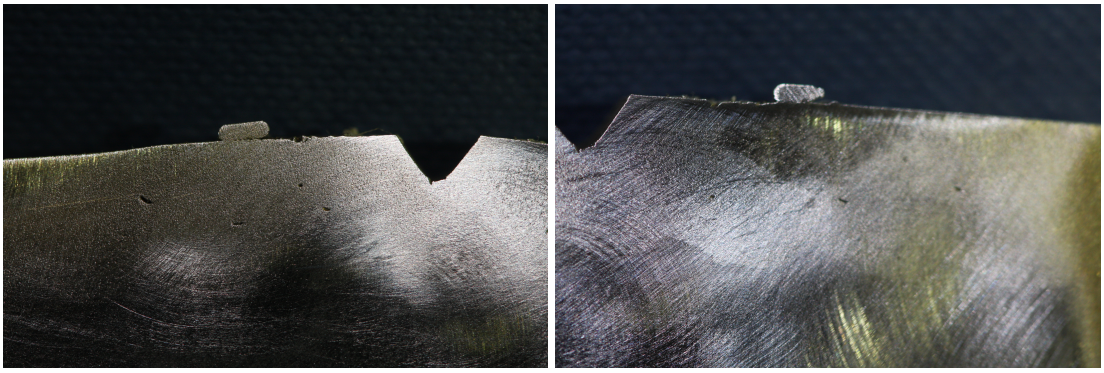

(a) (b)

Figure 7.20: Post-test imaging of clad embedded defects in specimen C21 (combined austenite and ferrite)

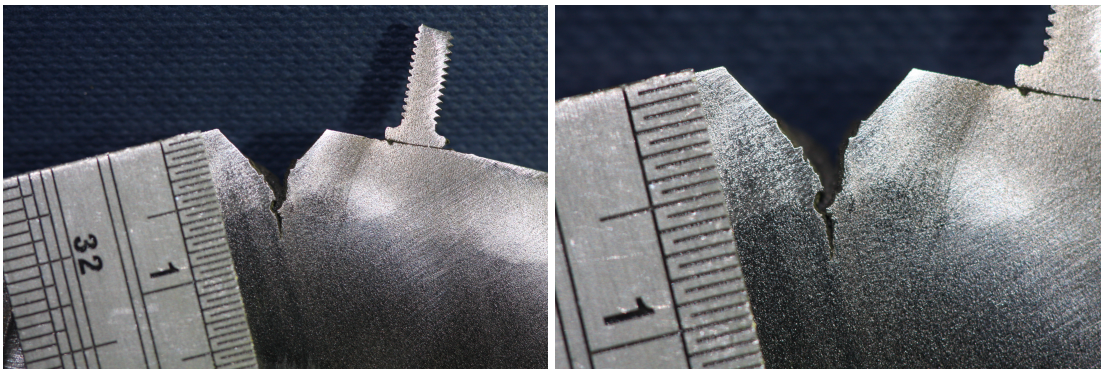

Figure 7.21: Post-test imaging of mid-thickness defect in specimen C24 (combined austenite and ferrite)

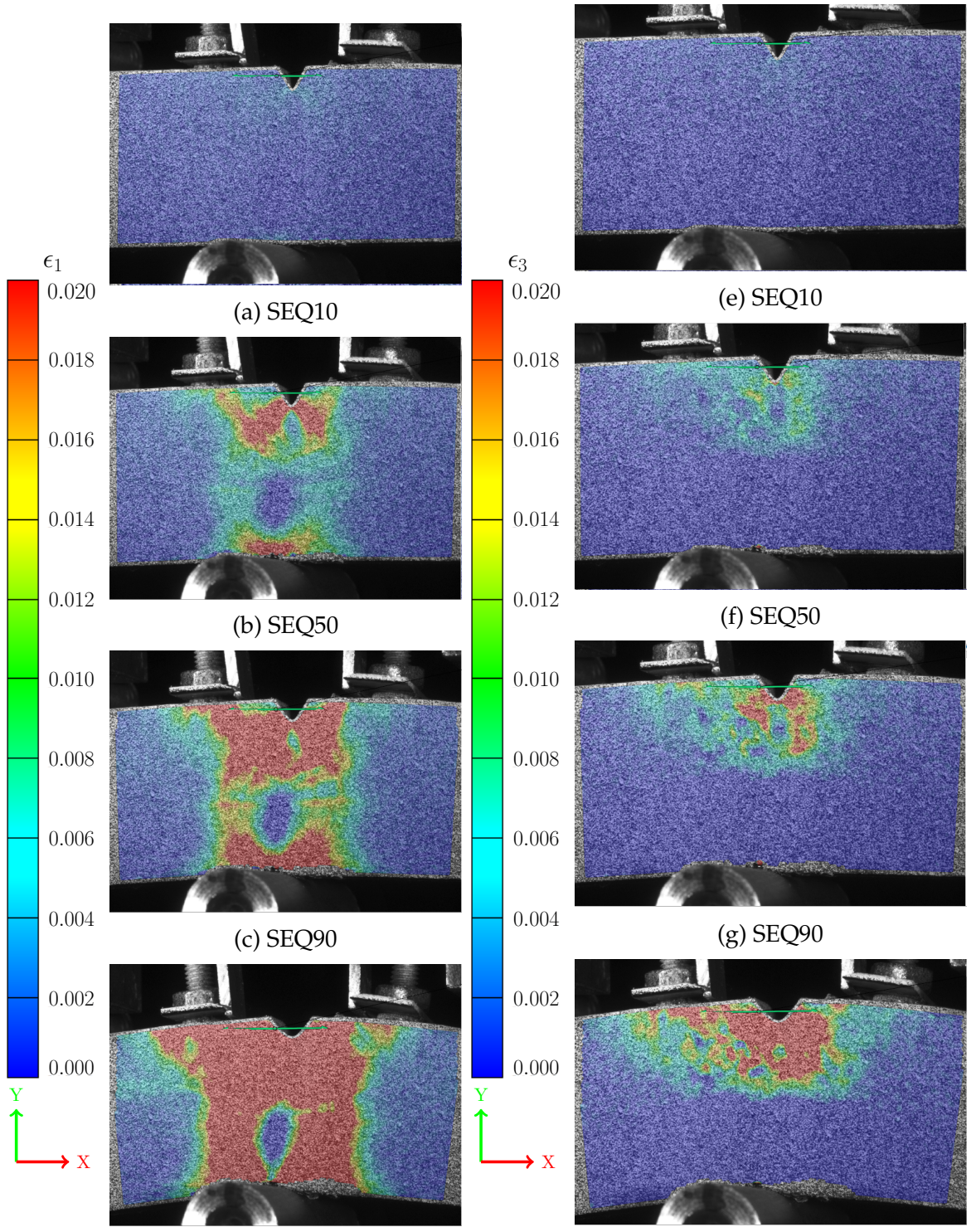

(a) SEQ10 (e) SEQ10

(b) SEQ50 (f) SEQ50

(c) SEQ90 (g) SEQ90

(d) SEQ180 (h) SEQ180

Figure 7.22: DIC data for combined specimen C21 with initial defect length $a/W = 0.15$. Figures 7.22a and 7.22d showing the true major strain and Figures 7.22e and 7.22h showing strains in thickness direction. Results of first, fifth, mid-test and final peak (force) unloading positions, respectively.

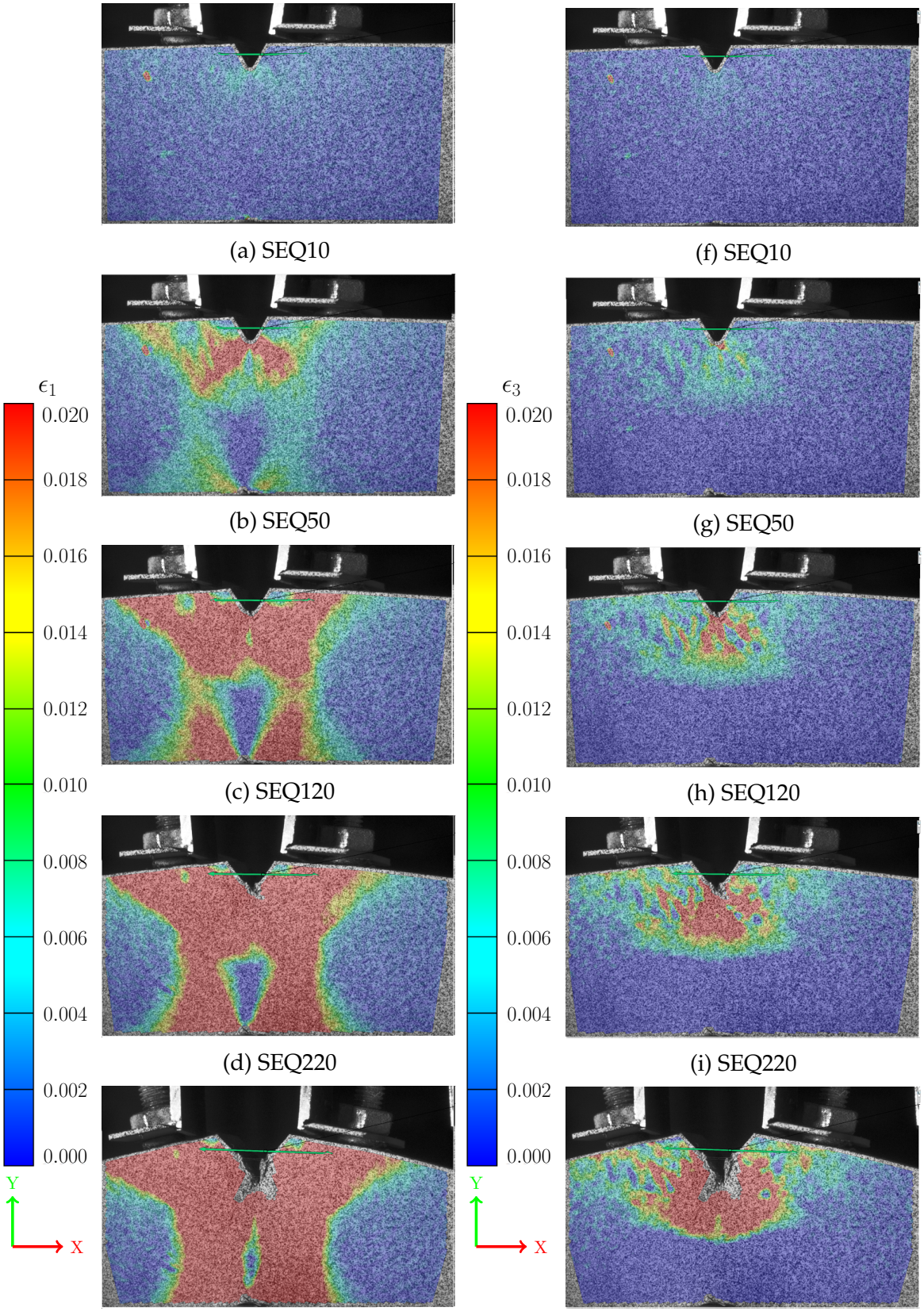

(a) SEQ10 (f) SEQ10

(b) SEQ50 (g) SEQ50

(c) SEQ120 (h) SEQ120

(d) SEQ220 (i) SEQ220

(e) SEQ430 (j) SEQ430

Figure 7.23: DIC data for combined specimen C24 with initial defect length $a/W = 0.15$. Figures 7.22a and 7.22d showing the true major strain and Figures 7.22e and 7.22h showing strains in thickness direction. Results of first, fifth, mid-test and final peak (force) unloading positions, respectively.

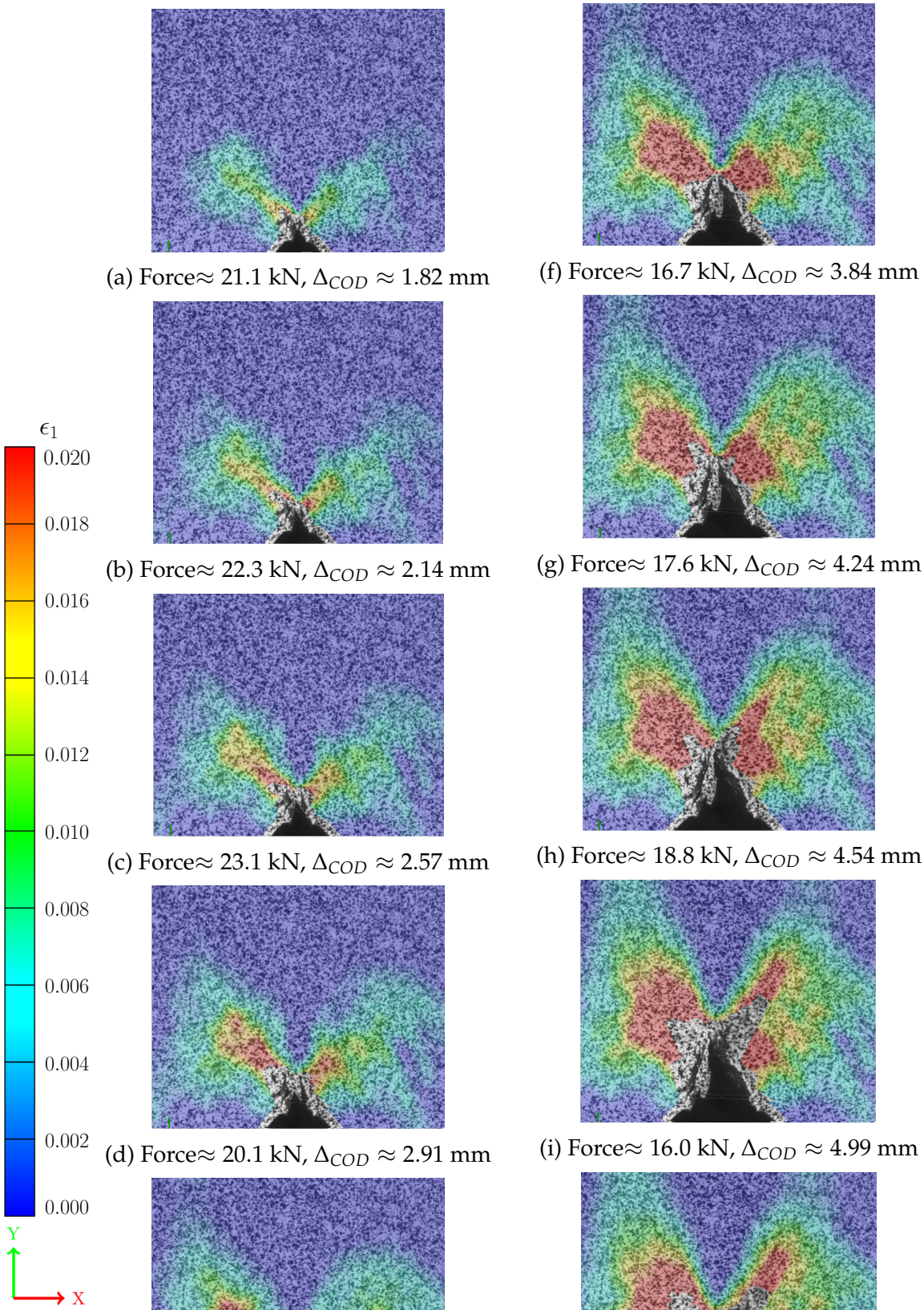

(a) Force≈ 21.1 kN, $\Delta_{COD} \approx 1.82$ mm

(b) Force≈ 22.3 kN, $\Delta_{COD} \approx 2.14$ mm

(c) Force≈ 23.1 kN, $\Delta_{COD} \approx 2.57$ mm

(d) Force≈ 20.1 kN, $\Delta_{COD} \approx 2.91$ mm

(e) Force≈ 18.0 kN, $\Delta_{COD} \approx 3.58$ mm

(f) Force≈ 16.7 kN, $\Delta_{COD} \approx 3.84$ mm

(g) Force≈ 17.6 kN, $\Delta_{COD} \approx 4.24$ mm

(h) Force≈ 18.8 kN, $\Delta_{COD} \approx 4.54$ mm

(i) Force≈ 16.0 kN, $\Delta_{COD} \approx 4.99$ mm

(j) Force≈ 16.3 kN, $\Delta_{COD} \approx 4.99$ mm

Figure 7.24: DIC data showing crack propagation on surface of combined sample C24

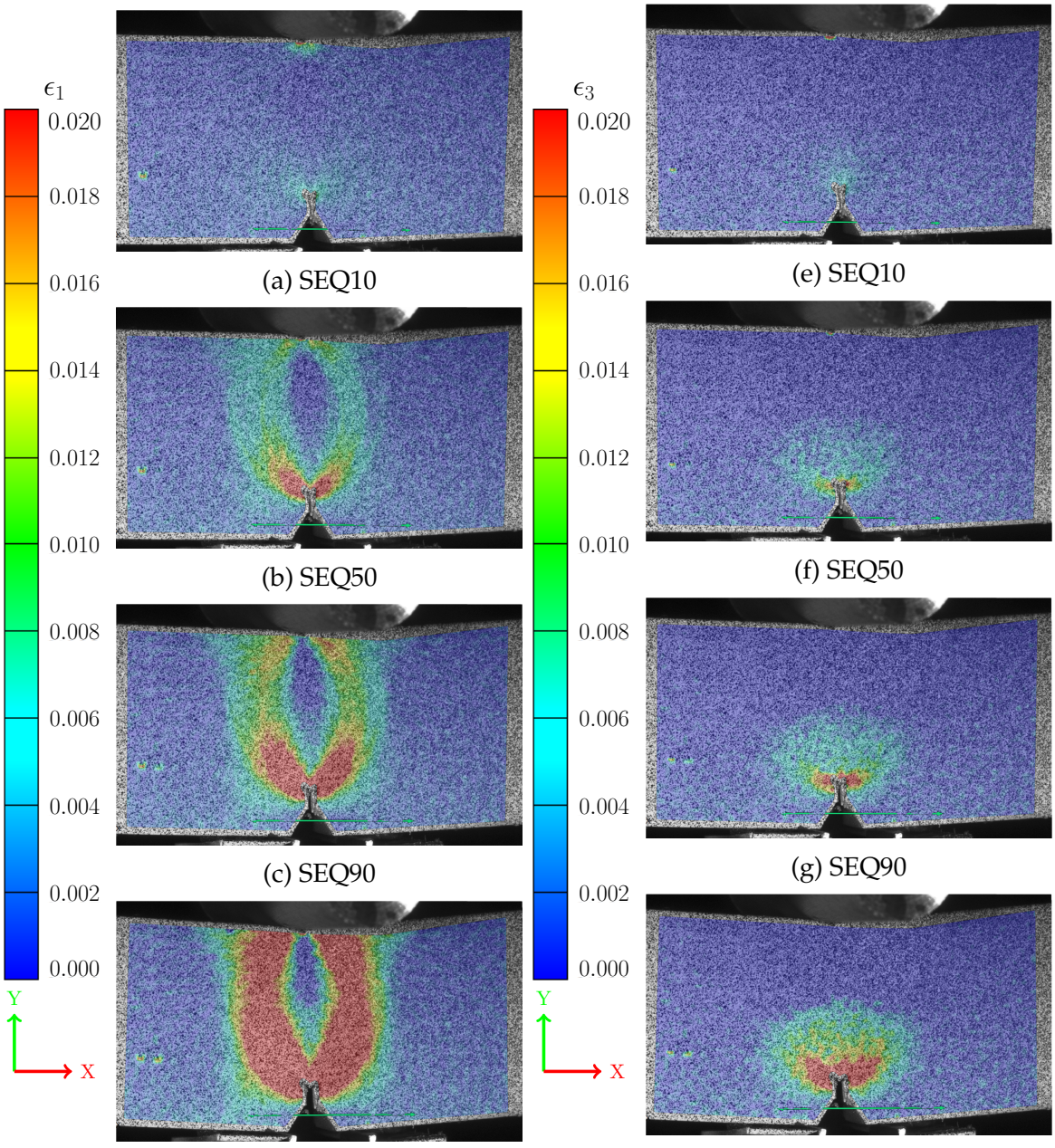

(a) SEQ10 (e) SEQ10

(b) SEQ50 (f) SEQ50

(c) SEQ90 (g) SEQ90

(d) SEQ180 (h) SEQ180

Figure 7.25: DIC data for homogeneous ferrite specimen C26 with initial defect length $a/W = 0.15$. Figures 7.25a and 7.25d showing the true major strain and Figures 7.25e and 7.25h showing strains in thickness direction. Results of first, fifth, ninth and eighteenth peak (force) unloading positions, respectively.

Table 7.3: Fracture toughness of SENB Group C2. Initial machined notch a_0 = 2.7 mm.

Sample & Test No.	**Material**	**Gauge length**	**Fatigue Cycles**	$a_{0\ elastic}$	$a_{0\ test}$	$a_{f\ test}$	$a_{f\ measured}$	**Comments**
		mm	N	mm	mm	mm	mm	
C21	Combined	10	100,000	3.28	3.26	2.78	3.89	No visible fatigue pre-crack. Blunting of machined notch, possible initiated defect on mid-thickness.
C22	Ferrite	5	175,636	4.44	3.83	3.84	-	
C22_2	Ferrite	10	142,298	5.70	5.76	7.43	9.05	Deviation of surface crack. Evidence of crack tunnelling.
C23	Ferrite	5	175,636	7.16	7.10	7.08	-	
C23_2	Ferrite	10	86,289	5.41	5.49	5.26	8.92	Deviation of surface crack. Bifurcation of crack tip in the mid-thickness.
C24	Combined	5	137,690	2.87	2.89	2.86	-	
C24_2	Combined	10	1,268	5.44	5.37	6.44	9.20	Deviation of surface crack. Clear indication of crack tunnelling. Crack propagating through cladding in the mid-thickness
C25	Ferrite	5	182,949	4.02	4.01	4.00	-	
C25_2	Ferrite	-	10	6.35	6.35	7.14	9.26	Bifurcation on surface. Evidence of crack tunnelling.
C26	Ferrite	5	56,860	4.30	3.52	3.52	-	
C26_2	Ferrite	10	-	4.00	5.16	7.74	8.69	Deviation of surface crack. Evidence of crack tunnelling.

Where $a_{0\ elastic}$ represents the initial crack length estimated during the elastic unloading prior to fracture testing, $a_{0\ test}$ the initial crack length estimated after first unloading sequence (SEQ10), $a_{f\ test}$ represents the final crack length estimated from final unloading sequence, and $a_{f\ measured}$ represents the measured crack length at the mid-thickness of the sample post-test.

7.2 2D Modelling of SENB specimens

7.2.1 Comparison of homogeneous and combined material models

Plane stress and plane strain 2D models investigating the response of homogeneous and combined samples under three point bending were investigated. The model geometry was based on experimental specimen geometries. Elastic-plastic material properties (as outlined in Table 4.2) were assigned to the relevant areas. In the case of single material models ferrite or austenite material properties were assigned to the entire model. For combined material models austenite material properties were assigned to a region 6 mm in depth from the top surface (Figure 7.26) similar to that of the experimental test specimens. The remainder of the model was assigned ferrite material properties. Large strain analyses were conducted using the non-linear option in Abaqus.

The crack tip was modelled at 0.1 mm distance from the machined notch using a seam to reproduce a sharp defect similar to what is expected from fatigue pre-cracking. Collapsed wedge elements with duplicated nodes and a midside position of 0.25 were applied to the first contour to enable crack tip blunting. Structured elements were used in all other areas. A boundary condition was applied to one node in the center of the specimen to prevent rigid body motion (U1 = 0) of the specimen. The rollers were modelled as analytical rigid bodies with a frictionless, hard contact specified between the surface of the specimen and the surface of the pins. Boundary conditions were applied to reference nodes in the center of the pins which were then kinematically coupled to the surface of the pins so that (U1 = U2 = UR1 = UR2). The two supporting rollers were constrained using the encastre boundary condition (U1 = U2 = UR1 = UR2 = 0), the third roller was displaced in the position Y-direction to a maximum displacement of 1 mm.

Specimens were meshed using element types CPE8R for plane strain and CPS8R for plane stress. In all cases a minimum of 6000 elements were used. Figure 7.26 shows

the boundary conditions and mesh applied to each specimen geometry. For clarity Figure 7.26 indicates the material properties used in the combined material models. The homogeneous material modes assumed identical material properties for the entire geometry.

Figure 7.27 plots the force versus displacement trace for each specimen type under plane stress and plane strain conditions. As shown that higher forces are predicted in the plane strain condition for each displacement compared to the plane stress analysis. This is expected given that plane strain conditions are more highly constrained in comparison to their plane stress counterparts. Figure 7.27a shows that for a crack depth of $a/W = 0.15$ the combined model has a response identical to the homogeneous austenite material model. Considering that the defect in the combined material model is located in the austenite material and, given that for this notch depth ($a/W = 0.15$) a significant portion of the remaining ligament is in austenitic material, this is not unexpected. Similarly Figure 7.27c shows that for defects located in the ferrite material results are identical to that of a homogeneous ferrite material model. Interestingly Figure 7.27b shows that for defects located in the austenite material close to the materials boundary the response is similar, though not identical, to that of the homogeneous ferrite model.

Given the clear increase in load-displacement for the plane strain assumption in comparison to the plane stress assumption the plane strain analyses were investigated in-depth. The stresses perpendicular to the notch tip (i.e. the x-direction) were investigated along the remaining ligament for the combined material models assuming a plane strain assumption. Figure 7.28 plots the direct stress (σ_{xx}) along the remaining ligament for each initial crack depth. For short defects ($a/W = 0.15$, Figure 7.28a) the stress at the weld boundary is similar for both the austenite and ferrite materials. Indeed over the range of displacement values investigated the stresses at the materials interface do not appear to be influenced by the presence of a materials interface and the resulting trend is similar to what is expected from a single material model. For a deeper defect ($a/W = 0.30$, Figure 7.28b) however there is a distinct change in stress

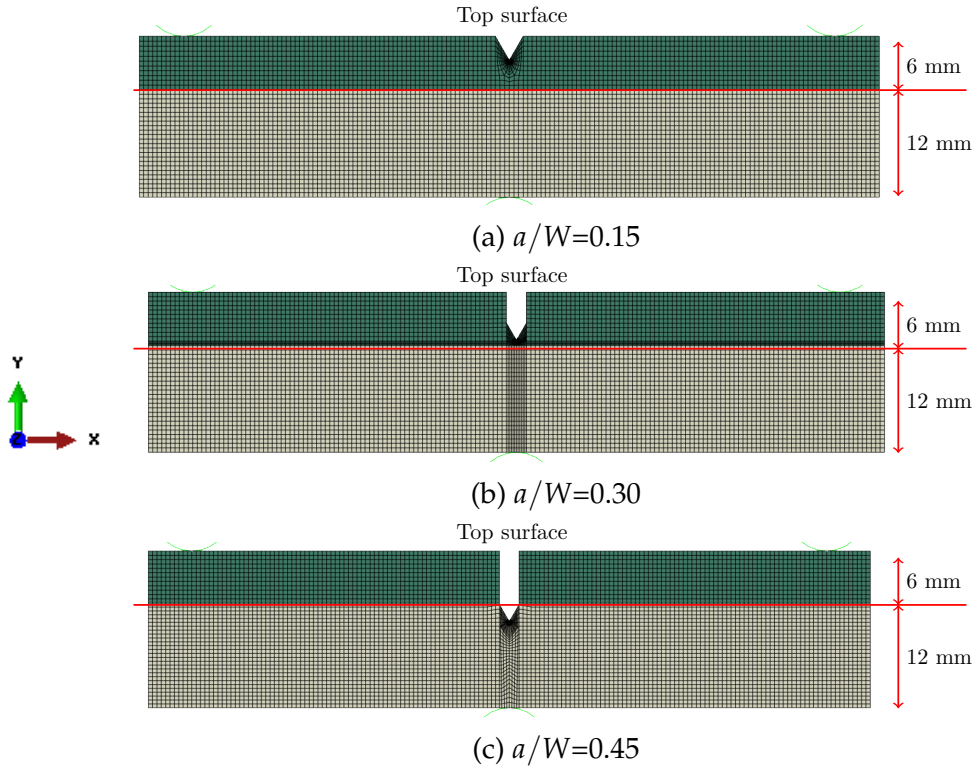

(a) a/W=0.15

(b) a/W=0.30

(c) a/W=0.45

Figure 7.26: FE models showing boundary conditions and meshing for notch depths: 7.26a) $a/W = 0.15$, 7.26b) $a/W = 0.30$, 7.26c) $a/W = 0.45$

at the weld boundary furthermore as the displacement increases so to does the disparity between stresses in the base and clad materials. At displacements equal to, or greater than, 0.150 mm the stress in the base material is predicted to exceed that of the cladding. Defects extending past the materials boundary ($a/W = 0.45$, Figure 7.28c) do not appear to be impacted by the presence of the weld.

Given that the austenite and ferrite materials have significantly different yield strengths it is not immediately clear whether the the ferrite or austenite materials have yielded. The normalised stress ($\sigma_{xx}/\sigma_{yield}$) is plotted in Figures 7.29a and 7.29b for initial crack lengths of $a/W = 0.15$ and $a/W = 0.30$, respectively. A magnified view of the materials boundary region is shown in Figures 7.29c and 7.29d. These plots give some indication of which material is most likely to yield first. From Figure 7.29c and 7.29d it can be seen that the stress decreases as distance from the crack tip increases. The rate at which the stress decreases changes with respect to the applied displacement so that at small displacements the rate of decrease in stress is significant, whilst at larger displacements the rate of decrease is less. This is due to the increasing size of the plastic

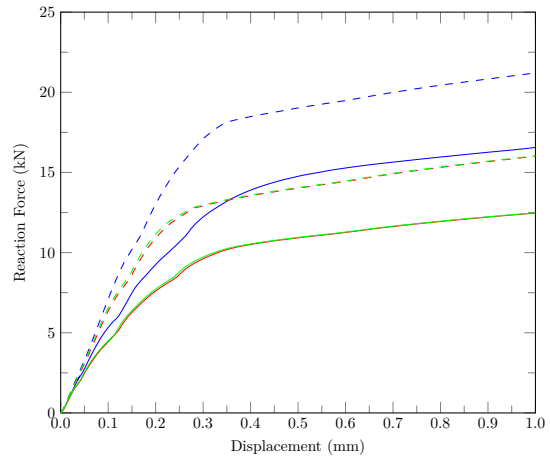

(a) $a/W = 0.15$

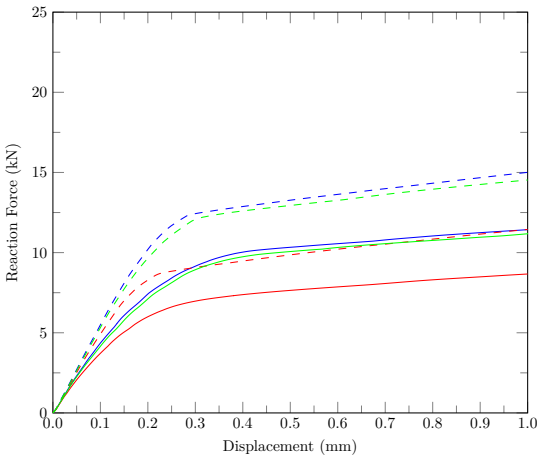

(b) $a/W = 0.30$

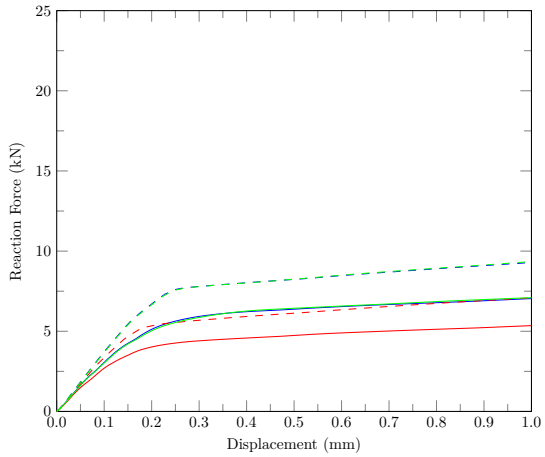

(c) $a/W = 0.45$

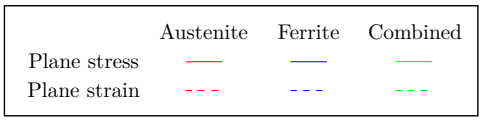

Figure 7.27: Comparison of force versus displacement curves for defects of size a/W=0.15 under plane stress and plane strain conditions

zone at larger applied displacements. As shown the austenite material is predicted to reach yield prior to the ferrite material. Figures 7.29c and 7.29d also show that as the displacement increases the disparity between each material on the interface increases. Nevertheless the prediction is that the cladding material is subject to higher stresses compared to the base material.

The stress was normalised using the yield strength of the relative material. Figure 7.29b shows yield occurring at the materials interface at relatively small applied displacements, this is not unexpected as, given the proximity of the defect to the weld boundary. From Figure 7.29d it can be seen that the entire cladding is predicted to have yielded at an applied displacement of $\Delta = 0.88$ mm. At this displacement the base material at the weld boundary is also predicted to have surpassed its yield strength.

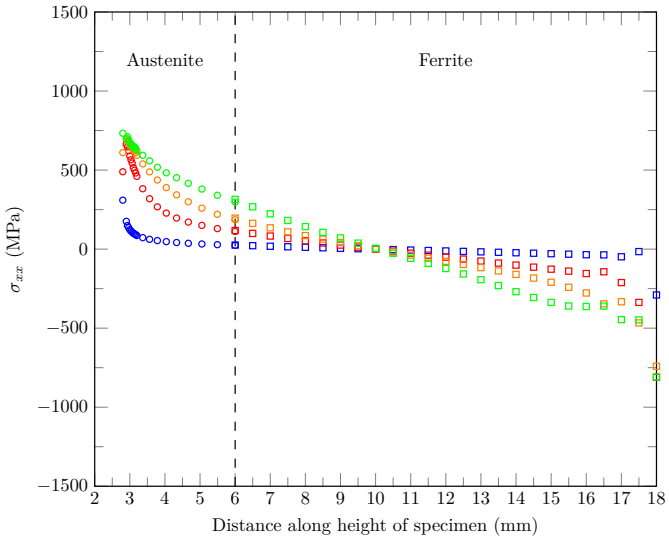

(a) $a/W = 0.15$

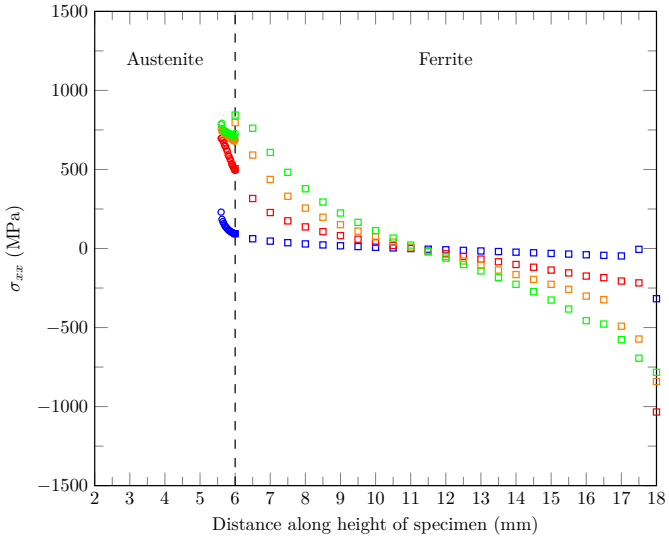

(b) $a/W = 0.30$

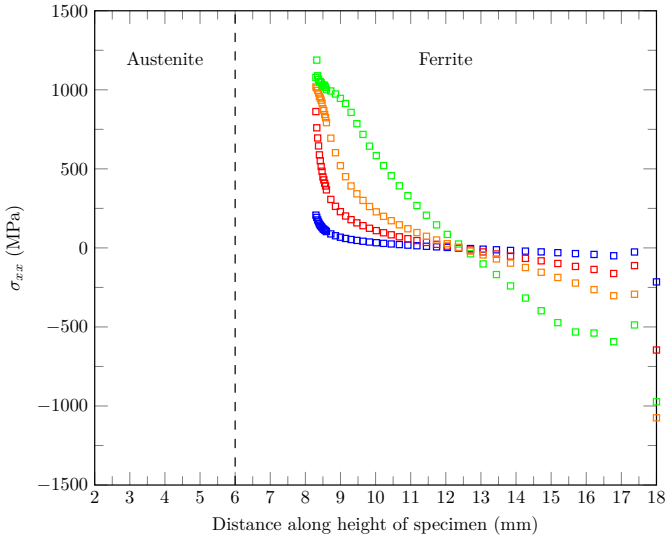

(c) $a/W = 0.45$

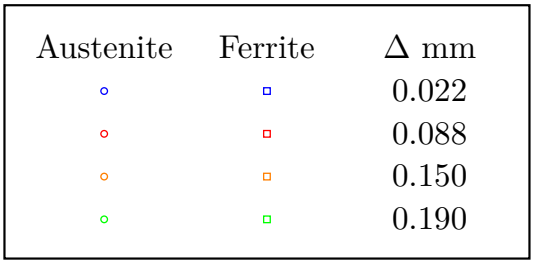

Figure 7.28: Principal stresses (σ_{xx}) along the remaining ligament for combined material model assuming plane strain conditions

Figure 7.30 shows contour plots of equivalent plastic strain (PEEQ) and Mises stress for these specimens at a fixed load of ≈ 5 kN. As shown the combined material cases (Figure 7.30c and Figure 7.30f) are significantly different compared to the homogeneous material models. The deviation in stress profile is more clearly seen in Figure 7.30f due to the proximity of the crack tip to the materials interface.

Figures 7.31, 7.32 and 7.33 plot the direct stress (σ_{xx}) at the TIG weld boundary over the span of the specimen for each of the crack depths analysed ($a/W = 0.15$, $a/W = 0.30$ and $a/W = 0.45$, respectively). As can be seen from Figures 7.31a - 7.31c the stresses are symmetrical around the centreline. For clarity and visualisation Figures 7.31d - 7.31f reduces the span to plot regions close to the crack tip only.

At a displacement of 0.190 mm the homogeneous material models shown in Figures 7.31a and 7.31b indicate that yield stress has not be surpassed. The figures also show a similar trend (compared to one another), where the peak stress is not directly at the crack tip but approximately 2 to 3 mm to the left and right. In the case of the homogeneous austenite only model (Figure 7.31b) the stress 2 to 3 mm from the crack tip is close to the yield strength of the material. Figure 7.31c shows that the stresses in the base material of the combined material model are higher, in the majority of cases, than those of the austenite region. One exception exists at the region of high stress 2 to 3 mm offset from the crack tip where the stress in the base and cladding appear to equalise.

Comparing Figures 7.31a and 7.31b with Figure 7.31c shows that the stresses in both the clad and base regions are slightly higher in the combined material model when compared to the respective predicted values for the homogeneous material model indicating that the combination of clad and base material properties may give rise to an increase in stress at the weld boundary. Similar trends, with greater disparity between the clad and base values were noted for the deeper defect size (Figure 7.35). For example: Figure 7.32f predicts stresses exceeding 500 MPa in the ferrite and austenite regions close to the crack tip at an applied displacement of 0.088 mm, in comparison

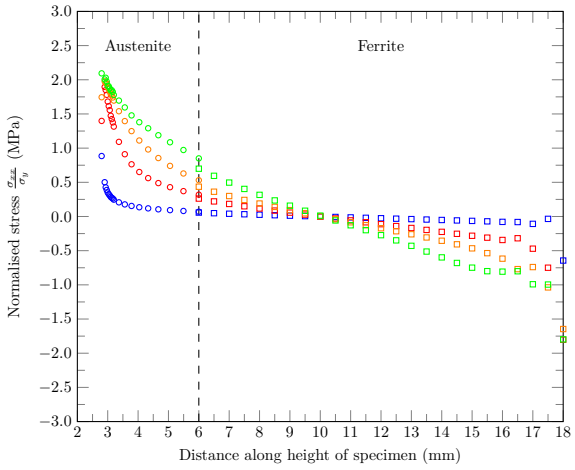

(a) $a/W = 0.15$

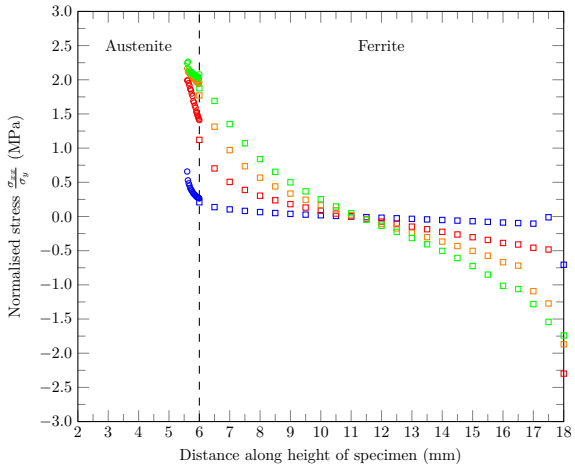

(b) $a/W = 0.30$

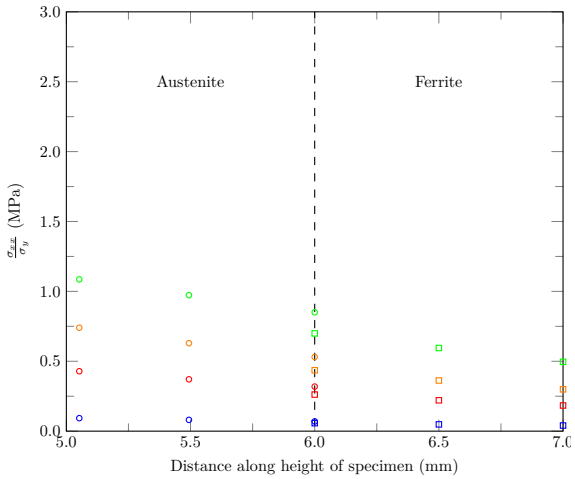

(c) Magnified view of 7.29a

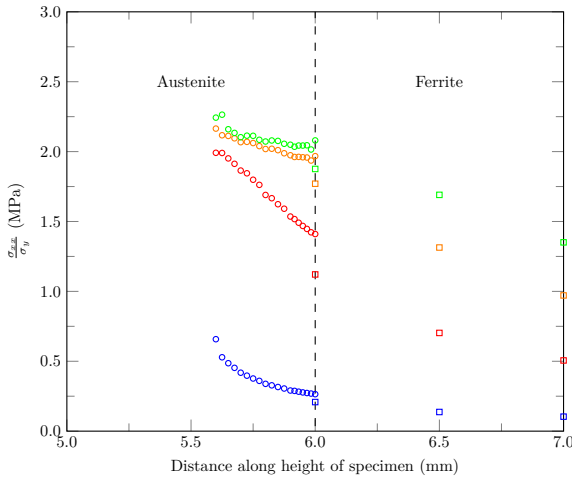

(d) Magnified view of 7.29b

Austenite	Ferrite	Δ mm
○	□	0.022
○	□	0.088
○	□	0.150
○	□	0.190

Figure 7.29: Normalised stress along the ligament for combined material model assuming plane strain conditions. Figures 7.29a and 7.29b showing the entire section along the specimen height. Figures 7.29c and 7.29d showing the region surrounding the materials interface.

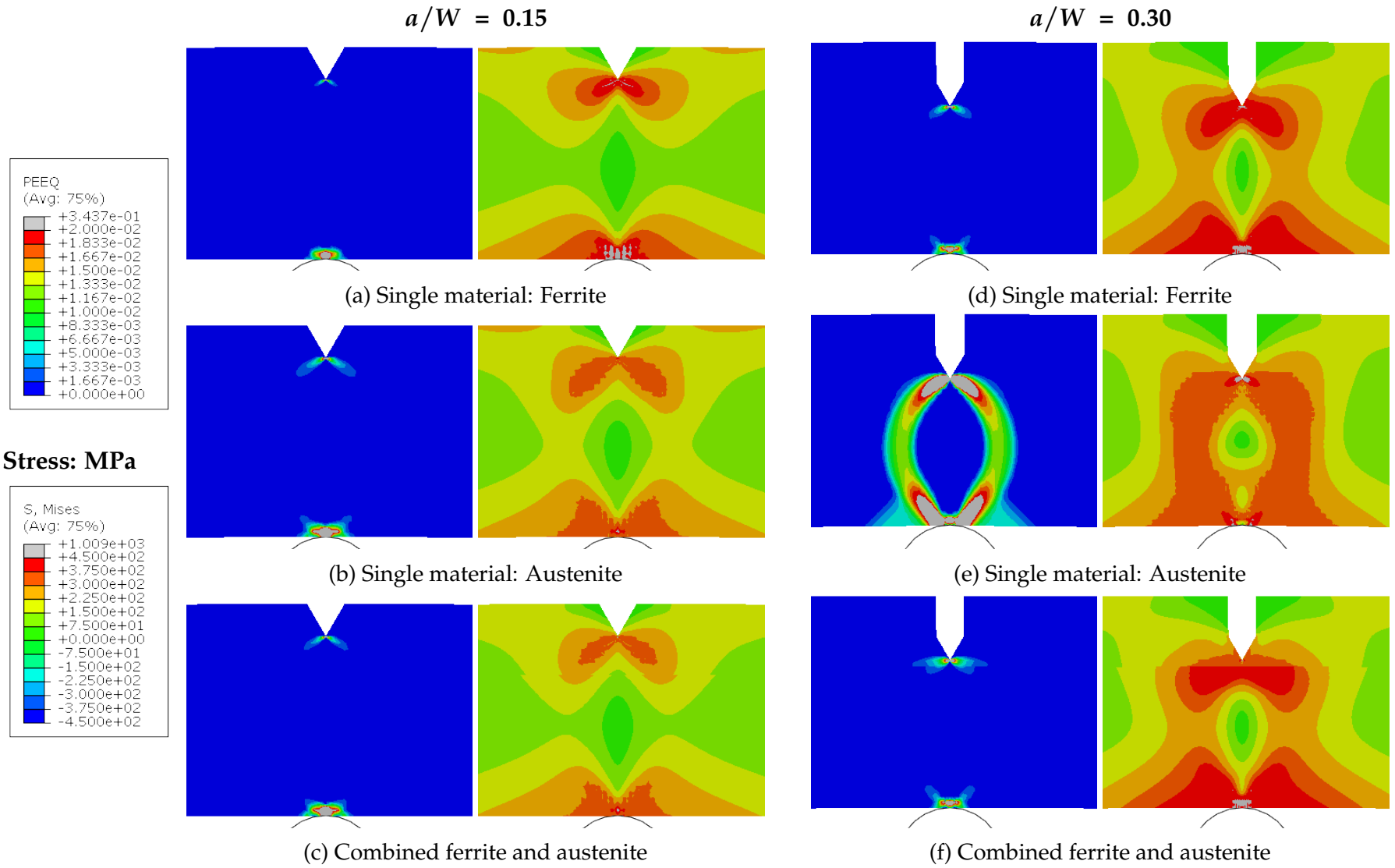

(a) Single material: Ferrite

(b) Single material: Austenite

(c) Combined ferrite and austenite

(d) Single material: Ferrite

(e) Single material: Austenite

(f) Combined ferrite and austenite

Figure 7.30: Contour plots of plane strain analyses for equivalent plastic strain (PEEQ) and Mises stress for $a/W = 0.15$ and $a/W = 0.30$. Force$\approx$ 5 kN

Figure 7.32d predicts stresses of less than 400 MPa for the same positions along the specimen length at the same level of applied displacement. It should be noted however that Figure 7.32e predicts similar levels of stress (approximately 500 MPa) to those predicted in the combined case. This indicates that high levels of stress in the cladding increases the stress in the base to well above what would be seen in a homogeneous ferrite model.

Interestingly Figure 7.33 shows that once the defect has propagated through the materials boundary the stresses along the weld boundary fall significantly in comparison to shorter crack depths. This indicates that the stress concentrating feature of the notch tip and its proximity to the weld boundary has a significant impact on the analyses. Also of note is the reduction in disparity of stresses when comparing the base and cladding materials along the weld boundary of the combined model. The disparity between the cladding and base regions is negligible in comparison to those seen for shorter crack depths (Figures 7.31d to 7.31f and Figures 7.32d to 7.32f). While the disparity increases with increasing displacement the magnitude of variation between the clad and base materials is less than approximately 20 MPa, a significant reduction when compared to the magnitudes noted for defects $a/W = 0.15$ and $a/W = 0.30$.

Also of interest in Figure 7.32f is the disparity between the clad and base regions. At displacements of less than 0.10 mm the clad and base regions, while not identical, are within approximately 20 MPa of one another. However, at displacements above 0.10 mm the disparity between the increases significantly with stresses in the base region differing from those in the cladding by up to approximately 200 MPa. Furthermore, increases in displacement appear to influence the lateral distance over which this disparity occurs. For example at a displacement of 0.15 mm significant disparities between stresses in the base and clad regions occur from the crack tip up to distances some 3 mm away, at displacements of 0.19 mm the disparity appears at distances up to 4 mm away from the crack tip.

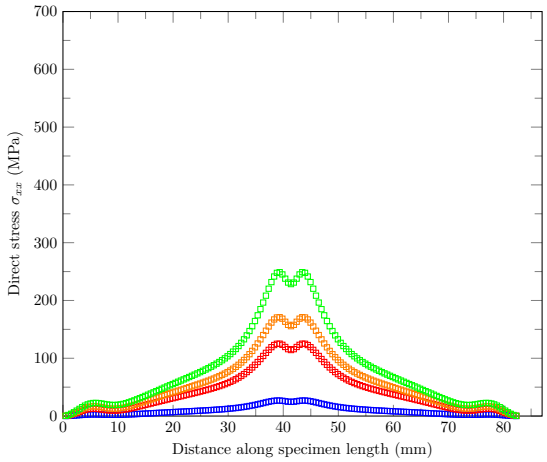

(a) Single material: Ferrite

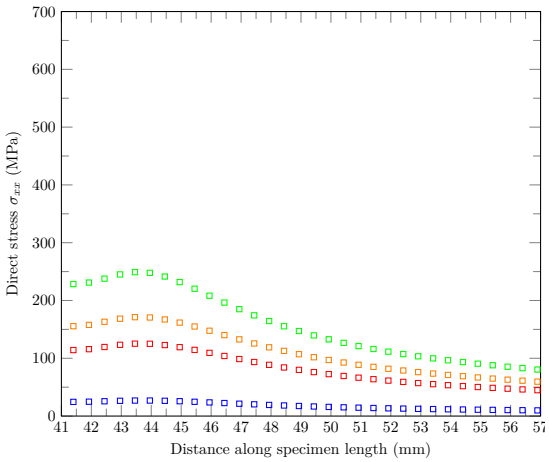

(d) Magnified view of Figure 7.31a

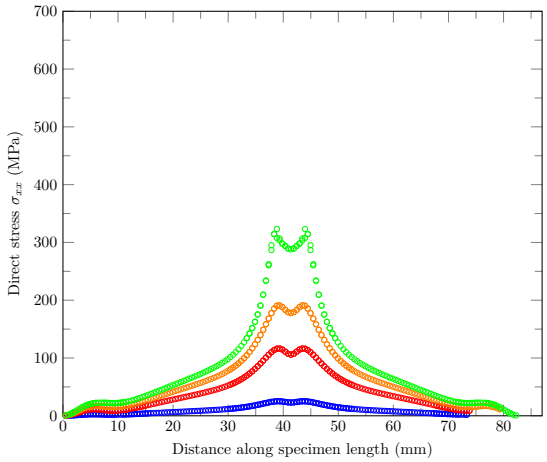

(b) Single material: Austenite

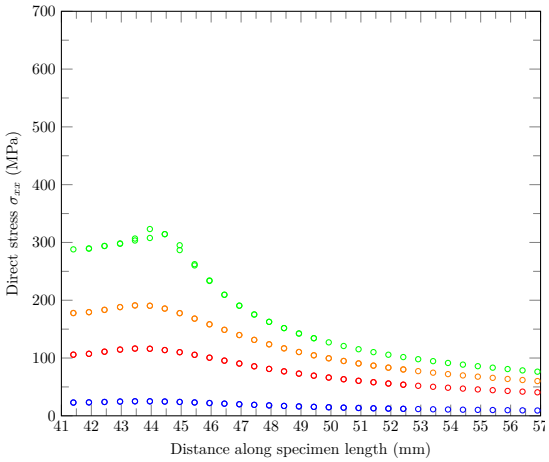

(e) Magnified view of Figure 7.31b

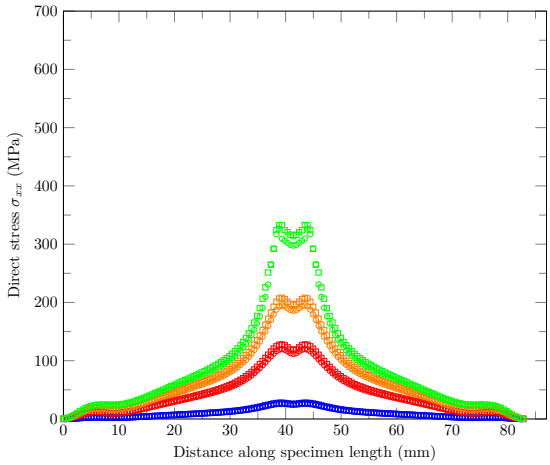

(c) Combined ferrite and austenite

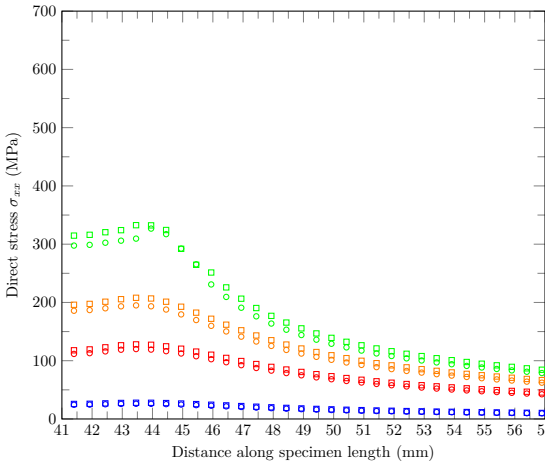

(f) Magnified view of Figure 7.31c

Austenite	Ferrite	Δ mm
○	□	0.022
○	□	0.088
○	□	0.150
○	□	0.190

Figure 7.31: Direct stresses along the materials interface for $a/W = 0.15$

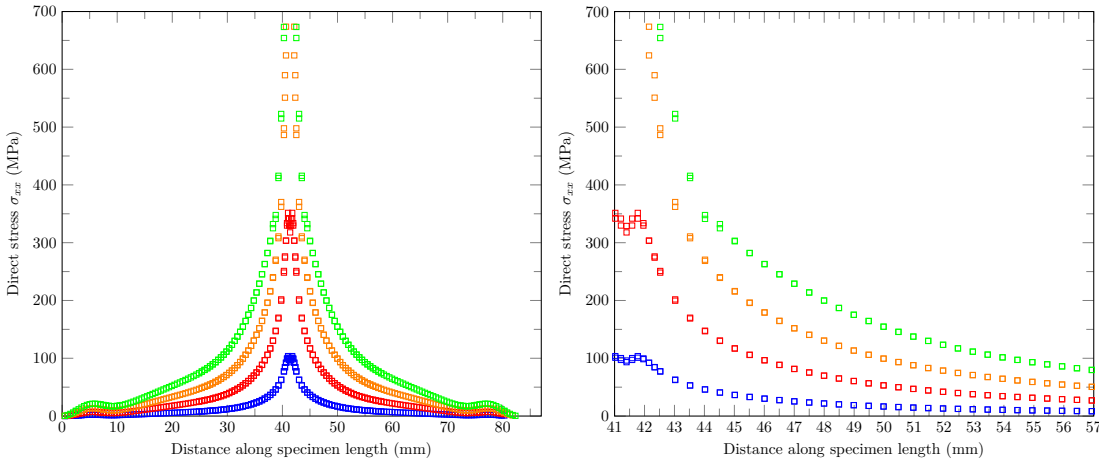

(a) Single material: Ferrite

(d) Magnified view of Figure 7.32a

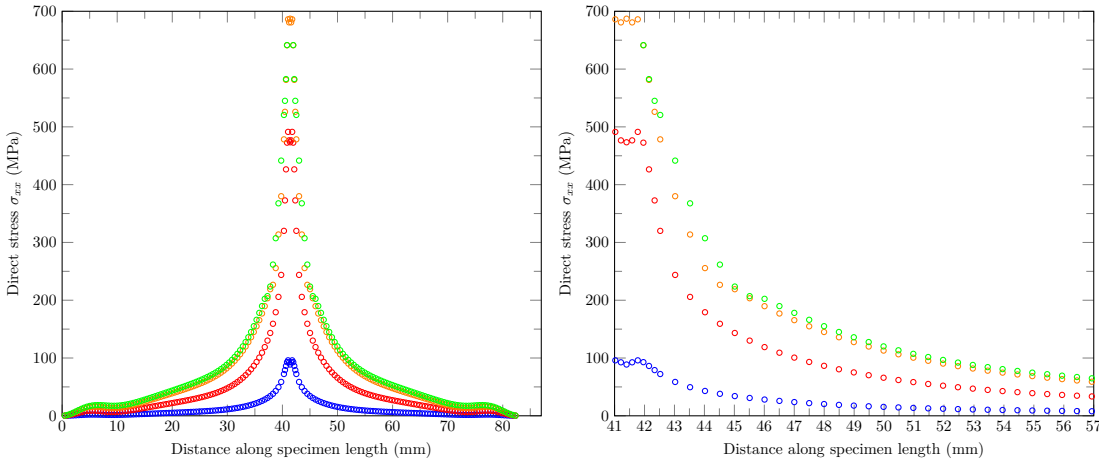

(b) Single material: Austenite

(e) Magnified view of Figure 7.32b

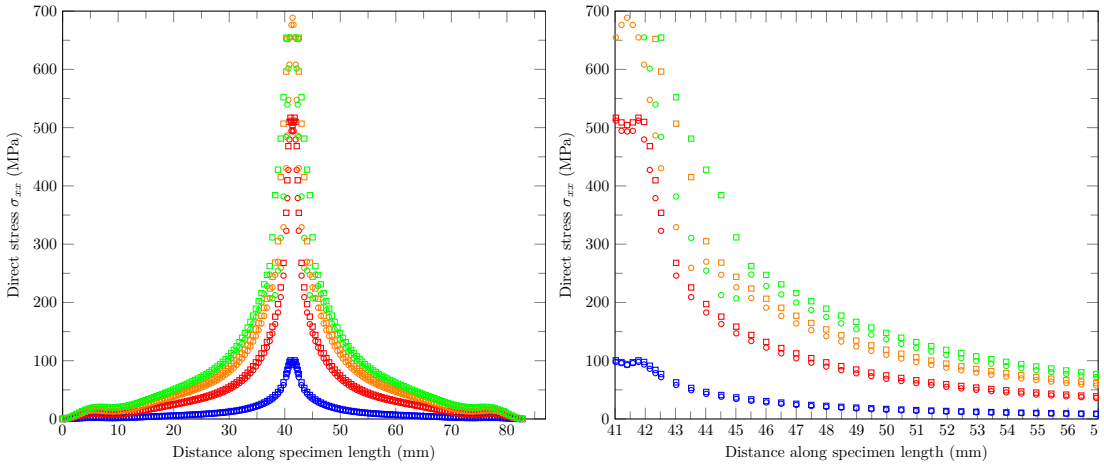

(c) Combined ferrite and austenite

(f) Magnified view of Figure 7.32c

Austenite	Ferrite	Δ mm
○	□	0.022
○	□	0.088
○	□	0.150
○	□	0.190

Figure 7.32: Direct stresses along the materials interface for $a/W = 0.30$

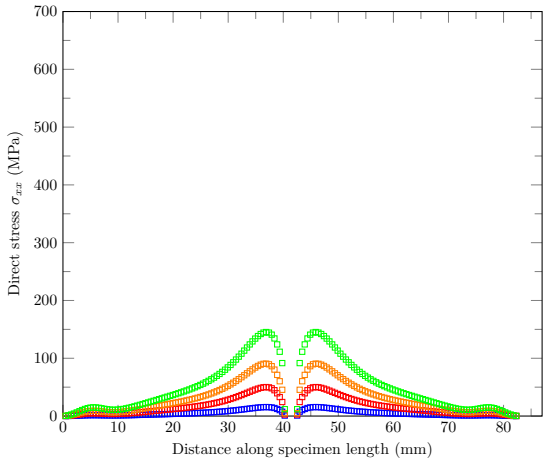

(a) Single material: Ferrite

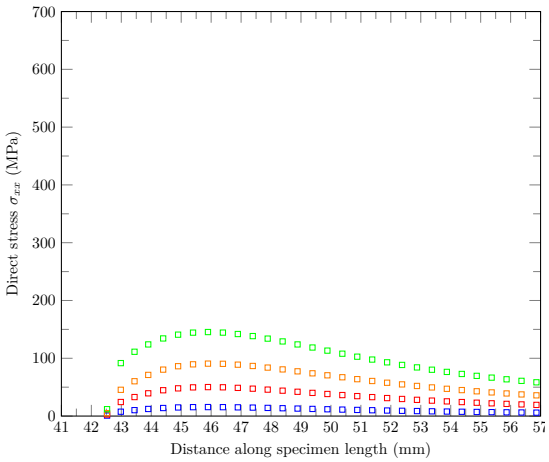

(d) Magnified view of Figure 7.33a

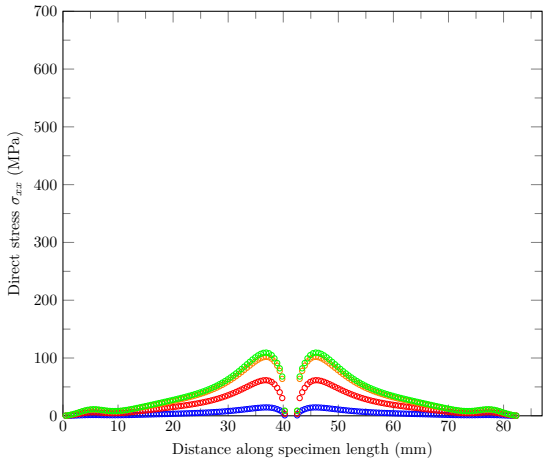

(b) Single material: Austenite

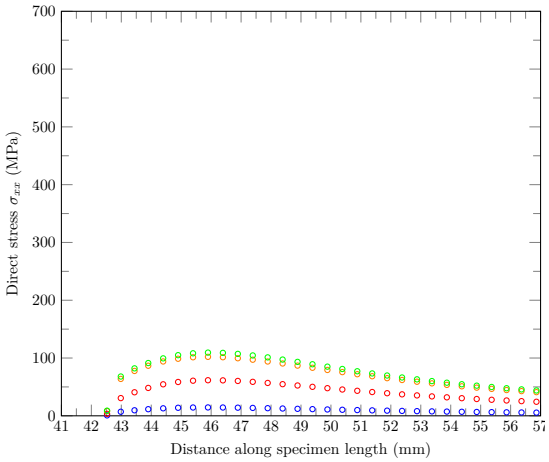

(e) Magnified view of Figure 7.33b

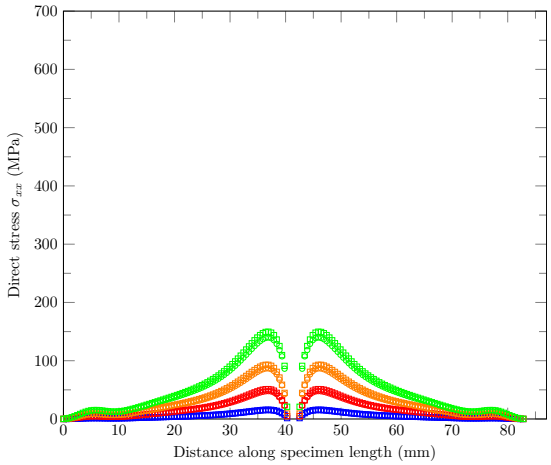

(c) Combined ferrite and austenite

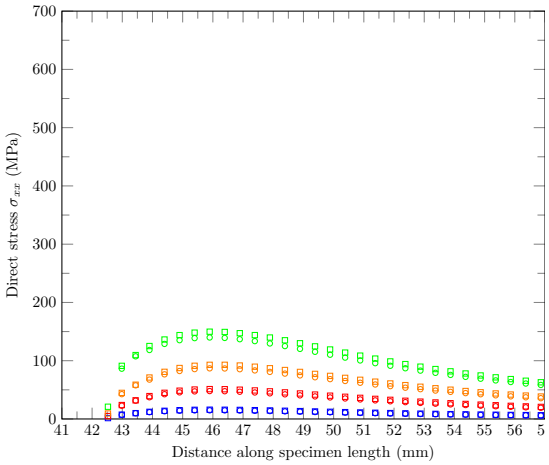

(f) Magnified view of Figure 7.33c

Austenite	Ferrite	Δ mm
○	□	0.022
○	□	0.088
○	□	0.150
○	□	0.190

Figure 7.33: Direct stresses along the materials interface for $a/W = 0.45$

Figures 7.34 and 7.35 plot the normalised stresses ($\sigma_{xx}/\sigma_{yield}$) against the specimen length for the defect depths ($a/W = 0.15$ and $a/W = 0.30$). As detailed above the full stress profile is shown in Figures 7.34a - 7.34c and 7.35a - 7.35c. A magnified view of stresses close to the crack tip is shown in Figures 7.34d - 7.34f and 7.35d - 7.35f. Figure 7.34d shows that the homogeneous ferrite model does not reach yield stress for the displacement values studied. At the maximum applied displacement (Δ = 1.0 mm) nodes in the base material only just reach yield values. The homogeneous clad model (Figure 7.34e) reaches yield at the weld boundary when the applied displacement is approximately 0.2 mm. Figure 7.34f plots the combined model with results for each material. As can be seen at all values of displacement investigated the stress in the cladding is predicted to be higher than that of the base. This remains true even at the maximum applied applied displacement. These data are in agreement with what was discussed earlier with respect to stresses in the remaining ligament.

By comparing Figure 7.35d with Figure 7.35e it can be seen that the homogeneous clad model predicts stresses above yield at the crack tip when a displacement of 0.88 mm is applied. Comparatively the homogeneous ferrite model has not yielded at this displacement. This is not unexpected given the difference in yield strengths of the two materials. At displacements of 0.150 mm and 0.190 mm both models have yielded in regions up to approximately 2 mm either side of the crack tip. What is interesting is the change in profile of the curves as displacement increases. The homogeneous clad model (Figure 7.35e) predicts similar stresses in regions outside the plastic zone (i.e. from 44 - 52 mm positions), whereas the homogeneous base model, for the same displacements (Figure 7.35d) shows a significant disparity between stresses at similar positions. This disparity is likely due to the variation in hardening ability of the two materials with the clad material being significantly more ductile compared to the base material. The results for the combined material model are shown in Figure 7.35f. As shown at a position directly below the crack tip (41.5 mm) yield occurs in both the base and clad materials above a displacement of 0.022 mm. The normalised stress in the clad material is predicted to be higher, in all cases, than those in the base material.

Again this is in agreement with values noted earlier with respect to the remaining ligament. Figure 7.35f clearly shows that as displacement increases stresses in the base material start to overtake those of the cladding. Additionally those higher stresses expand lengthwise along the materials interface for each increasing values of displacement. This may indicate that should a defect initiate on the weld boundary it may not appear directly below a stress concentrating feature such as, in this case, a notch, but rather some distance lateral to the SCF. Given the symmetry of the specimen it must be considered that two such defects may initiate on the weld boundary for every stress concentrating detail in the cladding. Furthermore given the proximity of these possible defects to one another and considering the interaction effects it is conceivable that a significantly long defect may initiate along the weld boundary.

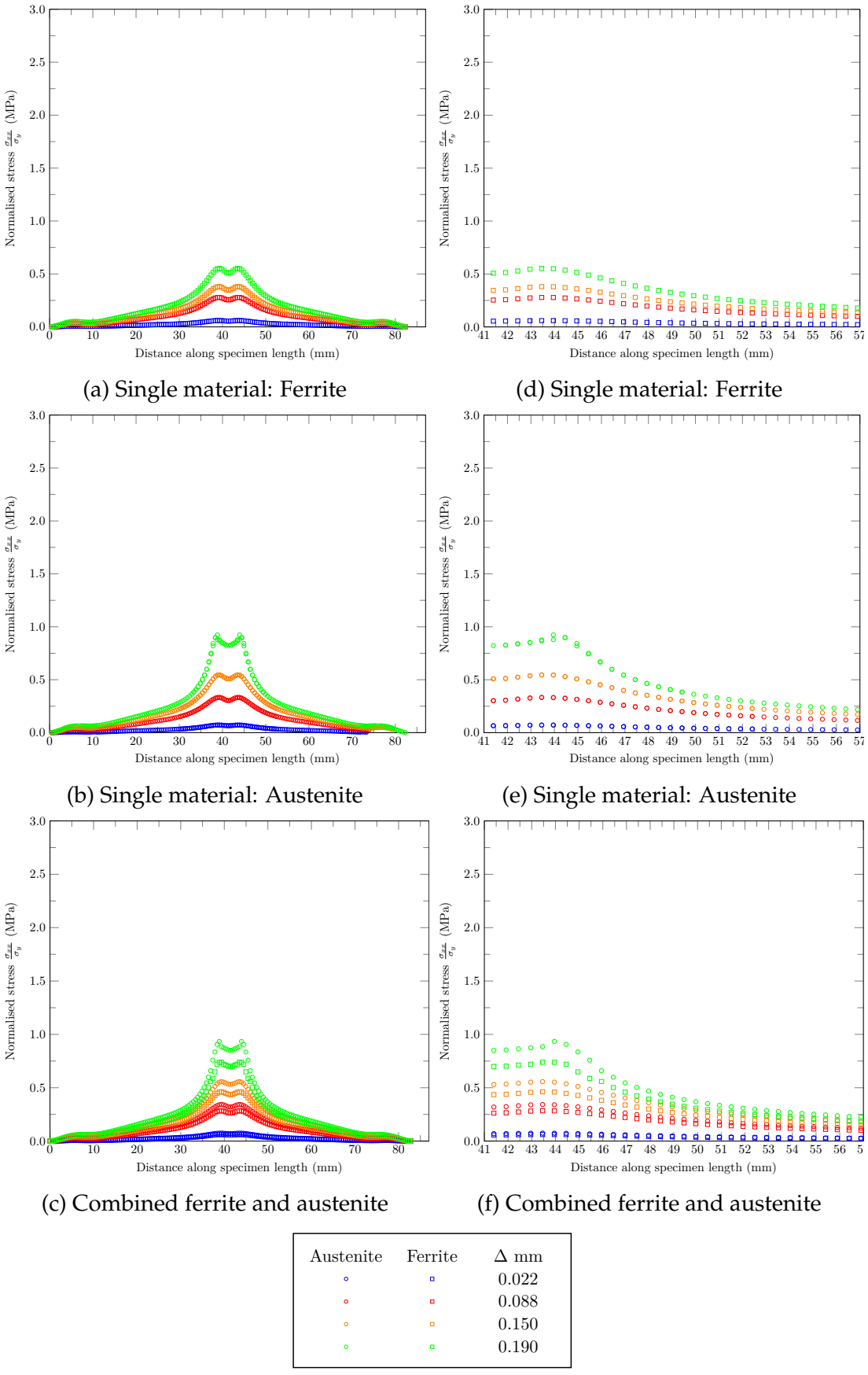

(a) Single material: Ferrite

(d) Single material: Ferrite

(b) Single material: Austenite

(e) Single material: Austenite

(c) Combined ferrite and austenite

(f) Combined ferrite and austenite

Figure 7.34: Normalised stresses along the materials interface for $a/W = 0.15$

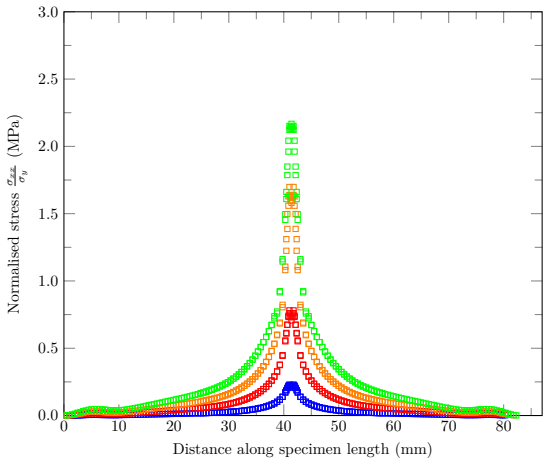

(a) Single material: Ferrite

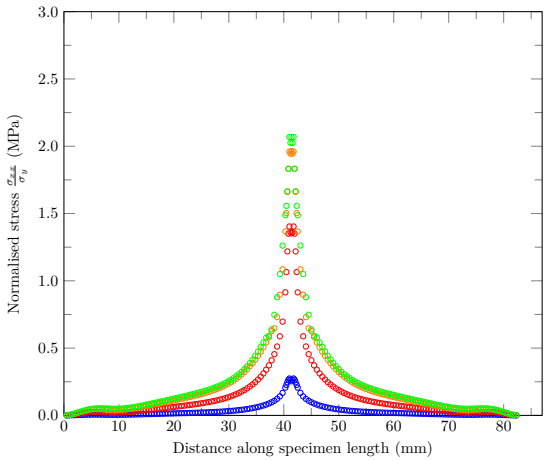

(b) Single material: Austenite

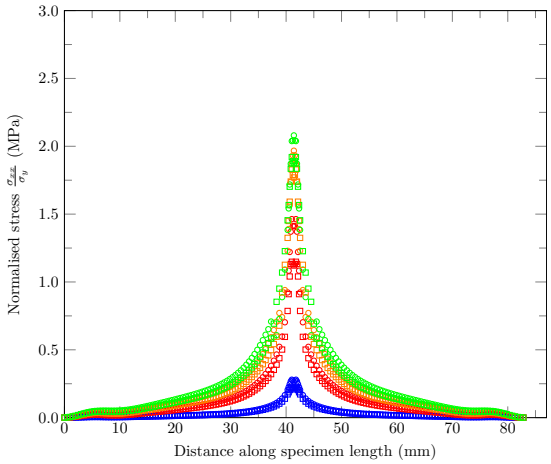

(c) Combined ferrite and austenite

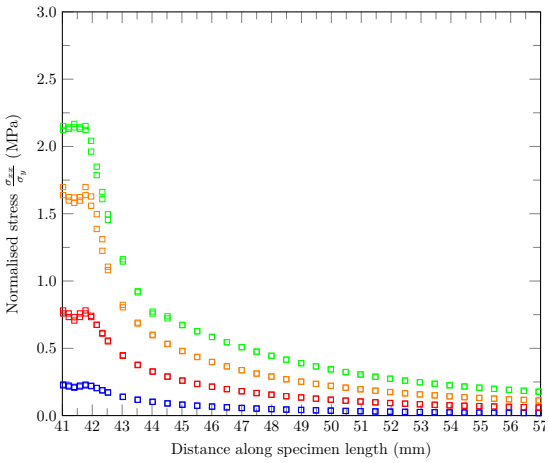

(d) Single material: Ferrite

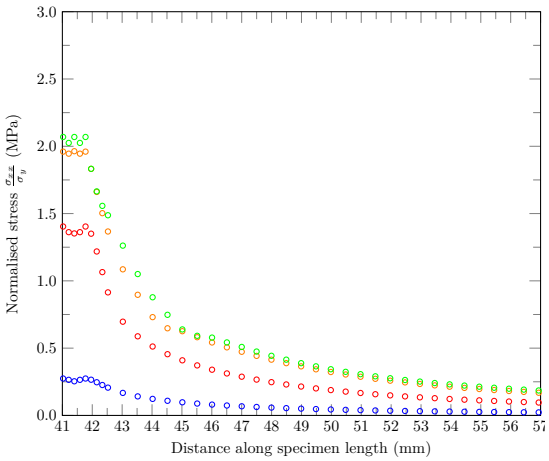

(e) Single material: Austenite

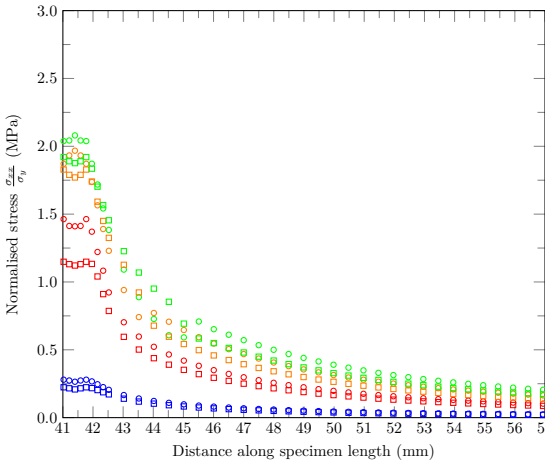

(f) Combined ferrite and austenite

Austenite	Ferrite	Δ mm
○	□	0.022
○	□	0.088
○	□	0.150
○	□	0.190

Figure 7.35: Normalised stresses along the materials interface for $a/W = 0.30$

7.2.2 Incorporating the HAZ into the combined material model

The previous analysis (Section 7.2.1) assumes a direct contact between the ferrite and austenite regions, neglecting to take into consideration the HAZ region. In Chapter 4 it was shown that a distinct HAZ zone exists between the cladding and base. Furthermore in Section 4.3 it was shown that incorporating the HAZ region significantly impacts the estimated distribution of stress. Two combined model cases are analysed here. The first case considers a combined base to clad assumption, the second case incorporates a 0.1 mm HAZ region to give a clad to HAZ to base material model. The HAZ region was assumed to exist between the cladding (6 mm thick) and the base. Figure 7.38 shows contour plots of equivalent plastic strain (PEEQ) and Mises stress for each notch depth under an applied load of $\approx$ 5 kN. From Figure 7.38 it can be seen that the inclusion of the HAZ region has a significant impact on the $a/W = 0.15$ and $a/W = 0.30$ crack depths and appears to have a comparatively negligible impact on the $a/W = 0.45$ crack depth.

Figure 7.36 plots the normalised stress in the remaining ligament for the two combined model cases. As shown the HAZ has a significant impact on the stress profile. Stresses at the crack tip are higher when the HAZ is incorporated. Additionally a larger disparity exists at the weld boundary between the cladding and the HAZ layer compared to that noted previously between the cladding and base material. Plots for specimen $a/W = 0.30$ are shown in Figure 7.37. As can be seen in Figure 7.37 the cladding material is likely to reach yield stress prior to either the HAZ or base. However, at displacements of 0.088 mm and greater, a significant portion of the remaining ligament in the base is predicted to reach yield prior to the failure of the HAZ region.

The normalised stresses (σ_{xx}/σ_y) along the weld boundary are plotted in Figures 7.39 and 7.40 for specimens with crack depths of $a/W = 0.15$ and $a/W = 0.30$, respectively. As outlined previously each material was analysed individually by removing respective element sets. Hence each plot has four series, each series representing the

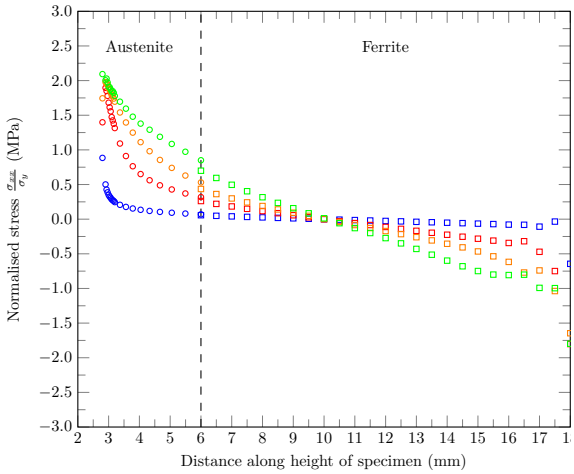

(a) Ferrite and austenite

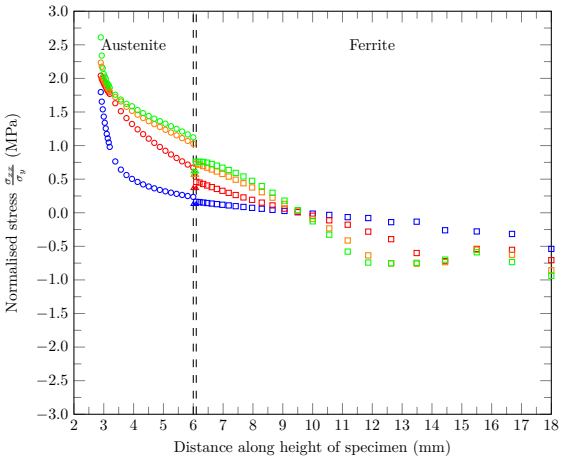

(b) Ferrite, austenite and HAZ

Austenite	HAZ	Ferrite	Δ mm
○	△	□	0.022
○	△	□	0.088
○	△	□	0.150
○	△	□	0.190

Figure 7.36: Normalised stress in remaining ligament for $a/W = 0.15$ when HAZ is neglected (Figure 7.29a) and included (Figure 7.36b)

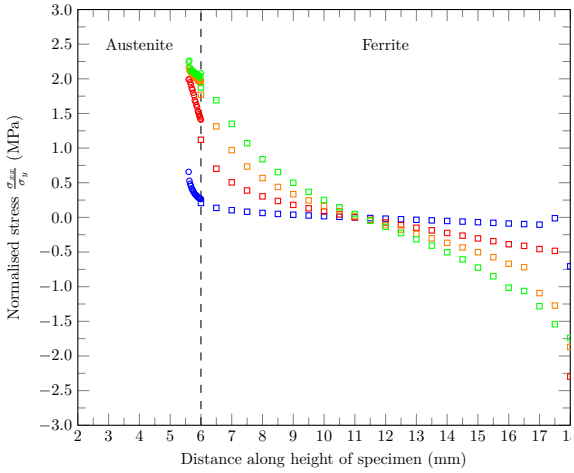

(a) Ferrite and austenite

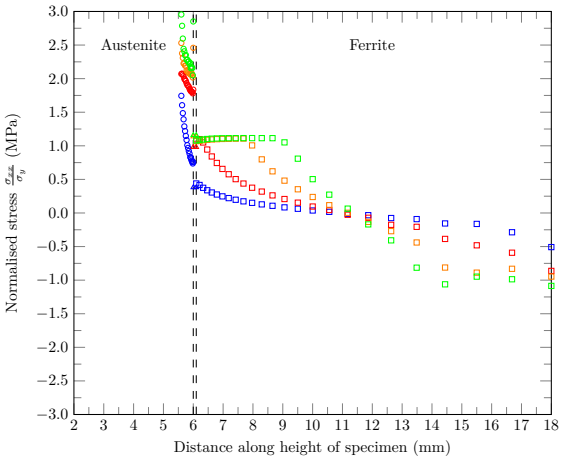

(b) Ferrite, austenite and HAZ

Austenite	HAZ	Ferrite	Δ mm
○	△	□	0.022
○	△	□	0.088
○	△	□	0.150
○	△	□	0.190

Figure 7.37: Normalised stress in remaining ligament for $a/W = 0.30$ when HAZ is neglected (Figure 7.29b) and included (Figure 7.37b)

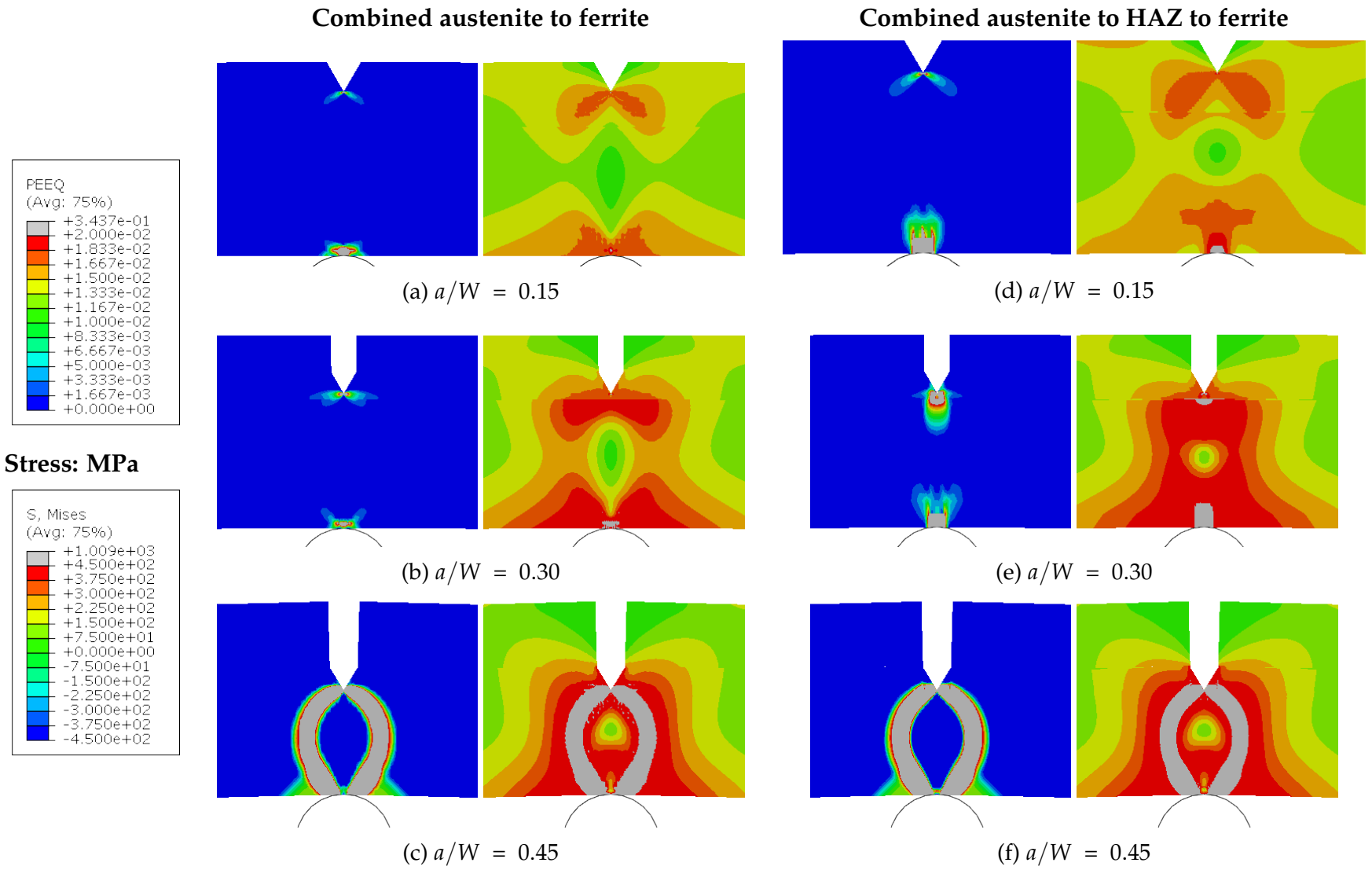

Figure 7.38: Comparison of contour plots for plane strain analyses. Combined austenite and ferrite model results for PEEQ strains and Mises stress shown in Figures 7.38a to 7.38c. Combined austenite to HAZ to ferrite model in Figure 7.38d to 7.38f. Force≈ 5 kN, except for Figures 7.38c and 7.38f where the maximum force was estimated to be ≈ 4.6 kN.

nodes associated with each of the material of interest. These materials are: homogeneous cladding, cladding to HAZ boundary, HAZ to base boundary and homogeneous ferrite. The trend along the entire length of the specimen for a specific value of displacement are shown in Figures 7.39a - 7.39c. Magnified views of the region near the crack are shown in Figures 7.39d - 7.39f.

Figure 7.39 shows that yielding has not occurred at an applied displacement of 0.088 mm (Figures 7.39a and 7.39d). The trends in all regions remain similar with peak stresses being located at the crack tip position and along the weld boundary to a region approximately 4 mm either side of the crack tip position. The highest stresses are located in the cladding followed by the base, the two HAZ positions have the lowest relative stresses and are identical to one another, as expected. At a displacement of 0.150 mm the clad material is predicted to have yielded (Figures 7.39b and 7.39e). The peak stress in the clad material is not the crack tip position but rather at a position 2 to 2.5 mm from the crack tip. The base material retains a similar trend to that noted at lower values of displacement with the peak stresses being located at the crack tip position and a smooth transition to lower stresses as one moves away from the crack tip position. The two HAZ regions are again identical to one another but the trend is significantly different; Rather than the previously noted smooth transition the HAZ regions retain lower stresses at the crack tip in comparison to the clad and base materials. At a position approximately 2 mm from the crack tip a sharp increase in stress occurs. This increase results in the relative stresses of the HAZ exceeding that of the base material quite significantly. However the stresses do not exceed that of the cladding nor do they exceed yield strength of the HAZ material. At a slightly higher level of displacement (Δ = 0.190 mm) the peak stresses in the cladding and base materials change relatively little in comparison to the previous level of displacement. The HAZ regions however both change significantly. While the HAZ regions around the crack tip do not change at positions approximately 3 mm from the crack tip the stress in the HAZ are predicted to exceed yield but they do not exceed the corresponding relative stress in the clad. This indicates that both the clad and HAZ are predicted to yield. Further along the mate-

rials boundary at a lateral position approximately 4 mm from the crack tip the stress in the HAZ exceeds that of the cladding region. This may be indicative HAZ failure prior to failure of the cladding particularly when one considers the relative ductilities of each material.

For deeper initial defects ($a/W = 0.30$) the material response is significantly different to that described above. From Figure 7.40 it can be seen that all four materials are predicted to yield at a displacement of 0.088 mm. Figure 7.40d shows that at an applied displacement of 0.088 mm at the crack tip the clad material has yielded significantly up to 2 mm along the weld boundary and that the base and HAZ materials have yielded up to 1 mm from the crack tip. While the cladding region is more likely to yield first the base material is predicted to yield prior to the HAZ. Indeed as the displacement increases (Figures 7.40b and 7.40e) stresses in the base material are predicted to be of greater relative magnitude than those in both the cladding and in HAZ for lateral distances up to approximately 2 mm from the crack tip.

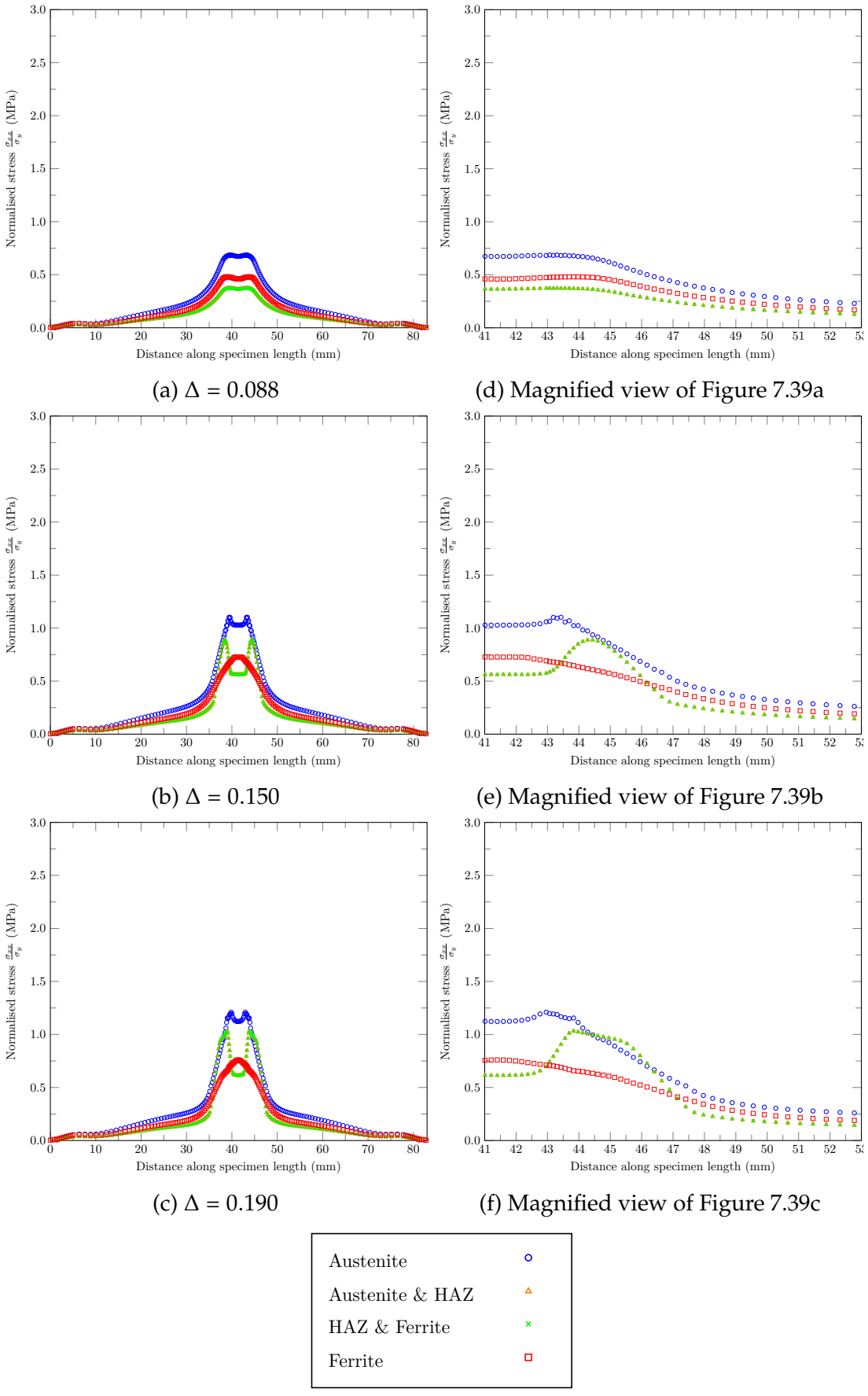

(a) $\Delta = 0.088$

(d) Magnified view of Figure 7.39a

(b) $\Delta = 0.150$

(e) Magnified view of Figure 7.39b

(c) $\Delta = 0.190$

(f) Magnified view of Figure 7.39c

Figure 7.39: Normalised stresses along the materials interface for $a/W = 0.15$

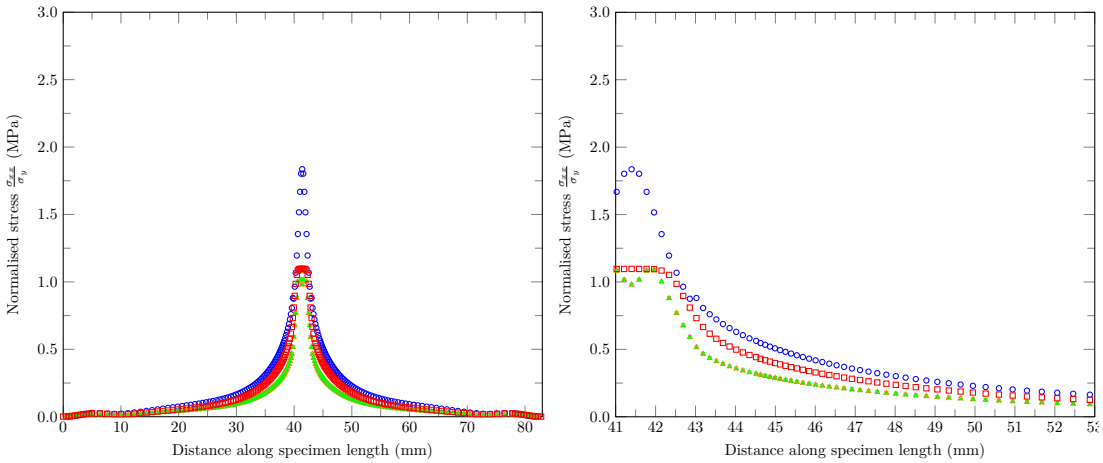

(a) Δ = 0.088

(d) Magnified view of Figure 7.40a

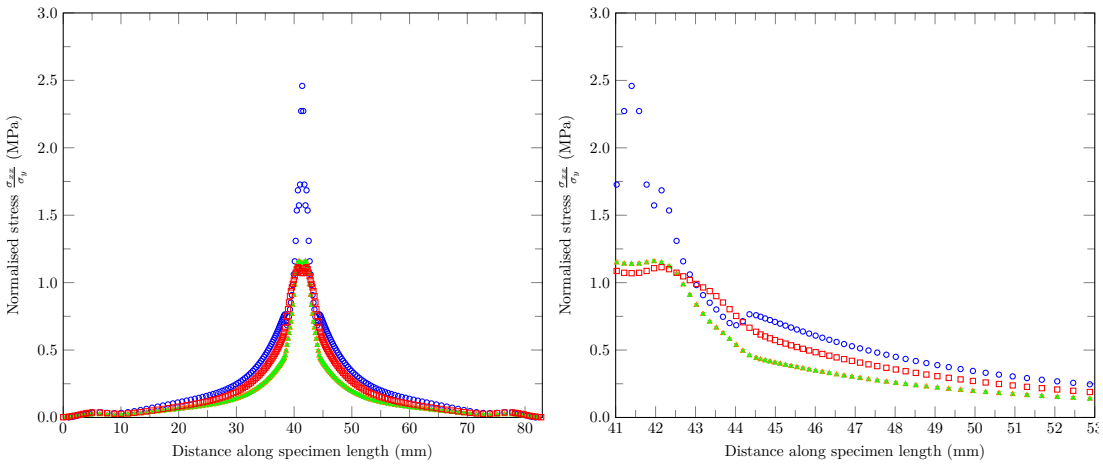

(b) Δ = 0.150

(e) Magnified view of Figure 7.40b

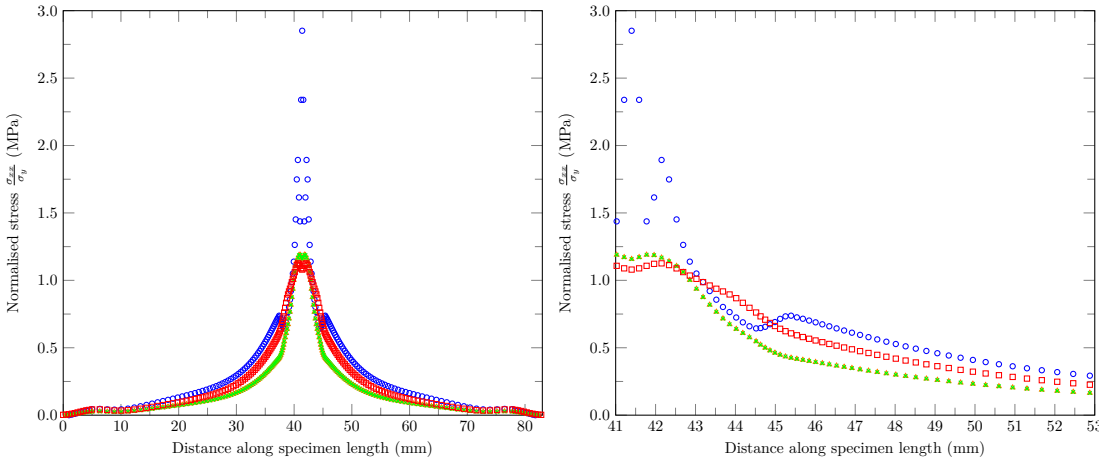

(c) Δ = 0.190

(f) Magnified view of Figure 7.40c

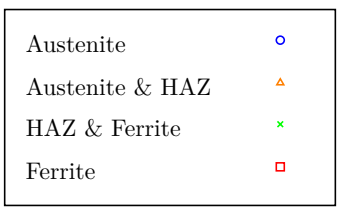

Figure 7.40: Normalised stresses along the materials interface for $a/W = 0.30$

7.3 Chapter 7 Summary

The single edge notch bend (SENB) specimens used for fracture testing were manufacture from the TIG welded plate close to the weld start/stop position as shown in Figure 3.3. This is undesirable given that weld start/stop positions frequently have variable microstructure and hardness in comparison with the mid-weld position but was unavoidable due to constraints on material availability. Three 'slices' (see Figure 3.8) of material were used to manufacture three sets of SENBs. Each set investigated a specific notch depth; $a/W = 0.15$, $a/W = 0.30$, and $a/W = 0.45$, respectively and contained six SENB specimens. Two specimens of each set consisted of both base (ferritic) and clad (austenitic) material (combined samples), the remaining four samples consisted of homogeneous ferrite material. Specimens were notched in the thickness direction (with respect to the original plate), through the thickness of the specimen. The notch ratios were chosen based on the position relative to the clad weld boundary. Hence, for the combined samples, defects with a ratio of $a/W = 0.15$ were located in the austenite cladding relatively distance from the weld boundary. Defects with a ratios of $a/W = 0.30$ were located in the austenite material close the the weld boundary, while the set containing defects with ratios of $a/W = 0.45$ were located, through the cladding in the base material only.

Microscopy and hardness testing was conducted on offcuts of the TIG welded plate. Specific details on measurement locations are provided in Section 3.3.2, Figures 3.16a and 4.3. It was clearly shown (Figure 4.1) that the base material had transformed to martensite at the weld boundary (the HAZ) but was bainitic in the remaining microstructure (Figure 4.2a to 4.2c). The cladding exhibited signs of distinct changes in microstructure when comparing subsequent clad layers (Figure 4.5e to 4.5c). The hardness was shown to of the highest magnitude in the HAZ (Figure 4.3). Relatively high magnitudes of hardness existed in the cladding when compared to the base material with increased hardness measured at the mid-width of the sample (i.e. the mid-width of the original plate) compared with the outer edge.

Similar to the CT specimens and for similar reasons to those outlined in the previous section, fracture toughness testing was only partially successful. Valid J_Q values could not be derived and, in all cases, the specimens exceeded the limits of J_{IC} testing outlined in the test method [ASTM International, 2001]. Crack propagation did not occur at every unloading cycle. Additionally post-test inspection showed the presence of shear deformation and bifurcation of the crack tip on the surfaces of samples, and longer crack depths in the mid-thickness region, indicative of ductile failure. This was not unexpected given the high measures of ductility noted during tensile testing.

Specimens were grouped according to initial defect length, each group contained four homogeneous and two combined samples, except for group C1 which contained only one combined sample. Specimens in group C1 were notched to depths of $a/W = 0.45$, this is the minimum crack depth that fulfils the test methods guidelines [ASTM International, 2001]. In the case of the combined sample, specimen C11, the depth of the notch exceeded the depth of the cladding. Hence the notch tip was located in the base material only. The remaining specimens in groups C3 ($a/W = 0.30$) and C2 ($a/W = 0.15$) were notched to depths that would not fulfil the requirements of the test standard but would place the defect in various locations of the cladding material. This was deliberate, so that the impact of the cladding and the presence of the weld boundary on strain initiation and propagation, in the combined samples, could be investigated. The true major strain (equivalent to true plastic strain in a FE model) profile of combined specimen C11 was shown to be identical to that of homogeneous specimen C13. A similar result was found when comparing strains in the thickness direction. This indicates that through thickness notches located in the ferrite material perform identically to homogeneous specimens. The cladding appears to have no further impact on the analysis. This was confirmed by 2D FE modelling.

For specimens in group C3 there were notable differences between the performance of combined and homogeneous specimens. Pre-fatigue cracking was conducted on all samples. The number of fatigue cycles were limited as the purpose was not to grow a long fatigue pre-crack but rather a short sharp crack at the tip of the machined notch.

In the case of the combined sample C31, despite the clip gauge indicating that a crack had formed, post-test inspection found no evidence of fatigue pre-cracking nor of defect initiation/propagation due to fracture testing. A higher number of samples were applied to C34 in a bid to initiate a defect. While a fatigue pre-crack was successfully formed it was noted to have been limited to the mid-thickness area and did not extend to the surface of the specimen. Comparatively fatigue pre-cracking was conducted successfully on all homogeneous samples. As per Table 7.2 the estimated fatigue pre-crack length appears to have been over-estimated for combined samples. During fatigue pre-cracking the Young's Modulus of the austenite material, derived from experimental tensile testing, was used to estimate the fatigue pre-crack length. Given that the notch was located in the austenite material this was considered a relevant approximation. One of the reasons for the incorrect fatigue pre-crack length estimate may be that the Young's Modulus of a fully austenitic sample differs significantly from the of a combined SENB specimen. Tensile testing of the 'mixed' tensile sample S5 was measured to have a Young's Modulus of 173,280 MPa. The clad samples were measured to have a Young's Modulus of 203,220 MPa. The impact of different values of Young's Moduli on fatigue pre-crack length cannot be assessed with the current information.

In terms of true major strain and through thickness strains there was distinct and measurable differences between the performance of combined and homogeneous specimens. With regards to true major strain, homogeneous samples performed as expected. High magnitudes of strain at approximately 45 °angles to the notch tip were formed, eventually propagating through the remaining ligament. The combined samples however appear to initiate strain in the expected orientation but rather than propagating through the remaining ligament the strains appear to be restricted, at least initially, to the cladding region and the ferrite region immediately below areas of high magnitude. The strain then grows both laterally (i.e. to the left and right of the notch) along the length of the specimen, vertically into the cladding and, through the remaining ligament. By the mid-point of the test strain in the cladding region surrounds the entirety of the notch region up to the surface of the specimen. Expected, homogeneous

sample behaviour, limits regions of higher strain typically to areas surrounding the notch tip and to the remaining ligament. This is not what was seen in experimental testing of combined samples. Similar trends were noted to have occurred for strains in the thickness direction. The propagation of strain in this manner indicates that the either the weld boundary or the HAZ acts as barrier to strains propagating towards the remaining ligament. Essentially strains unable to propagate through the barrier may be redistributed back into the cladding. However, it was additionally noted that strains in the thickness direction indicated localised regions of high magnitudes of strain - hotspots. These regions are likely a result of the variable microstructure in the cladding. It is considered equally possible that strains propagate laterally due to microstructural effects alone, or indeed, some combination of both of these effects.

Similar experimental results were noted in combined specimens from group C2 ($a/W = 0.15$) to those noted above for group C3. In the case of combined specimens (C21 and C24) the variation between strains in the cladding and strains in the ferrite (base) material were more pronounced. The lateral progression of strain along the length of the cladding region is of greater magnitude (in terms of length, mm) when compared with samples C31 and C34. Given that the two groups are of broadly similar microstructure and that both samples contain nominally identical HAZ regions then the lateral expansion of strains is more likely to be a result of the local cladding microstructure than a result of a barrier effect in the HAZ region. Samples C21 and C24 exhibited many more localised hotspots compared to C31 and C34. This might be indicative of variability in microstructure along the length of the original TIG welded plate. Although it should be noted that samples from groups C1, C2 and C3 were removed from regions close to weld start/stop positions and hence might be subject to microstructural changes that are not represented in other areas of the original TIG welded plate. Without further microscopic analysis it is difficult to comment further.

Both samples C21 and C24 initiated and propagated defects. The defect in sample C24 was, in contrast to the others, largely surface breaking. The evolution of defect propagation was shown in Figure 7.24, cracking initiated from the notch tip. The propagation

of the defect occurred largely by micro-cracking. It is possible that defect propagation is occurring along preferentially oriented grains but, as previously noted, additional microscopic analysis is required to confirm. Table 7.3 post-test inspection of sample C24 showed a defect of approximately 8.7 mm extending from the notch tip, through the cladding and into the base material. In comparing Table 7.3 with Table 7.2 and Table 7.1 it can be seen that post-test inspection of mid-thickness defects showed similar defect lengths for all specimens - irrespective of initial notch size. This is unexpected given that defects shorter than $a/W = 0.45$ are subject to lower in-plane constraint conditions. Other authors [Smith and Rolfe, 1994; Arun, 2015; Dolby et al., 2005] have shown that lower constraint leads to apparent increased measures of fracture toughness, as was briefly discussed in Section 2.3.3. In the case of comparable measures of fracture toughness, such as seen here, a corresponding decrease in final crack depth would be logical. Dolby [Dolby et al., 2005] stated that ductile crack extension in low constraint samples may occur via shear localisation as opposed to micro-void coalescence (MVC) but again, further microscopic analysis would be required to confirm whether failure occurred by MVC or some other mechanism.

Two dimension plane stress and plane strain models investigating the impact of the weld boundary on SENB specimens were analysed. It was shown that the force versus displacement curves for combined material models tended to mimic those of the respective homogeneous material models if the defect was located reasonably distant to the weld boundary. Defects located close to the weld boundary ($a/W = 0.30$) were found to be more similar to the base material than the cladding. This implies that the ligament between the crack tip and the weld boundary has an impact on results. This is supported when the stresses along the remaining ligament are investigated. It was shown that, for comparable values of applied displacement, nodes on the weld boundary have a greater disparity when the ligament between the crack tip and the weld boundary is smaller (i.e. when comparing crack depths of $a/W = 0.15$ to $a/W = 0.30$ see Figure 7.29). Contour plots of equivalent plastic strain (PEEQ) show that for a combined model of $a/W = 0.30$ the distribution of strain at the crack tip differs sig-

nificantly from homogeneous material models. Defects of $a/W = .15$ however are broadly similar to the homogeneous austenite (clad) model. When stresses along the weld boundary were investigated it was interesting to note that the maximum stress was not seen at the crack tip position but at lateral distances up to 4 mm away. This implies that the highest magnitude of stress does not occur in the remaining ligament, as is expected. This trend was noted to have occurred in all models, combined and homogeneous for all crack depths.

Incorporating the HAZ into the model had a significant impact on defects that had not propagated through the weld boundary (i.e. crack depths of $a/W = 0.15$ and $a/W = 0.30$). For defects in the base material ($a/W = 0.45$) incorporating the HAZ region had a minimal effect. For defects located close to the weld boundary ($a/W = 0.30$) stresses in the base material along the remaining ligament appear to be limited to those of the HAZ region. This supports the earlier hypothesis, and experimental observations, that the HAZ acts are a barrier to strains attempting to propagate from the cladding. Figure 7.37b shows this quite well. While it could be argued that the cladding is predicted to yield prior to the HAZ or base materials the ductility of the cladding with respect to the other materials must be considered. The HAZ was measured to have a ductility of only 13% while the cladding was measured to have a ductility of over 40%. The implication being that failure (i.e. separation of material) is likely to occur first in the HAZ region.

Chapter 8: Application to Industry

8.1 Synthesis

As discussed in Chapter 2 engineering critical assessments (ECAs) provide a method by which the structural integrity of a pressure vessel can be justified as being in a 'safe' or 'unsafe' condition. The method relies on material properties data taken from, ideally, the in-service component. It is often not possible to remove specimens from the component itself as doing so would essentially result in destruction of the component rendering it unfit for service. Additionally in-service material inevitably becomes irradiated increasing the risk associated with handling and testing such materials. Commonly additional components, manufactured from the same grades of material under identical manufacturing processes, are generated at the design stages of an engineering project. In the majority of cases it is these additional components that are used to manufacture specimens from which material properties data is gathered.

For homogeneous materials, improvements in manufacturing processes have ensured reproducible results, in terms of microstructure and mechanical properties, when comparing grades of materials from various batches. The variability of results however increases when welded components, even those of the same grade and same batch, are compared. Literature associates these variabilities with the chemical compositions of the constituent materials, the type welding process and to the proficiency of the welder [Gooch, 1976; Ashby and Jones, 2006]. It is not surprising that DMWs would be subject to higher variabilities in terms of mechanical properties in comparison to either base materials or homogeneous welds given that an additional chemical composition is added to the equation.

The impact of materials variability on the outcome of the ECA is often addressed via sensitivity studies (i.e. preforming multiple analyses, each analysis modifying a sin-

gle mechanical property). In the case of dis-similar metal welds (DMWs) where the accuracy of non-destructive testing (NDT) procedures is not clear, there is additional uncertainty surrounding the location and size of any postulated defect. When taken into consideration with the variability in material properties discussed above the uncertainties surrounding the result of the ECA increase substantially. Performing additional ECAs, addressing multiple defects (in terms of size and location), provide some insight into the sensitivity of the analysis to these parameters but fail to address the underlying issue, which is: where will a defect initiate and in what direction will it grow in a DMW. To better understand defect initiation and propagation in DMWs the following research questions (previously outlined in Chapter 2) were derived for this work:

- Does the cladding contribute to structural integrity? Can we quantify the contribution, if any, of the cladding?
- Are there locations where defects are likely to initiate? Are sub-surface defects more prevalent than surface breaking defects?
- If defects exist in multiple locations is one more likely to propagate in comparison with another? Are sub-surface or surface breaking defects more likely to propagate?
- Does the weld boundary influence defect propagation direction? Do defects oriented perpendicular to the weld boundary deviate along the weld interface (i.e. delamination of cladding)? Or, do they propagate through the weld boundary into the base material? Do defects oriented parallel to the weld boundary continue propagating along the boundary? Or, do they deviate into one of the materials specifically?
- How accurate is finite element modelling at predicting defect propagation in DMWs?

The original contribution to knowledge is the direct comparison of homogeneous (unclad, ferrite material only) and inhomogeneous (clad, austenite to ferrite combination) samples using digital image correlation (DIC) to assess the formation of strain distri-

bution during fracture toughness testing. It has been shown in this work that the inhomogeneous materials (samples containing cladding) absorb significantly more energy in comparison to homogeneous samples (samples containing base material only) when the defect is located in the cladding. Hence it is clear that, for materials and samples tested in this work, the cladding contributes significantly to the overall structural integrity of the RPV in cases where the defect does not extend beyond the cladding.

This work has addressed the issue of defect growth by comparing two defect orientations: defects perpendicular to the weld boundary (i.e. surface breaking defects) and defects parallel to the weld boundary (i.e. sub-surface defects). This work has shown that defects oriented perpendicular to the DMW boundary continue to propagate perpendicular to the loading direction. That is to say the direction of growth does not appear to be influenced by the weld boundary. Furthermore this has been shown to be the case irrespective of the relative position of the crack-tip compared to the DMW boundary. In terms of ECAs this has a significant impact as it implies that delamination of the cladding material from the base material is unlikely to occur when the initial defect is located on the surface of the cladding material. While this work did not investigate defects on the surface of the base material it is considered likely that a similar response would occur (though it should be noted that given the ratio of cladding material to base material, plastic collapse of the sample is almost inevitable prior to achievement of the required defect depth). In terms of defect initiation it is clear from work presented here that the presence of sub-surface defects in the cladding cannot be discounted. Hence, from an analysis perspective, the direction of propagation of these defects becomes of significance. Sub-surface defects (i.e. those oriented parallel to the weld boundary), in terms of the specimens manufactured for this work, are somewhat more complex to analyse in comparison to surface-breaking defects. Experimental tests have shown that defect propagation does not continue parallel to the loading direction but rather deviates away from the weld boundary into the austenite material. No initiation nor propagation was noted to have occurred in the ferrite regions of the samples. The implication is that defects existing on the boundary be-

tween the cladding and base material are more likely to propagate in the cladding. There are however several limitations to this finding which may have significance, in terms of impact, on this finding. The loading applied to the sub-surface defect (CT) samples is not representative of loading that is applied to the in-service component. Samples tested as part of this work were subject to additional EB laser welding and it has been shown that the microstructure, in the region of the notch, was affected. Hence the microstructure of samples containing sub-surface defects differ from samples testing surface-breaking defects (SENB samples) and it is not clear to what extent defect propagation direction was impacted by this change in microstructure. Numerical modelling of the laser welding processes showed significant residual stresses in the mid-thickness region of the sub-surface defect samples, which is the location where defect deviation was noted to have occurred. The presence of residual stresses was confirmed experimentally prior to fracture testing but did not include additional machining extending the notch tip. It is considered likely that the residual stress profiles measured experimentally are likely more onerous than those present during testing. Without additional neutron diffraction measurements however a measure of the levels of residual stresses present during the unloading compliance test is unknown. Additionally, given that the samples effectively plastically collapsed, the high plasticity seen during testing likely removed any influence of residual stress from the test samples. Hence the impact of residual stress on defect propagation at a component level is not clear. It should however be pointed out that other authors also noted deviations in defect propagation direction for similarly notched, multi-material, CT specimens which may indicate that defect deviation into lower strength materials is a generic occurrence for multi-material specimens [Brayshaw et al., 2018].

The overall implication for structural integrity assessments from the perspective of defect propagation is that while defects may initiate sub-surface either on the weld boundary or in the cladding material, it is more likely that propagation will occur in the lower strength material i.e. in the cladding. Hence defects initiating on the weld boundary, propagating in the cladding will, eventually, become surface breaking de-

fects. This result has several implications when assessing key input parameters for the ECAs, for example: It could be assumed, conservatively, that defects postulated at the weld boundary should be analysed as surface breaking with the depth of the defect being equal to the depth of the cladding. While this is conservative in terms of defect size it leads to the somewhat troubling, hypothetical, conclusion that the base material is now essentially exposed to the corrosive environment. The outcome of assessing the defect in this manner is that the operating life of the component would be significantly reduced. Alternatively one could conduct ECAs and assess the impact of defects of varying depths through the cladding and make an engineering judgement on the overall likelihood of failure whilst retaining the benefit of corrosion resistance. Hence, while the first option provided (assuming a surface breaking defect the same depth as that of the cladding) is considered extremely conservative, it does provide a exceptionally quantifiable 'safe' lifetime with only a single assessment required. This result may also be of interest to NDT operators. As previously discussed NDT procedures struggle to find and size defects in clad welded materials due to changes in the direction of ultrasonic waves propagating through the bi-metallic interface. Given that this work has shown that defects are unlikely to cause de-lamination of the cladding then NDT equipment could potentially be calibrated to focus on finding and sizing defects in the cladding only.

It is clear the above that, for either defect orientation, propagation occurs predominately in the cladding irrespective of initiation location. Hence it is undeniable that the cladding contributes to the overall integrity of the vessel. Quantifying the contribution however is more difficult as there is a clear dependency on numerous variables not least of which is the thickness of the cladding section relative to the base material. This work has shown that the proximity of the notch tip to the weld boundary has a clear impact on the strain distribution in both cases. For surface defects the in-plane constraint appears to be affected not only by the remaining ligament of the sample but also by the ligament between the notch tip and the weld boundary. For surface breaking defects in the cladding shallow defects were found to behave in a more un-

desirable fashion compared to deeper defects. This has been attributed to the local microstructure and the inhomogeneous (in comparison to the base material) nature of the cladding. It is clear that both parameters (in-plane constraint and microstructure) are impacting the strain distribution in the tested samples but accounting for the relative contribution from each is difficult if not impossible given the unique nature of each sample (i.e. positional location in the plate may influence results). Hence generalising this work to incorporate other material combinations cannot be made on the basis of the current work. The impact of varying cladding thickness was assessed for sub-surface defects using numerical computation but the models investigated did not encapsulate the local microstructural regions found to exist in the cladding. Hence while the influence of constraint on the tests could potentially be estimated the impact of neglecting local microstructural effects is unknown and in some respects unknowable without sample destruction.

Experimental fracture toughness data presented in this work are based on comparisons between inhomogeneous and homogeneous samples for three initial notch depths. While there was a clear trend in terms of strain distribution in inhomogeneous samples compared to the homogeneous samples it should be noted that only two inhomogeneous samples were tested per notch depth and no valid fracture toughness measurements could be computed. Investigating the strain distribution does not rely on the valid computation of a fracture toughness measurement and hence the data presented is considered acceptable from that perspective. The number of samples tested, and the fact that only one material combination was investigated leaves some uncertainty as to whether this trend can be generalised to other inhomogeneous material combinations. Indeed the distribution of strain noted in the cladding may be linked to the extreme ductility of the austenite material.

Numerical computations have been shown to be of value to these types of assessment. This work showed that 2D plane strain analyses could discern the correct defect propagation direction with relatively little computational power. However plane stress 2D models were found to be inadequate in describing surface strain/stress distribution.

Hence 2D modelling should be used cautiously and validation of 2D results should be required for cases were surface distributions are of interest. Three dimensional analyses were shown to be more accurate in their predictions particularly when considering strains/stresses on the surface of samples and while more computational power was required in comparison to the 2D models the benefit, in terms of accuracy, may outweight the computational costs depending on the investigation type. It would be interesting to investigate the influence of out-of-plane constraint (i.e. thickness effect) in terms of in-plane constraint for these inhomogeneous welded samples. In these types of assessment where surface strain/stress distribution is likely to have significant impact on the overall results 3D modelling should be applied. Additional 3D modelling was used to predict residual stresses in components post-welding. It was shown that the initial assumption that the combined 'sandwich' component (see Chapter 5) was inaccurate and likely accounted for deviations noted when compared to experimental data. A better correlation was noted when material was removed from the model (via element deletion) and the individual specimens were compared to experimental data. As previously discussed the comparison likely improved due to the superior comparison of element size when comparing individual specimens to the component specimen in terms of gauge section.

One of the key research areas that was not investigated in this work but has relevance to multiple industries incorporating these dissimilar welded materials is the influence of temperature on results. Particularly of the influence of lower temperatures. This was discussed briefly in Chapter 2 were it was stated that ferritic materials, due to their crystallographic structure, are subject to a temperature transition from ductile failure modes (at higher temperatures) to brittle failure modes (at lower temperatures). Austenitic materials however fail in a ductile manner irrespective of test temperature. It is unknown how this would impact the findings, in terms of defect propagation, reported here. For example considering a defect located sub-surface it is potentially possible, that at lower temperatures, failure could occur in the ferritic material rather than the cladding material.

8.2 Conclusions

For the readers clarity the following conclusions are grouped, by topic, and distinguished from one another by the use of labels.

The following conclusions can be made in reference to experimental work conducted on the TIG welded plate and, testing conducted on samples from the TIG welded plate.

A1 Post-test analyses showed several sub-surface defects in the cladding of the original TIG welded plate. The defects were noted to have occurred in samples taken from the weld start/weld stop positions and were located predominately in the first and/or second clad layers. Defects in cladding material were not found in samples taken from other locations.

A2 The TIG welded plate was found to have a banitic microstructure in the base material which is typical of grade A508. A layer of martensite was found between the base material and the cladding. The cladding was shown to have a complex and varying microstructure through the thickness of the cladding. The change in microstructure is due to the complex heating and re-heating of material as additional layers are added during the TIG welding process. The cladding exhibits numerous HAZ regions and regions of distinct changes in grain growth direction.

A3 Hardness measurements showed the peak hardness, measuring approximately 350 HV_{10}, occurred at the weld boundary between the base and clad materials. As noted earlier (see **A2**) a region of martensite material was found at this location. The hardness in the cladding was found to be lower than that of the martensite layer at approximately 300 HV_{10}. The base material was found to have a hardness of approximately 200 HV_{10}.

A4 Tensile testing was conducted on the base (ferrite), cladding (austenite) and HAZ materials. The yield strengths were measured to be approximately 440 MPa, 350 MPa and 510 MPa respectively. The strain at failure (ϵ_f) was noted to be 20%,

43% and 13% for the base, cladding and HAZ areas, respectively. The accuracy of the HAZ result is subject to debate given that only one specimen was available and the ratio of HAZ to ferrite/austenite is not clear. Similarly it should be noted that only two specimens comprised of cladding material were tested. Tensile results for the austenite material compared well with data taken from literature [Ficquet et al., 2009] providing some confidence as to their accuracy. Tensile testing on the ferrite (base) material samples was conducted for multiple specimens. The specimen results were in good agreement with one another and compared favourably with data provided by the industrial sponsor. The strain at failure was measured to be 21% in the ferrite, 43% in the cladding and 13% in the HAZ.

A5 Additional testing on sub-sized tensile specimens showed that the orientation of the specimens, with respect to the TIG weld direction, did not appear to impact the stress-strain response of the samples. Comparisons between the sub-sized and full-sized specimens were unsuccessful as a higher strain rate was applied to the sub-sized specimens. HAZ sub-sized samples were found to be of significantly higher magnitude in comparison to the full size specimens. While it is understood that the applied strain rates make these data directly incomparable it should also be noted that the microstructure sampled by the sub-sized specimens is limited to HAZ region only whereas the full sized specimen was likely a mixture of HAZ and austenite or ferrite material.

A6 The residual stress in the base plate was measured post-TIG welding by another work [Serasli, 2014]. The residual stress in the cladding was found to be approximately +400 MPa in the longitudinal and transverse directions and $\pm$200 MPa in the normal direction. In the base material, A508, the residual stress in the normal direction was measured to be negligible. In the longitudinal and transverse directions the residual stress was found to follow similar trend and measured in the range of $\pm$400 MPa.

A7 The d_0 values measured during neutron diffraction were oscillated around ten angles to reduce the error associated with coarse, textured grain structure. The residual stresses in tensile specimens, with thickness of 3 mm, were additionally measured. Applying the d_0 values to the measurement resulted in stresses that were considered to be excessively large in magnitude. A more reasonable approximation was made using the plane stress assumption. The variation in result, when comparing the d_0 method to the plane stress assumption, was attributed to the coarse, textured grain structure and the positionally dependent nature of the d_0 specimen. The application of the plane stress assumption to the tensile specimens resulted in residual stresses that fell within the error margin ($\pm$50 MPa) of the measurement.

A8 The following comments pertain to experimental fracture toughness test results of the SENB specimens:

A8a Valid fracture toughness data could not be measured experimentally within the validity limits stated by the test method [ASTM International, 2001].

A8b Crack propagation was not measured for every unloading cycle indicating that crack tip blunting occurred at multiple stages of the test.

A8c The appearance of shear deformations and bifurcation of defects on the surfaces of tested samples indicate ductile tearing occurred during testing. Additionally the defect depth was shown to be measurably greater in the mid-thickness region, indicative of crack tunnelling and further evidence of a ductile failure mode.

A8d Digital image correlation (DIC) data showed that for specimens where the initial notch depth exceeded that of the cladding (i.e. when $a/W \geq 0.45$) no discernible difference in strain, either in the principal direction or in the thickness direction, was found when comparing combined and

homogeneous samples. This indicates that should a defect propagate through the cladding the specimen acts in the same manner as a homogeneous, ferrite only, sample. It should be noted however, that only one combined sample with a notch penetrating the cladding was used in this work. Further tests should be conducted to confirm this finding.

A8e For defects located in the cladding close to the materials boundary ($a/W = 0.30$) the principal strains on the surface of combined samples indicated significant growth of strain in the austenite region prior to propagation of strain through the materials boundary into the ferrite material. Additionally strains in the thickness direction appear to preferentially grow laterally (i.e. in the x-direction) as opposed to symmetrically around the notch tip as was noted for homogeneous samples. These trends are clearly documented in Figures 7.13 and 7.14. The strain in the thickness direction was shown to have localised 'hotspot' areas. It is considered likely, given the points made in **A2** to **A4**, that these hotspots are formed due to local microstructural variations in the cladding. Homogeneous material samples, of the same initial defect size (Figure 7.16) did not indicate lateral strain growth nor hotspots. Hence the differences in strain profiles noted in samples C31 and C34 must be due to the presence of the cladding material and the weld boundary. The final measured defect length in the combined samples were measurably lower than those of the homogeneous samples, despite similar test conditions. This indicates that, in combined samples, the austenite material effectively absorbs more energy without defect propagation compared to similarly notched homogeneous specimens. This observation correlates with the respective material failure strains noted in **A4**.

A8f Similar to **A8e** combined samples with initial crack depth ratios of $a/W = 0.15$ indicated the presence of hotspot locations. In Figures 7.22 and 7.23

the 'barrier' effect of the weld boundary is clearly presented. Up to the mid-point of the test almost all the strain in the samples (excluding local strains due to the loading pin) are confined to the cladding. Furthermore there appears to be a larger variation between strain in the cladding and strain in the base materials in **A8e**. Similar to **A8e**, samples (with initial notch depths of $a/W = 0.15$) exhibited a significant difference when comparing the strain profiles of homogeneous and combined samples. Homogeneous samples of equivalent initial crack depths ($a/W = 0.15$) produced similar strain profiles as homogeneous samples of deeper crack depths.

A8g Given that the homogeneous samples perform similarly, in terms of strain profile, irrespective of initial notch depth, geometric constraint (i.e. the remaining ligament and thickness effect) alone cannot account for the differences noted when comparing combined samples of varying crack depth. A significant difference in strain profile was noted when comparing combined samples of initial depths $a/W = 0.15$ to those of $a/W = 0.30$. This change in strain profile may indicate that the in-plane constraint in combined samples is affected not only by the a/W ratio, but also by the relative position of the defect depth to the materials interface.

A8h Samples notched to $a/W = 0.15$ exhibited longer final crack depths in comparison to samples notched to $a/W = 0.30$. This is unexpected given that the literature consensus is that shorter defect depths result in a reduction in in-plane constraint. Additionally it has been shown that the strain to failure for the cladding material far exceeds that of the ferrite material. It was noted that, for shorter defect depths (i.e. $a/W = 0.15$), the affected area of cladding material was larger, for equivalent stages of testing, compared to samples of longer initial defect lengths. Furthermore strain was noted to initiate at local hotspots, likely due to the vari-

able microstructure through the thickness of the cladding. There were notably more hotspots in samples notched to $a/W = 0.15$ compared to samples notched to $a/W = 0.30$. It is therefore postulated, given the latter and taking points made in **A2** to **A4** into consideration, that the microstructure of the cladding has significantly affected defect propagation. For longer defect lengths (i.e. $a/W = 0.30$) the crack tip samples a relatively small amount of cladding before propagating into the ferrite material. Given that the ferrite material was found to be comparatively homogeneous in terms of microstructure it may be that defects are less likely to propagate in this region compared to the cladding material. In other words, the microstructure of the cladding may promote defect initiation and/or propagation in comparison to the ferrite material.

A8i Defects in the mid-thickness region of the combined samples did not appear to be affected by the presence of the weld boundary. Defects appear to have propagated in the expected manner (i.e. perpendicular to the loading direction) through the weld boundary into the ferrite material.

The following conclusions can be made to the laser welded component. Including comments pertaining to measurements on the component, specimens taken from the component and testing on specimens removed from the component:

B1 Orientating the notch parallel to the materials boundary was not possible without significant additional machining and welding of the original component. A double sided laser weld was used to join ferrite and austenite materials. Full fusion of the weld root was achieved and no welding defects, associated with either the laser welding process were found.

B2 The use of laser welding resulted in significant changes to the microstructure of the cladding. It was noted that the direction of grain growth and the morphology of the ferrite phase varied through the thickness of the clad region. The ferrite material did not indicate any significant changes attributed to the laser welding

process. However, the microscopy in this work was limited to optical microscopy, specific etchants (1 % nital solution for ferrite material and 10% oxalic acid for austenite material) and one orientation.

B3 Significantly higher measured values of hardness were found at the laser weld boundary. The highest magnitudes, measuring approximately 500 HV_{10}, were noted to occur at the weld cap position. There was a distinct reduction of hardness in the mid-width of the section analogous to the weld root overlap position. The hardness in the mid-width was similar to that measured at the TIG weld boundary. Both weld boundary positions were of higher magnitudes of hardness in comparison to the ferrite material regions. There was little difference, in terms of hardness, between the weld start and weld stop positions.

B4 Neutron diffraction measurements were conducted on the laser welded component prior to machining CT specimens. The stresses were measured to be tensile at both the laser weld boundary and at the approximate location of the TIG weld boundary. In the mid-thickness of the cladding material the residual stresses were measured to be compressive. The distinct double-peak at the weld boundaries implies that, prior to the laser welding process, the stress in the machined sections were not in a stress-free state.

B5 Neutron diffraction measurements on three CT specimens were measured using both the d_0 measurement and the plane stress assumption. Given the microstructure and texture issues associated with the d_0 measurement (see **A7**) the plane stress assumption was assumed to provide more accurate results. Comparisons of the three specimens showed similar trends and magnitudes of residual stress for each of the orthogonal directions, indicating that the position of the CT specimen in the component had relatively little effect on the measured residual stresses post-machining. The longitudinal stresses were noted to be compressive at the crack tip and predominately tensile in the remaining ligament. The transverse stresses were found to be predominately compressive.

B6 The following comments pertain to experimental fracture toughness test results of the CT specimens:

B6a Valid fracture toughness data could not be measured experimentally within the validity limits stated by the test method [ASTM International, 2001].

B6b Crack propagation was not measured for every unloading cycle indicating that crack tip blunting occurred at multiple stages of the test.

B6c The appearance of shear deformations and bifurcation of defects on the surfaces of tested samples indicate ductile tearing occurred during testing. Additionally the defect depth was shown to be measurably greater in the mid-thickness region, indicative of crack tunnelling and further evidence of a ductile failure mode.

B6d Digital image correlation (DIC) data showed that the strain on the surface of the sample was biased towards the two weld interface. The major strain appears to have propagated predominately in the austenite region. Limited propagation of strain outside of the cladding was noted to have occurred. Furthermore strains do not appear to propagate from the cladding region to the ferrite region until significant plasticity has occurred in the austenite region.

B6e Strains in the thickness direction are symmetrical around the notch tip, irrespective of the asymmetry of the sample.

B6f The largest magnitudes of strain, measured using the DIC technique, were noted to have occurred approximately 2 mm vertically from the notch tip position. Post-test inspection of the samples show this to be the approximate location of the TIG weld boundary.

B6g Defects on the surface of the sample initiated and propagated at 45 angles to the root of the notch. Defects in the mid-thickness region prop-

agated away from the TIG weld boundary into the austenite material. This indicates that sub-surface defects initiating in the austenite material preferentially grow in the austenite region rather than along the weld boundary.

The following conclusions can be made with reference to finite element modelling:

C1 Three dimensional modelling of the tensile test showed the expected results when homogeneous material properties were applied. For multi-material models it was found that, comparing normalised stresses, the stress in the austenite region was always comparatively higher than that in the ferrite region. When the HAZ material is taken into consideration the disparity between the ferrite, HAZ and austenite regions is of greater magnitude. This indicates that the HAZ region has a large impact on analyses results.

C2 The residual stresses in the laser welded component were estimated using the block dump model (BDM) and the moving heat source (MHS) techniques. With regards to the BDM the following conclusions can be made:

C2a The heat transfer and structural analyses were shown to predict a higher temperature than that noted experimentally. However, the location of the experimental temperature measurement was not adequately marked and hence some deviation between the model and the experimental measurement was expected.

C2b The transverse residual stresses were estimated to be compressive on the surface of the specimen and somewhat tensile in the mid-thickness region.

C2c The longitudinal stresses were predicted to be relatively low on the surface of the specimen and significantly tensile in the mid-thickness. In the mid-thickness region yield magnitude stresses were predicted to exist at the laser weld boundary, predominately in the austenite material.

C2d The normal stresses were predicted to be tensile on both the surface and in the mid-thickness regions. The magnitude of tensile stress was predicted to be greater in the mid-thickness region and was predominately restricted to the austenite material region.

C2e The nodal displacements, and hence the residual stresses, can be successfully mapped from a basic, coarse mesh, to a complex dense mesh without significant loss of residual stresses during the equilibrium phase.

C2.(cont.) With respect to the MHS technique the following conclusions can be made:

C2f The heat transfer and structural analyses were shown to predict lower temperatures on the first weld pass in comparison to the BDM. This was not unexpected given the significant differences between the two heat sources. The MHS predicted a temperature that was similar to that measured experimentally on the first weld pass. The model appeared to overestimate the temperature for the second weld pass, though it should be noted that the model failed to account for the additional time to pre-pressurise the EB chamber. Additional cooling of the component, resulting in a temperature similar to that found experimentally, is considered likely to have been achieved should this have been incorporated.

C2g The transverse residual stresses were estimated to be compressive on the surface. A notable increase in residual stress in the region of the weld overlap was found. This is not unexpected given the type of weld (i.e. double sided weld) utilised. In the mid-thickness region a mixture of tensile and compressive stresses were estimated.

C2h The longitudinal stress was estimated to be negligible on the surface of the specimen. In the mid-thickness the sample was predicted to be compressive towards to outer edges but highly tensile in the mid-section close to the austenite region.

C2i The normal stress was estimated to be a mixture of compressive and tensile stresses both on the surface and in the mid-thickness region.

C2.(cont.) In general the BDM and MHS predicted similar residual stress profiles and compare well. The magnitudes of stress were, as expected, somewhat larger in the MHS in comparison to the BDM. The difference in magnitudes of stress between the models is a reflection of the profiles of the respective heat sources and the volumes to which they were applied.

C3 Assumptions made in the BDM and MHS models can be improved to give better agreement when compared to experimental neutron diffraction measurements. The models did not accounted for residual stresses resulting from phase transformations during the heating and cooling cycles. The assumption that the sections, used to manufacture the laser welded component, were in a stress-free state prior to laser welding is considered inaccurate on the basis of the experimental results obtained. A better agreement between the estimated and measured values can be obtained using an averaging technique as opposed to specific nodal values presented here.

C4 Element deletion was used to estimate the residual stresses in CT specimens post-machining from the laser welded component. The mapping processing was conducted successfully with the majority of residual stress being maintained after equilibrium was achieved.

C4a Removing elements associated with the main block resulted in significant relaxation of stresses in the CT specimens blanks in all three orthogonal directions. In the majority of cases the yield strength tensile stresses in the austenite regions relaxed to a compressive state balanced by tensile stresses in ferrite regions.

C4b Removing singular CT specimens from the specimen blanks relaxed stresses even further. Post-element deletion predicted that tensile residuals stresses

were located in the longitudinal direction only. Furthermore these tensile residual stresses were predicted to be located the austenite material, close to the EB weld. Stresses along the remaining ligament close to the notch tip were predicted to be either compressive or negligible in the normal and transverse directions.

C4c The residual stresses in the CT specimens were predicted to be significantly variable through the thickness of the sample, with larger magnitudes of stress predicted, as expected, in the mid-thickness region.

C4d The predicted residual stresses in the CT specimens compares favourably with those measured experimentally, likely due to the element size being of similar size to the gauge volume used during experimental measurements.

C5 Based on two dimensional (2D) finite element modelling of the compact tension specimens the following conclusions can be made:

C5a Plastic collapse of a specimen with an initial defects of $a/W = 0.45$ and $a/W = 0.55$ is postulated to occur at a loads of approximately 35.8 kN and 26.3 kN respectively. The estimated J-integral values at plastic collapse for the aforementioned crack depths were 314.84 MPa mm (9.95 MPa m) and 482.7 MPa mm (15.26 MPa m), respectively.

C5b As expected, plane strain analyses were, in general, more limiting in terms of stress magnitudes compared to plane stress analyses. Furthermore analyses shown that at the weld boundary the strain in austenite material is always of greater magnitude compared with strains in the ferrite material. This is supported by experimental observations.

C5c Modifying the thickness of the austenite region has significant affects on computed results. Increasing the volume of austenite tends to reduce

strains along the remaining ligament for comparable applied displacements. Given that during ductile failure, such as those noted in **B6**, defect propagation occurs via strain exhaustion, the results indicate that defects are less likely to propagate in samples containing thicker regions of cladding.

C5d The proximity of the notch tip to the weld boundary was also found to have an impact on analyses results. Unsurprisingly notches located in closer proximity result in higher stresses at the weld boundary. The strains along the remaining ligament do not appear to be influenced by the presence of a weld boundary.

C5e Overall a good agreement was found between experimental DIC results of fracture testing on CT specimens and the 2D plane strain and plane stress assumption models.

C5f Inverting the material properties (so the majority of the specimen was manufactured from austenite with a notched 6 mm ferrite region) predicted significantly different results in comparison to the austenite cladding case. Strains initiate, as expected, at the crack tip however, strain is estimated to almost immediately propagate into the austenite material. Taking the ductility of the respective materials (see **A4**) into consideration this indicates that defects located in the ferrite material, close to the weld boundary, are likely to propagate in the ferrite material only. Further, while strains do propagate through the weld boundary into the bulk austenite region, they propagate at an angle to the crack tip. Hence, in a real-world specimen, the implication is that sub-surface defects in the ferrite material may propagate without any indications of failure in the austenite region.

C6 Three dimensional (3D) finite element modelling of the compact tension specimens under experimentally measured load-line displacement data was conducted. Based on the results the following conclusions can be made:

C6a The force versus reaction curve changes depending on whether the specimens is assumed to be notched in the ferrite or austenite material. This is not unexpected given the variation in yield strengths noted in **A4**. Specimens notched in ferrite material were estimated to reach lower magnitudes of force for comparable values of displacement. This was not unexpected given that the bulk of the specimen is comprised of austenite material which has a lower yield strength.

C6b Strains on both the surface and the mid-thickness of the 3D model were significantly larger than strains predicted in the 2D model.

8.3 Future work

Testing conducted in this work was limited due to material availability. In terms of structural integrity assessments the following additional tests are recommended:

- Additional microscopy of the EB laser welded component is recommended. The morphology of the ferrite phase in the cladding can be better assessed if additional orientations orientations are investigated. Furthermore better contrast between the various phases using a different chemical compositions for etching than those used in this work. The use of scanning electron microscopy (SEM) and energy dispersive x-ray (EDX) technologies would provide additional useful information about the microstructure.

- Tensile testing on cross-weld samples on both the TIG welded plate and the laser welded component would provide data on the likelihood of failure for the relative materials. The failure strain of a cross welded sample will additionally pro-

vide data on the Young's modulus value that should be used when fracture testing combined samples.

- Charpy impact testing of the relevant materials and the weld combinations would be of great interest. The transition temperature may be influenced by the microstructure and/or the combination of materials.

- Additional fracture toughness testing of combined and homogeneous samples should be conducted. The performance at temperatures other than ambient temperature would ensure valid fracture toughness data were gathered. High temperature testing would be of particular interest to the nuclear industry but is unlikely to be qualified to the test method used in this work.

- The applicability of the master curve approach should be assessed for dissimilar metal welds.

The finite element work conducted in this thesis could be improved by the following:

- The weld models could incorporate phase transformations in the ferritic material. The remaining residual stress in the TIG welded plate could be calculated using modelling. This information could then be incorporated into the laser welding model discussed here. An averaging technique, mimicking the neutron diffraction gauge volumes, could be applied to the nodal values of residual stress reported in this work. The application of these points is likely to significantly improve the correlation between experimental measurements and modelling predictions of residual stress.

- The 2D parametric studies detailed in this work were limited. A more comprehensive study of both CT and SENB type specimens could be implemented. The influence of material properties, yield strength, ultimate tensile strength, hardening ability etc. could be expanded and additional material grades could also be investigated. Furthermore additional fracture parameters such as T-stress and Q-

stress could be analysed and the sensitivity of each to geometrical conditions could be assessed.

- The estimated residual stress in the CT specimens should be incorporated into the 3D model assessment of the fracture toughness test. The impact, on residual stress and on elastic-plastic fracture parameters such as J-integral and Q-stress could be investigated.

- The 3D model of the fracture toughness test could be further expanded to incorporate damage. The propagation of damage could be compared to experimental data derived in this work.

References

Abburi Venkata, K., Truman, C., Khayatzadeh, S. and Coules, H. [2016], 'Interaction of residual stresses with applied stresses in a dissimilar metal electron beam welded specimen'.

Abburi Venkata, K., Truman, C. and Smith, D. J. [2015], 'Characterising residual stresses in a dissimilar metal electron beam welded plate', *Procedia Engineering* **130**, 973–975.

Abburi Venkata, K., Truman, C., Smith, D. J. and Bhaduri, A. [2016], 'Characterising electron beam welded dissimilar metal joints to study residual stress relaxation from specimen extraction', *International Journal of Pressure Vessels and Piping* (139-140), 237–249.

Aird, C., Smith, M., Kapadia, P., Abburi Venkata, K. and Muransky, O. [2013], 'Round robin prediction of residual stresses in the edge-welded beam r6 validation benchmark problem', (55713), V06BT06A088. 10.1115/PVP2013-98039.
URL: *http://dx.doi.org/10.1115/PVP2013-98039*

American Society of Mechanical Engineers ASME [2015*a*], 'BPVC Section ii - Materials -Part D - Properties (BPVC - IID - 2015)'.

American Society of Mechanical Engineers ASME [2015*b*], 'BPVC Section VIII - Rules for Construction of Pressure Vessels Division 1 (BPVC-VIII-1-2015)'.

American Society of Mechanical Engineers ASME [2015*c*], 'BPVC Section VIII - Rules for Construction of Pressure Vessels Division 2 - Alternative Rules (BPVC-VIII-2-2015)'.

Anderson, T. [2005], *Fracture mechanics: fundamentals and applications*, 3 edn, Boca Raton, FL: Taylor & Francis.

ARAMIS: User Information - Hardware [2013], Report, GOM-GmbH.

Arun, S. [2015], Finite element modelling of fracture & damage in austenitic stainless steel in nuclear power plant, Thesis, University of Manchester.

Ashby, M. F. and Jones, D. R. [2006], Chapter 11 - steels 1—carbon steels, *in* M. F. Ashby and D. R. Jones, eds, 'Engineering Materials 2 (Third Edition)', third edition edn, International Series on Materials Science and Technology, Butterworth-Heinemann, Boston, pp. 112 – 134.

ASM International Handbook Committee [2010], *Volume 1 - Properties and Selection: Irons, Steels and Higher-Performance Alloys*, Vol. 1 of *ASM Handbook*, 10 edn.
URL: *http://products.asminternational.org/hbk/index.jsp*

ASM International Handbook Committee [2011], *Superalloys*, Superalloys, ASM Handbook Supplements.

ASTM International [2001], ASTM E1820-01: Standard Test Method for Measurement of Fracture Toughness.

Bettinson, A. D. [2001], The influence of constraint on the creep crack growth of 316H stainless steel, Thesis, Imperial College London,,.

Bhadeshia, H. and Honeycombe, R. [2017], *Steels: Microstructure and Properties*, Elsevier Science & Technology, Oxford, UNITED KINGDOM.
URL: *http://ebookcentral.proquest.com/lib/imperial/detail.action?docID=4775700*

Boin, M. [2015], 'Setup specs'.
URL: *https://www.helmholtz-berlin.de/forschung/oe/em/mikro/methoden/ neutronendiffraktometer/setup_en.html*

Branco, C. M., Maddox, S. J., Infante, V. and Gomes, E. C. [1999], 'Fatigue performance of tungsten inert gas (tig) and plasma welds in thin sections', *International Journal of Fatigue* **21**(6), 587–601.

Brayshaw, W. J., Cooper, A., Sherry, A. H. and James, P. [2018], 'Advanced assessment of ductile fracture behaviour in dissimilar metal welds using x-ray tomography', (51685), V06BT06A042. 10.1115/PVP2018-84014.
URL: *http://dx.doi.org/10.1115/PVP2018-84014*

British Energy [2008], 'R6: Revision 4, Amendment 6: Assessment of the integrity of structures containing defects'.

British Standards Institute [2001], 'BS EN 10002-1:2001: Metallic materials - Tensile testing - Part 1: Method of test at ambient temperature'.

British Standards Institute [2015*a*], 'BS7910:2013+A1:2015 Guide to methods for assessing the acceptability of flaws in metallic structures'.

British Standards Institute [2015*b*], 'PD 5500:2015: Specification for unfired fusion welded pressure vessels'.

British Standards Institute [2018*a*], 'BS EN 13445-2:2014 + A3:2018: Unfired pressure vessels'.

British Standards Institute [2018*b*], 'BS ISO 21432: Non-destructive testing. standard test method for determining residual stresses by neutron diffraction.'.
URL: *https://bsol.bsigroup.com/Bibliographic/BibliographicInfoData/000000000030372101*

Buongiorno, J. [2010], 'BWR Description'.
URL: *http://ocw.mit.edu/courses/nuclear-engineering/22-06-engineering-of-nuclear-systems-fall-2010/lectures-and-readings/MIT22_06F10_lec06b.pdf*

Caccese, V., Blomquist, P. A., Berube, K. A., Webber, S. R. and Orozco, N. J. [2006], 'Effect of weld geometric profile on fatigue life of cruciform welds made by laser/gmaw processes', *Marine Structures* **19**(1), 1–22.

Chater, J. [2005], 'A history of nuclear power', *Nuclear Exchange* .
URL: *http://www.nuclear-exchange.com/pdf/TP_History_nuclear.pdf*

Choi, S. N., Jang, K. S., Kim, J. S., Choi, J. B. and Kim, Y. J. [2000], 'Effect of cladding on the stress intensity factors in the reactor pressure vessel', *Nuclear Engineering and Design* **199**(1–2), 101–111.

Cooper, M. W. D. [2015], Atomic scale simulation of irradiated nuclear fuel, Thesis, Imperial College London.
URL: *http://abulafia.mt.ic.ac.uk/publications/theses/michael-cooper/Cooper-MWD-2015-PhD-Thesis.pdf*

Croften, S. [2007], 'Lecture notes: Fundementals of fracture mechanics'.

Crupi, V., Guglielmino, E., Maestro, M. and Marinò, A. [2009], 'Fatigue analysis of butt welded ah36 steel joints: Thermographic method and design s–n curve', *Marine Structures* **22**(3), 373–386.
URL: *http://www.sciencedirect.com/science/article/pii/S0951833909000252*

Dassault Systemes Simulia Corp [2014], 'Abaqus 6.14 documentation'.

David, S. [1981], 'Ferrite morphology and variations in ferrite content in austenitic stainless steel welds', *Welding Journal Research Supplement* .
URL: *https://app.aws.org/wj/supplement/WJ˙1981˙04˙s63.pdf*

Davis, J. [1994], *Stainless steel cladding and weld overlays*, ASM International, p. 13.

Daw, J. E., Rempe, J. L. and Knudson, D. L. [2010], 'Thermal properties of structural materials used in lwr vessels', *Journal of Nuclear Materials* **401**(1–3), 65–70.

Dodds, R. H., Anderson, T. L. and Kirk, M. T. [1991], 'A framework to correlate a/w ratio effects on elastic-plastic fracture toughness (jc)', *International Journal of Fracture* **48**(1), 1–22.
URL: *https://doi.org/10.1007/BF00012499*

Dodge, M. [2014], The Effect of Heat Treatment on the Embrittlement of Dissimilar Welded Joints, Thesis.

Dolby, R. E., Wiesner, C. S., Ainsworth, R. A., Burdekin, F. M., Hancock, J., Milne, I. and O'Dowd, N. P. [2005], 'Review of a procedure for performing constraint and attenuation-corrected fracture mechanics safety case calculations for magnox reactor steel pressure vessels', *International Journal of Pressure Vessels and Piping* **82**(6), 496–508.

Duffy, C. J. [2014], Modelling the electron beam welding of nuclear reactor pressure vessel steel, Report, University of Cambridge.
URL: *https://www.phase-trans.msm.cam.ac.uk/2014/Duffy.pdf*

Dunnett, T. J. [2014], Linkage of intermediate damage in metallics to material and fracture models, Thesis.
URL: *https://spiral.imperial.ac.uk:8443/handle/10044/1/27253*

Ficquet, X., Smith, D., Truman, C. E., Kingston, E. and Dennis, R. [2009], 'Measurement and prediction of residual stress in a bead-on-plate weld benchmark specimen', *International Journal of Pressure Vessels and Piping* **86**, 20–30.

Francis, J. A., Bhadeshia, H. and Withers, P. J. [2007], 'Welding residual stresses in ferritic power plant steels', *Materials Science and Tecnology* .
URL: *http://dx.doi.org/10.1179/174328407X213116*

GOM [2017], 'Gom correlate professional 2017 hotfix 7, rev. 113517, build 2018-11-12'.

Gooch, T. G. [1976], Review of overlay welding procedures for light water nuclear reactor pressure vessels, Report, The Welding Institute (TWI),,.

Hanninen, H., Aaltonen, P., Brederholm, A., Ehrnsten, U., Gripenberg, H., Toivonen, A., Pitkanen, J. and Virkkunen, I. [2006], 'Dissimilar metal weld joints and their performance in nuclear power plant and oil refinery conditions'.

Hirdaris, S. E., Cheng, Y. F., Shallcross, P., Bonafoux, J., Carlson, D., Prince, B. and Sarris, G. A. [2014], 'Considerations on the potential use of nuclear small modular reactor (smr) technology for merchant marine propulsion', *Ocean Engineering* **79**, 101–130.

Honeycombe, J. and Gooch, T. G. [1985], Arc welding ferritic-austenitic stainless steels: prediction of weld area microstructures, Report, The Welding Institute.

Hutchinson, J. [1983], 'Fundamentals of the phenomenological theory of nonlinear fracture mechanics', *Journal of Applied Mechanics* **50**(4b), 10.
URL: *http://appliedmechanics.asmedigitalcollection.asme.org/mobile/article.aspx? articleID=1407320*

IAEA [1966], Pressure vessel codes: Their application to nuclear reactor systems. findings from a survey by the internation atomic energy agency, Report 56, International Atomic Energy Agency IAEA.

IAEA [1999], Pwr pressure vessels, Report, International Atomic Energy Agency IAEA.

IAEA [2005], Measurement of residual stress in materials using neutrons: Proceedings of a technical meeting held in vienna 13-17 october 2003, Report, International Atomic Energy Agency IAEA.

IAEA [2009*a*], Deterministic safety analysis for nuclear power plants: safety guide, Report, International Atomic Energy Agency IAEA.

IAEA [2009*b*], Integrity of reactor pressure vessels in nuclear power plants: assessment of irradiation embrittlement effects in reactor pressure vessel steels, Report, International Atomic Energy Agency IAEA.
URL: *http://www-pub.iaea.org/MTCD/publications/PDF/Pub1382_web.pdf*

IAEA [2010], Deterministic evaluation for the integrity of reactor pressure vessel., Report, International Atomic Energy Agency IAEA.
URL: *http://www-pub.iaea.org/MTCD/publications/PDF/te_1627_web.pdf*

IAEA [2014], Nuclear safety review 2014, Report, International Atomic Energy Agency IAEA.
URL: *https://www.iaea.org/About/Policy/GC/GC58/GC58InfDocuments/English/ gc58inf-3_en.pdf*

IAEA [2015], Ageing management for nuclear power plants: international generic ageing lessons learned (igall), Report, International Atomic Energy Agency IAEA.

Instron [2010*a*], '$\frac{da}{dN}$ fatigue crack propagation software application program'.

Instron [2010*b*], 'J_1*C* fracture toughness software application program'.

International Institute of Welding [2008], 'Recommendations for fatigue design of welded joints and components'.

James, M. N., Newby, M., Doubell, P., Hattingh, D. G., Serasli, K. and Smith, D. J. [2014], 'Weld residual stresses near the bimetallic interface in clad rpv steel: A comparison between deep-hole drilling and neutron diffraction data', *Nuclear Engineering and Design* **274**(0), 56–65.
URL: *http://www.sciencedirect.com/science/article/pii/S0029549314002039*

Jang, C., Cho, P.-Y., Kim, M., Oh, S.-J. and Yang, J.-S. [2010], 'Effects of microstructure and residual stress on fatigue crack growth of stainless steel narrow gap welds', *Materials & Design* **31**(4), 1862–1870.
URL: *http://www.sciencedirect.com/science/article/pii/S0261306909006177*

Kamel, S. [2010], The effects of constraint and residual Stress on ductile and brittle fracture, Thesis, Imperial College London.

Kapadia, P. [2014], Experimental and Numerical Analysis of Creep Cracking under Secondary and Combined Loading, Thesis, Imperial College London.

Köhler, H., Rajput, R., Khazan, P. and Kornmeier, J. R. [2014], 'On the influence of laser cladding and post-processing strategies on residual stresses in steel specimens', *Physics Procedia* **56**, 250–261.
URL: *http://www.sciencedirect.com/science/article/pii/S1875389214003149*

Kim, J. W., Lee, K., Kim, J. S. and Byun, T. S. [2009], 'Local mechanical properties of alloy 82/182 dissimilar weld joint between sa508 gr.1a and f316 ss at rt and 320∘c', *Journal of Nuclear Materials* **384**(3), 212–221.

Kiser, S. D., Hinshaw, E. B., Crum, J. R. and Shoemaker, L. E. [2005], 'Nickel alloy welding requirements for nuclear service'.
URL: *http://www.specialmetals.com/assets/smw_docs/Special-Metals.pdf*

Maddox, S. J. [1991], *Fatigue strength of welded structures*, 2nd ed. edn, Cambridge : Abington Publishing, Cambridge.

Maddox, S. J. [2000], 'Fatigue design rules for welded structures', *Progress in Structural Engineering and Materials* **2**(1), 102–109.
URL: *http://dx.doi.org/10.1002/(SICI)1528-2716(200001/03)2:1¡102::AID-PSE12¿3.0.CO;2-A*

Naveed, N. [2015], Improving the spatial resolution of the contour method, Thesis, Open University.

O'Connor, A., Davies, C. M., Garwood, S. J. and Hadley, I. [2019], 'Optimising the safe design of pressurised components'.

Pollard, B. and Cover, R. [1972], 'Fatigue of steel weldments'.
URL: *https://app.aws.org/wj/supplement/WJ_1972_11_s544.pdf*

Rathod, D. W., Pandey, S., Singh, P. K. and Kumar, S. [2017], 'Microstructure-dependent fracture toughness (jic) variations in dissimilar pipe welds for pressure vessel system of nuclear plants', *Journal of Nuclear Materials* **493**, 412–425.

Rathod, D. W., Pandey, S., Singh, P. K. and Prasad, R. [2015], 'Experimental analysis of dissimilar metal weld joint: Ferritic to austenitic stainless steel', *Materials Science and Engineering: A* **639**(0), 259–268.

Rosenthal, Y., Tobler, R. and Purtscher, P. [1990], 'Jic data analysis methods with a negative crack growth; correction procedure'.

Rowinski, M. K., White, T. J. and Zhao, J. [2015], 'Small and medium sized reactors (smr): A review of technology', *Renewable and Sustainable Energy Reviews* **44**, 643–656.

Seok, C.-S. [2000], 'Correction methods of an apparent negative crack growth phenomenon', *International Journal of Fracture* **102**(3), 259–269.
URL: *https://doi.org/10.1023/A:1007680608587*

Serasli, K. [2014], Measurement and mapping of residual stresses in welded nuclear components, Thesis.

Server, W. L. and Nanstad, R. K. [2015], *1 - Reactor pressure vessel (RPV) design and fabrication: the case of the USA*, Woodhead Publishing, pp. 3–25.

Slaughter, G. M. and Housely, T. R. [1962], The welding of ferritic steels to austenitic stainless steels, Report, Oak Ridge National Laboratory.

Smith, J. A. and Rolfe, S. T. [1994], 'The effect of crack depth (a) and crack depth to width ratio (a/w) on the fracture toughness of a533-b steel', *Journal of Pressure Vessel Technology* **116**(2), 115–121. 10.1115/1.2929564.

Smith, M. C. and Smith, A. C. [2009], 'Net bead-on-plate round robin: Comparison of residual stress predictions and measurements', *International Journal of Pressure Vessels and Piping* **86**(1), 79–95.

Smith, S. [1997], Comparison of the PD6493:1991 RHO factore with FEA results, Report, TWI Ltd.

Spence, J. and Nash, D. H. [2004], 'Milestones in pressure vessel technology', *International Journal of Pressure Vessels and Piping* **81**(2), 89–118.

Submerged-arc welding [n.d.].
URL: *http://www.twi-global.com/technical-knowledge/job-knowledge/submerged-arc-welding-process-005/*

The manual metal arc process (MMA Welding) [n.d.].
URL: *http://www.twi-global.com/technical-knowledge/job-knowledge/the-manual-metal-arc-process-mma-welding-002/*

Tomkins, B. [2003], *1.09 - Structural Integrity Issues in the Nuclear Industry*, Pergamon, Oxford, pp. 173–192.

Törrönen, K., Saario, T., Wallin, K. and Forstén, J. [1984], 'Mechanism based evaluation of materials behavior and reference curves', *Nuclear Engineering and Design* **81**(1), 35–50.

Verstraete, M. A., Hertelé, S., Denys, R. M., Van Minnebruggen, K. and De Waele, W. [2014], 'Evaluation and interpretation of ductile crack extension in sent specimens using unloading compliance technique', *Engineering Fracture Mechanics* **115**, 190–203.
URL: *http://www.sciencedirect.com/science/article/pii/S0013794413003585 https://ac.els-cdn.com/S0013794413003585/1-s2.0-S0013794413003585-main.pdf?_tid=c9dababc-c763-4c7c-983b-12ce22339112&acdnat=1544556810_a2d536f54927cba69748eabfe56b2f4d*

Vitale, E. [1989], 'Trends in the evaluation of the structural integrity of rpvs', *Nuclear Engineering and Design* **116**(2), 73–100.
URL: *http://www.sciencedirect.com/science/article/pii/002954938990229X*

Voss, B. [1983], *On the problem of 'negative crack growth' and 'load relaxation' in single specimen partial unloading compliance tests*, OECD, Nuclear Energy Agency of the OECD (NEA).
URL: *http://inis.iaea.org/search/search.aspx?orig_q=RN:15025413*

Washko, S. and Aggen, G. [1990], *Wrought Stainless Steels*, Vol. 1, ASM International.
URL: *https://matdata.asminternational.org/hbk/index.jsp*

Wei, L., Johnston, C. and Gallegillo, M. [2010], A review of fabrication technologies, residual stresses and structural integrity in clad components, Report, TWI Ltd.

Weiss, K. and Nyilas, A. [2006], 'Specific aspects on crack advance during j-test method for structural materials at cryogenic temperatures', *Fatigue & Fracture of Engineering Materials & Structures* **29**(2), 83–92.
URL: *https://onlinelibrary.wiley.com/doi/abs/10.1111/j.1460-2695.2006.00963.x https://onlinelibrary.wiley.com/doi/pdf/10.1111/j.1460-2695.2006.00963.x*

World Nuclear Association [2015], 'Nuclear power reactors'.

URL: *http://www.world-nuclear.org/info/Nuclear-Fuel-Cycle/Power-Reactors/Nuclear-Power-Reactors/*

Appendix A: Appendix Chapter 4 Mechanical Properties and Metallography

Table A.1: Hardness HV10 values for weld start position

Measurement Line	**1**	**2**	**3**
Distance fom top (mm)	**HV10 Value**		
6	226.0	202.6	188.1
12	211.5	188.1	211.5
14	229.7	194.9	194.5
16	252.1	190.1	203.0
18	281.4	241.5	268.9
20	189.0	193.9	271.3
22	220.8	166.7	217.3
24	219.8	174.8	238.9
26	453.1	248.4	234.5
28	534.8	232.3	483.2
30	253.4	201.7	201.9
36	222.1	228.4	238.7
40	232.8	229.2	220.9

Table A.2: Hardness HV10 values for weld end position

Measurement Line	**1**	**2**	**3**
Distance fom top (mm)	**HV10 Value**		
6	207.8	199.9	201.8
12	209.6	236.0	210.3
14	206.5	219.5	214.8
16	201.3	197.5	198.9
18	317.1	224.1	247.3
20	244.1	196.6	246.9
22	201.8	177.9	183.0
24	205.2	231.3	209.6
26	174.1	250.4	220.8
28	486.6	208.3	462.2
30	208.5	196.4	228.1
36	207.4	201.4	218.3
40	216.8	208.5	199.2

Table A.3: HV10 hardness measurements on original TIG weld plate

Measurement line number	5	4	3	2	1
Distance from left side of plate (mm)	**HV10 Hardness values**				
5	173.1	205.7	240.8	208.5	-
10	178.6	205.9	256.6	277.2	-
15	174.3	201.0	272.0	295.5	228.6
20	176.3	214.8	278.8	301.7	201.1
25	175.0	193.8	250.4	233.3	231.2
30	179.6	206.3	220.9	242.3	207.8
35	202.1	213.0	219.8	275.5	223.8
40	192.3	234.8	210.5	339.8	252.8
45	201.3	229.5	222.7	249.7	254.1
50	209.5	225.1	213.0	334.9	209.8
55	192.9	219.2	225.7	223.5	259.1
60	195.8	206.4	214.2	305.6	256.0
65	185.1	208.1	240.2	302.7	278.5
70	192.8	211.5	220.0	265.2	230.5
75	188.0	198.1	218.0	277.0	225.4
80	190.7	220.3	197.2	392.3	207.0
85	181.6	204.6	206.7	295.9	195.2

Table A.4: Engineering Stress-Strain Data

Specimen Number		17	15	14	13	12	11	10	8	7	6	5	4	3
Yield strength	MPa	450.00	450.00	460.00	450.00	450.00	450.00	450.00	400.00	400.00	400.00	500.00	350.00	300.00
0.2% proof stress	MPa	485.00	475.00	475.00	490.00	440.00	480.00	480.00	480.00	470.00	460.00	580.00	470.00	380.00
Young's Modulus	GPa	215.23	197.88	205.90	205.30	176.51	186.19	186.18	193.23	221.21	186.02	185.00	171.01	185.73
UTS	MPa	621.96	612.86	608.47	624.93	573.05	612.88	618.22	622.51	613.94	594.01	676.37	615.93	580.69

Table A.5: Power law constants for calculation of true stress-true strain data for ferrite samples

Specimen Number	17	15	14	13	12	11	10	8	7	6
A	4.54E-13	5.27E-13	3.05E-13	3.84E-13	3.80E-13	1.66E-13	7.22E-13	9.73E-13	1.40E-12	3.09E-13
n	4.01	4.00	4.09	4.04	4.06	4.19	3.95	3.89	3.84	4.09

Table A.6: Power law constants for calculation of true stress-true strain data for austenite and mixed samples

Specimen Number	5	4	3	2
A	1.90E-16	1.16E-13	2.20E-16	2.34E-15
n	5.11	4.21	5.24	5.09

Figure A.1: Temperature dependent thermal conductivity curve digitalised from literature [Serasli, 2014]

Figure A.2: Temperature dependent specific heat curve digitalised from literature [Serasli, 2014]

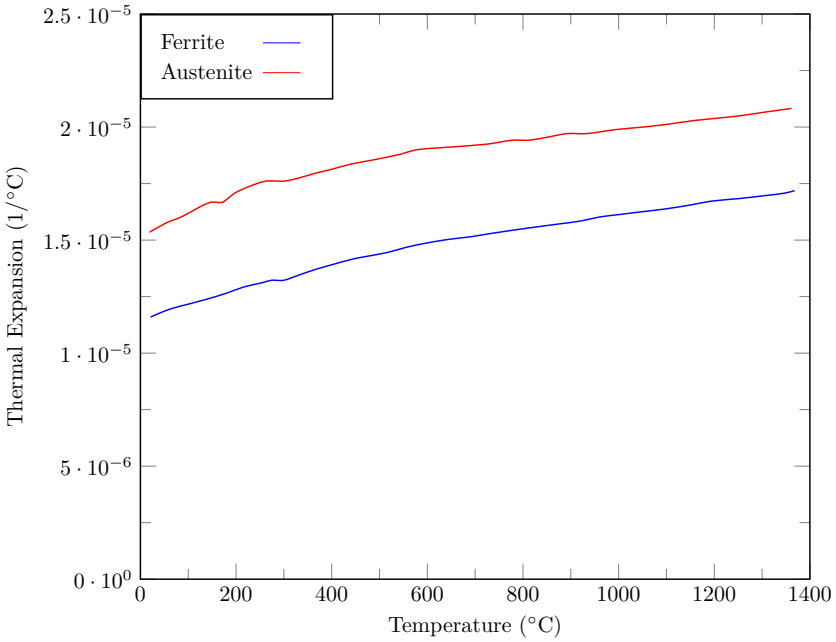

Figure A.3: Temperature dependent thermal expansion curve digitalised from literature [Serasli, 2014]

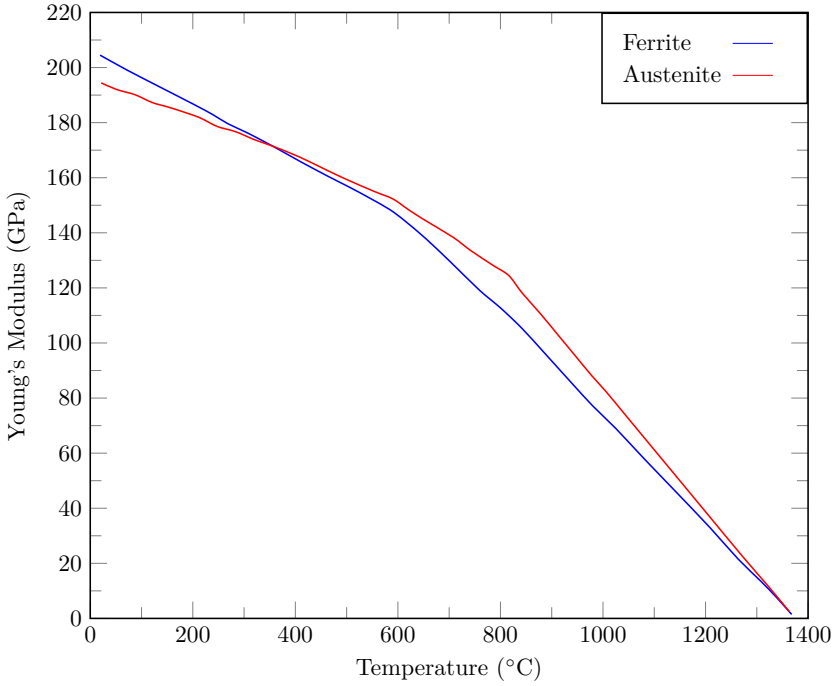

Figure A.4: Temperature dependent Young's modulus curve digitalised from literature [Serasli, 2014]

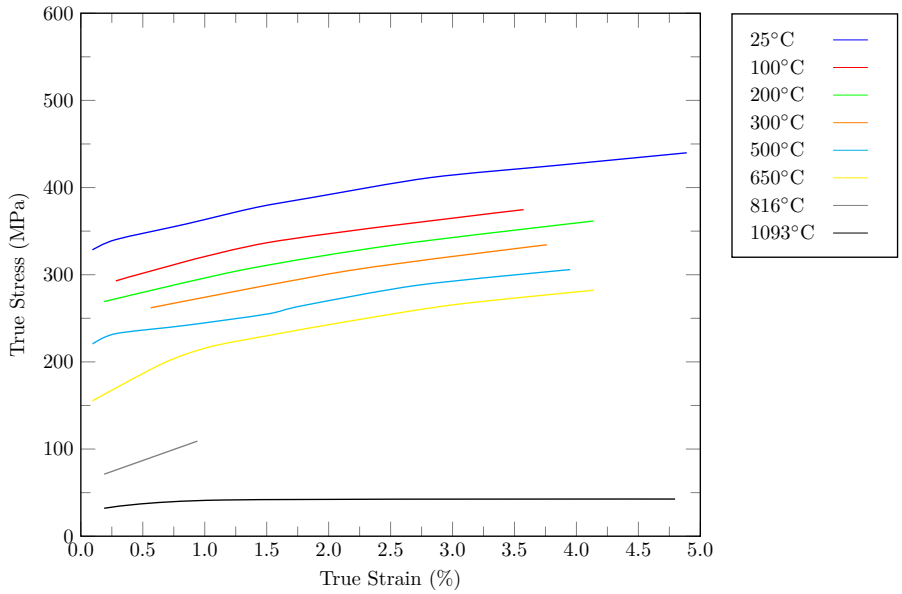

Figure A.5: Temperature dependent true stress - true strain curve for ferrite material digitalised from literature [Serasli, 2014]

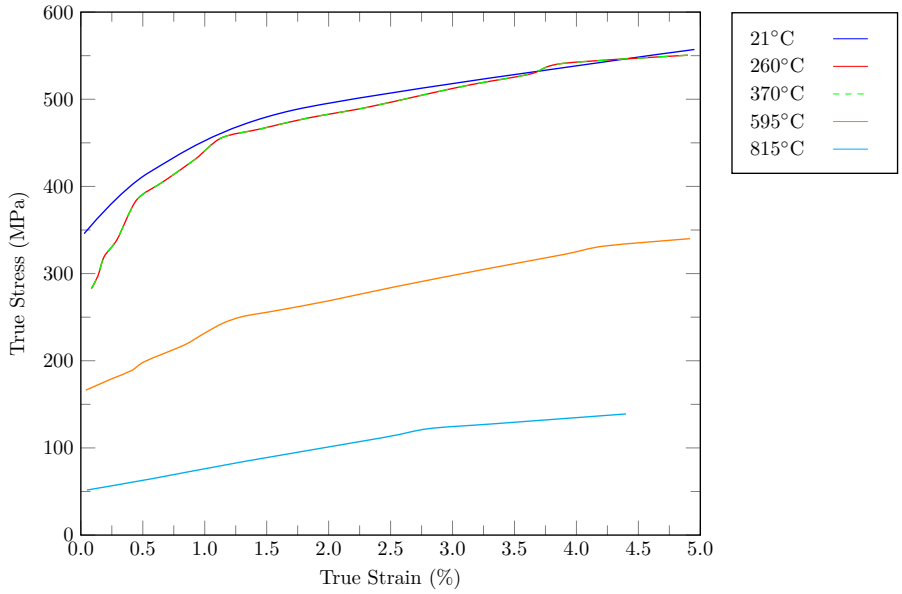

Figure A.6: Temperature dependent true stress - true strain curve for austenite material digitalised from literature [Serasli, 2014]

Appendix B: Appendix Chapter 5 Residual Stresses

B.1 Tensile Residual Stress Measurements

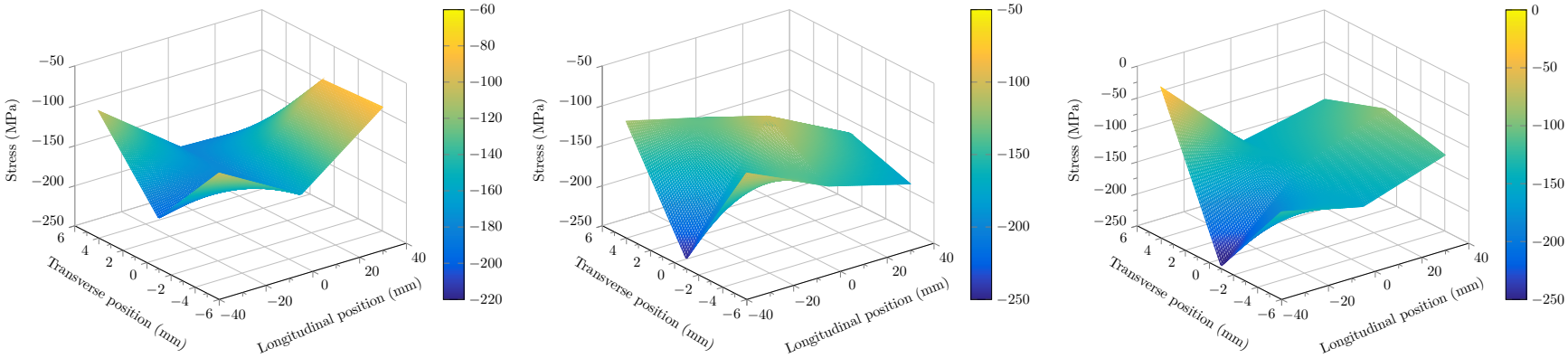

(a) Longitudinal (b) Transverse (c) Normal

Figure B.1: Surface plot of residual stress in tensile specimen 3 using d_0 values

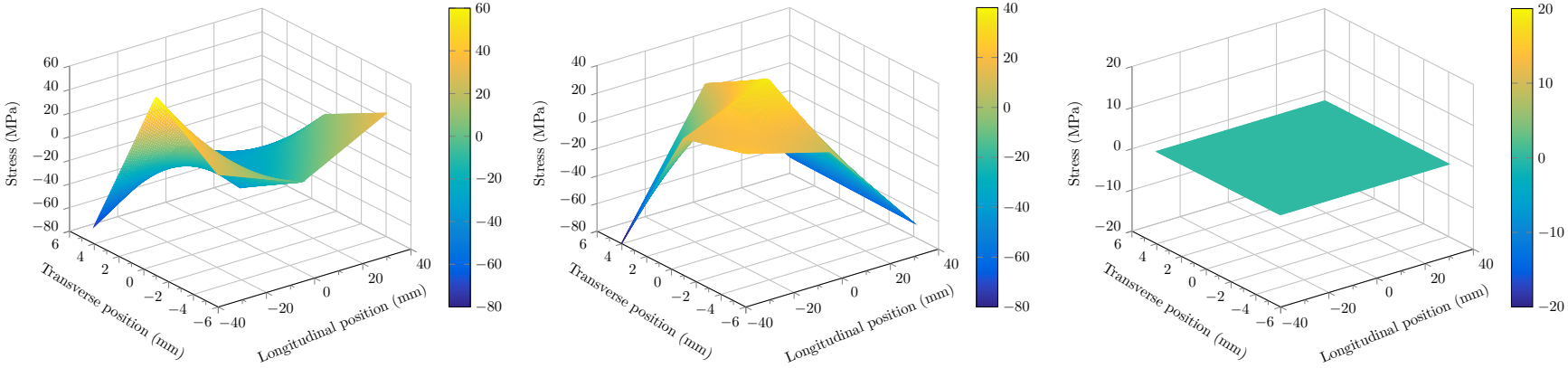

(a) Longitudinal (b) Transverse (c) Normal

Figure B.2: Surface plot of residual stress in tensile specimen 3 assuming plane stress condition

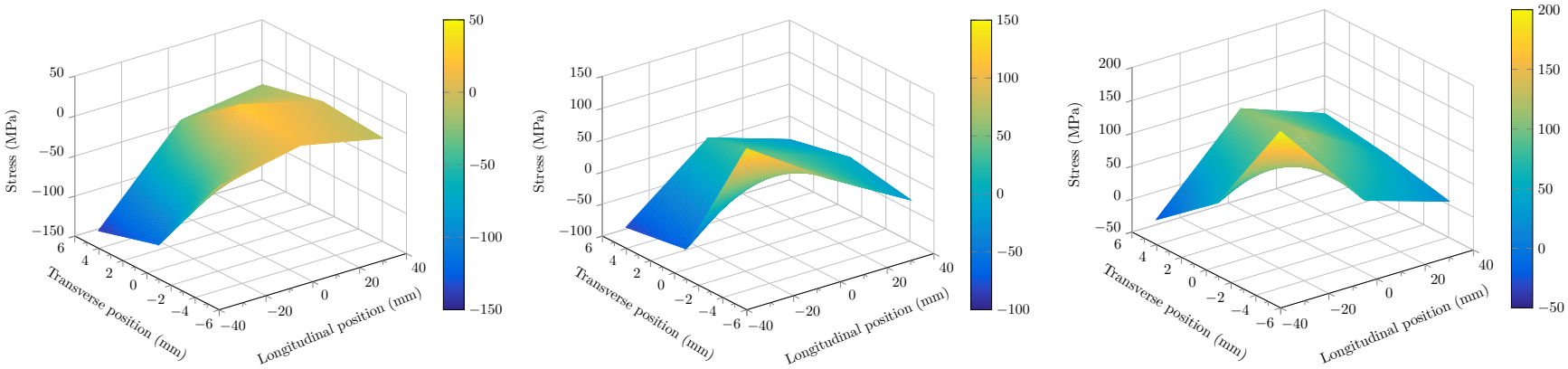

(a) Longitudinal (b) Transverse (c) Normal

Figure B.3: Surface plot of residual stress in tensile specimen 4 using d_0 values

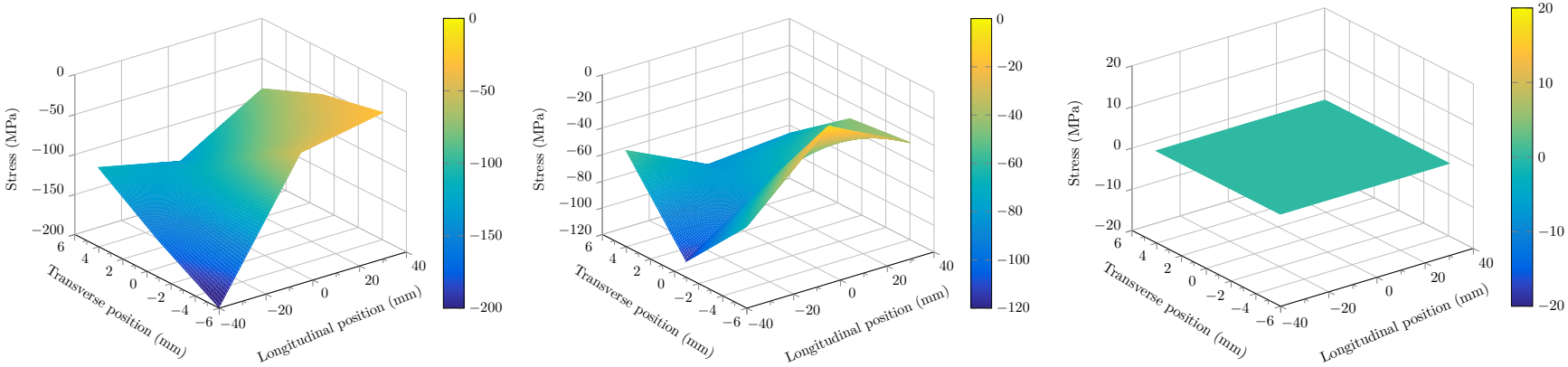

(a) Longitudinal (b) Transverse (c) Normal

Figure B.4: Surface plot of residual stress in tensile specimen 4 assuming plane stress condition

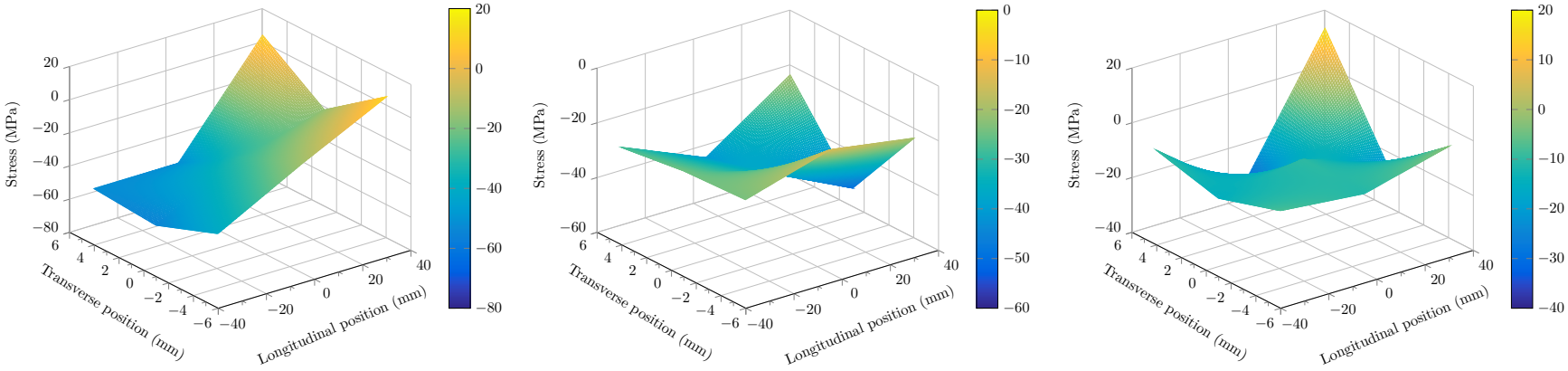

(a) Longitudinal (b) Transverse (c) Normal

Figure B.5: Surface plot of residual stress in tensile specimen 18 using d_0 values

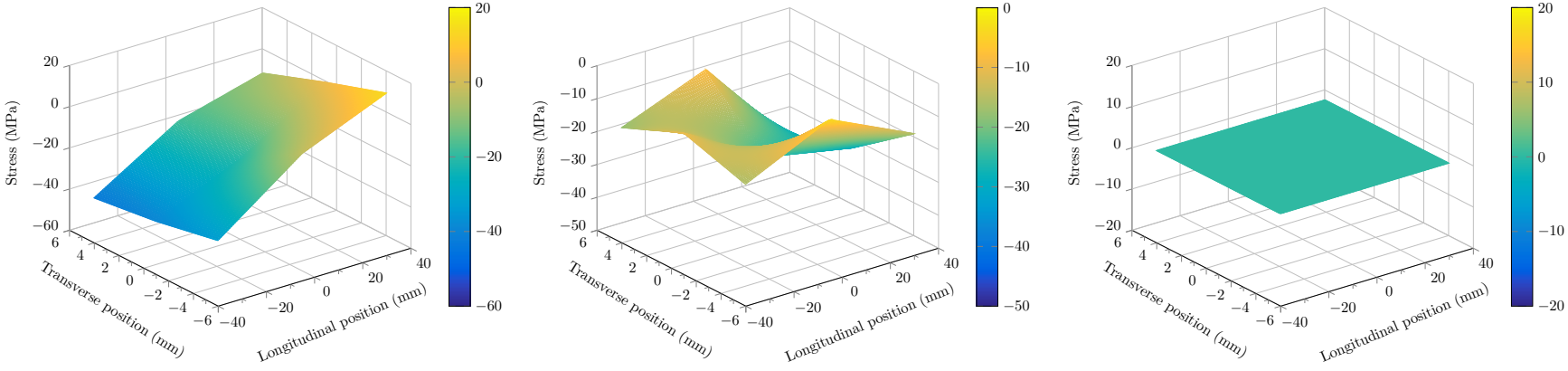

(a) Longitudinal (b) Transverse (c) Normal

Figure B.6: Surface plot of residual stress in tensile specimen 18 assuming plane stress condition

Table B.1: Longitudinal stresses measured in tensile specimens using d_o values

X	Y	Austenite						Ferrite			
		Specimen 2		Specimen 3		Specimen 4		Specimen 4		Specimen 18	
		Stress	Error	Stress	Error	Stress	Error	Stress	Error	Stress	Error
35	-5	-159	37	-83	21	-	36	-9	37	11	29
35	0	-128	31	-87	22	22	24	-2	40	-16	28
35	5	-129	39	-183	19	59	21	-19	48	10	27
0	-5	-109	24	-162	26	-	31	13	49	-14	31
0	0	-60	23	-176	27	48	22	25	53	-30	31
0	5	-89	27	-179	26	50	22	-33	46	-52	28
-35	-5	-136	23	-104	25	11	25	-8	59	-41	33
-35	0	-215	27	-199	25	4	25	-119	87	-55	31
-35	5	-84	31	-103	24	-22	27	-140	66	-52	31

Table B.2: Transverse stresses measured in tensile specimens using d_o values

X	Y	Austenite						Ferrite			
		Specimen 2		Specimen 3		Specimen 4		Specimen 4		Specimen 18	
		Stress	Error	Stress	Error	Stress	Error	Stress	Error	Stress	Error
35	-5	-132	32	-179	23	-	18	-20	44	-20	27
35	0	-125	25	-154	27	90	23	-2	44	-50	28
35	5	-153	28	-186	25	119	21	-22	52	-20	28
0	-5	-159	24	-151	24	-	17	52	58	-15	26
0	0	-99	24	-102	26	33	25	42	46	-35	28
0	5	-106	29	-142	29	52	23	19	42	-41	25
-35	-5	-96	21	-104	23	13	25	137	60	-24	28
-35	0	-199	28	-250	24	13	26	-68	83	-25	29
-35	5	-107	31	-116	26	4	25	-82	78	-28	26

Table B.3: Normal stresses measured in tensile specimens using d_o values

X	Y	Austenite						Ferrite			
		Specimen 2		Specimen 3		Specimen 4		Specimen 4		Specimen 18	
		Stress	Error	Stress	Error	Stress	Error	Stress	Error	Stress	Error
35	-5	-73	30	-116	23	-	23	20	48	-3	26
35	0	-138	29	-92	24	-2	25	42	52	-21	27
35	5	-142	33	-125	22	66	22	57	57	17	27
0	-5	-236	31	-158	24	-	26	60	55	-11	28
0	0	-103	28	-139	25	13	24	117	46	-10	28
0	5	-104	28	-152	26	68	22	103	50	-33	25
-35	-5	-62	25	-128	27	1	24	203	97	-8	28
-35	0	-251	34	-261	29	-34	27	47	127	-15	27
-35	5	-135	27	-29	26	-12	26	-27	97	-9	25

Table B.4: Longitudinal stresses measured in tensile specimens assuming plane stress condition

X	Y	Austenite						Ferrite			
		Specimen 2		Specimen 3		Specimen 4		Specimen 4		Specimen 18	
		Stress	Error	Stress	Error	Stress	Error	Stress	Error	Stress	Error
35	-5	-86	37	33	21	-	-	-29	37	14	29
35	0	10	31	5	22	25	24	-45	40	4	28
35	5	14	39	-58	19	-7	21	-76	48	-7	27
0	-5	127	24	-4	26	-	-	-48	49	-3	31
0	0	42	23	-36	27	35	22	-92	53	-21	31
0	5	15	27	-27	26	-18	22	-136	46	-18	28
-35	-5	-74	23	24	25	10	25	-211	59	-33	33
-35	0	37	27	63	25	39	25	-166	87	-39	31
-35	5	51	31	-74	24	-9	27	-113	66	-43	31

Table B.5: Transverse stresses measured in tensile specimens assuming plane stress condition

X	Y	Austenite						Ferrite			
		Specimen 2		Specimen 3		Specimen 4		Specimen 4		Specimen 18	
		Stress	Error	Stress	Error	Stress	Error	Stress	Error	Stress	Error
35	-5	-59	32	-63	23	-	-	-40	44	-16	27
35	0	13	25	-62	27	92	23	-45	44	-30	28
35	5	-10	28	-61	25	53	21	-79	52	-37	28
0	-5	76	24	7	24	-	-	-9	58	-4	26
0	0	4	24	37	26	21	25	-74	46	-25	28
0	5	-2	29	11	29	-15	23	-84	42	-8	25
-35	-5	-34	21	24	23	13	25	-66	60	-16	28
-35	0	53	28	12	24	48	26	-115	83	-10	29
-35	5	28	31	-87	26	16	25	-55	78	-18	26

Table B.6: Normal stresses measured in tensile specimens assuming plane stress condition

X	Y	Austenite						Ferrite			
		Specimen 2		Specimen 3		Specimen 4		Specimen 4		Specimen 18	
		Stress	Error	Stress	Error	Stress	Error	Stress	Error	Stress	Error
35	-5	0	30	0	23	-	-	0	48	0	26
35	0	0	29	0	24	0	25	0	52	0	27
35	5	0	33	0	22	0	22	0	57	0	27
0	-5	0	31	0	24	-	-	0	55	0	28
0	0	0	28	0	25	0	24	0	46	0	28
0	5	0	28	0	26	0	22	0	50	0	25
-35	-5	0	25	0	27	0	24	0	97	0	28
-35	0	0	34	0	29	0	27	0	127	0	27
-35	5	0	27	0	26	0	26	0	97	0	25

B.2 Block A

Table B.7: Residual stresses measured in EB weld specimen Block A

Position from clad surface of plate (mm)	Stress (MPa)					
	Longitudinal	Transverse	Normal	Longitudinal error	Transverse error	Normal error
5	-105	-34	42	49	38	24
15	-117	-101	-123	33	36	34
20	130	-31	327	90	73	90
21	87	-223	242	56	53	67
22	-50	-349	77	47	49	67
23	-114	-530	-70	52	59	83
25	-51	-413	21	61	72	87
27	21	-274	239	111	84	93
30	82	-200	60	35	44	36
32	43	-59	10	32	36	31
35	-78	-102	-91	27	19	20
40	-122	-38	53	31	13	15
45	-116	-12	150	36	15	15

B.3 CT Residual Stress Measurements

Table B.8: Residual stresses measured in CT1: Weld start

Distance from notch (mm)	Stress (MPa)					
	Longitudinal	Transverse	Normal	Longitudinal error	Transverse Error	Normal error
0	-125	-82	-40	32	54	38
2	36	-111	-34	29	54	31
4	146	-110	40	25	34	23
6	75	-32	2	35	42	39
8	115	-51	57	34	46	34
10	70	-103	-48	30	36	26
12	2	-76	-103	34	40	39
14	145	102	104	40	44	50
16	74	-73	0	30	45	34
18	13	-101	-24	29	45	33
20	13	-12	62	31	41	34
22	11	-44	52	31	34	25

Table B.9: Residual stresses measured in CT2: Mid-weld

Distance from notch (mm)	Stress (MPa)					
	Longitudinal	Transverse	Normal	Longitudinal error	Transverse Error	Normal error
0	136	81	171	24	36	29
2	160	5	82	22	35	28
4	249	37	156	30	42	35
6	158	-86	47	37	49	41
8	180	-12	102	34	52	40
10	301	123	238	35	44	35
12	209	15	44	32	26	34
14	192	38	142	28	34	38
16	132	44	153	27	28	30
18	78	13	118	31	48	30
20	25	-30	81	31	30	31
22	-85	-171	-15	32	42	29

Table B.10: Residual stresses measured in CT3: Weld end

Distance from notch (mm)	Stress (MPa)					
	Longitudinal	Transverse	Normal	Longitudinal error	Transverse Error	Normal error
0	25	-106	167	30	55	34
2	129	-40	120	28	48	30
4	31	-64	1	28	47	34
6	263	148	241	30	49	29
8	244	116	280	33	34	31
10	224	65	210	41	43	34
12	246	101	166	26	29	27
14	138	44	171	32	41	30
16	137	76	147	28	40	25
18	185	111	143	33	50	33
20	-43	-96	60	43	53	36
22	-242	-251	-155	37	35	31

Appendix C: Appendix Chapter 6 Defects oriented parallel to materials boundary

C.1 Experimental

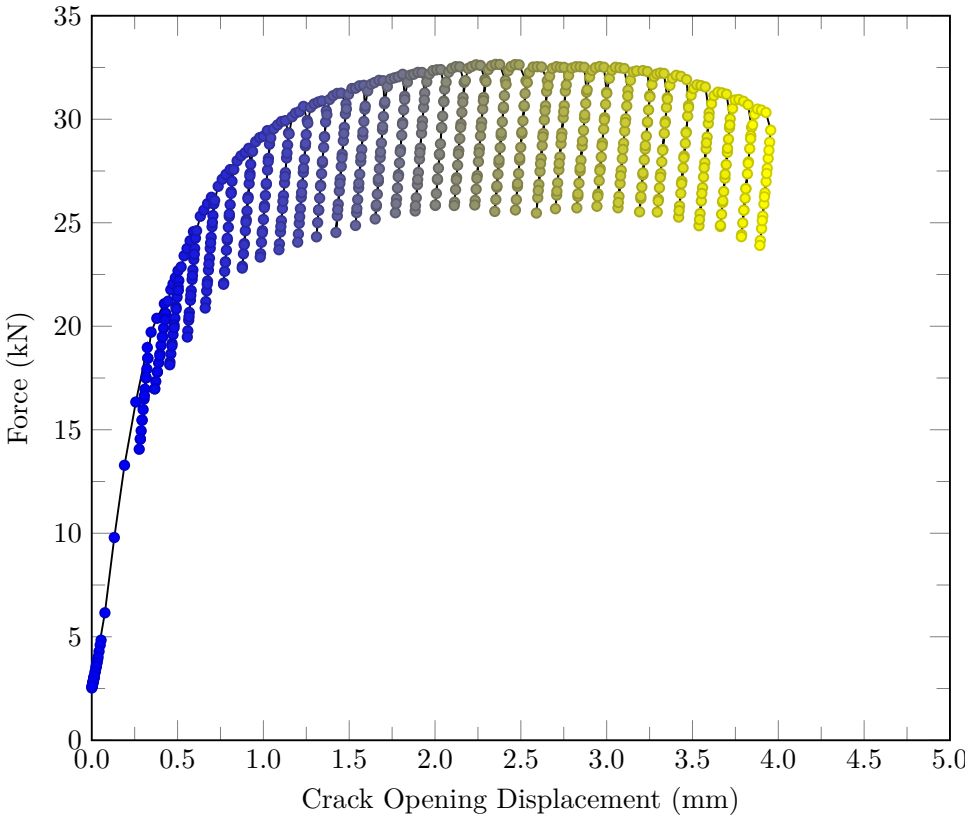

Figure C.1: Force versus displacement for CT specimen S1, initial defect in austenite material

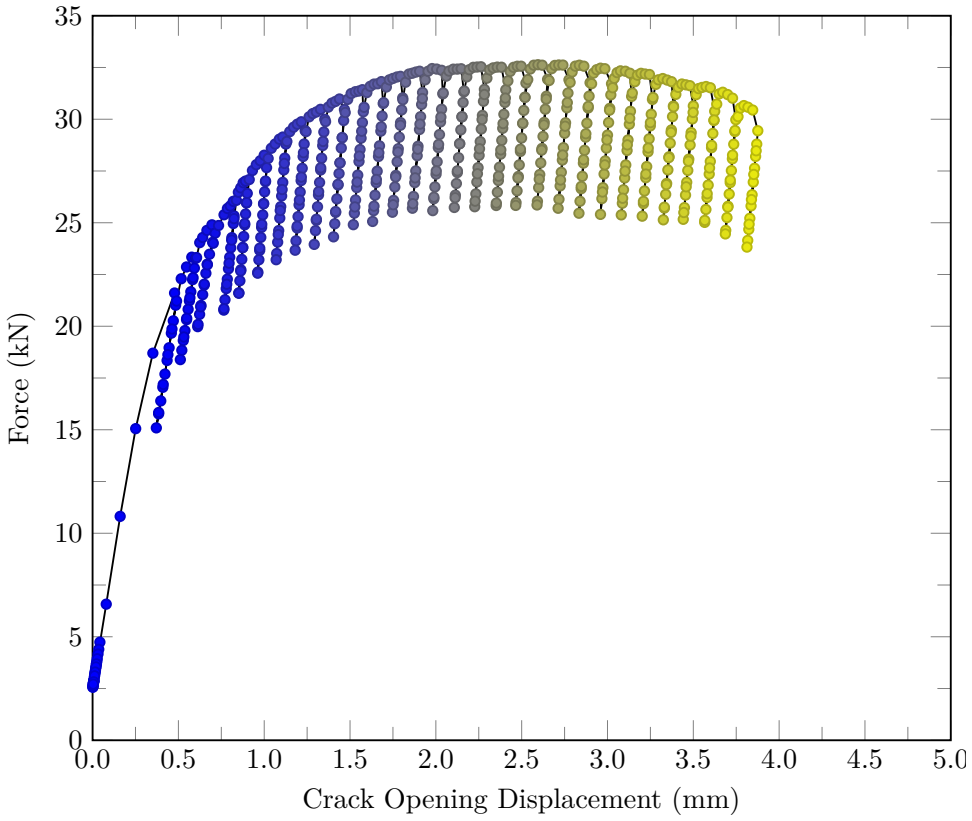

Figure C.2: Force versus displacement for CT specimen S2, initial defect in austenite material

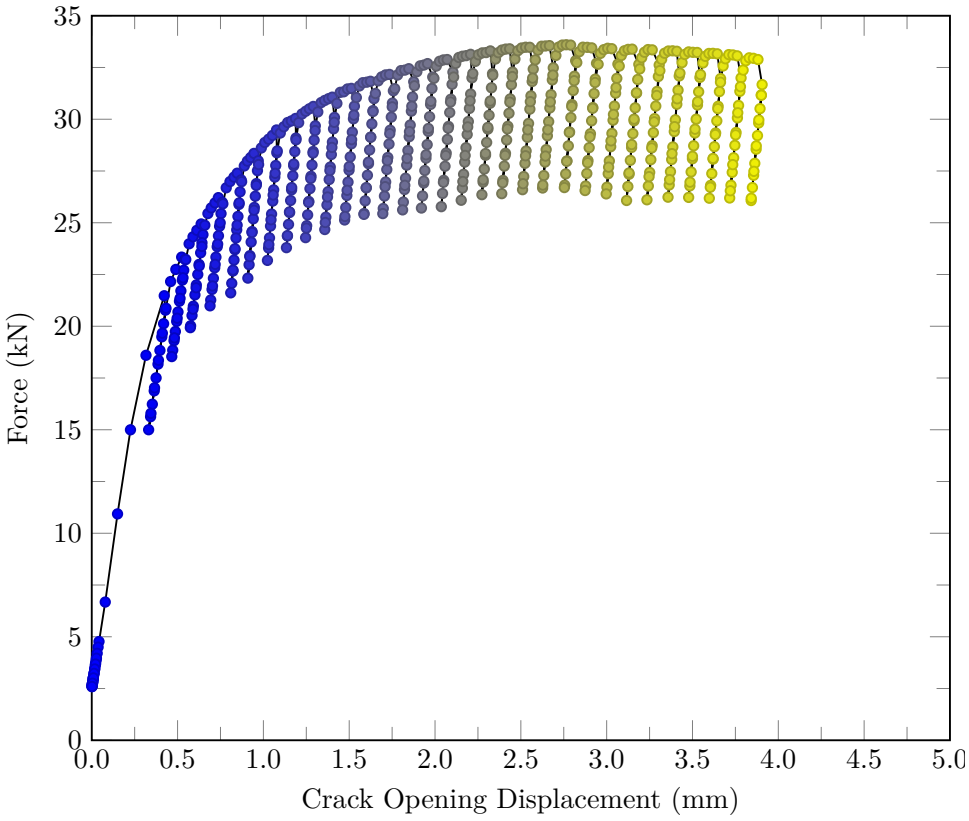

Figure C.3: Force versus displacement for CT specimen S3, initial defect in austenite material

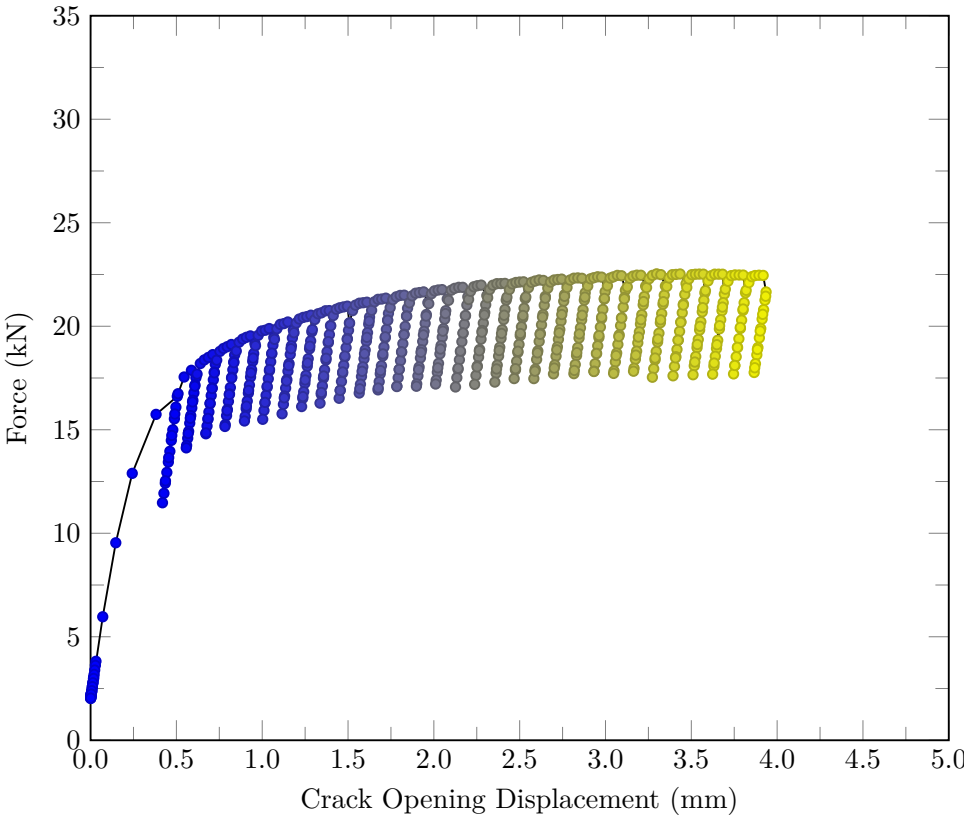

Figure C.4: Force versus displacement for CT specimen S4, initial defect in austenite material

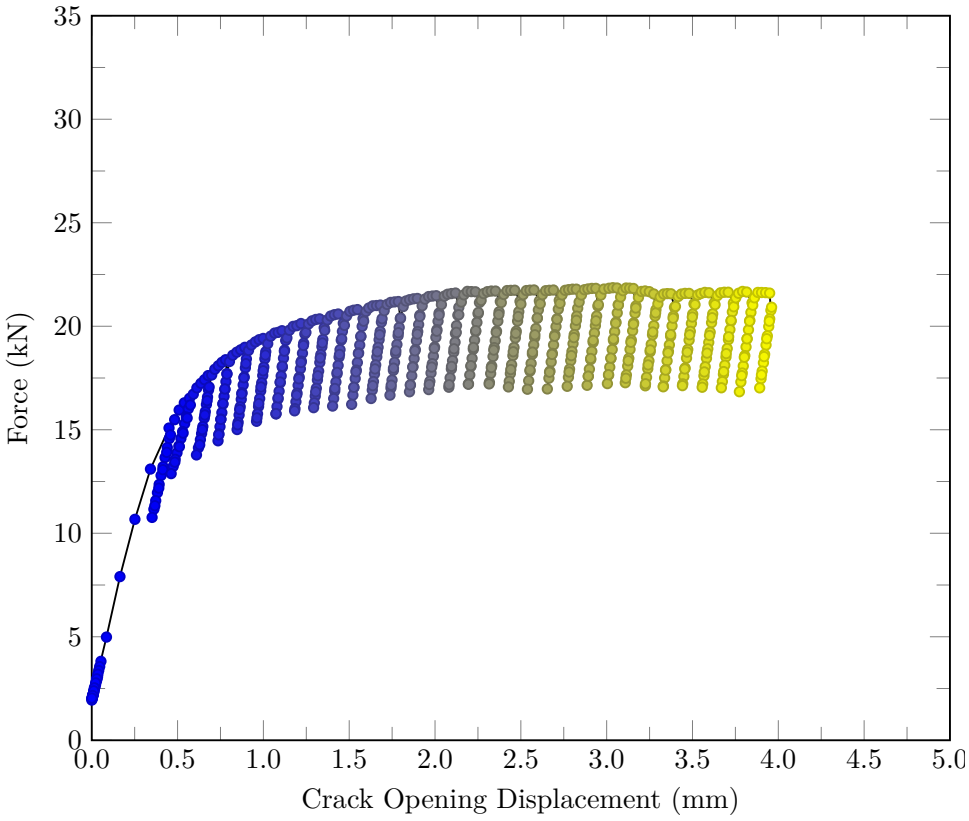

Figure C.5: Force versus displacement for CT specimen S5, initial defect in austenite material

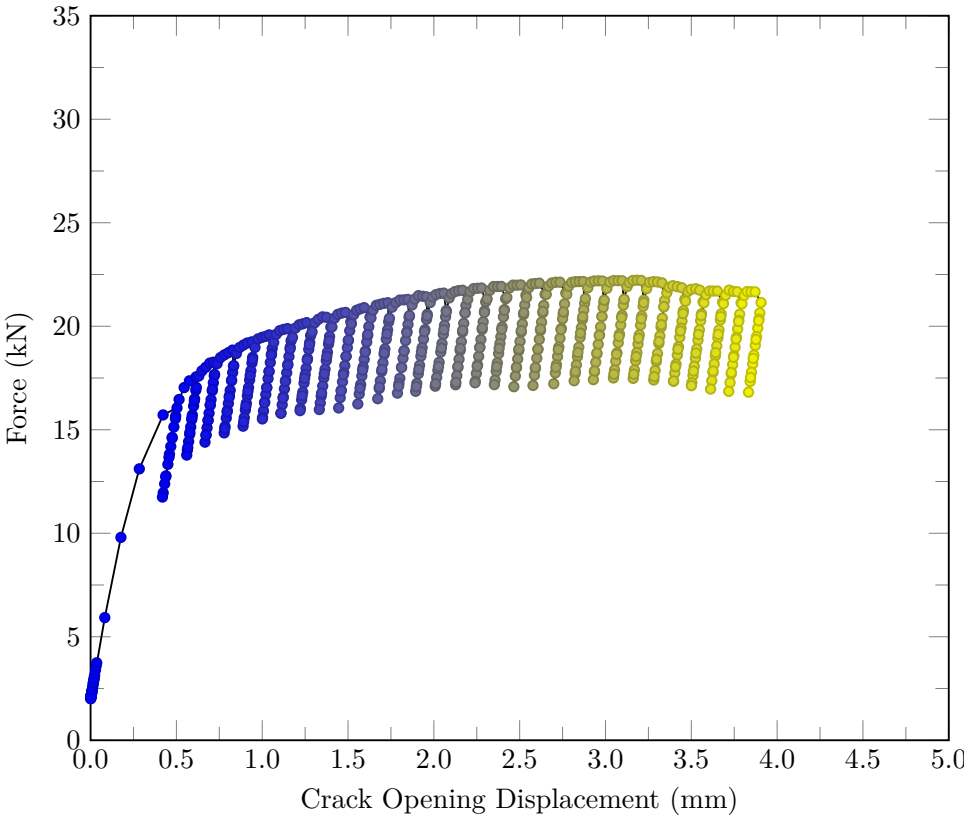

Figure C.6: Force versus displacement for CT specimen S6, initial defect in austenite material

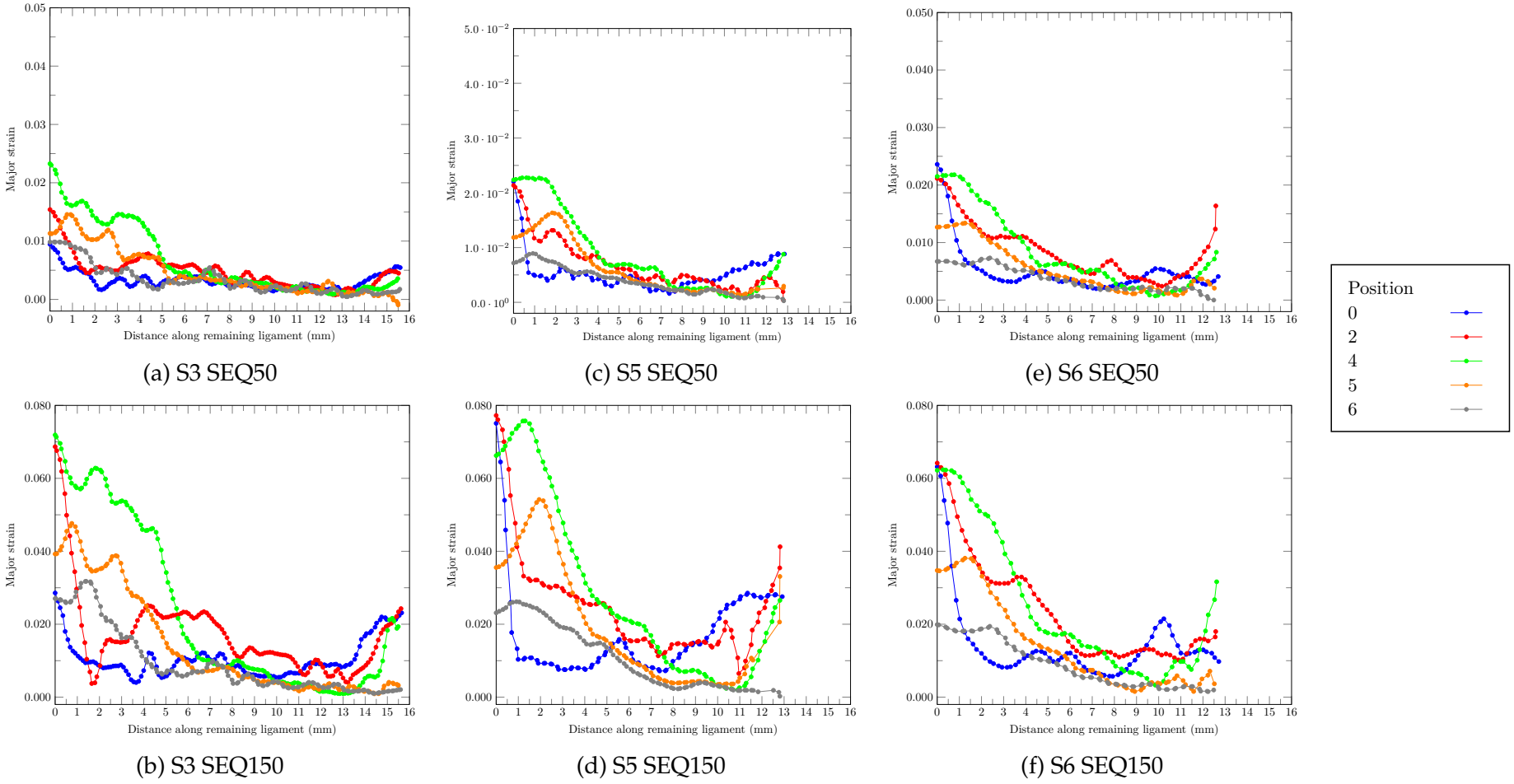

(a) S3 SEQ50 (c) S5 SEQ50 (e) S6 SEQ50

(b) S3 SEQ150 (d) S5 SEQ150 (f) S6 SEQ150

Figure C.7: Major strain along the remaining ligament at various positions. Positions are positive relative to the crack tip towards the TIG weld boundary. Results shown for Samples S3, S5 and S6 at fifth and mid-test sequences, respectively.

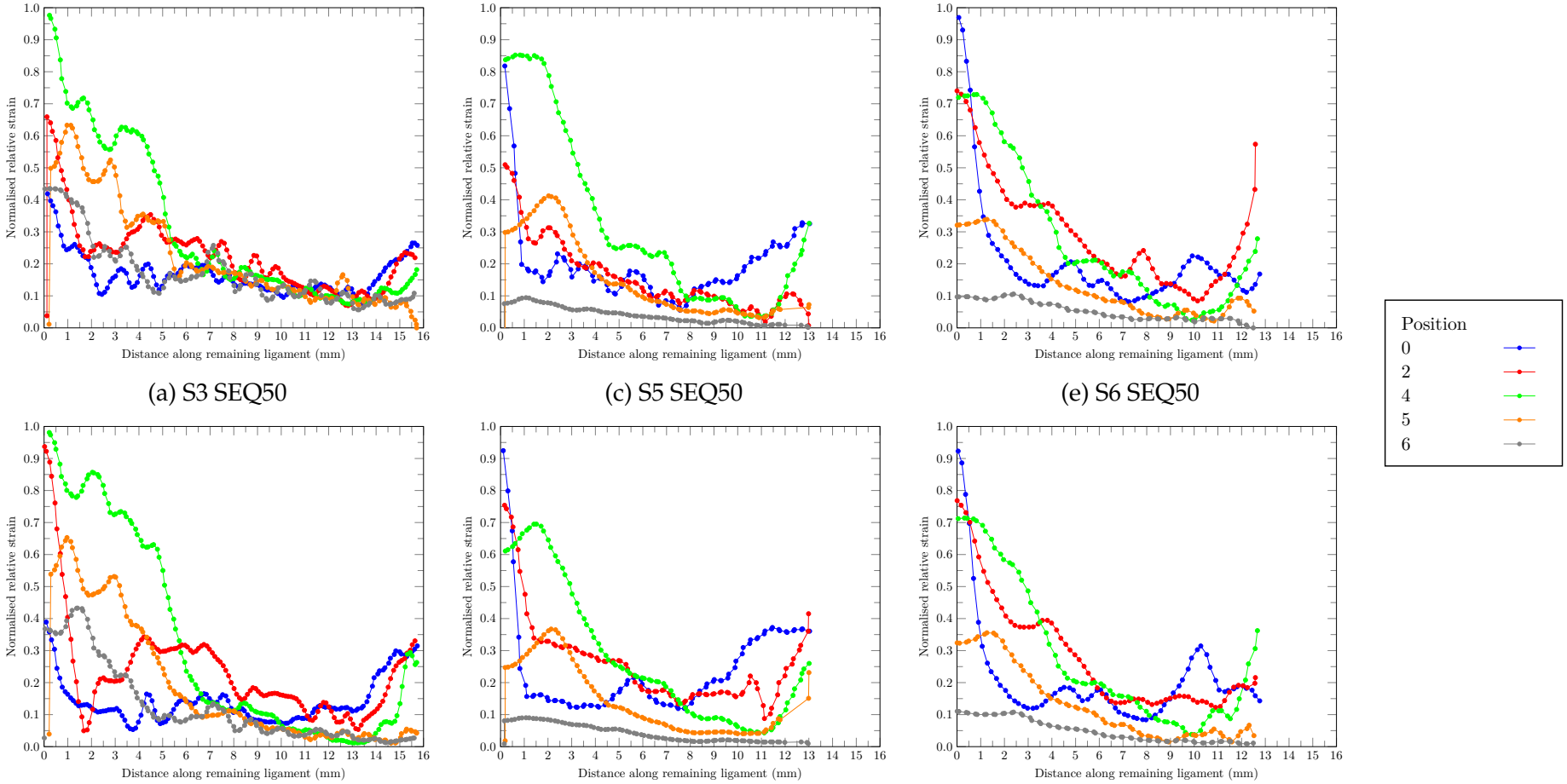

(a) S3 SEQ50 (c) S5 SEQ50 (e) S6 SEQ50

(b) S3 SEQ150 (d) S5 SEQ150 (f) S6 SEQ150

Figure C.8: Normalised relative strain along the remaining ligament at various positions. Positions are positive relative to the crack tip towards the TIG weld boundary. Results shown for Samples S3, S5 and S6 at fifth and mid-test sequences, respectively.

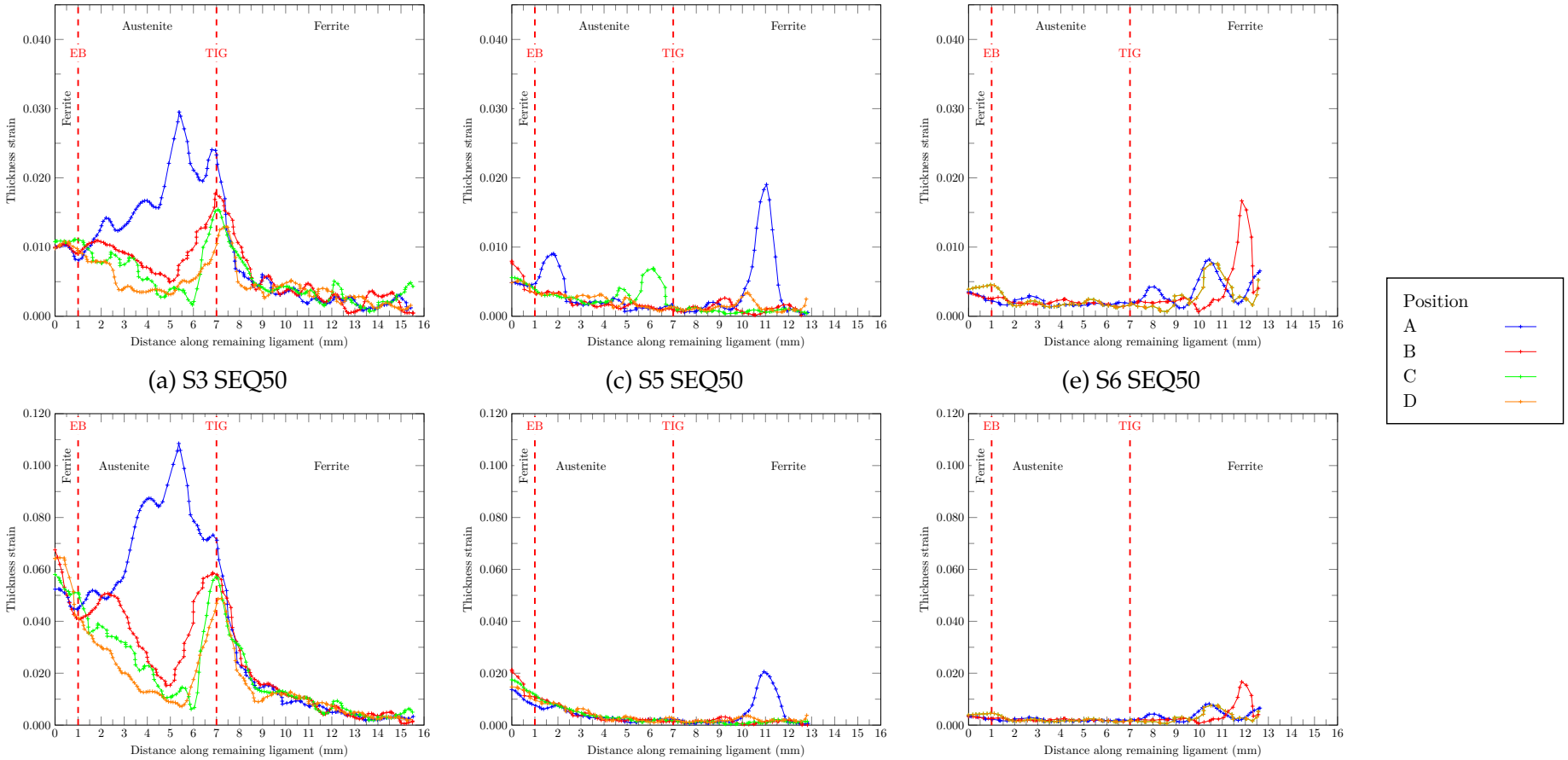

(a) S3 SEQ50 (c) S5 SEQ50 (e) S6 SEQ50

(b) S3 SEQ150 (d) S5 SEQ150 (f) S6 SEQ150

Figure C.9: Major strain parallel to loading direction. Position 'A' at the crack tip, Positions 'B' to 'D' offset from preceding section by 1 mm. Results shown for Samples S3, S5 and S6 at first and final sequences, respectively.

C.2 Finite element 2D: Defect in austenite

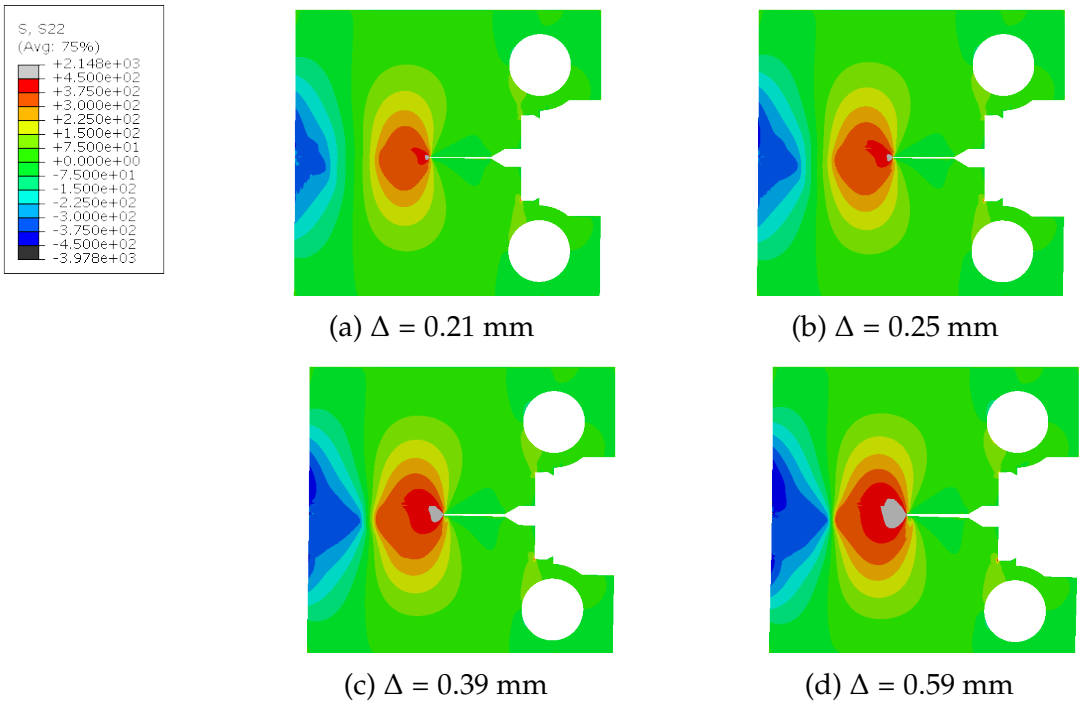

(a) Δ = 0.21 mm (b) Δ = 0.25 mm

(c) Δ = 0.39 mm (d) Δ = 0.59 mm

Figure C.10: Plane stress analysis contour plots of direct stress (σ_{yy}), in MPa, for multiple values of pin displacement (Δ)

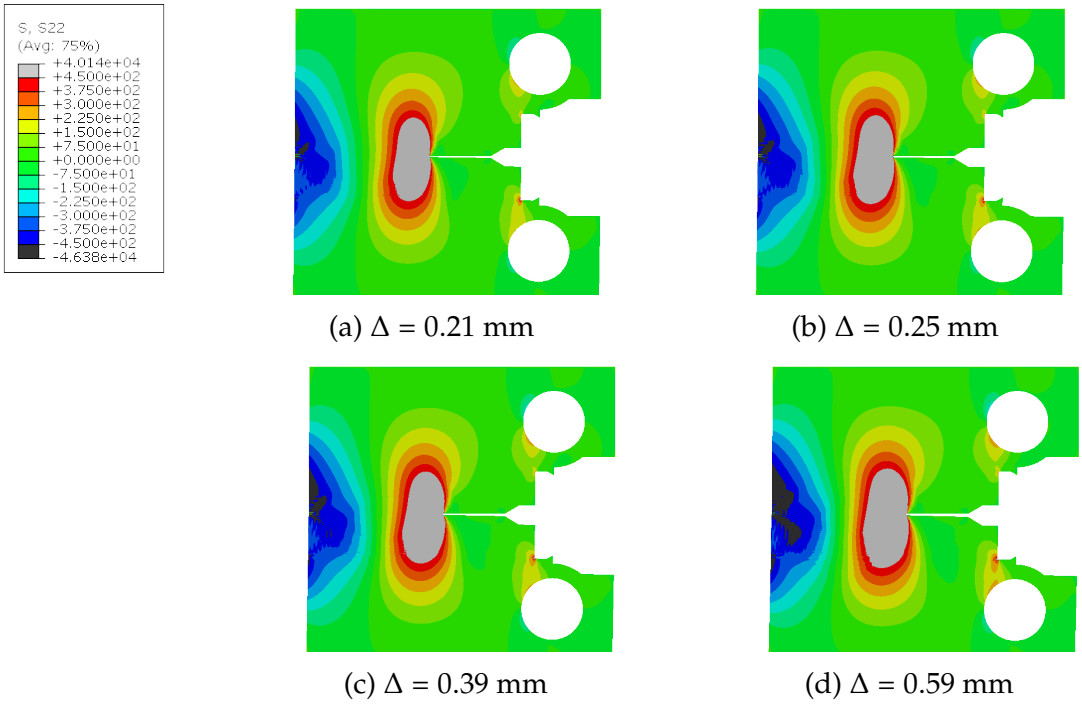

(a) Δ = 0.21 mm (b) Δ = 0.25 mm

(c) Δ = 0.39 mm (d) Δ = 0.59 mm

Figure C.11: Plane strain analysis contour plots of direct stress (σ_{yy}), in MPa, for multiple values of pin displacement (Δ)

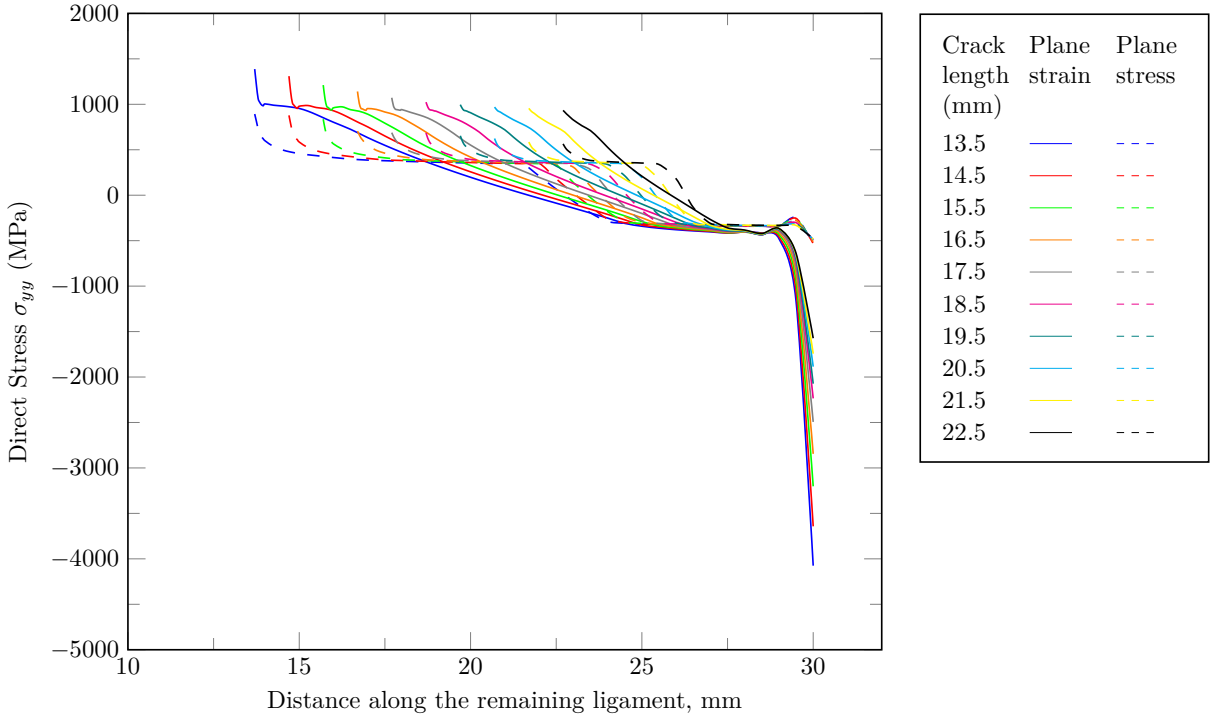

Figure C.12: Direct stress (σ_{yy}) along the remaining ligament for multiple initial crack depths (a_0) for plane stress and plane strain analyses at a displacement (Δ = 0.4 mm)

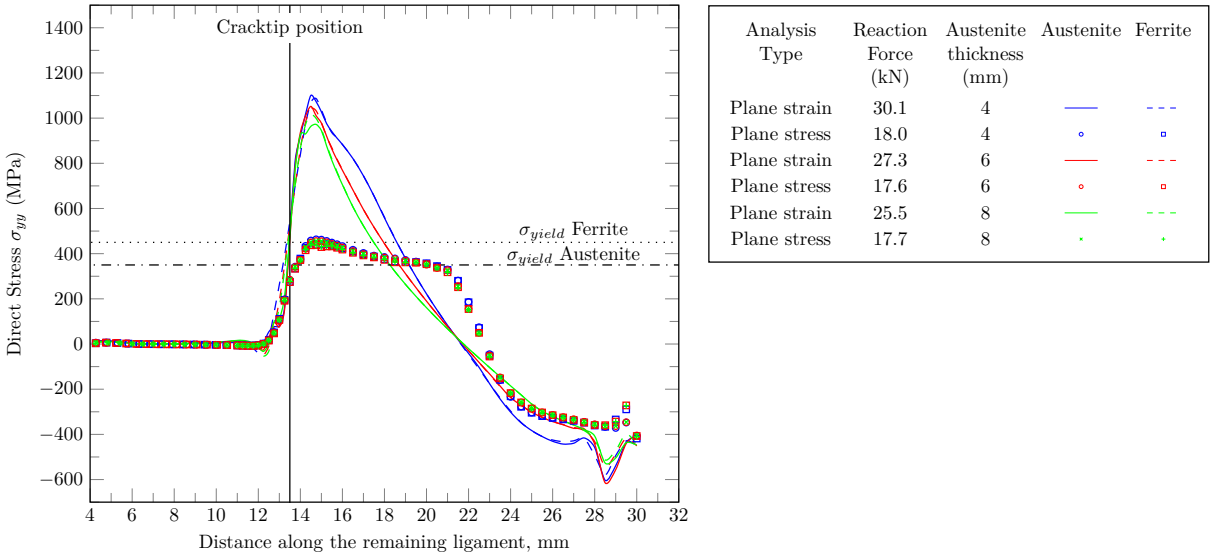

Figure C.13: Comparison of direct stress σ_{yy} along the materials interface for plane strain and plane stress conditions varying austenite thickness. Displacement Δ = 0.4 mm.

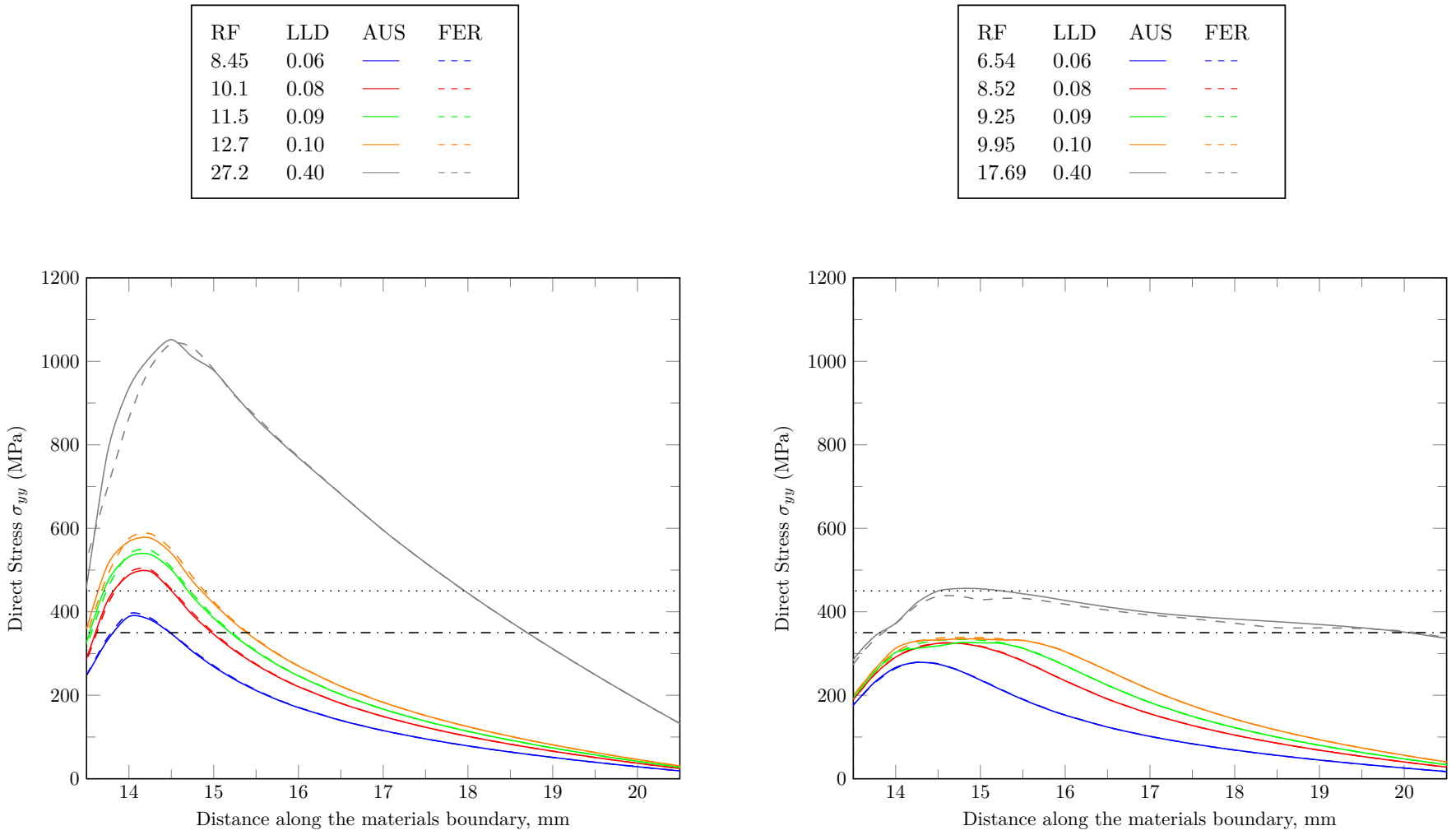

(a) Plane Strain

(b) Plane Stress

Figure C.14: Direct stress (σ_{yy}) along the materials boundary when $\frac{a}{W} = 0.45$ for multiple load-line displacement values for plane strain (Figure C.16a) and plane stress (Figure C.16b) conditions.

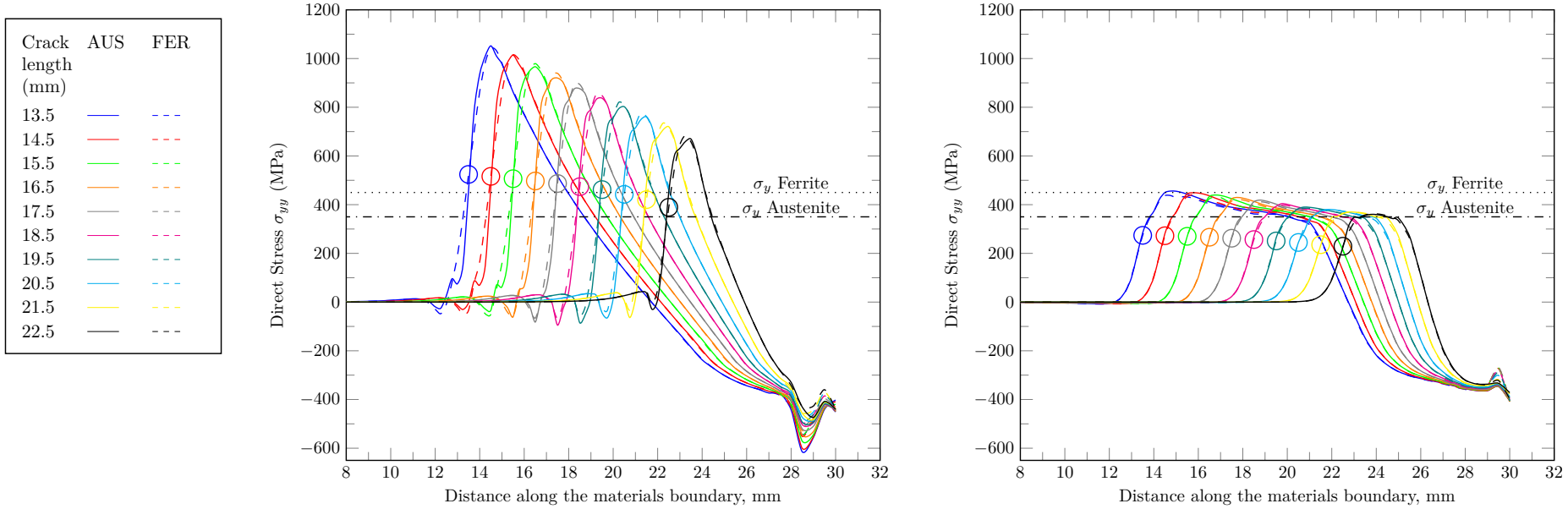

(a) Plane Strain

(b) Plane Stress

Figure C.15: Direct stress (σ_{yy}) along the materials boundary for multiple initial crack depths (a_0) for 2D Plane Strain (Figure C.15a) and Plane Stress (Figure C.15b) analyses at a displacement (Δ = 0.4 mm). Cracktip positions marked with circle.

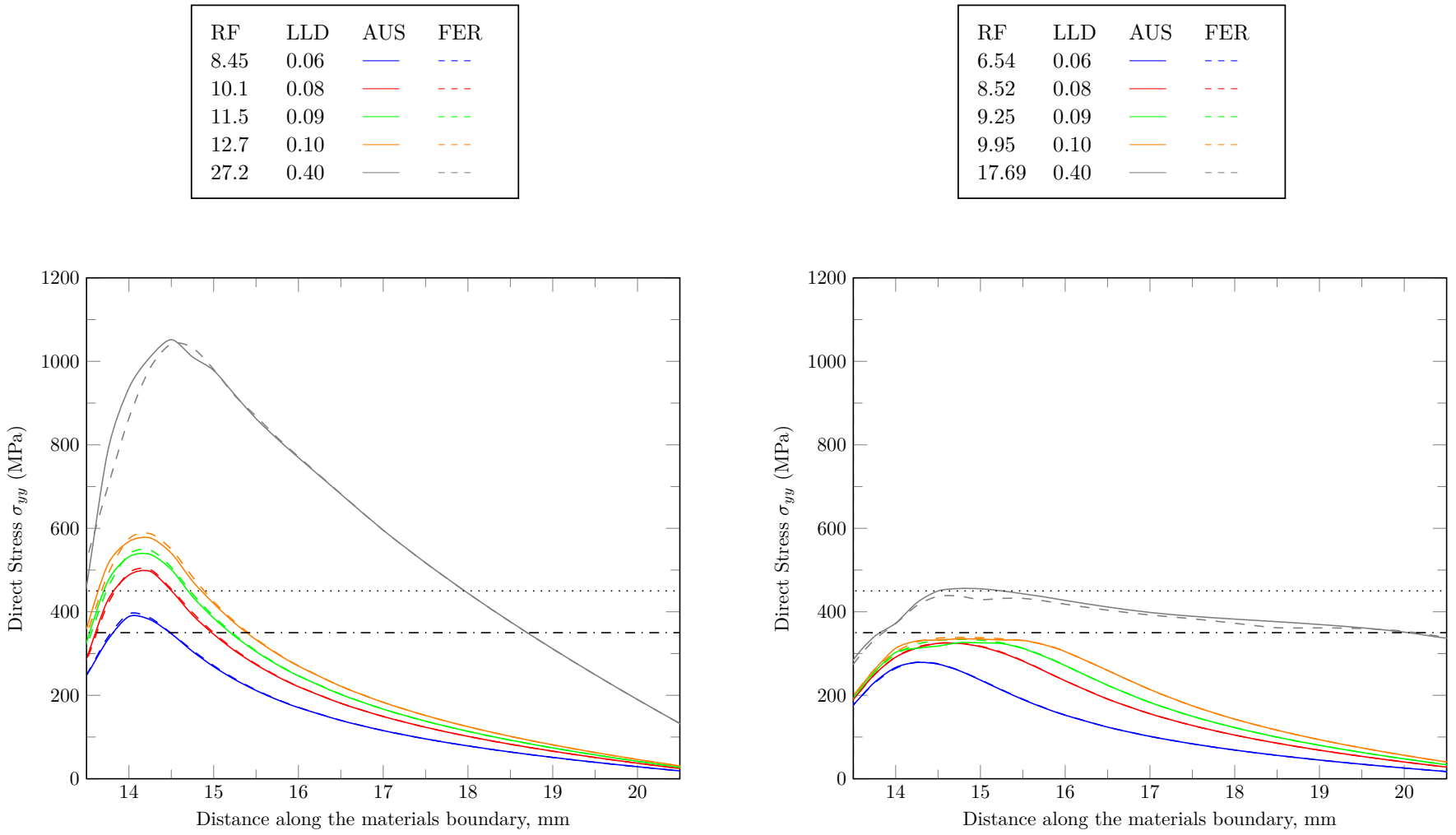

(a) Plane Strain

(b) Plane Stress

Figure C.16: Direct stress (σ_{yy}) along the materials boundary when $\frac{a}{W} = 0.45$ for multiple load-line displacement values for plane strain (Figure C.16a) and plane stress (Figure C.16b) conditions.

Figure C.17: Contour plots for the Plane Stress and Plane Strain conditions varying the austenite thickness.

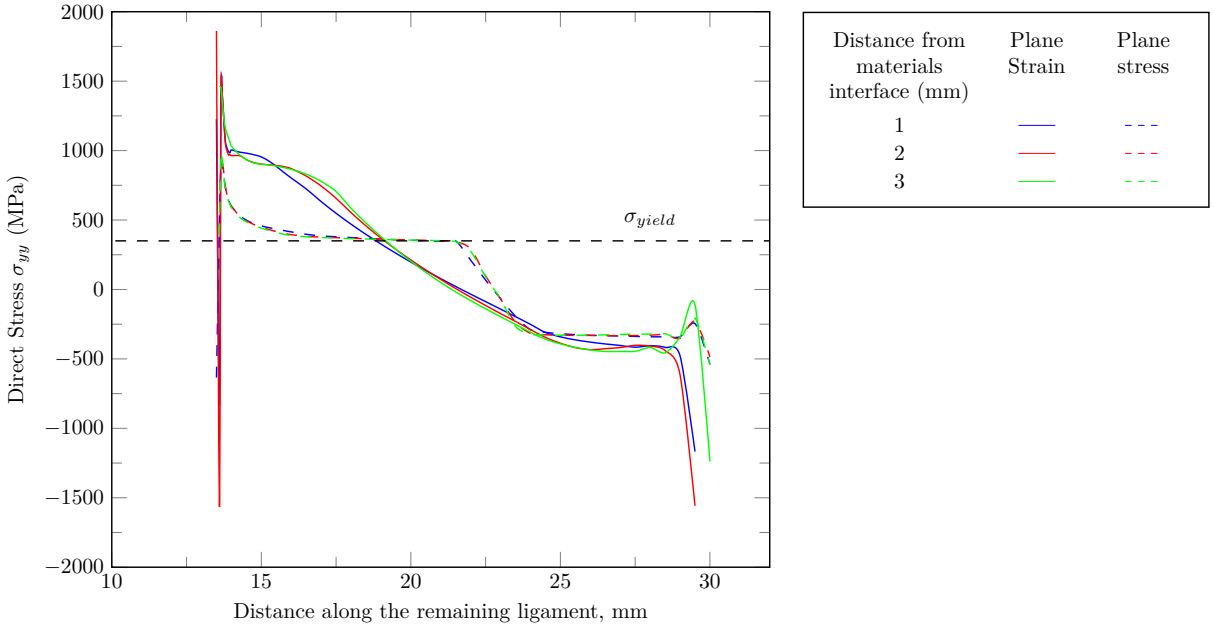

Figure C.18: Comparison of direct stress σ_{yy} along the remaining ligament for plane strain and plane stress conditions varying the proximity of the notch to the materials interface (Δ = 0.4 mm).

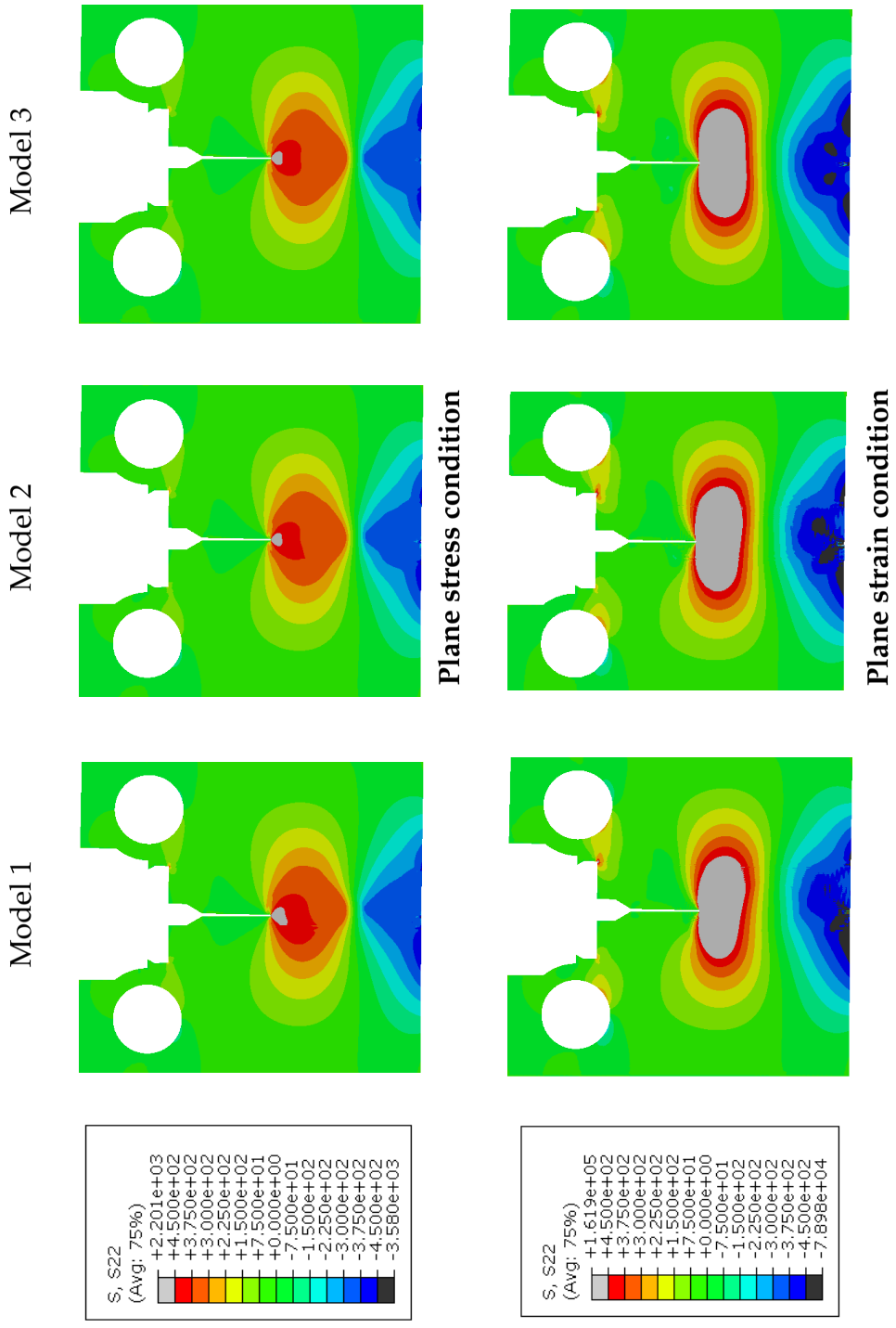

Figure C.19: Contour plots for the plane stress and plane strain conditions varying the proximity of the notch to the materials interface.

C.3 Finite element 2D: Defect in ferrite

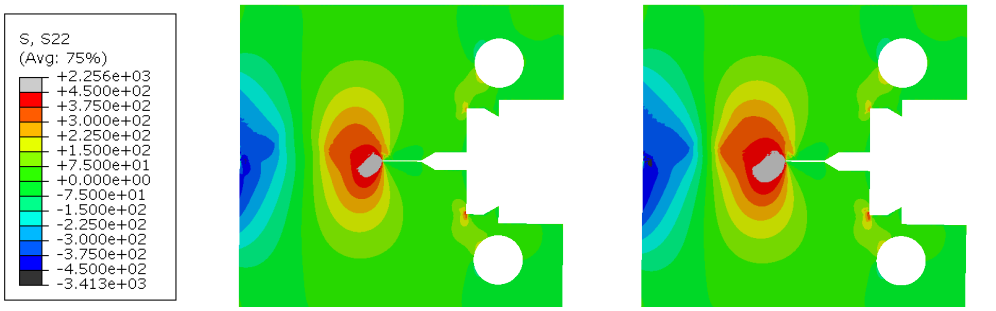

(a) Δ = 0.22 mm (b) Δ = 0.32 mm

(c) Δ = 0.42 mm (d) Δ = 0.52 mm

Figure C.20: Plane stress contour plots of direct stress (σ_{yy}) for multiple values of pin displacement (Δ)

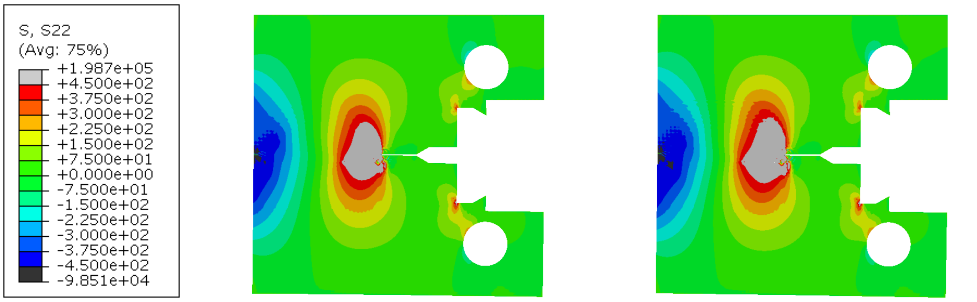

(a) Δ = 0.25 mm (b) Δ = 0.32 mm

(c) Δ = 0.38 mm (d) Δ = 0.45 mm

Figure C.21: Plane strain contour plots of direct stress (σ_{yy}) for multiple values of pin displacement (Δ)

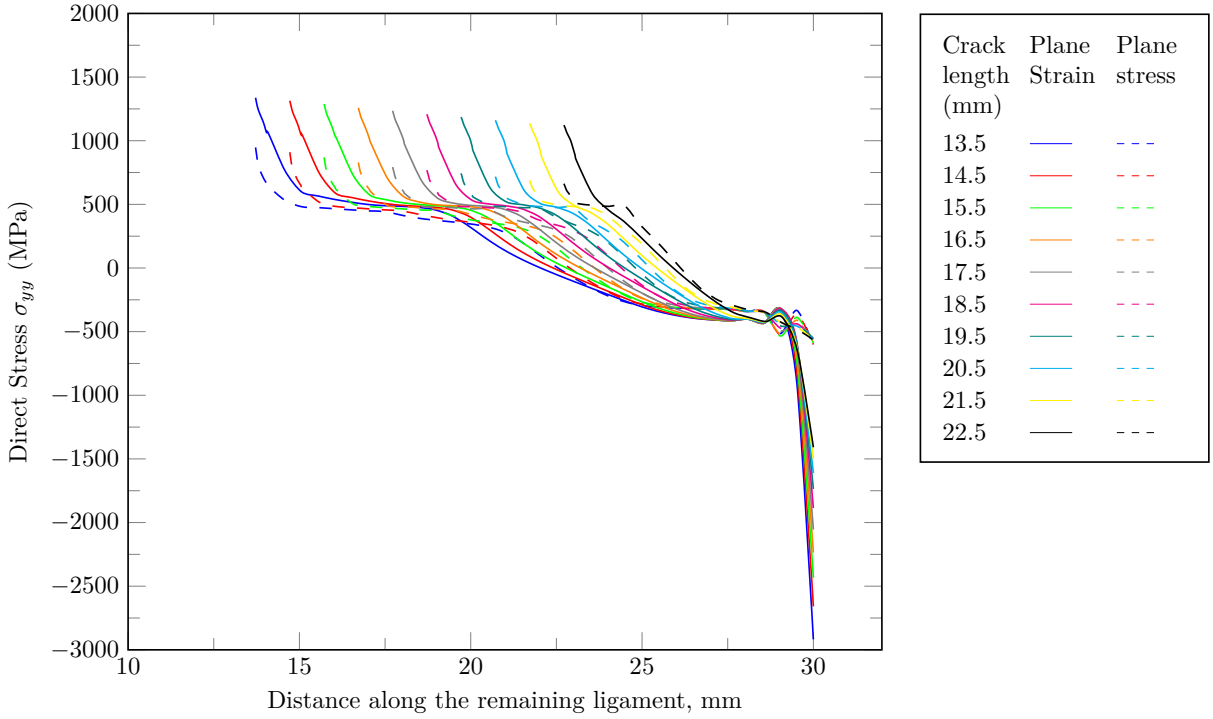

Figure C.22: Direct stress (σ_{yy}) along the remaining ligament for multiple initial crack depths (a_0) for plane stress and plane strain analyses at a displacement (Δ = 0.4 mm)

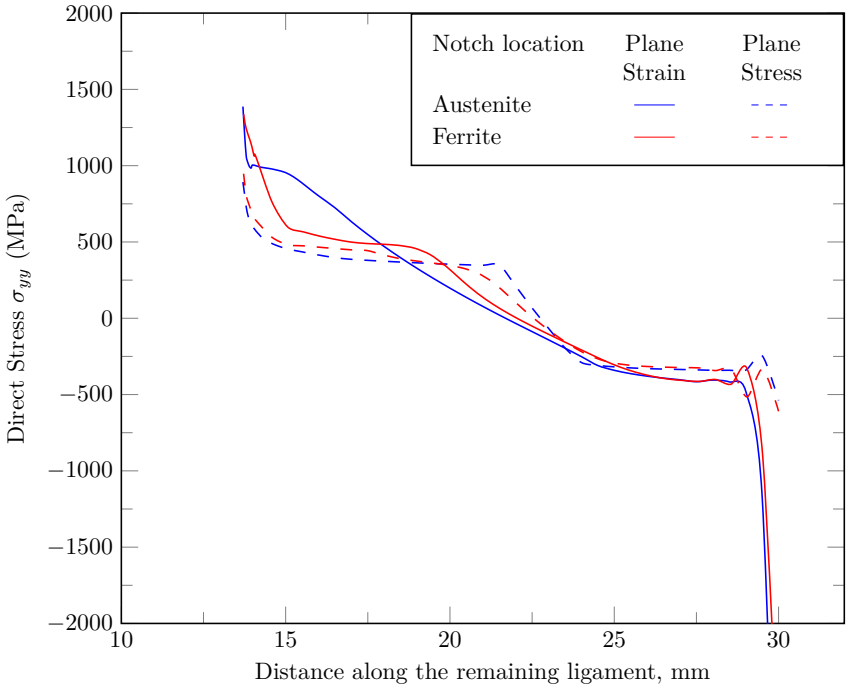

Figure C.23: Direct stress (σ_{yy}) along the remaining ligament for initial crack length (a_i) 13.5 mm for plane stress and plane strain analyses at a displacement (Δ = 0.4 mm)

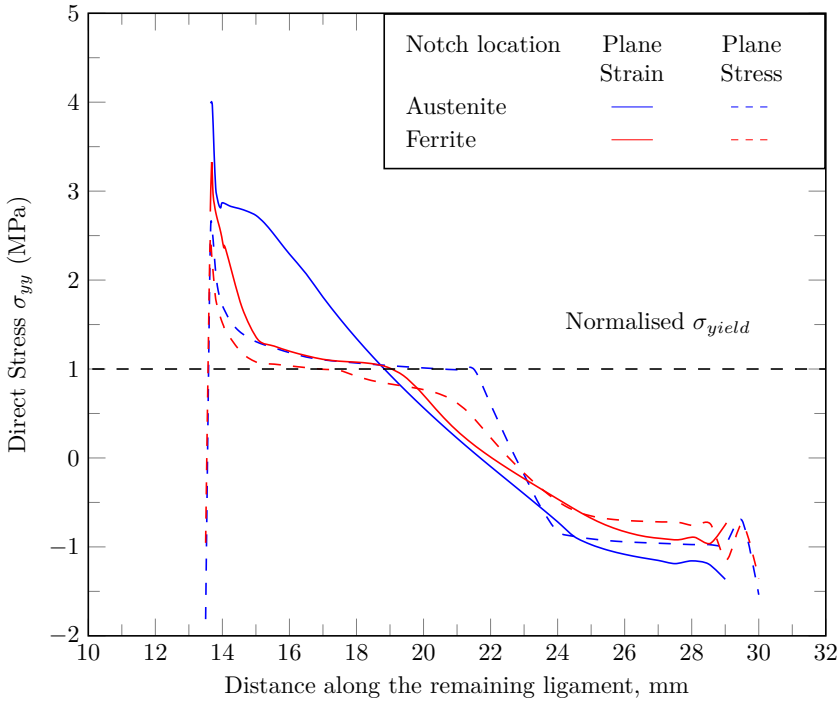

Figure C.24: Comparison of normalised direct stress (σ_{yy}) along the remaining ligament for initial crack length (a_i) 13.5 mm for plane stress and plane strain analyses at a displacement (Δ = 0.4 mm) for specimens notched in austenite material and specimens notched in ferrite material

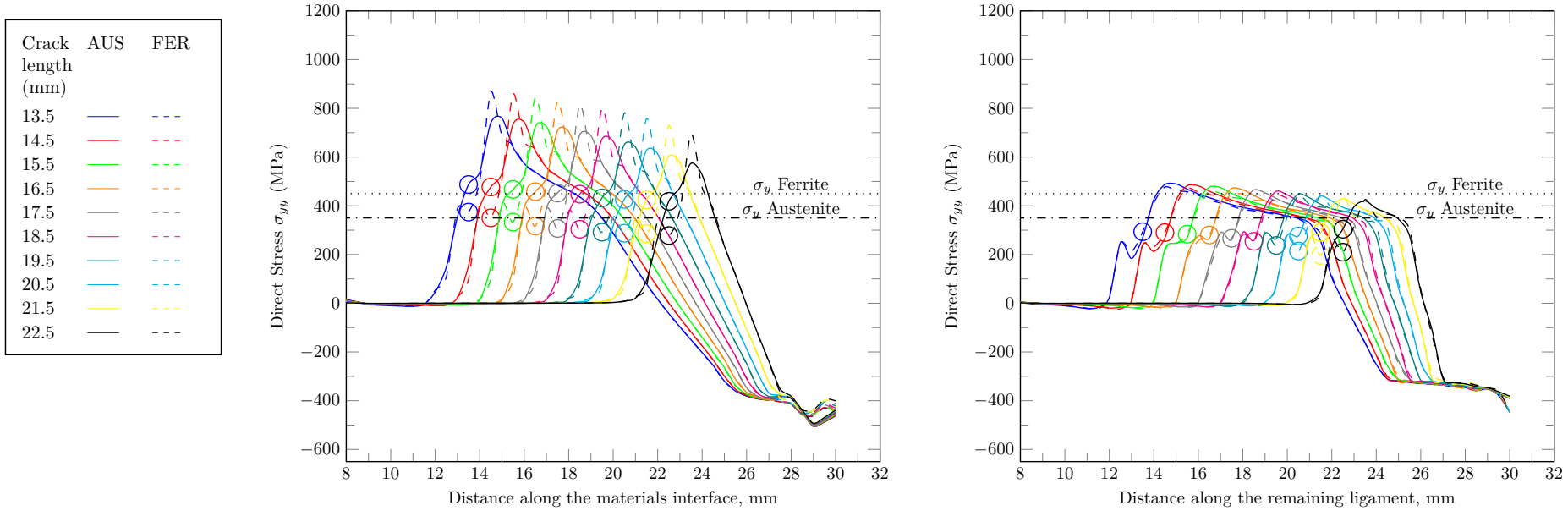

(a) Plane Strain

(b) Plane Stress

Figure C.25: Direct stress (σ_{yy}) along the materials boundary for multiple initial crack depths (a_0) for 2D Plane Strain (Figure C.15a) and Plane Stress (Figure C.15b) analyses at a displacement (Δ = 0.4 mm). Cracktip positions marked with circle.

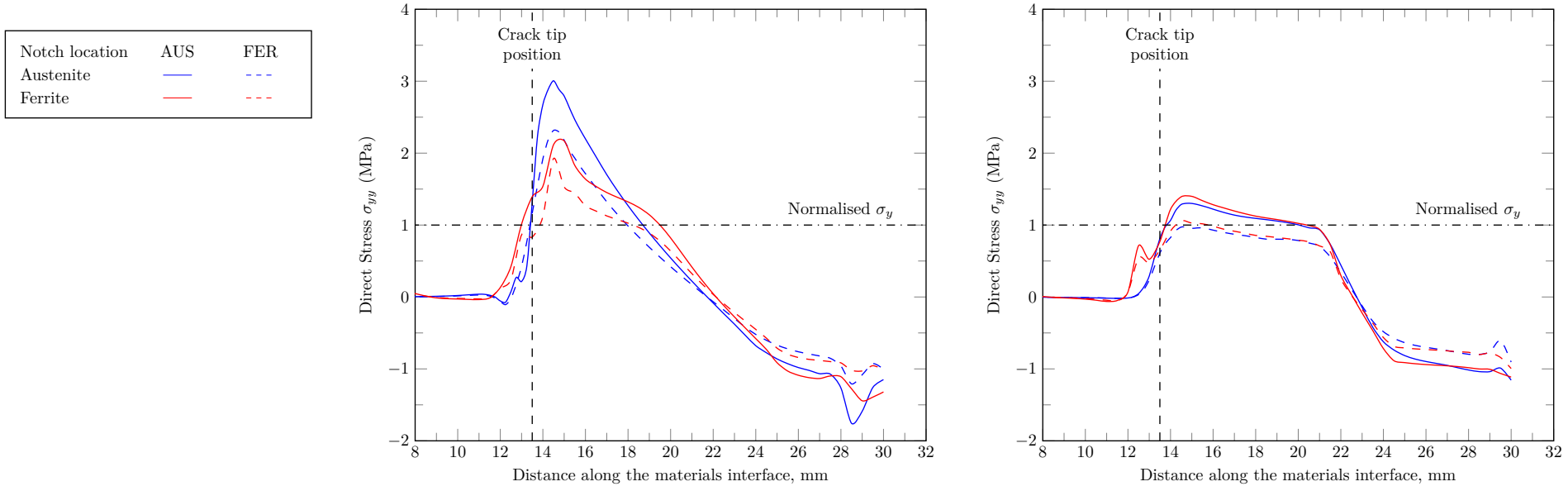

(a) Plane Strain

(b) Plane Stress

Figure C.26: Comparison of normalised direct stress (σ_{yy}) along the materials boundary for initial crack depth (a_i=13.5 mm) for 2D Plane Strain (Figure C.26a) and Plane Stress (Figure C.26b) analyses at a displacement (Δ = 0.4 mm) for specimens notched in austenite material and specimens notched in ferrite material

C.4 Assessment of CT's using 3D Finite Element

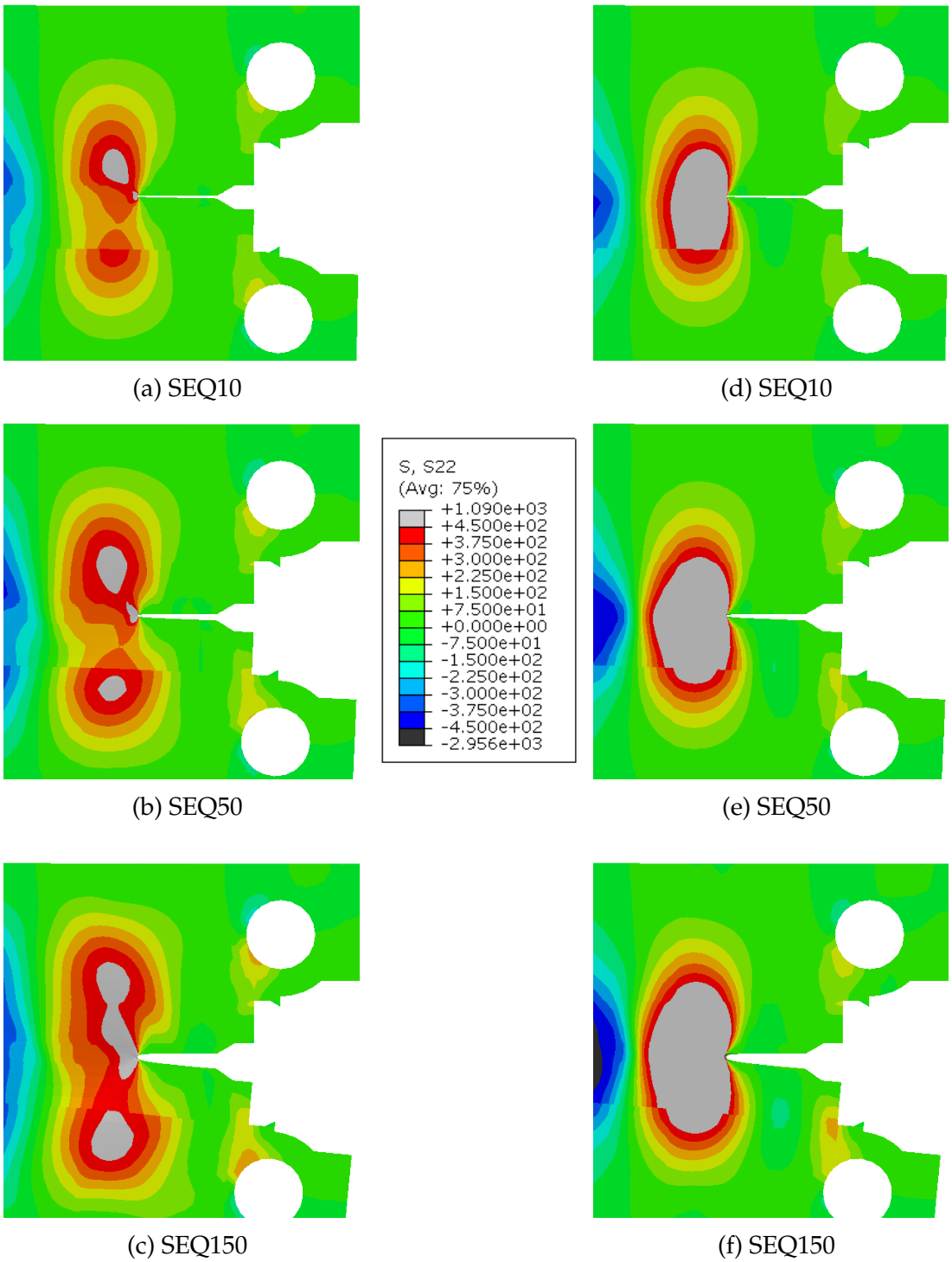

(a) SEQ10

(d) SEQ10

(b) SEQ50

(e) SEQ50

(c) SEQ150

(f) SEQ150

Figure C.27: Contour plots of direct strain ϵ_{yy} in 3D model of fracture toughness test during peak loading conditions. Figures C.27a to C.27c showing estimated strain on surface. Figures C.27d to C.27f showing strains in the mid-thickness region.

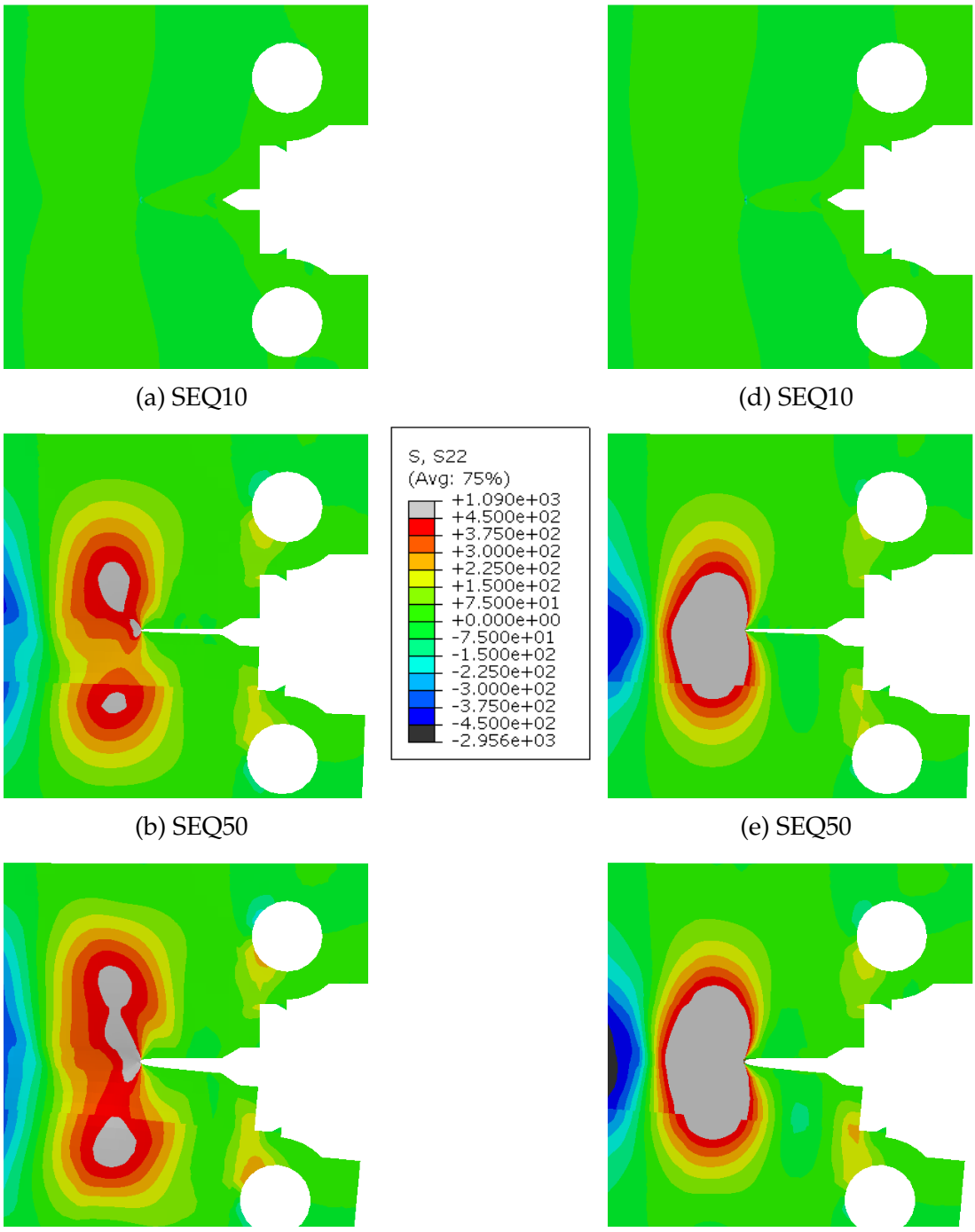

(a) SEQ10 (d) SEQ10

(b) SEQ50 (e) SEQ50

(c) SEQ150 (f) SEQ150

Figure C.28: Contour plots of direct strain ϵ_{yy} in 3D model of fracture toughness test during peak unloading conditions. Figures C.28a to C.28c showing estimated stress on surface. Figures C.28d to C.28f showing stress in the mid-thickness region.

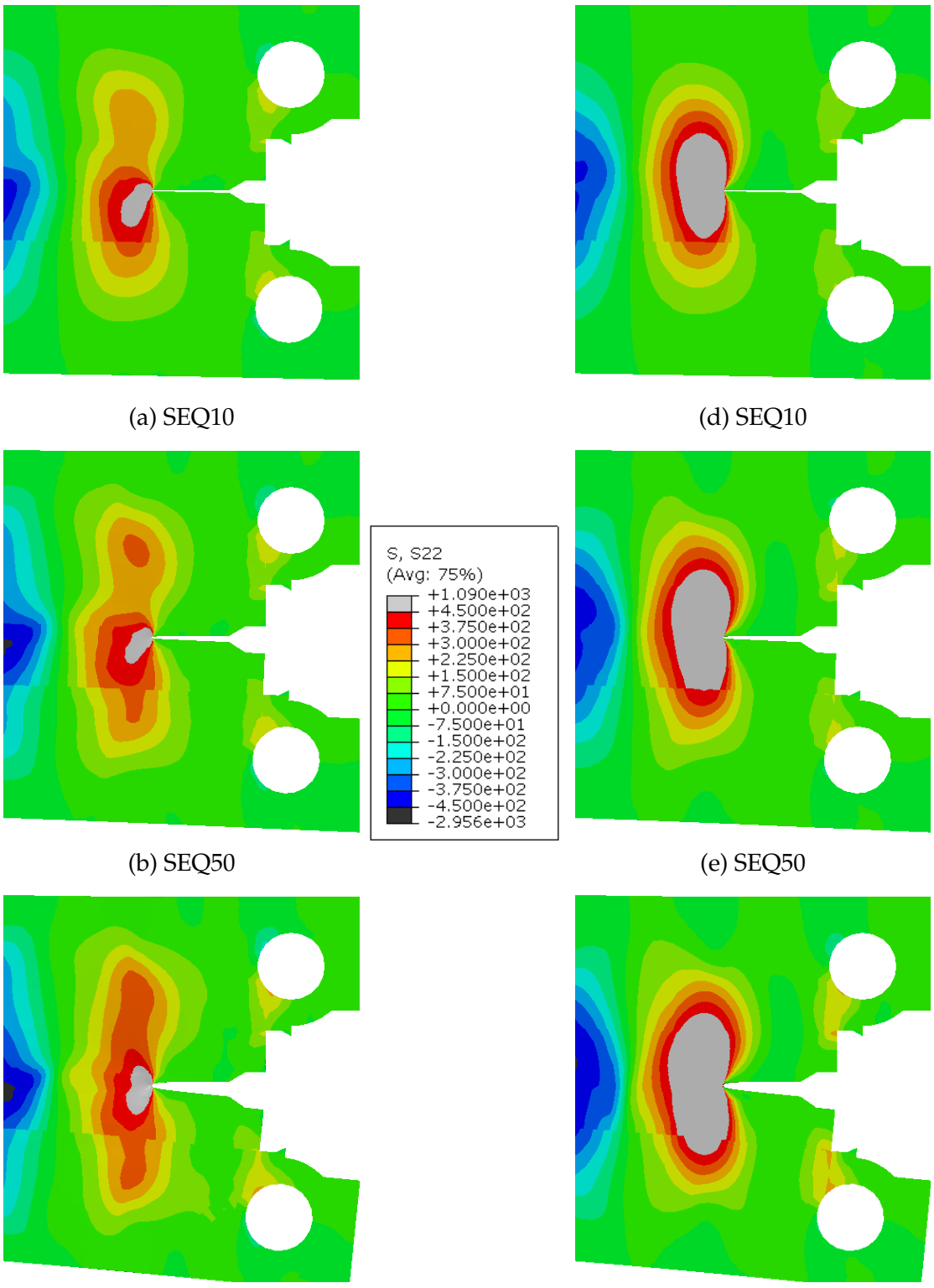

(a) SEQ10

(d) SEQ10

(b) SEQ50

(e) SEQ50

(c) SEQ150

(f) SEQ150

Figure C.29: Contour plots of direct strain ϵ_{yy} in 3D model of fracture toughness test during peak loading conditions. Figures C.29a to C.29c showing estimated strain on surface. Figures C.29d to C.29f showing strains in the mid-thickness region.

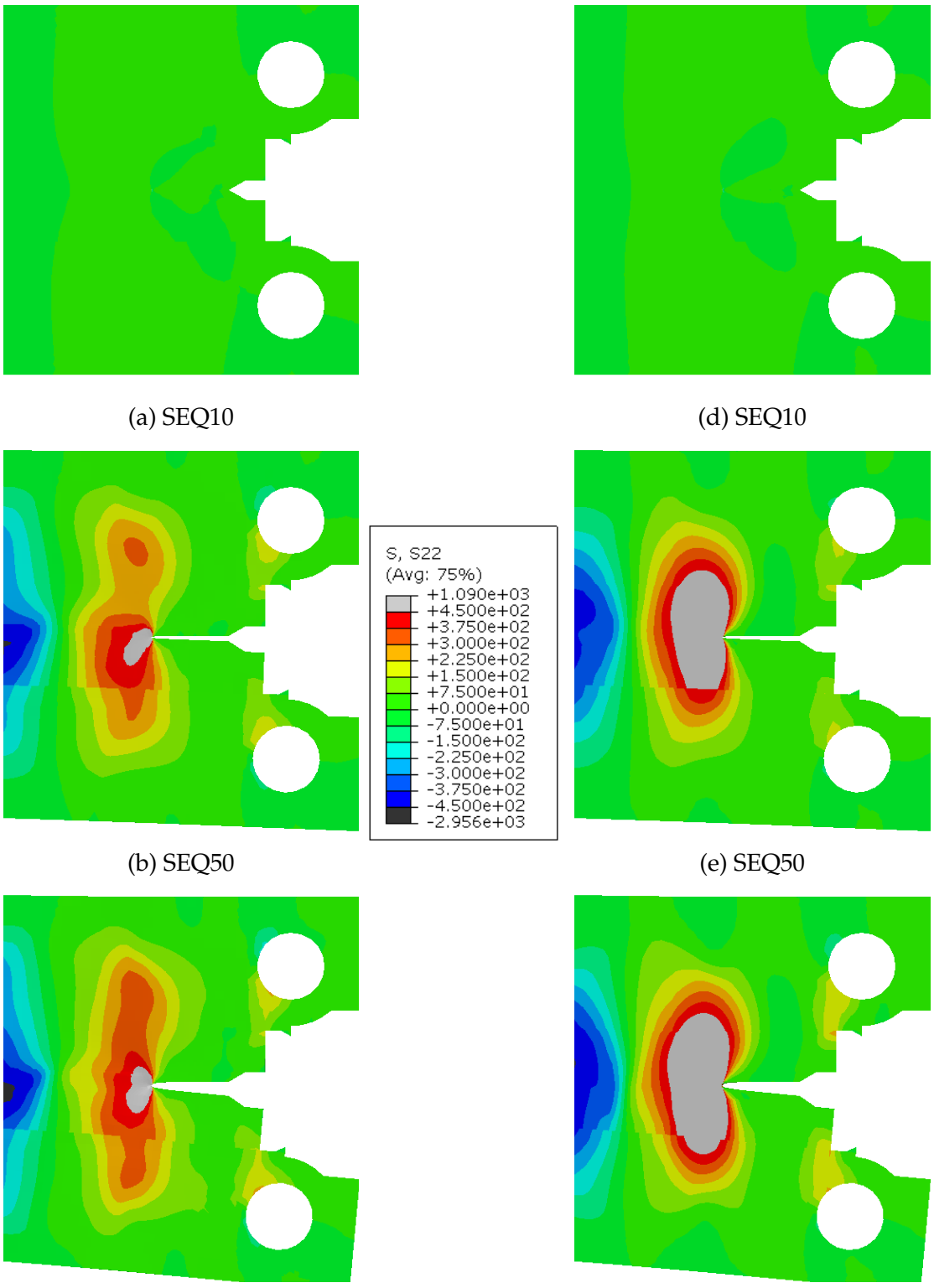

(a) SEQ10

(d) SEQ10

(b) SEQ50

(e) SEQ50

(c) SEQ150

(f) SEQ150

Figure C.30: Contour plots of direct strain ϵ_{yy} in 3D model of fracture toughness test during peak unloading conditions. Figures C.30a to C.30c showing estimated stress on surface. Figures C.30d to C.30f showing stress in the mid-thickness region.

Appendix D: Appendix Chapter 7 Defects oriented perpendicular to materials interface

D.1 Compliance Functions for Austenite Material

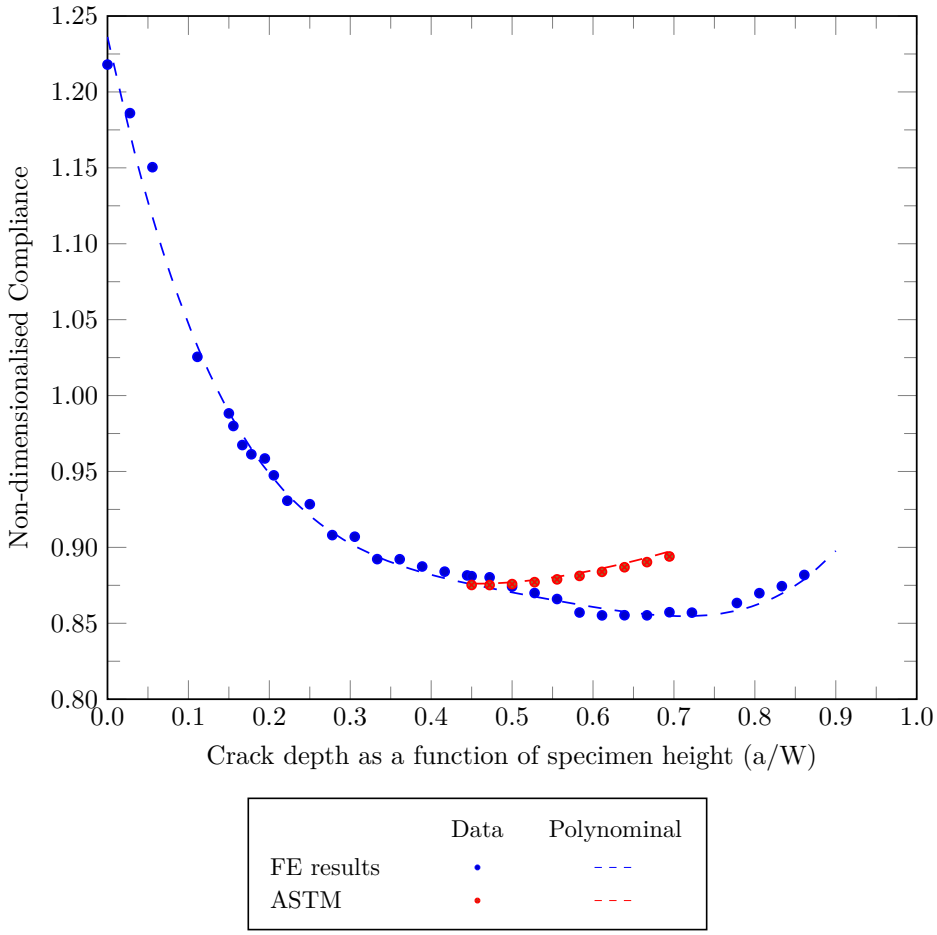

Figure D.1: Compliance as a function of crack depth, including polynomial fit for austenite material

Table D.1: Coefficients for calculation of compliance, austenite material properties

Analysis	A_0	A_1	A_2	A_3	A_4	A_5
ASTM	1.193	-1.980	4.478	-4.443	1.739	0
FE	1.2376962	-2.4426889	6.3856790	-7.2973943	2.3552200	0.8075576

Table D.2: Coefficients for calculation of crack depth from crack mouth opening displacements for austenite material properties. Note: ASTM coefficients only valid for surface measurements.

Analysis	U_0	U_1	U_2	U_3	U_4	U_5
ASTM	0.9997480	-3.9504	2.9821	-3.21408	51.51564	-113.031
CMOD0	0.9973780	-3.7886114	2.0503374	2.0616605	17.6609550	-31.4093580
CMOD1	1.0007495	-4.0503287	4.4917107	-14.7461140	69.5390730	-85.7407550
CMOD2	1.0016039	-4.2091670	5.6627622	-24.9096270	106.8409100	-128.7241300
CMOD3	1.0016717	-4.3328084	6.4290541	-33.2642490	142.0025600	-172.55113000

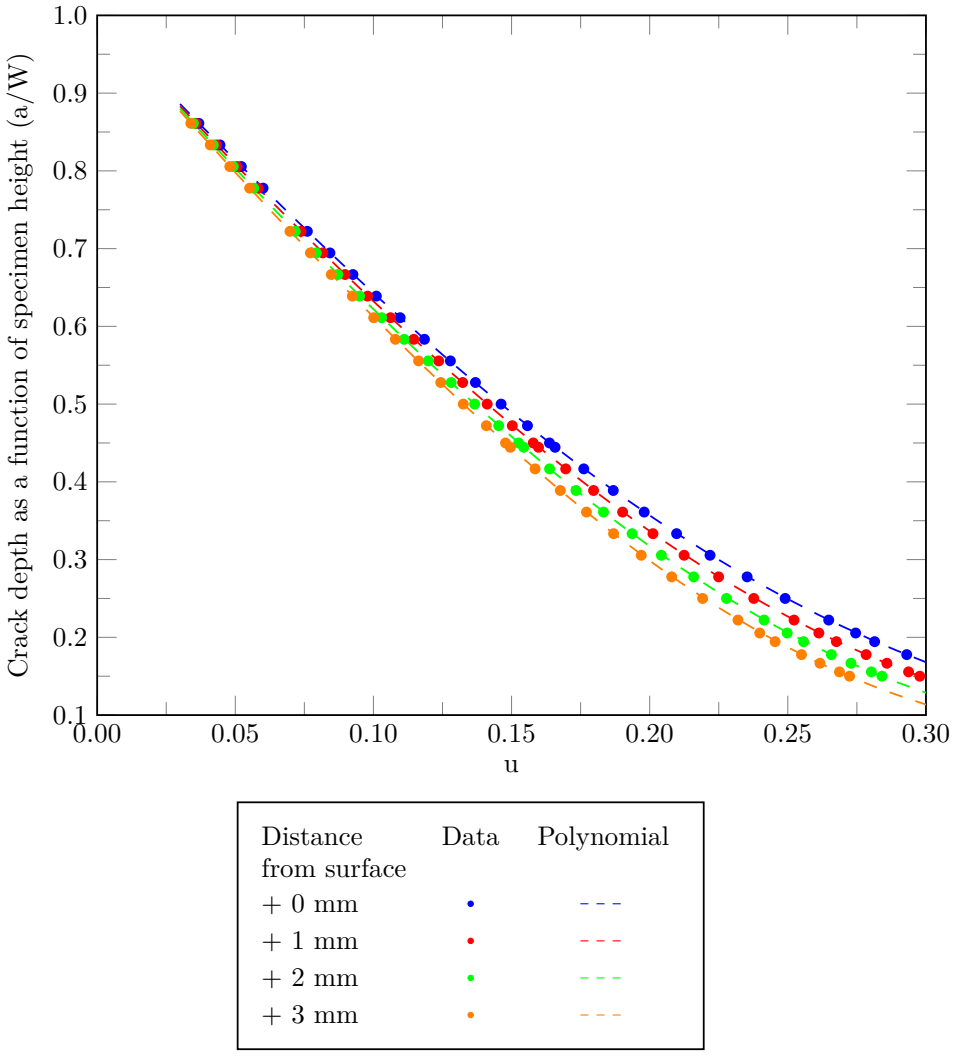

Figure D.2: Crack depth as a function of crack mouth opening, including polynomial fit

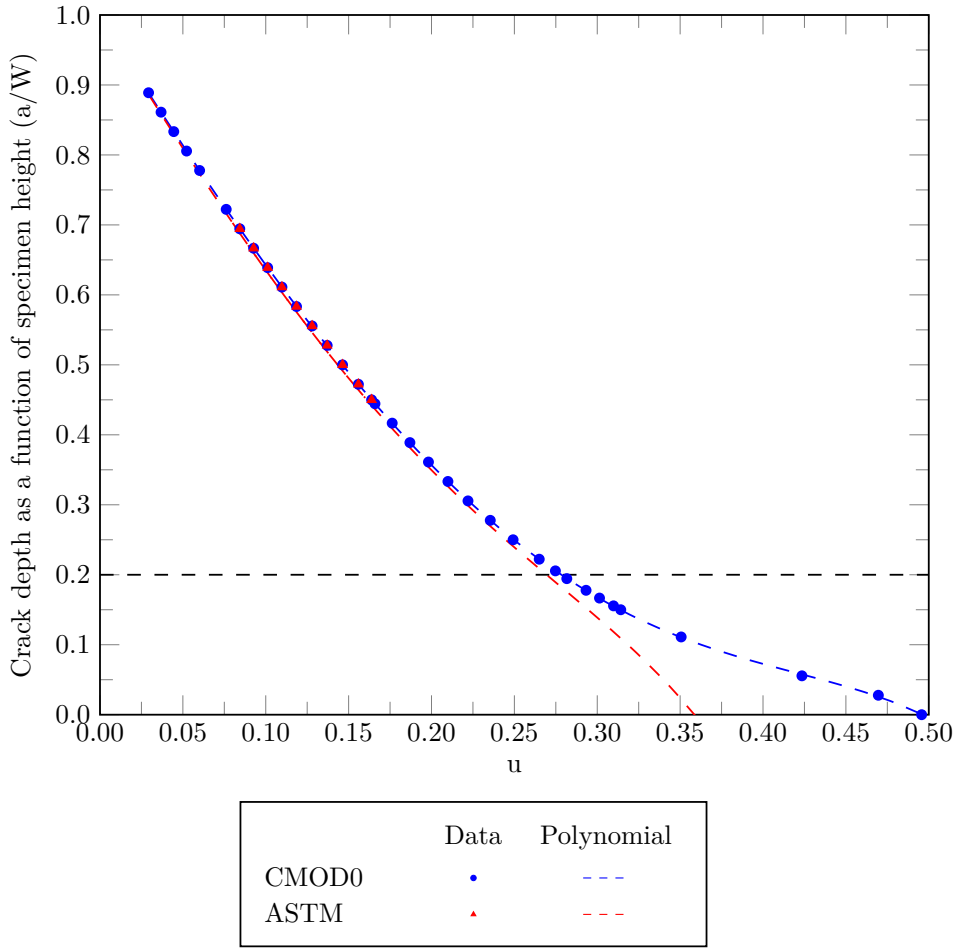

Figure D.3: Comparison of polynomial fit for ASTM coefficients and FE derived coefficients for austenite material properties

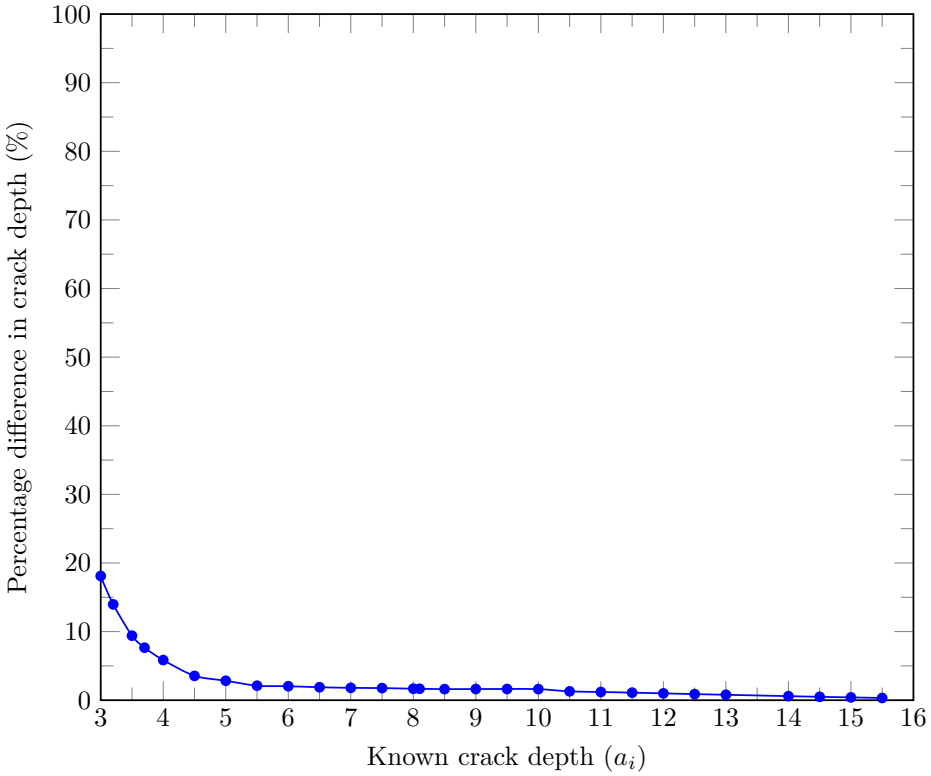

Figure D.4: Percentage difference in calculated crack depth compared to the known crack depth for $0 \geq a/W \leq 0.85$. Austenite material properties

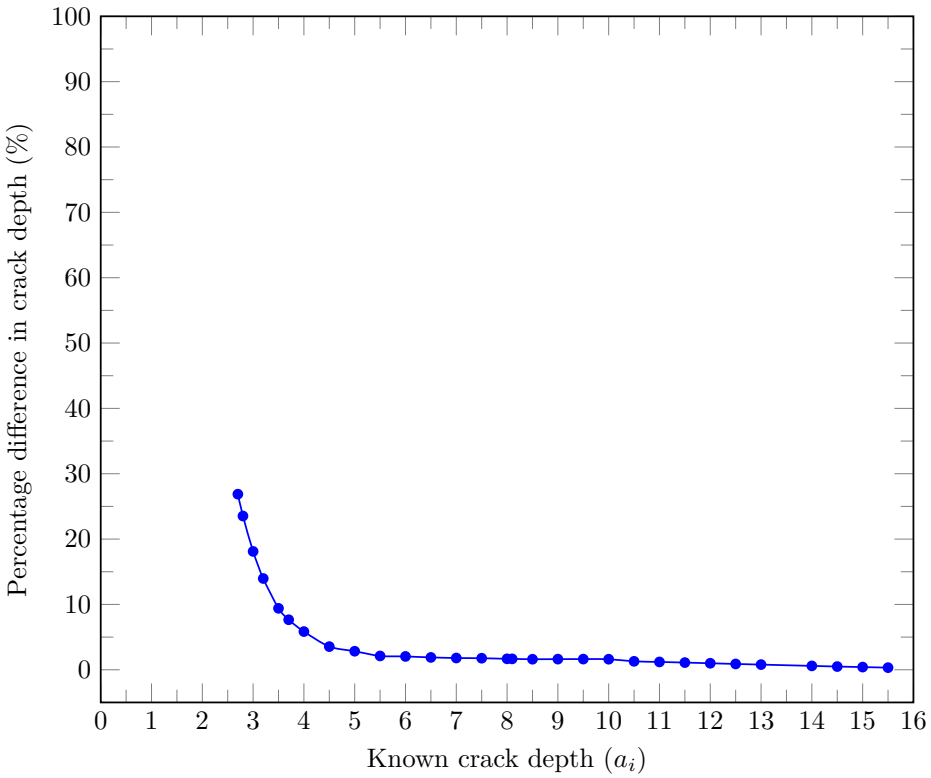

Figure D.5: Percentage difference in calculated crack depth compared to the known crack depth for $0.30 \geq a/W \leq 0.85$. Austenite material properties

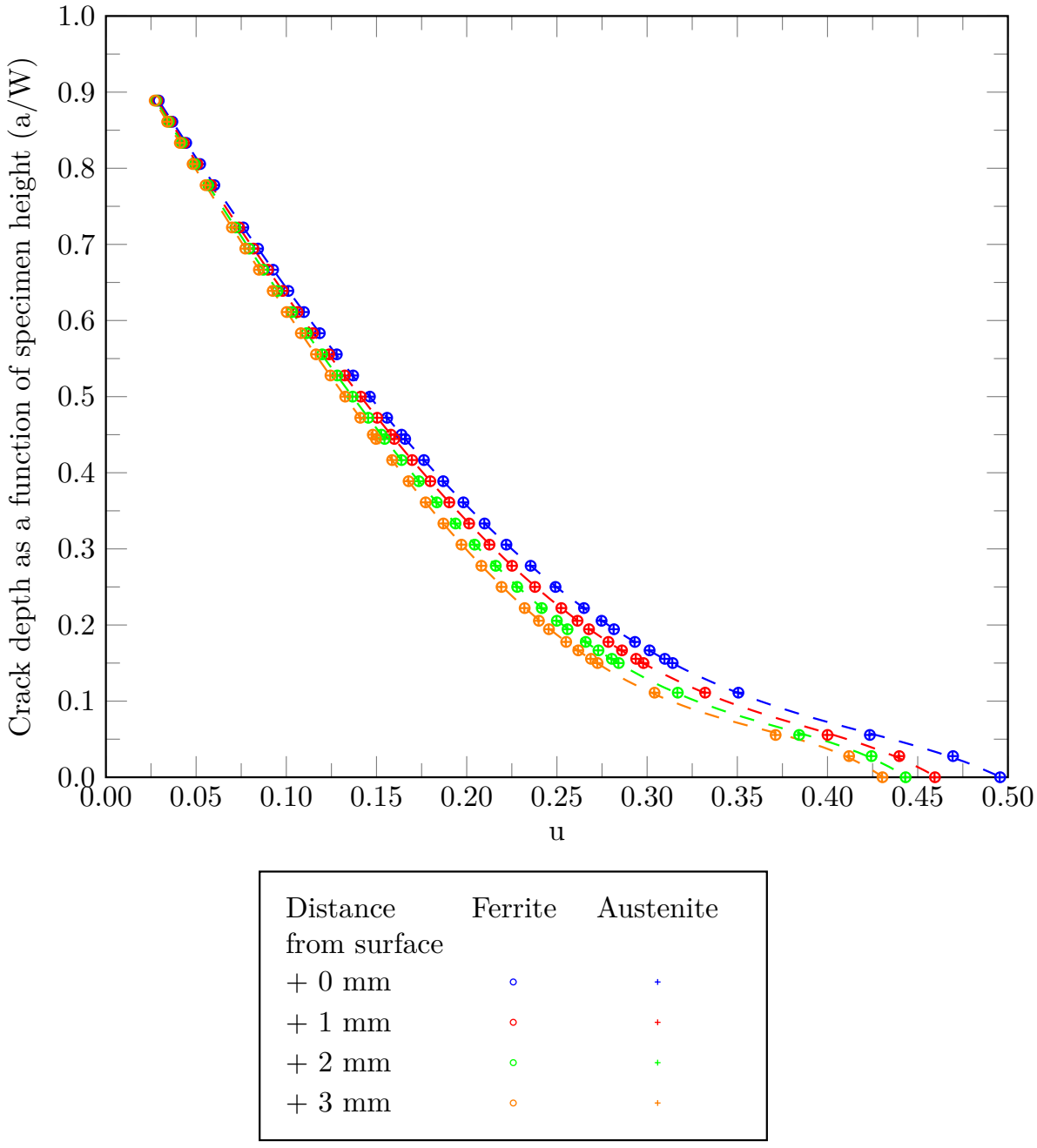

Figure D.6: Comparison of crack mouth opening polynomials using data from both the ferrite and austenite material models.

D.2 Force versus Displacement curves for individual samples

Initial defect size $a/W = 0.45$

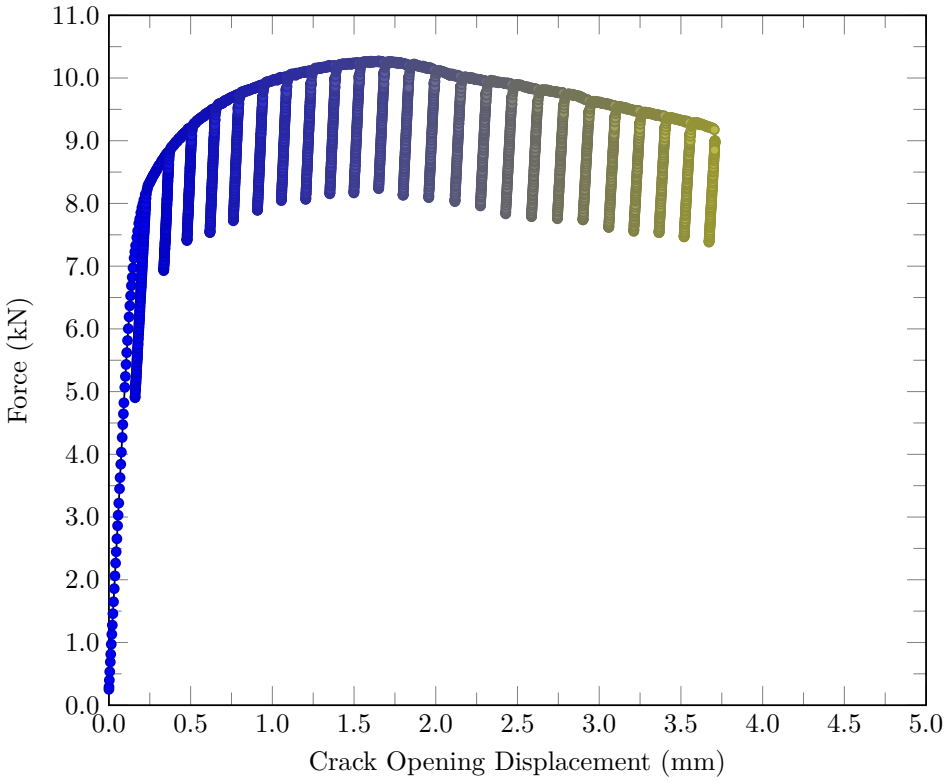

Figure D.7: Force versus displacement for specimen C11

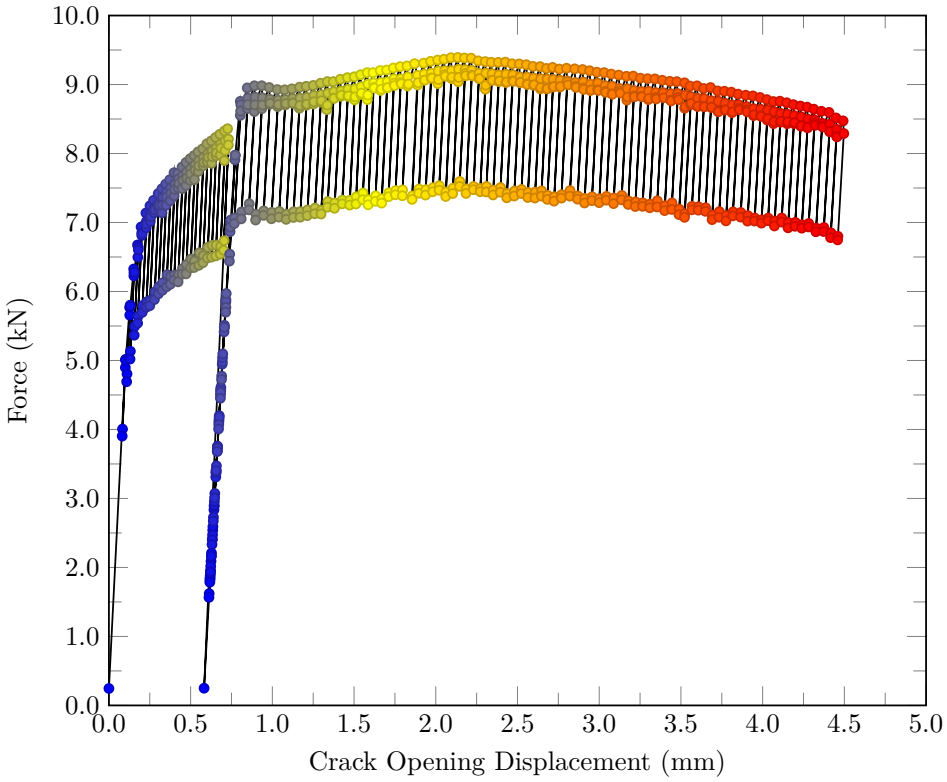

Figure D.8: Force versus displacement for specimen C12

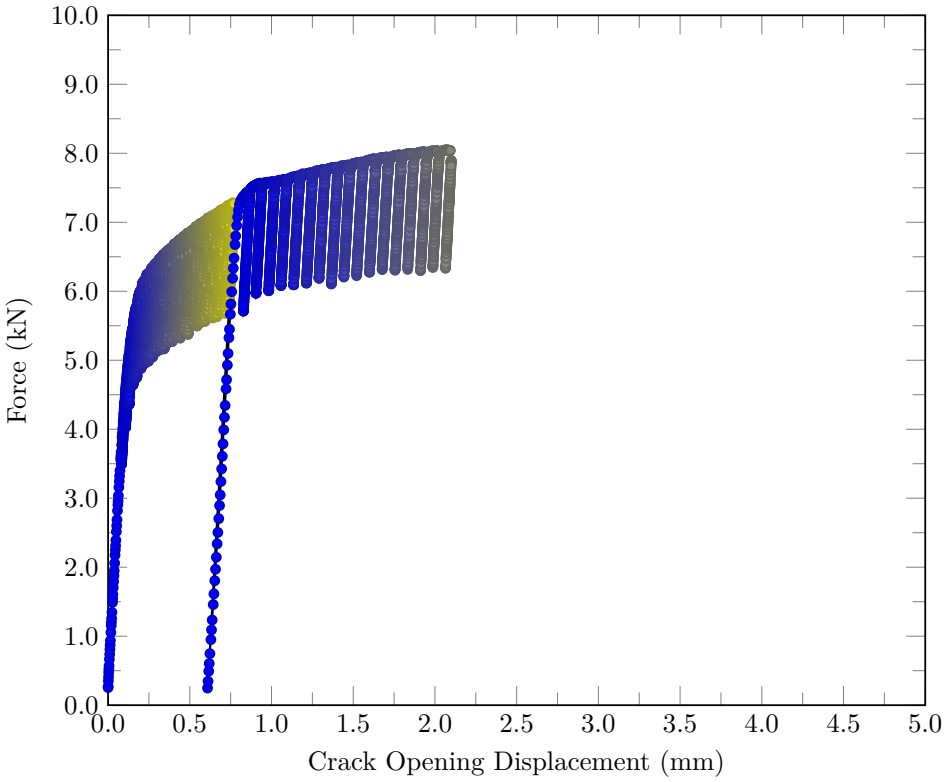

Figure D.9: Force versus displacement for specimen C13

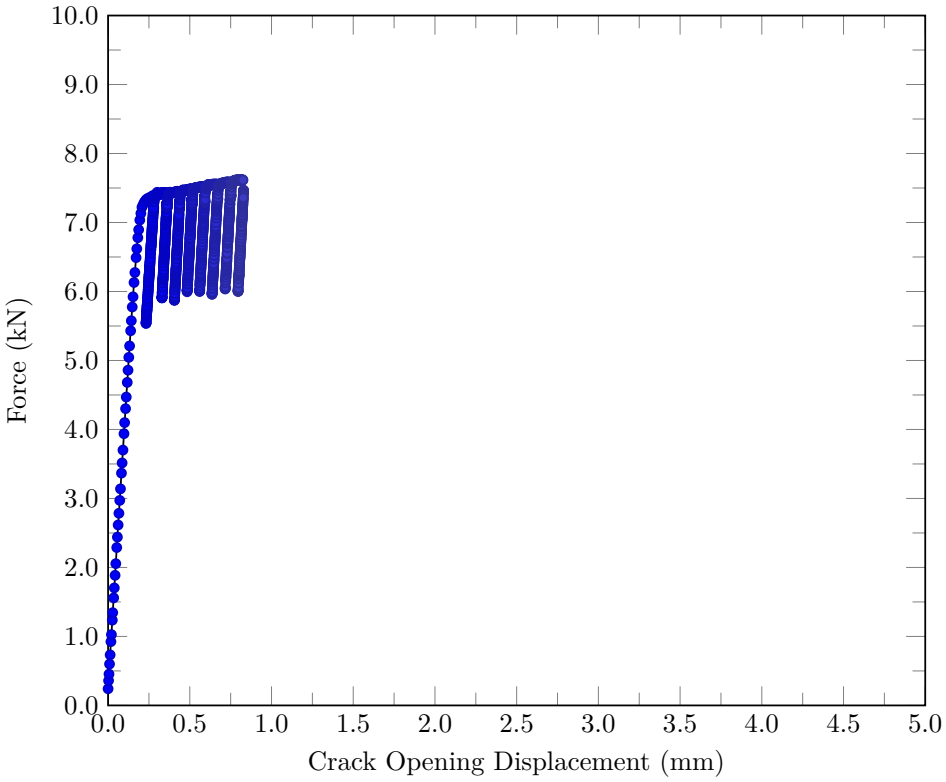

Figure D.10: Force versus displacement for specimen C15

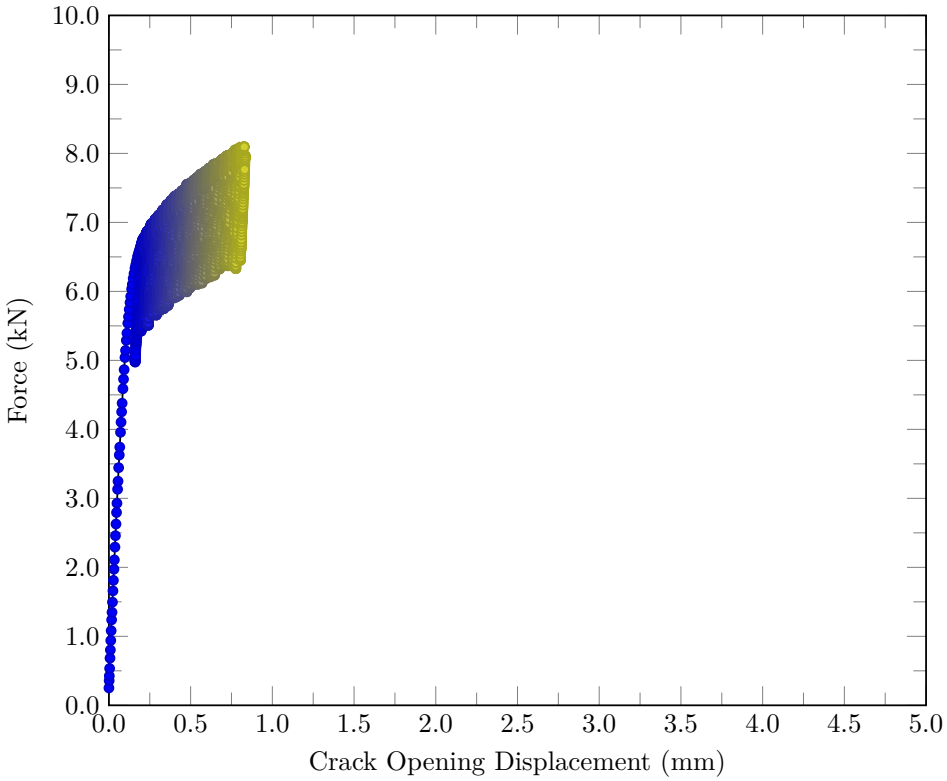

Figure D.11: Force versus displacement for specimen C16

Initial defect size $a/W = 0.30$

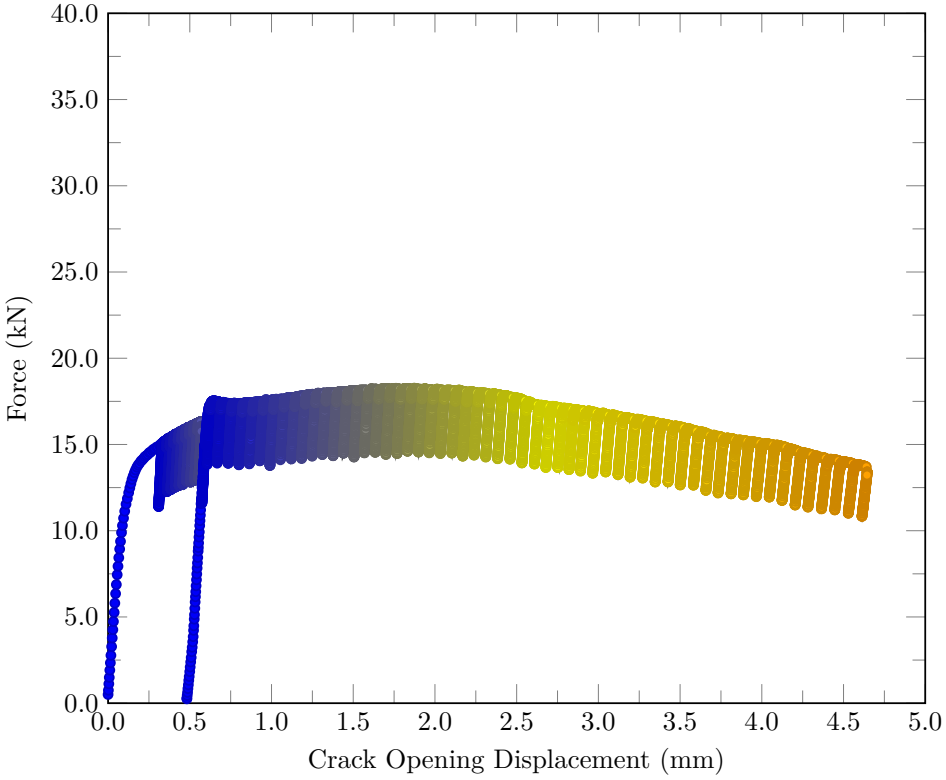

Figure D.12: Force versus displacement for specimen C31

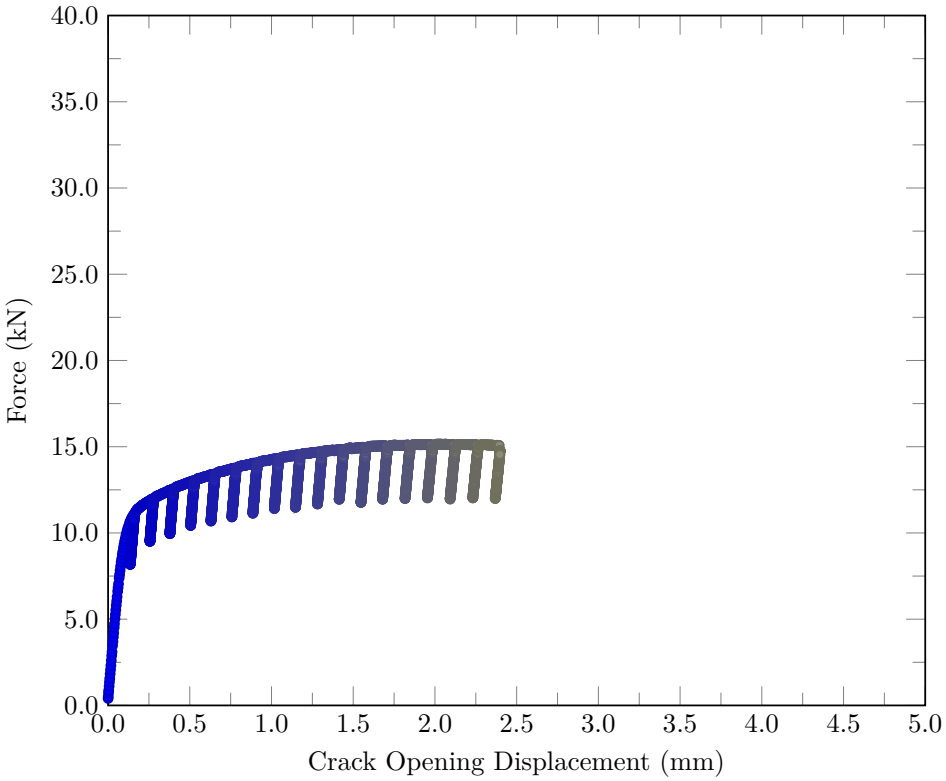

Figure D.13: Force versus displacement for specimen C32

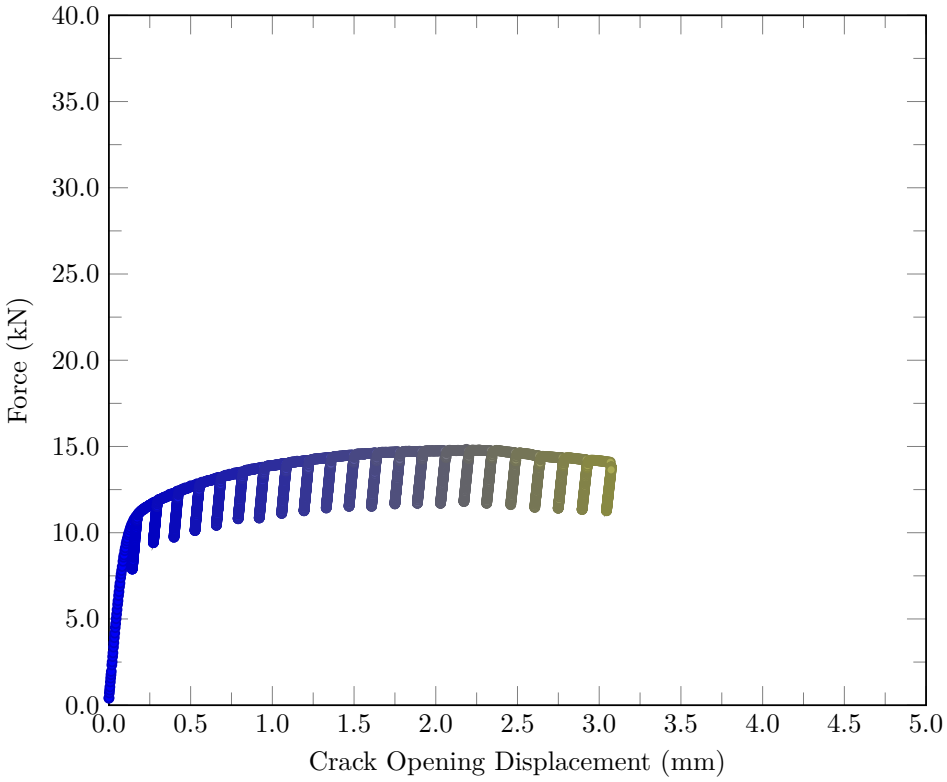

Figure D.14: Force versus displacement for specimen C33

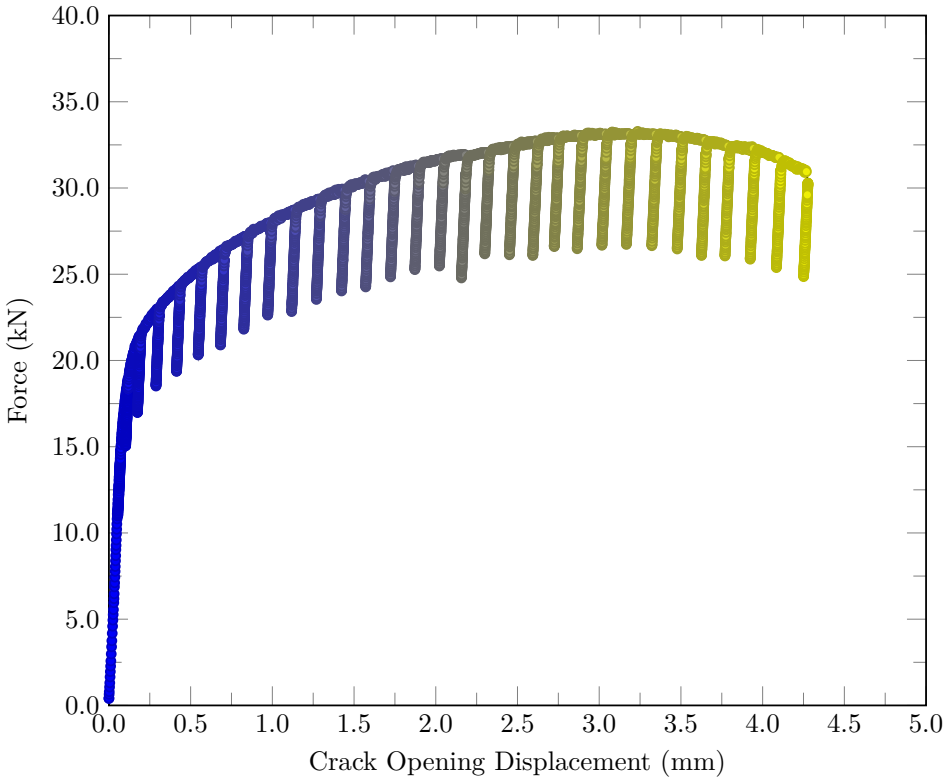

Figure D.15: Force versus displacement for specimen C34

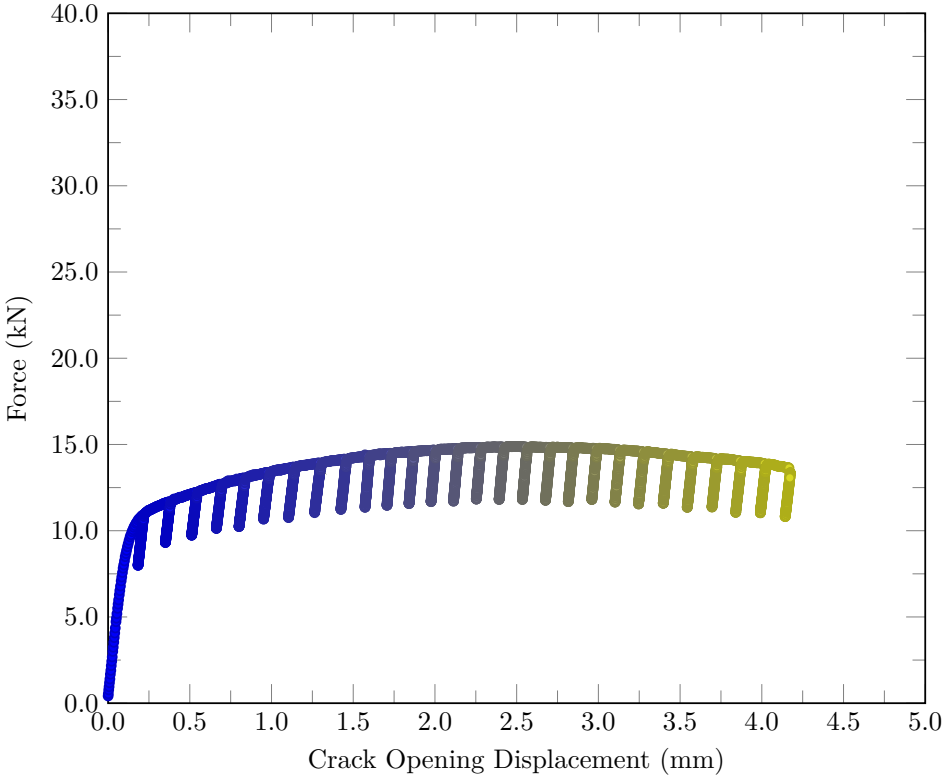

Figure D.16: Force versus displacement for specimen C35

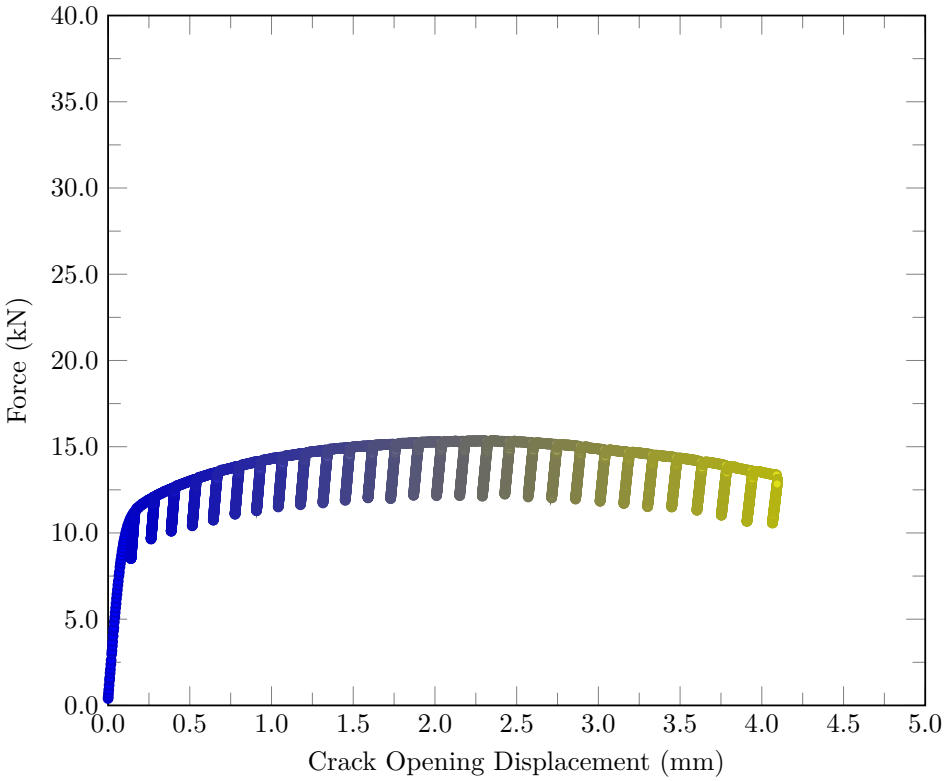

Figure D.17: Force versus displacement for specimen C36

Initial defect size $a/W = 0.15$

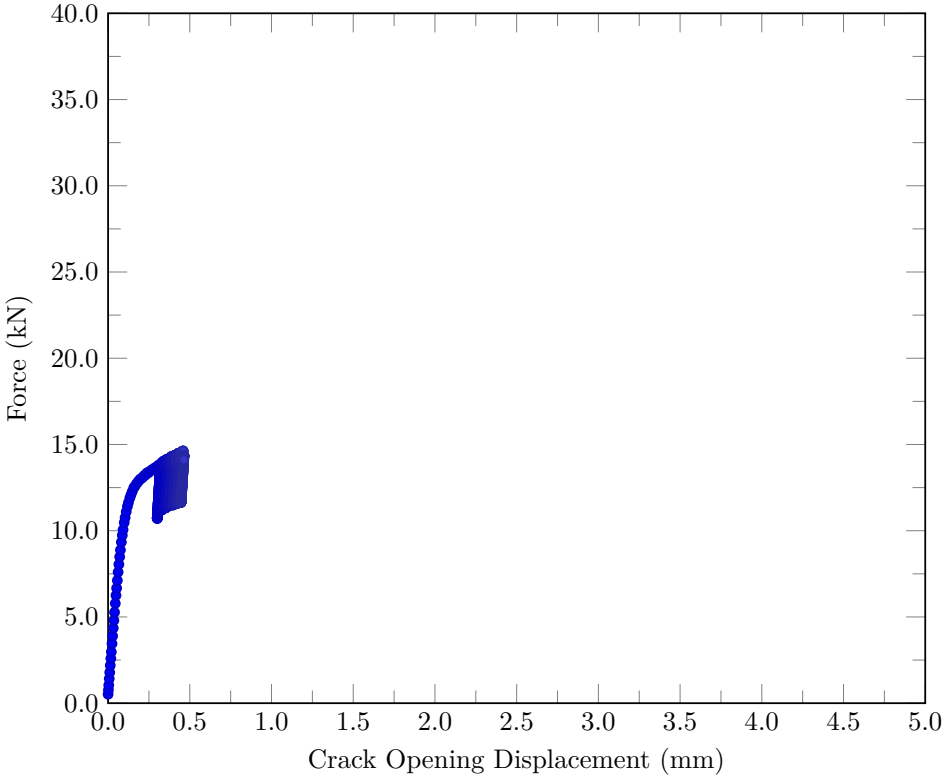

Figure D.18: Force versus displacement for specimen C21

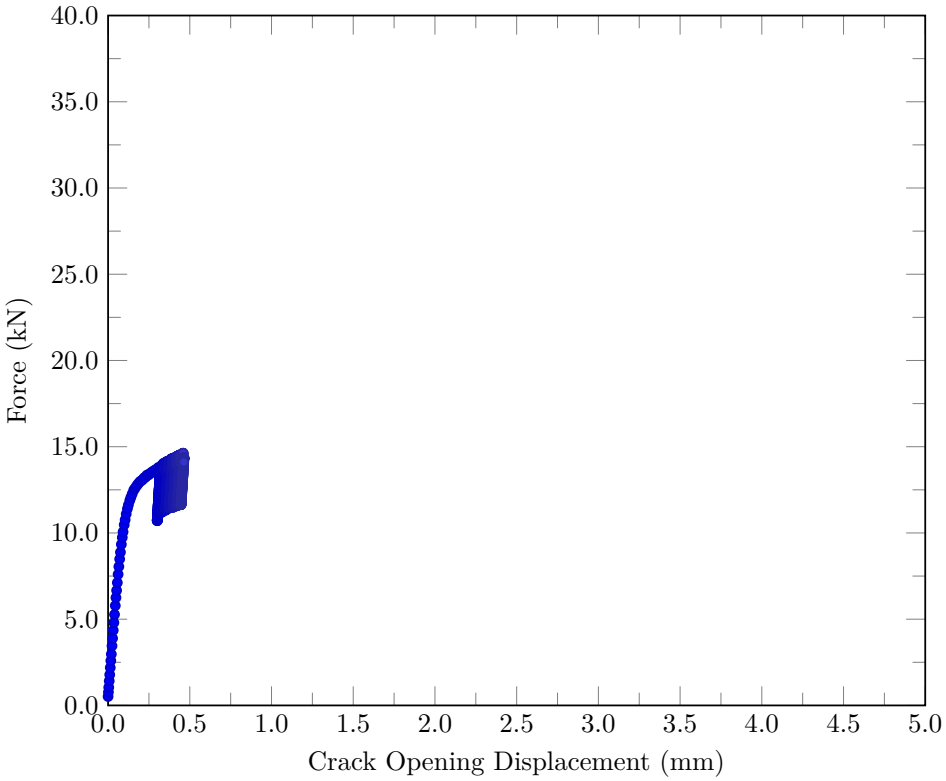

Figure D.19: Force versus displacement for specimen C22

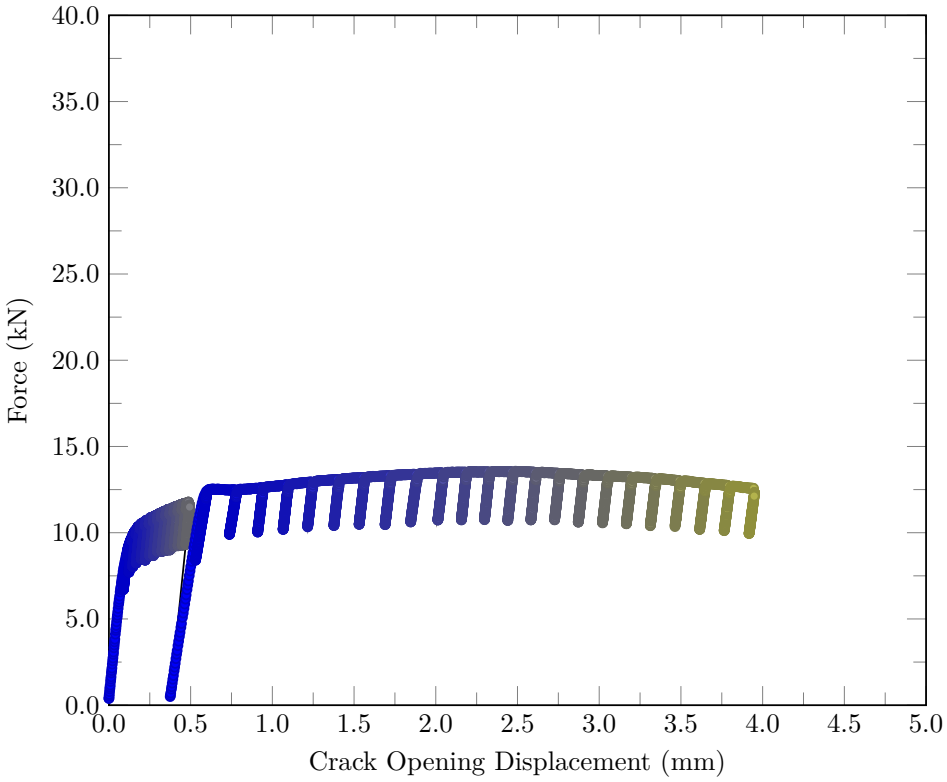

Figure D.20: Force versus displacement for specimen C23

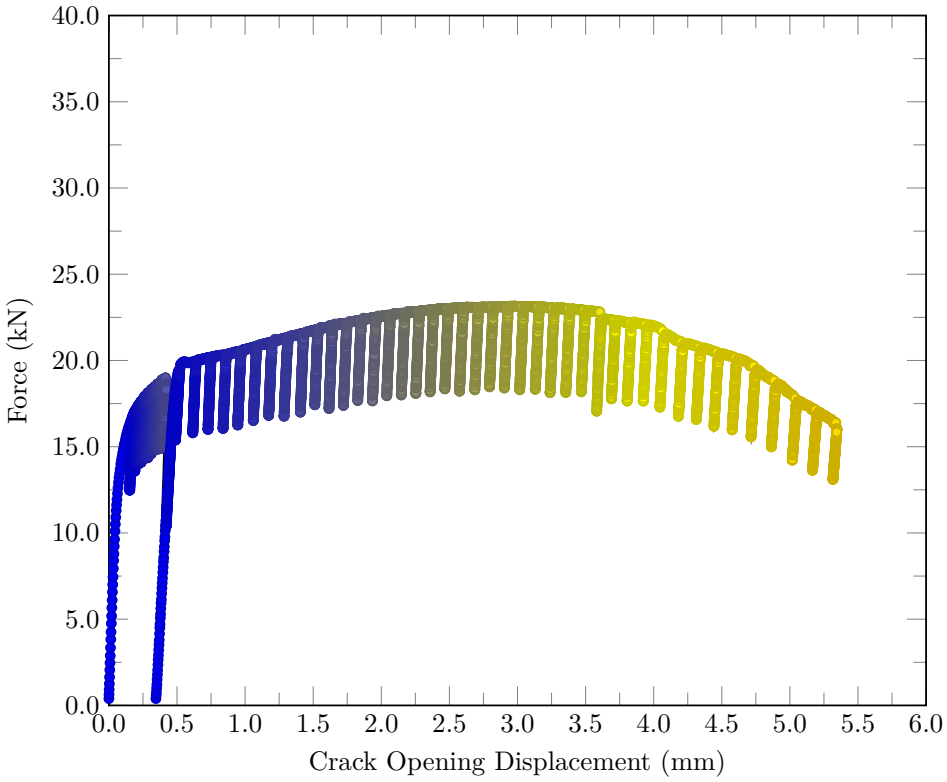

Figure D.21: Force versus displacement for specimen C24

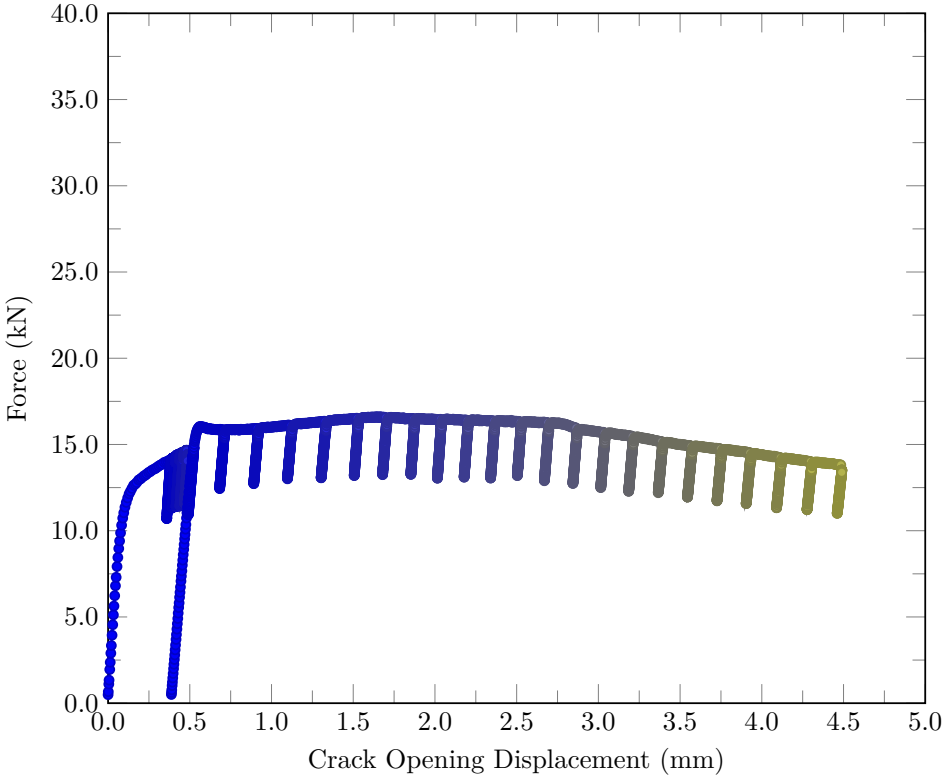

Figure D.22: Force versus displacement for specimen C25

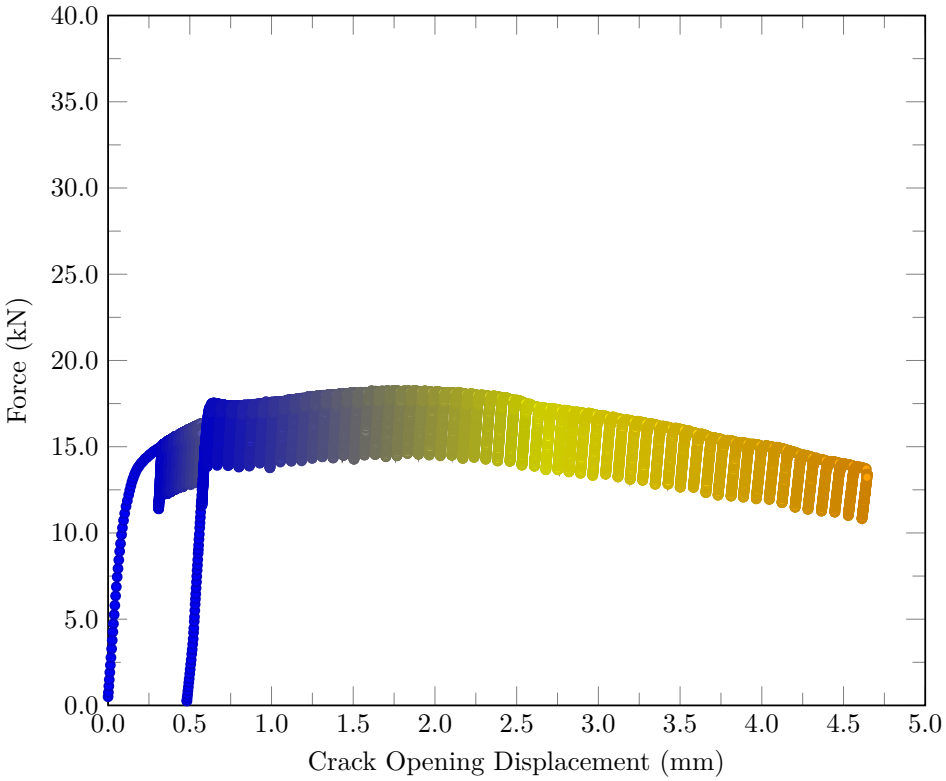

Figure D.23: Force versus displacement for specimen C26

D.3 2D FEA

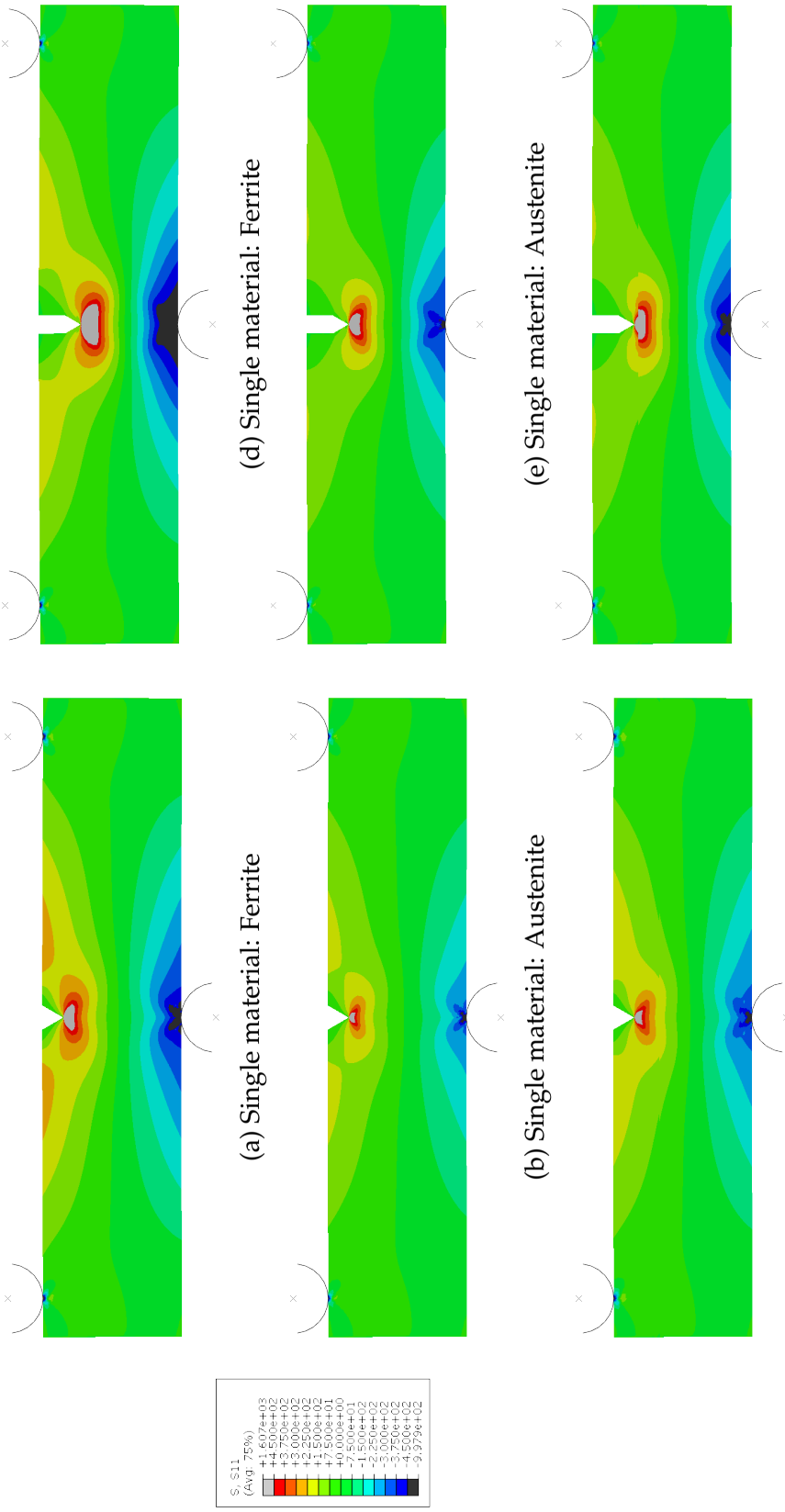

(a) Single material: Ferrite (b) Single material: Austenite (c) Combined ferrite and austenite

(d) Single material: Ferrite (e) Single material: Austenite (f) Combined ferrite and austenite

Figure D.24: Contour plots of plane strain analysis direct stress (σ_{xx}) for $a/W = 0.15$ and $a/W = 0.30$ at displacment $\Delta = 0.150$ mm